Élaboration de nanoparticules adressées pour une thérapie photodynamique anti-cancéreuse activée par rayons X

Batoul Dhaini

Thèse

Une thèse soumise pour l'obtention du titre de
Docteur de l'Université de Lorraine

Ecole Doctoral **SIMPPE**
Science et **I**ngénierie, des **M**olécules, des **P**roduits, des **P**rocédés et de l'**E**nergie

Spécialité : Génie des Procédés et des Produits et des Molécules

Sous la direction de Céline FROCHOT
Présentée et soutenue publiquement le **18 Novembre 2022**

Par:

Batoul DHAINI

Elaboration des nanoparticules adressées pour une thérapie photodynamique anti-cancéreuse activée par rayons X

Membre de jury :

Gilles Lemercier	Professeur, HdR - Université de Reims Champagne-Ardenne	Rapporteur-Président
Véronique Rosilio	Professeur, HdR - Institut Galien Paris-Saclay	Rapporteur
François Lux	Maître de conférences, HdR - Université de Lyon	Examinateur
Anne-Laure Bulin	Chargée de Recherche INSERM – INSERM, Institute for Advanced Biosciences	Examinateur
Joumana Toufaily	Professeur, HdR - Université Libanaise	Examinateur
Joël Daouk	Ingénieur de Recherche CNRS - CNRS, Université de Lorraine	Examinateur
Céline Frochot	DR CNRS, HdR - CNRS, Université de Lorraine	Directeur de thèse
Tayssir Hamieh	Professeur, HdR- Université Libanaise	Co-directeur de thèse
Samir Acherar	Maître de conférences, HdR - Université de Lorraine	Invité

Remerciement

Je remercie Dieu qui nous console et nous donne la force pour pouvoir continuer nos chemins et réaliser nos objectifs.

Je tiens à remercier toutes les personnes qui ont contribuées à réussir ce travail. Ce travail a été réalisé en codirection entre l'Université de Lorraine (LRGP) et l'Université Libanaise (MCEMA).

Je tiens à remercier Monsieur Gilles LEMRCIER et Mme Véronique Rosilio pour avoir accepté d'être les rapporteurs de cette thèse. Je remercie également les membres du jury, Monsieur François LUX, Mme Anne-Laure Bulin, Mme Joumana Toufaily, Monsieur Joël DAOUK, et Monsieur Samir ACHERAR pour avoir fait partie du jury.

Un grand merci à Monsieur Joël DAOUK, Monsieur Hervé SCHOHN et Mme Valérie JOUAN-HUREAUX pour tout le coup de main que vous m'avez donné dans les expériences biologiques et radiologique, j'apprécie beaucoup, et à Mme Muriel BARBERI-HEYOB pour l'accueil qui m'a été réservé lors de mon travail au CRAN.

Je remercie Monsieur Olivier TILLEMENT et Monsieur François LUX et toutes les personnes dans leurs équipes qui ont aidées pour des caractérisations physico-chimiques. Merci aux membres de l'entreprise NHtherAGuIX pour nous fournir l'opportunité d'utiliser les AGuIX.

Je tiens, avant tout, à remercier ma directrice de thèse, Mme Céline FROCHOT, pour son soutien, sa disponibilité et sa confiance en mes capacités, je ne saurais assez exprimer ma gratitude pour les connaissances et l'expérience que vous partagez, sa gentillesse et son tendre cœur qui nous entourait toujours.

Mon directeur de thèse libanais Monsieur Tayssir Hamieh, merci d'avoir cru en mes compétences et l'opportunité que vous m'avez donnée pour que je me situe là où je suis aujourd'hui. Philippe et Samir, merci d'avoir être disponible pour toutes questions, de toujours me tendre la main. Les membres de l'équipe, Mathilde, Francis, Morgane, Laurène merci de me faire sentir que j'appartiens à une famille. Pour tous mes anciens collègues, Albert, Amina et Ludivine avec qui je manque d'emmener et de partager des moments.

Merci à tous mes chers amis, Zahraa, Zeinab, Hoda, Rim, Layla, Ghadir, Danielle, Israa. Merci à ceux qui ont partagé avec moi cette expérience 'Nancéienne', Zahraa, Malak, Sarah, Hanine, Jazia, Rim et un tas de merveilleux amis que j'ai eu la chance de rencontrer à Nancy, merci d'avoir toujours été là pour moi.

Je tiens à exprimer ma reconnaissance infinie à tous mes camarades du laboratoire du LRGP, du LCPM et du CRAN pour les bons moments passés.

Ma plus profonde gratitude, du fond du cœur, est dédiée à toute ma famille, mon père Adnan, ma mère Hanaa, mes frères Jalal, Mohamad et Hadi. Mes belles sœurs et neveux. Pour ma grande famille, tantes, oncles, cousines et cousins. Merci à mon porte-bonheur et joie Mohamad. Merci à vous tous de m'avoir toujours soutenu, de m'avoir écouté et d'avoir pris soin de moi quand dans les plus difficiles moments. Je vous aime plus que ces mots ne peuvent l'exprimer.

Sommaire

Liste des figures

Liste des Tableaux

Abréviations

A	Absorption
AB3	*Anti-cancer drug*
ABDA	*9,10-Anthracenediyl-bis(methylene) dimalonic acid*
ABMDMA	*9,10-Anthracenediyl-bis(methylene)dimalonic acid*
ABS	*Acetate buffer solution*
ACN	Acétonitrile
ADN	Acide désoxyribonucléique
ADPA	*10-dipropionic acid, disodium salt*
ADPA	*Anthracene-9,10-dipropionic acid disodium salt*
AEP	*2-Aminoethyl dihydrogen phosphate*
AFM	*Atomic force microscope*
Ahx	Acide 6-aminohexanoïque
APMA	*3(Aminopropyl)methacrylamide hydrochloride*
APTES	*aminopropyltriethoxysilane*
ATF	*Amino terminal fragment of urokinase plasminogen activator*
AuNPs	Nanoparticules d'or
AVT	*Angiogenic vessel-targeting*
Azo	*Azobenzene*
BBB	*Blood brain barrier*
BFNS	Bifunctional nanosphere
BHE	Barrière hémato-encéphalique
BHQs	*Black hole quenchers*
BP	*Bis-pyrene*
bPEI	*Branched polyethylenimine*
BRET	*Bioluminescence resonance energy transfer*
BSA	*Bovine serum albumin*
BT	Barium–titanate
BTSA	*Bis(trimethylsilyl)acetamide*
C_{18}RB	Hydrocarbonized Rose Bengal
CaB	Cathepsin B
CCM	chromatographie sur couche mince

CD	Cyclodextrine
cDDP	*Cis-diaminedichloroplatine(II)*
Ce	Cérium
Ce6	Chlorine e6
CendR	*C-end Rule*
CI	Conversion interne
CIRC	Centre international de recherche sur le cancer
CIS	Conversion inter-système
CLSM	*Confocal laser scanning microscopy*
CQDs	*Carbon quantum dots*
CR	*Core satellite superstructure*
CR-PDT	PDT induite par Cerenkov
Cs-Na	*Nitroimidazole-modified chitosan*
CTAB	*Cetyltrimethylammoniumbromide*
CTS	Chitosane
Cy3	Cyanine 3
D_2O	Oxyde de Deutérium
DCF	2',7'-Dichlorofluorésceine
DCF-2DA	2',5'(Di-acétate) dichlorofluorésceine
DCFH	Dichlorofluorésceine
DCFH-DA	Dichlorodihydrofluorescéine-diacetate
DCM	Dichlorométhane
DER	*Dose enhanced ratio*
DHR123	Dihydrorhodamine 123
DLS	*Dynamic light scattering*
DMA	9,10-Diméthylanthracène
DMF	N,N-Diméthylformamide
DMSO	Diméthylsulfoxyde
DNA	*Deoxyribonucleic acid*
DO	Densité optique
DOPE	*Dioleoyl L-α-phosphatidylethanolamine*

DOTA	Acide 1,4,7,10-Tétraazacyclododécane-1,4,7,10-tetrayl tétraacétique
DOX	Doxorubicine
DPBF	1,3-diphénylisobenzofuran
DPBS	*Dulbecco's phosphate buffer saline*
EADC	*1-Ethyl-3-(3-dimethylaminopropyl)carbodiimide*
EBR	Efficacité Biologique Relative
EDC	*N-Ethyl-N′-(3-(dimethylamino)propyl)carbodiimide*
EDC.HCl	N,N′-dicyclohexylcarbodiimide
EDCI	Chlorhydrate de N–éthyl–N′–(3diméthylaminopropyl)carbodiimide)
EGF	*Epidermal growth factor*
EPR	*Enhanced permeability effect*
ER	*Endoplasmic reticulum*
EtOH	Ethanol
FA	*Folic acid*
FAM	*Carboxyfluorescein*
FITS	*Fluorescein isothiocyanate*
FRET	*Förster resonance energy transfer*
FT-IR	Spectroscopie infrarouge à transformée de Fourier
GBM	Glioblastoma multiforme
GC	*Gastric cancer*
GG	Guar gum
GNPs	*Gold nanoprisms*
GRDs	*Gadolinium-rose bengal coordination polymer nanodots*
GSH	Glutathione
HA	Acide 6-Bromohexanoïque
HA	*Hyaluronic acid*
HAPPE	*Peptide (i.e. hybrid apamin-p32 polypeptide)*
HAx	*Hexamethylenediamine*
HBTU	Hexafluorophosphate de N,N,N′,N′–tétraméthyl–O–(1H-benzotriazole–1–yl)uranium)

HCPT	*10-Hydroxycamptothecin*
HDL	*High-density lipoproteins*
HIF-1-α	*Hypoxia-inducible factor*
HMSNs	*Hollow mesoporous silica nanoparticles*
HNSCC	*Head and neck squamous cell carcinoma*
HO•	Radical hydroxyle
Hp	Hématoporphyrine
HpD	Hématoporphyrine dérivée
HPLC	Chromatographie liquide à haute performance
HSA	Human serum albumin
HSPC	Hydrogenated soy L-a-phosphatidylcholine
HUVEC	Human umbilical vein endothelial cells
ICG	Indocyanine green
ICRP	Commission internationale de protection radiologique
ICRU	Commission internationale des unités et mesures de rayonnement
IgG	Immunoglobuline G
iPDT	*Interstitial photodynamic therapy*
IR	*Infrared*
IR825	*NIR-absorbing dye*
IDL	Intervalle-Drogue-lumière
IRM	Imagerie par résonance magnétique
KA	Kératose actinique
Ksv	Constante de Stern-Volmer
LCR	Liquide céphalo-rachidien
LD	*Light dose*
LED	*Light-emitting diode*
LIFU	*Low-intensity focused ultrasound*
Ln	Lanthanides
LNP	Luminescent lanthanide nanoparticles
MB	*Methylene blue*
MB2	*Methylene blue derivative*
MC540	Merocyanine 540

MeOH	Méthanol
MF	*Multifunctional*
MIPNPs	Molecularly imprinted polymeric NPs
MMSN	Magnetic mesoporous silica nanoparticle
MNCs	Magnetic nanoclusters
MOF	Metal–organic frameworks
MPD	Mistearoyl-sn-glycero-3-phosphoethanolamine-N[maleimide(polyethylene glycol)-2000]
MPM	Mésothéliome pleural malin
MRI	Magnetic resonance imaging
MS	Mesoporous silica
$mSiO_2$	Mesoporous silica shell
MSNs	Mesoporous silica nanoparticles
MTD	Maximum tolerated dose
*m*THPC	5,10,15,20-Tetrakis(3-hydroxyphenyl)chlorin
MTT	3-(4,5-Dimethylthiazol-2-yl)-2,5-diphenyl tetrazolium
MUCNPs	Multi-shelled upconversion nanoparticles
NCs	Nanocarriers
nd	Not determined
NHS	N-hydroxysuccinimide
NIR	*Near infrared*
NIRF	*Near infrared fluorescence*
NMM	N-méthylmorpholine
NMP	Méthylpyrrolidinone
NMP	Polymérisation médiée par les nitroxydes
NPs	Nanoparticules
NRP-1	Neuropiline-1
O_2	Oxygène moléculaire
$O_2^{-\bullet}$	Anion superoxyde
P	Probabilité
p.i	Post injection

P1	*5-(4-Carboxyphenyl succinimide ester)-10,15,20-triphenyl porphyrin*
PAA	*Polyacrylic acid*
PAH	*Poly(allylamine)*
PAMAM	*Poly(amidoamine)*
PAMAM-G7, P	*Generation poly (amidoamine) dendrimer*
PARN	*Amphiphilic peptide nanocapsules*
PBS	*Phosphate buffer solution*
Pc4	Phthalocyanine 4
PCL	*PEG-block-poly(ε-caprolactone)*
PD-1	*Programmed death-1*
Pdots	*Polymer dots*
PDT	*Photodynamic therapy*
PDTA	*Propylenediaminetetra-acetic acid*
PE	*Phosphoethanolamine*
PEG	Polyéthylène Glycol
PEG-b-PAsp	*Polyethylene glycol-b-poly(aspartic acid)*
PEG-PCL	*Polyethylene glycol-poly (α-caprolactone)*
PEI	*Polyethylene imine*
PE-NH_2	*1,2-Dioleoyl-sn-glycero-phosphoethanolamine-N(hexanoylamine)*
PFH	Perfluorohexane
PFOB	*Oxygen depot perfluorooctyl bromide*
PGA	*Poly(glycolic acid)*
PHLA	*Partially hydrolyzed α-lactalbumin*
PLA	*Poly(lactic acid)*
PLGA	*Poly(lactic-co-glycolic acid)*
PMAO	*Poly(maleic anhydride-alt-1-octadecene))*
PPADT	*Poly-(1,4-phenyleneacetone dimethylenethioketal)*
PpIX	Protoporphyrine IX
PS	Photosensibilisateur
PTT	*Photothermal therapy*
PTX	Paclitaxel

PVA	*Poly(vinyl alcohol)*
PVK	*Poly(N-vinyl carbazole)*
QDs	*Quantum dots*
RB	Rose Bengal
RBD	*Rose bengal ω-carboxyheptyl ester*
RCMI	Radiothérapie conformationnelle par modulation d'intensité
RET	*Resonance energy transfer*
Rhod-TAT	TAT peptide functionalized with rhodamine
RMN	Résonance magnétique nucléaire
ROS	*Reactive oxygen species*
RPMI	*Roswell Park Memorial Institute medium;*
S_0	Etat fondamental singulet
S1	Premier état singulet excité
ScNPs	*Scintillating nanoparticles*
SHG	*Second harmonic generation*
S_n	Etat excité singulet
SOSG	*Singlet Oxygen Sensor Green*
SPION	*Superparamagnetic Iron Oxide Nanoparticles*
SPR	*Surface plasmon resonance*
SSTRs	*Somatostatin receptors*
SWI	*Susceptibility weighted imaging*
T1	Premier état triplet excité
TEM	*Transmission emission microscopy*
TEOS	*Tetraethyl orthosilicate*
Tf	*Transferrin*
TFA	Acide trifluoroacétique
TfR	*Transferrin receptor*
TGM2	Transglutaminase
tHPP	*5,10,15,20-Tetrakis(4-hydroxyphenyl)-21H,23H-porphine*
TiO_2	Oxyde de Titanium
TIPS	Triisopropylsilane
TMP–OH	*2,2,6,6-Tetramethyl-4-piperidinol*

TNBC	*Ttriple negative breast cancer*
TOPO	*Trioctylphosphine oxide*
TPA	*Two-photon activation*
TPC	*Triphenyl-chlorin*
TPC PS	*(5-(4-Carboxyphenyl)-10, 15,20-tris(3-hydroxyphenyl)chlorin)*
TPGS-PLA NPs	*D-α-Tocopheryl polyethylene glycol 1000 succinate-poly(lactic acid) NPs*
TPP	*5-(4-Carboxyphenyl)-10,15,20 triphenylporphyrin*
TTB	*Matrix encapsulating a fluorogen*
TCSPC	*Time Correlated Single Photon Counting*
TUNEL	*Terminal deoxynucleotidyl transferase dUTP nick end labeling*
UCL	*Upconversion luminescence*
UCNP	*Upconversion nanoparticle*
UPA	*Urokinase plasminogen activator*
US	*Ultrasound*
USPIO	*Ultrasmall superparamagnetic iron oxide*
UV	Ultraviolet
VEGF	*Vascular Endothelial Growth Factor*
VEGFR	*vascular endothelial growth factor receptor*
VTP	*Vascular Targeted Photodynamic therapy*
WEN	*White emitting $NaYF_4$*
XLNPs	*X-Ray-luminescent nanoparticles*
X-PDT	Thérapie photodynamique induite par rayons X
ZIF-90	*Zeolitic imidazolate framework-90*
Zn3PyP1	*Zinc(II) 5-(4-carboxyphenyl)-10,15,20-(tri-N-methyl-4-pyridyl) porphyrin trichloride.*
ZnPc	*Zinc phthalocyanine*
ZnPc-COOH	*Zinc β-carboxyphthalocyanine*
ε	Coefficient d'extinction molaire
λ	Longueur d'onde
ν	Fréquence
τ	Durée de vie

τf	Durée de vie de fluorescence
τΔ	Durée de vie de l'oxygène singulet
Φf	Rendement quantique de fluorescence
ΦΔ	Rendement quantique de production d'oxygène singulet
18F-FDG	18F-fluorodeoxyglucose
$^1O_2$	Oxygène singulet
$^3O_2$	Oxtgène triplet
5-ALA	Acide 5-aminolévulinique
5FU	*5-Fluorouracil*
68Ga-BSA	*Ga-68 labeled bovine serum albumin*

Résumé

Les thérapies anticancéreuses (radiothérapie, chimiothérapie, etc.), bien que très performantes, présentent des effets secondaires. Aujourd'hui, la thérapie photodynamique (PDT) représente une véritable option dans le monde de la thérapie contre le cancer. Sous action de la lumière, une molécule photo-activable nommée photosensibilisateur va pouvoir transférer son énergie à l'oxygène environnant pour induire la formation d'espèces réactives de l'oxygène, capables de détruire les cellules cancéreuses. Le traitement par PDT de certaines tumeurs primaires et métastatiques a montré des résultats très encourageants. Les limitations de la PDT sont la faible pénétration de la lumière dans les tissus et le manque de sélectivité de la plupart des photosensibilisateurs actuellement utilisés en clinique.

Une approche relativement nouvelle, appelée X-PDT, consiste à utiliser des rayons X au lieu de la lumière UV-visible pour surmonter la faible profondeur de pénétration de la lumière visible dans les tissus. Lors de l'exposition aux rayons X ionisants, les nanoscintillateurs transfèrent leur énergie aux PS, qui sont alors activés et peuvent engendrer une action PDT. Dans cette thèse, nous avons développé des nanoscintillateurs à base de nanoparticules AGuIX contenant des chélates de Gadolinium ou de Terbium. Le Rose Bengale (RB) a été couplé de façon covalente aux AGuIX. Pour cibler spécifiquement NRP-1, récepteur membranaire surexprimé sur les cellules endothéliales, un peptide a également été couplé (DKPPR ou autre séquence).

L'étude photophysique de ces nouvelles nanoparticules nous a permis de confirmer qu'il existe un transfert d'énergie entre le lanthanide chélaté et le Rose Bengal sous illumination ou excitation par rayons X. Nous avons montré que le Rose Bengale produit de l'oxygène singulet capable de détruire les cellules cancéreuses. Le peptide, même couplé aux nanoparticules, conserve sa capacité à cibler NRP-1.

Abstract

Cancer therapies (radiotherapy, chemotherapy, etc.), although very effective, have side effects. Today, photodynamic therapy (PDT) represents a real option in the world of cancer therapy. Under the action of light, a photo-activatable molecule called a photosensitizer is able to transfer its energy to the surrounding oxygen to induce the formation of reactive oxygen species capable of destroying cancer cells. PDT treatment of some primary and metastatic tumors has shown very encouraging results. The limitations of PDT are the low penetration of light into the tissues and the lack of selectivity of most photosensitizers currently used in the clinic.

A relatively new approach, called X-PDT, is to use X-rays instead of UV-visible light to overcome the shallow penetration depth of visible light into tissue. Upon exposure to ionizing X-rays, nanoscintillators transfer their energy to PSs, which are then activated and can initiate PDT action. In this thesis, we have developed nanoscintillators based on AGuIX nanoparticles containing Gadolinium or Terbium chelates. Rose Bengal (RB) was covalently coupled to AGuIX. To specifically target NRP-1, a membrane receptor overexpressed on endothelial cells, a peptide was also coupled (DKPPR or another sequence).

The photophysical study of these new nanoparticles allowed us to confirm that there is an energy transfer between the chelated lanthanide and the Rose Bengal under illumination or excitation by X-rays. We have shown that the Rose Bengal produces oxygen singlet capable of destroying cancer cells. The peptide, even coupled to the nanoparticles, retains its ability to target NRP-1.

Introduction générale

Introduction générale

L'une des tumeurs les plus sévères est le glioblastome. C'est une tumeur cérébrale maligne. Les traitements traditionnels tels la chirurgie, la chimiothérapie et la radiothérapie ne montrent pas une efficacité suffisante pour soigner le glioblastome.

La thérapie photodynamique (PDT) anti-cancéreuse semble être un excellent candidat pour traiter le glioblastome et d'autres types de cancer. La PDT consiste à injecter une molécule photoactivable nommée photosensibilisateur (PS) par voie intraveineuse, puis à l'exciter dans la zone de la tumeur après un intervalle de temps appelé « intervalle drogue–lumière ». Cette excitation conduit à la production d'espèces réactives de l'oxygène (ROS) dont l'oxygène singulet $^1O_2$.

La PDT présente plusieurs avantages par rapport à d'autres types de traitement comme le non toxicité des PS dans le noir, pas de résistance au traitement, peu d'effets secondaires. En revanche, la PDT rencontre plusieurs obstacles : le manque de sélectivité des PS, la limitation de la pénétration de la lumière dans les tissus profonds et le manque d'oxygénation.

Dans cette thèse, nous nous intéressons à développer des nanoparticules (NPs) excitables par rayon-X. Les rayons X ont la capacité de pénétrer profondément dans les tissus. De plus, les NPs ont la capacité de cibler les tumeurs d'une manière passive grâce à l'effet EPR (*Enhanced Permeability Effect*). Les NPs envisagées sont des AGuIX, développées par la société NH TherAguix et actuellement en phase 2 pour le traitement par radiothérapie de métastases cérébrales. Un autre type de ciblage est visé dans cette thèse, c'est le ciblage actif. L'une des formes de ciblage actif est l'utilisation de peptides pour cibler des récepteurs surexprimés sur les membranes des cellules cancéreuses ou des néovaisseaux.

Dans le premier chapitre, nous décrivons l'historique du cancer, les différents types de traitements utilisés, la PDT et ses limitations, les caractéristiques des lanthanides. Dans les sous chapitre I, II et III nous décrivons comment il est possible d'utiliser les rayons Cerenkov en PDT, l'intérêt de coupler des peptides sur les NPs pour un ciblage actif et l'avantage d'utiliser le Rose Bengal (RB), couplé aux NPs.

Dans le deuxième chapitre, nous étudions le transfert d'énergie entre différents donneurs lanthanide (Terbium et Gadolinium) et le RB comme PS accepteur après excitation lumineuse au rayon X. Le terbium et le Gadolinium sont soit libres en solution, soit chélatés dans les AGuIX.

Dans le troisième chapitre, nous étudions le transfert d'énergie entre Tb/Gd, AGuIX Gd et AGuIX Tb et le Photofrin. Nous étudions également le transfert d'énergie entre les AGuIX couplé au fluorophore cyanine 5,5 et le Photofrin.

Nous présentons dans le quatrième et le cinquième chapitre le couplage covalent entre PS et les AGuIX. Dans le quatrième chapitre, nous présentons les résultats de la PDT induite par rayons X (X-PDT) avec des AGuIX Tb@ porphyrine tétraphényl monocarboxylique (P1).

Dans le dernier chapitre, nous décrivons le couplage covalent des AGuIX Tb et AGuIX Gd avec le RB, soit directement, soit *via* un bras espaceur. Nous couplons alors les peptides DKPPR et XXXXX.

Ce travail a été réalisé grâce à plusieurs collaborations :

- Les AGuIX sont fournies par l'entreprise NHtherAGuIX et l'équipe d'Olivier Tillement et François Lux du laboratoire ILM, UMR 5306 CNRS-Universté de Lyon, synthétisées par Paul Rocchi.
- Les mesures TDA-MS des AGuIX sont faites par l'équipe d'Olivier Tillement et François Lux à l'ILM, par Agnès Hagege.
- La synthèse des peptides est faite en collaboration avec le laboratoire LCPM, UMR 7375 à Nancy, Samir Acherar et Mathilde Achard.
- Les irradiations X et les tests biologiques sont faits avec l'équipe de Muriel Barberi-Heyob au CRAN, UMR 7039 à Nancy, Joël Daouk, Hervé Schohn et Valérie Jouan-Hureaux.

Chapitre I : Bibliographie

I. Cancer

I.1 Statistiques

Quelle que soit la situation économique et sociale des pays, le cancer reste la principale source de mortalité dans le monde. D'après les statistiques publiées par le centre international de recherche sur le cancer (CIRC) dans 185 pays des différents continents [1], 19 292 789 nouveaux cas ont été diagnostiqués en 2020 et 9 958 133 personnes sont décédées. Ces statistiques toujours effrayantes concernent tous les âges et les deux sexes.

La distribution de ces données montre que 23,4 % des cas de cancer sont dans le continent européen, 48,4 % en Asie, 13,2 % en Amérique du Nord, 7,8 % en Amérique latine, 5,8 % en Afrique et 1,4 % en Océanie. Les grands pourcentages en Asie et l'Afrique peuvent être dus au manque de soins sanitaires et un manque d'équipements nécessaires à diagnostiquer et traiter le cancer [1].

La **Figure 1** montre la distribution des nouveaux cas de cancer et des morts, selon le type de cancer, en 2020.

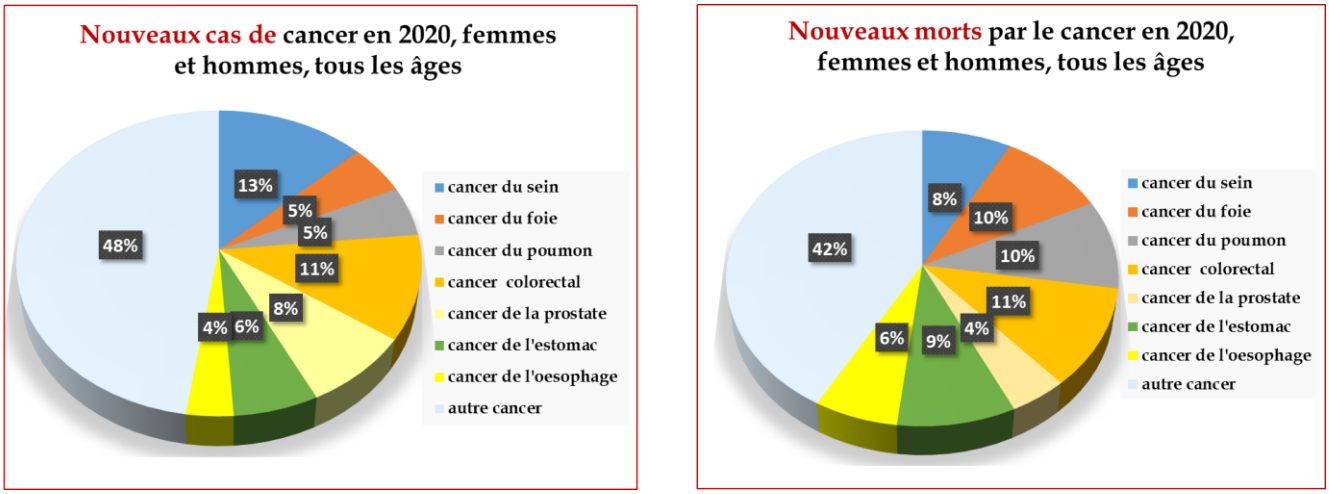

Figure 1 : Statistique sur le nombre des nouveaux cas et de morts causés par les différents types de cancer. Adapté du site officiel du centre international de recherche sur le cancer (CIRC).

I.2 Définition

Le cancer est une maladie qui cause une prolifération incontrôlée des cellules, qui est l'unité vitale du corps humain. Chaque cellule joue un rôle spécifique et sa durée de vie est limitée. Les cellules vieillissent constamment, meurent et se font remplacer par d'autres. Pour des raisons encore inconnues, il est possible que certaines cellules changent et continuent de se multiplier plutôt que de disparaître naturellement. Ces vieilles cellules se propagent, produisant des mutations qui affectent leur division normale [2]. La propagation incontrôlée de ces cellules empêche le système immunitaire de se défendre. Ainsi, elles s'accumulent et forment la tumeur. Plusieurs paramètres sont à la source de ces mutations : la génétique, le type d'alimentation, les rayonnements ionisants, l'environnement pollué, et certains produits chimiques [3, 4].

Le cancer est classé, selon les scientifiques, comme une maladie génétique qui a une identité distincte par rapport à la plupart des autres maladies génétiques. En général, les maladies génétiques héréditaires sont causées par des altérations génétiques, appelées mutations au

niveau des cellules germinales (sperme, ovules). Cependant, le cancer, principalement, est causé par des mutations somatiques et non germinales [5, 6], sachant que le corps d'un organisme multicellulaire est formé de cellules somatiques.

I.3 Type des cancers

I.3.1 Catégories des cancers selon leur aspect

Il existe deux grandes catégories de cancers classées selon leur aspect :

- Les cancers solides qui se développent dans tout type de tissus, sachant que 90 % des cancers humains sont des cancers solides,
- Les cancers liquides ou sanguins,

I.3.2 Catégorie des cancers selon leur stade

Il existe trois types de tumeurs selon leur stade :

- Tumeurs bénignes qui sont des tumeurs non cancéreuses qui se développent lentement et restent localisées. Une fois traitées, ces tumeurs ne se propagent pas [7].
- Tumeurs malignes qui sont des tumeurs cancéreuses. Elles se développent plus rapidement que les tumeurs bénignes et ont tendance à envahir d'autres zones que celles où elles sont apparues au départ. Elles peuvent développer alors de nouvelles tumeurs appelées métastases [8].
- Tumeurs « atypiques » ou « évolutives » qui sont des tumeurs intermédiaires dites bénignes au début, qui peuvent se transformer en cancer dans un laps de temps variable [9].

I.3.3 Catégorie des cancers selon leur genre

Le cancer est un nom générique qui regroupe plusieurs genres en fonction de la position de la tumeur au sein du corps :

- La *leucémie* est un cancer qui se développe dans la moelle osseuse à partir de cellules qui produisent habituellement des globules blancs [10],
- Les *lymphomes* sont des tumeurs malignes qui apparaissent surtout dans les ganglions et les vaisseaux lymphatiques [11],
- Les *sarcomes* sont des tumeurs malignes formées à partir des tissus de soutien du corps, qui sont essentiellement des muscles et des os [12],
- Les *adénocarcinomes* ont des récepteurs du facteur de croissance HER2, mais aucun récepteur œstrogénique et/ou progestérone (RE- et/ou RP- et HER2+) [13]. Ce sont des facteurs de croissance épidermique humaine cancérigènes, c'est-à-dire des récepteurs du facteur de croissance épidermique humain,
- Les *carcinomes* proviennent de l'épithélium, c'est-à-dire du tissu intérieur ou extérieur de certains organes (poumon, sein, peau, côlon, prostate...) [14].

Le cancer humain malin solide commence par la formation d'une tumeur qui ensuite se propage jusqu'à l'angiogenèse et les métastases [15].

Angiogenèse : Les cellules humaines ont besoin d'un apport permanent d'aliments et d'oxygène par la circulation sanguine. Le sang véhicule l'oxygène des poumons vers les cellules et transporte les nutriments de l'intestin vers les cellules. D'autre part, les cellules génèrent des déchets toxiques qui sont emportés par la circulation sanguine, filtrés par les reins puis éliminés dans l'urine. Les cellules doivent être suffisamment rapprochées des vaisseaux sanguins pour être servies par la circulation sanguine, le réseau vasculaire est donc très développé pour nourrir toutes les cellules du corps humain [16, 17]. À mesure que les tissus se développent et que leur épaisseur et leur taille augmentent, les cellules nouvellement formées s'éloignent progressivement des vaisseaux sanguins. Pour que les cellules continuent à se développer normalement, des nouveaux vaisseaux sanguins se forment par des cellules endothéliales. Ce processus physiologique est appelé « l'angiogenèse ». Dans la situation sanitaire normale, l'angiogenèse prend place. La prolifération cellulaire tumorale est anormale et donc la croissance tumorale n'est pas accompagnée d'angiogenèse. Cependant, les tissus tumoraux ont une carence en oxygène et les éléments nutritifs génèrent des signaux angiogèniques tel que le VEGF (*Vascular Endothelial Growth Factor* : facteur de croissance de l'endothélium vasculaire) qui stimulent l'angiogenèse et permet ainsi une vascularisation de la zone tumorale **(Figure 2)**.

Métastase : Chez les patients atteints de cancer, les métastases sont la principale cause de mortalité. Ce sont des tumeurs indépendantes générées par des cellules cancéreuses malignes migratrices (tumeur primitive) qui ont tendance à se détacher de la tumeur primaire [18]. Pour que les métastases se produisent efficacement, elles doivent surmonter plusieurs obstacles. Les cellules cancéreuses en circulation échappent aux résistances immunitaires et pénètrent dans les tissus et les organes distants, elles persistent en tant que graines dormantes de départ de tumeur et finalement s'emparent de l'organe hôte et le remplacent. Les métastases se produisent principalement dans les poumons, le foie, les os et le cerveau [19-22].

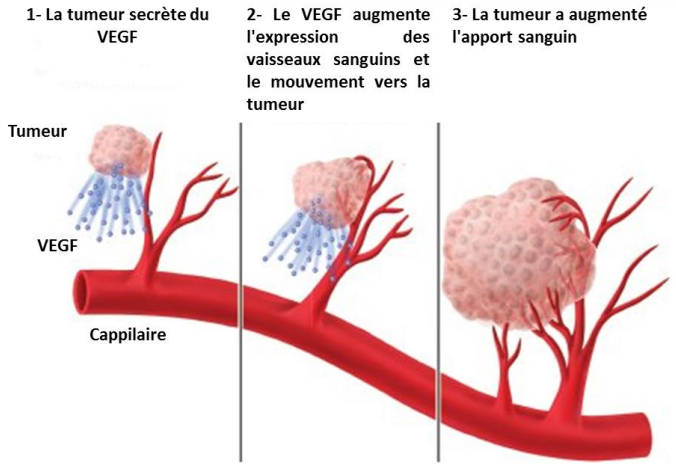

Figure 2 : Processus d'angiogenèse tumorale. [23]

La propagation des tumeurs se fait par plusieurs voies : par *extinction directe* [24] si le cancer primitif se répand dans les tissus voisins, par *dissémination à travers le système lymphatique* [25], par *dissémination par la circulation sanguine* [26], lorsque les cancers détachés circulent dans le sang vers d'autres organes.

Le cancer du cerveau reste un cancer des plus agressifs et compliqué à traiter.

II. Cancer du cerveau

II.1 Constituant du cerveau

Le cerveau est constitué de plusieurs zones qui sont protégées par plusieurs barrières. La première barrière est l'os du crâne qui le protège des chocs, puis trois membranes appelées les «méninges » qui enveloppent le cerveau et la moelle épinière pour les protéger des blessures et des infections. Il est aussi protégé du déséquilibre grâce au liquide céphalo-rachidien (LCR) qui assure une pression constante. Ce liquide joue le rôle d'isolant et d'amortisseur présent à l'intérieur du crâne et le long de la colonne vertébrale [27, 28].

Chaque zone du cerveau a un rôle précis et gère des activités spécifiques **(Figure 3)** :

- Les hémisphères cérébraux

Ceux sont les parties les plus volumineuses du cerveau constituées de deux hémisphères : droit et gauche. Ces deux cerveaux droit et gauche contrôlent les fonction mentales supérieures, les mouvements volontaires, les pensées, l'apprentissage, etc ..[29].

- Le tronc cérébral

Le tronc cérébral établit un lien entre les hémisphères cérébraux et la moelle épinière. Il contrôle également la mobilité et les fonctions vitales du corps : rythme cardiaque, respiration, pression artérielle des yeux, mouvements du visage et déglutition [30].

- Le cervelet

Le cervelet est localisé derrière le tronc cérébral, en-dessous des lobes occipitaux. Cela permet d'avoir des réflexes, de coordonner les mouvements et de garder l'équilibre [31].

- L'hypophyse et l'hypothalamus

L'hypophyse ainsi que l'hypothalamus sont des structures nerveuses situées à la base du cerveau, au centre du crâne. L'hypophyse a un rôle principal dans la production hormonale (croissance, production de lait maternel, puberté, fertilité) [32]. L'hypothalamus, qui se trouve légèrement au-dessus de l'hypophyse, est en contact avec toutes les autres parties du cerveau. Il règle les sentiments de faim et de soif, la température corporelle, le sommeil, la sexualité et le rythme cardiaque.

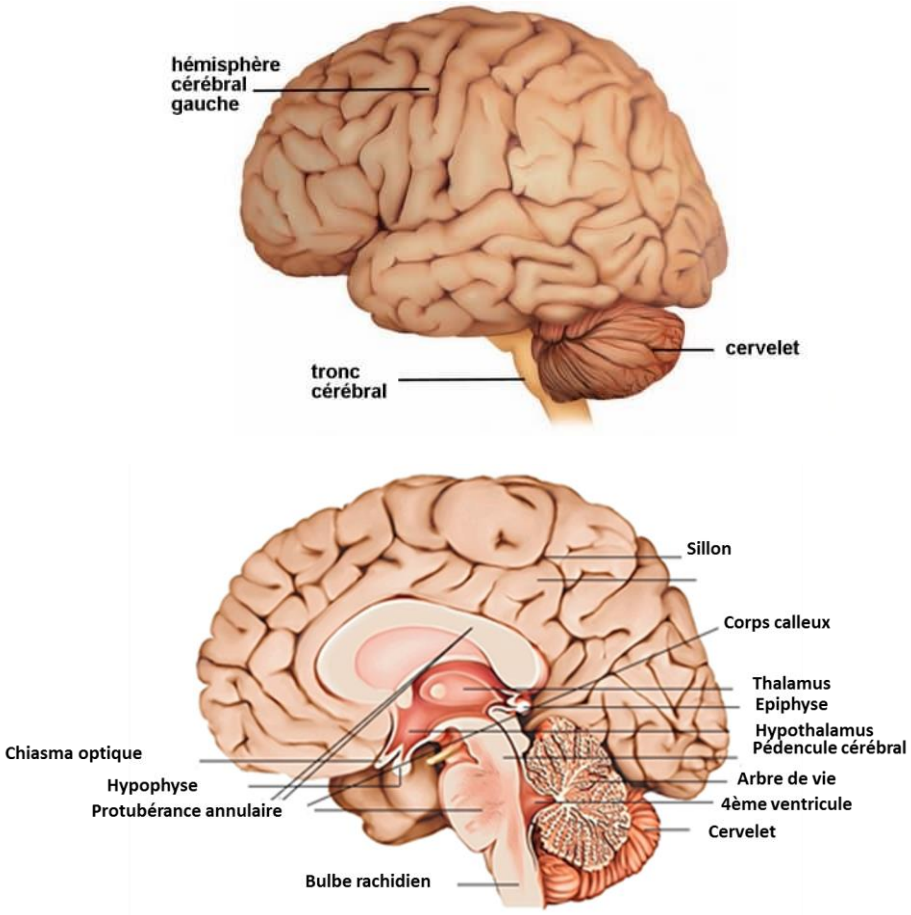

Figure 3 : Différentes parties du cerveau. Adapté par Archives Larousse- Dessin Michel Saemann.

II.2 Tumeur du cerveau

Il faut bien différencier la tumeur du cerveau des métastases du cerveau. Lorsque le cancer du cerveau naît directement dans le crane, il est nommé tumeur primitive, tandis que les tumeurs secondaires sont des métastases qui se sont développées à partir d'un cancer situé dans une autre partie du corps : le sein, les poumons, etc. Le traitement de ces métastases dépend des traitements reçus pour le premier cancer qui se propage.

Les tumeurs du cerveau sont variées, elles dépendent de leur localisation dans le cerveau, du type de la cellule qui est à l'origine du cancer, du degré d'agressivité (I à IV, de moins au plus agressif). Elles sont classées aussi selon l'état et la vitesse de propagation. Le glioblastome est la tumeur la plus agressive des tumeurs du cerveau qui ne répond souvent pas aux traitements classiques.

II.3 Symptôme de la tumeur du cerveau

Les symptômes des tumeurs cérébrales ne sont pas systémiques, ils peuvent être [33] :

- Maux de tête persistants,
- Crises épileptiques ou désordres plus ou moins significatifs des fonctions gérées par le cerveau,
- Changement de personnalité et d'humeur,
- Déficits moteurs,

- Troubles de la vue ou du langage,
- Perte de sensibilité…

II.4 Diagnostic et traitement

Pour détecter une tumeur cérébrale, un examen IRM précédé ou suivi d'un scanner est fait ainsi qu'un prélèvement et l'analyse d'un échantillon de la tumeur. La chirurgie est le premier traitement à envisager, qui a pour but d'éliminer autant de tumeur que possible. Après l'intervention chirurgicale, la tumeur est analysée en laboratoire d'anatomie. Cette analyse permet de préciser le diagnostic et de déterminer les traitements suivants [34].

Il est possible de recourir à la radiothérapie et/ou à la chimiothérapie. Ces traitements visent à éliminer les cellules cancéreuses restantes et à limiter le risque de récurrence. Dans certains cas, notamment lorsque la tumeur n'évolue pas ou ne présente pas de risque immédiat, aucun traitement contre la tumeur n'est envisagé. En revanche, des traitements sont proposés pour soulager les éventuels symptômes provoqués par la tumeur (maux de tête, crises d'épilepsie).

III. Traitement des cancers

III.1 La chirurgie

Par définition, la chirurgie est une opération de résection utilisée pour éliminer la tumeur avec parfois une marge du tissu sain qui l'entoure afin de garantir l'élimination totale des cellules malignes. La résection chirurgicale est la plus ancienne et la principale approche thérapeutique du cancer [35, 36].

La chirurgie peut être utilisée comme moyen de prévention, de diagnostic et de traitement du cancer. Il s'agit d'un traitement efficace de divers types de cancers, en particulier dans le cas de tumeurs solides de petite taille et localisées, détectées à un stade précoce. Dans le cas de la chirurgie préventive, il s'agit de retirer un tissu susceptible de devenir cancéreux. Elle est réalisée pour les personnes présentant des facteurs à risques élevés. Chez ces patients, la chirurgie permet l'analyse des cellules afin de déterminer leur nature cancéreuse ou non et, le cas échéant, le type de cancer dont il s'agit. La chirurgie peut aussi permettre d'évaluer le stade d'avancement d'un cancer. Dans ce cas, ce sont les nodules lymphatiques ainsi que les organes à proximité de la tumeur qui sont examinés, ce qui permet d'orienter une décision dans le traitement à appliquer.

Lorsqu'un cancer solide n'est pas métastasé, il peut être classiquement éradiqué par la chirurgie, en association parfois avec d'autres traitements comme la chimiothérapie ou la radiothérapie. Lorsque le cancer ne peut être retiré totalement, d'autres traitements sont utilisés en complément de la chirurgie. La chirurgie n'est efficace que lorsque le cancer est présent dans une seule partie du corps. S'il est métastasé, il faut alors envisager des traitements à plus large spectre.

III.2 La chimiothérapie

Depuis le début du 20ème siècle, la chimiothérapie a été introduite comme traitement du cancer. La **Figure 4** décrit brièvement l'histoire de la chimiothérapie depuis 1900. En 1900, Paul Ehrlich, le célèbre chimiste allemand, a défini le terme "chimiothérapie". Dès lors, les médicaments contre le cancer sont développés [37].

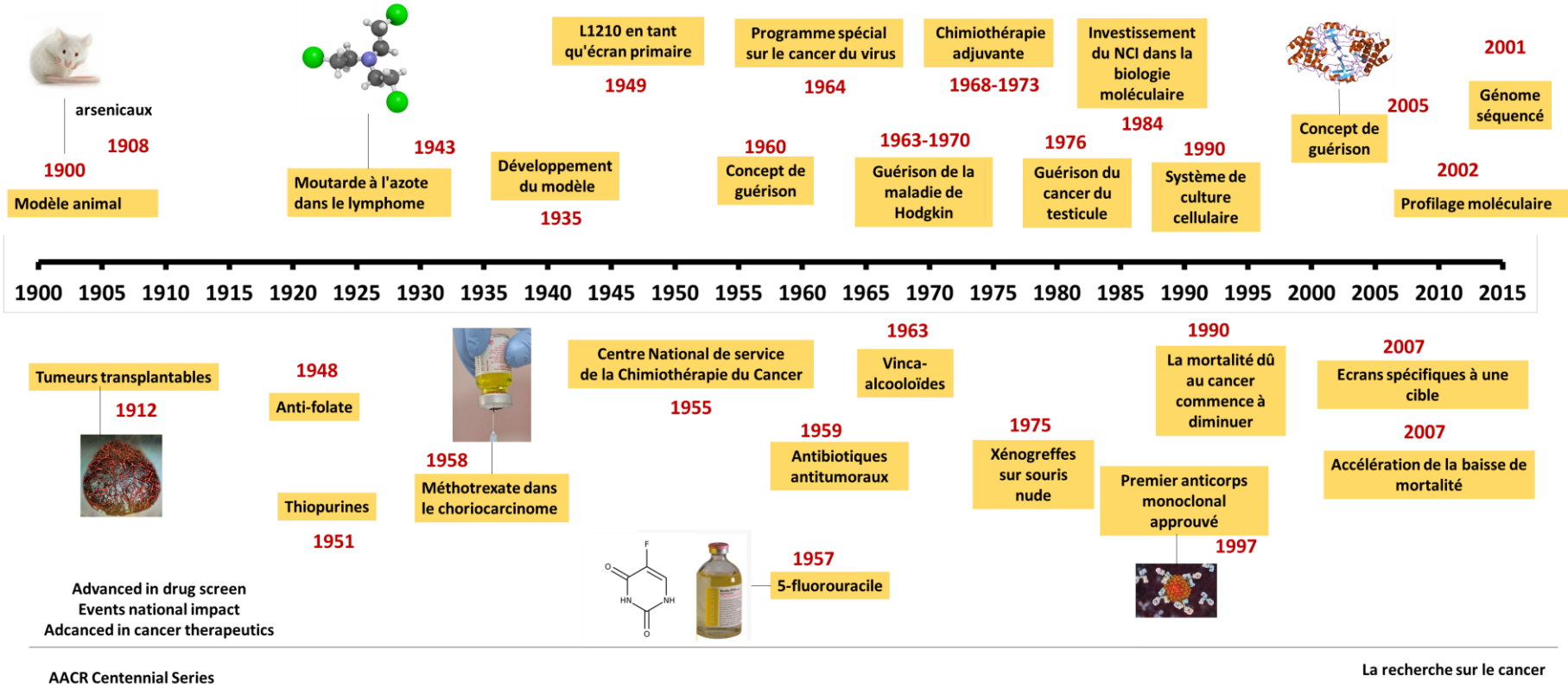

Figure 4 : Avancées majeures dans l'histoire de la chimiothérapie anti-cancéreuse. [38]

Les médicaments chimiothérapiques anti-cancéreux de première génération sont des agents alkyles (Moutarde azotée, cyclophosphamide, méthotrexate, doxorubicine..) [39]. La deuxième génération sont les médicaments de la famille cisplatine (cisplatine, ifosfamide, mitomycine C, vindésine) [40]. La troisième génération sont les cisplatine ou carboplatin (gemcitabine, paclitaxel, docétaxel, irinotécan et vinorelbine) [41].

Généralement, l'introduction du médicament chimiothérapeutique se fait par voie intraveineuse [42]. Chaque séance de traitement est suivie d'une période de repos, pour atténuer les effets secondaires du traitement et permettre à l'organisme de fabriquer de nouvelles cellules saines. Les cycles sont espacés généralement de 21 jours [43]. Le nombre des cycles de traitement est entre 4 et 6 cycles, il est variable d'un traitement à autre selon le type du cancer et la situation du patient [44]. Si les effets indésirables sont très durs, les conditions du traitement peuvent être adaptés (dose, temps de repos et nombre de cycles).

La chimiothérapie engendre des effets secondaires sévères [45] : nausées, vomissements, diarrhée, mucites (inflammation muqueuse et buccale pouvant causer une difficulté pour manger et boire), toxicité hématologique (toxicité des globules rouges entraînant une anémie, toxicité des globules blancs entraînant une dépression du système immunitaire, toxicité des plaquettes entraînant des hémorragies), cardiotoxicité, hépatotoxicité, néphrotoxicité, toxicité unguéale (lésions des ongles des mains et pieds), anomalie dans l'ADN des cellules reproductives. Les effets secondaires dépendent de plusieurs facteurs tels que le type et la dose de médicament chimiothérapeutique, l'état sanitaire du patient et le stade du cancer [46].

Selon le type de cancer et le stade de la maladie, la chimiothérapie peut être utilisée seule ou en complémentaire de la radiothérapie et de la chirurgie dans la plupart des cas [47]. Une chimiothérapie *néoadjuvante* [48] dure généralement de 3 à 5 mois, et se pratique avant une chirurgie, dans le but de diminuer la taille de la tumeur et faciliter l'opération chirurgicale. Une chimiothérapie *adjuvante* [49] dure en général de 6 mois à 2 ans, se pratique après une chirurgie complète de la tumeur, pour diminuer les risques de récidive à l'endroit de la tumeur d'origine ou ailleurs dans l'organisme. Une chimiothérapie *métastatique* qui dure en moyenne de 3 mois à 1 an traite les métastases propagées dans l'organisme [50].

Un inconvénient majeur de la chimiothérapie est le non sélectivité des molécules qui détruisent les cellules tumorales et les cellules saines. Les efforts des chercheurs visent à améliorer la sélectivité du traitement [51].

III.3 La radiothérapie

La radiothérapie peut être utilisée seule lorsque le type de cancer ne permet pas une chirurgie comme certaines tumeurs du cerveau, du poumon ou gynécologique. Dans beaucoup d'autres cas, la radiothérapie peut être aussi utilisée avec d'autres traitements, après une chimiothérapie ou/et une chirurgie soit pour continuer le traitement du cancer, soit pour soulager les symptômes du cancer (traitement palliatif) [52].

A forte dose, l'un des effets des rayonnements et leurs capacités de tuer les cellules cancéreuses ou de ralentir leur prolifération en endommageant leur ADN [53]. Les brins d'ADN des cellules tumorales sont cassés, soit directement, soit par le biais de la formation de radicaux libres. Ces ADN endommagés sont irréparables, la cellule se décompose et s'élimine du corps. Ce

processus de mort cellulaire prend des semaines ou des moins après la fin de la radiothérapie [54]. Les cellules tumorales sont plus sensibles à la radiothérapie que les cellules saines du fait que les cellules cancéreuse prolifèrent beaucoup plus rapidement que celles saines.

La radiothérapie peut être faite par un faisceau externe ou interne. L'usage de l'un des deux principaux types de radiothérapie dépend de plusieurs facteurs : de l'état de santé du patient, du type de cancer, de sa taille et de son emplacement dans l'organisme, de la sensibilité des tissus normaux adjacents aux tissus cancéreux, d'autres types de traitement utilisés pour le même patient. [55]. Les doses de rayonnement sont dépendantes du nombre de séance de radiothérapie adressé sur une zone précise et de sa sensibilité [56]. La radiothérapie peut être associée avant, avec et après la chirurgie [57].

La radiothérapie peut provoquer des effets secondaires [58] : perte des cheveux, fatigue, problème de mémoire, nausées et vomissement, mal de tête, vue floue, acnés, diarrhée, problèmes de gorge, difficulté à avaler, problèmes de fertilité (hommes) et problèmes sexuels (femmes), problèmes urinaires et vésicaux, problèmes d'estomac et d'abdomen. De plus, les radiations affectent aussi les cellules saines. Des effets secondaires peuvent apparaître plusieurs années après le traitement causant des effets appelés « tardifs » comme des cancers secondaires.

III.3.1 Radiothérapie externe

Le corps est irradié dans de nombreuses directions. Les doses utilisées sont de 20 à 80 grays (Gy) selon la tumeur et l'organe. La radiothérapie externe est appliquée sur plusieurs séances [59].

III.3.2 Radiothérapie interne

La radiothérapie interne se fait par une source placée à l'intérieur du corps humain à proximité ou dans la tumeur. Cette source peut-être solide ou liquide [60]. En particulier, le radium est utilisé dans la radiothérapie interne. La source solide nommée « curiethérapie » est sous forme de grains, capsules ou rubans. Ils émettent généralement des rayonnements alpha et bêta. Ces rayonnements courts délivrent une dose et un débit de dose élevés en un petit volume, sauvant au maximum les tissus sains environnants [61, 62].

Divers types de cancers comme les cancers de la tête et du cou, du sein, du col de l'utérus, de la prostate et des yeux sont traités par la « curiethérapie ».

Un autre type de radiothérapie interne se fait grâce à une source liquide appelée « thérapie systémique » appelé aussi I^{131} iode radiatif. C'est surtout le cancer de la thyroïde qui est traité par la radiothérapie systémique [63]. Par voie orale, intraveineuse ou par injection, les atomes radiatifs sont déplacés dans le sang vers les cellules tumorales. Suite à un rayonnement ou systémique, les fluides corporels (urine, sueur et salive..) émettent un rayonnement pendant un certain temps [64].

III.3.3 Effet et mécanisme des rayons ionisants

L'interaction entre la matière vivante et les rayons ionisants entraînent des réactions physico-chimiques (**Figure 5**) :

- Au niveau de la cellule, les rayons X ont le pouvoir d'arracher des électrons aux molécules qu'ils rencontrent, et induisent la création d'ions et de radicaux libres. Ces ions provoquent des dommages moléculaires.
- À l'échelle tissulaire, l'effet des rayons X dépend du pourcentage de cellules atteintes.

III.3.4 Type de radiothérapie

Plusieurs types d'irradiation sont utilisés :

- La radiothérapie conformationnelle 3D [65]

Cette technique vise à utiliser 4 à 6 orientations de faisceaux pour adapter les rayonnements au volume et à la forme de la tumeur en évitant l'attaque des cellules saines. Cette technique utilise des images 3D de la tumeur et d'organes traités et les organes voisins.

- La radiothérapie conformationnelle par modulation d'intensité (RCMI) [66]

RCMI ajuste le débit de dose de chaque faisceau pendant la session de manière à protéger les tissus sains. Il permet également de modifier la forme du faisceau en fonction du volume de la tumeur traitée. Cette modulation est assurée par un collimateur multi-lames qui se déplace dans les deux sens pour cibler la tumeur avec la meilleure dose possible.

- Radiothérapie synchronisée à la respiration [67]

Certains organes situés à proximité de l'appareil respiratoire sont difficiles à traiter en raison de leur mouvement. Afin d'éviter ces problèmes, des techniques innovantes sont utilisées pour contrôler le rayonnement émis par les mouvements des organes.

- La radiothérapie stéréotaxique [68]

Elle est appelée aussi la radiochirurgie. Cette radiothérapie est guidée par une image à haute précision. En effet, des microfaisceaux de photons ou de protons convergent au centre de la lésion permettant de délivrer une grande dose pour des petites lésions et des malformations vasculaires cérébrales.

- La tomothérapie [69]

La tomothérapie consiste à coupler un scanner et un accélérateur de particules qui tourne autour du malade pendant le déplacement de la table. Cela permet un meilleur ciblage de la tumeur.

- Le Cyberknife [70]

Cette technique peut traiter les tumeurs partout dans l'organisme. Ce dispositif radiochirurgical associe les techniques d'imagerie médicale avec la robotique assistée par ordinateur.

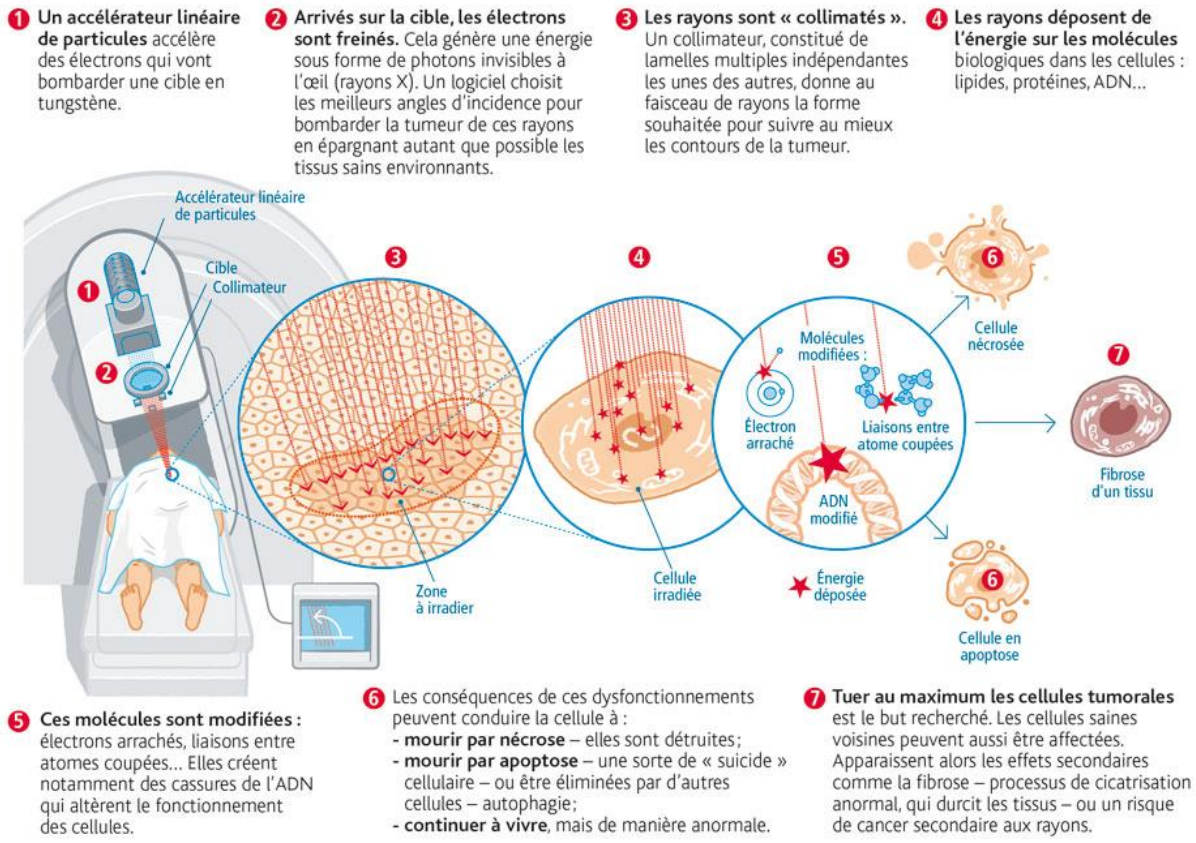

Figure 5 : Action des rayonnements ionisants en radiothérapie. Adapté du site officiel de l'institut de radioprotection et de sureté nucléaire.

- La protonthérapie [71]

La plupart des radiothérapies produisent des photons et des électrons, ces électrons sont secondaires à la production des photons. Certaines tumeurs sensibles comme la tumeur de l'œil exigent des doses légères pour éviter l'attaque des cellules saines. Pour cela, des faisceaux de protons sont utilisés.

III.4 Immunothérapie

L'immunothérapie consiste à utiliser les défenses immunitaires de l'organisme pour qu'elles s'attaquent aux cellules cancéreuses ou autres maladies. Cet objectif peut être atteint :

- Soit en stimulant une réponse immunitaire propre renforcée pour combattre les cellules tumorales,
- Soit en introduisant certains anticorps de l'extérieur.

Les anticorps monoclonaux, les médicaments à point de contrôle immunitaire et les vaccins anticancéreux sont les types les plus courants d'immunothérapie anticancéreuse. Cette modalité de traitement prend de plus en plus d'importance depuis les dernières décennies [72, 73].

III.5 Hormonothérapie

Elle est utilisée dans le cas des cancers qui ont besoin d'hormones pour se développer. L'hormonothérapie a pour but de stopper la stimulation de la tumeur par les hormones suivant

deux stratégies : le bloquage de la production des hormones ou l'empêchement de leur action au niveau de la tumeur.

III.5.1 Effets secondaires de l'hormonothérapie

Les effets secondaires de l'hormonothérapie sont essentiellement liés au type d'hormonothérapie, la dose du médicament ou de la combinaison des médicaments administrés et l'état de santé général : fatigue, nausées, diarrhée et vomissements, gain de poids, intérêt réduit ou perte totale d'intérêt pour les rapports sexuels, ménopause, bouffées de chaleur, sensibilité mammaire, problèmes de fertilité, douleurs musculaires ou articulaires, caillots de sang, ostéoporose.

Il existe un autre type de traitement anti-cancéreux, la thérapie photodynamique (PDT), qui fait l'objet de ma thèse.

IV. La thérapie photodynamique (PDT)

IV.1 Principe de la PDT

La lumière est le point commun entre la radiothérapie et la PDT, mais cette dernière utilise de la lumière visible. Ce sont des radiations non ionisantes de plus faible énergie, non mutagènes. La PDT est une technique de traitement anti-bactérien et anti-cancéreux basée sur l'association d'une molécule photosensible appelée photosensibilisateur (PS) capable de s'internaliser dans les cellules malignes et d'une lumière de longueur d'onde appropriée pour activer le PS. Le PS activé par la lumière interagit avec l'oxygène moléculaire pour générer des ROS dont l'$^1O_2$. L'$^1O_2$ et les autres ROS produits sont des espèces cytotoxiques qui réagissent avec les composants cellulaires et induisent des désordres biochimiques dans la cellule. Ces processus photophysiques localisés et ces réactions photochimiques sont au cœur de la PDT. Ainsi, la lumière, le PS et l'oxygène sont les éléments constitutifs essentiels de la PDT. Séparément, ces composants ne présentent aucune toxicité et l'absence de l'un d'entre eux supprime l'effet photodynamique. C'est la combinaison de ces trois éléments, avec une dosimétrie bien réglée de la lumière et du PS, qui détermine l'efficacité globale de la PDT [74-76]. La PDT est une opération en plusieurs étapes illustrées dans la **Figure 6** [74] :

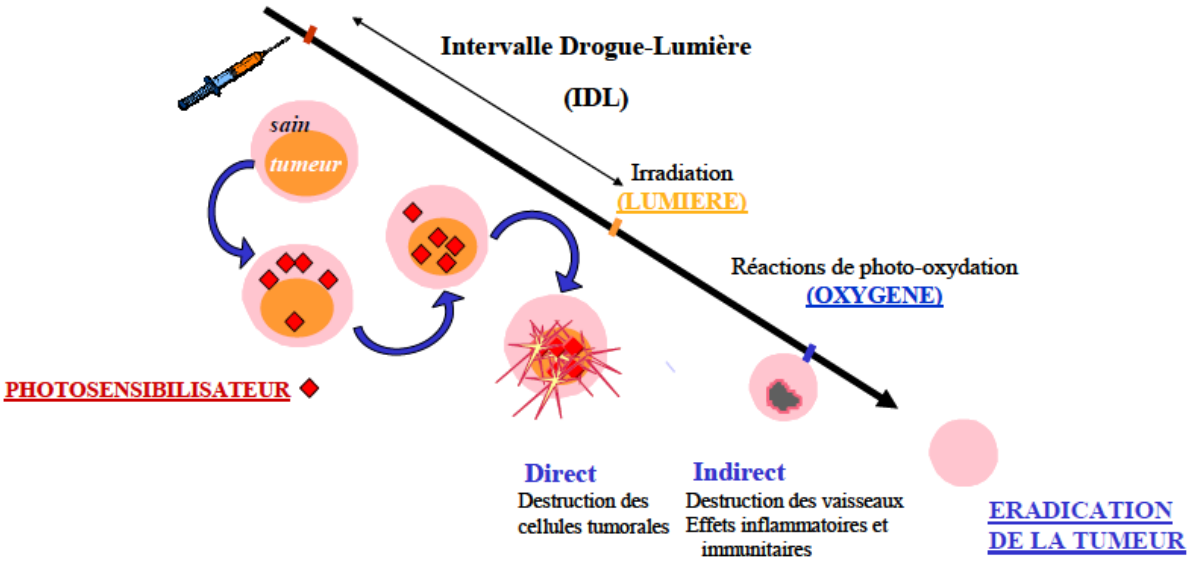

Figure 6 : Principe de la PDT [77]

1. Le PS est administré, par voie intraveineuse, orale ou topique dans le corps du patient. Le patient est laissé à l'obscurité pendant un intervalle de temps (intervalle-Drogue-lumière IDL) pouvant aller de quelques minutes à plusieurs jours.
2. Le PS se lie à certaines protéines plasmatiques comme les lipoprotéines, l'albumine et la globuline. Il s'accumule dans le tissu néoplasique malin ou reste dans la vascularisation [78].
3. La lumière à une longueur d'onde et une dose appropriée est appliquée sur le tissu malade pendant un temps spécifique,
4. Les cellules cancéreuses sont endommagées et la mort cellulaire par l'apoptose ou la nécrose induites en résulte (**Figure 7**).

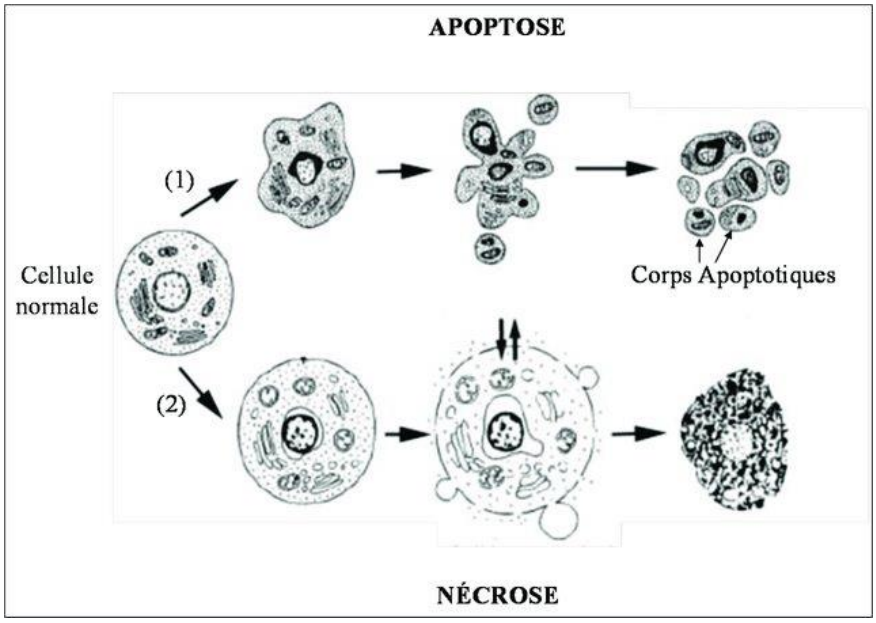

Figure 7 : La différence entre les modifications structurales de (1) l'apoptose et (2) la nécrose adapté d'après [79]

IV.2 Historique et avantage de la PDT

L'idée de considérer la lumière comme outil thérapeutique essentiel pour plusieurs maladies existe depuis 4000 ans. Ce sont les égyptiens, à cette époque, qui ont utilisé la plante Amni Majus et l'exposaient à la lumière du soleil pour guérir une maladie de la peau appelée vitiligo. L'effet désirable obtenu était dû au composant actif de la plante qui est le psoralène. Le psoralène est actuellement utilisé dans le monde entier pour le traitement du psoriasis [74].

Historiquement, et d'après le livre sacré hindou nommé « Atharva », les indiens utilisaient la lumière dans les thérapies médicales 1500 ans avant J.C. Les civilisations après ont montré que les Grecs, les Chinois et les Egyptiens, utilisaient aussi la lumière pour traiter diverses maladies tels que le psoriasis, le vitiligo et le cancer de la peau. D'après des livres de la civilisation arabe, au 13ème siècle, la médicine populaire égyptienne près du Nil utilisait un végétal appelé *Ammi majus* pour une dépigmentation de la peau.

C'est au 19ème siècle que l'utilisation de la lumière pour des traitements a été utilisée en Europe. Lorsque des maladies infectieuses ont commencé à se propager chez des patients vivant dans des logements insalubres et surpeuplés, très peu éclairés par la lumière naturelle, les autorités de cette époque en Europe n'avaient pas de véritables médicaments à leur disposition, et recommandèrent à ces malades, notamment atteints de la tuberculose, de mettre en place des séances d'exposition de leur corps et de leur visage à la lumière du soleil. Ce traitement a montré une excellente efficacité suggérant que les rayons solaires pouvaient induire une activité du système immunitaire.

En 1900, Oscar Raab, Niels Finsen, Tappeiner et Jesionek ont découvert la PDT par l'utilisation de l'éosine comme PS. En 1912, Meyer-Betz a osé essayer sur lui-même la première PDT humaine en utilisant l'hématoporphyrine et en s'exposant aux rayons solaires. En 1978, Dougherty a réussi à traiter un cancer de la peau en utilisant un dérivé de l'hématoporphyrine (HpD) sur des patients [80]. L'historique de la PDT est résumé dans la **Figure 8**.

Par définition, la PDT est une modalité de traitement peu invasive. La PDT peut être utilisée comme une alternative aux thérapies conventionnelles contre certains cancers mais souvent combinée à d'autres méthodes thérapeutiques. Elle peut être appliquée avant ou après l'un de ces traitements [81, 82].

La PDT présente divers avantages par rapport aux traitements conventionnels. La PDT est peu invasive, elle est ciblée, elle peut être répétée plusieurs fois sans engendrer de résistance. La PDT n'implique aucun échauffement des tissus et aucun endommagement des tissus conjonctifs. De plus, d'un point de vue cosmétique, la PDT laisse peu ou pas de cicatrices. C'est pour cette raison que la PDT convient pour les lésions de la peau, du cou, de la tête et de la cavité buccale. Le potentiel curatif de la PDT a été reconnu il y a environ 25 ans et son utilisation en clinique a commencé en 1993. La PDT traite les dysplasies et les carcinomes *in situ* pré-malins des muqueuses, les cancers de l'œsophage, les cancers du poumon [82, 83]. La PDT est utilisée en dermatologie (kératoses actiniques (KA)) [84], en ophtalmologie (dégénérescence maculaire liée à l'âge, Visudyne®) [85], en urologie (cancer de la prostate, Tookad®) [86],

en gastro-entérologie (cancers superficiels de l'œsophage, dysplasie et cholangiocarcinome inopérable) [87], en gynécologie (lésions dysplasiques de haut grade du col utérin) [88], en neurochirurgie (glioblastome), en pneumologie (mésothéliome pleural malin (MPM)) [89], etc.

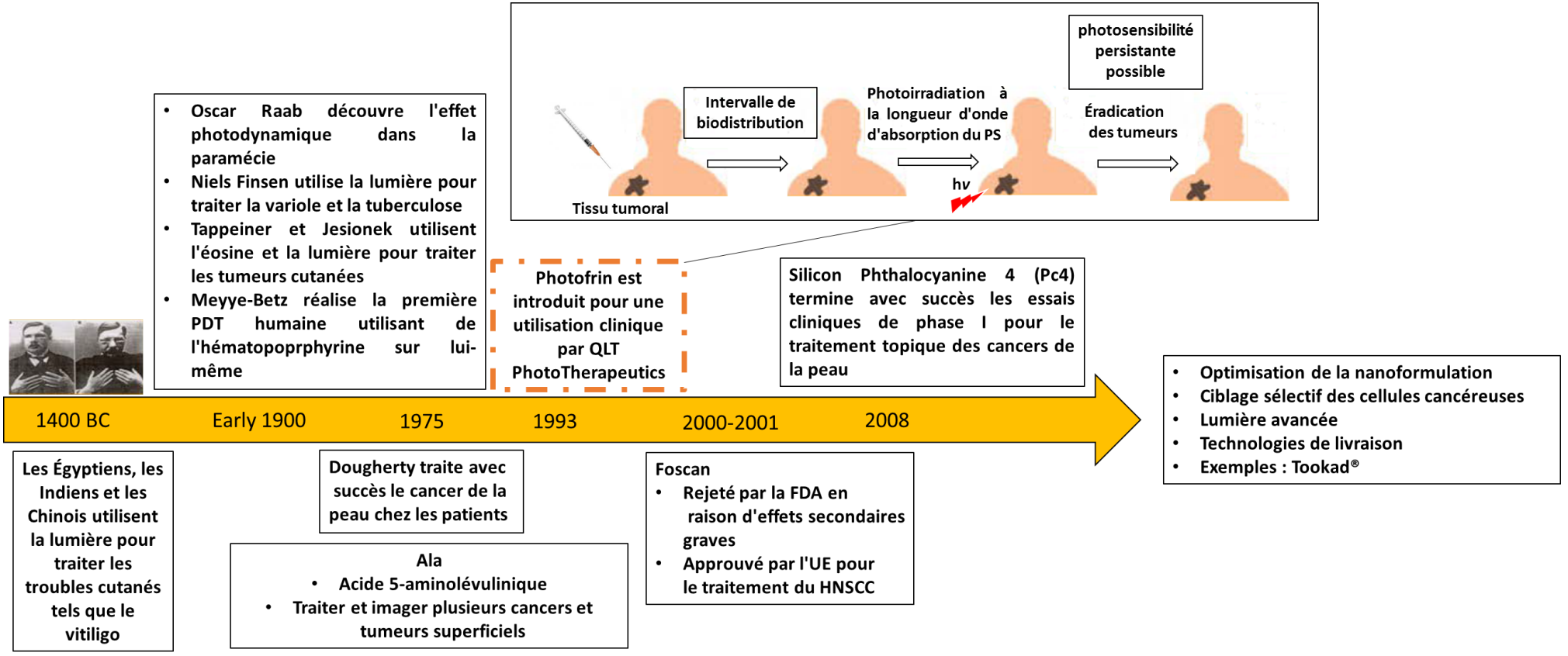

Figure 8 : Historique de la PDT. Adapté d'après [38]

IV.3 Mécanisme de la PDT

Les processus photochimiques et photophysiques impliqués dans la PDT ont été largement étudiés et sont illustrés par le diagramme de Perrin-Jablonski et les équations 1-13 (**Figure 9**) [76] (détaillé encore plus dans la partie transfert d'énergie-chapitre II). L'illumination à une longueur d'onde appropriée du PS permet à cette molécule photosensible d'absorber un photon (hv) et de passer de son état fondamental (S_0) à un état excité singulet (S_n) (équation 1). Le PS excité se relaxe ensuite dans l'état singulet excité le plus bas S_1 (équation 2), suivi par

i) la conversion vers l'état triplet du sensibilisateur (T_1) généré par le processus de croisement intersystème non radiatif (équation 5),

ii) le retour à S_0 avec émission de lumière (Fluorescence) (équation 3),

iii) le retour à S_0 sans émission de lumière (équation 4).

$$PS\ (S_0) \xrightarrow{hv} PS\ (S_n) \quad \text{(équation 1)}$$

$$PS\ (S_n) \xrightarrow{Kic} PS\ (S_1) \quad \text{(équation 2)}$$

$$PS\ (S_n) \xrightarrow{fluorescence} PS\ (S_0) + hv \quad \text{(équation 3)}$$

$$PS\ (S_1) \xrightarrow{hv} PS\ (S_0) \quad \text{(équation 4)}$$

$$PS\ (S_1) \xrightarrow{Kisc} PS\ (T_1) \quad \text{(équation 5)}$$

La durée de vie de l'état triplet T_1 (µs) est plus longue que celle de l'état singulet S_1 (ns). L'interaction du PS dans son état excité T_1 avec les autres molécules proches est renforcée avec des durées de vie τ plus longues. Par conséquent, l'état T_1 est capable de réagir de deux manières, classées comme mécanismes de type I et II.

Le mécanisme de type I produit des ROS tels que $HO^{\bullet}$, $O_2^{\bullet-}$, $HOO^{\bullet}$, etc. Ce mécanisme est basé sur des réactions d'abstraction d'atomes d'hydrogène ou de transfert d'électrons se produisant généralement entre le PS dans son état T_1 excité et un autre substrat, la réaction de type I est favorisée dans les environnements polaires et déficients en oxygène. Les ROS produits sont très réactifs et causent de graves dommages à la cellule.

Photoréaction-Type I

$$PS\ (T_1) + PS\ (T_1) \rightarrow PS^{+\bullet} + PS^{-\bullet} \quad \text{(équation 6)}$$

$$PS\ (T_1) + Substrat \rightarrow Substrat^{+\bullet} + PS^{-\bullet} \quad \text{(équation 7)}$$

$$PS^{-\bullet} + {}^3O_2\ (^3\Sigma_g^-) \rightarrow PS + O_2^{-\bullet} \quad \text{(équation 8)}$$

$$Substrat^{+\bullet} + {}^3O_2\ (^3\Sigma_g^-) \rightarrow Stress\ oxydatif \quad \text{(équation 9)}$$

$$Substract + O_2^{-\bullet} \rightarrow Stress\ oxydatif \quad \text{(équation 10)}$$

Le mécanisme photochimique de type II implique un processus de transfert d'énergie par collision entre le PS excité et l'oxygène dans son état triplet. Ce transfert d'énergie génère $^1O_2$ qui est considéré comme le principal agent cytotoxique responsable de l'activité photobiologique. Les réactions de type I et II peuvent se produire simultanément avec un rapport qui dépend du type de PS et de son environnement. Les deux réactions présentent des dommages oxydatifs analogues [76, 90].

Photoréaction-Type II

$$PS\ (T_1) + \quad {}^3O_2\ ({}^3\Sigma_g^-) \xrightarrow{ken} PS\ (S_0) + \quad {}^1O_2\ ({}^1\Delta_g) \quad \text{(équation 11)}$$

$${}^1O_2\ ({}^1\Delta_g) + \ substract \ \rightarrow Stress\ oxydatif \quad \text{(équation 12)}$$

$$PS\ (T_1) \xrightarrow{phosphorescence} PS\ (S_0) + \ hv \quad \text{(équation 13)}$$

$$PS\ (T_1) \rightarrow PS\ (S_0) \quad \text{(équation 14)}$$

${}^3\Sigma_g^-$ désigne l'état triplet de l'$^1O_2$ et ${}^1\Delta_g$ désigne l'état singulet de l'$^1O_2$

In vivo, tout constituant cellulaire, comme les noyaux, les mitochondries, la membrane cytoplasmique, les lysosomes, etc. représente une cible pour les ROS cytotoxiques. La cellule néoplasique est éradiquée par apoptose ou par nécrose selon la cible attaquée, le type et la quantité de PS utilisés et la dose de lumière mise en œuvre. Il a été reconnu que la PDT provoque la mort cellulaire en provoquant inflammations et certaines réponses immunitaires spécifiques à la tumeur [76].

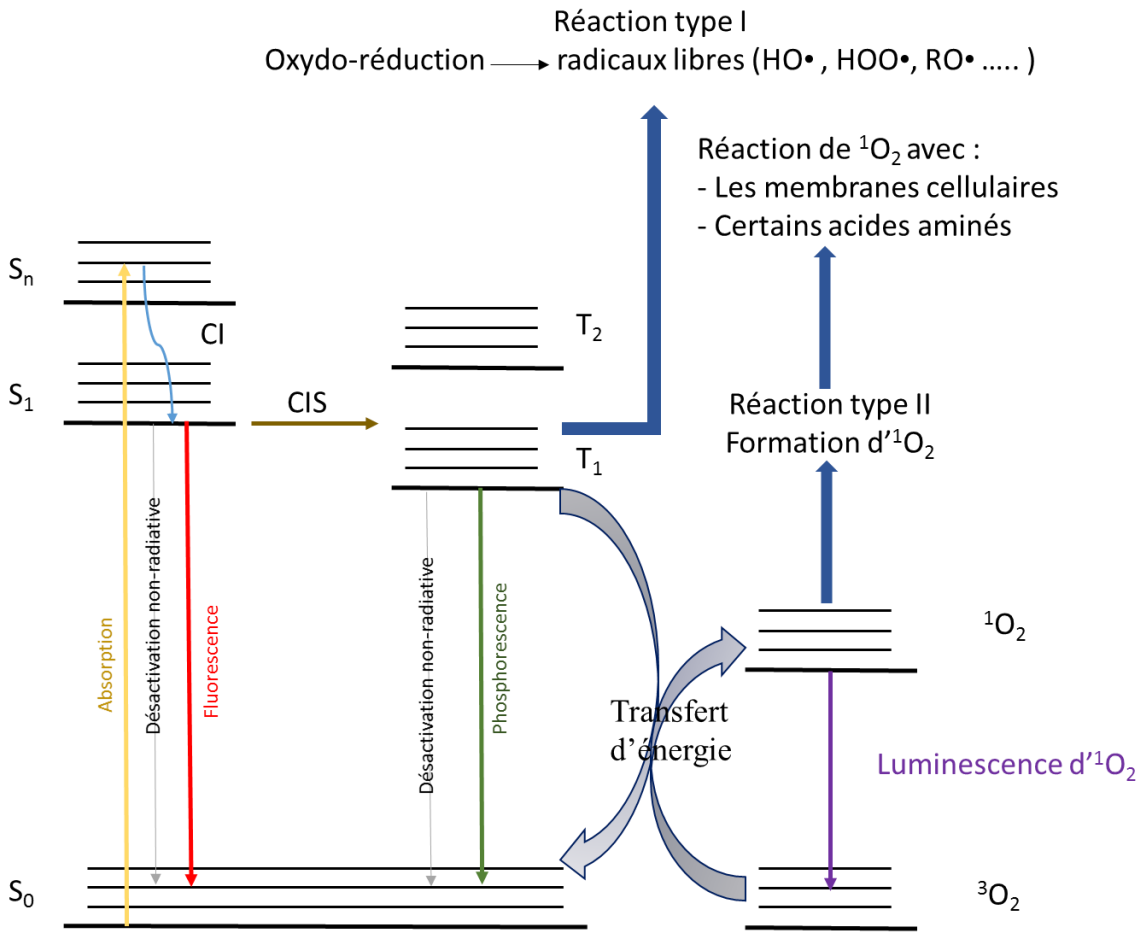

Figure 9 : Diagramme de Perrin-Jablonski modifié illustrant le principe de la PDT, où S_0, S_1 et T_1 sont respectivement l'état fondamental singulet, le premier état singulet excité et le premier état triplet excité du PS. [76, 91]. CI = Conversion interne, CIS = Conversion inter-système.

IV.4 Oxygène

L'oxygène dans son état fondamental possède deux électrons célibataires à spins parallèles. Il est donc paramagnétique. En absorbant 22 kcal, l'oxygène apparie ses deux électrons célibataires dont les spins sont anti-parallèles. Il devient diamagnétique. D'après la règle de Hund, l'état stable correspond à l'état paramagnétique (**Figure 10**).

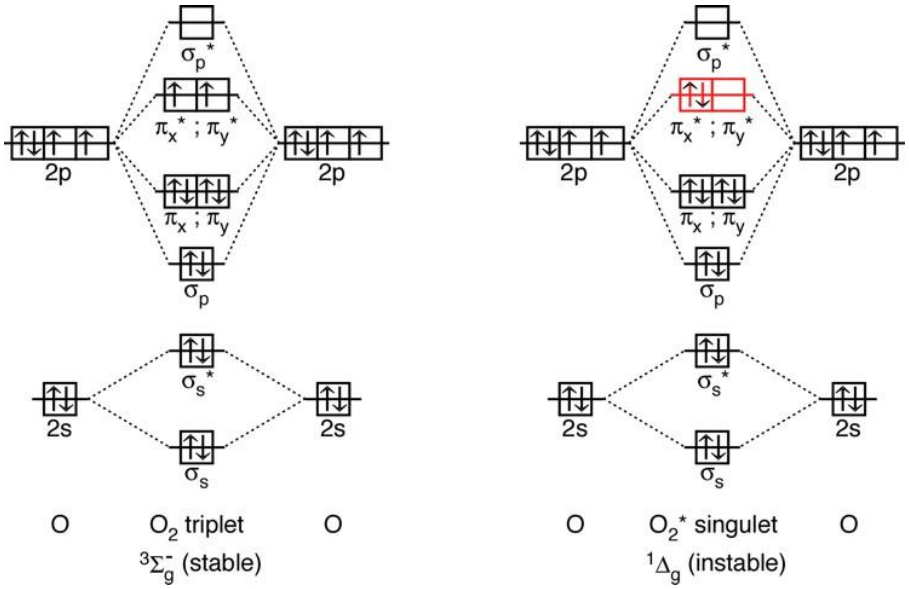

Figure 10 : Diagramme des niveaux d'énergie électroniques de l'oxygène triplet et singulet

IV.5 Composants de la PDT

Pour que la PDT soit mieux mise en œuvre dans les cliniques, il doit exister une combinaison bien planifiée d'un système d'administration, de la lumière appropriée et d'une concentration adéquate du PS en présence d'O_2.

IV.5.1 La lumière

Pour faire passer la technique de traitement par PDT de la paillasse du laboratoire et de la préclinique à la pratique clinique, il a fallu mettre au point des sources lumineuses et des dispositifs d'émission de lumière. La profondeur de la pénétration de la lumière dans les tissus dépend de la longueur d'onde de la lumière émise. La **Figure 11** montre que la capacité de la pénétration des différents types de lumière dans le tissu est variée. Les grandes longueurs d'onde de la lumière sont capables de pénétrer plus efficacement dans les tissus que les petites longueurs d'onde. Ainsi, la pénétration de la lumière bleue (400-450 nm) dans le tissu est superficielle avec une profondeur de <1 mm, contrairement à la lumière orange (590-620 nm) et à la lumière rouge (600-720 nm) qui pénètrent respectivement à environ 1,5 et 3 mm de profondeur [80, 92]. Les lasers sont considérés comme les sources de lumière les plus cohérentes pour la PDT. Le développement de systèmes d'administration de la lumière plus avancés a été un défi, ces systèmes comprennent les lasers à argon et à colorant, les lasers à vapeur métallique, les lasers à colorant KTP:YAG, les lasers à diode, les sources de lumière non laser, mais également les dispositifs d'administration de la lumière comme les fibres optiques, les fibres cylindriques, les cathéters à ballonnet. Les LED remplacent désormais souvent les lasers.

La **Figure 11** montre la profondeur de pénétration de la lumière dans les tissus pour les différentes longueurs d'onde [92]. Plus récemment, les chercheurs ont développé des dispositifs basés sur des fibres et des textiles émetteurs de lumière, pour une transmission de la lumière efficace, flexible et homogène (**Figure 12**) [93].

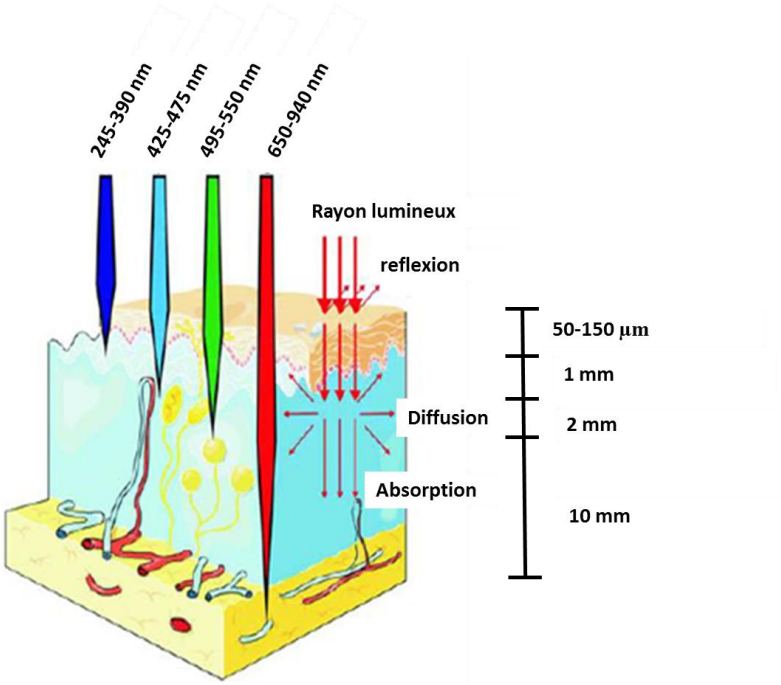

Figure 11 : La profondeur de pénétration de la lumière dans les tissus [94]

Dans le cadre de la PDT, le terme "fenêtre thérapeutique" fait référence à la gamme de longueurs d'onde la plus utilisée, à savoir entre 650 et 850 nm. En général, cette gamme est appropriée pour exciter une large série de PSs utilisés pour la PDT et assure en même temps une pénétration maximale de la lumière dans les tissus. A noter que la lumière transmise au PS dépend des espèces biologiques qui absorbent une partie de la lumière comme le graisse, l'hémoglobine, etc … Cependant, la longueur d'onde et le type de lumière utilisés dépendent du type de cancer et de l'application. Par exemple, le traitement des cancers de la peau peut être réalisé par la lumière du soleil ou une lumière bleue, tandis que le traitement des tumeurs de l'œsophage nécessite une lumière verte. Par conséquent, l'optimisation d'un dosage idéal de la lumière, suffisamment puissant pour activer le PS et tuer les cellules néoplasiques sans endommager les cellules saines est nécessaire [92].

Figure 12 : Photographie d'un textile lumineux [93].

IV.5.2 Les photosensibilisateurs

Les PSs sont des molécules capables d'absorber la lumière à des longueurs d'onde spécifiques. Les PSs peuvent soit être présents naturellement comme dans les plantes, soit synthétiques.

Pour qu'un PS soit efficace dans la PDT, il doit produire des agents cytotoxiques létaux tels que les ROS dont $^1O_2$ [76].

Les PS sont divisés en trois générations :

IV.5.2.1 Première génération de PS

Deux PS forment la première génération de PS autorisés pour l'utilisation en PDT: le Photofrin et l'HpD.

En 1898, le « Paramecium caudatum » en combinaison avec la lumière a montré des effets cytotoxiques par O. Raab [95]. En 1903, les professeurs de O.Raab, Jesionek et von Tappeiner ont traité des tumeurs cutanées par application locale d'éosine et de la lumière blanche [96]. En 1911, Hausmann et al. ont montré que l'hématoporphyrine (Hp) en association avec la lumière UV présente une efficacité sur des petites lésions de psoriasis [97].

En 1924, Policard et al. ont montré que l'Hp s'accumule dans les tumeurs [98]. L'Hp est utilisé comme sonde fluorescente pour diagnostiquer et éliminer la tumeur par Figge et al. [99]. En 1955, Schwartz et al. [100] purifient l'Hp, qui est un mélange complexe de porphyrines. La dernière purification fut introduite par Lipson et à donner naissance à l'hématoporphyrine dérivée (HpD) [101]. En 1975, Dougherty et al. ont montré que la PDT est bien efficace pour le traitement du cancer, en couplant une lampe à arc à xénon avec HpD et en traitant des tumeurs mammaires de souris [102]. En 1978, la même équipe réalisa les premiers essais sur l'homme et des résultats encourageants ont été obtenus [103]. Entre 1983 et 1985, l'introduction des fractions actives (l'éther et l'ester de dihématoporphyrine) de l'HpD donnait naissance au Photofrin®.

L'HpD et le Photofrin présentent plusieurs avantages :

- Ils possèdent un bon rendement quantique de génération d'$^1O_2$ (0,60 dans le D_2O),
- Ils sont connus depuis longtemps.

En revanche, ces PSs possèdent plusieurs inconvénients :

- Ce sont de mélanges complexes,
- Ils ne sont pas sélectifs,
- Ils présentent un faible coefficient d'extinction molaire à une longueur d'onde d'absorption peu élevée c'est-à-dire 630 nm.

Pour pallier à ces problèmes, des PSs de seconde génération ont été développés.

IV.5.2.2 Deuxième génération de PS

Les PSs de deuxième génération présentent certains avantages : ils sont purs et ont été élaborés pour absorber à de plus hautes longueurs d'onde. Ce sont principalement les porphyrines, les chlorines et les bactériochlorines.

- Les porphyrines

Les porphyrines sont des molécules cycliques tétrapyrroliques avec un noyau hétérocyclique appelé porphine [74] (**Figure 13(a)**). Ces structures jouent un rôle important dans le métabolisme respiratoire, dans la composition de l'hémoglobine et des globules rouges. Inspirés par leurs rôles biologiques vitaux dans les systèmes naturels tels que la photosynthèse et le transport de l'oxygène, les porphyrines ont ouvert la voie au domaine médicinal. Les dérivés de porphyrine constituent une classe majeure de PSs. Elles ont été largement utilisées dans les domaines de l'imagerie de fluorescence, des médicaments, etc. Les porphyrines constituent un groupe de composés naturels caractérisés par une couleur pourpre intense, d'où leur nom (porphura = pourpre en grec). La chlorophylle et l'hème, qui sont des métallophorphyrines en raison de la présence d'un métal occupant le centre de leur anneau porphyrique, sont les représentants naturels des porphyrines **(Figure 13(b)**).

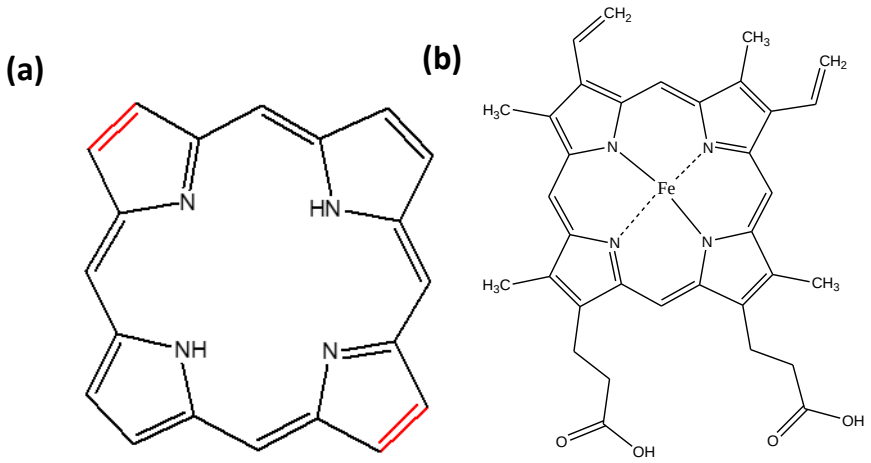

Figure 13 : (a) structure d'une porphyrine, (b) structure d'une métalloporphyrine

Le système d'électron π fortement conjugué des porphyrines leur permet une absorption dans le domaine du visible avec des spectres d'absorption très caractéristiques qui sont fonction de la structure et de la présence ou non d'un métal (**Figure 14**). Les spectres d'absorption des porphyrines non métallées se composent d'une bande intense entre 390 et 430 nm (proche UV) appelée bande de Soret ou bande B et de quatre bandes de moindre intensité aux plus grandes longueurs d'onde (entre 500 et 680 nm) nommées bandes Q. Les porphyrines métallées n'ont que 2 bandes Q.

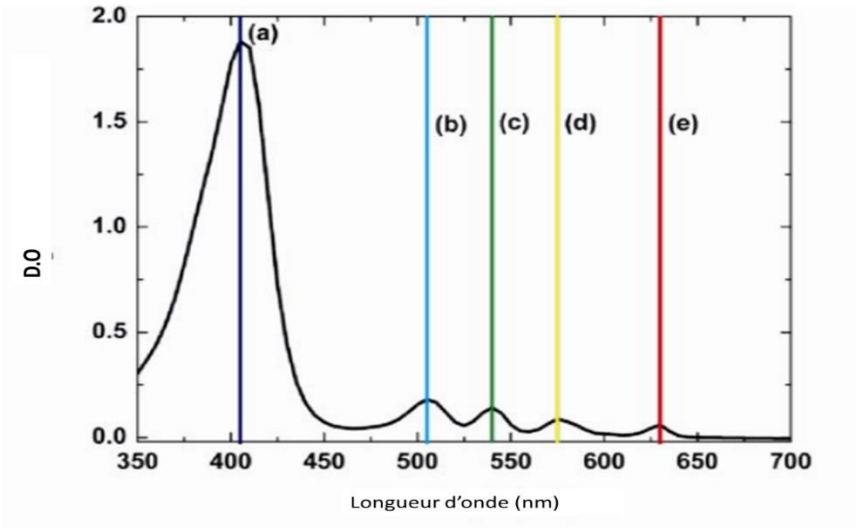

Figure 14 : Spectre UV-visible caractéristique d'une porphyrine base libre (a) Bande Soret (b) Q_{IX} (c) Q_{III} (d) Q_{II} (e) Q_{I}.

- Chlorines et bactériochlorines

Elles sont considérées comme une catégorie majeure de PSs pour la PDT. Par rapport aux porphyrines, la structure des chlorines diffère par une liaison exocyclique réduite avec la présence de deux atomes d'hydrogène supplémentaires dans un cycle pyrrole **(Figure 15)** [104, 105]. Cette modification structurelle est à l'origine du décalage rouge bathochrome de la bande d'absorption des chlorines [104, 105]. Les bactériochlorines présentent deux liaisons exocycliques réduites.

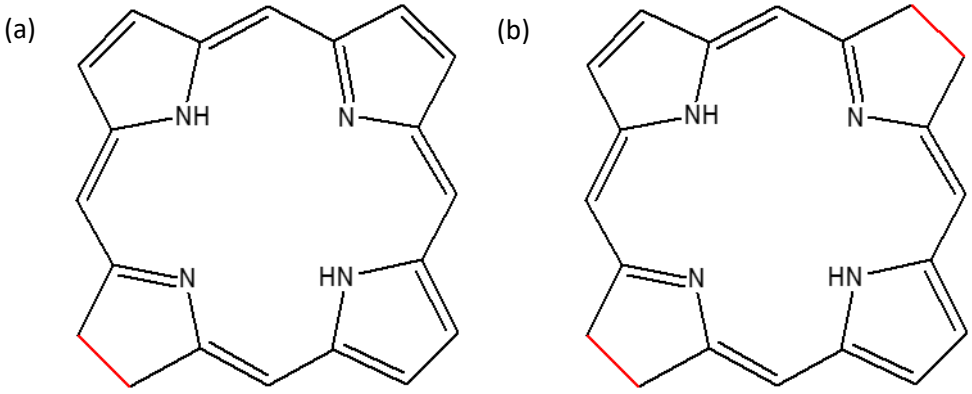

Figure 15 : (a) structure d'une chlorine, (b) structure d'une bactériochlorine

IV.5.2.3 Troisième génération de PS

L'un des inconvénients des PSs de la première et deuxième génération est leur manque de sélectivité et donc d'accumulation dans la tumeur. Pour éviter ce problème, des vecteurs peuvent être couplés de façon covalente au PS pour cibler des récepteurs membranaires sur-exprimés dans les cellules cancéreuses ou les néo-vaisseaux (ciblage actif) ou les PSs peuvent être encapsulés ou greffés à des nanoparticules (NPs, ciblage passif). Ce point sera discuté dans le paragraphe (4.7.2) [106].

IV.5.2.4 Quatrième génération de PS

Les PSs de 4ème génération sont non seulement sélectifs mais peuvent également servir à détecter les tumeurs. Des agents de détection sont ajoutés (fluorophore, radiomarqueur..)

Le **Tableau 1** résume les PSs utilisés cliniquement.

Tableau 1 : PSs utilisés cliniquement, leurs noms commerciaux, leur longueur d'onde maximale d'absorption, le type de tumeur traité, le pays où ils sont utilisés et leur structure chimique développée [38, 107].

Nom commercial du médicament	Photosensibilisateur	λ_{max} absorption (nm)	Tumeur traitée	Pays	Structure chimique du PS
Photofrin®	HpD, Porfimère sodique	630	Cancer du poumon et de l'oesophage	Canada, Etats-Unis (USA), Royaume-Uni (RU) et union Européenne (UE)	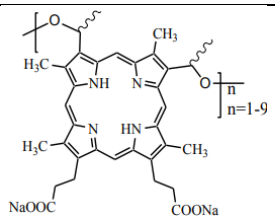
Levulan®	Acide 5-aminolévulinique (5-ALA), précurseur de la Protoporphyrine IX	635	Kératose actinique	UE et USA	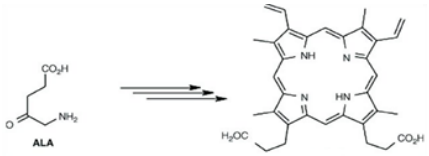
Cysview®	Hexaminolevulinate (HAL)	632	Diagnostic du cancer de la vessie	USA	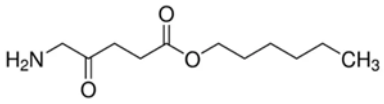
Foscan®	Méta-tétra(hydroxyphényl)chlorine (m-THPC ou temoporfin)	652	Cancer tête et cou	UE Islande et Norvège	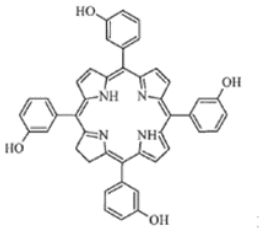
Purlytin®	Tin ethyl etiopurpurin	664	Dénocarcinome du sein, carcinome basocellulaire, sarcome de Kaposi, dégénérescence maculaire liée à l'âge	USA	

					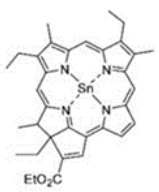
Laserphyrin, Litx®	N-aspartyl chlorin e6 (NPe6)	664	Cancer du poumon	Japon	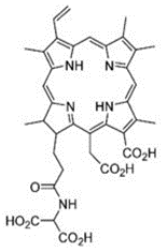
Photochlor®	2-(1-héxyloxyéthyl)-2-devinyl pyrophéophorbide-alpha	650	Cancer de l'œsophage, des poumons, tête et cou et larynx.	Japon	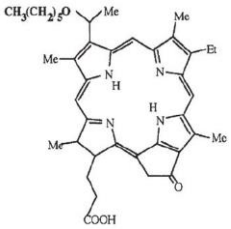
Tookad®	Palladium bacteriopheophorbide (WST09)	763	Cancer de la prostate	UE	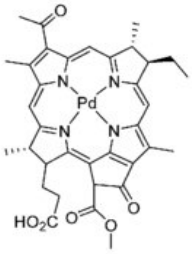
Stakel®	WST11	763	Cancer de la prostate	Mexique	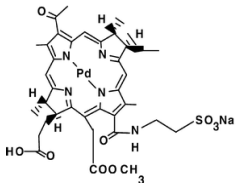
Lutrin®, Optrin®, Antrin®	Motexafin lutetium (Lu-Tex)	732	Cancer de la prostate, lié à l'âge dégénérescence maculaire, sein cancer, cancer du col de l'utérus, artériel maladie	USA	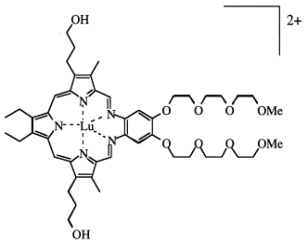

Photosense®	Phtalocyanine d'aluminium	676	Ventre, peau, lèvres, cavité orale, langue, cancer du sein	Russie	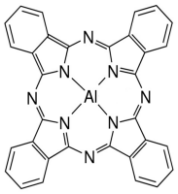
Visudyne®	Verteporphin, Dérivé monoacide de la Benzoporphyrine	690	Ophtalmique	USA UE	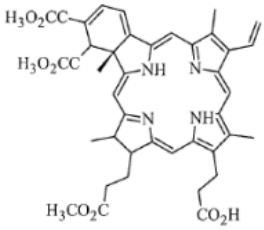
Pc4®	Phtalocyanine-4	670	Lésions cutanées/subcutanées de tumeurs solides divers	USA	
SnET2®	Etiopurpurine d'étain	660	Cancer du sein, de la prostate et sarcome de Kaposi	USA Canada	-
Xcytrin®	Texaphyrine	732	Cancer de la prostate, DMLA	USA	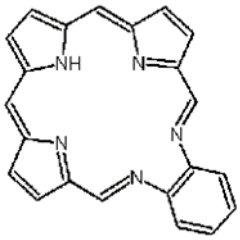
Benzvix®	Acide benzyl δ - aminolévulinique	635	Tumeurs gastrointestinales	USA Canada UE	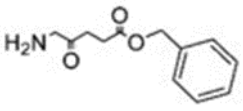

Lu-Tex®	Texaphyrine de lutétium	720-760	Tumeurs cérébrales, cancer de la prostate et du col de l'utérus	Canada	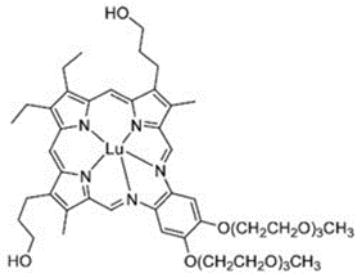
Photoditazine®	Chlorine e6	662	Cancer du poumon et de la prostate	Russie	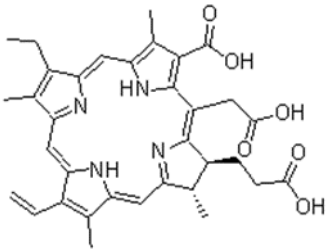

IV.5.2.5 Le Rose Bengale

Le RB est un PS soluble dans l'eau. C'est un composé organique dérivé de la fluorescéine (**Figure 16**). Dans l'eau, la longueur d'onde d'absorption maximale est de 545 nm. Dans l'éthanol, son rendement quantique d'$^1O_2$ est de 0,68. Il montre aussi une fluorescence significative avec un rendement quantique de 0,15.

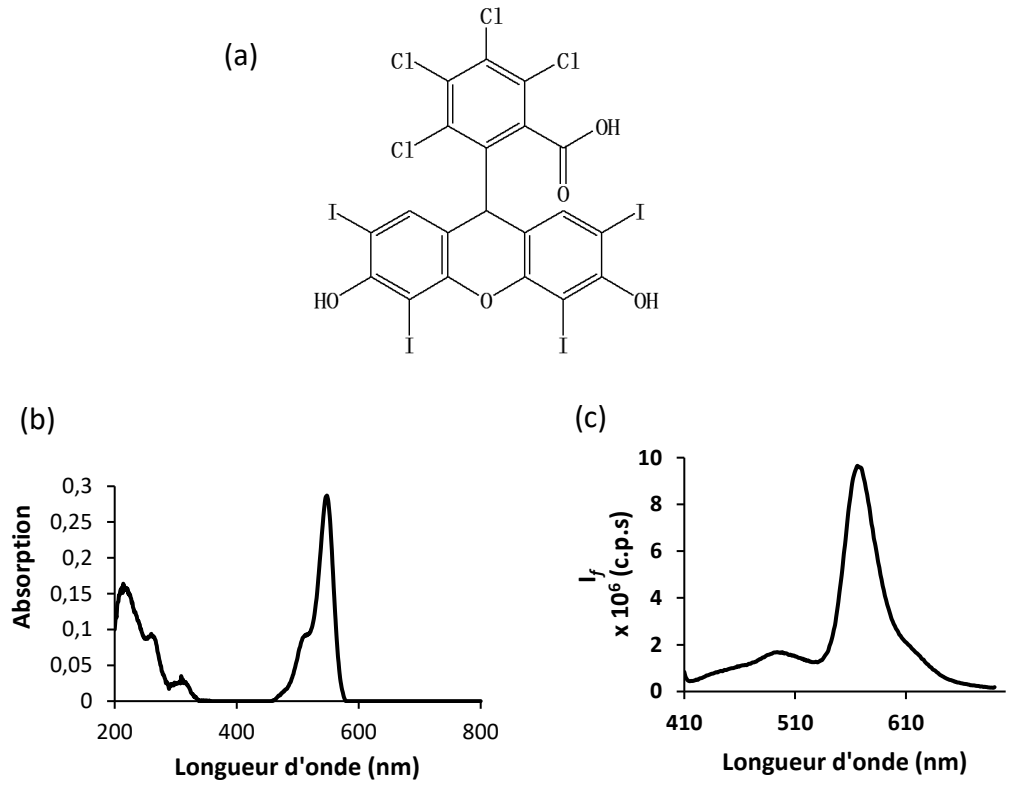

Figure 16 : (a) Formule développée du Rose Bengale (RB) (b) spectre d'absorption du RB (c) spectre d'émission du RB (solvant : eau , λ_{exc}=558 nm)

Le RB, à l'origine, a été utilisé comme teinture pour la laine. En 1882, Robert Ghnem, un chimiste suisse, a préparé le RB comme analogue de la fluorescéine [108]. Rudolf Nietzki, de l'université de Bâle, a identifié les principaux constituants du RB comme étant des dérivés iodés de la di et tétra-chlorofluorescéine [109]. Le RB est déjà utilisé en clinique en collyre permettant de visualiser les lésions éventuelles de la cornée [110]. Il est utilisé également pour tester l'activité du foie [111].

Le RB stimule le système immunitaire pour le traitement du cancer par l'activation des lymphocytes T [112]. Il produit aussi de l'$^1O_2$ après excitation lumineuse et peut-être utilisé en PDT. Le RB permet le diagnostic sérologique des brucelloses dûes à Brucella abortus, par la détection des IgG (immunoglobuline G) [113, 114]. Nous avons écrit une revue, publiée dans *Pharmaceuticals*, sur l'utilisation du RB en PDT, située en sous-chapitre III.

IV.6 Limitations de la PDT

IV.6.1 Pénétration de la lumière

Une des limitations de la PDT est la faible pénétration de la lumière dans les tissus. Pour y remédier, il existe plusieurs pistes :

IV.6.1.1 L'excitation biphotonique et l'up-conversion

L'excitation biphotonique dans le proche infrarouge se fait par absorption simultanée de deux photons [115] (**Figure 17**). Suite à l'absorption du premier photon, la molécule passe à un état excité intermédiaire, simultanément l'absorption du deuxième photon lui permet de passer vers l'état excité final [116]. Récemment, il est décrit également l'utilisation des UCNPs (Upconversion NPs) contenant des terre rares ayant une durée de vie de l'ordre de ms à µs qui

permet à ces NPs d'absorber séquentiellement deux photons à travers un état d'énergie métastable [117, 118].

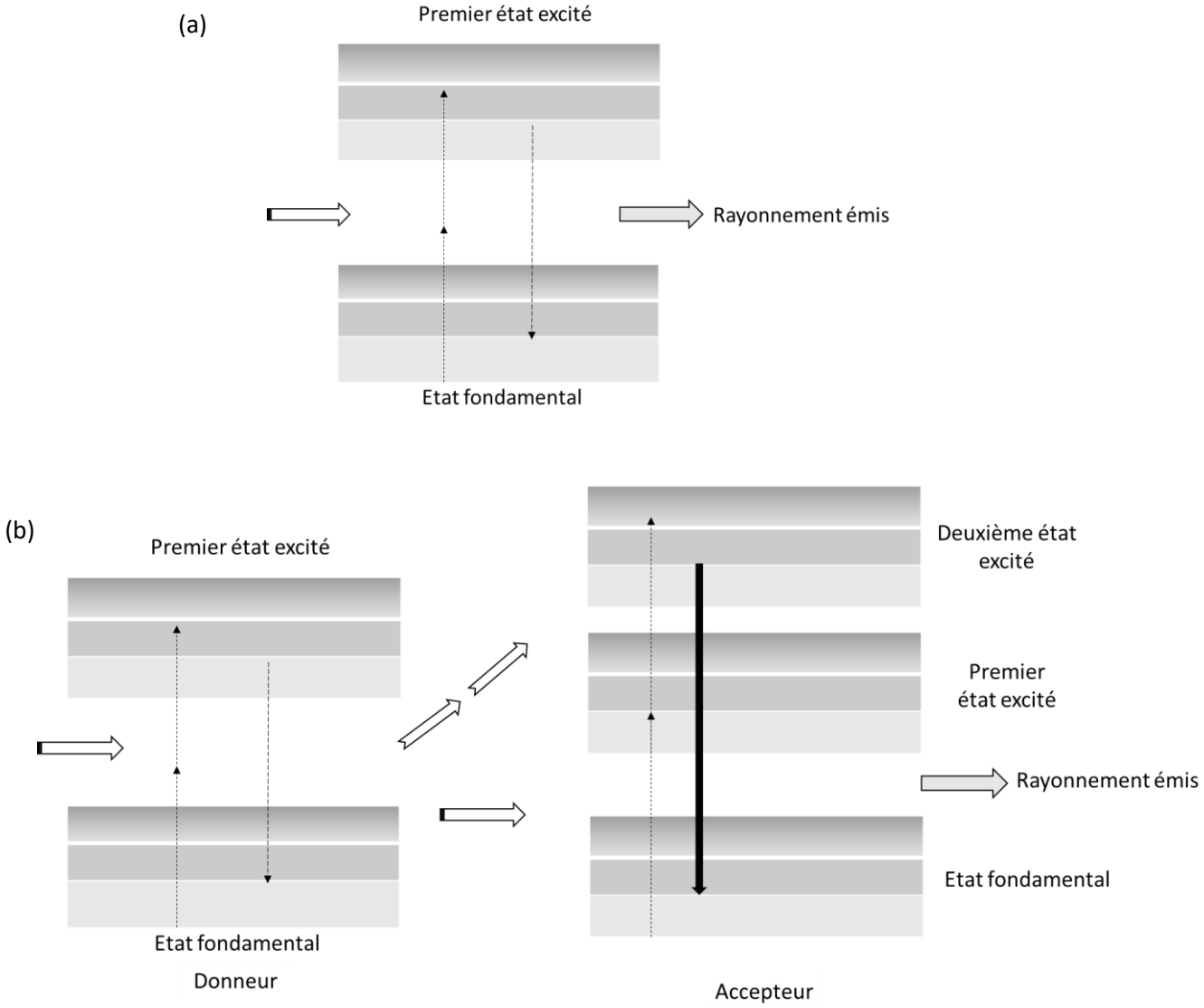

Figure 17: schématisation de (a) l'excitation biphotonique et (b) upconversion

IV.6.1.2 L'utilisation des rayons X

IV.6.1.2.1 L'énergie des rayons X incidents en radiothérapie (source)

En radiothérapie externe X, les faisceaux de basse énergie (jusqu'à 200 kV) ont très peu d'applications et sont dédiés aux traitements cutanés (< 5 mm de profondeur, par exemple mélanome, carcinome basocellulaire, carcinome épidermoïde, chéloïde). Les moyennes énergies 200 kV à 1 MV (rayons X orthovoltage et supervoltage) ont été largement utilisées pour les traitements superficiels depuis les années 1930-1940 mais sont devenues moins avantageuses avec l'avènement des électrons de haute énergie dans les années 1960-1970. De nos jours, les faisceaux à haute énergie, encore appelés faisceaux mégavoltage, (1 à 25 MV)

sont de loin les plus utilisés car ils permettent le traitement de tumeurs profondes (> 2 cm de profondeur).

L'utilisation des rayons X en radiothérapie est bien connue et exploite les effets des rayonnements ionisants pour produire des ROS et détruire les cellules malignes. Dans ce processus, il y a une radiolyse de l'eau produisant des ROS (radical hydroxyle ($OH^{\bullet}$), le peroxyde d'hydrogène (H_2O_2) et le radical superoxyde ($O_2^{\bullet -}$) et de l'$^1O_2$. La dose des rayons X est exprimée en Gray (Gy). En 2010, les recherches de Borgh et al. [119] démontrent que la dose tolérée en Gray est fixée à 60 Gy (2 Gy sur 30 fractions séparées).

Pour évaluer le gain d'efficacité en radiobiologie classique, il est d'usage d'utiliser l'Efficacité Biologique Relative (EBR) [120] qui se définit comme le rapport d'une dose de rayonnement standard (par exemple photons) à une dose de tout autre type de particules ionisantes (c'est-à-dire protons, neutrons, etc) pour produire le même effet biologique [16]. L'EBR est cliniquement pertinente car elle peut permettre aux cliniciens d'adapter les doses délivrées en fonction des performances du nouveau système ou stratégie thérapeutique, par rapport aux traitements conventionnels. Par exemple, les physiciens médicaux et les radio-oncologues devraient délivrer 30 Gy avec des NPs au lieu de délivrer 60 Gy, si la stratégie thérapeutique « Rayons X avec des NPs » était caractérisée par un EBR de 2. Le concept d'EBR a déjà été discuté par la Commission internationale de protection radiologique (ICRP) [121] et la commission internationale des unités et mesures de rayonnement (ICRU) [122].

Les principes théoriques des interactions des rayons X avec les NPs ont déjà été décrits dans la littérature [123]. Les interactions des rayons X avec la matière se produisent principalement à basse énergie où l'effet photoélectrique est dominant. L'effet photoélectrique se produit lorsque le photon X incident est absorbé par l'atome, ce qui entraîne l'éjection d'un électron. Cet effet prévaut jusqu'à ce que l'énergie du photon atteigne une énergie moyenne (par exemple 500 keV pour Au) avec une section efficace variant avec Z^4 ou Z^5 selon le matériau et est renforcée par une absorption accrue par les couches d'électrons (K, L, M, etc.) aux basses énergies. C'est pourquoi les NPs radiosensibilisantes sont basées sur des matériaux à Z élevé.

Comme l'atome est dans un état ionisé, un rayon de fluorescence X ou une émission d'électrons suit l'éjection d'un photoélectron. Des études plus théoriques peuvent être trouvées dans la littérature [124]. L'effet Auger concerne surtout les atomes à faible Z [125] et ne serait donc pas un contributeur majeur à la dose déposée en présence de NP à Z élevé. En effet, il est dominant pour $Z < 15$ mais presque égal à 0 pour $Z > 60$ [126]. Un photoélectron est émis avec toute l'énergie du photon incident diminuée de l'énergie de liaison. Un électron Auger peut également être émis avec une énergie représentant la différence énergétique entre deux couches électroniques (**Figure 18**).

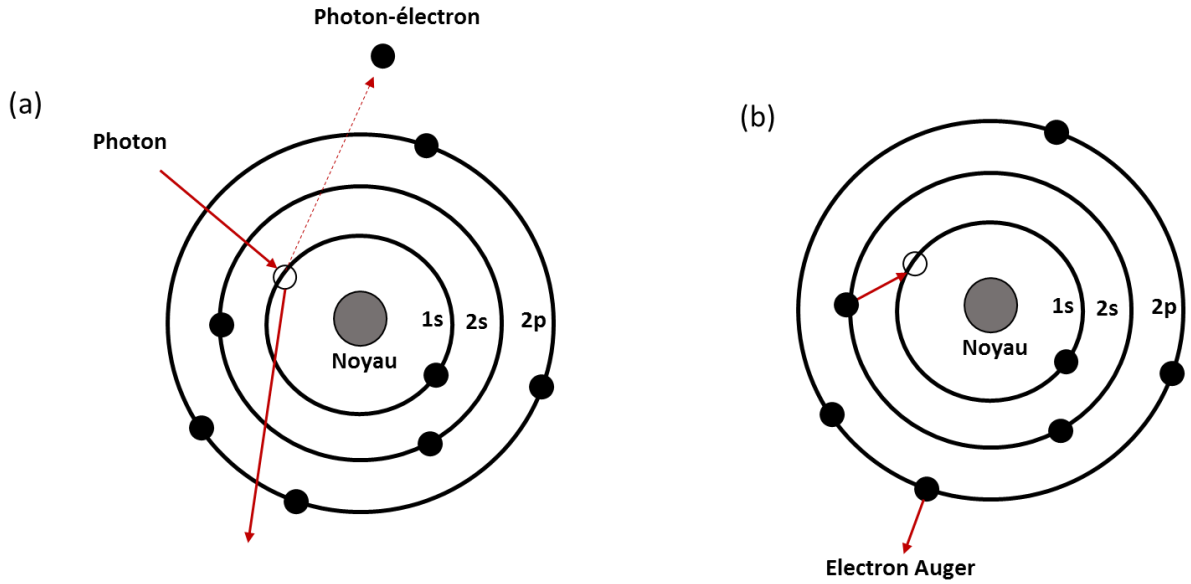

Figure 18 : Effet Auger. (a) illustre séquentiellement les étapes impliquées dans la désexcitation Auger. (b) Un électron incident (ou un photon) crée un trou de cœur dans le niveau 1s. Un électron du niveau 2s remplit le trou 1s et l'énergie de transition est transmise à un électron 2p qui est émis. Le niveau atomique final a ainsi deux trous, un sur l'orbitale 2s et un autre sur l'orbitale 2p.

Pour les faisceaux de moyenne ou haute énergie (toujours polyénergétiques en routine clinique), la composante de basse énergie du spectre interagit avec la matière par effet photoélectrique et les composantes de moyenne et haute énergie sont plus susceptibles d'interagir par effet Compton. L'effet Compton est dû à une déviation du photon incident qui cède une partie de son énergie à l'électron éjecté. Cet effet ne dépend pas du Z des cibles. Le photon diffusé, selon son énergie, déclenchera soit des effets photoélectriques, soit des effets Compton.

L'excitation par rayons X induit l'émission d'électrons secondaires qui seraient responsables de la majorité des dommages cellulaires. Il convient de noter que pour les photons de très basse énergie, le photoélectron éjecté peut ne pas transporter une énergie suffisante pour provoquer des ionisations ultérieures. Des informations contraires sur la dose déposée par Auger ou les photoélectrons au voisinage des NPs ont été publiées dans la littérature.

McMahon et al. [127] ont trouvé que la contribution des électrons Auger était dominante et Douglass et al. [128] ont affirmé que la contribution des électrons Auger était insignifiante même s'ils utilisaient le même code de simulation. Certains auteurs ont décrit un phénomène d'auto-absorption qui peut être amplifié par la taille des NPs et la présence d'autres atomes à Z élevé dans son voisinage (par exemple un groupe de NP). Les espèces secondaires à faible énergie seraient les premières à être absorbées. Par conséquent, la conception des NPs est de la plus haute importance concernant l'amélioration de la radiothérapie ; les composants à Z élevé peuvent augmenter le nombre d'espèces secondaires en raison d'un Z^5 la dépendance de l'effet photoélectrique et des NPs ou clusters plus grands tend à favoriser l'auto-absorption des électrons de faible énergie.

Les NPs à base de métaux lourds ont également été suggérés comme agents théranostiques efficaces ciblant les tumeurs avec une double fonction : système ciblé efficace pour l'imagerie tumorale et amplificateur de dose d'irradiation pour la radiothérapie sous la direction de

l'imagerie par tomodensitométrie [129]. Guidés par l'imagerie par tomodensitométrie à rayons X ciblée sur la tumeur, leur effet radiosensibilisant a été étudié à l'aide d'un faisceau de photons clinique à mégavoltage.

IV.6.1.2.2 Génération de ROS sous les rayons X

Les mécanismes impliqués dans la génération de ROS lors d'une irradiation aux rayons X en présence de NPs diffèrent selon la composition, la taille et le potentiel de ces NPs.

Il a été démontré que les SPION (*Superparamagnetic Iron Oxide Nanoparticles*) recouverts de citrate peuvent fonctionner comme d'excellents radiosensibilisateurs en améliorant l'impact des rayons X sur la génération de ROS d'environ 240 % par rapport aux cellules traitées aux rayons X sans SPION internalisés. La production de ROS dans les cellules chargées d'oxyde de fer NP a été expliquée comme provenant à la fois de la libération d'ions de fer et des surfaces catalytiquement actives des NP de silice avec une oxydation de SiO_2 après irradiation [130].

Fait intéressant, un lien a été mis en évidence entre la localisation intracellulaire des SPION et la génération de ROS ; la fonctionnalisation avec une fonction amine des NPs de silice peut augmenter significativement la production de ROS en raison de leur charge de surface positive, ce qui facilite l'accumulation de NPs dans les membranes du réticulum endoplasmique, des vésicules et surtout des mitochondries. La présence de SPIONs dans les membranes induit également une peroxydation des lipides membranaires, améliorant l'effet radiosensibilisant [131].

IV.6.1.2.3 X-PDT

Toujours dans l'objectif d'améliorer l'efficacité de la PDT, une nouvelle approche a été proposée. Cette nouvelle approche, que nous appellerons X-PDT, est l'utilisation des rayons X, qui peuvent pénétrer plus profondément dans les tissus que la lumière. Un nombre croissant de publications décrit la conception de nouveaux systèmes pour X-PDT.

Dans les années 90, Kokotov et al. ont réussi à activer l'hématoporphyrine dérivée (HpD) par les rayons X [132]. Dans les années suivantes, d'autres PS ont été testés pour confirmer que ce sont également des radiosensibilisateurs comme : PpIX [133], 5-ALA [134], Photofrin II [135].

Depuis 2006, l'idée de l'utilisation des rayons X avec des NPs a été publiée par Chen et al. [136] (**Figure 19**). Une fois irradié par des rayons X, le scintillateur émet une lumière visible qui peut être absorbée par le PS, qui, à son tour génère de l'$^1O_2$. Ils ont été les premiers à utiliser la X-PDT. Ils ont démontré qu'il suffit d'irradier avec 0,44 Gy/min une nanoparticule LaF_3 : Tb^{3+} couplé à une porphyrine pour produire de l'$^1O_2$ et induire le mort cellulaire. La production d'$^1O_2$ était plus importante avec les NPs-PS qu'avec les PS seuls. L'énergie utilisée dans cette étude (250 Kev) est beaucoup plus petite que celle de la radiothérapie classique (en Mev).

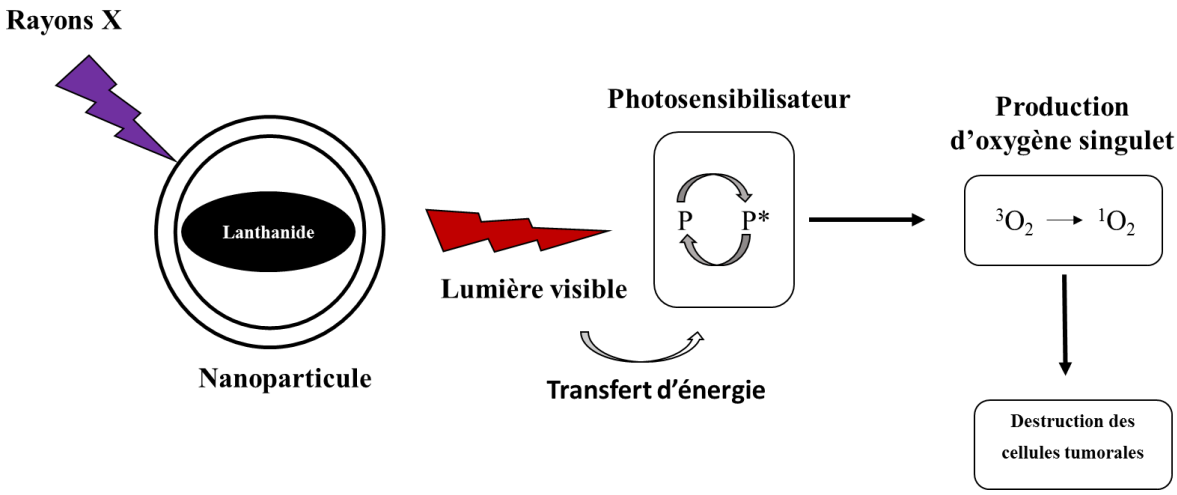

Figure 19 : Effet X-PDT. P= Photosensibilisateur à l'état fondamental, P = Photosensibilisateur à l'état excité*

Pour être efficace en tant qu'agent pour la X-PDT, les NPs sélectionnées avec, dans le cœur un scintillateur, et un PS au niveau matriciel, doivent répondre aux exigences suivantes : le spectre d'émission du nanoscintillateur doit correspondre au spectre d'absorption du PS garantissant par transfert d'énergie une activation efficace de la molécule photo-activable et la production d'$^1O_2$; le nanoscintillateur doit émettre après excitation aux rayons X et produire de la luminescence; le PS doit être facilement couplé à la NP avec un taux de charge ajustable; la NP doit être non-toxique, stable dans un environnement biologique avec une biocompatibilité optimisée par *coating* afin d'empêcher les opsonines de s'adsorber à sa surface. L'absorption des rayons X est directement dépendante de Z^4 ou Z^5 (Z étant le numéro atomique de l'élément considéré). Ainsi, les matériaux lourds facilitent le phénomène d'absorption [137].

Il n'est pas possible actuellement de définir la X-PDT comme une modalité clinique au même titre que la radiothérapie ; en effet, de nombreux paramètres restent à être optimisés

- Le rendement quantique des nanoscintillateurs : les matériaux de forte densité auront un pouvoir d'arrêt des grandes radiations et un plus grand cœfficient d'absorption. Les NPs présentant un déplacement de Stokes petit auront une efficacité de luminescence plus grande. Cette propriété provient du couplage électron-phonon ; s'il est petit, le déplacement de Stokes est petit, et le rendement de scintillation est grand.

- L'optimisation du transfert d'énergie entre scintillateur et le chromophore : choix du PS, de la concentration (le rendement dépend de la distance entre scintillateur et PS mais également de la distance PS-PS pour éviter des transferts non radiatifs, et de la distance (inférieure en tout état de cause à quelques dizaines de nm pour avoir un transfert efficace).

- L'optimisation de la formation en $^1O_2$ (choix du PS, taille des NPs permettant une bonne diffusion de l'oxygène et une bonne diffusion de l'$^1O_2$ en dehors de la NP pour atteindre la cible).

IV.6.1.3 γ-PDT

C'est l'activation directe du PS par le rayonnement de Cerenkov, appelée PDT induite par Cerenkov (CR-PDT) [13,14]. Il a été prouvé qu'un tel traitement pourrait être une synergie entre l'effet radiothérapeutique et photothérapeutique, ce dernier impliquant uniquement l'activation des PSs. Cependant, malgré les différentes études récentes démontrant un réel bénéfice en termes de diminution de la croissance tumorale, il existe toujours un débat sur la présence d'un effet photothérapeutique cytotoxique. En effet, le nombre de photons absorbés par le PS étant inférieur à ceux impliqués dans la PDT, la quantité d'$^1O_2$ produite est très faible. La γ-PDT pourrait donc, en optimisant ces conditions, former une révolution dans la PDT pour surmonter le problème de la mauvaise pénétration de la lumière et des effets secondaires des rayons X. Nous avons écrit une revue à ce sujet, située dans le sous-chapitre I.

Outre la limitation de la faible pénétration de la lumière dans les tissus, un autre inconvénient de la PDT traditionnelle est le manque de sélectivité des PSs. Il est possible de vectoriser les PSs.

IV.6.2 Ciblage des PSs

Le manque de sélectivité des PSs commerciaux présente des inconvénients. Les chercheurs travaillent depuis des années à la recherche de PS beaucoup plus spécifiques. Il est possible de distinguer deux types de ciblage :

Ciblage passif

Dans le cas des cancers solides, les tumeurs présentent une néo-vascularisation qui se développe en parallèle de la prolifération des cellules pour compenser les besoins croissants en nutriments et en oxygène. La croissance de ces vaisseaux sanguins en milieu inflammatoire entraîne l'apparition de défauts de jonction dans les cellules endothéliales, conduisant à la formation de pores, et augmentant la perméabilité vasculaire. Les cellules cancéreuses compriment aussi les canaux lymphatiques, réduisant le drainage lymphatique. Mécaniquement, ces deux phénomènes vont permettre aux NPs de pénétrer et de s'accumuler dans le tissu cancéreux par diffusion, c'est l'effet EPR (*Enhanced Permeability and Retention*) [138]. Dans les tissus sains, les jonctions intercellulaires sont serrées, ce qui prévient les nanovecteurs. Cet effet découvert en 1986 par Maeda et ses collaborateurs peut être exploité pour le ciblage passif des tissus tumoraux (**Figure 20**).

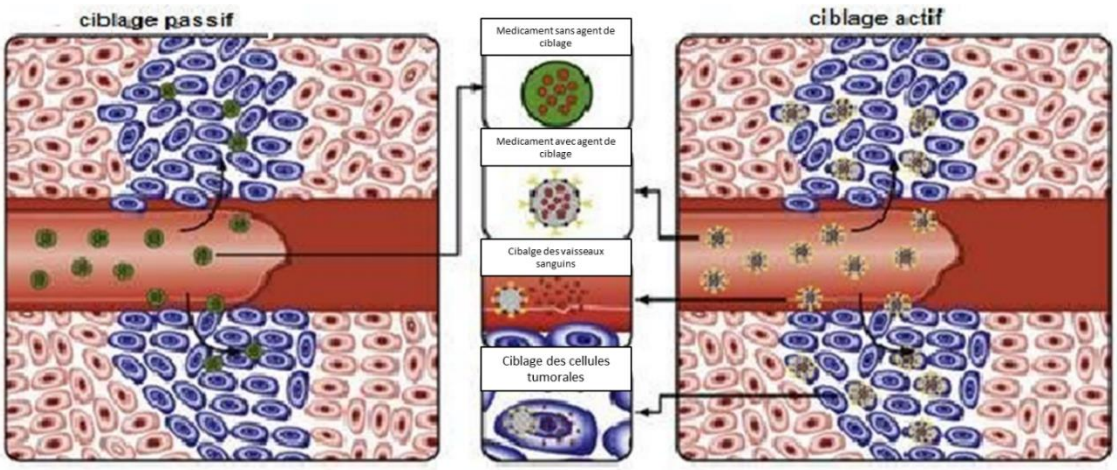

Figure 20 : Les ciblages actif et passif adapté de Wang et al. 2016.

Cet effet est exprimé dans de nombreuses tumeurs solides ainsi que certains nodules tumoraux métastatiques. Des composés de haut poids moléculaire comme les polymères ou des NPs dont le diamètre est compris entre 10 et 500 nm peuvent, par ce biais, s'accumuler préférentiellement dans les tissus tumoraux [139].

Pour cibler de manière spécifique les cellules cancéreuses, il faut avoir recours à un ciblage dit actif.

Ciblage actif

Les PS peuvent être fonctionnalisés avec des ligands capables d'interagir avec les récepteurs surexprimés à la surface des cellules cancéreuses [140]. L'interaction entre ligand et récepteur permet une internalisation sélective par endocytose. Il s'agit ici d'un ciblage actif. (voir sous-chapitre II) [141].

Deux types de cellules peuvent être ciblés : les cellules cancéreuses et l'endothélium tumoral. Le ciblage des cellules cancéreuses vise à améliorer l'accumulation des PSs ou NPs dans ces dernières pour éliminer la tumeur tandis que le ciblage de l'endothélium tumoral a pour but de détruire la néovascularisation pour priver les cellules cancéreuses en oxygène et en nutriments en les asphyxiant [142].

IV.6.3 Nécessité en Oxygène

L'un des problèmes de la PDT est le besoin d'oxygène pour induire un effet photodynamique. Les tumeurs ont souvent de faibles concentrations en oxygène, liées à la structure anormale des microvaisseaux conduisant à une distribution sanguine inefficace. De plus, PDT consomme de l'$^1O_2$. Afin d'améliorer l'oxygénation de la tumeur ou de diminuer l'hypoxie, différentes stratégies sont développées et décrites dans la littérature : L'utilisation de véhicules de O_2, la modification du microenvironnement tumoral, la combinaison avec d'autres thérapies, une PDT indépendante de l'oxygène, l'utilisation de la PDT fractionnée [143].

V. Les nanoparticules

V.1 Généralité

D'après la commission de l'Union européen, et l'encadrement juridique des nano-objets et matériaux, le nanomatériau est un matériau dont les principaux composants se situent entre 1 et 100 nm (**Figure 21**). Une NP est une particule qui se situe dans la gamme des tailles des protéines. C'est un assemblage des milliers d'atomes [144].

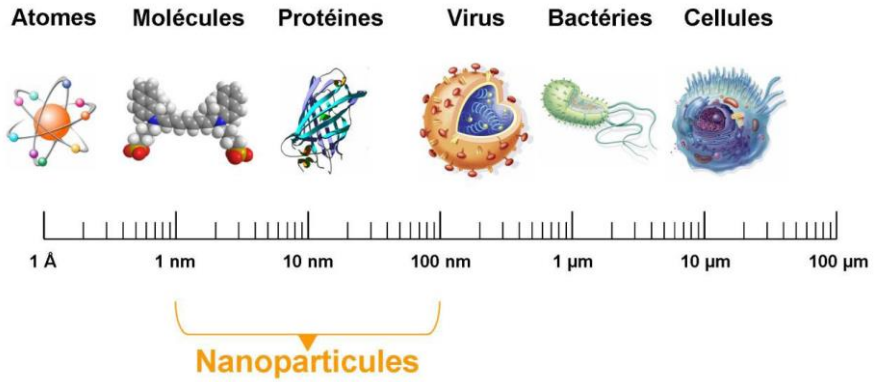

Figure 21 : Échelle de taille des NPs comparées aux principales structures chimiques et biologiques [145].

V.2 Nano-objets

On désigne par nano-objets les matériaux nanostructurés qui ont une, deux ou trois dimensions externes à l'échelle nanométrique **(Figure 22)** [146] :

- Dendrimères, NPs polymériques ou micelles (polymères)
- Liposomes (Lipidique)
- NP virales (Virus)
- Matériaux en silicone ou en carbone
- NPs magnétiques
- Nanofibres :
  - nanotubes, si les nanofibres sont creuses, (nanotubes de carbone),
  - nanotiges, si les nanofibres sont pleines, (nanofibres de polyesters),
  - nanoconducteurs, dans le cas de nanofibres électriquement conductrices ou semi-conductrices,
- Nanoplaques :
  - nanofeuillets, (nanofeuillets d'argile)
  - nanocouches
  - nanorevêtements.

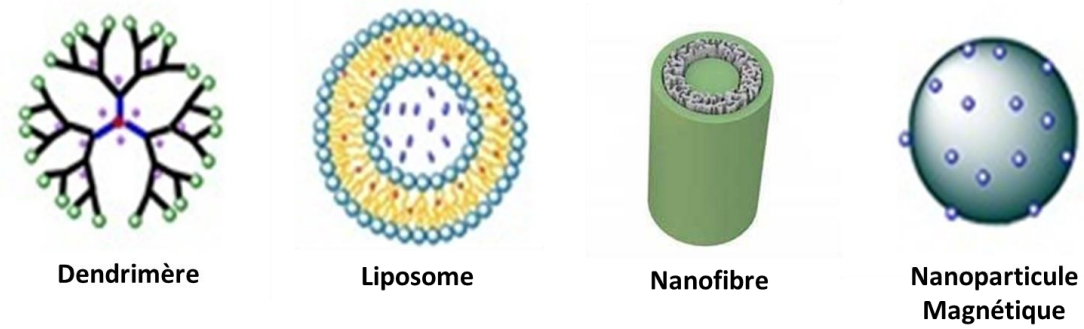

Figure 22 : Représentation schématique de certaines NPs

V.3 Caractéristique des NPs

Un nano-vecteur utilisable en PDT doit répondre à certaines caractéristiques [147] :

- Il doit être biocompatible et/ou biodégradable, il ne doit pas induire d'effets secondaires liés à son administration,
- Il doit présenter des propriétés de furtivité afin d'échapper au système immunitaire et ainsi éviter sa capture par des cellules du système réticulo-endothélial (macrophages),
- Il doit faciliter le transport de la molécule thérapeutique jusqu'à sa cible et la protéger dans les conditions physiologiques,
- Il doit libérer la molécule au niveau de sa cible de manière efficace si ces NPs jouent le rôle d'une capsule.

Différents types de nano-vecteurs sont actuellement développés pour améliorer le traitement de différentes pathologies, dont le cancer. A ce jour, seule la visudyne® (liposome) est un nano-objet utilisé cliniquement en PDT.

V.4 Paramètres physiologiques à prendre en compte dans la conception des nano-vecteurs

V.4.1 Le système réticuloendothélial

Le système réticulo-endothélial correspond à un ensemble de cellules disséminées dans l'organisme, plus particulièrement au niveau du foie, de la rate et la moelle osseuse. Ce système possède diverses fonctions dont la fabrication des éléments du sang et la destruction des corps considérés comme étrangers que peuvent représenter les nano-vecteurs. Lorsqu'ils entrent dans l'organisme, les nano-vecteurs peuvent être pris en charge par des phagocytes et être éliminés. Ce traitement peut activer la sécrétion de cytokines provoquant une inflammation locale et une détérioration des tissus. Afin d'éviter la prise en charge non spécifique des NPs par des tissus sains, leur chimie de surface peut être modifiée pour empêcher l'adsorption de certaines protéines. La fonctionnalisation avec la PEGylation peut empêcher l'adsorption non spécifique de certaines protéines ainsi que l'opsonisation. Ce processus correspond à la fixation de protéines du plasma (appelées opsonines) à la surface des NPs, favorisant ainsi leur prise en charge par les macrophages et par conséquent leur phagocytose. La présence de PEG à la

surface des NPs augmente leur temps de circulation dans le sang [148]. La forme, la taille, la charge de surface, l'hydrophobie ainsi que la chimie de surface jouent aussi un rôle dans la reconnaissance au niveau du système immunitaire.

V.4.2 Le système rénal

Le procédé d'ultrafiltration rénale peut réguler la pharmacocinétique des NPs. La taille, la forme et la charge des NPs sont des paramètres importants dans la voie d'élimination rénale. Les NPs sphériques, lorsqu'elles ont un diamètre inférieur à 6 nm, sont éliminées par cette voie. En revanche, les particules de diamètre supérieur à 8 nm passent avec difficulté la barrière de filtration glomérulaire [149].

V.4.3 La barrière hémato-encéphalique

La barrière hémato-encéphalique (BHE) bloque près de 98 % des molécules. Le franchissement de cette barrière est l'un des plus grands défis à relever pour parvenir à transporter des principes actifs au niveau du système nerveux central. Des études ont montré que des NPs peuvent passer la BHE par l'intermédiaire de récepteurs exprimés au niveau de cellules endothéliales, entraînant une endocytose et le transport vers le système nerveux central. Pour ce faire, les NPs doivent être fonctionnalisées avec des ligands de ciblage, ou des surfactants (comme le polysorbate 80 ou le poloxamère 188) qui permettent l'adsorption spécifique de certaines protéines (apo-lipoprotéines E ou A-I) qui sont capables d'interagir avec les récepteurs spécifiques exprimés au niveau de la BHE. La taille des NPs a également de l'importance avec un diamètre idéalement compris entre 20 et 70 nm. La charge joue aussi un rôle car les NPs neutres ou chargées négativement en surface n'altèrent pas la BHE alors que celles chargées positivement sont neurotoxiques du fait de la perméabilité augmentée. En dehors de ces considérations physiologiques, dans le cadre du traitement de tumeurs solides, les nano-vecteurs doivent parvenir à atteindre les cellules cancéreuses de manière spécifique [149, 150].

V.5 Génération des nanoparticules

V.5.1 Les nanomédicaments de première génération : nanoparticules nues

Au cours de l'administration intraveineuse de NPs, les NPs de première génération se concentrent principalement dans le foie, sous-entendu dans les tissus du système réticulo-endothélial. Ce phénomène est principalement dû au fait qu'ils ont une grande surface spécifique, sur laquelle plusieurs protéines plasmatiques, en particulier les opsonines, sont adsorbées, qui seront ensuite reconnues de façon sélective par les macrophages hépatique. Ces derniers interagissent ensuite avec les nanovecteurs, c'est pourquoi les nanovecteurs de première génération se concentrent rapidement au niveau du foie. Ceci peut être considéré comme un désavantage, mais il est possible d'en tirer profit. En effet, ces systèmes constituent de véritables navettes pour l'administration sélective de médicaments au tissu hépatique. De cette façon, il est possible de traiter efficacement les maladies hépatiques graves, comme le cancer résistant de l'hépatome et les métastases hépatiques [151].

V.5.2 Les nanoparticules de deuxième génération : nanoparticule furtives

Comme déjà mentionné, l'idée est d'ajouter à la surface des NPs de première génération des polymères hydrophiles et flexibles de type polyéthylèneglycol PEG. Ces polymères sont capables de repousser les opsonines qui sont responsables de la capture des NPs par le foie après qu'elles se soient fixées à leur surface. Ce sont les NPs de deuxième génération dites furtives [152].

Cela se fait suivant le principe physico-chimique de « répulsion stérique ». Les modifications présentes à la surface des NPs crée un encombrement stérique rendant ces particules furtives pour le corps humain et le foie ne les reconnait pas [153].

V.5.3 Les nanoparticules de troisième génération : nanoparticules ciblantes

Ces NPs sont conçues pour pénétrer à l'intérieur des cellules pour un ciblage intracellulaire. Il est possible d'ajouter des agents de ciblage qui sont reconnus par des récepteurs situés dans les membranes tumorales, leur permettant de former des complexes ligand-récepteur. Cette génération de NPs va permettre une accumulation préférentielle des NPs dans les tissus à traiter et diminuer les effets secondaires dus à la non-spécificité et l'incorporation dans les tissus sains.

Parmi les agents de ciblage qui peuvent être greffés en surface de NPs pour favoriser la reconnaissance avec un type cellulaire, il existe l'acide folique, des anticorps monoclonaux, des peptides (Sous-chapitre I.2)…

VI. NPs dans la PDT

VI.1 Importance des NPs dans la PDT

La plupart des PSs sont hydrophobes et insolubles dans l'eau ou le milieu biologique. Les NPs sont considérées comme des véhicules pour les PSs. Le transport des PS par les NPs peut être réalisé par adsorption, liaison covalente ou encapsulation. La liaison covalente stable semble être plus avantageuse que les autres méthodes car elle permet de contrôler la quantité de PS greffée sur les nanoporteurs [154]. Des agents de ciblage peuvent être aussi couplés sur ces NPs induisant un ciblage actif en plus du ciblage passif apporté par les NPs elles-mêmes (voir sous-chapitre III).

VI.2 Les AGuIX®

VI.2.1 Structure et généralité

La société NHTherAguix développe des nanoplateformes nommées AGuIX®. C'est un nanomédicament hybride ultrapetit. Ces NPs de quelques nanomètres sont composées d'une matrice de polysiloxane et de complexes de lanthanide (Gd : agent de contraste positif en IRM) greffés dans les DOTA. Les AGuIX ont un diamètre hydrodynamique moyen d'environ 3,5 ± 1,0 nm et une masse d'environ 10 kDa permettant une simple élimination rénale [155]. Elles ont été développées initialement à l'Université Claude Bernard à Lyon puis par la société NhTherAguix. Un essai de phase 1 a été fait en radiothérapie sur 15 patients ayant 4 types de tumeurs différents (colon, poumon, sein et mélanome). Après l'évaluation clinique de ces essais, les AGuIX sont entrées en phase 2 pour traiter, par radiothérapie, les métastases du

cancer du cerveau. Notre équipe a montré qu'il était possible de les coupler à des PSs pour faire de la PDT ciblée [156] (**Figure 23**).

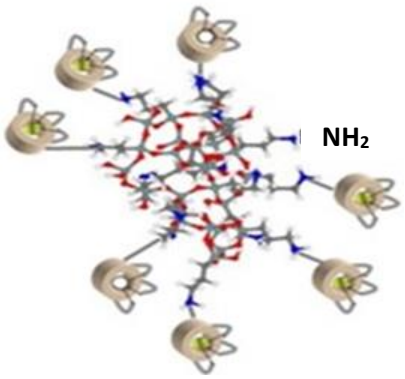

Figure 23 : Représentation des NPs AGuIX

La structure polysiloxane confère une bonne biocompatibilité aux AGuIX. Les AGuIX sont biodégradables en milieu dilué, les sous-produits dégradés ne sont pas toxiques. Elles sont facilement éliminées du corps et ne présentent pas d'élimination rénale retardée, ni d'absorption dans le système phagocytaire mononucléaire. Les AGuIX montrent une incorporation rapide dans la tumeur et une élimination *via* les reins sans rétention significative dans les autres organes. Les AGuIX n'affectent ni la fonction neurologique, ni les fréquences cardiaques et respiratoires. Aucune réaction d'hypersensibilité n'a été remarquée.

VII. Les lanthanides

VII.1 Généralités

Les lanthanides constituent une ligne dans la classification chimique périodique de Mendeleïev des éléments chimiques. Ces éléments chimiques ont des numéros atomiques compris entre 57 et 71. Ils comprennent : le Lanthane (La), le Cérium (Ce), le Praséodyme (Pr), le Néodyme Nd, le Prométhéum (Pm), le Samarium (Sm), l'Europium (Eu), le Gadolinium (Gd), Terbium (Tb), le Dysprosium (Dy), l'Holmium (Ho), l'Erbium (Er), le Thulium (Tm), l'Ytterbium (Yb), le Lutécium (Lu). En ajoutant le Scandium et l'Yttrium à cette famille de 15 éléments, la famille de « terres rares » est formée.

Les terres rares sont de plus en plus recherchées dans l'industrie pour des applications automobile, informatique, technologique et aéronautique. Elles sont utilisées dans les LED [157], dans les batteries de voitures électriques et hybrides [158], dans les éoliennes [159], dans les puces de smartphone [160], les écrans d'ordinateur portable [161] et dans les panneaux photovoltaïques [162]. Les systèmes d'arme et de ciblage [90], les capteurs de radars et sonars [163] se basent dans leur composition sur les lanthanides. Elles sont aussi aujourd'hui indispensables dans des applications d'imagerie et de traitement médical [164, 165]. Ces métaux « stratégiques » ont été découverts pour la première fois en 1787 par le Suédois, Carl Axel Arrhenius dans une carrière près de Stockholm [166].

VII.2 Caractéristique électronique des lanthanides [167]

A l'exception du lanthane et du lutétium, la famille lanthanide est l'ensemble des éléments chimiques de la classification périodique ayant 4f au cours de remplissage comme sous couche [168]. A l'état atomique, les lanthanides ont la configuration électronique suivante :

$$[Ln]\ 6s^2\ 5d^1\ 4f^n \quad \text{avec } 0 \leq n \leq 14$$

Le **Tableau 2** regroupe les configurations électroniques des différents lanthanides

Tableau 2 : Caractéristiques électroniques des lanthanides : numéro atomique, configuration électronique Ln et de son ion trivalent.

Nom	Numéro atomique	Symbole	Configuration électronique (Ln)	Configuration électronique (Ln^{3+})
Lanthane	57	La	[Xe] $6s^2\ 5d^1$ (*)	[Xe] $4f^0$
Cérium	58	Ce	[Xe] $6s^2\ 4f^1\ 5d^1$ (*)	[Xe] $4f^1$
Praséodyme	59	Pr	[Xe] $6s^2\ 4f^3$	[Xe] $4f^2$
Néodyme	60	Nd	[Xe] $6s^2\ 4f^4$	[Xe] $4f^3$
Prométhium	61	Pm	[Xe] $6s^2\ 4f^5$	[Xe] $4f^4$
Samarium	62	Sm	[Xe] $6s^2\ 4f^6$	[Xe] $4f^5$
Europium	63	Eu	[Xe] $6s^2\ 4f^7$	[Xe] $4f^6$
Gadolinium	64	Gd	[Xe] $6s^2\ 4f^7\ 5d^1$ (*)	[Xe] $4f^7$
Terbium	65	Tb	[Xe] $6s^2\ 4f^9$	[Xe] $4f^8$
Dysprosium	66	Dy	[Xe] $6s^2\ 4f^{10}$	[Xe] $4f^9$
Holmium	67	Ho	[Xe] $6s^2\ 4f^{11}$	[Xe] $4f^{10}$
Erbium	68	Er	[Xe] $6s^2\ 4f^{12}$	[Xe] $4f^{11}$
Thulium	69	Tm	[Xe] $6s^2\ 4f^{13}$	[Xe] $4f^{12}$
Ytterbium	70	Yb	[Xe] $6s^2\ 4f^{14}$	[Xe] $4f^{13}$
Lutécium	71	Lu	[Xe] $6s^2\ 4f^{14}\ 5d^1$	[Xe] $4f^{14}$

(*) Exceptions à la règle de Klechkowski concernant le lanthane $_{57}$La, le cérium $_{58}$Ce et le gadolinium $_{64}$Gd. [169]. La contraction lanthanidique [170] est expliqué par le fait que la force d'attraction entre le noyau et les électrons est plus importante avec l'augmentation de la charge apparente du noyau. La charge apparente du noyau augmente avec l'augmentation du numéro atomique de gauche à droite de la série.

L'électron *4f* est le plus externe. Il est bien protégé par les électrons des sous niveaux *5s* et *5p* [171]. L'électron de l'orbitale *4f* ne participe pas à la liaison chimique et à la stabilisation du champ cristallin des complexes. L'orbitale *4f* est plus proche du noyau que *5d* et *6s* [172]. Puisque les orbitales *5d* et *6s* sont déjà remplies à l'état fondamental, les électrons de ces niveaux sont protégés par les couches électroniques supplémentaires. Elles ne sont pas ou peu influencées par l'environnement. L'orbitale 4*f* non remplie est celle responsable des propriétés optiques et magnétiques.

Cependant, l'orbitale la plus externe est remplie ou vide, a peu d'effets sur les propriétés chimiques, n'affecte pas les propriétés magnétiques et les spectres d'émission. L'état d'oxydation le plus élevé se trouve généralement dans les fluorures et les oxydes [173], et l'état d'oxydation le plus faible dans les halogénures (bromures et iodures) [174]. En général, les lanthanides ont une tendance à perdre facilement trois électrons de leur couche externe pour former les ions trivalents Ln (III). L'état +3 est le plus stable et saturé en couche externe.

C'est donc les électrons 4f des lanthanides qui confèrent les propriétés optiques et magnétiques particulièrement intéressantes.

VII.3 Propriétés physiques

Comme les ions lanthanides ont des configurations électroniques différentes, ils ont aussi des structures cristallines différentes. Ils ont cinq structures cristallines à la température ambiante : structure 9-hcp (hexagonale compacte), une structure 4-dhcp (double axe c hcp), des 2-fcc (cubique à faces centrées) et 1-bcc et des structures rhombiques. Un changement de température entraîne un changement de la structure cristalline [175]. Ainsi, la terre rare est utilisée pour les oxydes de Ln^{3+}. La plupart de Ln^{3+}sous forme de sel sont solubles dans l'eau [176].

Les propriétés physiques de Ln^{3+} dépendent de leur solubilité, leur couleur, leurs propriétés magnétiques, leurs états d'oxydation, leur formation de complexes, etc [177].

VII.4 Propriétés magnétiques

A l'exception du lanthane, de l'ytterbium et du lutécium qui n'ont pas d'électrons célibataire, tous les lanthanides ont des électrons célibataires 4f, et sont des éléments paramagnétiques, qui leur donnent une susceptibilité magnétique élevée [178].

L'ion Gadolinium Gd^{3+} a le nombre maximum d'électrons célibataires, mais les électrons du Gd^{3+} sont de spins parallèles, c'est pour cela qu'il est utilisé comme agent de contraste positif en imagerie par résonance magnétique [179].

VII.5 Propriétés spectroscopiques

C'est l'orbitale f qui met en valeur les caractéristiques magnétique et spectroscopique des lanthanides [180]. Les électrons des orbitales f n'interagissent pas avec des vibrations moléculaires, parce qu'ils sont relativement proches du noyau et ne sont pas influencés par leur environnement. Cet aspect explique les spectres d'émission fins. L'aspect de ces spectres dépend des niveaux d'énergie de chaque lanthanide, ainsi le coefficient d'extinction des lanthanides est très faible, il est de l'ordre de 3 $M^{-1}.cm^{-1}$).

Selon la règle de Laporte [181], les transitions entre les orbitales symétrique f-f sont interdites. Le retour des électrons à l'état fondamental des ions excités est défavorisé, ce qui donne aux lanthanides la caractéristique de longue durée de vie de luminescence.

Trois des lanthanides ne sont pas soumis à ces règles : le lanthane, le lutécium et le Prométhéum. Le lanthane a l'orbitale 4f vide, le lutécium est saturé par des électrons appariés et le Prométhéum possède 4 électrons f non-appariés, est certainement radioactif et ne possède pas d'isotope stable [182].

Les spectres d'émission des lanthanides sont distribués sur toute la zone des longueurs d'onde du visible à l'infra-rouge, à l'exception du Gadolinium qui émet dans l'UV parce qu'il a son premier état excité trop haut **(Figure 24)** [183]. L'aspect de ces spectres d'émission est le résultat des transitions électroniques entre différents niveaux énergétiques.

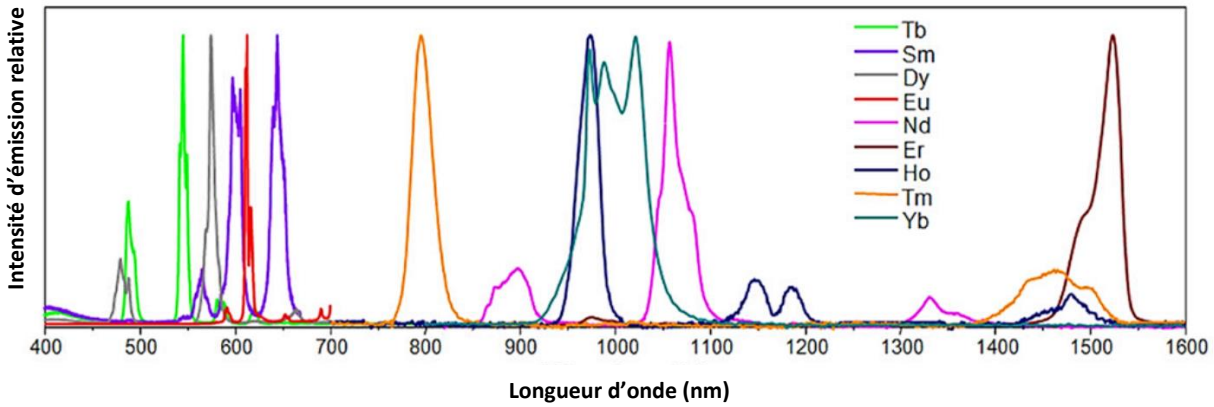

Figure 24 : Spectres d'émission de différents lanthanides dans l'eau [184, 185].

VIII. Objectif de la thèse

L'objectif est de trouver un traitement complémentaire à ceux déjà existants pour traiter le glioblastome, qui reste parmi des cancers les plus graves. La radiosensibilisation des tumeurs hypoxiques, et surtout l'augmentation de la dose d'irradiation délivrée n'ont pas permis d'améliorer significativement les résultats du traitement de ces tumeurs. La radiothérapie standard nécessite une adaptabilité des doses délivrées pour réduire la toxicité et ne pas altérer les tissus sains adjacents. Les recherches actuelles se concentrent à la fois sur l'adjonction d'une thérapie complémentaire locale au sein du foyer opératoire après intervention mais aussi sur la mise au point de technologies innovantes qui contribueraient à rendre moins toxique la radiothérapie pour les tissus sains environnants. Les récentes avancées technologiques nous permettent d'envisager une stratégie thérapeutique novatrice pouvant combiner PDT et radiothérapie *via* l'utilisation de scintillateurs nanoparticulaires excitables par des rayons X.

Les avantages de cette approche thérapeutique associant radiothérapie et PDT sont de pouvoir envisager le synergisme de deux thérapies anti-cancéreuses efficaces, d'être applicable aux tumeurs profondes jusqu'ici non traitables par PDT, et de diminuer le risque de dommage aux tissus sains adjacents grâce à l'adjonction d'une thérapie complémentaire locale. Ceci pourra être source de ramifications considérables en matière de thérapie anti-cancéreuse.

D'après la bibliographie, nous désignons une nanoparticule à base de lanthanide, vu son importance en excitation sous rayon X. nous choisissons le Gadolinium puisqu'il un agent de contraste positif en IRM et le Terbium puisqu'il émet dans une large gamme dans le visible. Sur ces nanoparticules nous avons choisis de coupler ou adsorber un PS qui répond d'une part aux caractéristiques des PS utilisés en PDT et d'autres part qu'il soit accessible de permettre un transfert d'énergie avec les lanthanides choisies. C'était le RB, son importance est introduite dans le sous-chapitre I.3. Nous choisissons aussi un peptide pour un ciblage actif du glioblastome. L'utilisation des peptides couplés sur les nanoparticules est présentée dans le sous-chapitre I.2.

Nous intéressons donc dans cette thèse, à étudier initialement la possibilité d'avoir un transfert d'énergie entre un donneur et un accepteur dans le but d'exciter ce donneur sous rayons X pour qu'il puisse transférer son énergie au PS voisin. Dans un premier temps, nous étudions le transfert d'énergie entre des lanthanides et un PS, en solution. Les AGuIX contenant du Gd ou du Tb ont été choisies comme nanoscintillateurs. Concernant le PS, nous en avons sélectionné plusieurs : une porphyrine, le photofrin et le RB. Pour le RB, une étude sur l'influence de la distance entre le donneur et l'accepteur a également été entreprise.

Dans ce but nous étudions (**Figure 25**):

- Le recouvrement entre le spectre d'absorption de l'accepteur et le spectre d'émission du donneur pour voir la possibilité d'avoir un transfert d'énergie.
- La variation de l'intensité de luminescence et de la durée de vie du donneur en fonction de la concentration de l'accepteur pour préciser le type de transfert d'énergie, lorsque le donneur et l'accepteur sont en solution, adsorbés, ou couplés de façon covalente.

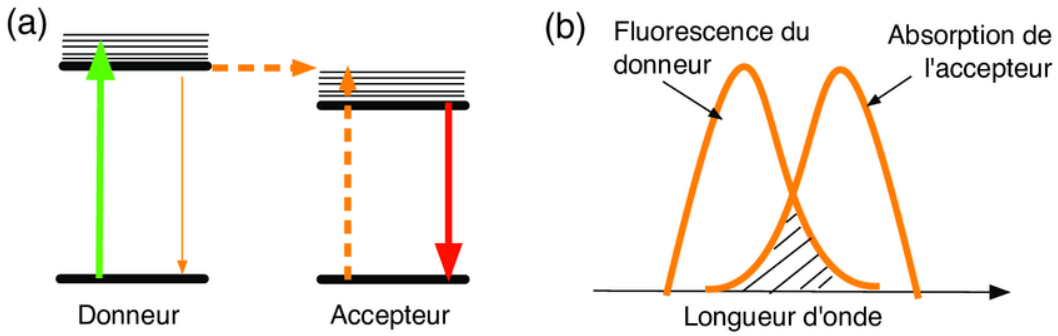

Figure 25: (a) Schématisation du transfert d'énergie entre donneur et accepteur (b) Schématisation du recouvrement entre émission du donneur et absorption de l'accepteur [186].

- Dans un deuxième temps, nous nous sommes attachés à coupler le PS de façon covalente aux AGuIX.
- Enfin, un peptide de ciblage qui a une affinité pour les récepteurs NRP-1a également été greffé aux NPs multifonctionnelles.

Toutes les AGuIX développées ont été caractérisées (taille, potentiel zéta), les propriétés photophysiques ont été réalisées (absorption, émission de fluorescence, formation d'$^1O_2$ après illumination ou irradiation). Des tests biologiques d'affinité des peptides couplés à l'AGuIX ont été faits ainsi que de tests MTT *in vitro* pour évaluer la PDT.

Reference

[1] M. Gultekin, P. T. Ramirez, N. Broutet, and R. Hutubessy, "World Health Organization call for action to eliminate cervical cancer globally," *International Journal of Gynecological Cancer,* vol. 30, pp. 426-427, 2020.

[2] J. C. Fisher and J. H. Hollomon, "A hypothesis for the origin of cancer foci," *Cancer,* vol. 4, pp. 916-918, 1951.

[3] J. E. Visvader, "Cells of origin in cancer," *Nature,* vol. 469, pp. 314-322, 2011/01/01 2011.

[4] O. Warburg, "On the Origin of Cancer Cells," *Science,* vol. 123, pp. 309-314, 1956.

[5] B. Vogelstein and K. W. Kinzler, "The multistep nature of cancer," *Trends in genetics,* vol. 9, pp. 138-141, 1993.

[6] E. Farber, "The multistep nature of cancer development," *Cancer research,* vol. 44, pp. 4217-4223, 1984.

[7] A. Coulon, S. Milin, E. Laban, C. Debiais, C. Jamet, and J.-M. Goujon, "Aspects histopathologiques des principales tumeurs des nerfs périphériques," *Neurochirurgie,* vol. 55, pp. 454-458, 2009.

[8] F. Clère, E. Carola, C. Halimi, A. De Gramont, S. Bonvalot, Y. Panis, *et al.*, "Actualités sur les tumeurs stromales gastro-intestinales: à partir de sept observations de tumeurs malignes," *La Revue de médecine interne,* vol. 23, pp. 499-507, 2002.

[9] C. d. l. Fouchardière, J.-C. Lifante, J.-L. Peix, and J.-P. Droz, "Tumeurs atypiques de la thyroïde et formes réfractaires," in *Tumeurs malignes rares*, ed: Springer, 2010, pp. 451-457.

[10] S. Gisselbrecht, "Oncogènes et leucémies: historique et perspectives," *médecine/sciences,* vol. 19, pp. 201-210, 2003.

[11] P. Gaulard, "Classification des lymphomes non hodgkiniens," *Médecine thérapeutique,* vol. 6, pp. 343-52, 2000.
[12] J.-M. Coindre, "Biologie moléculaire des sarcomes," *Bulletin du cancer,* vol. 97, pp. 1337-1345, 2010.
[13] P. Maroun, J. Gligorov, J. Ohnona, C. Murariu, and Y. Belkacémi, "Détermination de HER2 dans les adénocarcinomes pour établir le pronostic et prédire la réponse aux traitements," *Bio tribune magazine,* vol. 36, pp. 30-35, 2010.
[14] J.-P. Thiery, "Transitions épithélium mésenchyme dans le développement et la progression des carcinomes," *Bulletin de l'Académie Nationale de Médecine,* vol. 193, pp. 1969-1979, 2009.
[15] M. S. O'Reilly, L. Holmgren, Y. Shing, C. Chen, R. A. Rosenthal, M. Moses*, et al.*, "Angiostatin: a novel angiogenesis inhibitor that mediates the suppression of metastases by a Lewis lung carcinoma," *cell,* vol. 79, pp. 315-328, 1994.
[16] L. Brannon-Peppas and J. O. Blanchette, "Nanoparticle and targeted systems for cancer therapy," *Advanced drug delivery reviews,* vol. 56, pp. 1649-1659, 2004.
[17] M. J. Bissell and D. Radisky, "Putting tumours in context," *Nature Reviews Cancer,* vol. 1, pp. 46-54, 2001.
[18] A. Schroeder, D. A. Heller, M. M. Winslow, J. E. Dahlman, G. W. Pratt, R. Langer*, et al.*, "Treating metastatic cancer with nanotechnology," *Nature Reviews Cancer,* vol. 12, pp. 39-50, 2012.
[19] A. Niwińska, M. Murawska, and K. Pogoda, "Breast cancer brain metastases: differences in survival depending on biological subtype, RPA RTOG prognostic class and systemic treatment after whole-brain radiotherapy (WBRT)," *Annals of Oncology,* vol. 21, pp. 942-948, 2010.
[20] W. Wu, X. He, D. Andayani, L. Yang, J. Ye, Y. Li*, et al.*, "Pattern of distant extrahepatic metastases in primary liver cancer: a SEER based study," *Journal of Cancer,* vol. 8, p. 2312, 2017.
[21] V. Adamo, T. Franchina, B. Adamo, G. Scandurra, and A. Scimone, "Brain metastases in patients with non-small cell lung cancer: focus on the role of chemotherapy," *Annals of oncology,* vol. 17, pp. ii73-ii75, 2006.
[22] T. Yoneda, A. Sasaki, and G. R. Mundy, "Osteolytic bone metastasis in breast cancer," *Breast cancer research and treatment,* vol. 32, pp. 73-84, 1994.
[23] K. Moussa, "Domain of Attraction Estimation and Optimization-Based Control : Application to Tumor Growth Models

Estimation de domaines d'attraction et contrôle basé sur l'optimisation : application à des modèles de croissance tumorale," Université Grenoble Alpes [2020-....], 2020.
[24] E. A. Ostrander, B. W. Davis, and G. K. Ostrander, "Transmissible Tumors: Breaking the Cancer Paradigm," *Trends in Genetics,* vol. 32, pp. 1-15, 2016/01/01/ 2016.
[25] P. O. Van Trappen and M. S. Pepper, "Lymphatic dissemination of tumour cells and the formation of micrometastases," *The lancet oncology,* vol. 3, pp. 44-52, 2002.
[26] K. Pantel and C. Alix-Panabières, "Detection methods of circulating tumor cells," *Journal of thoracic disease,* vol. 4, p. 446, 2012.
[27] N. S. Al-Waili, G. J. Butler, J. Beale, R. W. Hamilton, B. Y. Lee, and P. Lucas, "Hyperbaric oxygen and malignancies: a potential role in radiotherapy, chemotherapy, tumor surgery and phototherapy," *Medical science monitor,* vol. 11, p. RA279, 2005.
[28] L. Sakka, G. Coll, and J. Chazal, "Anatomy and physiology of cerebrospinal fluid," *European annals of otorhinolaryngology, head and neck diseases,* vol. 128, pp. 309-316, 2011.
[29] R. W. Sperry, "Left-brain, right-brain," *Saturday Review,* vol. 2, pp. 30-32, 1975.
[30] R. A. Ramadan, S. Refat, M. A. Elshahed, and R. A. Ali, "Basics of brain computer interface," in *Brain-Computer Interfaces*, ed: Springer, 2015, pp. 31-50.
[31] M. Itō, *The cerebellum: brain for an implicit self*: FT press, 2012.

[32] S. V. Meethal and C. S. Atwood, "The role of hypothalamic-pituitary-gonadal hormones in the normal structure and functioning of the brain," *Cell Mol Life Sci,* vol. 62, pp. 257-270, 2005.
[33] M. P. Lovely, "Symptom management of brain tumor patients," in *Seminars in oncology nursing*, 2004, pp. 273-283.
[34] W. H. Organization, *Diagnosis and treatment* vol. 4: World Health Organization, 2008.
[35] R. Sullivan, O. I. Alatise, B. O. Anderson, R. Audisio, P. Autier, A. Aggarwal*, et al.*, "Global cancer surgery: delivering safe, affordable, and timely cancer surgery," *The Lancet Oncology,* vol. 16, pp. 1193-1224, 2015/09/01/ 2015.
[36] L. Wyld, R. A. Audisio, and G. J. Poston, "The evolution of cancer surgery and future perspectives," *Nature Reviews Clinical Oncology,* vol. 12, pp. 115-124, 2015.
[37] V. T. DeVita and E. Chu, "A history of cancer chemotherapy," *Cancer research,* vol. 68, pp. 8643-8653, 2008.
[38] Z. Youssef, "Nanoparticules de TiO2 couplées à des photosensibilisateurs pour des applications en photocatalyse et en thérapie photodynamique," 2017.
[39] D. A. Karnofsky, W. H. Abelmann, L. F. Craver, and J. H. Burchenal, "The use of the nitrogen mustards in the palliative treatment of carcinoma. With particular reference to bronchogenic carcinoma," *Cancer,* vol. 1, pp. 634-656, 1948.
[40] D. M. Finkelstein, D. Ettinger, and J. Ruckdeschel, "Long-term survivors in metastatic non-small-cell lung cancer: an Eastern Cooperative Oncology Group Study," *Journal of Clinical Oncology,* vol. 4, pp. 702-709, 1986.
[41] R. Rudd, N. Gower, S. Spiro, T. Eisen, P. Harper, J. Littler*, et al.*, "Gemcitabine plus carboplatin versus mitomycin, ifosfamide, and cisplatin in patients with stage IIIB or IV non–small-cell lung cancer: A phase III randomized study of the London Lung Cancer Group," *Journal of Clinical Oncology,* vol. 23, pp. 142-153, 2005.
[42] H. D. Riordan, N. H. Riordan, J. A. Jackson, J. J. Casciari, R. Hunninghake, M. J. González*, et al.*, "Intravenous vitamin C as a chemotherapy agent: a report on clinical cases," *Puerto Rico health sciences journal,* vol. 23, 2004.
[43] J. C. Panetta and K. R. Fister, "Optimal control applied to cell-cycle-specific cancer chemotherapy," *SIAM Journal on Applied Mathematics,* vol. 60, pp. 1059-1072, 2000.
[44] V. Trillet-Lenoir, J. Green, C. Manegold, J. Von Pawel, U. Gatzemeier, B. Lebeau*, et al.*, "Recombinant granulocyte colony stimulating factor reduces the infectious complications of cytotoxic chemotherapy," *European Journal of Cancer,* vol. 29, pp. 319-324, 1993.
[45] M. S. Aslam, S. Naveed, A. Ahmed, Z. Abbas, I. Gull, and M. A. Athar, "Side effects of chemotherapy in cancer patients and evaluation of patients opinion about starvation based differential chemotherapy," *Journal of Cancer Therapy,* vol. 2014, 2014.
[46] A. Coates, S. Abraham, S. B. Kaye, T. Sowerbutts, C. Frewin, R. Fox*, et al.*, "On the receiving end—patient perception of the side-effects of cancer chemotherapy," *European Journal of Cancer and Clinical Oncology,* vol. 19, pp. 203-208, 1983.
[47] E. S. Kim, J. B. Putnam, R. Komaki, G. L. Walsh, J. Y. Ro, H. J. Shin*, et al.*, "Phase II study of a multidisciplinary approach with induction chemotherapy, followed by surgical resection, radiation therapy, and consolidation chemotherapy for unresectable malignant thymomas," *Lung cancer,* vol. 44, pp. 369-379, 2004.
[48] C. Vale and A. B. C. M.-a. Collaboration, "Neoadjuvant chemotherapy in invasive bladder cancer: a systematic review and meta-analysis," *The Lancet,* vol. 361, pp. 1927-1934, 2003.
[49] H. E. Skipper, "Adjuvant chemotherapy," *Cancer,* vol. 41, pp. 936-940, 1978.
[50] D. Rosner, T. Nemoto, and W. W. Lane, "Chemotherapy induces regression of brain metastases in breast carcinoma," *Cancer,* vol. 58, pp. 832-839, 1986.
[51] P. Gotwals, S. Cameron, D. Cipolletta, V. Cremasco, A. Crystal, B. Hewes*, et al.*, "Prospects for combining targeted and conventional cancer therapy with immunotherapy," *Nature Reviews Cancer,* vol. 17, pp. 286-301, 2017.
[52] A. S. Allal, K. Nicoucar, N. Mach, and P. Dulguerov, "Quality of life in patients with oropharynx carcinomas: assessment after accelerated radiotherapy with or without chemotherapy

versus radical surgery and postoperative radiotherapy," *Head & Neck: Journal for the Sciences and Specialties of the Head and Neck,* vol. 25, pp. 833-840, 2003.
[53] M. Lomax, L. Folkes, and P. O'neill, "Biological consequences of radiation-induced DNA damage: relevance to radiotherapy," *Clinical oncology,* vol. 25, pp. 578-585, 2013.
[54] H. W. Wieringa, A. G. van der Zee, E. G. de Vries, and M. A. van Vugt, "Breaking the DNA damage response to improve cervical cancer treatment," *Cancer treatment reviews,* vol. 42, pp. 30-40, 2016.
[55] M. Sadeghi, M. Enferadi, and A. Shirazi, "External and internal radiation therapy: past and future directions," *Journal of cancer research and therapeutics,* vol. 6, p. 239, 2010.
[56] C. S. Reft, "The energy dependence and dose response of a commercial optically stimulated luminescent detector for kilovoltage photon, megavoltage photon, and electron, proton, and carbon beams," *Medical physics,* vol. 36, pp. 1690-1699, 2009.
[57] S. Bonvalot, F. Rimareix, A. Paumier, E. Roberti, H. Bouzaiene, and C. Le Péchoux, "Actualisation de la stratégie thérapeutique locorégionale dans les sarcomes des tissus mous et les tumeurs desmoïdes des membres," *Cancer/Radiothérapie,* vol. 14, pp. 455-459, 2010.
[58] L. Barazzuol, R. P. Coppes, and P. van Luijk, "Prevention and treatment of radiotherapy‐induced side effects," *Molecular oncology,* vol. 14, pp. 1538-1554, 2020.
[59] C. Ortholan, S. Estivalet, I. Barillot, A. Costa, and J. Gérard, "Guide des procédures de radiothérapie externe 2007 Guide for External Beam Radiotherapy. Procedures 2007," *Cancer/Radiothérapie,* vol. 11, pp. 329-330, 2007.
[60] C. Lepage, "La radiothérapie interne vectorisée en pratique," *Hépato-Gastro & Oncologie Digestive,* vol. 28, pp. 21-28, 2021.
[61] F. El Ghissassi, R. Baan, K. Straif, Y. Grosse, B. Secretan, V. Bouvard*, et al.*, "A review of human carcinogens—part D: radiation," *The lancet oncology,* vol. 10, pp. 751-752, 2009.
[62] D. Chassagne, A. Gerbaulet, J. Perrin, and C. Haie, "Cancer of the prostate: technics of curietherapy. Review of the literature and experience at the Institut Gustave-Roussy," *Bulletin du Cancer,* vol. 72, pp. 578-584, 1985.
[63] A. S. Riley, G. A. McKenzie, V. Green, G. Schettino, R. J. A. England, and J. Greenman, "The effect of radioiodine treatment on the diseased thyroid gland," *International journal of radiation biology,* vol. 95, pp. 1718-1727, 2019.
[64] M. Puerto, F. Borson-Chazot, and A. Tabarin, "Updates on therapy for medullary thyroid cancer in 2021," in *Annales d'Endocrinologie*, 2021.
[65] K. L. Baglan, M. B. Sharpe, D. Jaffray, R. C. Frazier, J. Fayad, L. L. Kestin*, et al.*, "Accelerated partial breast irradiation using 3D conformal radiation therapy (3D-CRT)," *International Journal of Radiation Oncology* Biology* Physics,* vol. 55, pp. 302-311, 2003.
[66] A. J. Khan, M. C. Kirk, S. Mehta, N. S. Seif, K. L. Griem, D. A. Bernard*, et al.*, "A dosimetric comparison of three-dimensional conformal, intensity-modulated radiation therapy, and MammoSite partial-breast irradiation," *Brachytherapy,* vol. 5, pp. 183-188, 2006.
[67] R. Wurm, F. Gum, S. Erbel, L. Schlenger, D. Scheffler, D. Agaoglu*, et al.*, "Image guided respiratory gated hypofractionated Stereotactic Body Radiation Therapy (H-SBRT) for liver and lung tumors: Initial experience," *Acta oncologica,* vol. 45, pp. 881-889, 2006.
[68] D. W. Andrews, C. B. Scott, P. W. Sperduto, A. E. Flanders, L. E. Gaspar, M. C. Schell*, et al.*, "Whole brain radiation therapy with or without stereotactic radiosurgery boost for patients with one to three brain metastases: phase III results of the RTOG 9508 randomised trial," *The Lancet,* vol. 363, pp. 1665-1672, 2004.
[69] T. R. Mackie, "History of tomotherapy," *Physics in Medicine & Biology,* vol. 51, p. R427, 2006.
[70] J. R. Adler Jr, S. D. Chang, M. J. Murphy, J. Doty, P. Geis, and S. L. Hancock, "The Cyberknife: a frameless robotic system for radiosurgery," *Stereotactic and functional neurosurgery,* vol. 69, pp. 124-128, 1997.
[71] A. R. Smith, "Proton therapy," *Physics in Medicine & Biology,* vol. 51, p. R491, 2006.
[72] S. Farkona, E. P. Diamandis, and I. M. Blasutig, "Cancer immunotherapy: the beginning of the end of cancer?," *BMC medicine,* vol. 14, pp. 1-18, 2016.

[73] M. Schuster, A. Nechansky, and R. Kircheis, "Cancer immunotherapy," *Biotechnology Journal: Healthcare Nutrition Technology,* vol. 1, pp. 138-147, 2006.
[74] L. B. Josefsen and R. W. Boyle, "Photodynamic therapy and the development of metal-based photosensitisers," *Metal-based drugs,* vol. 2008, 2008.
[75] C. Frochot, M. Barberi-Heyob, M. Blanchard-Desce, L. Bolotine, S. Bonneau, M. Chiara*, et al.*, "La thérapie photodynamique : état de l'art et perspectives," *L'Actualité Chimique,* pp. 46-50, 2015-06 2015.
[76] W. M. Sharman, C. M. Allen, and J. E. Van Lier, "Photodynamic therapeutics: basic principles and clinical applications," *Drug discovery today,* vol. 4, pp. 507-517, 1999.
[77] S. Rajendiran, *Post-transcriptional and epigenetic regulation of MIEN1 in prostate cancer*: University of North Texas Health Science Center at Fort Worth, 2014.
[78] T. J. Dougherty, C. J. Gomer, B. W. Henderson, G. Jori, D. Kessel, M. Korbelik*, et al.*, "Photodynamic therapy," *J Natl Cancer Inst,* vol. 90, pp. 889-905, Jun 17 1998.
[79] B. Busser, "IDENTIFICATION AND CHARACTERIZATION OF AN ORIGINAL MECHANISM OF RESISTANCE TO GEFITINIB IN NON-SMALL LUNG CANCERS: ROLE OF AMPHIREGULIN
IDENTIFICATION ET CARACTÉRISATION D'UN NOUVEAU MÉCANISME DE RÉSISTANCE AU GEFITINIB DANS LE CANCER DU POUMON NON-À PETITES CELLULES : ROLE DE L'AMPHIRÉGULINE," Université Joseph-Fourier - Grenoble I, 2009.
[80] A. Master, M. Livingston, and A. S. Gupta, "Photodynamic nanomedicine in the treatment of solid tumors: perspectives and challenges," *Journal of controlled release,* vol. 168, pp. 88-102, 2013.
[81] C. Frochot, M. barberi-heyob, M. Blanchard-Desce, L. Bolotine, S. Bonneau, C. Mauriello-Jimenez*, et al.*, "La thérapie photodynamique: état de l'art et perspectives," 06/01 2015.
[82] C. Hopper, "Photodynamic therapy: a clinical reality in the treatment of cancer," *The lancet oncology,* vol. 1, pp. 212-219, 2000.
[83] S. B. Brown, E. A. Brown, and I. Walker, "The present and future role of photodynamic therapy in cancer treatment," *The lancet oncology,* vol. 5, pp. 497-508, 2004.
[84] K. L. Du, S. Both, J. S. Friedberg, R. Rengan, S. M. Hahn, and K. A. Cengel, "Extrapleural pneumonectomy, photodynamic therapy and intensity modulated radiation therapy for the treatment of malignant pleural mesothelioma," *Cancer biology & therapy,* vol. 10, pp. 425-429, 2010.
[85] G. C. Brown, M. M. Brown, J. Campanella, and G. R. Beauchamp, "The cost-utility of photodynamic therapy in eyes with neovascular macular degeneration—a value-based reappraisal with 5-year data," *American journal of ophthalmology,* vol. 140, pp. 679. e1-679. e10, 2005.
[86] J. A. Cadeddu, "Re: TOOKAD® Soluble Vascular-Targeted Photodynamic (VTP) Therapy: Determination of Optimal Treatment Conditions and Assessment of Effects in Patients with Localised Prostate Cancer," *The Journal of Urology,* vol. 191, pp. 1290-1290, 2014.
[87] H. Moole, H. Tathireddy, S. Dharmapuri, V. Moole, R. Boddireddy, P. Yedama*, et al.*, "Success of photodynamic therapy in palliating patients with nonresectable cholangiocarcinoma: A systematic review and meta-analysis," *World journal of gastroenterology,* vol. 23, p. 1278, 2017.
[88] P. Soergel, M. Loning, I. Staboulidou, C. Schippert, and P. Hillemanns, "Photodynamic diagnosis and therapy in gynecology," *Journal of Environmental Pathology, Toxicology and Oncology,* vol. 27, 2008.
[89] A. F. Degen, T. Gabrecht, L. Mosimann, M. K. Fehr, R. Hornung, V. A. Schwarz*, et al.*, "Photodynamic endometrial ablation for the treatment of dysfunctional uterine bleeding: a preliminary report," *Lasers in Surgery and Medicine: The Official Journal of the American Society for Laser Medicine and Surgery,* vol. 34, pp. 1-4, 2004.
[90] T. Banerjee, S. Abhilash, D. Kabiraj, S. Ojha, G. Umapathy, M. Shareef*, et al.*, "Fabrication of thin targets for nuclear reaction studies at IUAC," *Vacuum,* vol. 144, pp. 190-198, 2017.

[91] E. D. Sternberg, D. Dolphin, and C. Brückner, "Porphyrin-based photosensitizers for use in photodynamic therapy," *Tetrahedron,* vol. 54, pp. 4151-4202, 1998.
[92] I. Yoon, J. Z. Li, and Y. K. Shim, "Advance in photosensitizers and light delivery for photodynamic therapy," *Clinical endoscopy,* vol. 46, p. 7, 2013.
[93] C. Cochrane, S. R. Mordon, J. C. Lesage, and V. Koncar, "New design of textile light diffusers for photodynamic therapy," *Materials Science and Engineering: C,* vol. 33, pp. 1170-1175, 2013.
[94] F. Zhou, B. Zheng, Y. Zhang, Y. Wu, H. Wang, and J. Chang, "Construction of near-infrared light-triggered reactive oxygen species-sensitive (UCN/SiO₂-RB + DOX)@PPADT nanoparticles for simultaneous chemotherapy and photodynamic therapy," *Nanotechnology,* vol. 27, p. 235601, 2016/05/03 2016.
[95] O. Raab, "On the effect of fluorescent substances on infusoria," *Z Biol,* vol. 39, pp. 524-6, 1900.
[96] H. Von Tappeiner, "Therapeutische versuche mit fluoreszierenden stoffen," *Munch Med Wochenschr,* vol. 1, pp. 2042-2044, 1903.
[97] P. G. Calzavara-Pinton, R.-M. Szeimeis, B. Ortel, and C. Zane, "Photodynamic therapy with systemic administration of photosensitizers in dermatology," *Journal of Photochemistry and Photobiology B: Biology,* vol. 36, pp. 225-231, 1996.
[98] A. Policard, "Etude sur les aspects offerts par des tumeurs experimentales examinees a la limiere de wood," *Biologue Comptes Rendus,* vol. 91, p. 1423, 1924.
[99] G. Jori, L. Tomio, E. Reddi, E. Rossi, L. Corti, P. Zorat*, et al.*, "Preferential delivery of liposome-incorporated porphyrins to neoplastic cells in tumour-bearing rats," *British journal of cancer,* vol. 48, p. 307, 1983.
[100] R. Thaller, D. Lyster, and D. Dolphin, "Potential use of radiolabelled porphyrins for tumor scanning," in *Porphyrin Photosensitization*, ed: Springer, 1983, pp. 265-278.
[101] H. Kato, "History of photodynamic therapy--past, present and future," *Gan to Kagaku ryoho. Cancer & Chemotherapy,* vol. 23, pp. 8-15, 1996.
[102] B. Kjeldstad, T. Christensen, and A. Johnsson, "Geitmyrsv. 75, 0462 Oslo 4, Norway," *Methods in Porphyrin Photosensitization,* vol. 193, p. 155, 2012.
[103] R. L. Ruff and J. H. Dougherty Jr, "Complications of lumbar puncture followed by anticoagulation," *Stroke,* vol. 12, pp. 879-881, 1981.
[104] A. B. Ormond and H. S. Freeman, "Dye sensitizers for photodynamic therapy," *Materials,* vol. 6, pp. 817-840, 2013.
[105] M. P. Uliana, L. Pires, S. Pratavieira, T. J. Brocksom, K. T. de Oliveira, V. S. Bagnato*, et al.*, "Photobiological characteristics of chlorophyll a derivatives as microbial PDT agents," *Photochemical & Photobiological Sciences,* vol. 13, pp. 1137-1145, 2014.
[106] I. S. Mfouo-Tynga, L. D. Dias, N. M. Inada, and C. Kurachi, "Features of third generation photosensitizers used in anticancer photodynamic therapy," *Photodiagnosis and Photodynamic Therapy,* vol. 34, p. 102091, 2021.
[107] I. S. Mfouo-Tynga, L. D. Dias, N. M. Inada, and C. Kurachi, "Features of third generation photosensitizers used in anticancer photodynamic therapy: Review," *Photodiagnosis and Photodynamic Therapy,* vol. 34, p. 102091, 2021/06/01/ 2021.
[108] W. Alexander, "American society of clinical oncology, 2010 annual meeting and rose bengal: From a wool dye to a cancer therapy," *Pharmacy and Therapeutics,* vol. 35, p. 469, 2010.
[109] R. Nietzki, *Chemistry of the Organic Dye-stuffs*: Gurney & Jackson, 1892.
[110] M. J. Doughty, "Rose bengal staining as an assessment of ocular surface damage and recovery in dry eye disease—a review," *Contact Lens and Anterior Eye,* vol. 36, pp. 272-280, 2013.
[111] J. M. Lowenstein, "Radioactive rose bengal test as a quantitative measure of liver function," *Proceedings of the Society for Experimental Biology and Medicine,* vol. 93, pp. 377-378, 1956.

[112] J. Qin, N. Kunda, G. Qiao, J. F. Calata, K. Pardiwala, B. S. Prabhakar*, et al.*, "Colon cancer cell treatment with rose bengal generates a protective immune response via immunogenic cell death," *Cell death & disease,* vol. 8, pp. e2584-e2584, 2017.
[113] L. JN, T. Vo, C. Saegerman, L. De Waele, A. Tibor, and A. Cloeckaert, "Identification et clonage des antigènes de diagnostic de la brucellose: perspectives d'application," *Prevention of Brucellosis in the Mediterranean countries,* p. 252.
[114] I. Sow, "Evaluation du risque de brucellose lié à la consommation du lait frais dans la commune rurale de Cinzana," Universite de Bamako, 2011.
[115] N. Ž. Knežević, V. Stojanovic, A. Chaix, E. Bouffard, K. E. Cheikh, A. Morère*, et al.*, "Ruthenium(ii) complex-photosensitized multifunctionalized porous silicon nanoparticles for two-photon near-infrared light responsive imaging and photodynamic cancer therapy," *Journal of Materials Chemistry B,* vol. 4, pp. 1337-1342, 2016.
[116] R. Liang, L. Liu, H. He, Z. Chen, Z. Han, Z. Luo*, et al.*, "Oxygen-boosted immunogenic photodynamic therapy with gold nanocages@ manganese dioxide to inhibit tumor growth and metastases," *Biomaterials,* vol. 177, pp. 149-160, 2018.
[117] Z. He, Y. Xiao, J.-R. Zhang, P. Zhang, and J.-J. Zhu, "In situ formation of large pore silica–mnO 2 nanocomposites with H+/H 2 O 2 sensitivity for O 2-elevated photodynamic therapy and potential MR imaging," *Chemical Communications,* vol. 54, pp. 2962-2965, 2018.
[118] T. Lin, X. Zhao, S. Zhao, H. Yu, W. Cao, W. Chen*, et al.*, "O2-generating MnO2 nanoparticles for enhanced photodynamic therapy of bladder cancer by ameliorating hypoxia," *Theranostics,* vol. 8, p. 990, 2018.
[119] E. Borghi, P. Saïd, A. Pottier, and L. Lévy, "Les nanoparticules thérapeutiques: une voie novatrice pour la radiothérapie appliquée à la cancérologie," *Réalités Industrielles,* p. 39, 2010.
[120] S. Moore, F. K. Stanley, and A. A. Goodarzi, "The repair of environmentally relevant DNA double strand breaks caused by high linear energy transfer irradiation–no simple task," *DNA repair,* vol. 17, pp. 64-73, 2014.
[121] J. Valentin, "Relative biological effectiveness (RBE), quality factor (Q), and radiation weighting factor (wR): ICRP Publication 92," *Annals of the ICRP,* vol. 33, pp. 1-121, 2003.
[122] I. C. o. R. Units and Measurements, *Quantitative concepts and dosimetry in radiobiology*: International Commission on Radiation Units and Measurements, 1979.
[123] K. T. Butterworth, S. J. McMahon, F. J. Currell, and K. M. Prise, "Physical basis and biological mechanisms of gold nanoparticle radiosensitization," *Nanoscale,* vol. 4, pp. 4830-4838, 2012.
[124] J. F. Hainfeld, F. A. Dilmanian, D. N. Slatkin, and H. M. Smilowitz, "Radiotherapy enhancement with gold nanoparticles," *Journal of pharmacy and pharmacology,* vol. 60, pp. 977-985, 2008.
[125] J. Martin, "Nuclear Interactions. W: Martin, JE Physics for Radiation Protection (s. 98-100)," ed: Wiley-VCH, 2013.
[126] L. C. Feldman and J. W. Mayer, "Fundamentals of surface and thin film analysis," *North Holland, Elsevier Science Publishers, P. O. Box 211, 1000 AE Amsterdam, The Netherlands, 1986.,* 1986.
[127] S. J. McMahon, W. B. Hyland, M. F. Muir, J. A. Coulter, S. Jain, K. T. Butterworth*, et al.*, "Biological consequences of nanoscale energy deposition near irradiated heavy atom nanoparticles," *Scientific reports,* vol. 1, pp. 1-10, 2011.
[128] M. Douglass, E. Bezak, and S. Penfold, "Monte Carlo investigation of the increased radiation deposition due to gold nanoparticles using kilovoltage and megavoltage photons in a 3D randomized cell model," *Medical physics,* vol. 40, p. 071710, 2013.
[129] H. Xing, X. Zheng, Q. Ren, W. Bu, W. Ge, Q. Xiao*, et al.*, "Computed tomography imaging-guided radiotherapy by targeting upconversion nanocubes with significant imaging and radiosensitization enhancements," *Scientific reports,* vol. 3, pp. 1-9, 2013.
[130] S. Klein, A. Sommer, L. V. Distel, W. Neuhuber, and C. Kryschi, "Superparamagnetic iron oxide nanoparticles as radiosensitizer via enhanced reactive oxygen species formation," *Biochemical and biophysical research communications,* vol. 425, pp. 393-397, 2012.

[131] S. Klein, M. L. Dell'Arciprete, M. Wegmann, L. V. Distel, W. Neuhuber, M. C. Gonzalez*, et al.*, "Oxidized silicon nanoparticles for radiosensitization of cancer and tissue cells," *Biochemical and biophysical research communications,* vol. 434, pp. 217-222, 2013.

[132] S. Kokotov, A. Lewis, R. Neumann, and S. Amrusi, "X‐RAY INDUCED VISIBLE LUMINESCENCE OF PORPHYRINS," *Photochemistry and photobiology,* vol. 59, pp. 385-387, 1994.

[133] K. Berg, Z. Luksiene, J. Moan, and L. Ma, "Combined treatment of ionizing radiation and photosensitization by 5-aminolevulinic acid-induced protoporphyrin IX," *Radiation research,* vol. 142, pp. 340-346, 1995.

[134] R. Allman, P. Cowburn, and M. Mason, "Effect of photodynamic therapy in combination with ionizing radiation on human squamous cell carcinoma cell lines of the head and neck," *British journal of cancer,* vol. 83, pp. 655-661, 2000.

[135] U. Kulka, M. Schaffer, A. Siefert, P. M. Schaffer, A. Ölsner, K. Kasseb*, et al.*, "Photofrin as a radiosensitizer in an in vitro cell survival assay," *Biochemical and biophysical research communications,* vol. 311, pp. 98-103, 2003.

[136] Y. Liu, W. Chen, S. Wang, A. G. Joly, S. Westcott, and B. K. Woo, "X-ray luminescence of La F 3: Tb 3+ and La F 3: Ce 3+, Tb 3+ water-soluble nanoparticles," *Journal of Applied Physics,* vol. 103, p. 063105, 2008.

[137] A.-L. Bulin, C. Truillet, R. Chouikrat, F. Lux, C. Frochot, D. Amans*, et al.*, "X-ray-Induced Singlet Oxygen Activation with Nanoscintillator-Coupled Porphyrins," *The Journal of Physical Chemistry C,* vol. 117, pp. 21583-21589, 2013/10/17 2013.

[138] A. M. Jhaveri and V. P. Torchilin, "Multifunctional polymeric micelles for delivery of drugs and siRNA," *Frontiers in pharmacology,* vol. 5, p. 77, 2014.

[139] R. A. Petros and J. M. DeSimone, "Strategies in the design of nanoparticles for therapeutic applications," *Nature reviews Drug discovery,* vol. 9, pp. 615-627, 2010.

[140] E. Bouyer, G. Mekhloufi, V. Rosilio, J.-L. Grossiord, and F. Agnely, "Proteins, polysaccharides, and their complexes used as stabilizers for emulsions: alternatives to synthetic surfactants in the pharmaceutical field?," *International journal of pharmaceutics,* vol. 436, pp. 359-378, 2012.

[141] T. Lammers, F. Kiessling, W. E. Hennink, and G. Storm, "Drug targeting to tumors: principles, pitfalls and (pre-) clinical progress," *Journal of controlled release,* vol. 161, pp. 175-187, 2012.

[142] P. Yingchoncharoen, D. S. Kalinowski, and D. R. Richardson, "Lipid-based drug delivery systems in cancer therapy: what is available and what is yet to come," *Pharmacological reviews,* vol. 68, pp. 701-787, 2016.

[143] L. Larue, A. Ben Mihoub, Z. Youssef, L. Colombeau, S. Acherar, J. C. André*, et al.*, "Using X-rays in photodynamic therapy: an overview," *Photochem Photobiol Sci,* vol. 17, pp. 1612-1650, Nov 1 2018.

[144] A. P. S. Sawhney, B. Condon, K. V. Singh, S.-S. Pang, G. Li, and D. Hui, "Modern applications of nanotechnology in textiles," *Textile Research Journal,* vol. 78, pp. 731-739, 2008.

[145] Y. Wan, "Développement de nanovecteurs polymériques et lipidiques fonctionnalisés par des anticorps pour cibler des cellules cancéreuses," 2012.

[146] M. A. Zarbin, C. Montemagno, J. F. Leary, and R. Ritch, "Nanomedicine in ophthalmology: the new frontier," *American journal of ophthalmology,* vol. 150, pp. 144-162. e2, 2010.

[147] K. Ulbrich, K. Holá, V. Šubr, A. Bakandritsos, J. Tuček, and R. Zbořil, "Targeted Drug Delivery with Polymers and Magnetic Nanoparticles: Covalent and Noncovalent Approaches, Release Control, and Clinical Studies," *Chemical Reviews,* vol. 116, pp. 5338-5431, 2016/05/11 2016.

[148] N. Mackiewicz, E. Gravel, A. Garofalakis, J. Ogier, J. John, D. M. Dupont*, et al.*, "Tumor‐Targeted Polydiacetylene Micelles for In Vivo Imaging and Drug Delivery," *Small,* vol. 7, pp. 2786-2792, 2011.

[149] C. von Roemeling, W. Jiang, C. K. Chan, I. L. Weissman, and B. Y. Kim, "Breaking down the barriers to precision cancer nanomedicine," *Trends in biotechnology,* vol. 35, pp. 159-171, 2017.

[150] Y. Zhou, Z. Peng, E. S. Seven, and R. M. Leblanc, "Crossing the blood-brain barrier with nanoparticles," *Journal of controlled release,* vol. 270, pp. 290-303, 2018.
[151] A. Albanese, P. S. Tang, and W. C. Chan, "The effect of nanoparticle size, shape, and surface chemistry on biological systems," *Annual review of biomedical engineering,* vol. 14, pp. 1-16, 2012.
[152] S. Tran, P.-J. DeGiovanni, B. Piel, and P. Rai, "Cancer nanomedicine: a review of recent success in drug delivery," *Clinical and Translational Medicine,* vol. 6, p. 44, 2017/12/11 2017.
[153] D. K. Chatterjee, L. S. Fong, and Y. Zhang, "Nanoparticles in photodynamic therapy: an emerging paradigm," *Advanced drug delivery reviews,* vol. 60, pp. 1627-1637, 2008.
[154] A. Z. Wilczewska, K. Niemirowicz, K. H. Markiewicz, and H. Car, "Nanoparticles as drug delivery systems," *Pharmacological reports,* vol. 64, pp. 1020-1037, 2012.
[155] F. Lux, V. L. Tran, E. Thomas, S. Dufort, F. Rossetti, M. Martini*, et al.*, "AGuIX® from bench to bedside—Transfer of an ultrasmall theranostic gadolinium-based nanoparticle to clinical medicine," *The British journal of radiology,* vol. 92, p. 20180365, 2019.
[156] P. Couleaud, D. Bechet, R. Vanderesse, M. Barberi-Heyob, A.-C. Faure, S. Roux*, et al.*, "Functionalized silica-based nanoparticles for photodynamic therapy," *Nanomedicine,* vol. 6, pp. 995-1009, 2011.
[157] A. Tiwari and S. Dhoble, "Tunable lanthanide/transition metal ion ‐ doped novel phosphors for possible application in w ‐ LEDs: a review," *Luminescence,* vol. 35, pp. 4-33, 2020.
[158] E. Dobrescu, "General characterization of rare earth elements," *Anuarul Institutului de Cercetari Economice" Gheorghe Zane"-Iasi,* vol. 21, p. 25, 2012.
[159] M. Carsky and V. Gruber, "New technology for lanthanide recovery from spent Nd-Fe-B magnets," *South African Journal of Chemical Engineering,* vol. 33, pp. 35-38, 2020.
[160] J. Yan, J. Zhang, M. Zhang, and G. Shi, "Lanthanide metal-organic framework as a paper strip sensor for visual detection of sulfonamide with smartphone-based point-of-care platform," *Talanta,* vol. 237, p. 122920, 2022.
[161] A. Getsis and A. V. Mudring, "Lanthanide containing ionic liquid crystals: EuBr2, SmBr3, TbBr3 and DyBr3 in C12mimBr," ed: Wiley Online Library, 2010.
[162] B. M. Van Der Ende, L. Aarts, and A. Meijerink, "Lanthanide ions as spectral converters for solar cells," *Physical Chemistry Chemical Physics,* vol. 11, pp. 11081-11095, 2009.
[163] J. Martins, C. A. Diaz, M. F. Domingues, R. A. Ferreira, P. Antunes, and P. S. André, "Low-cost and high-performance optical fiber-based sensor for liquid level monitoring," *IEEE Sensors Journal,* vol. 19, pp. 4882-4888, 2019.
[164] K. H. Thompson and C. Orvig, "Lanthanide compounds for therapeutic and diagnostic applications," *Chemical Society Reviews,* vol. 35, pp. 499-499, 2006.
[165] R. Delgado, J. Costa, K. P. Guerra, and L. M. Lima, "Lanthanide complexes of macrocyclic derivatives useful for medical applications," *Pure and applied chemistry,* vol. 77, pp. 569-579, 2005.
[166] J.-C. G. Bünzli, "Spectrochemical properties of lanthanide coordination and supramolecular compounds," *Chimia,* vol. 50, pp. 603-603, 1996.
[167] G. V. Samsonov and I. Y. Gil'man, "Electronic structure and physical properties of the oxides of the lanthanides — A review," *Soviet Powder Metallurgy and Metal Ceramics,* vol. 13, pp. 925-932, 1974/11/01 1974.
[168] J.-C. G. Bünzli, "Benefiting from the unique properties of lanthanide ions," *Accounts of chemical research,* vol. 39, pp. 53-61, 2006.
[169] F. BENNAR, "Contribution a l'étude des propriétés structurales, électroniques, élastiques et thermodynamiques des composés binaires XY (X= Lu, Yb et Y= N, Sb, Bi) par la méthode ab initio FP-LMTO," 2017.
[170] J. A. Peters, K. Djanashvili, C. F. Geraldes, and C. Platas-Iglesias, "The chemical consequences of the gradual decrease of the ionic radius along the Ln-series," *Coordination Chemistry Reviews,* vol. 406, p. 213146, 2020.

[171] K. A. Gschneidner, *Rare earths: the fraternal fifteen*: US Atomic Energy Commission, Division of Technical Information, 1964.
[172] I. Annexe, "Annexe I: Caractéristiques générales des éléments de terre rare et de transition," *Structure et propriétés physiques de composés magnétiques de type RT12B6 et (Hf, Ta) Fe2 et leur dépendance en fonction de la pression (physique ou chimique),* p. 285, 2014.
[173] S. Riedel and M. Kaupp, "The highest oxidation states of the transition metal elements," *Coordination Chemistry Reviews,* vol. 253, pp. 606-624, 2009.
[174] G. Meyer, T. Gloger, and J. Beekhuizen, "Halides of titanium in lower oxidation states," *Zeitschrift für anorganische und allgemeine Chemie,* vol. 635, pp. 1497-1509, 2009.
[175] J. F. Cannon and H. T. Hall, "Effect of high pressure on the crystal structures of lanthanide trialuminides," *Journal of the Less Common Metals,* vol. 40, pp. 313-328, 1975.
[176] Y. Rong, M. M. Hassan, Q. Ouyang, and Q. Chen, "Lanthanide ion (Ln3+) ‐ based upconversion sensor for quantification of food contaminants: A review," *Comprehensive Reviews in Food Science and Food Safety,* vol. 20, pp. 3531-3578, 2021.
[177] L. Armelao, S. Quici, F. Barigelletti, G. Accorsi, G. Bottaro, M. Cavazzini*, et al.*, "Design of luminescent lanthanide complexes: From molecules to highly efficient photo-emitting materials," *Coordination Chemistry Reviews,* vol. 254, pp. 487-505, 2010.
[178] M. Woods, D. E. Woessner, and A. D. Sherry, "Paramagnetic lanthanide complexes as PARACEST agents for medical imaging," *Chemical Society Reviews,* vol. 35, pp. 500-511, 2006.
[179] S. W. Young, M. K. Sidhu, F. Qing, H. H. Muller, M. Neuder, G. Zanassi*, et al.*, "Preclinical evaluation of gadolinium (III) texaphyrin complex. A new paramagnetic contrast agent for magnetic resonance imaging," *Investigative radiology,* vol. 29, pp. 330-338, 1994.
[180] A. Vogler and H. Kunkely, "Excited state properties of lanthanide complexes: beyond ff states," *Inorganica Chimica Acta,* vol. 359, pp. 4130-4138, 2006.
[181] J. H. CO, B. INSTITU, and J. LALVANICOLLEGE, "Affiliated to University of Mumbai," *Inorganic Chemistry,* vol. 2, p. 8.
[182] V. K. Fischer, "A study of the Isotopes of Promethium," 1952.
[183] B. Wybourne, "Energy levels of trivalent gadolinium and ionic contributions to the ground-state splitting," *Physical Review,* vol. 148, p. 317, 1966.
[184] J. Zhang, P. D. Badger, S. J. Geib, and S. Petoud, "Sensitization of near ‐ infrared ‐ emitting lanthanide cations in solution by tropolonate ligands," *Angewandte Chemie,* vol. 117, pp. 2564-2568, 2005.
[185] A. Louie, "Multimodality imaging probes: design and challenges," *Chemical reviews,* vol. 110, pp. 3146-3195, 2010.
[186] F. Treussart, "Light from single emitters, applications," 12/16 2004.

Sous-chapitre I.1: Can Cerenkov Light Really Induce an Effective Photodynamic Therapy?

Joël Daouk [1], Batoul Dhaini [2], Jérôme Petit [1], Céline Frochot [2], Muriel Barberi-Heyob [1,*] and Hervé Schohn [1]

[1] Centre de Recherche en Automatique de Nancy (CRAN), UMR 7039, CNRS, Université de Lorraine, Campus Santé Bât D, 9 avenue de la forêt de Haye, F54518 Vandoeuvre-lès-Nancy, France; joel.daouk@univ-lorraine.fr (J.D.); jerome.petit9@etu.univ-lorraine.fr (J.P.); herve.schohn@univ-lorraine.fr (H.S.)

[2] Laboratoire Réactions et Génie des Procédés (LRGP), UMR 7274, CNRS, Université de Lorraine, F54000 Nancy, France; batoul.dhaini@univ-lorraine.fr (B.D.); celine.frochot@univ-lorraine.fr (C.F.)

Review published in MDPI-Radiation journal

Résumé : La thérapie photodynamique (PDT) est une stratégie thérapeutique prometteuse pour les cancers pour lesquels la chirurgie et la radiothérapie ne sont pas efficaces. La PDT repose sur la photoactivation de photosensibilisateurs, la plupart du temps par des lasers pour produire des espèces réactives de l'oxygène et notamment de l'oxygène singulet. L'inconvénient majeur de cette stratégie est la faible pénétration de la lumière dans les tissus. Pour surmonter ce problème, des études récentes ont proposé de générer de la lumière visible in situ avec des isotopes radioactifs émettant des particules chargées capables de produire un rayonnement Cerenkov. Les résultats in vitro et précliniques sont séduisants, mais l'existence d'un véritable effet photothérapeutique létal reste controversée. Dans cet article, nous avons passé en revue les travaux originaux antérieurs traitant de la PDT induite par Cerenkov (CR-PDT). De plus, nous proposons une résolution d'équation analytique simple pour démontrer que la lumière Cerenkov peut potentiellement générer un effet photo-thérapeutique, bien que la plupart des photons Cerenkov soient émis dans les domaines UV-B et UV-C. Nous suggérons que le CR-PDT et l'interaction directe UV-tissus agissent en synergie pour produire l'effet thérapeutique observé dans la littérature. De plus, l'ajout d'un nanoscintillateur à proximité du photosensibilisateur augmenterait l'efficacité de la PDT, car il convertirait les photons UV Cerenkov en lumière absorbée par le photosensibilisateur.

Can Cerenkov Light Really Induce an Effective Photodynamic Therapy?

Abstract: Photodynamic therapy (PDT) is a promising therapeutic strategy for cancers where surgery and radiotherapy cannot be effective. PDT relies on the photoactivation of photosensitizers, most of the time by lasers to produced reactive oxygen species and notably singlet oxygen. The major drawback of this strategy is the weak light penetration in the tissues. To overcome this issue, recent studies proposed to generate visible light in situ with radioactive isotopes emitting charged particles able to produce Cerenkov radiation. In vitro and preclinical results are appealing, but the existence of a true, lethal phototherapeutic effect is still controversial. In this article, we have reviewed previous original works dealing with Cerenkov-induced PDT (CR-PDT). Moreover, we propose a simple analytical equation resolution to demonstrate that Cerenkov light can potentially generate a photo-therapeutic effect, although most of the Cerenkov photons are emitted in the UV-B and UV-C domains. We suggest that CR-PDT and direct UV-tissue interaction act synergistically to yield the therapeutic effect observed in the literature. Moreover, adding a nanoscintillator in the photosensitizer vicinity would increase the PDT efficacy, as it will convert Cerenkov UV photons to light absorbed by the photosensitizer.

Keywords: Cerenkov radiations; photodynamic therapy; nanoparticles; radiopharmaceuticals

I. Introduction

Photodynamic therapy (PDT) uses specific molecules, namely photosensitizing agents, photo-agents or photosensitizers (PS), along with light illumination, in the presence of oxygen, to kill cancer cells, ultimately leading to tumor eradication. PDT is also known as photoradiation therapy or photochemotherapy. PDT involves the presence of PS, light and endogenous molecular oxygen ($^3O_2$) to generate photochemical reactions. Over the past few decades, diverse synthesized PS activation by visible and near-infrared (NIR) light has been widely investigated [1]. The mechanism of PDT is based on type I and II photo-oxidation reactions. At a specific excitation wavelength (light photon absorption), the PS produces ROS causing oxidative cell damage which is highly dependent on the $^3O_2$ content within the tissue [2].

Unfortunately, due to shallow visible light penetration depth into tissues, the photodynamic therapeutic strategy currently has largely been restricted to the treatment of surface localized tumors. Additional invasive strategies, i.e., interstitial PDT, through optical fibers are currently used for getting the visible light into the intended deep-seated targets [3,4]. Indeed, compared to ionizing-radiations, the light could not penetrate deeply because most tissue chromophores absorb in the range of the visible light spectrum commonly used in clinical practice. Moreover, the optimization of PDT modalities must consider numerous phenomena, regarding one or several main factors (photosensitizer, light, oxygen) involved in the treatment efficacy. A specific dosimetry remains challenging owing to their nonlinear interactions. Light penetration in the target tissue depends on its specific optical properties. If the tissue is hypoxic or becomes hypoxic because of the PDT treatment which consumes $^3O_2$, the yield of singlet oxygen $^1O_2$

will be lower than expected. Furthermore, making things tricky, PS concentration, light penetration and tissue oxygenation can vary during treatments and one parameter can influence the others.

To knock down the biotechnological barriers limiting the effectiveness of radiotherapy (i.e., curative X-ray dose to the tumor tissue without increasing it in the healthy adjoining tissue) and PDT (low penetration of the light), it has been proposed to use a bimodal therapy using biocompatible high-Z nanoparticles (NPs). This concept could combine both radiotherapy and PDT strategies, two clinical proven modalities, while maintaining the main benefits of each therapeutic strategy. Only PDT can generate $^1O_2$, but unfortunately, the low penetration of light remains a limiting factor. To treat deep lesions without an invasive approach, X-ray could be used as an excitation source instead of normal light. This therapeutic approach is known as X-ray-induced PDT (X-PDT) [5–9]. The light penetration limitation in the tumor tissue will be overcome and PS activation within the tumor cells will be performed by radiotherapy. This methodology requires a material composition exhibiting appropriate physical properties: high density for a good ionizing radiation interaction, high scintillation quantum yield and efficient energy transfer toward the PS as well as a biocompatibility and adapted in vivo bio-distribution. However, most of the X-PDT studies were mainly obtained with cancer cell lines or animal models bearing subcutaneous grafted cancer cells, limiting therefore clinical relevance [10]. The potential toxicity of nanoscintillators, in fact, mostly relies on nanoparticles stability, which can be enhanced by an inorganic shell among other things. As an example, AGuIX-designed nanoplatforms which originally chelate gadolinium have been assessed in phase I and phase II clinical trials without evidence of any toxicity [11,12]. AGuIX nanoparticle being a chelator, Gd^{3+} cations can be easily replaced by another 3+ lanthanide.

Recently, another therapeutic strategy has been proposed, direct PS activation through Cerenkov radiation, referred as Cerenkov-induced PDT (CR-PDT) [13,14]. Ran et al., in their proof-of principle article, postulated that such a treatment could be a synergy between the radiotherapeutic and phototherapeutic effect, the latter involving solely PSs activation [15]. However, despite the various recent studies demonstrating a real benefit in terms of tumor growth decrease, there is still a debate about the presence of a cytotoxic phototherapeutic effect [16]. Indeed, the number of photons absorbed by the PS being lower than those involved in PDT, the amount of $^1O_2$ produced is dramatically low.

In this article, we review the recent results obtained by researchers dealing with CR-PDT. Then, we propose an analytical assessment of $^1O_2$ production for the most used PS (photofrin) and radioisotopes used in nuclear medicine to determine whether Cerenkov radiation could produce a true phototherapeutic effect or not.

II. Cerenkov Light

Cerenkov light is a luminescence signal produced by charged particles. Two conditions must be present to enable such an effect: the medium must be dielectric and the charged particle must travel faster than the phase velocity of light in that medium. Cerenkov photons are produced by successive polarization/depolarization of the medium along the particle path, yielding constructive interferences [17]. To make it clearer, Cerenkov radiation can be compared with sound barrier crossing, but for light.

The Cerenkov photon yield can be computed with the Frank–Tamm formula [18]:

$$\frac{dN}{dx} = 2\pi\alpha\left(1 - \frac{1}{n^2\beta^2}\right)\int_{\lambda_1}^{\lambda_2}\frac{1}{\lambda^2}d\lambda, \qquad \text{(equation 15)}$$

Where *dN/dx* is the number of photons emitted per step length; *n* is the refractive index of the considered medium; α is a time constant defined as 1/137; and β is the ratio between the actual particle velocity and light speed in vacuum. Only particles, where $\beta n > 1$, will be able to produce Cerenkov light. β is directly related to the particle energy following the formula:

$$\beta = \sqrt{1 - \left[\frac{1}{\left(\frac{E}{mc^2}+1\right)}\right]^2} \qquad \text{(equation 16)}$$

Thus, to allow Cerenkov radiation, the initial particle's energy must be:

$$E > mc^2\left(\frac{1}{\sqrt{1-n^{-2}}} - 1\right) \qquad \text{(equation 17)}$$

In biological tissues, where the refractive index is considered around 1.4, this energy threshold is around 250 keV. This threshold is much lower than most of the radionuclides emitting β^+ or β^- particles.

The Cerenkov spectrum is a continuous spectrum from UV to infra-red light where the number of photons per wavelength is proportional to $1/\lambda^2$. Cerenkov photons are not emitted isotropically from the particle, but within a cone aligned with the direction of the travelling particle. The cone aperture of the distribution (**Figure 26**) is related to the particle velocity as

$$\cos\theta = \frac{1}{n\beta}$$

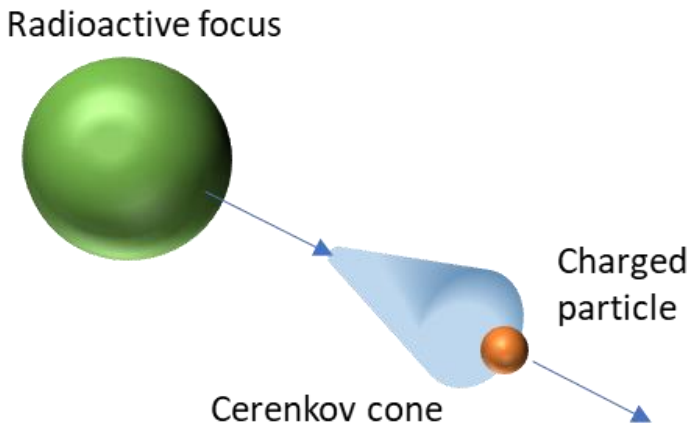

Figure 26 : Illustration of Cerenkov effect in a dielectric medium. A charged particle is emitted from the radioactive focus. Its velocity in the medium is higher than light in that medium yielding Cerenkov light production in a cone. The cone orientation is colinear to particle trajectory and its aperture is defined by particle velocity. As the particle is faster than light, Cerenkov photons appear behind it.

Gill et al. highlighted the luminescence yield of several isotopes commonly used in nuclear medicine and biology [19]. They used simulations (including the true resolution of Franck–Tamm formula at each length step) to determine the quantity and spatial distribution of Cerenkov light for each assessed element. Moreover, they validated their simulation kernel by true experiments for five radionuclides covering energies from 0.611 up to 2.3 MeV. **Table 3** summarizes the photon yield of the most common radionuclides used in nuclear medicine and **Figure 27** presents the corresponding Cerenkov spectra for the same isotopes. It is noteworthy that most of them are dedicated to positron emission tomography. Monte Carlo simulations assessed the spatial distribution of Cerenkov photons in biological medium. Mitchell et al. computed the volume where the charged particles energy was still higher than the Cerenkov threshold, allowing for the conclusion that many β emitters produced Cerenkov light in a 2 mm-diameter sphere [18].

Table 3 : Cerenkov photon yield for main nuclear medicine elements. Data extracted from [16].

Element	Z	Half life	Main Emission Type	Photon Yield	E_{max} (MeV)	E_{mean} (Mev)
^{11}C	6	20.4 min	b^+	6.87	0.970	0.390
^{18}F	9	110 min	b^+	1.32	0.63	0.252
^{68}Ga	31	67.7 min	b^+	33.9	1.92	0.844
^{82}Rb	37	1.27 min	b^+	80.8	3.378	1.551
^{89}Zr	40	78.4 h	b^+	2.29	0.909	0.396
^{90}Y	39	64.1 h	b^-	47.3	2.28	0.935

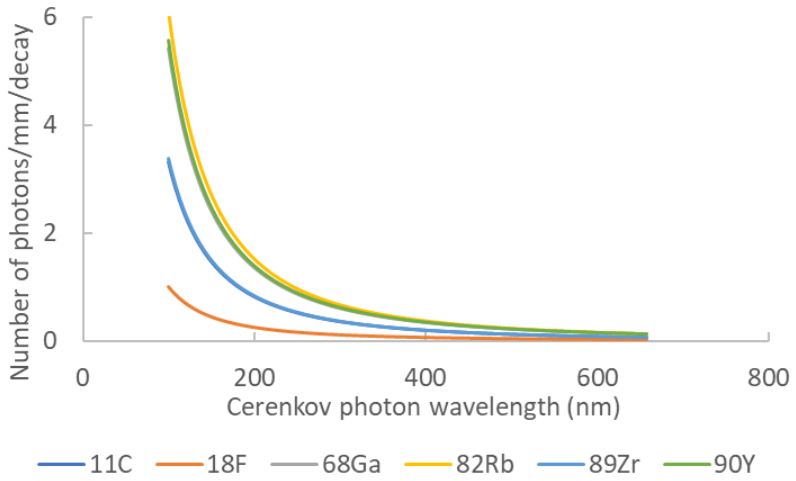

Figure 27 : Cerenkov spectrum for ^{18}F, ^{68}Ga and ^{89}Zr decay in biological medium. Spectra were defined between 100 and 650 nm. To ease reading, number of photons are expressed relatively to ^{18}F at 100 nm.

III. Photosensitizer (PS) Activation Mechanisms

PS are molecules able to absorb visible light to reach an excited singlet state. Then, return to the ground state is possible following three ways: (i) non radiative deactivation, (ii) emission of a fluorescence photon, whose wavelength is higher than the absorbed photon, or (iii) formation of a triplet state. The triplet excited PS can also decay back to the ground state by non radiative deactivation or emitting phosphorescence, but most importantly it can interact directly with surrounding biological substrates: The photo oxidative reactions, namely type I reactions, lead to an electron or proton transfer to generate radicals such as superoxide, hydroxyl or hydrogen peroxide as a consequence of dismutation of superoxide. Alternatively, the energy of the excited PS can be directly transferred to $^3O_2$ (itself as a triplet in the ground state) to form $^1O_2$, corresponding to type II reaction [20]. It is worth nothing that both type I and type II reactions occur simultaneously, and the ratio between these processes is affected by the nature of the PS, as well as by the concentration of endogenous $^3O_2$ and near/adjacent biomolecules targets. However, the production of $^1O_2$ plays a dominant role in in vivo PDT efficiency with most of the PS used for clinical applications. The reactivity of $^1O_2$, through the formation of endoperoxide derivatives, with unsaturated fatty acids within membranes, cyclic amino acyl residues within protein (Histidine, Tryptophane, or Methionine), and nucleic acids (Guanosine), is the main characteristic of the photodynamic effect [21–24].

The most popular PSs used in practice are porphyrins and their derivatives. These PS present a high intensity Soret band around 400 nm and from 2 to 4 Q-bands of lower intensity up to 630 nm. Soret band excitation is much more efficient than Q-band excitation However, UV/blue light does not penetrate deeply into tissue and red light is often used to overcome this issue. As stated before, Cerenkov radiation produce a continuous spectrum from 100 up to 650 nm following a monotonous $1/\lambda^2$ decay. Cerenkov radiation involves more UV/blue than red photons. Considering the Frank–Tamm formula, Cerenkov light should produce an infinite spectrum. In fact, high and low wavelength cut-offs can be defined: for long wavelengths (above 650~700nm) due to medium self-absorption and for wavelengths approaching the X-

ray domain (i.e., below 100 nm) [25]. However, these limitations do not interfere with the ability to activate a PS since their Soret band is classically located around 400–500 nm.

IV. Cerenkov-Induced PDT Main Results

Original studies providing detailed methods and results can be separated into in vitro and in vivo works. Collectively, it has been always reported that cancer cell death is increased when PS and β emitters are associated in the same treatment protocol. A dose-dependent effect of radioactivity and PS concentrations is observed. Obviously, close co-localization of both radio-emitters and PS is required to induce an efficient therapeutic effect [26–31]. In addition, after cellular uptake, intracellular PS level is related to a significant greatest part/ratio of Cerenkov radiation [30]. However, the photodynamic effect was not observed for all the assessed cell lines. Nakamura et al. postulated that such differences could be attributed to variable radiotracer accumulation [31]. Moreover, the sensitivity to the ionizing radiations and Cerenkov light differs according to the tested cell lines. Such a direct effect leads to the decrease of the participation of CR-PDT cytotoxicity to the overall therapeutic effect. The effect of the chosen isotope has been partly evaluated by Duan et al. Even though ^{18}F-FDG was six times more incorporated in cells than ^{68}Ga-BSA, the total amount of Cerenkov photons was still higher for the latter tracer and the phototherapeutic effects were higher as well [29]. These results are consistent with the greater ^{68}Ga Cerenkov yield as compared to ^{18}F yield (33.90 vs 1.32 photons/decay/mm respectively).

As a consequence of the use of radionuclides, γ-H_2AX expression was studied as a marker of DNA strand break in genotoxic stress conditions γ-H_2AX is a variant sequence of histone H2A, the expression of which is often increased following a DNA strand break, and the protein localizes as foci within the nuclei. γ-H_2AX plays therefore a major role in response to DNA damage and during the initial step of the DNA repair mechanism [32]. Recently, the protein levels were found to be enhanced in breast cancer cells after cell exposure to PSs and radionuclides [27,29]. This observed increase could not be attributed solely to cell damage induced by the ionizing nature of β emitters. Indeed, Duan et al. demonstrated that cell exposure to 400 µCi of ^{68}Ga or ^{18}F alone was not associated with any γ-H_2AX nuclei focus. The same trend has been observed by Kotagiri et al. when they pointed out DNA damage in numerous fibroblasts (i.e., γ-H_2AX-induces foci), when combining PS and ^{18}F-FDG in the treatment protocol [26]. These results are consistent with the previous PDT studies which demonstrated also DNA alteration while cells did not undergo cell death [33,34]. Nevertheless, γ-H_2AX foci were not observed in all conditions. Duan et al. reported γ-H_2AX levels increase only when the PS was associated with ^{68}Ga but not with ^{18}F [29]. Similar results, such as DNA repair activation, were obtained with^{89}Zr [35], in agreement with the Cerenkov photon yield of each isotope (33.90 vs 2.29 for ^{68}Ga and ^{89}Zr, respectively). Therefore, the PDT efficacy would not be similar considering the same radioactive deposit and PS concentration. The number of observed γ-H_2AX foci may probably be due to a cumulative effect from initial kinetic energy released by the isotope decay and PS activation. Indeed, cell exposure to ^{89}Zr isotope alone induced only a few foci compared to the treatment of both ^{89}Zr isotope and a PS [35]. Considering the $1/\lambda^2$ Cerenkov spectrum, nearly all of the produced photons are in the UV-C domain, which corresponds to the absorption area for nucleic acids (DNA and RNA)

supporting the concept that Cerenkov radiation alters DNA and RNA integrity but also proteins present in the absorption range of this radiation domain. The UV-C effect is enhanced when introducing silver NPs as demonstrated by Efthekari et al. [36]. They found a significant increase of the γ-H_2AX RNA levels when cells were exposed to silver NPs and UV-C compared to cells exposed to UV-C alone. Then, they suggested a synergistic effect of UV-C and Ag NPs in altering DNA and then increasing γ H_2AX expression. At least, a great γ-H_2AX expression was associated with the generation of ROS during ^{89}Zr-induced oxidative stress [28]. The increase of ROS levels was only observed within the cells incubated with NPs bearing both the PS and the ^{89}Zr radioisotope.

In vivo assessments seem to confirm Cerenkov efficacy. Indeed, tumor progression decreased when the PS treatment was associated with isotopes. Kotagiri et al. used a HT1080 tumor model in mice. A complete tumor regression within 30 days was observed when exposing the tumor to ^{64}Cu and TiO_2 [26]. The results were all the more impressive as the tumor represented a viable hypoxic tumor model. These findings supported the concept that Cerenkov light could induce a cytotoxic phototherapeutic effect, even in a hypoxic environment. The same trend was observed with other cell lines and PS/isotope couples. As an example, the impact of a Porphyrin/^{89}Zr association on tumor development was evaluated in a mouse breast cancer model, in breast cancer cells grafted in mice. Ni et al. performed serial imaging using Cerenkov luminescence and found that the synthesized NPs remained in tumors for several days, allowing a long term PS illumination, gradual singlet oxygen production and the decrease of the tumor development, when ^{89}Zr was embedded with porphyrin into the same nanostructure [28]. Moreover, the same group highlighted an additional antiangiogenic effect [35]. Similar to the in vitro studies, the charged particle energy is a crucial point for treatment efficacy. Using TiO_2 NPs, tumor regression has been reported to be higher with ^{68}Ga decay rather than ^{18}F, despite a lower cell uptake [29]. Therefore, the co-injection of ^{68}Ga and custom TiO_2 NPs significantly inhibited tumor growth in grafted cells in a heterotopic site as compared to tumor growth in animals in the control group.

Thus, considering these various studies, Cerenkov radiation-mediated PS activation appears to be an effective phototherapeutic strategy to overcome low light penetration in tissue. Another great advantage of CR-PDT is the fact that it allows the treatment of disseminated tumors, whereas PDT or X-PDT are limited to one or a few masses due to the need of an external device [37].

Nevertheless, despite these encouraging results, there is still debate about the existence of a real phototherapeutic effect through CR-PDT [16]. To support this assertion, the authors estimated the number of hydroxyl radicals produced by a ^{18}F decay. In fact, for a positron emitted at 250 keV energy, 6,800 molecules are produced through water radiolysis. Due to the TiO_2 bond, energy was too high to produce more than a few more radicals. To explain these exciting results, it has been postulated that positron could directly interact with photosensitizers, like other photocatalysts, to induce water radiolysis and then hydroxyl radicals, among other phenomena [16]. However, considering PDT efficacy through hydroxyl radical quantitation boils down to considering this therapeutic strategy like a “soft

radiotherapy". The PDT effect is mainly due to $^1O_2$ production involved in type II reaction and should not be assessed through other produced ROS.

V. Singlet Oxygen Production Estimation

$^1O_2$ is generated at the site of the parent PS molecule. Due to the short diffusion distance (10–100 nm), there is a higher probability that the molecule reacts with the parent PS than with the adjacent PS molecules. Previous studies stated that the cytotoxic effect could be obtained for $^3O_2$ concentrations around 0.5 mM, that corresponds to 2×10^8 to 2×10^9 $^1O_2$ molecules per cell to be effective [38–40]. Thus, to assess whether Cerenkov photons could provide enough $^1O_2$, we propose to study, analytically, the production of $^1O_2$ for photofrin which is, at the date of preparation of this manuscript, the most clinically relevant PS, and most isotopes used in medicine.

The most used factor to predict PDT efficiency is the PDT dose, which can be expressed as the product of the light power by the PS concentration. This criterion only reflects the energy absorbed by the PS and does not consider local environment factors, such as local $^3O_2$ concentration [41,42]. Photochemical parameters are now integrated to improve dosimetry in vitro. Recent advances have provided also such information for in vivo preclinical models [43]. To assess the CR-PDT effect, we used an analytic, macroscopic model of $^1O_2$ production [44]. This model considers light diffusion, PDT kinetics and $^3O_2$ supply terms. This model has been used in vivo and has been proven to be more predictive than PDT dose or light fluence alone [45,46].

In this model, the reaction rate equations can be expressed as [45]:

$$\frac{d[S_0]}{dt} + \left(\xi_\lambda \sigma \frac{\phi([S_0]+\delta)[\,^3O_2]}{[\,^3O_2]+\beta}\right)[S_0] = 0 \qquad \text{(equation 18)}$$

$$\frac{d[\,^3O_2]}{dt} + \left(\xi_\lambda \frac{\phi[S_0]}{[\,^3O_2]+\beta}\right)[\,^3O_2] - g\left(1 - \frac{[\,^3O_2]}{[\,^3O_2]_{t=0}}\right) = 0 \qquad \text{(equation 19)}$$

$$\frac{d[\,^1O_2]}{dt} - \left(\xi_\lambda \frac{\phi[S_0][\,^3O_2]}{[\,^3O_2]+\beta}\right) = 0 \qquad \text{(equation 20)}$$

Where $[S_0]$ is the PS concentration; □, the light fluence; $[^3O_2]$, the triplet oxygen concentration; and $[^1O_2]$, the singlet oxygen concentration. ξ_λ, σ, δ, β and g are specific PS characteristics and are defined as oxygen consumption rate at wavelength λ, photobleaching ratio, low-concentration correction factor, oxygen quenching threshold concentration and macroscopic oxygen maximum perfusion rate, respectively.

In PDT, the $^3O_2$ consumption and PS photobleaching are due mainly to the high light fluence. Thus, equations 18 and 19 cannot be ignored. On the contrary, in CR-PDT, the total number of photons emitted are dramatically lower than with an external laser source. In this condition, the $^3O_2$ consumption can reasonably be considered lower than the $^3O_2$ supply rate. Then, PS and $^3O_2$ concentrations can be considered constant during time.

The total light energy absorbed by the PS can be expressed by considering Cerenkov light as an external light source. Indeed, Cerenkov photons can be emitted in a sphere with a diameter up to 2 mm [18]. Thus, the Cerenkov fluence can be expressed as:

$$\phi_\lambda = \frac{E_\lambda . N_\lambda}{4\pi d^2}, \qquad \text{(equation 21)}$$

Where E_λ is the photon energy (J) for the considered wavelength, and N_λ is the number of Cerenkov photons of the same wavelength computed by the Franck–Tamm formula in the Cerenkov light sphere having diameter d (cm).

The energy transfer cannot be considered as a Förster resonance energy transfer (FRET) phenomenon. Hence, we computed the energy absorbed per wavelength following the Beer–Lambert formula:

$$\phi_\lambda = \phi_{\lambda 0} - \phi_{\lambda 0} . e^{(\epsilon . l . c)} \qquad \text{(equation 22)}$$

Where ε is the molar extension coefficient ($M^{-1}.cm^{-1}$), l is the absorption length (cm) and c is the PS concentration (M).

Introducing equation 22 in equation 20 results in the expression of $^1O_2$ concentration production per wavelength. Thus, the total $^1O_2$ molecules produced per second and per decay can be defined as:

$$\frac{n\,{}^1O_2}{dt} = \int_{\lambda_1}^{\lambda_2} \left(\xi_\lambda \frac{(\phi_{\lambda 0} - \phi_{\lambda 0} . e^{(\epsilon . l . c)})[S_0][\,{}^3O_2]}{[\,{}^3O_2] + \beta} \right) dt \,.\, N_A, \qquad \text{(equation 23)}$$

At last, the radioactive decay can be introduced in the latter equation to take the physical decay into consideration.

$$n\,{}_{{}^1O_2 t} = A_{t=0} . \int_{\lambda_1}^{\lambda_2} \left(\xi_\lambda \frac{(\phi_{\lambda 0} - \phi_{\lambda 0} . e^{(\epsilon . l . c)})[S_0][\,{}^3O_2]}{[\,{}^3O_2] + \beta} \right) dt . N_A . e^{\left(-\frac{\ln(2)}{T} . t\right)} \qquad \text{(equation 24)}$$

Where $n\,{}_{{}^1O_2 t}$ is the number of $^1O_2$ at time t, $A_{t=0}$ is the initial activity and T is the physical decay time of the considered isotope.

Under these conditions, the total produced $^1O_2$ depends directly on the initial kinetic energy of the emitted particle and the isotope half-life time.

We applied equation 10 with photofrin and various isotopes to assess the amount of $^1O_2$ produced through Cerenkov activation of the PS. PS characteristics used in this study were extracted from [45] and are summarized in **Table 4**.

Table 4 : Photofrin photodynamic therapy (PDT) parameters used in the macroscopic PDT kinetic equations. Parameters taken from [42].

Parameter	Definition	Value
x ($cm^2.s^{-1};mW^{-1}$) (630 nm)	Specific oxygen consumption rate	3.7×10^{-3}
$[^3O_1]$ (µM)	Triplet oxygen concentration	40
b (µM)	Oxygen quenching threshold concentration	11.9
[PS] (µM)	PS concentration	1

Figure 28 presents the $^1O_2$ production for the most common isotopes used in nuclear medicine with photofrin. For these computations, we used the β particle mean energy of each isotope and a 2-mm diameter sphere. A 10 kBq activity inside this volume is a reasonable activity which can be frequently encountered. Indeed, Kotagiri et al. estimated that a $50mm^3$ tumor could accumulate more than 1 MBq of FDG (after a 30 MBq injection). Then, a 2-mm diameter sphere represents a 5 mm^3 sphere and could contain easily up to 100 kBq, depending on the radiotracer affinity [47].

Despite having the greatest Cerenkov yield, ^{82}Rb is the less effective $^1O_2$ producer. Indeed, its physical decay is the lowest among the isotopes (roughly 90s). The total produced $^1O_2$ with 10 kBq ^{82}Rb was estimated at 2.71×10^{11} $^1O_2$ molecules. This is enough to destroy a hundred cancerous cells. Then, classical β^+ emitters used in positron emission tomography (i.e., ^{11}C, ^{18}F and ^{68}Ga) can produce from 2×10^{12} to 8.5×10^{12} $^1O_2$ molecules within two hours. ^{11}C and ^{18}F yield roughly the same amount of reactive oxygen species.

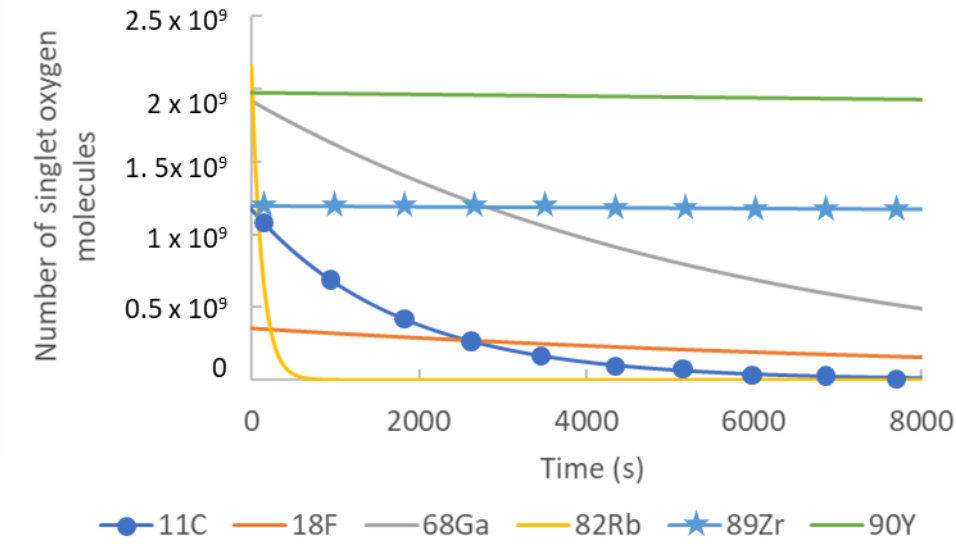

Figure 28 : Dynamic singlet oxygen produced by Cerenkov photons for various isotopes. Presented curves were computed for a 2-mm diameter sphere containing 10 kBq of isotope as well as 1µM and 40 µM of photofrin and triplet oxygen concentrations respectively.

The main difference between them is the dynamics of $^1O_2$ production. ^{11}C has a higher Cerenkov yield than ^{18}F, but its physical lifetime is much lower (20 vs 112 min respectively). ^{68}Ga can produce, on average, 8.5×10^{12} $^1O_2$. As stated in previous studies, the effective threshold dose of $^1O_2$ estimated for murine breast tumor spheroids was 2×10^8 molecules per

cell [40]. Similarly, a dose of 5×10^8 molecules per cell has been reported to induce liver necrosis in living rat [39]. Considering these values, the amount of $^1O_2$ produced by ^{68}Ga can destroy between 4×10^3 and 4×10^4 cancerous cells for 10 kBq associated with 1 µM of photofrin after a 2 h exposure. The most effective emitters are ^{89}Zr and ^{90}Y. Both isotopes have the longest lifetime. The amount of $^1O_2$ produced yields the destruction of 7.6×10^3 to 7.6×10^4 cells with the same radioactive concentration as before. Collectively, our estimation supported the concept that lifetime should be the most important factor to consider when CR-PDT is set-up.

VI. Nanoscintillators Would Increase PDT Efficacy

This $^1O_2$ production estimation only considered the direct PS activation through Cerenkov radiation. However, an easy way to improve CR-PDT would involve using nanoscintillators in nanoparticles. Indeed, as stated before, most of the Cerenkov light is in the UV domain and many lanthanides (e.g., Terbium) has a strong UV absorption yielding a high luminescence. This strategy is similar to the X-PDT approach where X-rays are used to excite nanoscintillator which, in turn, activate PS [9]. It requires nanoparticles exhibiting appropriated physical properties to establish energy transduction from the nanoscintillator to the PS, a high scintillation quantum yield and an optimal energy transfer from the scintillator onto the PS [48,49]. However, one of the biggest X-PDT pitfall is that, only a small fraction of the X-ray emitted photons will be converted into scintillations [50]. In addition, X-PDT has been studied in preclinical conditions, with X-ray energies ranging from dozen to a few hundred keV. In a clinical context here X-ray beam is set around 6 MeV, scintillation yield is dramatically lower since the probability of photoelectric interaction becomes minimal [38]. In these conditions, it is of great interest to find another way to activate the entire system nanoscintillator/PS in clinically compatible condition. In this way, b emitters are relevant not only because they can produce Cerenkov radiation able to excite both PS and nanoscintillators; but also, for positron emitters, because the 511 keV annihilation photons can also be converted to visible light by the scintillators to offer a third PS activation way. Then, PS would be excited from both scintillating element and direct Cerenkov photons (**Figure 29**).

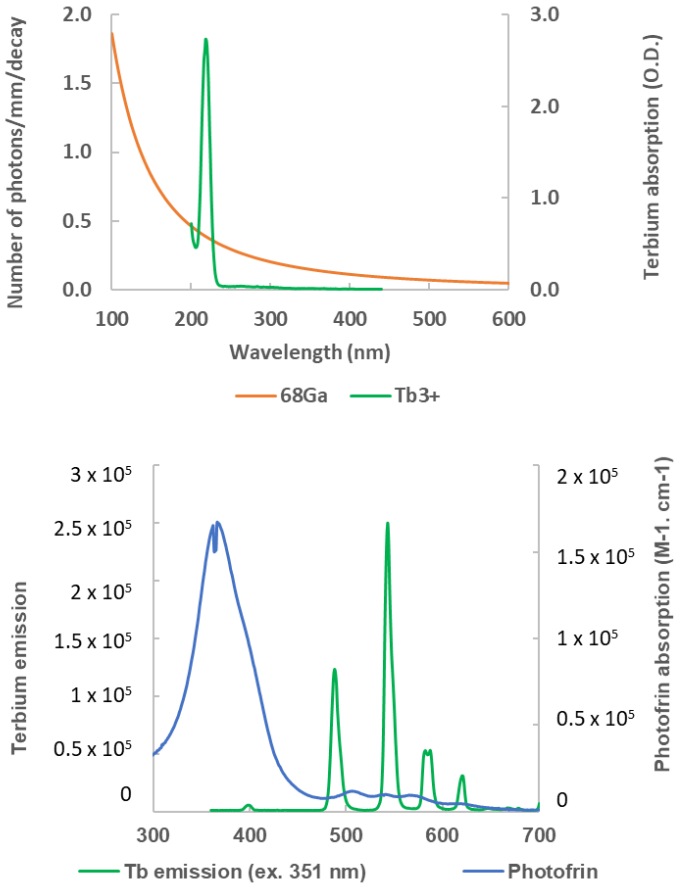

Figure 29 : Up: 68Ga Cerenkov spectrum overlapping Terbium absorption spectrum (between 280 and 520 nm). Terbium presents a high absorption band around 220 nm. Bottom: Terbium emission overlapping photofrin absorption spectra. Terbium was excited with 351 nm UV source and presented 4 characteristic peaks (490, 545, 590 and 620 nm). These Terbium emission wavelengths are able to excite the photosensitizers (PS) and thus to produce photodynamic therapy (PDT) effect. Hence, Cerenkov light can both excite the PS, mostly between 350–400 nm, and the Terbium, used as a scintillator, to involve two PS activation ways.

VII. Conclusions

Cerenkov light should be able to induce a PDT effect yielding cell death in tumor tissue with a minimal local radioactive concentration. The fact the greatest part of Cerenkov photons is in the UV-C domain means that this must be taken into consideration, when dealing with CR-PDT. Indeed, PSs absorb the light between 400 and 650 nm (i.e., the visible domain), suggesting that most of Cerenkov photons do not activate type II photoreactions which generate $^1O_2$. Nevertheless, UV-B and UV-C induce oxidative stress and DNA damage which trigger cell to cell death. An easy way to improve CR-PDT would be the addition of nanoscintillators to convert UV photons to wavelengths absorbed by the PS. Hence, the overall mechanism, involved in a possible synergy of direct UV and Cerenkov photon interactions, should be detailed to fully explain the observed CR-PDT efficacy.

References

1. Niedre, M.; Patterson, M.S.; Wilson, B.C. Direct near-infrared luminescence detection of singlet oxygen generated by photodynamic therapy in cells in vitro and tissues in vivo. *Photochem. Photobiol.* **2002**, *75*, 382–391, doi: 10.1562/0031-8655(2002)0750382DNILDO2.0.CO2.
2. Hirschberg, H.; Berg, K.; Peng, Q. Photodynamic therapy mediated immune therapy of brain tumors. *Neuroimmunol. Neuroinflamm.* **2018**, *5*, 27, doi:10.20517/2347-8659.2018.31.
3. Gill, I.S.; Azzouzi, A.-R.; Emberton, M.; Coleman, J.A.; Coeytaux, E.; Scherz, A.; Scardino, P.T.; PCM301 Study Group Randomized Trial of Partial Gland Ablation with Vascular Targeted Phototherapy versus Active Surveillance for Low Risk Prostate Cancer: Extended Followup and Analyses of Effectiveness. *J. Urol.* **2018**, *200*, 786–793, doi:10.1016/j.juro.2018.05.121.
4. Bechet, D.; Mordon, S.R.; Guillemin, F.; Barberi-Heyob, M.A. Photodynamic therapy of malignant brain tumours: A complementary approach to conventional therapies. *Cancer Treat. Rev.* **2014**, *40*, 229–241, doi:10.1016/j.ctrv.2012.07.004.
5. Chen, W.; Zhang, J. Using Nanoparticles to Enable Simultaneous Radiation and Photodynamic Therapies for Cancer Treatment. *J. Nanosci. Nanotechnol.* **2006**, *6*, 1159–1166, doi:10.1166/jnn.2006.327.
6. Popovich, K.; Tomanova, K.; Čuba, V.; Procházková, L.; Pelikánová, I.T.; Jakubec, I.; Mihóková, E.; Nikl, M. LuAG:Pr3+-porphyrin based nanohybrid system for singlet oxygen production: Toward the next generation of PDTX drugs. *J. Photochem. Photobiol. B: Biol.* **2018**, *179*, 149–155, doi:10.1016/j.jphotobiol.2018.01.015.
7. Chen, M.-H.; Jenh, Y.-J.; Wu, S.-K.; Chen, Y.-S.; Hanagata, N.; Lin, F.-H. Non-invasive Photodynamic Therapy in Brain Cancer by Use of Tb3+-Doped LaF3 Nanoparticles in Combination with Photosensitizer Through X-ray Irradiation: A Proof-of-Concept Study. *Nanoscale Res. Lett.* **2017**, *12*, 1–6, doi:10.1186/s11671-017-1840-3.
8. Bulin, A.-L.; Truillet, C.; Chouikrat, R.; Lux, F.; Frochot, C.; Amans, D.; LeDoux, G.; Tillement, O.; Perriat, P.; Barberi-Heyob, M.; et al. X-ray-Induced Singlet Oxygen Activation with Nanoscintillator-Coupled Porphyrins. *J. Phys. Chem. C* **2013**, *117*, 21583–21589, doi:10.1021/jp4077189.
9. LaRue, L.; Ben Mihoub, A.; Youssef, Z.; Colombeau, L.; Acherar, S.; André, J.-C.; Arnoux, P.; Baros, F.; Vermandel, M.; Frochot, C. Using X-rays in photodynamic therapy: an overview. *Photochem. Photobiol. Sci.* **2018**, *17*, 1612–1650, doi:10.1039/c8pp00112j.
10. Sun, W.; Zhou, Z.; Pratx, G.; Chen, X.; Chen, H. Nanoscintillator-Mediated X-Ray Induced Photodynamic Therapy for Deep-Seated Tumors: From Concept to Biomedical Applications. *Theranostics* **2020**, *10*, 1296–1318, doi:10.7150/thno.41578.
11. Verry, C.; Sancey, L.; Dufort, S.; Le Duc, G.; Mendoza, C.; Lux, F.; Grand, S.; Arnaud, J.; Quesada, J.L.; Villa, J.; et al. Treatment of multiple brain metastases using gadolinium nanoparticles and radiotherapy: NANO-RAD, a phase I study protocol. *BMJ Open* **2019**, *9*, e023591, doi:10.1136/bmjopen-2018-023591.
12. Verry, C.; Dufort, S.; Lemasson, B.; Grand, S.; Pietras, J.; Troprès, I.; Crémillieux, Y.; Lux, F.; Mériaux, S.; Larrat, B.; et al. Targeting brain metastases with ultrasmall theranostic nanoparticles, a first-in-human trial from an MRI perspective. *Sci. Adv.* **2020**, *6*, eaay5279, doi:10.1126/sciadv.aay5279.
13. Dothager, R.S.; Goiffon, R.J.; Jackson, E.; Harpstrite, S.; Piwnica-Worms, D. Cerenkov Radiation Energy Transfer (CRET) Imaging: A Novel Method for Optical Imaging of PET Isotopes in Biological Systems. *PLoS ONE* **2010**, *5*, e13300, doi:10.1371/journal.pone.0013300.
14. Liu, H.; Zhang, X.; Xing, B.; Han, P.; Gambhir, S.S.; Cheng, Z. Radiation-Luminescence-Excited Quantum Dots for in vivo Multiplexed Optical Imaging. *Small* **2010**, *6*, 1087–1091, doi:10.1002/smll.200902408.
15. Ran, C.; Zhang, Z.; Hooker, J.M.; Moore, A. In Vivo Photoactivation Without "Light": Use of Cherenkov Radiation to Overcome the Penetration Limit of Light. *Mol. Imaging Biol.* **2012**, *14*, 156–162, doi:10.1007/s11307-011-0489-z.
16. Pratx, G.; Kapp, D.S. Is Cherenkov luminescence bright enough for photodynamic therapy? *Nat. Nanotechnol.* **2018**, *13*, 354, doi:10.1038/s41565-018-0142-y.
17. Jelley, J.V. Cherenkov radiation and its applications; Pergamon press: London, UK, 1958; pp. 314.
18. Mitchell, G.S.; Gill, R.K.; Boucher, D.L.; Li, C.; Cherry, S.R. In vivo Cerenkov luminescence imaging: a new tool for molecular imaging. *Philos. Trans. R. Soc. A.* **2011**, *369*, 4605–4619, doi:10.1098/rsta.2011.0271.

19. Gill, R.K.; Mitchell, G.S.; Cherry, S.R. Computed Cerenkov luminescence yields for radionuclides used in biology and medicine. *Phys. Med. Biol.* **2015**, *60*, 4263–4280, doi:10.1088/0031-9155/60/11/4263.
20. Moan, J.; Berg, K. The photodegradation of porphyrins in cells can be used to estimate the lifetime of singlet oxygen. *Photochem. Photobiol.* **1991**, *53*, 549–553, doi:10.1111/j.1751-1097.1991.tb03669.x.
21. Calixto, G.M.F.; Bernegossi, J.; De Freitas, L.M.; Fontana, C.R.; Chorilli, M. Nanotechnology-Based Drug Delivery Systems for Photodynamic Therapy of Cancer: A Review. *Molecules* **2016**, *21*, 342, doi:10.3390/molecules21030342.
22. Karunakaran, S.C.; Babu, P.S.S.; Madhuri, B.; Marydasan, B.; Paul, A.K.; Nair, A.S.; Rao, K.S.; Srinivasan, A.; Chandrashekar, T.K.; Rao, C.M.; et al. In VitroDemonstration of Apoptosis Mediated Photodynamic Activity and NIR Nucleus Imaging through a Novel Porphyrin. *ACS Chem. Biol.* **2013**, *8*, 127–132, doi:10.1021/cb3004622.
23. Liu, K.; Liu, X.; Zeng, Q.; Zhang, Y.; Tu, L.; Liu, T.; Kong, X.; Wang, Y.; Cao, F.; Lambrechts, S.A.G.; et al. Covalently Assembled NIR Nanoplatform for Simultaneous Fluorescence Imaging and Photodynamic Therapy of Cancer Cells. *ACS Nano* **2012**, *6*, 4054–4062, doi:10.1021/nn300436b.
24. Sharman, W.M.; Allen, C.M.; Van Lier, J.E. Photodynamic therapeutics: basic principles and clinical applications. *Drug Discov. Today* **1999**, *4*, 507–517, doi:10.1016/s1359-6446(99)01412-9.
25. Ciarrocchi, E.; Belcari, N. Cerenkov luminescence imaging: physics principles and potential applications in biomedical sciences. *EJNMMI Phys.* **2017**, *4*, 14, doi:10.1186/s40658-017-0181-8.
26. Kotagiri, N.; Sudlow, G.P.; Akers, W.J.; Achilefu, S. Breaking the depth dependency of phototherapy with Cerenkov radiation and low-radiance-responsive nanophotosensitizers. *Nat. Nanotechnol.* **2015**, *10*, 370–379, doi:10.1038/nnano.2015.17.
27. Kamkaew, A.; Cheng, L.; Goel, S.; Valdovinos, H.F.; Barnhart, T.E.; Liu, Z.; Cai, W. Cerenkov Radiation Induced Photodynamic Therapy Using Chlorin e6-Loaded Hollow Mesoporous Silica Nanoparticles. *ACS Appl. Mater. Interfaces* **2016**, *8*, 26630–26637, doi:10.1021/acsami.6b10255.
28. Ni, D.; Ferreira, C.A.; Barnhart, T.E.; Quach, V.; Yu, B.; Jiang, D.; Wei, W.; Liu, H.; Engle, J.W.; Hu, P.; et al. Magnetic Targeting of Nanotheranostics Enhances Cerenkov Radiation-Induced Photodynamic Therapy. *J. Am. Chem. Soc.* **2018**, *140*, 14971–14979, doi:10.1021/jacs.8b09374.
29. Duan, D.; Liu, H.; Xu, Y.; Han, Y.; Xu, M.; Zhang, Z.; Liu, Z. Activating TiO2 Nanoparticles: Gallium-68 Serves as a High-Yield Photon Emitter for Cerenkov-Induced Photodynamic Therapy. *ACS Appl. Mater. Interfaces* **2018**, *10*, 5278–5286, doi:10.1021/acsami.7b17902.
30. Hartl, B.A.; Hirschberg, H.; Marcu, L.; Cherry, S.R. Activating Photodynamic Therapy in vitro with Cerenkov Radiation Generated from Yttrium-90. *J. Environ. Pathol. Toxicol. Oncol.* **2016**, *35*, 185–192, doi:10.1615/jenvironpatholtoxicoloncol.2016016903.
31. Nakamura, Y.; Nagaya, T.; Sato, K.; Okuyama, S.; Ogata, F.; Wong, K.J.; Adler, S.; Choyke, P.L.; Kobayashi, H. Cerenkov Radiation–Induced Photoimmunotherapy with 18F-FDG. *J. Nucl. Med.* **2017**, *58*, 1395–1400, doi:10.2967/jnumed.116.188789.
32. Ivashkevich, A.; Redon, C.E.; Nakamura, A.J.; Martin, R.F.; Martin, O.A. Use of the γ-H2AX assay to monitor DNA damage and repair in translational cancer research. *Cancer Lett.* **2012**, *327*, 123–133, doi:10.1016/j.canlet.2011.12.025.
33. Robertson, C.A.; Evans, D.H.; Abrahamse, H. Photodynamic therapy (PDT): A short review on cellular mechanisms and cancer research applications for PDT. *J. Photochem. Photobiol. B: Biol.* **2009**, *96*, 1–8, doi:10.1016/j.jphotobiol.2009.04.001.
34. Baldea, I.; Olteanu, D.; Bolfa, P.; Tăbăran, A.-F.; Ion, R.-M.; Filip, G.A. Melanogenesis and DNA damage following photodynamic therapy in melanoma with two meso-substituted porphyrins. *J. Photochem. Photobiol. B: Biol.* **2016**, *161*, 402–410, doi:10.1016/j.jphotobiol.2016.06.012.
35. Yu, B.; Ni, D.; Rosenkrans, Z.T.; Barnhart, T.E.; Wei, H.; Ferreira, C.A.; Lan, X.; Engle, J.W.; He, Q.; Yu, F.; et al. A "Missile-Detonation" Strategy to Precisely Supply and Efficiently Amplify Cerenkov Radiation Energy for Cancer Theranostics. *Adv. Mater.* **2019**, *31*, e1904894, doi:10.1002/adma.201904894.
36. Eftekhari-Kenzerki, Z.; Fardid, R.; Behzad-Behbahani, A. Impact of Silver Nanoparticles on the Ultraviolet Radiation Direct and Bystander Effects on TK6 Cell Line. *J. Med. Phys.* **2019**, *44*, 118–125.

37. Kotagiri, N.; Cooper, M.L.; Rettig, M.; Egbulefu, C.; Prior, J.; Cui, G.; Karmakar, P.; Zhou, M.; Yang, X.; Sudlow, G.; et al. Radionuclides transform chemotherapeutics into phototherapeutics for precise treatment of disseminated cancer. *Nat. Commun.* **2018**, *9*, 1–12, doi:10.1038/s41467-017-02758-9.
38. Clement, S.; Deng, W.; Camilleri, E.; Wilson, B.C.; Goldys, E.M. X-ray induced singlet oxygen generation by nanoparticle-photosensitizer conjugates for photodynamic therapy: determination of singlet oxygen quantum yield. *Sci. Rep.* **2016**, *6*, 19954, doi:10.1038/srep19954.
39. Farrell, T.J.; Wilson, B.C.; Patterson, M.S.; Chow, R. Dependence of photodynamic threshold dose on treatment parameters in normal rat liver in vivo. In Proceedings of Optics, Electro-Optics, and Laser Applications in Science and Engineering, Los Angeles, CA, USA, 1 June 1991.
40. Georgakoudi, I.; Nichols, M.G.; Foster, T.H. The Mechanism of Photofrin Photobleaching and Its Consequences for Photodynamic Dosimetry. *Photochem. Photobiol.* **1997**, *65*, 135–144, doi:10.1111/j.1751-1097.1997.tb01889.x.
41. Rizvi, I.; Anbil, S.; Alagic, N.; Celli, J.P.; Zheng, L.Z.; Palanisami, A.; Glidden, M.D.; Pogue, B.W.; Hasan, T. PDT dose parameters impact tumoricidal durability and cell death pathways in a 3D ovarian cancer model. *Photochem. Photobiol.* **2013**, *89*, 942–952, doi:10.1111/php.12065.
42. Penjweini, R.; Liu, B.; Kim, M.M.; Zhu, T.C. Explicit dosimetry for 2-(1-hexyloxyethyl)-2-devinyl pyropheophorbide-a-mediated photodynamic therapy: macroscopic singlet oxygen modeling. *J. Biomed. Opt.* **2015**, *20*, 128003, doi:10.1117/1.jbo.20.12.128003.
43. Kim, M.M.; Ghogare, A.A.; Greer, A.; Zhu, T.C. On thein vivophotochemical rate parameters for PDT reactive oxygen species modeling. *Phys. Med. Biol.* **2017**, *62*, R1–R48, doi:10.1088/1361-6560/62/5/r1.
44. Wang, K.K.-H.; Finlay, J.C.; Busch, T.M.; Hahn, S.M.; Zhu, T.C. Explicit dosimetry for photodynamic therapy: macroscopic singlet oxygen modeling. *J. Biophotonics* **2010**, *3*, 304–318, doi:10.1002/jbio.200900101.
45. Qiu, H.; Kim, M.M.; Penjweini, R.; Zhu, T.C. Macroscopic singlet oxygen modeling for dosimetry of Photofrin-mediated photodynamic therapy: an in-vivo study. *J. Biomed. Opt.* **2016**, *21*, 88002, doi:10.1117/1.JBO.21.8.088002.
46. Qiu, H.; Kim, M.M.; Penjweini, R.; Finlay, J.C.; Busch, T.M.; Wang, T.; Guo, W.; Cengel, K.A.; Simone, C.B.; Glatstein, E.; et al. A Comparison of Dose Metrics to Predict Local Tumor Control for Photofrin-mediated Photodynamic Therapy. *Photochem. Photobiol.* **2017**, *93*, 1115–1122, doi:10.1111/php.12719.
47. Kotagiri, N.; Laforest, R.; Achilefu, S. Reply to Is Cherenkov luminescence bright enough for photodynamic therapy? *Nat. Nanotechnol.* **2018**, *13*, 354–355, doi:10.1038/s41565-018-0143-x.
48. Kamkaew, A.; Chen, F.; Zhan, Y.; Majewski, R.L.; Cai, W. Scintillating Nanoparticles as Energy Mediators for Enhanced Photodynamic Therapy. *ACS Nano* **2016**, *10*, 3918–3935, doi:10.1021/acsnano.6b01401.
49. Zou, X.; Yao, M.; Ma, L.; Hossu, M.; Han, X.; Juzenas, P.; Chen, W. X-ray-induced nanoparticle-based photodynamic therapy of cancer. *Nanomed.* **2014**, *9*, 2339–2351, doi:10.2217/nnm.13.198.
50. Ren, X.-D.; Hao, X.-Y.; Li, H.-C.; Ke, M.-R.; Zheng, B.-Y.; Huang, J. Progress in the development of nanosensitizers for X-ray-induced photodynamic therapy. *Drug Discov. Today* **2018**, *23*, 1791–1800, doi:10.1016/j.drudis.2018.05.029.

Sous-chapitre I.2: Peptide-conjugated nanoparticles for targeted Photodynamic therapy

Batoul Dhaini[1,2], Bibigul Kenzhebayeva[3,4], Amina Ben-Mihoub[3], Mickaël Gries[5], Samir Acherar[3], Francis Baros[1], Noémie Thomas[5], Joël Daouk[5], Hervé Schohn[5], Tayssir Hamieh[2,6] and Céline Frochot*[1]

[1]*Université de Lorraine, CNRS,* Reactions and Chemical Engineering Laboratory *LRGP, F-54000 Nancy, France.* [2]*Université Libanaise, Faculté des sciences, MCEMA, Laboratoire des Matériaux, Catalyses, Environnement et Méthodes Analytiques, Beirut, Liban.*
[3]*Université de Lorraine, CNRS,* Laboratory of Macromolecular Physical Chemistry *LCPM, F-54000 Nancy, France.*
[4]*University of Satbayev, the department of chemical and biochemical engineering, Almaty, Kasakhstan.*
[5]*Université de Lorraine, CNRS,* Department of Biology, Signals and Systems in Cancer and Neuroscience *CRAN, F54000 Nancy, France.*
[6]*Faculty of Science and Engineering, Maastricht University, P.O. Box 616, 6200 MD Maastricht, The Netherlands.*

Review published in Nanophotonics journal

Résumé : Le cancer est la deuxième cause de décès dans le monde après les maladies cardiovasculaires. En fonction du type et de la localisation de la tumeur, plusieurs traitements du cancer sont mis en œuvre. Parmi ceux-ci, les trois thérapies les plus conventionnelles sont la chirurgie, la radiothérapie et la chimiothérapie. Cependant, il existe d'autres approches thérapeutiques telles que la thérapie photodynamique (PDT). La PDT repose sur l'action combinée de la lumière, d'une molécule photoactivable appelée photosensibilisateur (PS) et de l'oxygène moléculaire. La plupart des PS utilisés pour les applications cliniques ne sont pas spécifiques des cellules cancéreuses. L'une des solutions pour surmonter ce problème est l'utilisation de nanoparticules (NPs) pour induire un ciblage passif. Il est également possible de greffer un vecteur sur les NP pour cibler spécifiquement les récepteurs membranaires surexprimé dans les cellules tumorales ou les néovaisseaux entourant la tumeur. Dans cette revue, nous nous concentrons sur les NPs chargés de PSs et couplés à des peptides pour une PDT ciblée. Nous avons décrit des nanosystèmes qui ciblaient la neuropiline-1 (NRP-1), les intégrines αvβ3, le récepteur membranaire du nucléole, le récepteur du facteur de croissance épidermique (EGF), la protéine-glutamine-gamma-glutamyltransférase (TGM2), p32, la transferrine, PD-1 et la membrane mitochondriale. L'utilisation d'un peptide absorbant les cellules est également décrite.

Peptide-conjugated nanoparticles for targeted Photodynamic therapy

Abstract: Cancer is the second leading cause of death worldwide after cardiovascular disease. Depending on the type and the location of the tumor, several cancer treatments are implemented. Among these, the three most conventional therapies are surgery, radiotherapy and chemotherapy. However, there are other therapeutic approaches such as photodynamic therapy (PDT). PDT relies on the combined action of light, a photoactivable molecule called photosensitizer (PS) and molecular oxygen. Most of the PSs used for clinical applications are not cancer-cell specific. One of the solutions to overcome this problem is the use of nanoparticles (NPs) to induce a passive targeting. It is also possible to graft a vector onto the NPs to specifically target membrane receptors overexpressed in the tumor cells or neovessels surrounding the tumor. In this review, we focus on the NPs loaded with PSs and coupled to peptides for targeted PDT. We described nanosystems that targeted Neuropilin-1 (NRP-1), $\alpha_v\beta_3$ integrins, nucleolin membrane receptor, epidermal growth factor (EGF) receptor, protein-glutamine-gamma-glutamyltransferase (TGM2), p32, transferrin, PD-1 and mitochondrial membrane. The use of a cell absorbingpeptide is also described.

Keywords: Photodynamic therapy, cancer, nanoparticle, targeting, peptide, photosensitizer

I. Introduction

Cancer is the second leading cause of death in the world after cardiovascular disease [1]. Cancer treatment is mainly based on surgery, radiotherapy and/or chemotherapy, where the used therapeutic strategy depends on the cancer type and localization [2, 3]. The chemoradiotherapy treatment, which combines both radiotherapy and chemotherapy, exerts adverse effects on the normal cells surrounding the tumors. It is also well-known that the anticancer drugs could lead to the appearance of cell resistance mechanisms, resulting in the progression of tumors and rendering drug-treatment ineffective. An alternative strategy is the photodynamic therapy (PDT) [4]. PDT has been discovered more than 100 years ago by Raab and Tappeiner [5]. The principle of PDT consists of the transfer of light photons to a molecule, a photosensitizer (PS), which, in the presence of molecular oxygen, produces mainly singlet oxygen ($^1O_2$) and other reactive oxygen species (ROS), through photoreaction of type II and I, respectively (**Figure 30**). The production of reactive oxygen species (ROS/Singlet oxygen) at the loci of the mitochondrial, lysosomal or endoplasmic reticulum (ER) can directly initiate cell death by apoptosis [6]. Apoptosis is an irreversible pathway to cell death. One of the triggers for apoptosis is the release of cytochrome C into the cytoplasm, the photodamaged mitochondria trigger an anapoptotic response and result in the destruction of anti-apoptotic proteins. When cells are unable to undergo apoptosis, the autophagy pathway will be proposed as the cell death pathway. Autophagy allows the recycling of cellular components under conditions of starvation. The third pathway to cell death is necrosis.

Necrosis is often the consequence of an external cell injury. This injury is due to a supralethal dose of drug / light causing loss of membrane integrity. It can also occur after direct photodamage to the plasma membrane. When no apoptotic mechanism is involved, a fourth cell death pathway is proposed: paraptosis [7]. The hallmark is a substantial degree of vacuolation which appears to involve the endoplasmic reticulum (ER) and possibly the mitochondria. PDT may also have implications for the treatment of distant metastases, as an increased immunologic effect may result [8]. In 1978 Dougherty performed the first clinical applications in digestive oncology, demonstrating the interest of PDT strategy in a clinical context [9, 10]. The treatment by PDT presents many advantages. It is of low cost, less invasive than surgery, localized, presents little or no side effects, can be combined with other treatments and can be repeated many times at the same site without causing unwanted effects [10, 11].

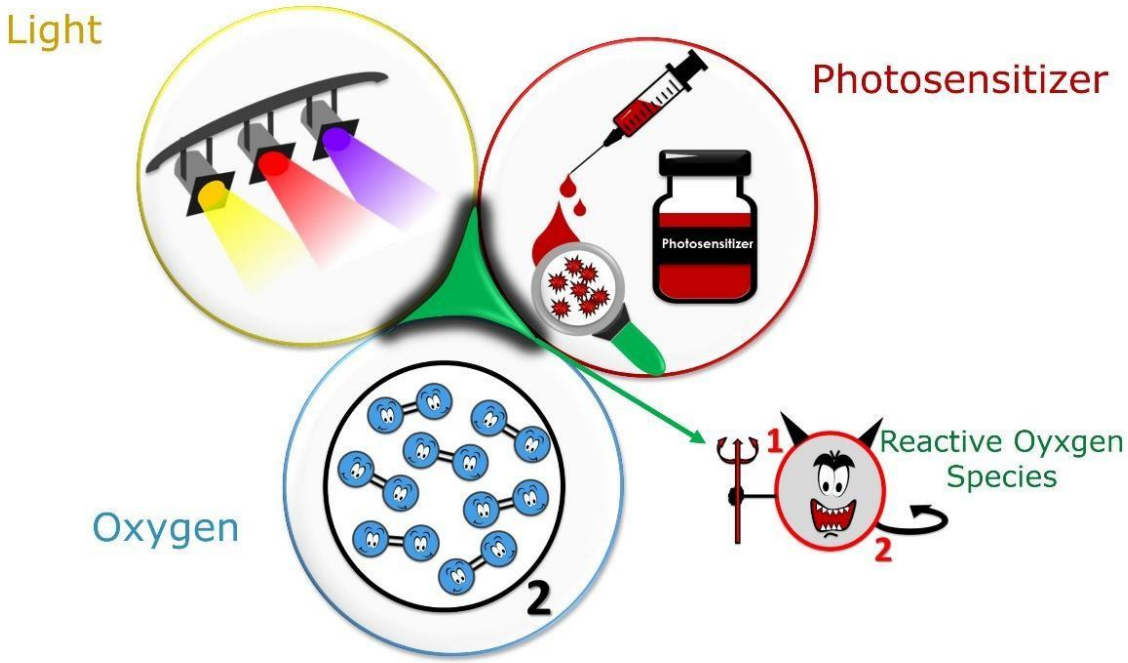

Figure 30 : Schematic presentation of PDT functionalization

PDT is used in dermatology, urology, gastroenterology, gynecology, neurosurgery, and pneumology [10]. Although it is currently in clinic, there are several difficulties that hinder the application of PDT. These include the poor penetration of light into the tissues, the hydrophobicity of the PSs, which in its turn increases the self-aggregation and decreases the cell incorporation efficiency, as well as their low selectivity towards tumor cells [12].

To overcome this, a breakthrough strategy based on nanoparticles (NPs) doped with PSs had been developed [13]. NPs could be delivered into the tumor areas via the enhanced permeability and retention (EPR) effect, consisting of the modeling of the vascular system surrounding tumors with concomitant fenestration of the neoplastic vessels [14]. Moreover, the delivery of NPs into the tumor was improved by coupling peptides that

target membrane receptors localized on the cancer cell surface or the surrounding neovessels. In addition, receptors involved in cell trafficking were also used for NP absorption. Noting that some peptide based nanoparticles are developed to be pH sensitive for photodynamic therapy (PDT) with prolonged tumor retention times [15].

The selectivity of PDT relies both upon the targeting of the light delivery and on the preferential uptake of the photosensitizer by malignant tissue. The majority of photosensitizers are taken up non-selectively by all cell types studied in vitro, and can also accumulate in normal cells. Different strategies can be addressed to improve the selectivity of PS. By using nanoparticles, the Enhanced Permeability retention (EPR) Effect allow the passive accumulation of the NP into the tumor. This is called the passive targeting. To target receptors overexpressed onto membranes of tumor cells or neovessels, it is possible to attach a vector to the photosensitizer or the nanoparticle. It is active targeting. Different vectors are described in the literature such as folic acid that targets folic acid receptor over-expressed on many tumoral cell membranes [16], but can suffer from low stability [17]. Stability of folic acid under several parameters [18], anti-tumor monoclonal antibodies [19] that present drawbacks such as their the large size and non-specific uptake of the antibody molecules by the liver and the reticulo-endothelial system [18]. Moreover, anti-tumor monoclonal antibodies exhibit low tissue penetration and poor cellular uptake when used in vivo [20]. Protein [21] can also be coupled with success to PS as well as aptamer [22]. Small peptides represent excellent targeting agents for receptors over-expressed in human cancers. We already describe in a review [23] all the advantages of using peptides such as their small size, they present good tissue permeability, rapid access to the tumor site, they can cross a disturbed bloodbrain barrier, they present low antigenicity. They are easy to synthesize in liquid or solid phases, easy to modify (pseudo-peptides), easy to link to a spacer via amide bond for example, they can present high affinity for receptors and rapid clearance from the body. Two drawbacks can be cited: they are potentially degraded by endo- and/or exo-peptidases ans they do not cross a normal blood-brain barrier.

Different receptors overexpressed in tumor or endothelial cells that had been chosen for cell targeting are described in this review: Neuropilin-1 (NRP-1), $\alpha_v\beta_3$ integrins, nucleolin membrane receptor, epidermal growth factor (EGF), protein-glutamine-gammaglutamyltransferase (TGM2), p32, as well as transferrin and mitochondrial membrane. The use of a specific cell absorbing-peptide is also described.

II. Nanoparticles loaded with photosensitizer and coupled to peptide

II.1 Peptides targeting Neuropilin-1 receptor

II.1.1 NPs@PS@ATWLPPR

The Neuropilin-1 (NRP-1) is a transmembrane glycoprotein and a co-receptor of the vascular endothelial growth factor receptor (VEGFR). It is involved in the axon guidance, angiogenesis, and immune responses [24]. NRP-1 is overexpressed in many types of cancers such as colon carcinoma, prostate, pancreatic carcinoma, lung carcinoma, melanoma, astrocytoma and neuroblastoma [25].

NRP-1 has been described as a potential target against glioblastoma [26]. A high NRP-1 expression in a glioblastoma sample is correlated with increased malignancy. In contrast, NRP-1 under-expression is associated to low cancer stem cell migration and proliferation *in vitro*, and to reduce tumor growth, *in vivo*. The enhanced NRP-1 expression has been observed in endothelial cells and is correlated to the development of tumor neovascularization [27, 28]. Vascular Targeted Photodynamic therapy (VTP) was applied using ATWLPPR heptapeptide as a part of specific NRP-1 recognizing sequence. Linked by a spacer arm (6-aminohexanoic acid, Ahx) to chlorin PS, the peptide accumulated in the tumor tissue and potentiated the photodynamic activity. However, the biodistribution studies conducted on mice demonstrated a rapid uptake of the peptide by the liver and the spleen. Consequently, 2 hours after intravenous injection (IV), 85% of the total amount of the compound was degraded in the liver [29]. Since the peptide arm, conjugated to the PS, was responsible for its selectivity, the degradation of this peptide fragment was related to the decrease in the PS accumulation in the tumor tissue [30].

In order to reduce the hepato-splenic clearance and peptide degradation, functionalized silica-based NPs, grafted with ATWLPPR-peptide by hydrophilic polymer, were designed for vessel targeting. The NP was also designed as a magnetic resonance imaging (MRI) contrast agent, since it is composed of a silica shell coupled to polyethylene glycol (PEG), doped with gadolinium oxide (Gd_2O_3). The PS was a chlorin derivative, 5-(4-carboxyphenyl)-10, 15, 20 triphenyl-chlorin (TPC), substituted with a succinimidyl ester. In brief, aminopropyltriethoxysilane (APTES) reacted with PEG or propylenediaminetetra-acetic acid (PDTA) containing Gd_2O_3 and was cyclehydrolysis to obtain the NPs (referred to as NP-TPC) [31-33] (**Figure 31A**). The size of the NPs was estimated between 3.3 and 3.8 nm [31, 33]. The coupling of the peptide (referred to as NP-TPC-ATWLPPR) raised the NPs' size to 4.6 ± 3.8 nm. NP-TPC-ATWLPPR were tested for their affinity to NRP-1 using biotinylated VEGF in competitive binding assays. The IC50 values were estimated to be 27 and 56.6 µM for NP-TPC-ATWLPPR and NP-TPC, respectively. The photocytotoxic effect was tested on human breast MDA-MB-231 cells that overexpress a high level of NRP-1. The calculated LD50 (Light dose) for P-TPC-ATWLPPR was estimated at 2.8 to 5.0 J.cm-² when cells were treated with 1 µM of NP-TPC-ATWLPPR (power 0.7 W, irradiance 4.54 J.cm-²). The LD50 value was close to that obtained by a similar treatment with 1 µM NP-TPC [31, 32]. In vivo, the maximal MRI enhancement was found at 2-7 min, after the IV injection of NPTPC-ATWLPPR in nude mice. The biodistribution, analysed 75 min after the IV injection, suggested both renal and hepatic clearance for NP-TPC and NP-TPC-ATWLPPR. However, the renal elimination was higher for NP-TPC. The exposure of the tumor U87 grafted cells to NP-TPC-ATWLPPR, revealed that the NPs targeted the peripheral vessels surrounding the tumors in accordance with the high expression of NRP-1 observed in endothelial cells [31, 32] (**Figure 31B**).

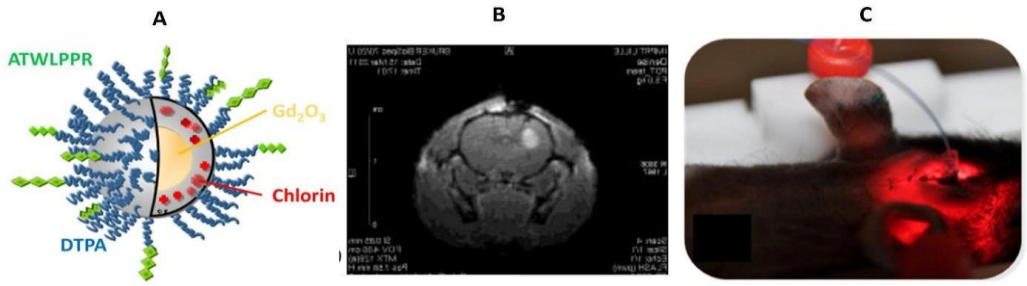

Figure 31 : (A) Schematic presentation of NP-TPC-ATWLPPR, (B) Maximal MRI signal intensity after injecting 84.2 µmol of Gd for a body weight of 250 g for cerebral biodistribution and brain tumor tissue selectivity of NP-TPC-ATWLPPR (C) overview clinical picture of the device applied on the mice [32] with permission from Elsevier and Copyright Clearance Center.

II.1.2 NPs@PS@KDKPPR

Based on the sequence homology of the natural ligand of NRP-1, VEGF-A165, a screening of several peptides was performed. Among the selected sequences, KDKPPR peptide showed a higher affinity to NRP-1 than ATWLPPR; the inhibitor dissociation constant (Ki) was estimated to be 9.0×10^{-8} mol.L^{-1} for the former as compared to 1.4×10^{-4} mol.L^{-1} for the latter [34]. The measurement of the affinity to NRP-1 for the K(P1)DKPPR conjugate (*i.e.* monocarboxylic tetraphenyl porphyrin, P1COOH, linked to the first ε-NH_2 lysine of KDKPPR) was 6 µM versus 171 µM for the P1-ATWLPPR complexes [35, 36].

The K(Pyro)DKPPR conjugate, using pyropheophorbide-a (Pyro) as PS, was coupled to PEGylated gold nanorods (AuNRs@PEG) through a thiol-maleimide (MI) click reaction to attain a combined hyperthermia and PDT effect (**Figure 32**) [37]. The AuNRs were functionalized with PEG to prevent any cytotoxicity. The AuNRs@PEG-MI-K(Pyro)DKPPR, illustrated in Figure 3, possessed a length of about 44 nm and a width of about 8 nm. The photophysical properties of the free Pyro were preserved in AuNRs@PEG-MI-K(Pyro)DKPPR, thus showing an unmodified visible absorption profile, a good fluorescence intensity (ϕ_F = 0.30 in EtOH versus 0.38 for Pyro) and a preserved $^1O_2$ production (ϕ_0 = 0.40 in EtOH versus 0.51 for Pyro).

The affinity of the AuNRs@PEG-MI-K(Pyro)DKPPR and the K(Pyro)DKPPR free peptide to recombinant NRP-1 was evaluated by competitive binding assay giving IC_{50} values of 1.5 and 2.0 µM, respectively. The efficacy of AuNRs@PEG-MI-K(Pyro)DKPPR was tested *in vitro* on human glioblastoma U87 MG cells. No cytotoxicity was obtained with concentrations up to 30 µM (concentration relative to PS), in contrast to the cells treated with the PS alone. A good photodynamic efficiency was found when cells were treated with 30 µM of AuNRs@PEG-MI-K(Pyro)DKPPR for 24 h and then exposed to light irradiation at 652 nm (Fluence 10 J.cm^{-2}, fluence rate 4.54 mW.cm^{-2}) with a 67% decrease in cell viability. This result supported the effect of both photodynamic and photothermal therapies (PTT) due to the presence of Gold.

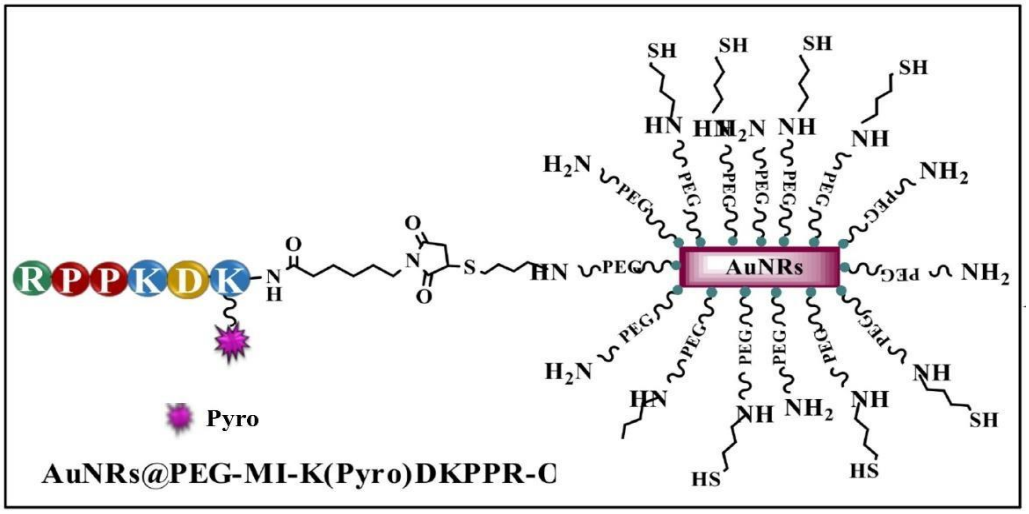

Figure 32 : Schematization of AuNRs@PEG-MI-K(Pyro)DKPPR. Adapted from Youssef et al. [24].

The same methodology was also used to graft K(P1)DKPPR conjugate on multifunctional NP platform, namely AGuIX[@] [38-40]. The designed NPs were first proposed as non-toxic resonance magnetic agents for their imaging properties [41]. The so-called AGuIX@MIK(P1)DKPPR NPs, illustrated in **Figure 33**, were tested for vascular-targeted interstitial photodynamic therapy (iPDT), using human umbilical vein endothelial cells (HUVEC) as an *in vitro* model and human U87 grafted tumors in rodents [38, 39].

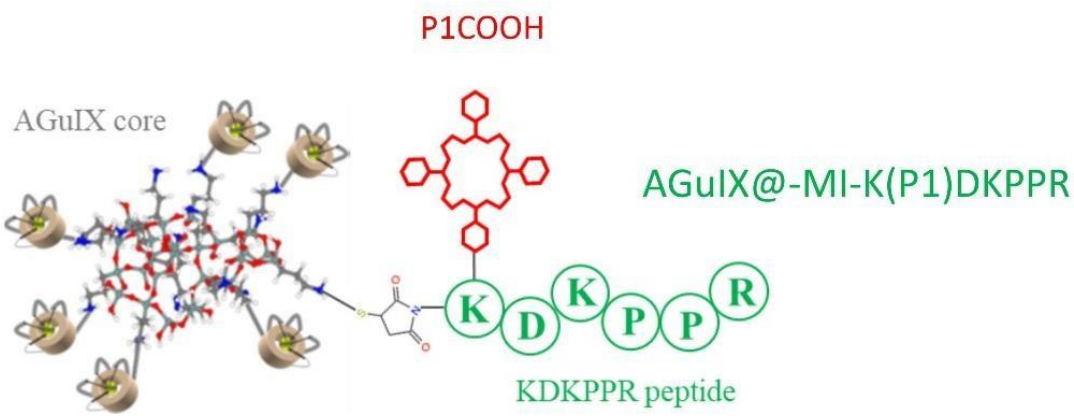

Figure 33 : Schematic presentation of AGuIX@MI-K(P1)DKPPR NPs. Adapted from Thomas et al. [39].

AGuIX@MI-K(P1)DKPPR NPs had a hydrodynamic diameter of approximately 10 nm, making them particularly suitable for rapid renal elimination [42]. The fluorescence (ϕ_F = 0.7 for P1COOH and ϕ_F = 0.1 for AGuIX@MI-K(P1)DKPPR in D_2O) and singlet oxygen (ϕ_O = 0.24 for P1COOH and ϕ_0 = 0.28 for AGuIX@MI-K(P1)DKPPR in D_2O) quantum yields of P1COOH PS were not altered after the peptide addition, demonstrating that the PS could be photoactivated to produce a photocytotoxic effect *in vitro* and *in vivo*.

HUVEC cell exposure to AGuIX@MI-K(P1)DKPPR NPs showed no dark cytotoxicity at PS concentrations up to 10 µM. However, the affinity to NRP-1 was altered as the peptide was coupled to the NPs (19 µM for AGuIX@MI-K(P1)DKPPR versus 2 µM for

the peptide alone). Similar changes were observed when the affinity of AGuIX@MI-K(P1)DKPPR was assessed for human and rat NRP-1. Using the Biacore technology based on the surface plasmon resonance (SPR), the Ki values were estimated at 0.5 µM for KDKPPR and 4.7 µM for AGuIX@MI-K(P1)DKPPR for human NRP-1. For mice NRP-1 cells, the Ki values were estimated at 8.7 µM for KDKPPR and 25.2 µM for AGuIX@MI-K(P1)DKPPR. The use of a scramble peptide (KRPKPD) revealed no binding to recombinant NRP-1 protein, in contrast to the KDKPPR peptide. The specificity of the AGuIX@MI-K(P1)DKPPR NPs was validated using HUVEC overexpressing NRP-1. The incorporation of AGuIX@-MI-K(P1)DKPPR NPs into the cells was increased twice when compared to the NPs carrying the scramble peptide (*i.e.* AGuIX@MI-K(P1)RPKPD NPs).

In vivo, the distribution of AGuIX@MI-K(P1)DKPPR NPs was assessed in rodents, rats and mice, 96 hours post-IV injection of 4 µmol.kg1 (PS equivalent) corresponding to 55 µmol.kg-1 (Gd equivalent). Throughout the experimental delay, no signs of clinical toxicity were observed. 96 hours post-IV injection, the fluorescence signal was mainly found in the organs of excretion such as the liver, bladder and kidneys. However, the contrast enhancement of Gd quantification was only observed in the kidneys and bladder. The selectivity of the AGuIX@MI-K(P1)DKPPR NPs to the tumor, compared to the healthy brain parenchyma, was validated in nude rats. This was applied on an orthotopic tumor developed from human glioblastoma U87 grafted cells, followed by MRI (T1 sequences). The selectivity of the AGuIX@MI-K(P1)DKPPR NPs towards the tumor vascular endothelium after IV injection was also assessed in nude mouse model either with dorsal chamber or cranial window. Non-targeting NPs (i.e. AGuIX@P1 without peptide and AGuIX@-MI-K(P1)RPKPD with scramble peptide) were visualized in the blood vessels 1 hour after injection but disappeared after 4 hours due to the fenestration of the tumor vascular system (**Figure 34**). In contrast, AGuIX@MI-K(P1)DKPPR NPs were more localized on the tumor vessel walls 1 hour after injection and were still present after 24 hours.

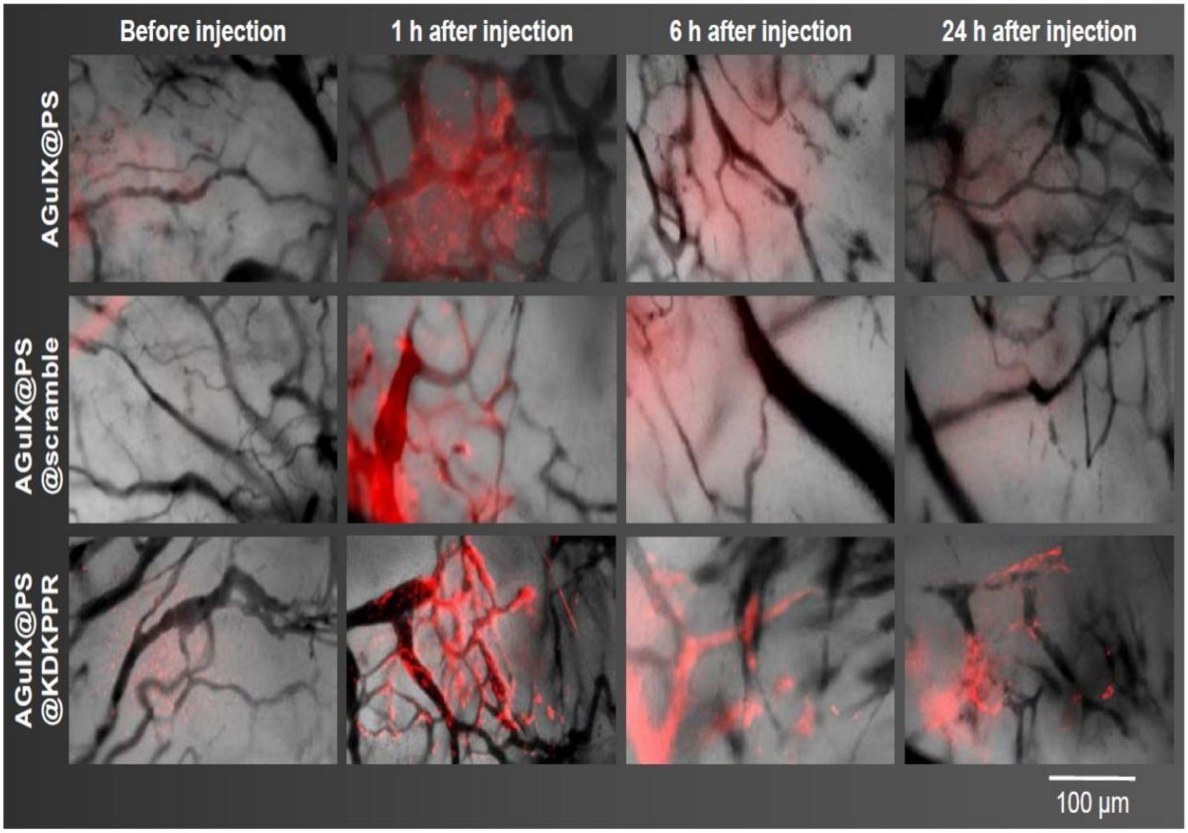

Figure 34 : In vivo selectivity: selectivity of NPs using a dorsal skinfold chamber model, before and 1, 6 and 24 h after IV injection of AGuIX@P1, AGuIX@MI-K(P1)RPKPD and AGuIX@MI-K(P1)DKPPR ([P1] = 6 µmol/Kg). Blood vessels are represented in black and P1 fluorescence in red. On the contrary to AguIX@P1 or AGuIX@MI-K(P1)RPKPD NPs, thanks to the targeting peptide, AGuIX@MI-K(P1)DKPPR NPs were fixed to the vessel walls of the tumor tissue. All pictures have been taken with the same magnification; scale bar represents 100 µm [38].

In addition, the efficacy of the treatment with the AGuIX@MI-K(P1)DKPPR NPs was studied by iPDT performed on nude rats with a cranial anchor (**Figure 35**). This vascular targeting strategy decreased the tumor growth and extended the rats' survival rate from 7 days, as in the case of AGuIX@P1 NPs, to 13 days ($p < 0.0001$). This result was associated with decreased tumor metabolism after treatment.

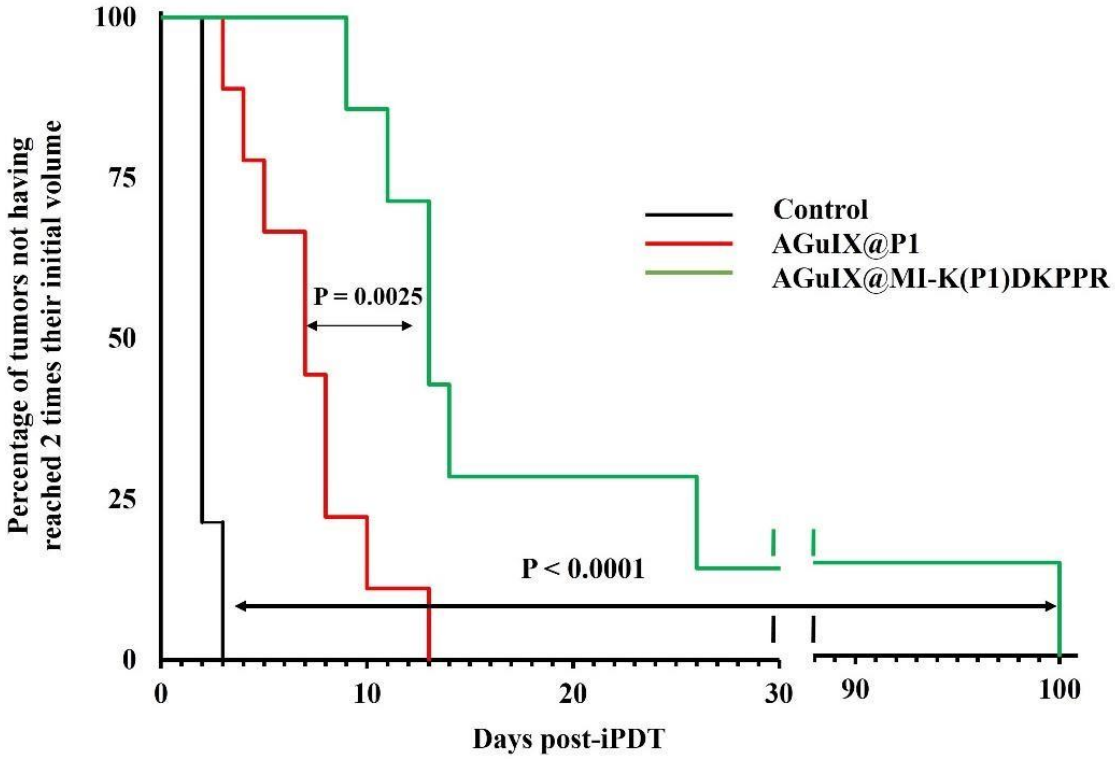

Figure 35 : Kaplan–Meier curves of control rats or rats treated by iPDT using AGuIX@P1 NPs (in red) or AGuIX@MI-K(P1)DKPPR (in green), considering the percentage of tumors not having reached 2 times their initial volume at the end point. At least seven animals were used for each experimental group. Statistical analysis was performed using the Log rank test and highlighted a statistically significantly difference between AGuIX@MI-K(P1)DKPPR group and control group ($p < 0.0001$) and between AGuIX@P1 ($P = 0.0025$). Adapted from Gries et al. [39].

In the field of brain tumors, the susceptibility weighted imaging (SWI) has recently been examined for glioma imaging [43, 44]. These recent studies showed that SWI can help in the glioma classification thanks to its high sensitivity to the microhemorrhage and the microvascularization itself, which correlates with the tumor grade. After VTP using AGuIX@-MI-K(P1)DKPPR NPs, the onset of microhemorrhages was rapid, occurring within the first few minutes (**Figure 36A**). Specifically, hemorrhages were concentrated at the tumor periphery as early as 1 hour after treatment and tended to resolve within 24-48 hours post-treatment (**Figure 36B-C**). This observation was consistent with the localization of the NRP-1 protein which was mainly expressed in the vessels of the tumor periphery and sometimes at the stromal level [32, 45]. The vascular impact of the treatment was restricted to the tumor borders and it did not affect the vessels of the healthy brain tissues, validating the selectivity of the targeting using the KDKPPR peptide.

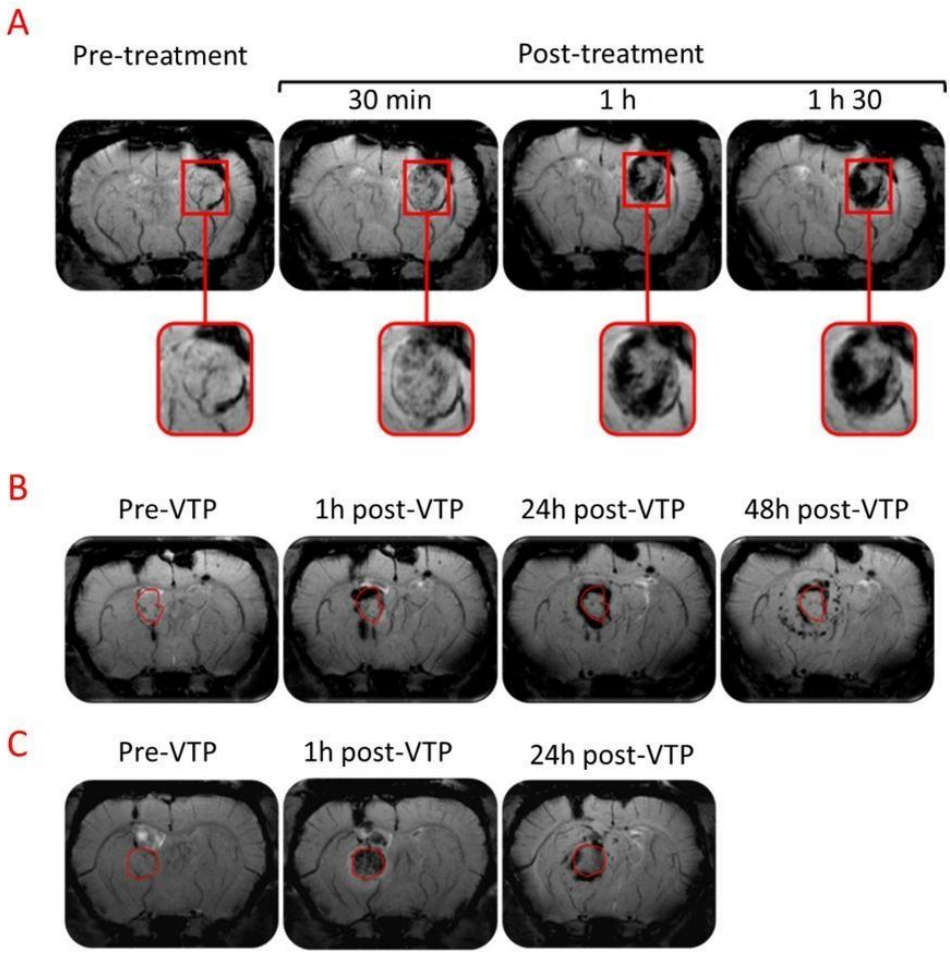

Figure 36 : Formation of microhemorrhages after VTP. The rat with human glioblastoma (U87) was treated with VTP (40 mW, 8 min 40 s, 20.8 J), 4 h after IV injection of AGuIX@MI-K(P1)DKPPR NPs (1.75 µmol.kg^{-1}, PS equivalent). Short (A) and medium (B-C) term monitoring of microhemorrhages was performed by MRI using a magnetic susceptibility sequence (SWI), which is extremely sensitive to venous blood, hemorrhages and iron storage. The diameter of the tumor visible in T2 at pre-treatment was reported on the SWI images (in red).

Recently, the designing of NPs coupled to different NRP-1 targeting peptides was performed by two other teams. They used CRGDK and tLyp-1 peptides covalently coupled to the NPs.

II.1.3 NPs@PS@CRGDK

Zhao *et al.* designed a very interesting multifunctional nanosystem composed of PEG-PCL (polyethylene glycol-poly (α-caprolactone)) NPs encapsulating the IR780 PS and the oxygen depot perfluorooctyl bromide (PFOB), and covalently coupled to the tumor homing peptide CRGDK. IR780 was used for its near-infrared light absorption and high fluorescence imaging capability and PFOB was chosen for oxygen storage.

By measuring the $^1O_2$ formation in solution *via* Singlet Oxygen Sensor Green (SOSG), they observed that the presence of PFOB enriched the environmental O_2 and decreased the hypoxia. In MDA-MB-231 human breast cancer cell line, the fluorescence of dichloro-dihydrofluorescein diacetate (DCFH-DA) was 1.8 times greater for CRGDK-targeted NPs than the untargeted ones. In MCF-7 resistant human breast adenocarcinoma cell line, no difference between the two types of NPs was observed. These results were

in correlation with the NRP1 expression level which is high in MDA-MB-231 cells and low in MCF-7 cells. By adding anti-NRP-1-monoclonal antibodies, the cellular incorporation of CRGDK targeted NPs strongly decreased. Multicellular tumor spheroids of HT-29 cells overexpressing NRP-1 receptor were prepared and incubated with the CRGDK-targeted NPs. For the NPs holding PFOB, the DCFH-DA fluorescence was detected in the whole sphere at the depth of 65 nm, whereas it was only observed at the edge of the tumor spheroid for the NPs lacking PFOB. However, no fluorescence was observed when the CRGDK-targeted NPs were incubated in multicellular tumor spheroids of MCF-7 with low expression of NRP-1 receptor. *In vivo* experiments in BALB/c nude mice bearing MDA-MB-231 tumor were conducted, where it was proved that the CRGDK-targeted NPs accumulated in tumor with a tumor-to-total organs ratio of 25%. After IV-injection, the fluorescence signal of IR780 was at the tumor periphery in the case of non-targeted NPs, however, with the CRGDK-targeted NPs, the signal occupied the whole tumor tissue. Indeed, CRGDK-targeted NPs could spread from the vascularized periphery to the avascular tumor area. Using a hypoxia marker (hypoxia-inducible factor (HIF)-1-α), it was proved that the tumor hypoxia decreased due to the presence of PFOB. To evaluate the phototoxicity, PDT treatment was performed at 808 nm (2 $W.cm^{-2}$, 20 s) 24 hours post-injection. As expected, the best efficiency was obtained with the CRGDK-targeted NPs (**Figure 37**) [45].

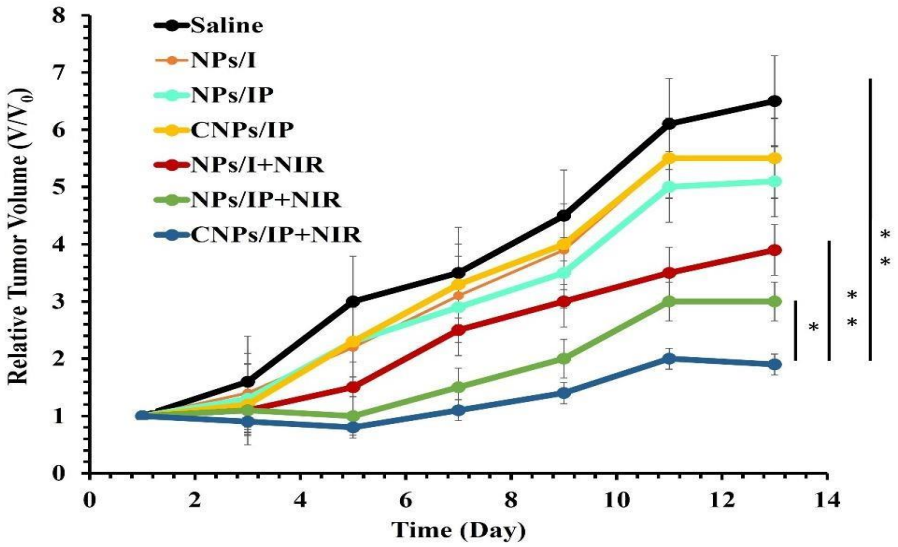

*Figure 37 : Tumor growth curves in mice treated in vivo on an MDA-MB-231 tumor model with saline solution, NPs/I with or without laser irradiation, NPs/IP with or without laser irradiation, and CNPs/IP with or without laser irradiation. The values are expressed as mean ± SD, (n = 5, * p <0.01, ** p <0.005, Student's t test). After 24 h, the tumors in laser treated groups were irradiated by an 808 nm laser with a power of 2 W cm^{-2} for 20 s. I = IR780, P = Perfluorooctyl bromide (PFOB), NPs = PEG-PCL (polyethylene glycol-poly (α-caprolactone)), C = CRGDK, V_0 = Initial tumoral volume before treatment Adapted from Zhao et al. [45].*

II.1.4 NPs@PS@tLyp1

In 2016, Jiang and co-workers designed a new targeted drug delivery system consisting of a PS (chlorin e6, Ce6, 3.8% loading capacity) chemically incorporated in the shell of D-α-tocopheryl polyethylene glycol 1000 succinate-poly(lactic acid) NPs (TPGS-PLA NPs). These NPs were surface-decorated with CGNKRTR (tLyp-1), a tumor homing and

penetrating peptide, to target NRP-1 receptor. The resulted spherical tLyp-1 NPs possessed an average size of around 140 nm. They encapsulated therein a chemo-drug (Doxorubicin, Dox, 9.56% loading capacity). The NPs were then used for chemo-photodynamic combination therapy of Dox-resistant breast cancer. In this combination therapy, the PS played multiple roles. On the one hand, it induced cell apoptosis by PDT. On the other hand, it disrupted the endolysosome membranes to release the encapsulated chemo-drug directly into cytoplasm for an enhanced treatment efficiency in drugresistant cancers. The *in vitro* studies on HUVEC and Dox-resistant human breast adenocarcinoma cells (MCF-7/ADR) revealed a cellular uptake enhancement and a photocytotoxicity improvement of tLyp-1 NPs compared to untargeted NPs (660 nm laser irradiation). The *in vivo* studies on mice bearing MCF-7/ADR tumors demonstrated the targeting efficiency and the penetrative ability of tLyp-1 NPs. This resulted in a considerable accumulation of the PS and Dox into the drug resistant tumors, and thus a more efficient chemo-photodynamic combination treatment. An increase in the anti-tumor efficiency was detected with tLyp-1 NPs exposed to Laser (170 mW.cm^{-2}) for 9.8 min at 660 nm (**Figure 38**) [46].

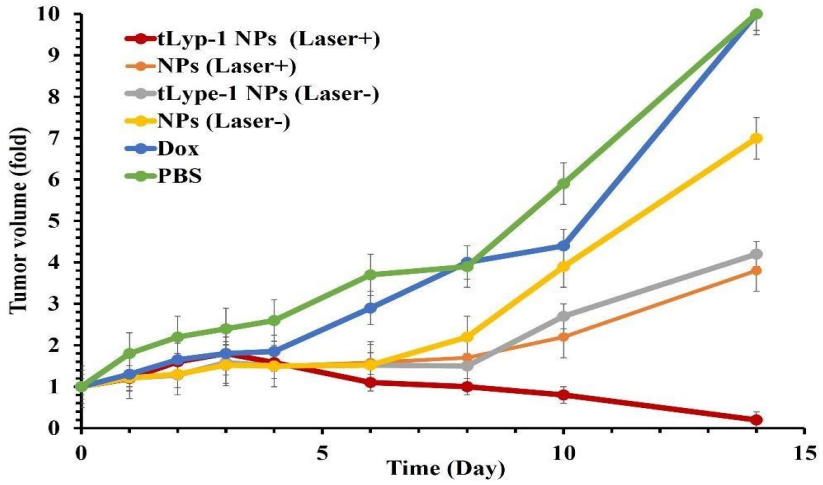

Figure 38 : Tumor growth curves showing the Anti-tumor efficiency of PBS, Free Dox, NPs with Ce6 and Dox without tLyp-1 in the surface (NPs), NPs with Ce6 and Dox with tLyp-1 in the surface (tLyp-1 NPs) with (Laser+) or without (Laser-) irradiation (170 mW.cm^{-2} for 9.8 min, 660 nm) Adapted from Jiang et al [46].

Table 5 describes the NPs@PS@peptide systems, targeting NRP-1 receptors, regarding the types of NPs, PSs and the coupling between them, in addition to the NPs size, excitation wavelength ($\lambda_{excitation}$), fluorescence quantum yield (ϕ_F), singlet oxygen quantum yield ($\Delta_{O.S}$) and the results obtained *in vitro* and/or *in vivo*.

Table 5 : The summary of NPs conjugated with PSs and peptides targeting Neuropilin-1 (NRP-1) in terms of different parameters

NPs@PS@Peptide tarhetting Neuropilin-1 (NRP-1)									
Reference	NPs	PS	Coupling btween NPs and PS	NPs size (nm)	$\lambda_{excitation}$ (nm)	Φ_F	$\Delta_{O.S}$	*In vitro*	*In vivo*
Peptide KDKPPR									
[38] [39]	AGuIX®	Monocarboxylic porphyrin (P1COOH)	Maleimide	4.9 ±1.4 for AGuIX® 11.2±3.9 for AGuIX@P1 11.6±6.3 for AGuIX@MIK(P1)DKPPR 10.6±2.3 for AGuIX@MIK(P1)RPKPD	652	0.07 for AGuIX@P1 0.1 for AGuIX@MI-K(P1)DKPPR 0.09 for AGuIX@MI-K(P1)RPKPD In H_2O	0.58 for AGuIX@P1 0.28 for AGuIX@MI-K(P1)DKPPR 0.35 for AGuIX@MI-K(P1)RPKPD In D_2O	HUVEC [38] U87 [39]	Nude rat with orthotopic U87 [38] Recombinant rat [39]
[37]	AuNRs	Pyropheophorbidea (Pyro)	Maleimide	AuNRs@PEG : 44.8	652	0.38 for Pyro 0.30 for AuNRs@PEG-MI-K(Pyro)DKPPR In toluene	0.51 for Pyro 0.40 for AuNRs@PEG-MI-K(Pyro)DKPPR In EtOH	U87	nd
Peptide ATWLPPR									
[31] [32] [33] [47]	silica shell gadolinium oxide core	5-(4-carboxyphenyl)-10,15,20-triphenyl-chlorin (TPC)	Amide bond NP-TPC-ATWLPPR	4.6 ±3.8 for NP-TPC-ATWLPPR	652	0.19 ± 0.02 for NP-TPC-ATWLPPR 0.18 ± 0.05 for NP-TPC 0.21 ±	0.66 ± 0.05 for MB-231 nude rats with ATWLPPR and NP-TPC 0.69 ± 0.05 for	MDA-U87 tumor	Male athymic

				0.05 for TPC in ethanol		TPC in ethanol			
Peptide CRGDK									
[45]	PEG-PCL (polyethylene glycol-poly (αcaprolactone))	IR780	Encapsulation	201.5 ± 4.7 for CNPs/IP	808	nd	nd	MDA-MB-231, MCF-7, HT-29	BALB/c nude mice bearing MDA-MB-231 tumor
Peptide tLyp-1									
[46]	TPGS-PLA (D-αtocopheryl polyethylene glycol 1000 succinate-poly(lactic acid)	Chlorin e6 (Ce6)	Ester bond	140.3± 13.45 for tLyp-1 NPs	660	nd	nd	HUVEC, MCF-7/ADR	Mice bearing MCF-7/ADR tumor

**nd: not determined*

II.2 Peptides targeting αvβ3 integrins

$\alpha_v\beta_3$ integrins are involved in the tumor angiogenesis and are highly expressed on activated endothelial cells and some tumor cells. However, they are not present in resting endothelial cells and most of the normal organ systems, making them interesting targets for antiangiogenic PDT [48].

II.2.1 NPs@PS@RGD

Arginyl-glycyl-aspartic acid (RGD) is a well-known peptide targeting $\alpha_v\beta_3$ integrins.

In 2014, Wang *et al.* reported the synthesis of lipid coated upconverting NPs (UCNs). The coating was constituted of RGD peptide functionalized by PMAO (poly(maleic anhydride-alt-1-octadecene)) grafted DOPE (dioleoyl L-α-phosphatidylethanolamine) (UCN/RGDPMAO-DOPE). Dextran merocyanine 540 (MC540) PS was adsorbed onto these NPs by hydrophobic interactions (MC540@UCN/RGDPMAO-DOPE). These upconverting NPs were monodispersed and presented a size of 20 nm. The amphiphilic lipid polymer coating was used to improve the hydrophilic properties of the UCNs' surface, and protect the drug, by electrostatic repulsion, from aggregation and leakage during the transport. The *in vitro* experiments were performed on MCF-7 cells overexpressing $\alpha_v\beta_3$ integrins. ROS, mainly $^1O_2$, were more importantly produced by MC540@UCN/PMAO-DOPE decorated by RGD peptide (MC540@UCN/RGD-PMAO-DOPE) as compared to NPs lacking RGD (MC540@UCN/PMAO-DOPE). This was attributed to the role of RGD in enhancing the cellular uptake of the NPs through receptor-mediated endocytosis. The production of ROS proved the successful energy transfer from the UCNs to the MC540 PS. In addition, MC540@UCN/RGD-PMAO-DOPE were capable of decreasing the cell viability to 35% after exposure to 980 nm laser for 30 min, thus revealing a more efficient photodynamic effect as compared to MC540@UCN/PMAO-DOPE (65% cell viability) (**Figure 39**). These results verified that the efficiency of PDT was enhanced by the presence of the RGD peptide [49].

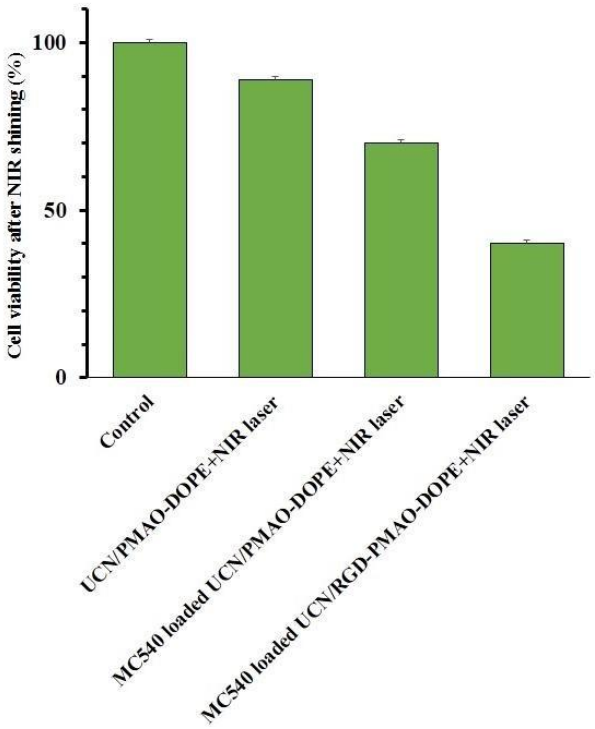

Figure 39 : PDT treatment efficiency on MCF-7 cells. Untreated cells as control group and cells treated with UCN/PMAO-DOPE NPs, MC540 loaded UCN/PMAO-DOPE NPs or MC540 loaded UCN/RGD-PMAO-DOPE NPs after NIR laser irradiation (980 nm, 30 min). Adapted from Wang et al. [49].

In 2018, Yuan *et al* reported a new platform based on mesoporous silica NPs (MSN). Black hole quenchers (BHQs) were doped in the inner walls of the MSN mesopores (MSN-BHQ). The resulted NPs were coupled to Photoporphyrin (PpIX) PS through a disulfide bond (SS) to afford MSN-BHQ-SS-PpIX. To prolong their blood circulation time, PEG was coupled to PpIX onto the NPs (MSN-BHQ-SSPpIX-PEG). A specific targeting agent, RGD peptide, was then conjugated to this nanoplatform (MSN-BHQ-SS-PpIX-PEG-RGD). The MSN-BHQ-SS-PpIX-PEG-RGD NPs had a spherical morphology with an average size of 50 nm. An oxidation-reduction reaction on this platform stimulated the glutathione (GSH)-mediated release of the therapeutic drug by breaking the SS link. GSH is present in large quantities in the tumor cells, which allowed to accelerate the release of the drugs. *In vitro* experiments were performed on cervical cancer cells (HeLa). The fluorescence of MSN-BHQ-SS-PpIX-PEG-RGD was higher than that of free RGD. The cellular incorporation of MSN-BHQ-SS-PpIX-PEG-RGD was measured in HeLa cells with and without GSH. With extra GSH, many red fluorescent spots appeared in the cytoplasm mainly around the nucleus. When tested on two other cell lines (SCC-7 and COS7), MSN-BHQ-SS-PpIX-PEG-RGD showed low cytotoxicity in the dark and good phototoxicity in the presence of light (**Figure 40**). In conclusion, MSN-BHQ-SS-PpIX-PEGRGD selectively targeted the tumor environment due to the presence of RGD. This selective toxicity was reinforced by GSH. The redox response of this nanoplatform in the tumor environment made it an important candidate in anti-cancer PDT and in tumor imaging therapy [50].

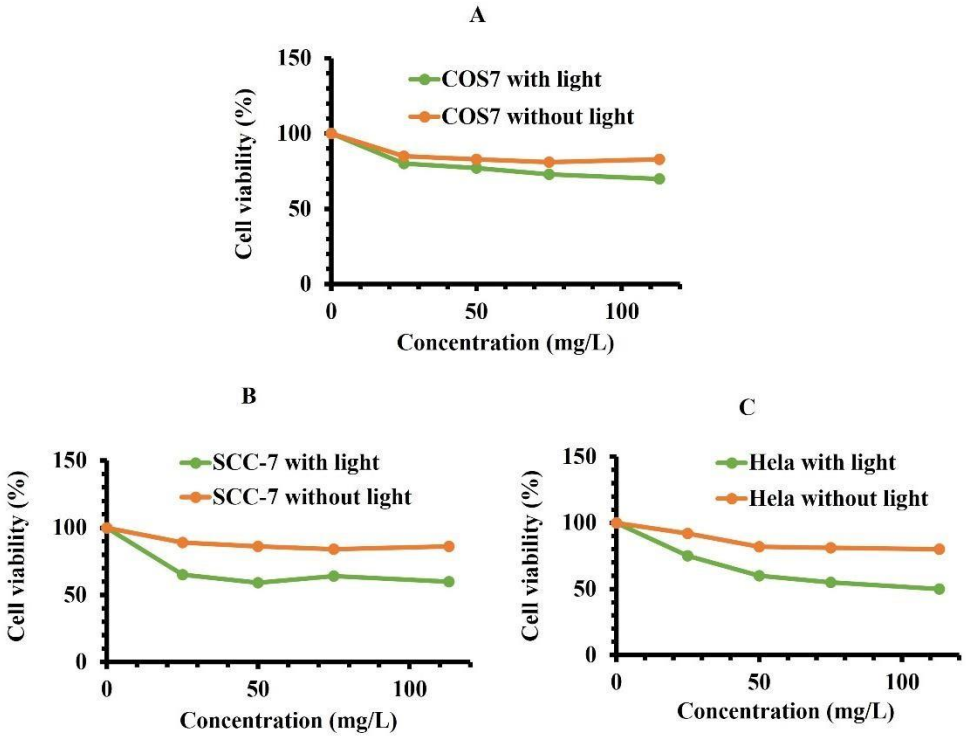

Figure 40 : In vitro cell viability of a) COS7, b) SCC-7 and c) HeLa cells incubated with different concentrations of MSN-BHQ-SS-PpIX-PEG-RGD without light and under 30 min. Data is shown as mean ± SD (n = 4). Adapted from Yuan et al. [38].

In the same year, Hou *et al* synthetized nanodumbbell ZnPc-UCN@lipid@RGD. Hydrophobic UCNs were transferred into water to form UCN@lipid. The UCN@lipid and zinc phthalocyanine (ZnPc) were both encapsulated into polymersome (PS) shell to form UCN@lipid@PS nanodumbbell. The exterior of the polymersome possessed many carboxyl functional groups that were coupled to RGD peptide. The UCN's core converted the NIR rays into visible ones, thus overcoming the problem of the limited light penetration into tissues. The ZnPc-UCN@lipid@PS had a high drug loading efficiency of 18.03%. The transmission electron microscopy (TEM) showed that the ZnPc-UCN@lipid@PS were of spherical form with a size of 150 nm. Whereas, the dynamic light scattering (DLS) gave an average diameter of 195 nm. After coupling the UCNs to ZnPc, the fluorescence intensity of the UCNs decreased, indicating an energy transfer between the UCNs and ZnPc. Following the excitation at 980 nm, ZnPc-UCN@lipid@PS and ZnPcUCN@lipid@PS–RGD showed the greatest production of $^1O_2$. These tests were carried out using 9,10-anthracenediylbis(methylene)dimalonic acid (ABDA) probe. The study of the *in vitro* cytotoxicity in HeLa cells exposed to different concentrations of NPs, showed a greater biocompatibility in the case of UCN@lipid@PS-RGD (97% of cell viability for 500 µg.mL^{-1} of NPs) as compared to UCN@lipid@PS (90%) and UCN@lipid (65%). This result was credited to the presence of RGD that induced the specific incorporation of the NPs in the cells, and hence decreased the unwanted cytotoxicity (**Figure 41A**). After incubation with Hela cells and excitation with a NIR source (980 nm, 1.5 W.cm^{-2}), ZnPc-UCN@lipid@PS-RGD showed the lowest tumor cell viability as compared to the untreated control cells and those exposed to the other ZnPc loaded-PS NPs (ZnPc-UCN@lipid@PS, UCN@lipid@PS

nanodumbbells) (**Figure 41(B) and (C)**) [51]. In the same conditions, ZnPc loaded UCN@lipid@PS with and withour RGD showed the best and higher production of singlet Oxygen in comparaison with other couples detailed in **Figure 41(C)**.

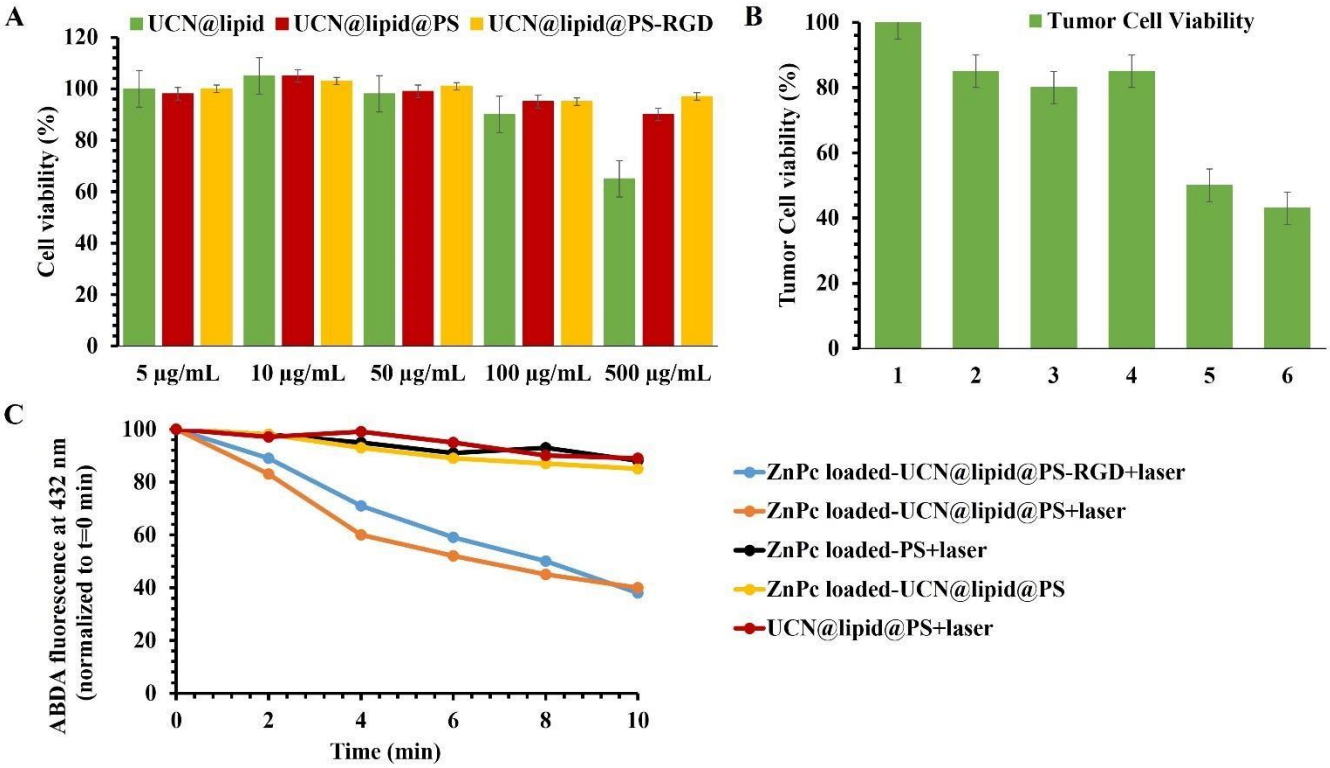

Figure 41 : (A) Cytotoxicity on Hela cells of UCN@lipid, UCN@lipid@PS, and UCN@lipid@PS-RGD. (B) Viability of Hela cells treated with 1 PBS (Control group), 2 UCN@lipid@PS nanodumbbells plus NIR laser, 3 ZnPc loaded-PS NPs plus NIR laser, 4 (ZnPc + UCN@lipid)@PS NPs, 5 (ZnPc + UCN@lipid)@PS NPs plus NIR laser, 6 (ZnPc + UCN@lipid)@PS-RGD NPs plus NIR laser (980 nm, 1.5 W.cm^{-2}). The concentration is 500 µg.mL^{-1}. (C) Comparison of $^1O_2$ production between control groups and experiment groups. Adapted from Hou et al. [39].

In 2015, Zhao *et al.* successfully synthesized a novel multi-arm polymeric nanosystem for PDT (RGD-8PEG-IR700). The RGD and the IR700 units were coupled to a PEG arm (8 polyethylene glycol). The hydrodynamic diameter of the nanosystem was 6.6 nm. The *in vitro* results on spheroid tumor model A375 and SKOV3 cells that express $\alpha_v\beta_3$ integrins, showed a stronger fluorescence of the RGD-8PEGIR700 NPs as compared to 8PEG-IR700. In contrast to IR700 and 8PEG-IR700, RGD-8PEG-IR700 induced a significant phototoxicity on A375 cells, under excitation at 504 nm with an IC_{50} value of 57.8 nM. No cytotoxic effect was observed in the dark even with a concentration of 1 µM (IR700 equivalent) **(Figure 42)** [52].

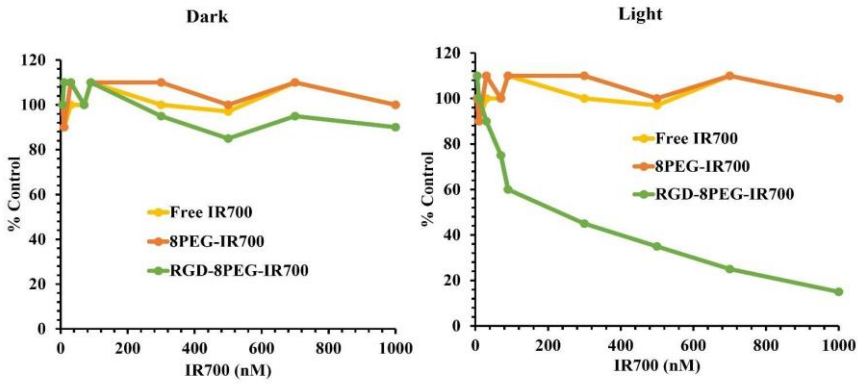

Figure 42 : Determination of the dose-dependent (A) cytotoxicity and (B) phototoxicity of free IR700, 8PEG-IR700 and RGD-8PEG-IR700 in A375 cells. Light irradiation at 660 nm with 3.5 mW.cm-2 for 30 min fluent rate. Adapted from Zhao et al. [40].

In 2015, Yuan *et al.* used the seventh generation poly (amidoamine) (PAMAM-G7, P) dendrimer of 8 nm. The PAMAM was coupled with Ce6 PS in addition to PEG or RGD, to obtain the PEG-P-Ce6 NPs and RGD-P-Ce6, respectively. The □ □ was 2.5 times higher for RGD-P-Ce6 than free Ce6 in water. *In vitro* experiments were performed in A375 cells (non-pigmented melanoma cell line expressing $\alpha_v\beta_3$ integrins (+)) and NIH_3T_3 cells (mouse fibroblast that do not express $\alpha_v\beta_3$ integrins (-)). Cellular uptake in (+) A375 cells was 4.7 fold superior for targeted RGD-P-Ce6 than non-targeted PEG-P-Ce6 NPs, whereas the incorporation into (-) NIH_3T_3 cells was the same for both NPs. The photocytotoxicity was evaluated with various concentrations in both types of cells by illumination at 660 nm (3.5 $mW.cm^{-2}$, 30 min). No cell killing was witnessed when A375 cells were treated with Ce6 due to its poor incorporation. RGD-P-Ce6 presented an enhanced phototoxicity in A375 cells compared to non-targeted NPs. As expected, in NIH_3T_3 cells, no difference in the phototoxicity between RGD-targeted NPs and PEG-P-Ce6 NPs was detected. The penetration of RGD-targeted NPs and free Ce6 was evaluated in A375 tumor spheroids. Using the same concentrations, *i.e.* 200, 400 and 800 nM, RGD-P-Ce6 showed a higher cellular uptake than free Ce6 with ratios of 40.8, 58.7 and 79.3, respectively (**Figure 43**) [53].

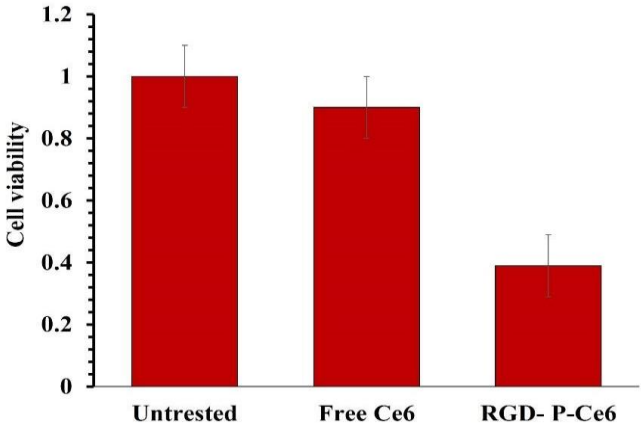

Figure 43 : A375 Cell viability after PDT treatment (660 nm, 3.5 mW.cm-2, 30 min). Adapted from Yuan et al. [41].

In 2017, Kim *et al.[42]* synthesized a nanoplatform consisting of C60 coupled to PEG and functionalized by Ce6 PS and cyclic RGD peptide (cyclic CKRGDf, denoted by cRGD). The nanosystem had a diameter of 3-4 nm. *In vitro* experiments were performed with SKOV3 (high $\alpha_v\beta_3$ expression (+)) and KB (low $\alpha_v\beta_3$ expression (-)) cells [54]. After exposure to light (670 nm, 5.2 $mW.cm^{-2}$, 10 min), the highest cell death was observed in (+) SKOV-3 with the targeted NPs. As expected, free Ce6 and non-targeted NPs were less phototoxic in both SKOV-3 and KB cells. The phototoxicity of the targeted NPs was also reduced in (-) KB cells. The *in vivo* experiments using BALB/c nu/nu female mice with SKOV-3 and KB xenografted tumors proved that the targeted NPs had a lower uptake in KB than in SKOV-3 tumors. Due to the small size of the NPs and the EPR effect, both targeted and non-targeted NPs were incorporated into the tumors. However, the highest uptake was achieved by the targeted NPs in SKOV-3 tumor. After realizing PDT treatment on the cells incubated with targeted NPs (670 nm, 5.2 $mW.cm^{-2}$, 40 min), the reached tumor volumes were 4.5 and 2.1 times smaller than those obtained in mice treated with Ce6 and non-targeted NPs,respectively.

In 2019, Shi *et al.* described the design of targeted RPTD/HP NPs made of chemo-drug Dox coupled to PEG, *via* a ROS-cleavable thioketal link, and a targeting cRGD peptide (cyclic RGDfC). This system also encapsulated hematoporphyrin (HP) PS (**Figure 44**) and was used for oral tongue squamous cell carcinoma treatment [55]. Due to the presence of both hydrophobic Dox and hydrophilic PEG, the molecules self-assembled to form RPTD/HP NPs with a size of about 180 nm.

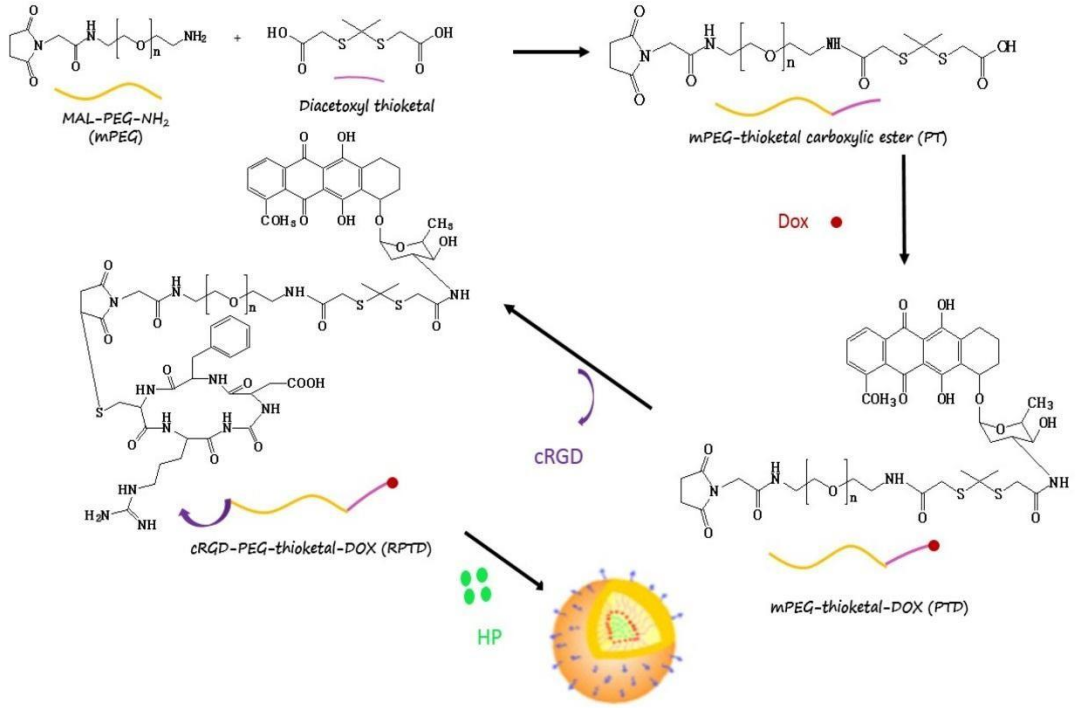

Figure 44 : Synthesis of RPTD/HP NPs. Adapted from Shi et al. [55].

In vivo studies were performed in HOEC (low $\alpha_v\beta_3$ integrin expression (-)) and CAL-27 (high $\alpha_v\beta_3$ integrin expression (+)) cells. The targeted RPTD/HP NPs were better incorporated in (+) CAL-27 than in (-) HOEC cells. After illumination (633 nm, 10 min, 100 $mW.cm^{-2}$), the ROS were formed, which triggered the cleavage of the thioketal bond. Consequently, the Dox was released and entered the nuclei of CAL-27 cells. Synergistic effects of PDT and chemotherapy was observed with both the targeted RPTD/HP and the nontargeted PTD/HP NPs with an IC_{50} value of 0.89 and 0.68 µM, respectively. Targeted RPTD/HP NPs displayed higher cytotoxicity and phototoxicity than non-targeted PTD/HP NPs, since they delivered more amounts of Dox and HP into the cells. The *in vivo* studies were implemented with free Dox, free HP, targeted RPTD/HP NPs and non-targeted PTD/HP NPs in CAL-27 tumor bearing BALB/c nude mice. All the treatments inhibited the tumor growth to a certain extent when compared to the control. However, the best results were obtained with the targeted RPTD/HP NPs (**Figure 45**). In addition to that, these NPs displayed a strong effect on tumor angiogenesis [55].

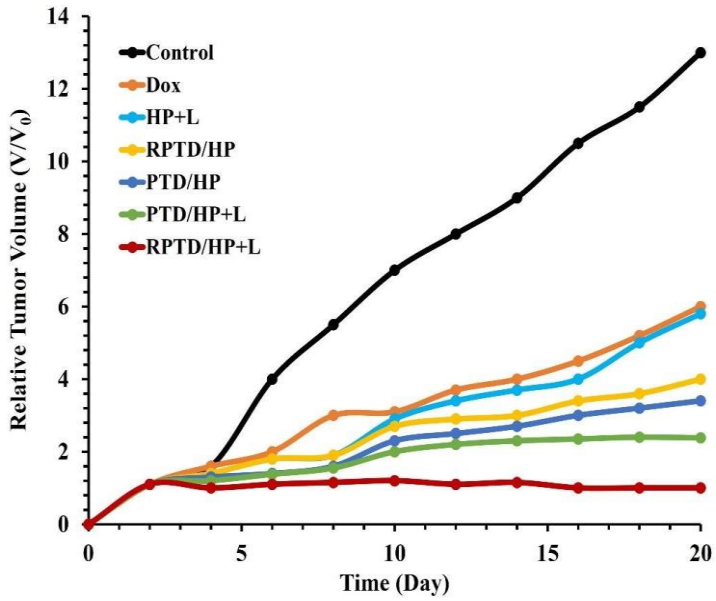

Figure 45 : Anti-tumor effects of Dox, HP+light, non-targeted PTD/HP NPs, non-targeted PTD/HP NPs+light, targeted RPTD/HP NPs, targeted RPTD/HP NPs+light (633 nm, 10 min, 100 mW.cm^{-2}), with free HP (4.0 μg/mL), PTD/HP, and RPTD/HP nanoparticles (4.0 μg/mL HP and 1.0 μg/mL DOX) and L = Light. Adapted from Shi et al. [43].

II.2.2 NPs@PS@iRGD

Internalizing-RGD (iRGD, sequence: CRGDKGPDC) is a disulfide-based cyclic RGD peptide that targets integrin $\alpha_v\beta_3$ receptors. The process of tumor-targeting by the iRGD peptide takes place in several steps: First, iRGD is proteolytically cleaved by binding to the surface of cells expressing α_v integrins ($\alpha_v\beta_3$ and $\alpha_v\beta_5$). This cleavage generates the CRGDK fragment, which then binds to NRP-1 and penetrates deeper into the tumor parenchyma. The affinity of iRGD for α_v integrins, compared to conventional RGD, is in the nanomolar range. Besides, the affinity of the CRGDK fragment is stronger for NRP-1 than for α_v integrins. This is due to the C-terminal exposure of a conditional C-end Rule (CendR) motif (R/KXXR/K). The receptor of this motif was proved to be NRP-1. On this basis, the CendR motif is able to bind to NRP-1, thus activating an endocytotic/exocytotic transport pathway that leads to a deeper penetration into the tumor [56].

In 2015, Yan *et al.* synthesized new NPs, named iRGD-ICG-LPs, by the thin-layer rehydration process [57]. These NPs were liposomebased (LP) in which the indocyanine green (ICG) PS was encapsulated (ICG-LPs) with an efficiency of 93.32 ± 1.25%. ICG-LPs were then grafted with iRGD peptide. The mean dynamic diameter of iRGD-ICG-LPs was 115.91 nm. The *in vitro* assays were performed using three different cell lines, HUVECs (high expression of $\alpha_v\beta_3$), 4T1 (high expression of $\alpha_v\beta_3$ and NRP-1) and MCF-7 (low expression of $\alpha_v\beta_3$). After the incubation of these cells with ICG-LPs and iRGD-ICG-LPs, iRGD-ICG-LPs showed 1.86-fold and 1.69-fold higher fluorescence intensity in HUVEC and 4T1 cells, respectively, as compared to ICG-LPs (**Figure 46A**). Due to their lower expression of $\alpha_v\beta_3$, MCF-7 cells exhibited an inferior fluorescence as compared to HUVEC and 4T1 cells. The cytotoxicity studies showed that iRGD-ICG-

LPs were biocompatible. Under laser illumination, iRGD-ICG-LPs and ICG-LPs exhibited a stronger cytotoxic effect than ICG alone (P <0.01) at the same dose of ICG. The amount of $^1O_2$ produced without light, but in presence of iRGD-ICG-LPs alone, was 1.91 times smaller than with iRGD-ICG-LPs excited by laser at 480 nm. The coupling of iRGD with ICG-LPs induced a very important PDT-PTT effect, thus demonstrating the specific targeting of the tumors. Using the luminescence of ICG, the *in vivo* results showed a stronger accumulation of the NPs in the tumors than that in the liver, spleen and other organs (**Figure 47A, B and C**). After light illumination of the cells exposed to iRGD-ICG-LPs, the growth of the tumor was suppressed (P<0.01) (**Figure 46B**). For these NPs, the amount of the generated ROS was 3.82 times greater than that produced in the tumors treated with PBS alone (control).

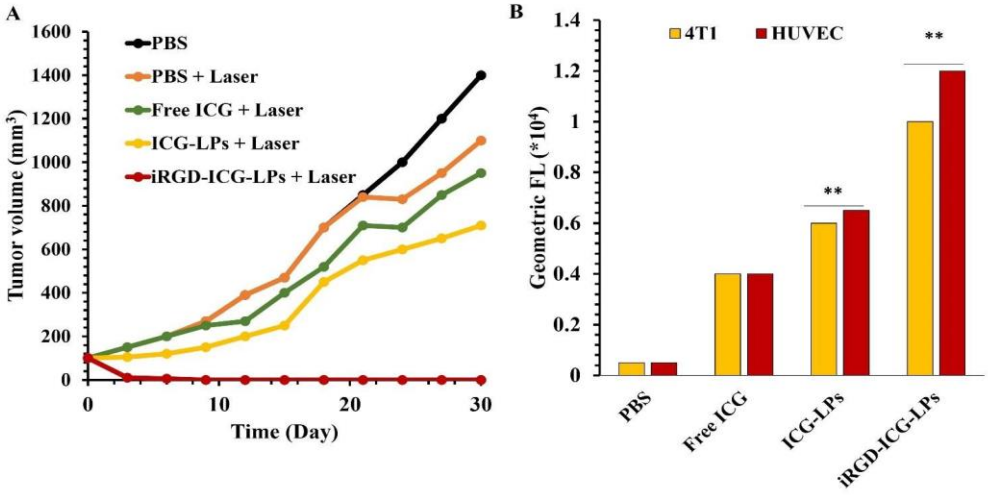

Figure 46 : In vivo anti-tumor effect and safety evaluation. (A) Geometric mean fluorescence intensity of HUVECs and 4T1 cells from flow cytometric analysis, (n = 3), (**) P < 0.01. (B) Tumor growth curves of non-treated mice or mice receiving iRGD-ICG-LPs, ICG-LPs, free ICG, PBS and laser irradiation within 30 days. (**)P <0.01. An 808 nm laser at a power density of 1.0 W.cm-2 was used to irradiate these samples for 8 min. Adapted from Yan et al. [45].

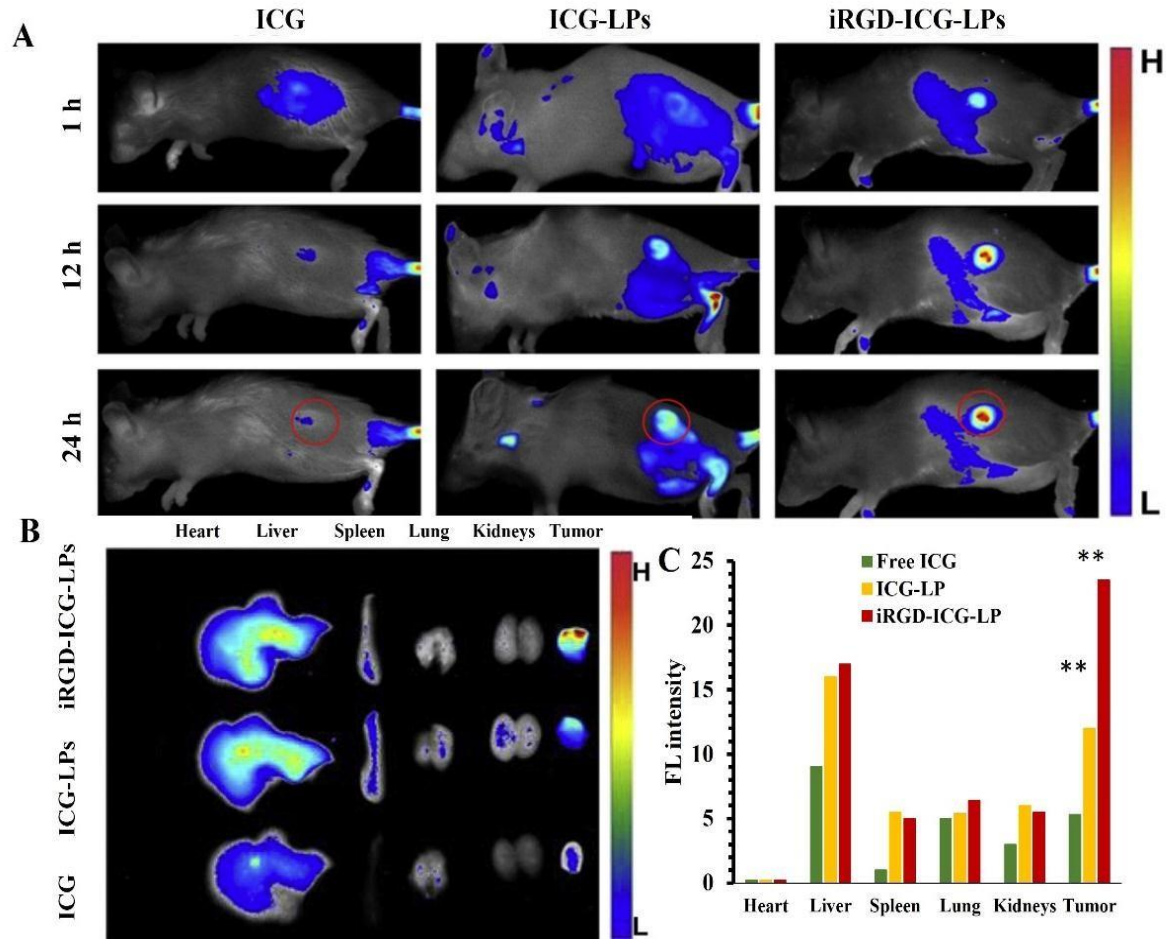

Figure 47 : In vivo molecular imaging and biodistribution. The free ICG, ICG-LPs or iRGD-ICG-LPs were IV administrated to the 4T1 tumor-bearing mice and the tumors and major organs were imaged with the ex/in vivo imaging system. (A) Fluorescence signal was obtained in tumor sites at 1 h, 12 h and 24 h after IV administration of free ICG, ICG-LPs or iRGD– ICG-LPs with 0.5 mg/Kg equivalent ICG. (B) Ex vivo fluorescence images of major organs and tumors were obtained at 24 h post-injection of free ICG, ICG-LPs or iRGD-ICG-LPs with 0.5 mg/Kg equivalent ICG. (C) Semiquantitative analysis of fluorescence intensity for the different organs and the tumor showed much higher signal intensity in the tumor of mice received with iRGD–ICG-LPs than those received with free ICG or ICG-LPs.(**) P <0.01. Laser excitation: 808 nm, 1.0 W.cm-2 for 10 min. Adapted from Yan et al. [45]. With permission from Elsevier and Copyright Clearance Center.

In 2019, Sheng *et al.* synthesized a novel nanoscale drug [58]. The basis of this NP was the high-density lipoproteins (HDL) in which ICG was encapsulated to give rHDL/ICG. The encapsulation of ICG in NPs presented several advantages such as the stability in the plasma and the lack of precipitation and aggregation. The iRGD peptide was coupled onto this system to afford iRGD-rHDL/ICG. These NPs possessed a hydrodynamic diameter of 90 nm. The *in vitro* assays in 4T1 cells overexpressing $\alpha_v\beta_3$ integrins, and the *in vivo* assays with the 4T1 murine breast cancer model, showed much higher fluorescence intensity for iRGD-rHDL/ICG than that of ICG and rHDL/ICG. This was ascribed to the efficient targeting displayed by iRGD. A strong tumor regression was observed after the treatment with iRGD-rHDL/ICG followed by light illumination at 808 nm (1.8 $W.cm^{-2}$, 5 min), whereas the tumor continued to grow in the absence of any treatment (**Figure 48**). The iRGD-rHDL/ICG induced necrotic and apoptotic effects on the tumor tissues due to the ROS generation and, consequently, exhibited a greater photocytotoxicity compared

to ICG and rHDL/ICG. In comparison with ICG, iRGD-rHDL/ICG accumulated specifically in tumors, exhibited a higher stability in blood, and showed a slower clearance from the body.

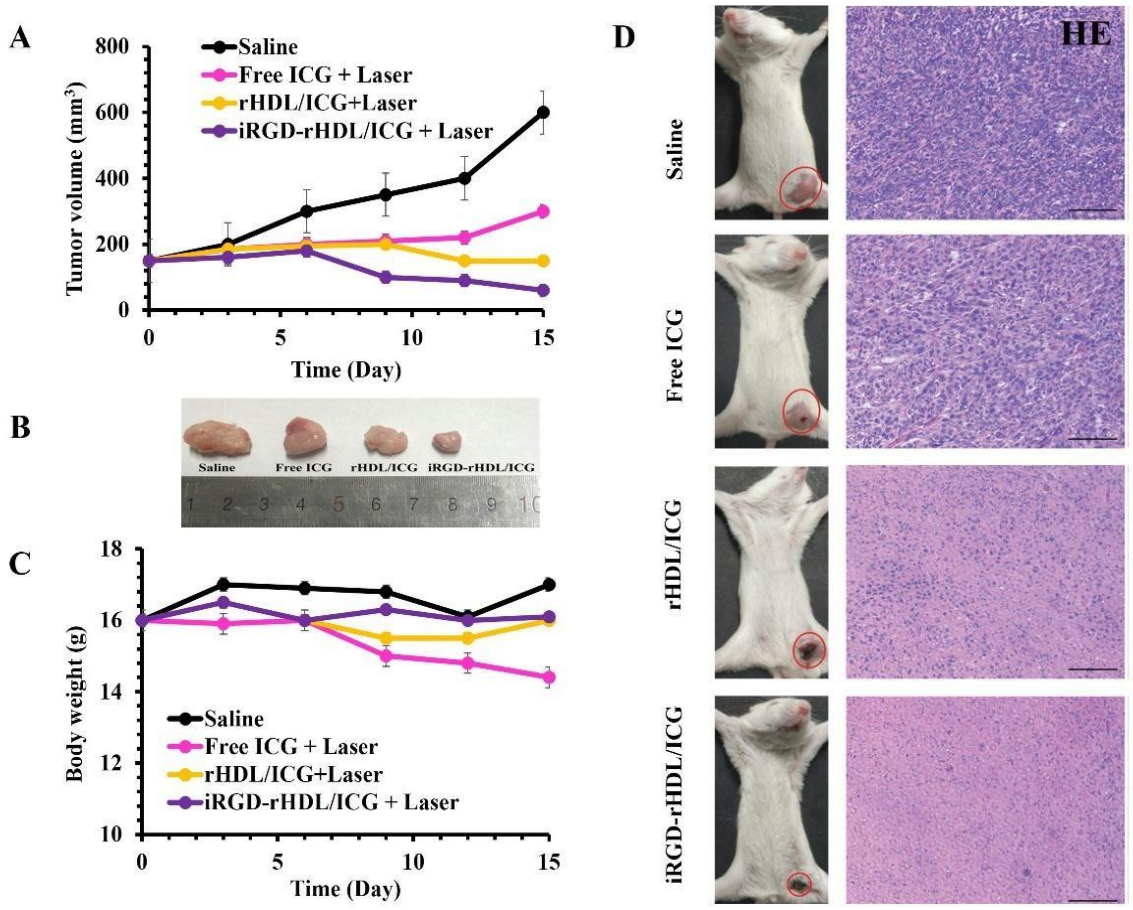

Figure 48 : In vivo PDT efficacy in 4T1 tumor-bearing mice. (A) Tumor growth curves after IV-injection of different formulations at an ICG concentration of 1.5 mg.kg−1 (n = 5). (B) Representative image of tumors from the 4T1 tumor-bearing mice sacrificed after being treated with different formulations with 1.5 mg.kg−1 of ICG1. (C) Changes in body weight over the PDT treatment period. (D) Hematoxylin and eosin (H&E) images of the tumor tissue section after PDT treatment with 1.5 mg.kg−1 of ICG1. Scale bar is 100 μm. Data are presented as mean ± SD, n = 3; the light excitation is at 808 nm, 1.8 W.cm−2 for 5 min. Adapted from Sheng et al. [58]. With permission from Royal Society of Chemistry.

In 2020, Wang *et al.* developed biodegradable NPs (iMSN/siRNA+miRNA+ICG) [59]. The mesoporous silica NPs (MSN) had a size of 15 nm. ICG was encapsulated in the MSN, with an efficiency of 91%, to afford MSN-ICG. MSN-ICG-iRGD was obtained after the coating of a lipid layer coupled to iRGD peptide on MSN-ICG. Carboxyfluorescein (FAM)-siRNA were adsorbed onto the MSN-ICG-iRGD to improve the targeting and to induce the apoptosis of the cancer cells. After light excitation at 808 nm, ROS were produced, especially $^1O_2$, The produced ROS had no significant influence on the genetic silencing activity of RNA, however, the exposure to the irradiation led to undesired heat generation. After irradiation at 808 nm (2.0 W.cm^{-2} for 5 min), the *in vitro* results in MDA-MB-231 cells treated with iRGD+MSN/FAM-siRNA+ICG revealed the destruction of the membrane of the endosomal vesicles by the released ROS. iRGD+MSN/FAM-siRNA+ICG induced cancer cell death due to the successful targeting of iRGD and siRNA . *In vivo*, a tumor of MDA-MB-231 cells expressing galectin-8-YFP

(Gal8) was grafted in mice. After light illumination at 808 nm, (2.0 W.cm^{-2}, 5 min), a significant fluorescence of iRGD+MSN/FAM-siRNA+ICG was observed in the tumor and the liver but not in other organs. The results showed that iRGD+MSN/FAM-siRNA+ICG displayed a strong tumor regression (**Figure 49**).

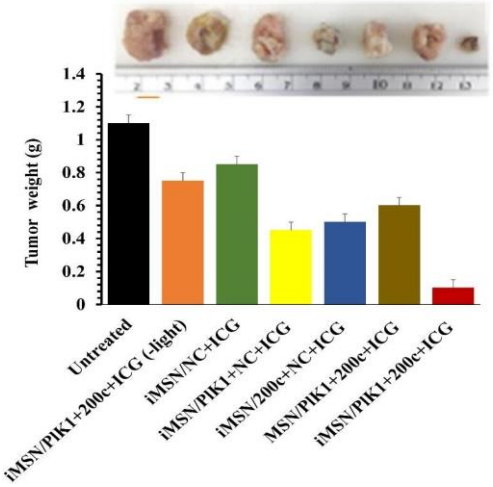

*Figure 49 : Representative images and weight of the isolated tumors from different groups. **p < 0.01 vs all of the groups, (1) saline, (2) iMSN/NC + ICG, iMSN/Plk1 + 200c + ICG (−light), (3) iMSN/Plk1 + NC + ICG, (4) iMSN/200c + NC + ICG, (5) MSN/Plk1 + 200c + ICG, (6) iMSN/Plk1 + 200c + ICG (+light) and (6) iMSN/Plk1 + 200c + ICG (−light) with . 1 mg/kg siPlk1, 1 mg/kg miR-200c and ICG 720 μg/kg. Light excitation: 808 nm, 2 W.cm-2, for 5 min. NC is a negative control, siRNA nonspecific to any human gene, Plk1 is a Polo-like kinase 1, 200c is a miR-200c mimic. Adapted from Wang et al. [47]. With permission from American Chemical Society.*

II.2.3 NPs@PS@c-RGD

In 2012, Zhou *et al.* described the synthesis of UCNPs (NaYF4:Yb/Er) coupled to chitosan, cRGD targeting peptide (cyclic RGDyK, named c(RGDK)) and Pyro PS [60]. The diameter of the resulted UCNP-Pyro-cRGD was 53 nm. U87-MG ($\alpha_v\beta_3$ integrin positive (+)) and MCF-7 ($\alpha_v\beta_3$ integrin negative (-)) cells were used for the *in vitro* studies. The targeted UCNP-Pyro-cRGD displayed a high affinity for U87-MG cells. An excess of the free cRGD peptide decreased this affinity, demonstrating the receptor-mediated endocytosis. After light illumination (980 nm, 5, min, 500 mW.cm^{-2}), MCF-7 cells treated with UCNP-Pyro-cRGD were intact, while on the contrary, the cell viability of the treated U87-MG cells was drastically decreased (**Figure 50**).

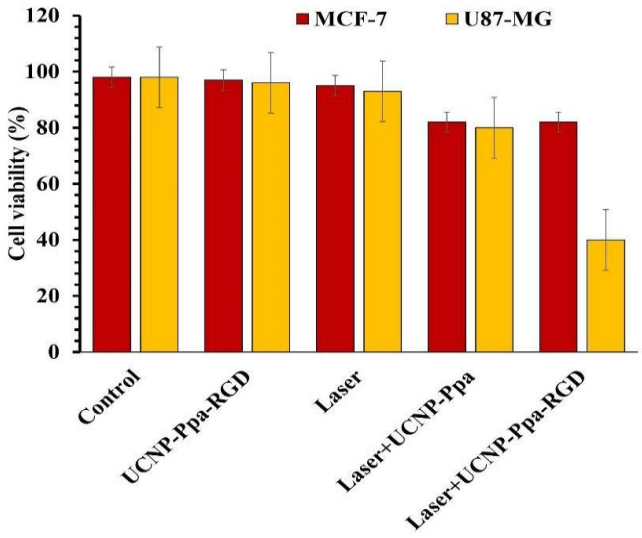

Figure 50 : PDT effect on (-) MCF-7 and (+) U87-MG cells treated with different concentration of 0, 50, 100, 200 µg/mL NPs (980 nm, 500 mW.cm^{-2} for 5 min). Adapted from Zhou et al. [48].

In 2015, the same team described *in vivo* studies applied in nude mice bearing U87-MG tumors. Two excitation types were chosen; *i.e.* 635 nm or continuous-wave at 980 nm, both at 500 mW.cm^{-2} during 60 min with 1 min interval after each minute of irradiation. Two PDT treatments were performed 3 days apart. In order to mimic the environment of a deep tumor, they used slices of pork to absorb the light. As expected, the highest phototoxicity was achieved when the tumor was treated with UCNP-Pyro-cRGD and NIR-illumination at 980 nm. This result was comparable to that obtained with Pyro and visible-light illumination at 635 nm [61] (**Figure 51**).

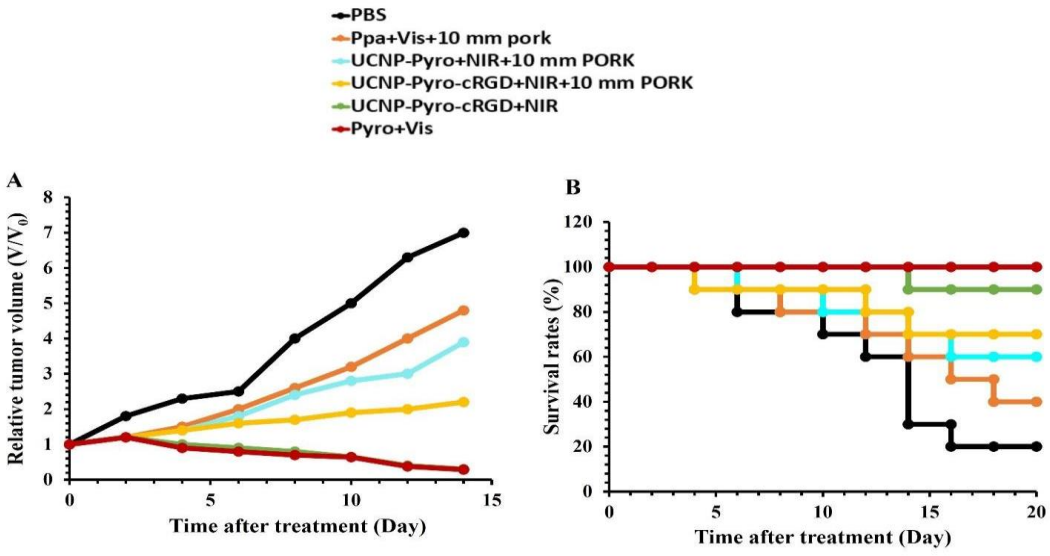

Figure 51 : In vivo PDT treatment with same concentration of pyro (10 µM). (A) time-dependent tumor growth rate, 14 days after the PDT treatment (B) mice survival rate after different kinds of PDT treatment with light excitation at 635 nm for Vis and 980 nm for NIR (500 mW.cm^{-2}) for 1 min. Adapted from Zhou et al. [49].

In 2018, Tang *et al.* focused on the development of NaScF4: 40% Yb, 2% Er@CaF2 UCNPs. Human serum albumin (HSA) was covalently coupled to the NPs. Ce6 chelating Mn^{2+}, for PDT and MRI, was loaded onto the HSA. Finally, the thiolated targeting c(RGDyK) peptide was coupled to the NPs to afford rUCNP@HSA(Ce6-Mn)-cRGD. *In vitro* studies were performed with human glioma U87 and rat glioma C6 cells. To detect ROS, SOSG and dichloro-dihydro-fluorescein diacetate (DCFH-DA) were used in solution and in cells, respectively. It was proved that upon excitation, a light resonance energy was transferred from rUCNPs to the Ce6-Mn complex leading to 1O2 generation. The highest uptake was observed for the targeted rUCNPs@HSA(Ce6-Mn)-cRGD due to the presence of HSA that could enhance the accumulation through the gp60 receptor and the cRGD peptide that targeted $\alpha_v\beta_3$ integrin. 24 hours post-treatment, the free Ce6 and the non-targeted rUCNPs@HSA(Ce6-Mn) were eliminated from the tumor, whereas the rUCNPs@HSA(Ce6-Mn)-RGD was still there, showing a great targeting and hence a superior retention ability. The cells were illuminated with a 980 nm laser (1.5 $W.cm^{-2}$ for 30 min with a 5-min interval between each 5 min illumination) after 6 hours of treatment with non-targeted rUCNPs@HSA(Ce6-Mn) or targeted rUCNPs@HSA(Ce6-Mn)-RGD. A strong phototoxic effect was observed with the targeted NPs. *In vivo* experiments were performed in U87 tumor-bearing mice. After 12 hours of incubation with the different compounds, the tumors were illuminated with a 980 nm laser every two days for 14 days (1.5 $W.cm^{-2}$ for 30 min with a 5-min interval between each 5 min illumination). The group treated with rUCNPs@HSA(Ce6-Mn)-RGD displayed the lowest tumor growth rate. The median survival times for the mice treated by PBS (control), light only, rUCNPs@HSA(Ce6-Mn) or rUCNsP@HSA(Ce6-Mn)-RGD were 45.0, 51.0, 54.5 and 59.2 days, respectively (**Figure 52**) [62, 63]**.**

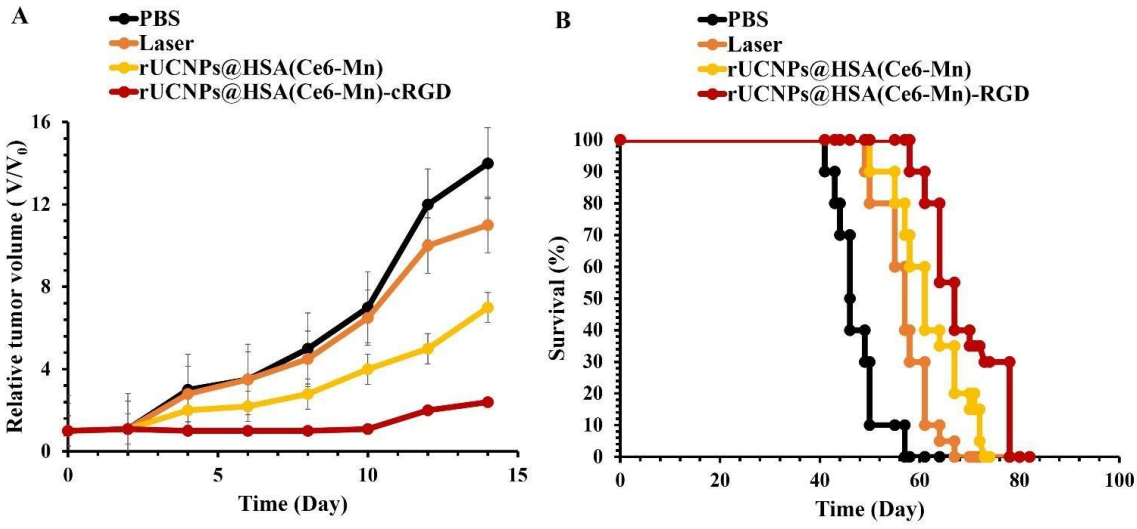

Figure 52 : (A) The relative tumor volume after treatment with PBS (control), light only, rUCNPs@HSA(Ce6-Mn) or rUCNsP@HSA(Ce6-Mn)-RGD, with a concentration of 5.2 mg/Kg (Ce6 equivalent) and (B) Kaplan-Meier survival time curve. Light excitation at 980 nm (1.5 $W.cm^{-2}$) for 5 min. Adapted from Tang et al. [50, 51].

In 2019, Kohle *et al.* studied the modification of the diagnostic Cornell prime dots (C′ dots) by encapsulating (design 1) or coupling (design 2) a Methylene blue derivative (MB2) PS. In both designs, the functionalization with a c(RGDyC) targeting peptide was performed. The TEM images presented a diameter of about 4.0 nm for each design. They estimated, respectively, 17 and 14 c(RGDyC) units per MB2 molecule for design 1 and 2. The ϕ_0 were determined using the singlet oxygen sensor 1,3-diphenylisobenzofuran (DPBF) and were found to be 111 ± 3% for design 1 and 161 ± 5% for design 2. The PS photostability was better in design 1 than in design 2. Surprisingly, the coupling of c(RGDyC) led to a decrease of ϕ_0 by 25% and 12% for design 1 and design 2, respectively. No *in vitro* or *in vivo* studies were performed [64].

In 2005, Kopelman *et al.* presented a combination of a NP consisting of a polyacrylamide (PAA) core, a cloaking PEG coat, a Photofrin® PS, a cRGD targeting peptide (cyclic CDCRGDCFC) and an MRI contrast agent, as shown in **Figure 53**. The size of PAA NPs was about 30-60 nm. The $^1O_2$ production was determined using anthracene-9,10-dipropionic acid disodium salt (ADPA) probe. *In vitro* studies were performed in 9L rat gliosarcoma cells incubated with or without different concentration of NPs. A concentration of 1050 $mg.mL^{-1}$ was required to obtain a PDT effect. Rats bearing intracerebral 9L tumors were used for the *in vivo* studies. Diffusion-weighted MR images were obtained from untreated rats and those treated either with laser alone or with laser and NPs. Only the latter showed necrosis of the tumor. The final step was the synthesis of targeted NPs using the cRGD peptide and testing them *in vitro* on (+) MDA-435 and (-) MCF-7 cells. The authors observed that targeted NPs bound only to (+) MDA-435 cells [65].

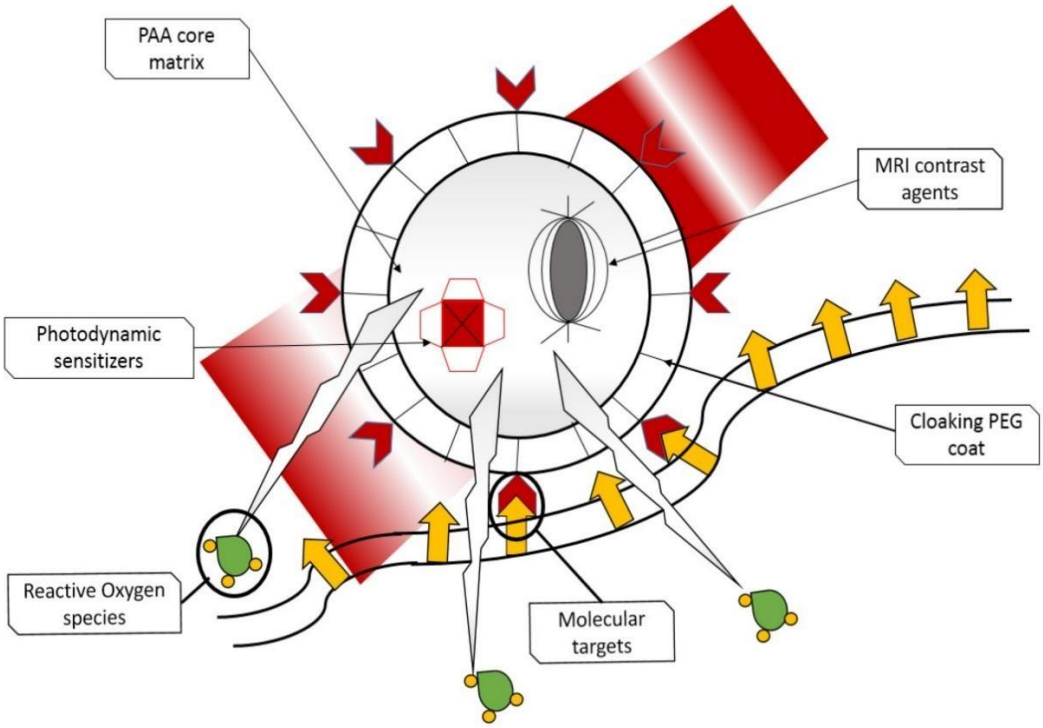

Figure 53 : The schematic nanoplatform consisting of PAA core matrix with PEG cloaking coat, photodynamic dye (Photofrin®), MRI contrast enhancement agents and molecular targeting (cRGD peptide). Adapted from Kopelman et al. [53].

II.2.4 NPs@PS@Fibronectin targeted-peptide

In 2013, Halig *et al.* formulated iron oxide (IO) NPs encapsulating phthalocyanine 4 (Pc4) PS. These NPs were conjugated to a targeting fibronectin mimetic peptide (Fmp: WQPPRARI), which is well-known to bind to $\alpha_v\beta_3$ integrin overexpressed in head and neck squamous cell carcinoma (HNSCC). Only *in vivo* multispectral imaging was achieved on mice bearing M4E cell induced tumor. These indicated a high accumulation of the non-targeted IO-Pc4 and the targeted Fmp-IO-Pc4 NPs in tumors as compared to Pc4 alone. No clear effect of Fmp was observed [66].

In 2014, the same team estimated the size of the targeted Fmp-IO-Pc4 NPs of about 41 nm. *In vitro* experiments were carried out on 4 HNSCC cell lines (M4E-15, TU212, 686LN, M4E CNT). The most significant tumor regression was observed 48 hours after laser treatment at 672 nm (100 $mW.cm^{-2}$, 30 min) for the cells exposed to Fmp-IO-Pc4 NPs as compared to free Pc4, IO-Pc4 NPs and IO NPs. *In vivo* experiments were then carried out on HNSCC xenografted mice. The initial tumor size in the mice was 5-7 mm^3 before the administration of the targeted and non-targeted NPs and the laser irradiation. 48 hours post-administration, the results showed that both NPs prompted a reduced tumor growth compared to free Pc4, but still led to a final increase in tumor volume compared to the initial volume (**Figure 54**) [67].

In 2020, *Y. Wang et al.* described the synthesis and characterization of Pep-SQ@USPIO nanoprobe used for imaging-guided PDT of triple negative breast cancer (TNBC) [59].

This new Cathepsin B (CTSB)-activatable nanoprobe was designed to achieve both fibronectintargeting magnetic resonance (MR) imaging and near infrared fluorescence (NIRF) imaging. SQ (squaraine-based) PS, known for its high NIR emission and photodynamic effect, was firstly synthesized. The PS was further conjugated with fibronectin-targeting peptide (CREKA) by means of the CTSB-cleavable peptide (GFLG) to form the Pep-SQ conjugate. The Pep-SQ@USPIO nanoprobe was finally obtained by the covalent coupling of the Pep-SQ conjugate onto the maleimide-DSPE-PEG2000-coated ultrasmall superparamagnetic iron oxide (USPIO) NPs. The hydrodynamic diameter of the NPs was 20 nm, as measured by DLS. In vitro PDT testing of the Pep-SQ@USPIO was done on MDA-MB-231 cells overexpressing fibronectin. After 24 h of cell incubation with Pep-SQ@USPIO, the irradiation was applied (5 min, 660 nm, 1 $W.cm^{-2}$). A significant decrease in the cell viabilities was induced by the increase of the laser power densities at 660 nm. In addition, cells treated with various concentrations of pep-SQ@USPIO, ranging between 100 and 800 µg.mL-1, showed different degrees of apoptosis, consequently verifying the PDT efficiency of this system. The assessment of the accumulation of these NPs by Prussian blue staining revealed a low amount of iron in the heart, lungs and kidneys, thus demonstrating the absence of pep-SQ@USPIO accumulation. However, the evident Prussian blue staining that occurred in both liver and spleen can arise from both nanoprobe accumulation and the endogenous iron. The obtained results of the NIRF imaging proved that the sufficiently high CTSB activity in the TNBC tumors enabled its detection by Pep-SQ@USPIO. The photodynamic efficiency of Pep-SQ@USPIO was also tested in vivo on MDA-MB-231 tumor-bearing mice. The tumor volume and mass decreased sharply when treated with Pep-SQ@USPIO in the presence of Laser irradiation (660 nm, 2 W.cm-2) as compared to those exposed to Pep-SQ@USPIO alone, control (PBS) and laser alone (PBS+L). Therefore, it was validated that the Pep-SQ@USPIO activated nanoprobe exhibited a high photodynamic efficiency under laser irradiation, which allows for an enhanced PDT guided by NIRF/MR bimodal imaging for the treatment of TNBC.

In 2021, *H. Cao et al*. described the elaboration of BKC-NPs (6 nm) formed by the self-assembly of the multifunctional peptide BPFFVLK-CREKA (BKC) in water. The NPs were constituted of three motifs; hydrophobic BP (bis(pyrene)) PS used for imaging and ROS production, FFVLK peptide for stabilizing the structure and CREKA peptide for fibrin-targeting on the extracellular matrix of tumors and new-born blood vessels [60]. Using ABDA ((9,10-anthracenediyl-bis(methylene)dimalonic acid)) as ROS detection reagent, the authors observed the formation of singlet oxygen after the two-photon excitation of the BKC-NPs at 800nm. The in vitro experiments were performed on MCF-7 and HUVECs that express fibrous protein onto their surfaces. No specificity was observed for MCF-7. Whereas, the robust interaction between BKC-NPs and the HUVECs was established by the strong fluorescence that was detected both inside and at the surface of these cells. This interaction was attributed to the abundant expression of fibrous protein onto the surface of HUVECs which allowed for a more specific recognition by the CREKA motif in the NPs. Cells incubated with the same concentration of BKC-NPs were tested under different conditions. After exposure to light illumination

at 800 nm, the cell viability attained 20.8 %, whereas it reached 16% for one photon (405 nm) and 73% for the control (two-photon laser of 800 nm (1 W) or a xenon lamp with a 405 nm cut-off filter for 20 minutes). In vivo experiments were then performed using BKC-NPs in BALB/c mice imaging. Confocal laser scanning microscopy revealed blood vessels in the ear and in the tumor. To explore the precision of the therapy in vivo, a selected region was illuminated by a two-photon laser for about 2 min. It was observed that the ROS generated by the accumulated BKC-NPs caused quick vessel breaking as compared to the control vessel that remained intact. It was proven that these new NPs could be used in precise surgery in the brain and eyes for example. Concerning PDT experiments, the mice were injected with these NPs and were illuminated with a two-photon laser at 800 nm at different time intervals. At day 16, it was observed that the tumor volumes increased to attain 695.8, 780.2 and 610.3 mm3 for the control, laser and BKC-NPs alone, respectively. However, an important tumor volume regression, reaching 67 mm3, was achieved by the BKC-NPs in the presence of irradiation.

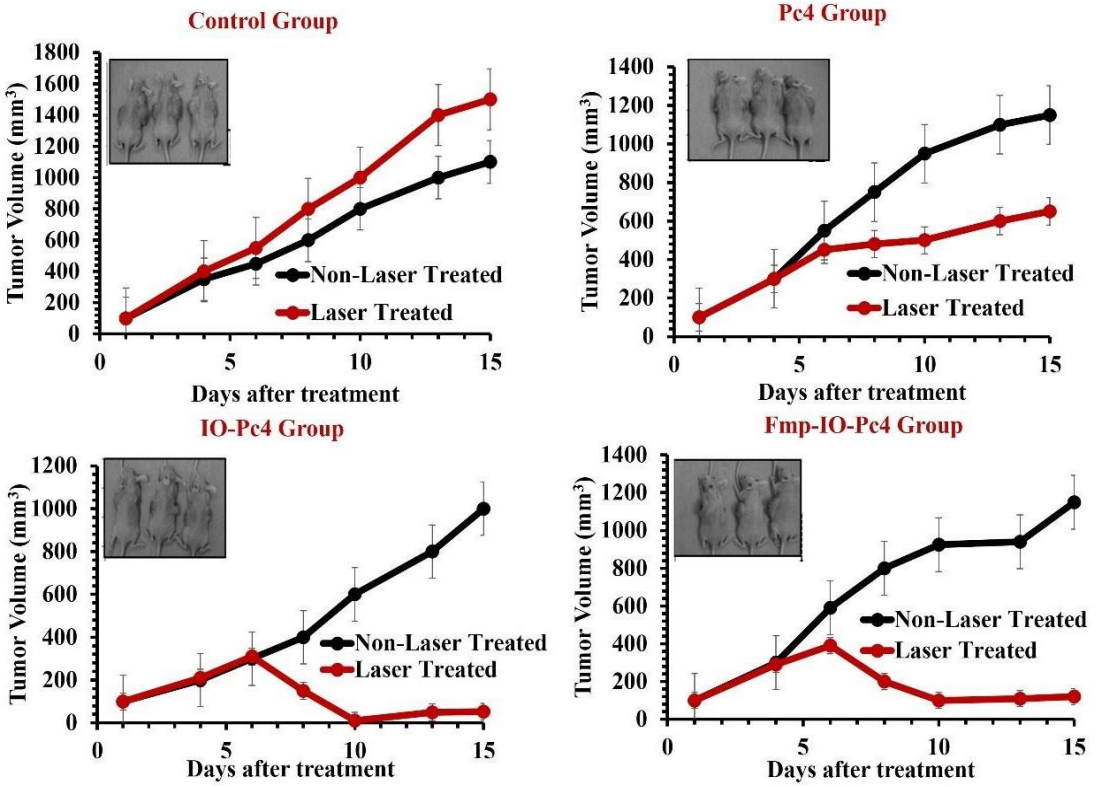

Figure 54 : Inhibition of xenograft tumor formation by Pc4 PDT treatment delivered by IO NPs. (A-D) Tumor growth and representative images of tumors on both sides of the mice in (A) PBS control, (B) free Pc4, (C) IO-Pc4, and (D) Fmp-IO-Pc4 groups, respectively with 0.4 mg/Kg Pc4. Laser treatment was performed at 48 h post-administration (672 nm, 100 mW/cm^2 for 30 min). Three out of six mice from each group are shown as representatives. Adapted from Halig et al. [55]. With permission from American Chemical Society.

II.2.5 NPs@PS@RGD-4R

In 2019, Dai *et al.* described the elaboration of polymeric NPs consisting of 1,2-distearoyl-sn-glycero-3-phosphoethanolamine-N[maleimide(polyethylene glycol)-2000] (MPD) matrix encapsulating a fluorogen (TTB). TTB displays an important aggregation-induced emission with strong NIR fluorescence and can efficiently produce ROS especially $^1O_2$. These MPD/TTB NPs were covalently coupled, *via* click reaction, to a

targeting peptide, either RGD or RGD-4R (*i.e.* modular peptide RGDFGGRRRRC), to produce targeted RGDMPD/TTB and RGD-4R-MPD/TTB NPs. ROS production was demonstrated using dichlorofluorescein (DCFH), dihydrorhodamine 123 (DHR123) and EPR spectroscopy to identify O_2•- and ABPA to detect $^1O_2$. The targeted NPs presented a high NIR luminescence at 730 nm and were efficient for real-time fluorescence monitoring. SKOV-3, HeLa and PC3 cell lines having high $\alpha_v\beta_3$ integrin expression and MCF-7 cell line with low $\alpha_v\beta_3$ integrin expression were used to prove the specificity of RGD-targeted NPs to $\alpha_v\beta_3$ integrins. The incorporation of the targeted NPs in MCF-7 was negligeable, while it was significant in the other cell lines. The targeted RGD-4R peptide presented a higher affinity than RGD. The PDT performed on cells incorporated with targeted RGD-4R-MPD/TTB NPs (730 nm, 200 mW.cm^{-2}, 10 min) revealed an apoptotic rate of 87% for PC3, 89 % for HeLa, and 91% for SKOV-3 cells. In comparison, it was only 17% for MCF-7 cells. The xenografted tumor model with HeLa, PC3 and SKOV-3 cells were used for the *in vivo* studies. A remarkable tumor growth delay was observed after the injection of targeted RGD-4R-MPD/TTB NPs and illumination at 730 nm (200 mW.cm^{-2}, 10 min) (**Figure 55**). This was accompanied with an inhibition of the expression of BCL2 and Ki-67 genes, and hence led to a reduction in the tumor proliferation and an advancement of apoptosis [68].

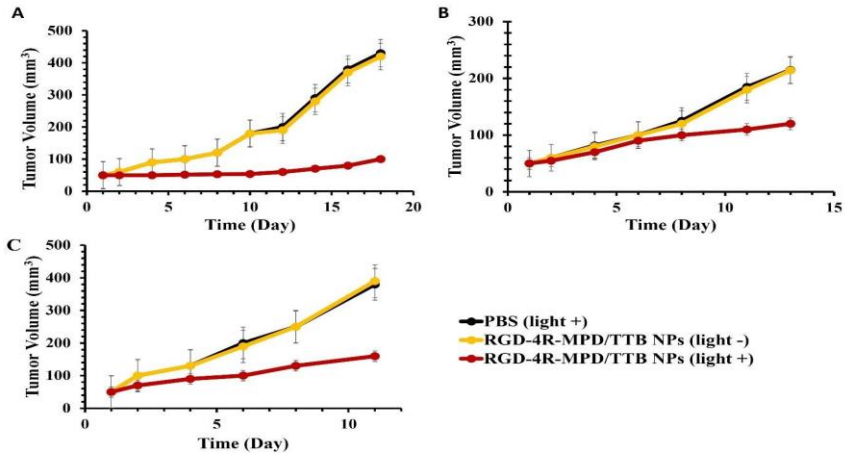

Figure 55 : RGD-4R-MPD/TTB (10 µg/ml) NPs mediated PDT for multiple xenograft tumors. Tumor volume changes in (A) HeLla, (B) PC3 and (C) SKOV-3 cells. Light excitation at 730 nm, 200 mW.cm^{-2} for 10 min. Adapted from Dai et al. [56].

II.2.6 NPs@PS@RGDfK

In 2014, Haedicke *et al.* developed calcium phosphonate NPs, in which they incorporated 5,10,15,20-Tetrakis(3-hydroxyphenyl)chlorin (*m*THPC) PS. The authors covalently coupled both a targeted RGD peptide (RGDfK) and a fluorescent dye (DY682) for near-infrared fluorescence (NIRF) emission. *In vitro* experiments were performed using tongue-squamous epithelium carcinoma cells CAL-27. A perinuclear localization of the NPs was observed. *In vivo* experiments were conducted in CAL-27 xenografted female athymic nude mice. The best accumulation for the non-targeted and the RGD targeted NPs was found at 8 hours and 24 hours post-treatment, respectively. A better internalization in the tumor was observed using RGD targeted NPs in comparison to the

non-targeted NPs or Foslip® PS. However, a strong accumulation was also detected in the lungs, kidneys, spleen and liver. After PDT (652 nm, 0.1 $W.cm^{-2}$, 100 $J.cm^{-2}$), a decrease of both tumor volume and tumor vascularization was demonstrated in 3 out 4 animals [69].

Table 6 describes the NPs@PS@peptide systems, targeting $\alpha_v\beta_3$ integrin, regarding the types of NPs, PSs and the coupling between them, in addition to the NPs size, excitation wavelength ($\lambda_{excitation}$), fluorescence quantum yield (ϕ_F), singlet oxygen quantum yield ($\Delta_{O.S}$) and the results obtained *in vitro* and/or *in vivo*.

Table 6 : The summary of NPs conjugated with PSs and peptides targeting αvβ3 integrin in terms of different parameters

NPs@PS@Peptide targeting $\alpha_v\beta_3$										
Reference	NPs	PS	Coupling between NPs and PS	NPs size (nm)	λexcitation (nm)	ϕF	ΔO.S	*in vitro*	*in vivo*
Peptide RGD									
[52]	Polymeric (PEG)	IR700	Maleimide	6.6 for RGD8PEGIR700	540	nd	nd	A375	Mouse fibroblast NIH/3T3
[50]	Mesoporous silica (MSN).	Photoporphyrin IX (PpIX)	Amide bond	50 for MSN-BHQSSPpIX-PEGRGD	nd	nd	nd	COS7 SCC-7 HeLa	Nd
[51]	Upconversion (UCN)	Zinc (II) phthalocyanine (ZnPc)	Encapsulation	150 for ZnPc-UCN@ lipid@ PS	980	nd	nd	Hela	Nd
[49]	Upconversion (UCN)	Merocyanine 540 (MC540)	Adsorption	225 for MC540 loaded UCN/RGDPMAO-DOPE	540	nd	nd	MCF-7	Nd
Peptide iRGD									

[58]	High-density lipoproteins (HDL)	Indocyanine green (ICG)	Encapsulation	86.7 for iRGD-rHDL/ICG	808	nd	nd	4T1	Female BALB/c mice
[59]	mesoporous silica (MSN)	Indocyanine green (ICG)	Encapsulation	100200 for Aminefunctionalized MSNs	808	nd	nd	MDA-MB-231.Luc B16F10.Luc .	Immuno compromised female NCG mice
[57]	Liposome (LP)	Indocyanine green (ICG)	Encapsulation	115.91 for iRGD-ICGLPs	808	nd	nd	4T1	4T1 Tumor-bearing mice
				Peptide cRGD					
[54]	Globular PEG	Chlorin e6 (Ce6)	Maleimide	3–4 for cRGDgPEG-Ce6	360	nd	nd	SKOV-3 KB	7-week-old Female nude mice (BALB/c nu/nu mice, Institute of Medical Science, Tokyo)
[53]	Poly (amido amine) dendrimer (PAMAM)	Chlorin e6 (Ce6)	Amide bond	28 for PEG-P-Ce6 and 273 RGDP-Ce6	488	nd	2.5-fold higher than that of free Ce6	A375 NIH3T3	Nd
[55]	Self assembly	Hematoporphyri n (HP)	Thioketal linkage	180 for RPTD/ HP	395	nd	nd	nd	Nd
				Peptide c(RGDyK)					

[60]	Upconversion (UCN)	Pyropheophorbi de-a (Pyro)	Amide bond	53 for OCMC-UCNP	414	nd	nd	U87-MG MCF-7	Nd
[64]	Silica	Methylene blue (MB)	Encapsulation (Design 1), Maleimide (Design 2)	below 10 for designed NPs 1 and 2	543	nd	111 ± 3% for Design 1 161 ± 5% for Design 2	nd	nd
[61]	Upconversion (UCN)	Pyropheophorbi de-a (Pyro)	Amide bond	55 for UCNP-PyroRGD	633	nd	nd	U87-MG	nude mice bearing U87-MG tumor
[63]	Upconversion (UCN)	Chlorin e6 Mn^{2+} (Ce6-Mn)	Encapsultation	101.6 for UCNPs@HSA	980	nd	nd	U87	U87-Bearing mice
				Peptide cRGD					
[65]	Polyacrylamide (PAA)	Photofrin®	Encapsultation	30-60 for PAA	630	nd	nd	9L rat	Rats bearing intracerebral 9L tumors
				Peptide Fmp fibronectin					
[66]	Iron oxide	Phthalocyanine 4 (Pc4)	Encapsultation	nd	586-820	nd	nd	nd	Mice bearing M4E tumor induced
[67]	Iron oxide	Phthalocyanine 4 (Pc4)	Encapsultation	41 for Fmp-IO-Pc4	672	nd	nd	M4E,M4E-15,686 LN, TU212	Mice bearing M4E tumor induced
				Peptide RGD or RGD-4R					

[68]	Polymeric matrix	TTB*	Encapsulation	79.1 for RGD-4R-MPD/T TB	400−700	0.10 in solid state	nd	MCF7, PC3, Hela, SKOV-3	BALB/c Nude mice (male for PC3 xenograft tumor and female for both Hela and SKOV-3 xenografted tumor models)
Peptide RGDfK									
[69]	Calcium Phosphate	5,10,15,20-Tetrakis(3hydroxyphenyl)chlorin (*m*THPC)	Encapsulation	205 for NP-DY682-*m*THP CRGD	652	nd	nd	CAL-27	Female athymic nude mice
Peptide CREKA									
[70]	self – assemble of bis(pyrene)-FFVLK	bis(pyrene)	amide bond	6	405 nm (one photon) and 800 nm (twophoton, day 1 and 4 : 7 min (3.5 W cm-2), day 8 : 8 min with 4 W cm-2 laser)	nd	60.1%	MCF-7 and HUVEC	BALB/C mice

[71]	ultrasmall superparamagnetic iron oxide	SQ (Squaraine)	amide bond	20	660	nd	nd	MDA-MB-231	MDA-MB-231 tumorbearing mice

**nd: not determined *TTB: Contains an electron-accepting benzo[1,2-b:4,5-b']dithiophene 1,1,5,5-tetraox-ide core and electron-donating 4,4'(2,2-diphenylethene-1,1-diyl)bis(N,N-diphenylaniline) groups for image-guided targeted PDT*

II.3 Peptide for nucleolin membrane receptors

Nucleolin is a nucleolar protein that has several roles in the intracellular pathways and is involved in tumorigenesis [72]. It is expressed in the nucleus of resting cells. In tumor cells, nucleolin cycles between the cell nucleus and the plasma membrane. Its overexpression was identified in different kind of cancers. Therefore, nucleolin is considered a target for anticancer therapies [73].

II.3.1 NPs@PS@F3-peptide

F3 peptide has a sequence of KDEPQRRSARLSAKPAPPKPEPKPKKAPAKK. It is well-known to target tumor neovessels as well as some tumor cells [74, 75]. F3 peptide can bind to the nucleolin membrane receptors, which allows its internalization into the cells and its further localization into the nucleolin.

Kopelman's team reported the elaboration of an F3-targeted nanosystem, consisting of a polyacrylamide core in which a photodynamic agent, Photofrin® PS, and an MRI agent, iron oxide, were embedded. The F3 targeting peptide was also attached to the NPs in addition to the coupling to Alexa Fluor 594 for fluorescent imaging. Six molecules of Photofrin® were encapsulated into each NP and an average of 30 F3 peptides were coupled. No cytotoxicity was observed in MDA-435 cells after 4 hours of incubation with the F3-targeted NPs. However, a significant phototoxic effect was achieved after light illumination (630 nm, 1.5 mW, 5 min) as 90 % of the cells were destroyed. Using fluorescence microscopy, the authors detected a cellular uptake and a nuclear localization of F3-targeted NPs. *In vivo* studies in rats bearing 9L gliomas were performed in the presence of non-targeted and F3-targeted NPs for comparative reasons. The F3-targeted NPs had about 3-fold prolonged tumor transit time. Their presence led also to an improved contrast-to-noise ratio of about 2-fold at 1 hour. A median survival time after treatment and illumination was found to be 7.0 days for the control untreated group, 8.5 days for the group treated only with laser and 13.0 days for the one treated with Photofrin® alone. Conversely, the median survival time was up to 33 days for the group treated with F3-targeted NPs (**Figure 56**) [76].

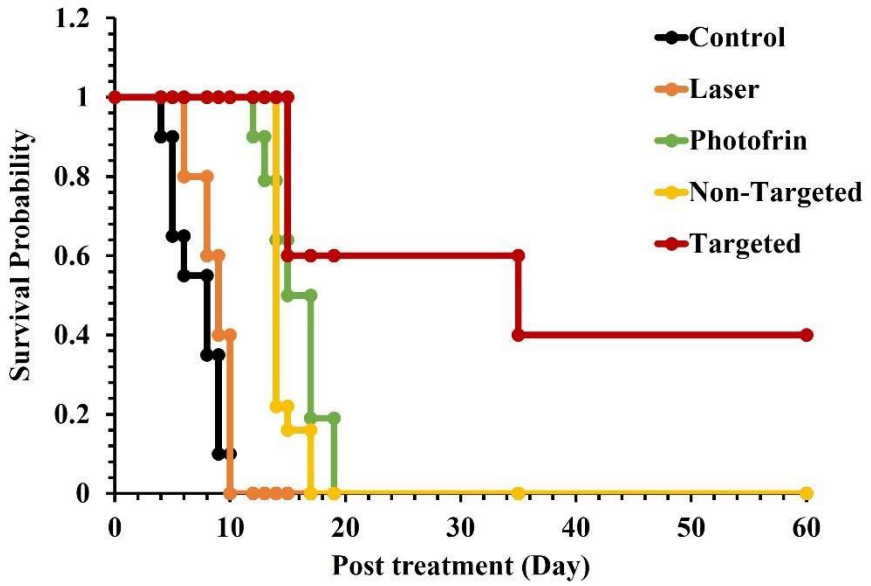

Figure 56 : Survival curves for animals bearing a brain tumor: untreated (control), laser only, Photofrin® + laser, non-targeted NPs + laser and F3targeted NPs + laser with a concentration of 7 mg.Kg^{-1} (Photofrin equivalent). Irradiation at 630 nm, 1.5 mW for 5 min. Adapted from Kopelman et al. [62].

The same team [77] reported polyacrylamide NPs conjugated with MB PS and F3 targeting peptide. First, MB was coupled to the 3(aminopropyl)methacrylamide hydrochloride (APMA) monomer before the formation of NPs in a reverse microemulsion. The amino functions of APMA were then used to couple the F3 peptide. 4 cell lines were cultivated, human melanoma MDA-MB-435, rat glioma F98, human breast adenocarcinoma MCF-7 and rat glioma 9L. The nucleolin expression was described previously by the same team [78]. The F3-targeted NPs presented the lowest affinity for MCF-7 cells. Yet, a better affinity by 2.5, 4 and 5.4 times was achieved for F98, MDA-MB-435 and 9L cells, respectively. No incorporation of the non-targeted MB-conjugated NPs was observed. Comparable results in terms of the photodynamic efficiency were obtained on all the four cell lines when the targeted NPs were tested at 1.5 mg.mL^{-1} and illuminated at 647 nm (20 J.cm^{-2}, 1 min). Further experiments performed on F98 cell lines proved that the cell death increased with illumination time and NPs concentration.

Feng *et al.* described the synthesis of targeted F3-PTX-(Pyro-PLA)$_2$PEG NPs (denoted by F3-targeted NPs). These consist of Pyroconjugated amphiphilic (Pyro-PLA)$_2$PEG NPs covalently attached to the F3 targeting peptide. Paclitaxel (PTX, Taxol) was then encapsulated to demonstrate a combination of PDT and chemotherapy [79]. (Pyro-PLA)$_2$PEG NPs presented a good stability *in vitro*. In HUVEC and human colorectal cancer cells (HCT-15), a better accumulation of the F3-targeted NPs was observed with a factor of 1.21 and 1.18, respectively, when compared with that of (Pyro-PLA)$_2$PEG. These NPs were localized mostly in the endolysosomal compartment. The production of ROS was demonstrated using 2',7'-dichlorofluorescein (DCF) fluorescence. The

IC_{50} values in HUVEC were 122.1 ng.mL^{-1} for Taxol, 84.09 ng.mL^{-1} for non-targeted NPs (*i.e.* PTX-(Pyro-PLA)$_2$PEG NPs) in the absence of laser, 41.21 ng.mL^{-1} for nontargeted NPs in the presence of laser and 17.0 ng.mL^{-1} for F3-targeted NPs accompanied by laser irradiation. The IC_{50} values in HCT-15 cells were 426.7 ng.mL^{-1} for non-targeted NPs in the absence of laser, 86.32 ng.mL^{-1} for non-targeted NPs in the presence of laser and 32.86 ng.mL^{-1} for F3-targeted NPs accompanied by laser irradiation. These outcomes validated the importance of adding a targeting peptide to boost the PDT efficiency. The *in vivo* experiments performed in Male BALB/c nude mice bearing colorectal tumor (HCT-15 injected subcutaneously) confirmed the *in vitro* results. After injection, the non-targeted NPs were slightly accumulated in the tumor and around the blood vessels, whereas the F3-targeted NPs were effectively accumulated into the tumor due to the efficient targeting of both the tumor cells and the neovessels. After light irradiation (660 nm,100 J.cm^{-2} for 9.8 min), the inhibition rate of the tumor was 79.92% for the F3 targeted NPs. F3-PTX-(Pyro-PLA)$_2$PEG NPs showed better results of tumor regression (**Figure 57 A and C**) and had a better survival rate in mice as compared to these NPs without laser or non-vectored NPs (Figure 28 B). However, the tumor inhibition rate was only 5.71 % for Taxol, 18.97 % for non-targeted NPs without irradiation, 38.08% for PTX-free non-targeted NPs (*i.e.* (Pyro-PLA)$_2$PEG NPs) in the presence of laser irradiation and 54.68% for non-targeted NPs without laser (Figure 28 D). The combination of PDT and chemotherapy was more efficient than any of these treatments alone. The addition of the F3 peptide allowed the NPs to accumulate specifically into the tumor parenchyma as well as around tumor angiogenesis [79].

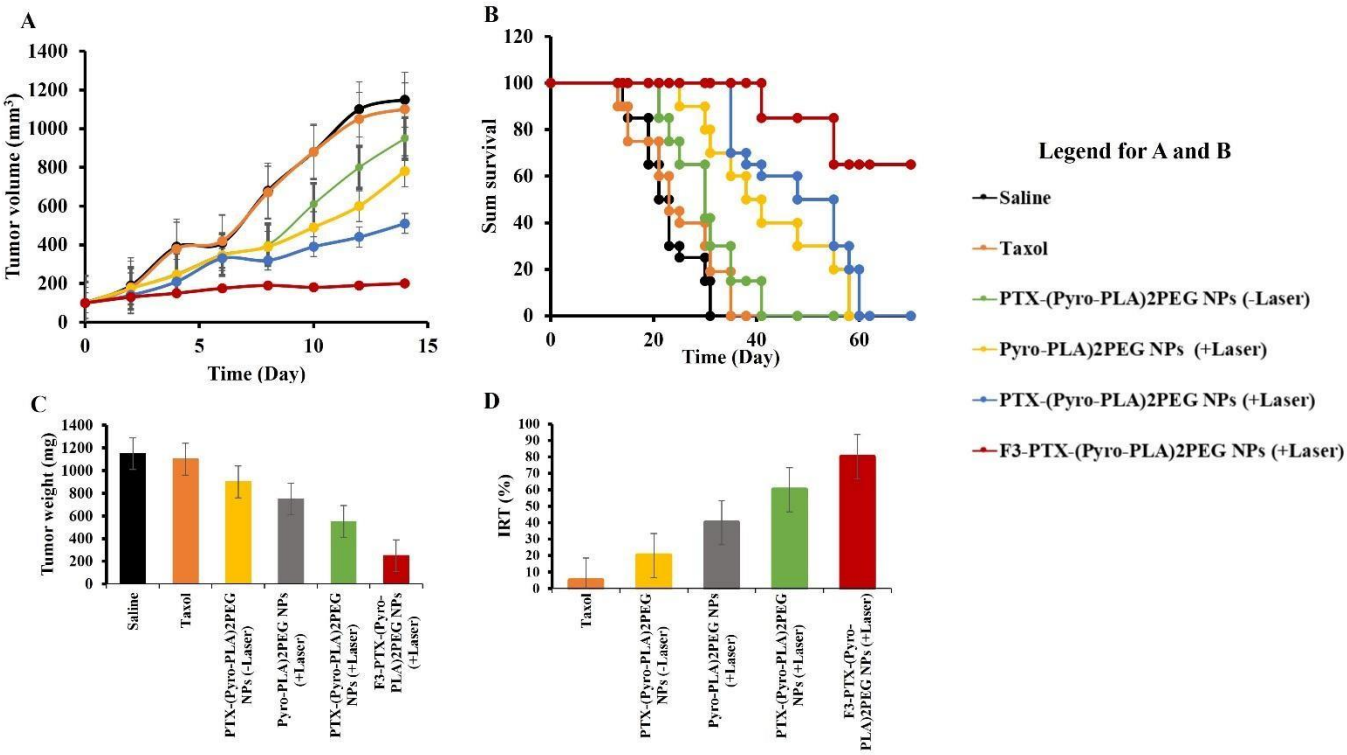

Figure 57 : Antitumor effect with 2.5 mg/Kg of Pyro, (Pyro-PLA)$_2$PEG NPs, PTX-(Pyro-PLA)2PEG NPs and F3-PTX-(Pyro-PLA)$_2$PEG NPs, respectively, with or without irradiation for 9.8 min with a 660 nm laser, 170 mW.cm^{-2}. The mice given with saline were applied as the negative control. (A) Changes in tumor volume of mice during the 14 days

experimental period. (B) Kaplan-Meir survival curve of mice. (C) Weight of dissected tumors. (D) Tumor-growth inhibition (IRT) rate of the various treatment strategies. Adapted from Feng et al. [65].

Table 7 describes the NPs@PS@peptide systems, targeting $\alpha_v\beta_3$ integrin, regarding the types of NPs, PSs and the coupling between them, in addition to the NPs size, excitation wavelength ($\lambda_{excitation}$), fluorescence quantum yield (ϕ_F), singlet oxygen quantum yield ($\Delta_{O.S}$) and the results obtained *in vitro* and/or *in vivo*.

Table 7 : The summary of NPs conjugated with PSs and F3 targeting peptides in terms of different parameters

NPs@PS@F3-Peptide										
Reference	NPs	PS	Coupling between NPs and PS	NPs size (nm)	λexcitation (nm)	ϕF	ΔO.S		*in vitro*	*in vivo*
F3-peptide targeting										
[77]	Polyacryla mide (PAA)	Methylene blue (MB)	Amide bond	55.8 ±5.0 for MBconjugated PAA NPs	647	nd	nd		MDA-MB-435, F98, MCF-7 9L	Nd
[79]	Hydroxylpoly(lactic acid)$_{19000}$poly-(ethylene glycol)$_{3000}$poly(lactic racid)$_{19000}$hydroxyl (HO-PLA-PEG-PLAOH)	Pyropheophorbide-a (Pyro)	Ester bond	109.81 ±3.55 for PTX-(Pyro-PLA)$_2$PEG NPs	660	nd	Nd		HUVEC HCT15	Male BALB/c nude mice
[76]	3aminoprolyl methacryla mide() encapsulati ng Iron oxide	Photofrin®	Encapsulation	40 for F3targeted NPs	630	nd	nd		MDA-MB-435	Rat 9L glioma in male Fischer 344

**nd: not determined*

II.4 Peptides for cell penetration

The plasma membranes form barriers, with a selective permeability, that hinder the intracellular transfer of the anticancer drugs. To overcome this obstacle, cell penetrating peptides of 5 to 30 amino acids can be used [80]. TAT (GRKKRRQRRRPQ) is a 12-amino acid peptide that allows the penetration into the cells [81]. Direct penetration has been proposed as the mechanism used for the internalization of the TAT protein. The first step in this model is the interaction between the membrane and the unfolded TAT fusion protein that causes the disruption of the membrane enough to allow its passage. Once internalized, the TAT fusion protein will then fold back using of a chaperone system. There is no consensus on this mechanism, and other ones that have been proposed involve clathrin-mediated endocytosis

II.4.1 NPs@PS@TAT

In 2013, Fales et al. synthetized Raman-labeled gold nanostars (AuNS-DTDC), where DTDC, 3,3'-diethylthiadicarbocyanine iodide, represents the Raman probe. The NPs were coated with a silica shell and loaded with PpIX PS and TAT peptide, where the latter was conjugated by passive adsorption, to afford AuNS-DTDC@SiO_2-PpIX-TAT. The size of NPs was 123 nm. The *in vitro* Raman imaging of BT-549 breast cancer cells incubated for 24 hours with AuNP-DTDC@SiO_2-PpIX without TAT displayed little to no signal, in contrast to that obtained in the presence of TAT. Such results indicated the convenience of this method in the delivery of the NPs into the cells. An *in vitro* phototoxic effect was observed after the excitation with a mercury arc lamp (filtered at 633 nm, 4.4 $W.cm^{-2}$, 30 second), in BT-549 breast cancer cells exposed to the NPs (Figure 29). The PDT effect induced by the developed NPs was clearly validated in the fluorescent microscopic images of the BT-549 breast cancer cells, incubated with the NPs with and without PpIX (**Figure 58**) [82].

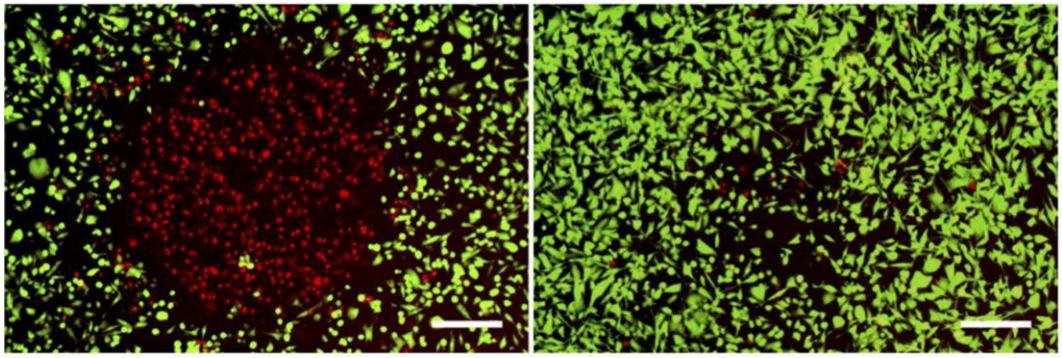

Figure 58 : Viability staining of BT-549 breast cancer cells incubated with AuNS-DTDC@SiO2-PpIX-TAT NPs (left) and AuNS-DTDC@SiO2-TAT NPs particle concentration of 0.1 nM (right) after 30 seconds of light irradiation 4.4 W.cm-2 for 30 second (mercury arc lamp, filtered at 633 nm). Live cells are stained green and dead cells are stained red. Scale bars are 250 μm [68]. With permission from American Chemical Society.

In 2014, Thandu et al. developed superparamagnetic iron oxide (SPION) NPs coupled to 5-(4-carboxyphenyl)-10,15,20 triphenylporphyrin (TPP) PS. The size of the SPION NPs alone was 20 nm. The coupling of TPP to SPION did not affect their $^1O_2$ production. Due to the poor cell affinity of these SPION-TPP NPs in B78-H1 murine amelanotic

melanoma cells, the authors conjugated a TAT peptide functionalized with rhodamine (Rhod-TAT) to the SPION-TPP NPs. The *in vitro* photodynamic effect of Rhod-TAT-SPION-TPP NPs was evaluated in B78-H1 cells after laser illumination at 543 nm (14 $J.cm^{-2}$, 30 min). An IC_{50} value of 500 nM was estimated. The rhodamine fluorescence was used to verify the incorporation of the targeted Rhod-TAT-SPION-TPP NPs into the cells (**Figure 59**) [83].

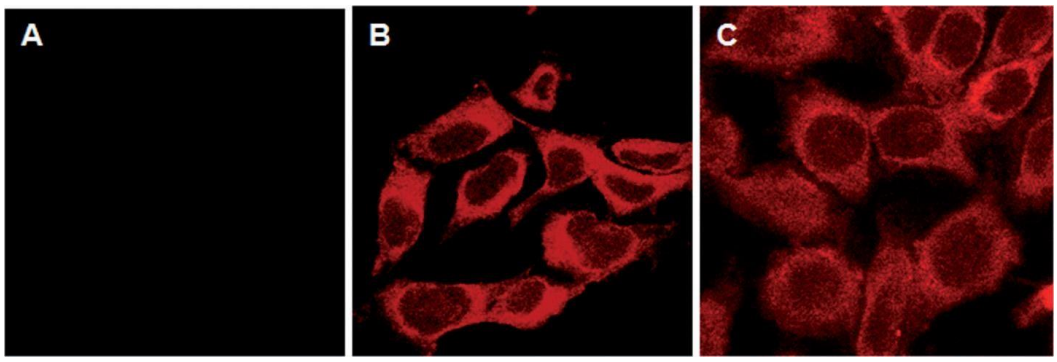

Figure 59 : Cellular uptake by confocal laser microscopy. Images of B78-H1 cells (A) untreated and treated with 400 nm Rhod-TAT-SPION-TPP after incubation for (B) 3 h and (C) 24 h [69]. With permission from John Wiley and Sons.

In 2017, Gao *et al.* synthetized a new polymeric NP decorated with tumor acidity (pHe)-activatable TAT peptide and loaded with Ce6 PS and Gd^{3+} contrast agent (^{DA}TAT-NP). These NPs were developed for the treatment of pancreatic cancer through fluorescence/MRI-guided PDT. ^{DA}TAT-NP comprised two diblock copolymers, PCL_{45}-*b*-$PAEP_{35}$-Cya/DTPA and ^{DA}TAT-PEG_{77}-*b*-PCL_{25}. The targeting effect of the TAT peptide was inactivated by masking the amines of the TAT lysine residues with 2,3-dimethylmaleic anhydride (DA). *In vitro* studies were performed on pancreatic BxPC-3 cancer cells incubated with different concentrations (Ce6 equivalent) of free Ce6, TAT-NP, ^{DA}TATNP and succinic anhydride TAT-NP (*i.e.* ^{SA}TAT-NP) in a medium with pH adjusted at 6.5 or 7.4, the extracellular pH of tumor and normal tissues, respectively. 4 hours post-incubation, a NIR laser irradiation (660 nm, 0.5 $W.cm^{-2}$) was applied for 20 min. **Figure 60** showed that the cell viability decreased linearly with the increase in the Ce6 concentration. Moreover, it was revealed that no significant difference was observed due to pH in TAT-NP and ^{SA}TAT-NP. Conversely, ^{DA}TAT-NP had a significant increasing effect on cell death when pH decreased. The intracellular ROS generation in BxPC-3 cancer cells was investigated under both pH conditions with all the tested compounds at a concentration of 20 $mg.mL^{-1}$ (Ce6 equivalent). ROS were detected using the DCFH-DA reagent. A similar ROS production was detected for all the three NPs in water [84].

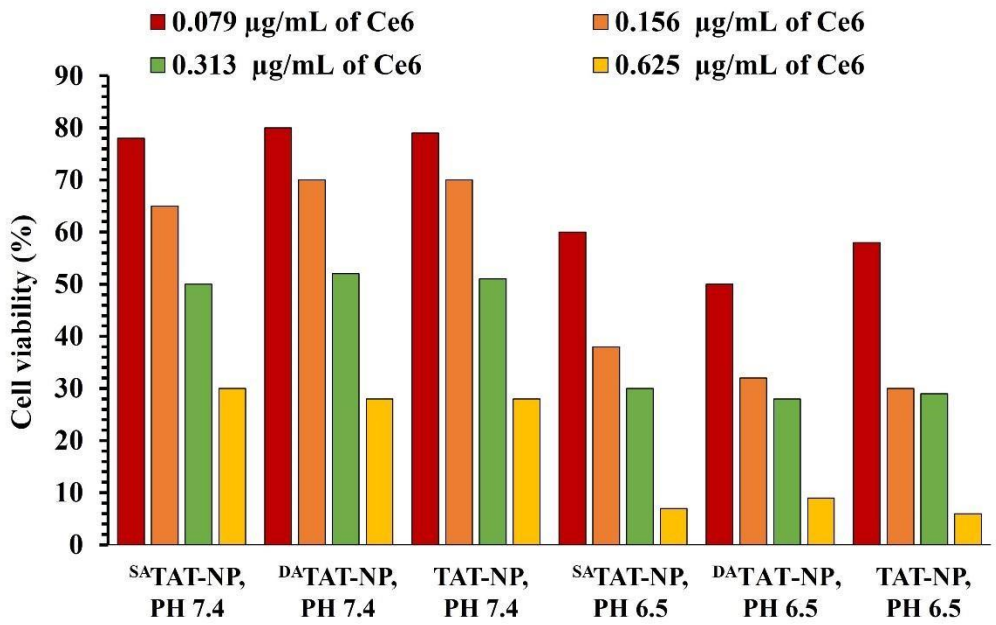

Figure 60 : The cytotoxicity performance of DATAT-NP, SATAT-NP and TAT-NP performance in BxPC-3 cells with NIR laser irradiation (660 nm, 0.5 mW.cm-2) for 20 min. Adapted from Gao et al. [70].

The *in vivo* studies were then realized on BxPC-3 xenograft-bearing mice, with a tumor volume around 100 mm^3 (**Figure 61**). Cancer tissues were imaged by fluorescence 48 hours after IV-injection of free Ce6, TAT-NP, ^{DA}TAT-NP and ^{SA}TAT-NP. ^{DA}TAT-NP treated mice exhibited the highest Ce6 fluorescence in the tumor when compared to other NPs and free Ce6. In healthy tissues, no difference was observed. This was in favor of a process in which ^{DA}TAT-NP had a prolonged blood circulation lifetime. In addition, the acidic environment in the tumor reactivated the masked TAT peptide, leading to an important reduction in the tumor volume by more than 65% after 16 days of therapy [84].

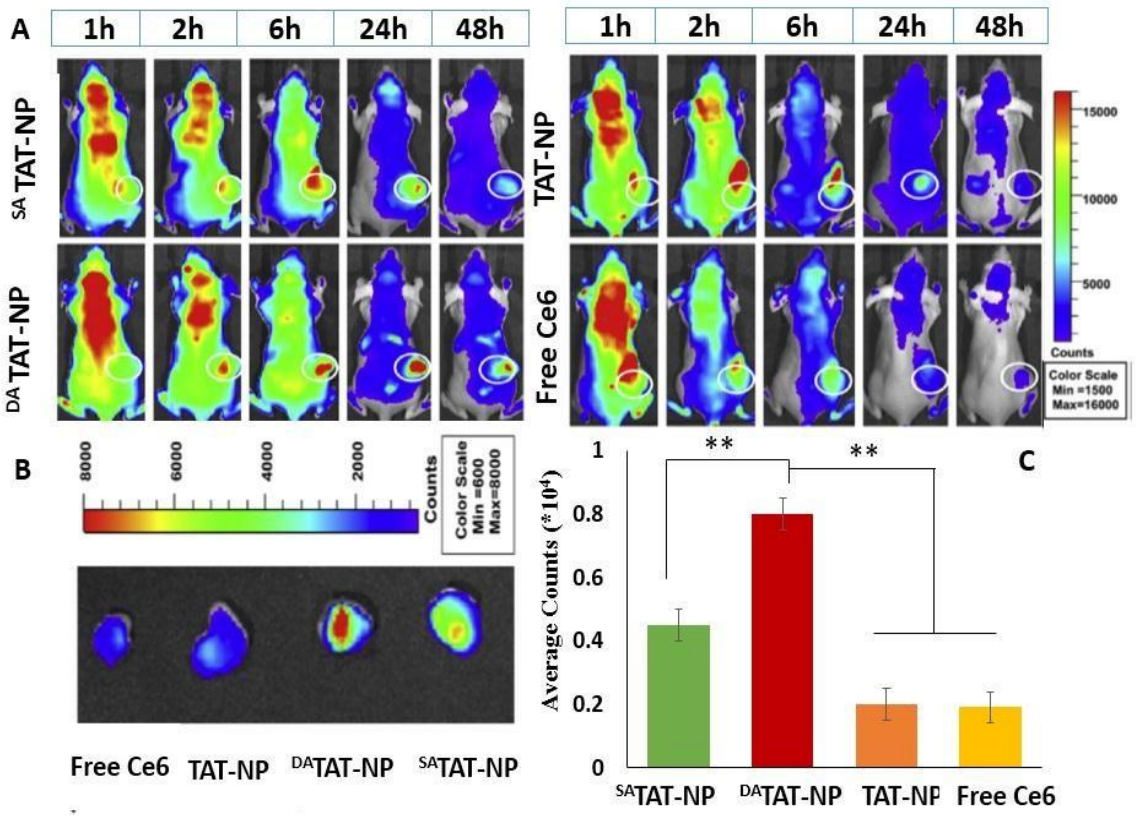

Figure 61 : (A) Fluorescence images of BxPC-3 xenograft-bearing mice after IV-injection of DATAT-NP, SATAT-NP and TAT-NP at different times. The tumor sites are denoted by white circles. (B) Ex vivo images of tumors excised at 48 h post-injection. (C) Quantification of Ce6 fluorescence in the tumors, as performed in (B) by the average counts. All of these experiment is on 2.5 mg.Kg-1 Ce6, 660-nm laser, 0.5 mW.cm-2, 20 min. Adapted from Gao et al. [70]. With permission from Elsevier.

In 2019, Wan *et al.* combined PDT, PTT and chemotherapy in order to treat breast cancer cells. The fluorescent infrared dye, IR780, was first conjugated with the nuclear targeting TAT peptide. Then, TAT-IR780 and chemotherapeutic Dox self-assembled using hydrophobic interactions to afford TID NPs (TAT-IR780-Dox). These NPs possessed a size of around 100 nm. For comparative reasons, the authors also tested TAT-IR780 in the absence of Dox (TIR). *In vitro* studies were performed on 4T1 cancer cells. 2- and 6-hours post-incubation, it was revealed that the fluorescence significantly increased when the NPs (TID or TIR) were administrated instead of IR780 alone. This proved the greater internalization of both NPs in the nuclear region (**Figure 62**) [85].

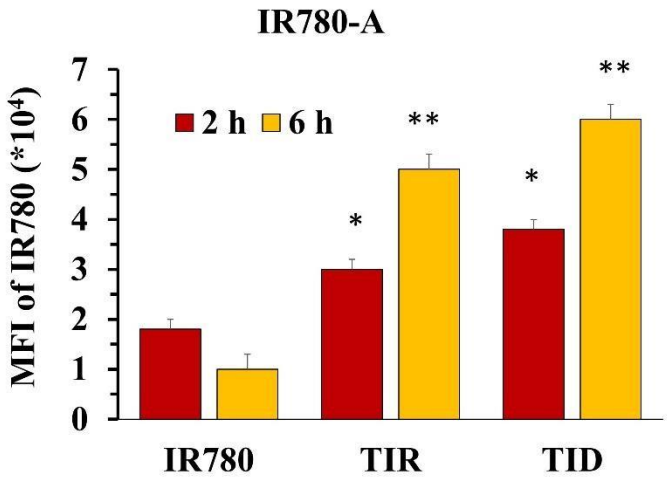

*Figure 62 : Quantitative analysis by flow cytometry of mean fluorescence intensity (MFI) of intracellular IR780 in 4T1 cells after 2-hour and 6-hour incubation with free IR780, TIR and TID NPs *P < 0.05 and **P < 0.01 as compared to the control (785 nm, of 1.0 W.cm-2, 5 min). Adapted from Wan et al. [71].*

24 hours after irradiation (785 nm, of 1.0 $W.cm^{-2}$, 5 min), the viability of the cells treated with Dox, IR780, TIR and TID reached 60%, 35%, 20% and >10%, respectively. This synergetic effect was also validated *in vivo* when 4T1 tumor-bearing mice were treated then sacrificed 6 hours later. The 100 mm^3 tumor was nearly ablated 6 days post-treatment with TID NP and IR irradiation, however, it was increased again, very slight, after 18 days (**Figure 63**) [85].

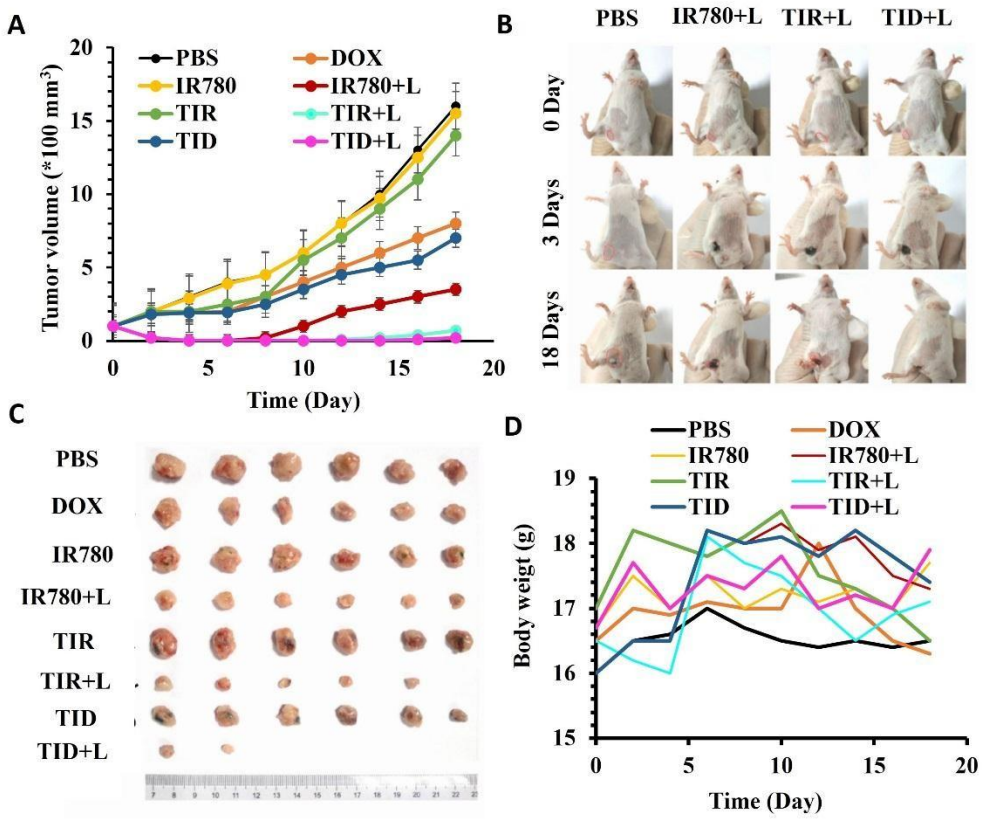

Figure 63 : Synergistic antitumor effects of TID NPs-mediated trimodal treatment of nucleus-targeted PTT/PDT and chemotherapy in 4T1 tumorbearing mice. (A) Tumor growth curves of the mice treated with free Dox, free IR780, TIR and TID NPs combined with (+L) and without laser irradiation. (B) Photos of the mice at 0-, 3- and 18-days post-treatment with free IR780, TIR and TID NPs combined with laser irradiation (+L). Red cycles indicate the recurrent tumors. (C) Photo of the tumors derived from the mice at the end of various treatments (D) Body weight changes of the mice with various treatments. **P < 0.01 for comparison between two treatment groups. IR780 and Dox doses were 1.0 and 0.5 mg.kg^{-1}, respectively. Laser irradiation was carried locally at the tumor at 785 nm at a power density of 1.0 W.cm^{-2} for 5 min. Adapted from Wan *et al.* [71]. With permission from Elsevier.

Table 8 describes the NPs@PS@peptide systems, targeting $\alpha_v\beta_3$ integrin, regarding the types of NPs, PSs and the coupling between them, in addition to the NPs size, excitation wavelength ($\lambda_{excitation}$), fluorescence quantum yield (ϕ_F), singlet oxygen quantum yield ($\Delta_{O.S}$) and the results obtained *in vitro* and/or *in vivo*.

Table 8 : The summary of NPs conjugated with PSs and cell penetrating peptides in terms of different parameters

NPs@PS@Cell Penetrating Peptide										
Reference	NPs	PS	Coupling between NPs and PS	NPs size (nm)	λexcitation (nm)	ϕF	ΔO.S		*in vitro*	*in vivo*
TAT Peptide										
[83]	Superparamagnetic iron oxide (SPION)	5-(4-Carboxyphenyl)10,15,20 triphenylporphyrin (TPP)	Click chemistry	20 for SPION NPs	White halogen lamp	nd	nd		B78-H1	Nd
[82]	Gold nanostar (AuNS)	Photoporphyrin IX (PpIX)	SiO_2-PpIX coating	123 ± 34 for AuNS-DTDC@SiO_2−PpIX	377	nd	nd		BT-549	Nd
[84]	PCL_{45}-*b*-$PAEP_{35}$-Cya/DTPA and ^{DA}TAT-PEG_{77}-*b*PCL_{25} blocks copolymers	Chlorin e6 (Ce6)	encapsulation	70 for TAT-NP, ^{DA}TAT-NP and ^{SA}TAT-NP	660	nd	nd		BxPC-3	BxPC-3 xenograft-bearing mice
[85]	Self-assembly of TAT-IR780 and Dox	IR780	Selfassembly	100 for TID NPs	785	nd	nd		4T1	4T1 tumor bearing Mice

*nd: not determined

II.5 Peptide targeting EGFR

Epidermal Growth Factor receptor (EGFR) has a role in the tumor progression in several cancers. EGFR also promotes tumor proliferation, angiogenesis and metastasis. The overexpression of EGFR in many types of cancer cells makes it a good candidate for targeted PDT [86]. The HER2 gene, one of the members of the EGFR family is expressed in two copies in healthy cells [87]. The modification of this gene and its amplification causes tumor proliferation.

II.5.1 NPs@PS@HER2 3-340

Narsireddy *et al.* synthesized 35-40 nm sized multimodal NPs constituting of an Fe_3O_4 core and a chitosan shell. The chitosan-covered Fe_3O_4 NPs were then deposited with gold NPs. 5,10,15,20-tetrakis(4-hydroxyphenyl)-21*H*,23*H*-porphine (tHPP) PS was attached *via* a lipoic acid linker to the gold NPs. A human EGFR2 (or HER2) targeting peptide, known as HER2 3-340 (MGSSHHHHHH SSGLVPRGSH MGVDNKFNKE MRNAYWEIAL LPNLNNQQKR AFIRSLYDDP SQSANLLAEA KKLNDAQAPK), was finally attached to the chitosan shell *via* a nickel-nitrilotriacetic acid linker. The uptake assays were performed in ovarian SKOV-3 cells. The obtained IC_{50} values for the PS alone, the non-targeted NPs and the targeted Peptide-NPs were 0.75 µM, 2.1 µM and 1.7 µM, respectively. The addition of the peptide did not significantly improve the selectivity for HER2. The positive effect of the NPs was demonstrated by the decrease of the dark cytotoxicity compared to the PS alone. The *in vivo* distribution was studied in FoxN1 nude mice. 24 hours after the injection of the nontargeted and the targeted peptide-NPs in the tumors, the estimated gold amount (ng of Au/gm of wet tissue) was found to be 477.5 ± 128 and 1794.2 ± 505, respectively, while a value of 361.4 ± 78 was recorded in the normal tissue. These outcomes validated the advantage of adding a peptide targeting HER2. 24 hours after the injection, PDT was performed (PDT-1200 set up, 640–720 nm, 120 $J.cm^{-2}$, 200 $mW.cm^{-2}$, 10 minutes). A notable retarding effect on tumor growth was observed with the targeted NP (**Figure 64**) [88].

One year later, the same team synthesized a fourth generation poly(amidoamine) (PAMAM) dendrimer (*i.e.* DPN and ADPN) coupled to the same PS and the same peptide to target HER2. Using confocal microscopy, the authors observed a greater fluorescence with the targeted ADPN dendrimer than with the non-targeted DPN dendrimer in SKOV-3 cells. PDT was performed on SKOV-3 (+) and human breast cancer MCF-7 cells (-) (PDT-1200 set up, 20 $J.cm^{-2}$, 50 mW/cm^2, 6.5 min). The IC_{50} values were 0.175 µM, 0.100 µM and 0.075 µM for the PS, the non-targeted DPN dendrimer and the targeted ADPN dendrimer, respectively. In MCF-7 cells, no difference in the IC_{50} values was detected between the PS and both dendrimers. The *in vivo* 137hototoxicity experiments (PDT-1200 set up, 120 $J.cm^{-2}$, 200 mW/cm^2, 10 min) revealed a delay in the tumor growth when exposed to the non-targeted DPN dendrimer or to the targeted ADPN dendrimer. However, no photodynamic effect was observed in tumors exposed to PBS (untreated) or PS alone. It seemed that grafting the targeted peptide did not enhance the efficacy of PDT [89].

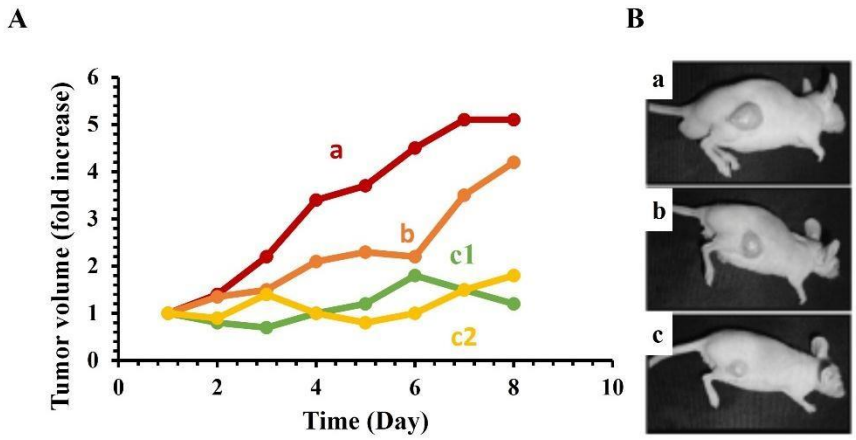

Figure 64 : Tumor growth curve in nude mice. On day 0, PS formulations were injected via tail vein; and on day 1, PDT was conducted. (A) PBS, (B) PS (2µM), (C1) ADPN (2µM of PS), and (C2) ADPN (2µM of PS). Laser irradiation with 640–720 nm (200 mW.cm-2 for 10 min). Adapted from Narsireddy et al.[75]. With permission from Elsevier.

II.5.2 NPs@PS@GE11

GE11 is a dodecapeptide with 12 amino acids (YHWYGYTPQNVI). Its affinity towards EGFR was identified by Li *et al*. GE11 has a lower affinity for EGFR (k_d = 22 nM) than EGF (k_d = 2 nM). It increases the endocytosis of the NPs due to an alternative EGFR-dependent actin-driven pathway. It has been shown that the EGFR level stays constant after the incorporation of GE11, indicating an EGFR recycling process with a prolonged cell receptivity for the circulating GE11 [90]. In 2012, Master *et al.* developed PEG-co-polycaprolactone (PEGPCL) NPs encapsulating phthalocyanine 4 (Pc4) PS and covalently coupled to GE11 peptide ligand to target EGFR overexpressed on many cancer cell lines. For their *in vitro* studies, the authors selected A431 human epidermoid carcinoma cells and MCF-7 human breast cancer cells overexpressing EGFR. After 1 hour and 5 hours of incubation, a better accumulation into A431 (+) cells was observed for the targeted NPs as compared to the untargeted ones. However, no accumulation was witnessed into the MCF-7 (-) cells. This was in favor of the receptor-mediated internalization of the targeted NPs. 24 hours post-incubation, no difference was detected between both NPs. This was due to the processes of passive uptake relying on the EPR effect and the active uptake *via* the EGF receptors. After 200 seconds of light illumination (diode array, 675 nm, 200 mJ.cm^{-2}), it was revealed that the cell viability evolves linearly with the amount of the accumulated NPs. The higher the accumulation, the greater the cell death. In the same year [91], the authors optimized various parameters, *i.e.* the density of the GE11 peptide ligand on the micelle surface, the Pc4 loading and the light dose, in order to enhance the PDT efficiency. They discovered that the micelle formulation should be of 10% mole GE11-modified polymer and 50 µg Pc4 per mg of polymer. In addition, the illumination using the Light-emitting diode array (675 nm, 200 mJ.cm^{-2}) was prolonged to 400 seconds [92].

Table 9 describes the NPs@PS@peptide systems, targeting $\alpha_v\beta_3$ integrin, regarding the types of NPs, PSs and the coupling between them, in addition to the NPs size, excitation

wavelength ($\lambda_{excitation}$), fluorescence quantum yield (ϕ_F), singlet oxygen quantum yield ($\Delta_{O.S}$) and the results obtained *in vitro* and/or *in vivo*.

Table 9 : The summary of NPs conjugated with PSs and human EGFR targeting peptides in terms of different parameters

NPs@PS@Peptide targeting human EGFR											
Reference	NPs	PS	Coupling between NPs	NPs size (nm)	$\lambda_{excitation}$ (nm) and PS	ϕ_F	ΔO.S	*in vitro*		*in vivo*	
HER2 3-340 Peptide											
[89]	Dendrimer (G4)	5, 10, 15, 20 – Tetrakis (4hydroxyphenyl)-21 H,23 H pophine (tHPP)	Amide bond	10	640	nd	nd	SKOV-3		FoxN1 Nude mice	
[88]	Fe_3O_4-ChitosanAu	5,10,15,20-Tetrakis (4hydroxyphenyl)-21*H*,23*H*porphine (tHPP)	Ester bond	35-40 for Fe_3O_4 NPs and 35 for MGPS*	640	nd	nd	SKOV-3		FoxN1 Nude mice	
GE11 Peptide											
[93] [94]		Polyethylene glycol-co-polycaprolactone (PEG-PCL)	Phthalocyanine 4 (Pc4)	Encapsulated	<100 for Pc4 in PEG-PCL micelles		675	nd	nd	A431 MCF-7c3	Nd

*MGPS: Magnetic/gold particles with PS. *nd: not determined

II.6 Peptides targeting vascular endothelial tumor

Tissue transglutaminase (TGM2) is a multifunctional protein that has been found to be a molecular marker of colorectal cancer [94]. It is mainly located in the cytoplasm and is involved in the cell growth and differentiation, remodeling and stabilization of extracellular matrix. TGM2 is overexpressed in different cancers such as ovarian, breast and colon cancers. The GX1 peptide (CGNSNPKSC) is an important new vector for targeting TGM2 and tumor vessels such as colorectal orthotopic vessels [95, 96].

II.6.1 NPs@PS@GX1

In 2017, Guo et *al.* developed new angiogenic vessel-targeting (AVT) NPs as delivery vehicles for a hypoxia-activated bioreductive prodrug (Tirapazamine, TPZ). The AVT NPs were formed by the self-assembly of a TPC-GX1 conjugate. This conjugate was composed of the TPC PS (5-(4-carboxyphenyl)-10, 15,20-tris(3-hydroxyphenyl)chlorin) covalently linked to an angiogenic vessel-targeting cyclopeptide GX1. The elaborated NPs had an average hydrodynamic size of about 109 nm. TPZ was then loaded on the AVT-NPs, at a capacity of 11.08%. The synthesized AVT-NP/TPZ system was designed for application in the chemo-photo synergistic cancer therapy. TPC-PEG micelles and chemotherapeutic cisplatin were used to track the distribution of the AVT-NPs and to demonstrate their targeting capability. The *in vitro* studies were performed on MCF-7, 3T3 and HUVEC cells. As for the *in vivo* assays, they were conducted on MCF7 and MDA-MB-231 xenograft mouse models. After exposure to the He-Ne laser irradiation (650 nm, 1.2 $W.cm^{-2}$, 10 min), TPC, in the AVT-NP/TPZ system, interacted with the molecular oxygen to produce $^1O_2$ that initiated firstly the cancer cell killing by PDT. The PDT induced hypoxia triggered a promoted angiogenesis, thus resulting in an enhanced targeted delivery of the NPs specifically to the tumor site, in addition to the activation of the bioreductive prodrug TPZ, that in its turn generate highly cytotoxic free radicals for a combinational chemophototherapy (**Figure 65**). This work showed the great potential of using hypoxia-induced enhancement of angiogenesis to mediate a specific accumulation of the NPs at the tumor site and initiate a chemo-photo combinational treatment [97].

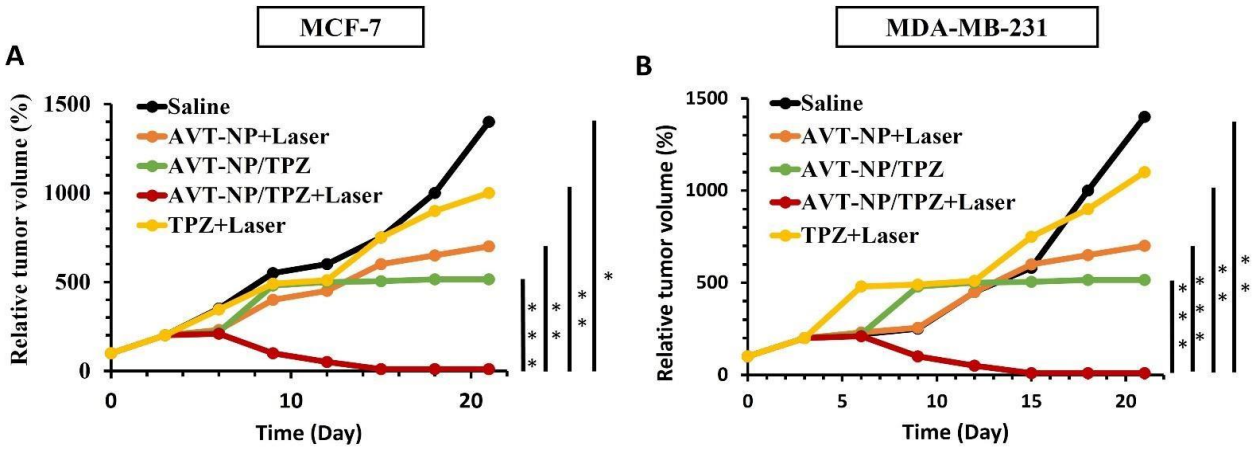

Figure 65 : MCF-7 tumor (A) and MDA-MB-231 (B) growth curves after intravenous injection of different drug formulations (0.1 mg/Kg; Ps/body weight). Error bars indicate standars deviation (n=5) *P<0.05, **P<0.01, ***P<0.001 (two-tailed Student's-test). He-Ne laser irradiation (650 nm, 1.2 W/cm^2 for 10 min). Adapted from Guo et al. [83].

Table 10 describes the NPs@PS@peptide systems, targeting $\alpha_v\beta_3$ integrin, regarding the types of NPs, PSs and the coupling between them, in addition to the NPs size, excitation wavelength ($\lambda_{excitation}$), fluorescence quantum yield (ϕ_F), singlet oxygen quantum yield ($\Delta_{O.S}$) and the results obtained *in vitro* and/or *in vivo*.

Table 10 : The summary of NPs conjugated with PSs peptides targeting tumor vasculature endothelium in terms of different parameters

NPs@PS@Peptide targeting tumor vasculature endothelium									
Reference	NPs	PS	Coupling between NPs and PS	NPs size (nm)	λexcitation (nm)	ϕ_F	ΔO.S	*in vitro*	*in vivo*
GX1 cyclopeptide									
[97]	Self-assembly of TPC/GX1-TPZ	5-(4-Carboxyphenyl)-10, 15,20-tris(3hydroxyphenyl)chlorin (TPC)	Self-assembly	109 for AVT-NP/TPZ	650	nd	nd	MCF-7, 3T3 HUVEC	MCF-7 and MDA-MB-231 xenograft mice models

**nd: not determined*

II.7 Peptide targeting p32

The p32 protein is a trimer with three homologous subunits [98]. It is a mitochondrial matrix protein in normal tissues, but it can also be detected on the cell surface, nucleus and endoplasmic reticulum. p32 is overexpressed on the cell membrane of certain human cancers making it a useful target in tumor diagnosis and therapy.

α-Helix p32 is a stick-shaped peptide expressed in the main cancer types. The coupling of α-helix p32 with anticancer drugs plays a rigorous role in targeting more than 50% of human cancers [99, 100].

II.7.1 NPs@PS@α-helix p32 membrane

In 2015, Zhang *et al.* described a new approach, called conformational epitope imprinting, to develop new targeted nanocarriers using the three-dimensional conformation of an epitope, rather than its linear structure, for the specific recognition of p32 membrane protein. To achieve this goal, the authors produced the HAPPE peptide (*i.e.* hybrid apamin-p32 polypeptide). It consisted of a disulfide-linked α-helixcontaining peptide, *i.e.* apamin, that mimics the extracellular structured *N*-terminal region of the p32 membrane protein, where seven residues were replaced by topologically equivalent ones from p32. For epitope imprinting, they designed molecularly imprinted polymeric NPs (MIPNPs), possessing selective cavities for the specific recognition of p32 membrane protein, using the HAPPE peptide as template. MIPNPs had a particle size of 37 nm. Non-imprinted polymeric NPs (NIPNPs), using a linear analogue of HAPPE peptide (*i.e.* four cysteines of apamin were replaced by alanines), were also synthesized to demonstrate the specific recognition. Compared to NIPNPs, a strong binding interaction of the MIPNPs with p32 was observed. A fluorescence probe, 6-aminofluorescein (FAM), was encapsulated into MIPNPs and NIPNPs. The uptake of both NPs by p32-positive cancer cells, namely 4T1 murine breast cancer and BxPC-3 human pancreatic cancer cells, was assessed by flow cytometric measurement. MIPNPs displayed a greater cellular uptake as compared to NIPNPs. The *in vivo* biodistribution of MIPNPs and NIPNPs, both encapsulating a near-infrared fluorophore (IR-783 dye), was also studied using 4T1-tumor-bearing mice. A higher accumulation in tumors was presented by MIPNPs. The pre-injection of Lyp-1 peptide, known to bind specifically to the *N*-terminal region of p32, significantly reduced this accumulation. This result confirmed that MIPNPs specifically bound to the targeted p32 protein. The *in vivo* antitumor effect of methylene blue (MB)-loaded NPs (MIPNPs and NIPNPs) was evaluated using laser light irradiation at 650 nm (800 $mW.cm^{-2}$, 10 min). It was demonstrated that the MB-loaded MIPNPs exhibited an efficient targeted photodynamic therapy (**Figure 66**) [101].

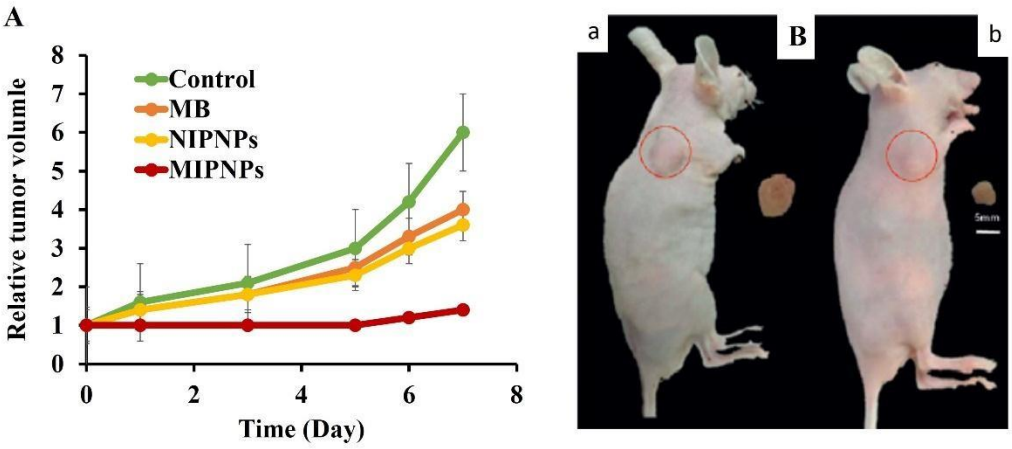

Figure 66 : (A) In vivo antitumor effect of PDT on 4T1-tumor bearing mice performed using distinct NP formulations. All injections were performed once at t=0, MIPNPs (1 mg/mL) loaded with the photosensitizer methylene blue (MB, 3 µm). Tumor volumes were measured every other day for one week. (B) Images of mice treated with (a) NIPNPs and (b) MIPNPs. Scale bar = 5mm. 650 nm laser light irradiation, 800 $mW.cm^{-2}$, 10 min. Adapted from Zhang et al. [87]. With permission from John Wiley and Sons.

Table 11 describes the NPs@PS@peptide systems, targeting $\alpha_v\beta_3$ integrin, regarding the types of NPs, PSs and the coupling between them, in addition to the NPs size, excitation wavelength ($\lambda_{excitation}$), fluorescence quantum yield (ϕ_F), singlet oxygen quantum yield ($\Delta_{O.S}$) and the results obtained *in vitro* and/or *in vivo*.

Table 11 : The summary of NPs conjugated with PSs and peptides targeting tumor suppressor protein p32 in terms of different parameters

NPs@PS@Peptide targeting tumor suppressor protein p32									
Reference	NPs	PS	Coupling NPs size (nm) and PS	NPs $\lambda_{excitation}$ between (nm)		ϕ_F	ΔO.S	*in vitro*	*in vivo*
α-helix containing peptide, apamin									
[101]	Molecularly imprinted polymeric (MIPNPs)	Methylene blue (MB)	Encapsulated	37 for MIPNPs	650	nd	nd	4T1 BxPC-3	4T1-Tumorbearing mice

**nd: not determined*

II.8 Peptide to target transferrin

Transferrin receptor (TfR) is also considered an attractive receptor for the targeted therapy since it is overexpressed on the surface of many cancer cells [102] and it is mostly expressed in epithelial cells. It is used to transfer iron from the liver to the bone marrow for incorporation into hemoglobin within red blood cells and distribution throughout the body [103]. Subsequently, the survival of human cells compels the body to manufacture transferrin. This emphasizes the importance of coupling transferrin to the NPs to improve the selectivity of PDT [104].

II.8.1 NPs@PS@transferrin

In 2017, Zhang and co-workers designed enzyme- and pH-responsive nanocarriers (UCNP@$mSiO_2$-Ce6) with a size of 75 nm. These nanocarriers consisted of an UCNP ($NaYF_4$:Yb,Er@$NaYF_4$) core embedded in a mesoporous silica shell ($mSiO_2$) doped with Ce6 PS. They were then surface-functionalized with transferrin (Tf) for targeting TfR overexpressed in tumor cells. In addition, Dox chemodrug was further loaded on the NPs, with an efficiency of about 4%, through a succinic acid-peptide linker (succinic acid-Gly-Phe-Leu-Gly, SGFLG linker). This linker established the pH- and enzyme-triggered drug release of Dox. The resulted enzyme/pH-responsive multifunctional nanocomposite (UCNP@$mSiO_2$/Ce6-Dox-SGFLG-Tf) was developed for application in synergistic PDT and chemotherapy. After the endocytic uptake of the nanocomposite into the tumor cells by pinocytosis or phagocytosis, various steps took place. First of all, the pH- and enzyme-triggered Dox release occurred due to the high concentration of cathepsin B and the low pH condition, thus illustrating a chemotherapeutic effect. Secondly, a 5 min NIR irradiation of UCNPs (980 nm, 0.5 $W.cm^{-2}$) led to a visible-light emission, which enabled the efficient excitation of Ce6 and the further generation of ROS, illustrating a photodynamic effect. The enzyme- and pH-dependent Dox release from UCNP@$mSiO_2$/Ce6-Dox-SGFLG-Tf was estimated in PBS using different parameters. With the pH fixed at 6.8, better values were obtained at high cathepsin concentration, for example 60.17% of Dox were released at 2 x 10^{-7} mol/L. By testing various pH conditions, from 1.2 to 6.8, better values were obtained at low pH, for instance 78.36% of Dox was released at pH 1.2. The *in vitro* cell viability assays were carried out on cancerous HeLa cells and L02 normal human liver cells. These tests demonstrated a synergistic PDT and chemotherapeutic effect under NIR irradiation. This effect was more drastic using UCNP@$mSiO_2$/Ce6-Dox-SGFLG-Tf nanocomposite and NIR irradiation (980 nm, 0.5 $W.cm^{-2}$, 15 min) leading to a HeLa cell viability of 33% (**Figure 67)** [105].

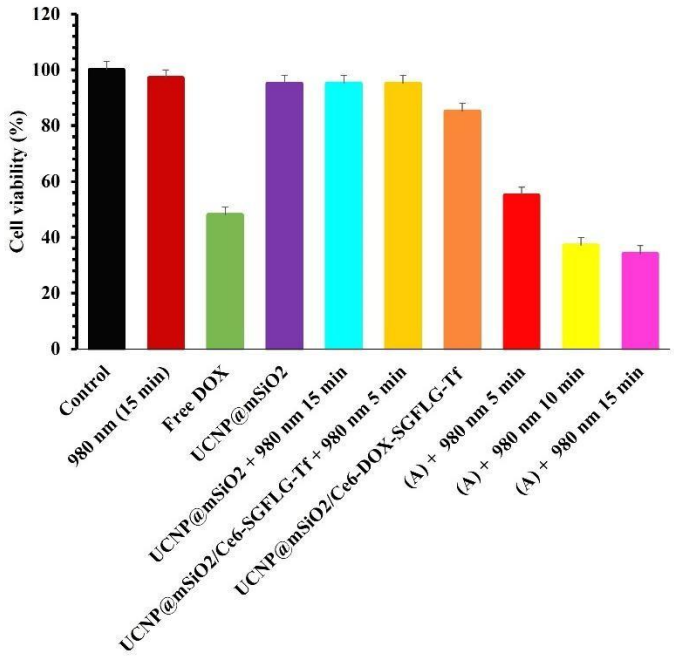

Figure 67 : Cell viability of HeLa cells under pure NIR, or incubated with free Dox (equal Dox concentration with NPs), UCNP@mSiO2, UCNP@mSiO₂/Ce6-SGFLG-Tf, and UCNP@mSiO2/Ce6-Dox-SGFLG-Tf without and with 5, 10 or 15 min NIR irradiation (980 nm, 0.5 W.cm^{-2}). Adapted from Zhang et al. [91]. With permission from Elsevier.

Table 12 describes the NPs@PS@peptide systems, targeting $\alpha_v\beta_3$ integrin, regarding the types of NPs, PSs and the coupling between them, in addition to the NPs size, excitation wavelength ($\lambda_{excitation}$), fluorescence quantum yield (ϕ_F), singlet oxygen quantum yield ($\Delta_{O.S}$) and the results obtained *in vitro* and/or *in vivo*.

Table 12 : The summary of NPs conjugated with PSs and peptides targeting blood brain barrier in terms of different parameters

NPs@PS@Peptide targeting blood brain barrier									
Reference	NPs	PS	Coupling between NPs and PS	NPs size (nm)	λexcitation (nm)	ϕ_F	ΔO.S	*in vitro*	*in vivo*
Transferrin									
[105]	Upconversion ($NaYF_4$:Yb,Er@$NaYF_4$)	Chlorin e6 (Ce6)	Mesoporous silica ($mSiO_2$)-Ce6 coating	75 for UCNP@$mSiO_2$/Ce6 NPs	980	nd	nd	HeLa L02	nd

**nd: not determined*

II.9 Peptide to target PD-1

Programmed death-1 (PD-1) is a cell surface molecule that regulates the adaptive immune response [106]. The engagement of PD-1 by its PD-L1 or PD-L2 ligands transduces a signal that inhibits T cell proliferation, cytokine production and cytolytic function. T lymphocytes are white blood cells that are specialized in certain immune reactions. It helps fight infections and destroy abnormal cells, including cancer cells.

II.9.1 NPs@PS@PD-L1

In 2020, *B. Liu et al*. described the development of multifunctional PEG-coated gold nanoprisms (GNPs) incorporating Ce6 PS and coupled to PD-L1 targeting peptide [97]. These NPs were designed for enhanced imaging and PTT/PDT applications. Using NIR and photoacoustic imaging, the authors proved that the NPs presented a high affinity for PD-L1 receptors both in vivo and ex vivo in the main organs and tissues. They also showed a synergetic PDT and PTT effect leading to the inhibition of the tumor growth in vivo.

Table 13 describes the NPs@PS@peptide systems, targeting PD-1, regarding the types of NPs, PSs and the coupling between them, in addition to the NPs size, excitation wavelength (λexcitation), fluorescence quantum yield (ϕF), singlet oxygen quantum yield (ΔO.S) and the results obtained in vitro and/or in vivo.

Table 13 : The summary of NPs conjugated with PSs and peptides targeting PD-1 in terms of different parameters

			Peptide						
NPs@PS@Peptide targeting PD-1 expressed on T cells									
Reference	NPs	PS	Coupling between NPs and PS	NPs size (nm)	λexcitation (nm)	ϕF	ΔO.S	*in vitro*	*in vivo*
				PD-1					
[107]	Gold NPsCe6	Mesoporous silica (mSiO2)-Ce6 coating	75 nm	980	nd	nd		Human Lung cancer HCC827	Nude mice

**nd: not determined*

II.10 Bioactive peptide targeting many cancer types

Bioactive peptides are short protein fragments of 2- 20 amino acids [108]. These peptides have revealed the ability to overcome cell membranes and cause cell death [109]. Since then, bioactive peptides have been used to target tumor cells in general [108]. Some researchers cited that coupling a bioactive targeting peptide can target plasma membrane and mitochondria.

II.10.1 NPs@PS@bioactive peptide

In 2019, Cheng *et al.* described the synthesis of a chimeric peptide that consisted of a hydrophobic PpIX PS conjugated, *via* a lysine linker, to a bioactive peptide (rFxrFxrFxr, r and Fx stand for D-arginine and L-cyclohexylalanine, respectively). Hydrophilic PEG_8 chain were also attached at the *C*-terminal extremity of the peptide. This amphipathic chimeric peptide self-assembled into spherical micelles in aqueous media, affording M-ChiP of a hydrodynamic size of about 167.9 nm. M-ChiP was used for mitochondria and plasma membrane dual-targeted PDT. The goal of this strategy was to have a M-ChiP insertion into the plasma membrane of tumor cells inducing its rupture via $^1O_2$ generation upon laser irradiation. The membrane rupture resulted in an enhanced membrane permeability, leading to endocytosis and mitochondria targeted delivery of M-ChiP, then to mitochondria destruction by the $^1O_2$ generated upon laser irradiation. The *in vitro* antitumor PDT efficacy of M-ChiP was carried out on murine mammary carcinoma 4T1 and African green monkey kidney COS7 cells using 630 nm LED light (29.8 $mW.cm^{-2}$, 20 or 30 s). This study showed negligible cytotoxicity and obvious phototoxicity on 4T1 and COS7 cells in a concentration-dependent manner where less than 10-15% of the cells remained viable at 20 $mg.L^{-1}$. The *in vivo* antitumor photodynamic efficiency was conducted in 4T1 tumor-bearing mouse using 630 nm He-Ne laser (250 $mW.cm^{-2}$, 10 min). This study revealed that M-ChiP had a remarkable tumor suppression effect upon laser irradiation (**Figure 68**) [110].

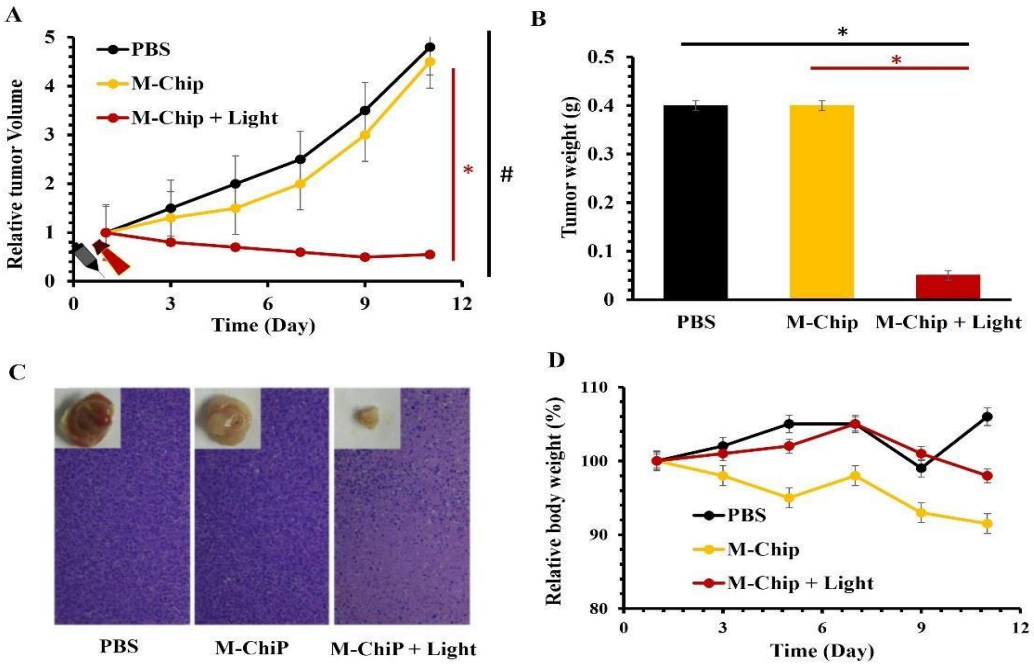

Figure 68 : Antitumor study of M-Chip. (A) The relative tumor volume changes after treatment with PBS, M-Chip (200 µL, 1.2 mg.mL^{-1}) and laser irradiation (150 J.cm^{-2}, 250 mW.cm^{-2} for 10 min). (B) The corresponding average tumor weight and (C) the scarified tumor images and HE staining analysis of tumor tissues after various treatments at the 11th day. (D) The relative body of the mice after various treatments in 11 days. Adapted from Cheng et al. [94].

Table 14 describes the NPs@PS@peptide systems, targeting $\alpha_v\beta_3$ integrin, regarding the types of NPs, PSs and the coupling between them, in addition to the NPs size, excitation wavelength ($\lambda_{excitation}$), fluorescence quantum yield (ϕ_F), singlet oxygen quantum yield ($\Delta_{O.S}$) and the results obtained *in vitro* and/or *in vivo*.

Table 14 : The summary of NPs conjugated with PSs and peptides targeting human muscular nicotinic acetylcholine receptors in terms of different parameters

NPs@PS@Peptide targeting human muscular nicotinic acetylcholine receptors									
Reference	NPs	PS	Coupling between NPs and PS	NPs size (nm)	$\lambda_{excitation}$ (nm)	ϕ_F	ΔO.S	*in vitro*	*in vivo*
Bioactive peptide									
[110]	Spherical micelles chimeric peptide (M-ChiP)	Photoporphyrin IX (PpIX)	Amide bond	167.9 for M-ChiP	630	nd	nd	4T1 COS7	4T1 Tumorbearing mouse

**nd: not determine*

III. Conclusion

The coupling of the peptides to the NPs enabled an important double targeting in PDT. The performed researches showed very encouraging results. The phototoxicity studies of these NPs confirmed their efficiency. In addition, the *in vivo* results presented a remarkable tumor regression and growth inhibition. NPs@PS@Peptide were considered the best candidates for PDT, since each peptide vector targeted specific tumor cells allowing better accumulation and, consequently, a superior photodynamic effect. Among these bioactive peptides, research results validated the effectiveness of the cell-penetrating peptides, such as TAT, that facilitated the penetration of the NPs into the cells. The *in vitro* and *in vivo* tests confirmed that the peptides DKPPR, ATWLPPR, CRGDK and tLyp-1 targeted NRP-1 receptor, which has been evaluated in the whole sections of 65 primary breast carcinomas, 95 primary colorectal adenocarcinomas, 90 primary lung carcinomas, 59 additional human metastases, and 16 xenografts. NRP-1 immunoreactivity had been observed in normal tissue vessels adjacent to the cancer cells and in 98-100% of carcinomas. The expression of NRP-1 in tumor cells was also observed in 36% of primary lung carcinomas and 6% of primary mammary carcinomas, but not in the colorectal adenocarcinoma. NRP-1 was also evaluated in mouse embryos, where their expression was limited to the nervous system, endocardium, vascular smooth muscle and in endothelium on subsets of vessels. Other peptides such as RGD, iRGD, cRGD, c(RGDyK), RGD-4R, RGDfK and fibronectin (Fmp), validated, by *in vitro* and *in vivo* tests, their ability to target $\alpha_v\beta_3$ integrins that are strongly expressed in normal mammary epithelium and in other primary invasive breast carcinomas. This integrin heterodimer was also abundant in all the breast cancer and the metastatic bone cancer cells. The *in situ* hybridization revealed high levels of mRNA at steady state corresponding to the protein expression sites. In addition to NRP-1 and $\alpha_v\beta_3$ integrins, transferrin was also a receptor of interest in the targeted PDT. Transferrin (TfR) is a receptor found on the blood brain barrier (BBB). Regarding the high selective permeability imposed by BBB, the photodynamic therapy with NPs@PS@transferrin allowed the penetration of transferrin protein, thus overcoming the difficulty of treating central nervous system (CNS) diseases by standard drugs such as chemotherapy. Coupling transferrin to the nanoparticles (NPs@PS@transferrin) enabled a superior and selective accumulation. This accumulation was confirmed by the fluorescence of the PS. On this basis, the Transferrin peptide targeted successfully the brain and blood cancers. Moreover, the efficiency of targeting by α-helix p32 peptide was also assessed. This peptide targeted all the tumors overexpressing p32 protein. In addition, the efficacy of F3 Peptide to target tissue factor F3 was confirmed. This factor is responsible for activating blood clotting and is expressed in most solid tumors. Other research efforts had also verified that GX1 peptide targeted the human gastric cancer (GC) vasculature by generally binding to the endothelial cells. The overexpression of EGFR contributes to the malignant transformation of human epithelial cells indicating gene mutations. It is mostly expressed in breast cancer. Various studies validated that the peptides GX1, HER2 3-340, GE11 are important vectors for

targeting EGFR due to the overexpression of tissue transglutaminase (TGM2). TGM2 is a multifunctional protein located in the cytoplasm which has been shown to be a molecular marker of colorectal cancer.

References

[1] A. l. Doerflinger, "Design and synthesis of polymerized micelles for the diagnosis and therapy of tumours," Université Paris-Saclay, 2017.

[2] M. S. Rajagopalan, D. E. Heron, R. E. Wegner, H. J. Zeh, N. Bahary, A. M. Krasinskas, *et al.*, "Pathologic response with neoadjuvant chemotherapy and stereotactic body radiotherapy for borderline resectable and locallyadvanced pancreatic cancer," *Radiat Oncol,* vol. 8, p. 254, Oct 31 2013.

[3] M. A. Bellavance, M. Blanchette, and D. Fortin, "Recent advances in blood-brain barrier disruption as a CNS delivery strategy," *Aaps j,* vol. 10, pp. 166-77, 2008.

[4] A. F. dos Santos, D. R. Q. de Almeida, L. F. Terra, M. S. Baptista, and L. Labriola, "Photodynamic therapy in cancer treatment - an update review," *Journal of Cancer Metastasis and Treatment,* vol. 5, p. 25, 2019.

[5] R.-M. Szeimies, J. Dräger, C. Abels, and M. Landthaler, "Chapter 1 History of photodynamic therapy in dermatology," in *Comprehensive Series in Photosciences*. vol. 2, P. Calzavara-Pinton, R.-M. Szeimies, and B. Ortel, Eds., ed: Elsevier, 2001, pp. 3-15, Amsterdam.

[6] C. Frochot, M. Barberi-Heyob, M. Blanchard-Desce, L. Bolotine, S. Bonneau, M. Chiara, *et al.*, "La thérapie photodynamique : état de l'art et perspectives," *L'Actualité Chimique,* pp. 46-50, 2015-06 2015.

[7] P. D. Silva, M. A. Saad, H. C. Thomsen, S. Bano, S. Ashraf, and T. Hasan, "Photodynamic therapy, priming and optical imaging: Potential co-conspirators in treatment design and optimization — a Thomas Dougherty Award for Excellence in PDT paper," *Journal of Porphyrins and Phthalocyanines,* vol. 24, pp. 1320-1360, 2020.

[8] D. Kessel and N. L. Oleinick, "Cell Death Pathways Associated with Photodynamic Therapy: An Update," *Photochem Photobiol,* vol. 94, pp. 213-218, Mar 2018.

[9] T. J. Dougherty, J. E. Kaufman, A. Goldfarb, K. R. Weishaupt, D. Boyle, and A. Mittleman, "Photoradiation therapy for the treatment of malignant tumors," *Cancer Res,* vol. 38, pp. 2628-35, Aug 1978.

[10] R. R. Allison and K. Moghissi, "Photodynamic Therapy (PDT): PDT Mechanisms," *Clin Endosc,* vol. 46, pp. 24-9, Jan 2013.

[11] S. B. Brown, E. A. Brown, and I. Walker, "The present and future role of photodynamic therapy in cancer treatment," *Lancet Oncol,* vol. 5, pp. 497-508, Aug 2004.

[12] M. Lan, S. Zhao, W. Liu, C.-S. Lee, W. Zhang, and P. Wang, "Photosensitizers for Photodynamic Therapy," *Advanced Healthcare Materials,* vol. 8, p. 1900132, 2019.

[13] X. Dai, T. Du, and K. Han, "Engineering Nanoparticles for Optimized Photodynamic Therapy," *ACS Biomaterials Science & Engineering*, vol. 5, pp. 6342-6354, 2019/12/09 2019.

[14] L. Larue, A. Ben Mihoub, Z. Youssef, L. Colombeau, S. Acherar, J. C. André, *et al.*, "Using X-rays in photodynamic therapy: an overview," *Photochem Photobiol Sci*, vol. 17, pp. 1612-1650, Nov 1 2018.

[15] B. Sun, R. Chang, S. Cao, C. Yuan, L. Zhao, H. Yang, *et al.*, "Acid-Activatable Transmorphic Peptide-Based Nanomaterials for Photodynamic Therapy," *Angewandte Chemie International Edition*, vol. 59, pp. 2058220588, 2020.

[16] H. Azaïs, C. Schmitt, M. Tardivel, O. Kerdraon, A. Stallivieri, C. Frochot, *et al.*, "Assessment of the specificity of a new folate-targeted photosensitizer for peritoneal metastasis of epithelial ovarian cancer to enable intraperitoneal photodynamic therapy. A preclinical study," *Photodiagnosis Photodyn Ther*, vol. 13, pp. 130138, Mar 2016.

[17] A. M. Gazzali, M. Lobry, L. Colombeau, S. Acherar, H. Azaïs, S. Mordon, *et al.*, "Stability of folic acid under several parameters," *Eur J Pharm Sci*, vol. 93, pp. 419-30, Oct 10 2016.

[18] W. M. Sharman, J. E. van Lier, and C. M. Allen, "Targeted photodynamic therapy via receptor mediated delivery systems," *Adv Drug Deliv Rev*, vol. 56, pp. 53-76, Jan 13 2004.

[19] D. Zahavi and L. Weiner, "Monoclonal Antibodies in Cancer Therapy," *Antibodies (Basel, Switzerland)*, vol. 9, p. 34, 2020.

[20] O. H. Aina, T. C. Sroka, M.-L. Chen, and K. S. Lam, "Therapeutic cancer targeting peptides," *Biopolymers*, vol. 66, pp. 184-199, 2002 2002.

[21] S. Li, Y. Jin, Y. Su, W. Li, Y. Xing, F. Wang, *et al.*, "Anti-HER2 Affibody-Conjugated Photosensitizer for Tumor Targeting Photodynamic Therapy," *Mol Pharm*, vol. 17, pp. 1546-1557, May 4 2020.

[22] J. Yan, T. Gao, Z. Lu, J. Yin, Y. Zhang, and R. Pei, "Aptamer-Targeted Photodynamic Platforms for Tumor Therapy," *ACS Appl Mater Interfaces*, vol. 13, pp. 27749-27773, Jun 23 2021.

[23] R. Schneider, L. Tirand, C. Frochot, R. Vanderesse, N. Thomas, J. Gravier, *et al.*, "Recent improvements in the use of synthetic peptides for a selective photodynamic therapy," *Anticancer Agents Med Chem*, vol. 6, pp. 46988, Sep 2006.

[24] R. Mehdi, A. Mary, and A. M. Shaker, "Peptide-Conjugated Nanoparticles as Targeted Anti-angiogenesis Therapeutic and Diagnostic in Cancer," *Current Medicinal Chemistry*, vol. 26, pp. 5664-5683, 2019.

[25] G. Graziani and P. M. Lacal, "Neuropilin-1 as Therapeutic Target for Malignant Melanoma," *Front Oncol*, vol. 5, p. 125, 2015.

[26] S. Sun, Y. Lei, Q. Li, Y. Wu, L. Zhang, P.-P. Mu, *et al.*, "Neuropilin-1 is a glial cell line-derived neurotrophic factor receptor in glioblastoma," *Oncotarget*, vol. 8, pp. 74019-74035, 2017.

[27] P. Hamerlik, J. D. Lathia, R. Rasmussen, Q. Wu, J. Bartkova, M. Lee, *et al.*, "Autocrine VEGF-VEGFR2-Neuropilin1 signaling promotes glioma stem-like cell viability and tumor growth," *J Exp Med,* vol. 209, pp. 507-20, Mar 12 2012.

[28] A. Starzec, P. Ladam, R. Vassy, S. Badache, N. Bouchemal, A. Navaza, *et al.*, "Structure-function analysis of the antiangiogenic ATWLPPR peptide inhibiting VEGF(165) binding to neuropilin-1 and molecular dynamics simulations of the ATWLPPR/neuropilin-1 complex," *Peptides,* vol. 28, pp. 2397-402, Dec 2007.

[29] E. Kamarulzaman, H. Benachour, M. barberi-heyob, C. l. Frochot, H. Wahab, F. o. Guillemin, *et al.*, "VascularTargeted Photodynamic Therapy (VTP)," ed, 2011.

[30] C. L. Thomas, E. M. Bayer, C. Ritzenthaler, L. Fernandez-Calvino, and A. J. Maule, "Specific Targeting of a Plasmodesmal Protein Affecting Cell-to-Cell Communication," *PLOS Biology,* vol. 6, p. e7, 2008.

[31] H. Benachour, A. Sève, T. Bastogne, C. Frochot, R. Vanderesse, J. Jasniewski, *et al.*, "Multifunctional PeptideConjugated Hybrid Silica Nanoparticles for Photodynamic Therapy and MRI," *Theranostics,* vol. 2, pp. 889-904, 09/29 2012.

[32] D. Bechet, F. Auger, P. Couleaud, E. Marty, L. Ravasi, N. Durieux, *et al.*, "Multifunctional ultrasmall nanoplatforms for vascular-targeted interstitial photodynamic therapy of brain tumors guided by real-time MRI," *Nanomedicine,* vol. 11, pp. 657-70, Apr 2015.

[33] P. Couleaud, D. Bechet, R. Vanderesse, M. barberi-heyob, A.-C. Faure, S. Roux, *et al.*, "Functionalized silicabased nanoparticles for photodynamic therapy," *Nanomedicine (London, England),* vol. 6, pp. 995-1009, 07/04 2011.

[34] E. E. Kamarulzaman, R. Vanderesse, A. M. Gazzali, M. Barberi-Heyob, C. Boura, C. Frochot, *et al.*, "Molecular modelling, synthesis and biological evaluation of peptide inhibitors as anti-angiogenic agent targeting Neuropilin-1 for anticancer application," *Journal of Biomolecular Structure and Dynamics,* vol. 35, pp. 26-45, 2017-01 2017.

[35] E. Kamarulzaman, R. Vanderesse, A. Gazzali, M. barberi-heyob, C. Boura, C. Frochot, *et al.*, "Molecular modelling, synthesis and biological evaluation of peptide inhibitors as anti-angiogenic agent targeting Neuropilin-1 for anticancer application," *Journal of biomolecular structure & dynamics,* vol. 35, pp. 1-49, 01/14 2016.

[36] L. Tirand, C. Frochot, R. Vanderesse, N. Thomas, E. Trinquet, S. Pinel, *et al.*, "A peptide competing with VEGF165 binding on neuropilin-1 mediates targeting of a chlorin-type photosensitizer and potentiates its photodynamic activity in human endothelial cells," *J Control Release,* vol. 111, pp. 153-64, Mar 10 2006.

[37] Z. Youssef, N. Yesmurzayeva, L. Larue, V. Jouan-Hureaux, L. Colombeau, P. Arnoux, *et al.*, "New targeted gold nanorods for the treatment of glioblastoma by photodynamic therapy," *Journal of Clinical Medicine,* vol. 8, p. 2205, 2019-12 2019.

[38] E. Thomas, L. Colombeau, M. Gries, T. Peterlini, C. Mathieu, N. Thomas, *et al.*, "Ultrasmall AGuIX theranostic nanoparticles for vascular-targeted interstitial photodynamic therapy of glioblastoma," *Int J Nanomedicine,* vol. 12, pp. 7075-7088, 2017.

[39] M. Gries, N. Thomas, J. Daouk, P. Rocchi, L. Choulier, J. Jubréaux, *et al.*, "Multiscale Selectivity and in vivo Biodistribution of NRP-1-Targeted Theranostic AGuIX Nanoparticles for PDT of Glioblastoma," *Int J Nanomedicine*, vol. 15, pp. 8739-8758, 2020.

[40] L. Sancey, S. Kotb, C. Truillet, F. Appaix, A. Marais, E. Thomas, *et al.*, "Long-Term in Vivo Clearance of Gadolinium-Based AGuIX Nanoparticles and Their Biocompatibility after Systemic Injection," *ACS Nano*, vol. 9, pp. 2477-2488, 2015/03/24 2015.

[41] O. Leduc, E. Fumière, S. Banse, C. Vandervorst, A. Clément, T. Parijs, *et al.*, "Identification and description of the axillary web syndrome (AWS) by clinical signs, MRI and US imaging," *Lymphology*, vol. 47, pp. 164-76, Dec 2014.

[42] L. Sancey, F. Lux, S. Kotb, S. Roux, S. Dufort, A. Bianchi, *et al.*, "The use of theranostic gadolinium-based nanoprobes to improve radiotherapy efficacy," *Br J Radiol*, vol. 87, p. 20140134, Sep 2014.

[43] C. C. Hsu, T. W. Watkins, G. N. Kwan, and E. M. Haacke, "Susceptibility-Weighted Imaging of Glioma: Update on Current Imaging Status and Future Directions," *J Neuroimaging*, vol. 26, pp. 383-90, Jul 2016.

[44] D. Schwarz, M. Bendszus, and M. O. Breckwoldt, "Clinical Value of Susceptibility Weighted Imaging of Brain Metastases," *Frontiers in Neurology*, vol. 11, 2020-February-04 2020.

[45] C. Zhao, Y. Tong, X. Li, L. Shao, L. Chen, J. Lu, *et al.*, "Photosensitive Nanoparticles Combining VascularIndependent Intratumor Distribution and On-Demand Oxygen-Depot Delivery for Enhanced Cancer Photodynamic Therapy," *Small*, vol. 14, p. e1703045, Mar 2018.

[46] D. Jiang, X. Gao, T. Kang, X. Feng, J. Yao, M. Yang, *et al.*, "Actively targeting d-α-tocopheryl polyethylene glycol 1000 succinate-poly(lactic acid) nanoparticles as vesicles for chemo-photodynamic combination therapy of doxorubicin-resistant breast cancer," *Nanoscale*, vol. 8, pp. 3100-3118, 2016.

[47] H. Benachour, T. Bastogne, M. Toussaint, Y. Chemli, A. Sève, C. Frochot, et al., "Real-time monitoring of photocytotoxicity in nanoparticles-based photodynamic therapy: a model-based approach," PLoS One, vol. 7, p. e48617, 2012.

[48] C. Frochot, B. Di Stasio, R. Vanderesse, M. J. Belgy, M. Dodeller, F. Guillemin, *et al.*, "Interest of RGD-containing linear or cyclic peptide targeted tetraphenylchlorin as novel photosensitizers for selective photodynamic activity," *Bioorg Chem*, vol. 35, pp. 205-20, Jun 2007.

[49] H. Wang, C. Dong, P. Zhao, S. Wang, Z. Liu, and J. Chang, "Lipid coated upconverting nanoparticles as NIR remote controlled transducer for simultaneous photodynamic therapy and cell imaging," *Int J Pharm*, vol. 466, pp. 307-13, May 15 2014.

[50] F. Yuan, J.-L. Li, H. Cheng, X. Zeng, and X.-Z. Zhang, "A redox-responsive mesoporous silica based nanoplatform for in vitro tumor-specific fluorescence imaging and enhanced photodynamic therapy," *Biomaterials Science,* vol. 6, pp. 96-100, 2018.

[51] B. Hou, B. Zheng, W. Yang, C. Dong, H. Wang, and J. Chang, "Construction of near infrared light triggered nanodumbbell for cancer photodynamic therapy," *Journal of Colloid and Interface Science,* vol. 494, pp. 363372, 2017/05/15/ 2017.

[52] Y. Zhao, F. Li, C. Mao, and X. Ming, "Multiarm Nanoconjugates for Cancer Cell-Targeted Delivery of Photosensitizers," *Molecular pharmaceutics,* vol. 15, pp. 2559-2569, 2018.

[53] A. Yuan, B. Yang, J. Wu, Y. Hu, and X. Ming, "Dendritic nanoconjugates of photosensitizer for targeted photodynamic therapy," *Acta Biomater,* vol. 21, pp. 63-73, Jul 2015.

[54] S. K. Kim, J. M. Lee, K. T. Oh, and E. S. Lee, "Extremely small-sized globular poly(ethylene glycol)-cyclic RGD conjugates targeting integrin α(v)β(3) in tumor cells," *Int J Pharm,* vol. 528, pp. 1-7, Aug 7 2017.

[55] S. Shi, L. Zhang, M. Zhu, G. Wan, C. Li, J. Zhang, *et al.*, "Reactive Oxygen Species-Responsive Nanoparticles Based on PEGlated Prodrug for Targeted Treatment of Oral Tongue Squamous Cell Carcinoma by Combining Photodynamic Therapy and Chemotherapy," *ACS Applied Materials & Interfaces,* vol. 10, pp. 29260-29272, 2018/09/05 2018.

[56] K. N. Sugahara, T. Teesalu, P. P. Karmali, V. R. Kotamraju, L. Agemy, O. M. Girard, *et al.*, "Tissue-penetrating delivery of compounds and nanoparticles into tumors," *Cancer Cell,* vol. 16, pp. 510-20, Dec 8 2009.

[57] F. Yan, H. Wu, H. Liu, Z. Deng, H. Liu, W. Duan, *et al.*, "Molecular imaging-guided photothermal/photodynamic therapy against tumor by iRGD-modified indocyanine green nanoparticles," *Journal of Controlled Release,* vol. 224, pp. 217-228, 2016/02/28/ 2016.

[58] Y. Sheng, Z. Wang, G. M. Ngandeu Neubi, H. Cheng, C. Zhang, H. Zhang, *et al.*, "Lipoprotein-inspired penetrating nanoparticles for deep tumor-targeted shuttling of indocyanine green and enhanced photo-theranostics," *Biomater Sci,* vol. 7, pp. 3425-3437, Aug 1 2019.

[59] Y. Wang, Y. Xie, K. V. Kilchrist, J. Li, C. L. Duvall, and D. Oupický, "Endosomolytic and Tumor-Penetrating Mesoporous Silica Nanoparticles for siRNA/miRNA Combination Cancer Therapy," *ACS Applied Materials & Interfaces,* vol. 12, pp. 4308-4322, 2020/01/29 2020.

[60] A. Zhou, Y. Wei, B. Wu, Q. Chen, and D. Xing, "Pyropheophorbide A and c(RGDyK) Comodified ChitosanWrapped Upconversion Nanoparticle for Targeted Near-Infrared Photodynamic Therapy," *Molecular Pharmaceutics,* vol. 9, pp. 1580-1589, 2012/06/04 2012.

[61] A. Zhou, Y. Wei, Q. Chen, and D. Xing, "In Vivo Near-Infrared Photodynamic Therapy Based on Targeted Upconversion Nanoparticles," *J Biomed Nanotechnol,* vol. 11, pp. 2003-10, Nov 2015.

[62] Z. Yi, X. Li, Z. Xue, X. Liang, W. Lu, H. Peng, *et al.*, *Tumor Detection: Remarkable NIR Enhancement of Multifunctional Nanoprobes for In Vivo Trimodal Bioimaging and Upconversion Optical/T2-Weighted MRIGuided Small Tumor Diagnosis (Adv. Funct. Mater. 46/2015) (page 7102)* vol. 25, 2015.

[63] X. L. Tang, J. Wu, B. L. Lin, S. Cui, H. M. Liu, R. T. Yu, *et al.*, "Near-infrared light-activated red-emitting upconverting nanoplatform for T(1)-weighted magnetic resonance imaging and photodynamic therapy," *Acta Biomater,* vol. 74, pp. 360-373, Jul 1 2018.

[64] F. F. E. Kohle, S. Li, M. Z. Turker, and U. B. Wiesner, "Ultrasmall PEGylated and Targeted Core–Shell Silica Nanoparticles Carrying Methylene Blue Photosensitizer," *ACS Biomaterials Science & Engineering,* vol. 6, pp. 256-264, 2020/01/13 2020.

[65] R. Kopelman, Y.-E. Lee Koo, M. Philbert, B. A. Moffat, G. Ramachandra Reddy, P. McConville, *et al.*, "Multifunctional nanoparticle platforms for in vivo MRI enhancement and photodynamic therapy of a rat brain cancer," *Journal of Magnetism and Magnetic Materials,* vol. 293, pp. 404-410, 2005/05/01/ 2005.

[66] L. V. Halig, D. Wang, A. Y. Wang, Z. G. Chen, and B. Fei, "Biodistribution Study of Nanoparticle Encapsulated Photodynamic Therapy Drugs Using Multispectral Imaging," *Proceedings of SPIE--the International Society for Optical Engineering,* vol. 8672, p. 10.1117/12.2006492, 2013.

[67] D. Wang, B. Fei, L. V. Halig, X. Qin, Z. Hu, H. Xu, *et al.*, "Targeted Iron-Oxide Nanoparticle for Photodynamic Therapy and Imaging of Head and Neck Cancer," *ACS Nano,* vol. 8, pp. 6620-6632, 2014/07/22 2014.

[68] J. Dai, Y. Li, Z. Long, R. Jiang, Z. Zhuang, Z. Wang, *et al.*, "Efficient Near-Infrared Photosensitizer with Aggregation-Induced Emission for Imaging-Guided Photodynamic Therapy in Multiple Xenograft Tumor Models," *ACS Nano,* vol. 14, pp. 854-866, 2020/01/28 2020.

[69] K. Haedicke, D. Kozlova, S. Gräfe, U. Teichgräber, M. Epple, and I. Hilger, "Multifunctional calcium phosphate nanoparticles for combining near-infrared fluorescence imaging and photodynamic therapy," *Acta Biomaterialia,* vol. 14, pp. 197-207, 2015/03/01/ 2015.

[70] H. Cao, Y. Qi, X. Gao, Z. J. Wei, J. Xia, L. Wang, *et al.*, "Two-photon excited peptide nanodrugs for precise photodynamic therapy," *Chemical Communications,* vol. 57, pp. 2245-2248, 2021.

[71] Y. Wang, L. Jiang, Y. Zhang, Y. Lu, J. Li, H. Wang, *et al.*, "Fibronectin-Targeting and Cathepsin B-Activatable Theranostic Nanoprobe for MR/Fluorescence Imaging and Enhanced Photodynamic Therapy for Triple Negative Breast Cancer," *ACS Applied Materials & Interfaces,* vol. 12, pp. 33564-33574, 2020/07/29 2020.

[72] L. S. Carvalho, N. Gonçalves, N. A. Fonseca, and J. N. Moreira, "Cancer Stem Cells and Nucleolin as Drivers of Carcinogenesis," *Pharmaceuticals,* vol. 14, p. 60, 2021.

[73] N. A. Fonseca, A. S. Rodrigues, P. Rodrigues-Santos, V. Alves, A. C. Gregório, Â. Valério-Fernandes, *et al.*, "Nucleolin overexpression in breast cancer cell sub-

populations with different stem-like phenotype enables targeted intracellular delivery of synergistic drug combination," *Biomaterials,* vol. 69, pp. 76-88, Nov 2015.

[74] K. Porkka, P. Laakkonen, J. A. Hoffman, M. Bernasconi, and E. Ruoslahti, "A fragment of the HMGN2 protein homes to the nuclei of tumor cells and tumor endothelial cells in vivo," *Proc Natl Acad Sci U S A,* vol. 99, pp. 7444-9, May 28 2002.

[75] M. E. Akerman, W. C. Chan, P. Laakkonen, S. N. Bhatia, and E. Ruoslahti, "Nanocrystal targeting in vivo," *Proc Natl Acad Sci U S A,* vol. 99, pp. 12617-21, Oct 1 2002.

[76] G. R. Reddy, M. S. Bhojani, P. McConville, J. Moody, B. A. Moffat, D. E. Hall, *et al.*, "Vascular targeted nanoparticles for imaging and treatment of brain tumors," *Clin Cancer Res,* vol. 12, pp. 6677-86, Nov 15 2006.

[77] H. J. Hah, G. Kim, Y. E. Lee, D. A. Orringer, O. Sagher, M. A. Philbert, *et al.*, "Methylene blue-conjugated hydrogel nanoparticles and tumor-cell targeted photodynamic therapy," *Macromol Biosci,* vol. 11, pp. 90-9, Jan 10 2011.

[78] D. A. Orringer, Y.-E. L. Koo, T. Chen, G. Kim, H. J. Hah, H. Xu, *et al.*, "In vitro characterization of a targeted, dyeloaded nanodevice for intraoperative tumor delineation," *Neurosurgery,* vol. 64, pp. 965-972, 2009.

[79] X. Feng, D. Jiang, T. Kang, J. Yao, Y. Jing, T. Jiang, *et al.*, "Tumor-Homing and Penetrating Peptide-Functionalized Photosensitizer-Conjugated PEG-PLA Nanoparticles for Chemo-Photodynamic Combination Therapy of DrugResistant Cancer," *ACS Appl Mater Interfaces,* vol. 8, pp. 17817-32, Jul 20 2016.

[80] A. Borrelli, A. L. Tornesello, M. L. Tornesello, and F. M. Buonaguro, "Cell Penetrating Peptides as Molecular Carriers for Anti-Cancer Agents," *Molecules (Basel, Switzerland),* vol. 23, p. 295, 2018.

[81] A. Subrizi, E. Tuominen, A. Bunker, T. Róg, M. Antopolsky, and A. Urtti, "Tat(48-60) peptide amino acid sequence is not unique in its cell penetrating properties and cell-surface glycosaminoglycans inhibit its cellular uptake," *J Control Release,* vol. 158, pp. 277-85, Mar 10 2012.

[82] A. M. Fales, H. Yuan, and T. Vo-Dinh, "Cell-penetrating peptide enhanced intracellular Raman imaging and photodynamic therapy," *Mol Pharm,* vol. 10, pp. 2291-8, Jun 3 2013.

[83] M. Thandu, V. Rapozzi, L. Xodo, F. Albericio, C. Comuzzi, and S. Cavalli, "“Clicking” Porphyrins to Magnetic Nanoparticles for Photodynamic Therapy," *ChemPlusChem,* vol. 79, pp. 90-98, 2014.

[84] M. Gao, F. Fan, D. Li, Y. Yu, K. Mao, T. Sun, *et al.*, "Tumor acidity-activatable TAT targeted nanomedicine for enlarged fluorescence/magnetic resonance imaging-guided photodynamic therapy," *Biomaterials,* vol. 133, pp. 165-175, Jul 2017.

[85] G. Wan, Y. Cheng, J. Song, Q. Chen, B. Chen, Y. Liu, *et al.*, "Nucleus-targeting near-infrared nanoparticles based on TAT peptide-conjugated IR780 for photo-

chemotherapy of breast cancer," *Chemical Engineering Journal,* vol. 380, p. 122458, 2020/01/15/ 2020.

[86] S. Gomez, A. Tsung, and Z. Hu, "Current Targets and Bioconjugation Strategies in Photodynamic Diagnosis and Therapy of Cancer," *Molecules,* vol. 25, p. 4964, 2020.

[87] T.-Y. Sun, Q. Wang, J. Zhang, T. Wu, and F. Zhang, "Trastuzumab-Peptide interactions: mechanism and application in structure-based ligand design," *International journal of molecular sciences,* vol. 14, pp. 1683616850, 2013.

[88] A. Narsireddy, K. Vijayashree, J. Irudayaraj, S. V. Manorama, and N. M. Rao, "Targeted in vivo photodynamic therapy with epidermal growth factor receptor-specific peptide linked nanoparticles," *Int J Pharm,* vol. 471, pp. 421-9, Aug 25 2014.

[89] A. Narsireddy, K. Vijayashree, M. G. Adimoolam, S. V. Manorama, and N. M. Rao, "Photosensitizer and peptideconjugated PAMAM dendrimer for targeted in vivo photodynamic therapy," *Int J Nanomedicine,* vol. 10, pp. 6865-78, 2015.

[90] I. Genta, E. Chiesa, B. Colzani, T. Modena, B. Conti, and R. Dorati, "GE11 Peptide as an Active Targeting Agent in Antitumor Therapy: A Minireview," *Pharmaceutics,* vol. 10, Dec 22 2017.

[91] R. S. Agnes, A. M. Broome, J. Wang, A. Verma, K. Lavik, and J. P. Basilion, "An optical probe for noninvasive molecular imaging of orthotopic brain tumors overexpressing epidermal growth factor receptor," *Mol Cancer Ther,* vol. 11, pp. 2202-11, Oct 2012.

[92] A. M. Master, M. Livingston, N. L. Oleinick, and A. Sen Gupta, "Optimization of a nanomedicine-based silicon phthalocyanine 4 photodynamic therapy (Pc 4-PDT) strategy for targeted treatment of EGFR-overexpressing cancers," *Molecular pharmaceutics,* vol. 9, pp. 2331-2338, 2012.

[93] A. M. Master, Y. Qi, N. L. Oleinick, and A. S. Gupta, "EGFR-mediated intracellular delivery of Pc 4 nanoformulation for targeted photodynamic therapy of cancer: in vitro studies," *Nanomedicine,* vol. 8, pp. 655-64, Jul 2012.

[94] N. Miyoshi, H. Ishii, K. Mimori, F. Tanaka, T. Hitora, M. Tei, *et al.*, "TGM2 is a novel marker for prognosis and therapeutic target in colorectal cancer," *Ann Surg Oncol,* vol. 17, pp. 967-72, Apr 2010.

[95] Z. J. Li, W. K. Wu, S. S. Ng, L. Yu, H. T. Li, C. C. Wong, *et al.*, "A novel peptide specifically targeting the vasculature of orthotopic colorectal cancer for imaging detection and drug delivery," *J Control Release,* vol. 148, pp. 292302, Dec 20 2010.

[96] A. de Oliveira É, B. L. Faintuch, D. Seo, A. B. Barbezan, A. Funari, R. C. Targino, *et al.*, "Radiolabeled GX1 Peptide for Tumor Angiogenesis Imaging," *Appl Biochem Biotechnol,* vol. 185, pp. 863-874, Aug 2018.

[97] D. Guo, S. Xu, N. Wang, H. Jiang, Y. Huang, X. Jin, *et al.*, "Prodrug-embedded angiogenic vessel-targeting nanoparticle: A positive feedback amplifier in hypoxia-induced chemo-photo therapy," *Biomaterials,* vol. 144, pp. 188-198, Nov 2017.

[98] V. Fogal, L. Zhang, S. Krajewski, and E. Ruoslahti, "Mitochondrial/cell-surface protein p32/gC1qR as a molecular target in tumor cells and tumor stroma," *Cancer Res,* vol. 68, pp. 7210-8, Sep 1 2008.

[99] L. Chen, H. Yin, B. Farooqi, S. Sebti, A. D. Hamilton, and J. Chen, "p53 alpha-Helix mimetics antagonize p53/MDM2 interaction and activate p53," *Mol Cancer Ther,* vol. 4, pp. 1019-25, Jun 2005.

[100] J. Banerjee, E. Radvar, and H. S. Azevedo, "10 - Self-assembling peptides and their application in tissue engineering and regenerative medicine," in *Peptides and Proteins as Biomaterials for Tissue Regeneration and Repair*, M. A. Barbosa and M. C. L. Martins, Eds., ed: Woodhead Publishing, 2018, pp. 245-281.

[101] Y. Zhang, C. Deng, S. Liu, J. Wu, Z. Chen, C. Li, *et al.*, "Active Targeting of Tumors through Conformational Epitope Imprinting," *Angewandte Chemie International Edition,* vol. 54, pp. 5157-5160, 2015, Germany.

[102] T. R. Daniels, E. Bernabeu, J. A. Rodríguez, S. Patel, M. Kozman, D. A. Chiappetta, *et al.*, "The transferrin receptor and the targeted delivery of therapeutic agents against cancer," *Biochim Biophys Acta,* vol. 1820, pp. 291-317, Mar 2012.

[103] M. Ruivard, M. Boursiac, G. Mareynat, A. F. Sapin, L. Gerbaud, H. Derumeaux, *et al.*, "Diagnostic de la carence en fer : évaluation du rapport « récepteur soluble de la transferrine/ferritine »," *La Revue de Médecine Interne,* vol. 21, pp. 837-843, 2000/10/01/ 2000.

[104] S. Li, H. Zhao, X. Mao, Y. Fan, X. Liang, R. Wang, *et al.*, "Transferrin Receptor Targeted Cellular Delivery of Doxorubicin Via a Reduction-Responsive Peptide-Drug Conjugate," *Pharmaceutical Research,* vol. 36, p. 168, 2019/10/25 2019.

[105] T. Zhang, S. Huang, H. Lin, N. An, R. Tong, Y. Chen, *et al.*, "Enzyme and pH-responsive nanovehicles for intracellular drug release and photodynamic therapy," *New Journal of Chemistry,* vol. 41, pp. 2468-2478, 2017.

[106] N. Kamimura, A. M. Wolf, and Y. Iwai, "Development of Cancer Immunotherapy Targeting the PD-1 Pathway," *J Nippon Med Sch,* vol. 86, pp. 10-14, 2019.

[107] B. Liu, G. Qiao, Y. Han, E. Shen, G. Alfranca, H. Tan, *et al.*, "Targeted theranostics of lung cancer: PD-L1-guided delivery of gold nanoprisms with chlorin e6 for enhanced imaging and photothermal/photodynamic therapy," *Acta Biomater,* vol. 117, pp. 361-373, Nov 2020.

[108] L. Wang, C. Dong, X. Li, W. Han, and X. Su, "Anticancer potential of bioactive peptides from animal sources (Review)," *Oncol Rep,* vol. 38, pp. 637-651, Aug 2017.

[109] S. Li, L. Liu, G. He, and J. Wu, "Molecular targets and mechanisms of bioactive peptides against metabolic syndromes," *Food Funct,* vol. 9, pp. 42-52, Jan 24 2018.

[110] H. Cheng, R. R. Zheng, G. L. Fan, J. H. Fan, L. P. Zhao, X. Y. Jiang, *et al.*, "Mitochondria and plasma membrane dual-targeted chimeric peptide for single-agent synergistic photodynamic therapy," *Biomaterials,* vol. 188, pp. 1-11, Jan 2019.

Sous-chapitre I.3: Importance of Rose Bengal Loaded with nanoparticles for Photo dynamic anti-cancer therapy

Batoul Dhaini[1], Laurène Wagner[2], Morgane Moinard[1], Joël Daouk[3], Philippe Arnoux[1], Hervé Schohn[3], Perrine Schneller[3], Samir Acherar[2], Tayssir Hamieh[4,5] and Céline Frochot[1*]

[1] Reactions and Chemical Engineering Laboratory, Université de Lorraine, LRGP-CNRS, F-54000, Nancy, France;
[2] Laboratory of Macromolecular Physical Chemistry, Université de Lorraine, LCPM-CNRS, F-54000, Nancy, France;
[3] Department of Biology, Signals and Systems in Cancer and Neuroscience, Université de Lorraine, CRAN-CNRS, F-54000 Nancy, France;
[4] Faculty of Science and Engineering, Maastricht University, P.O. Box 616, 6200 MD Maastricht, The Netherlands
[5] Laboratory of Materials, Catalysis, Environment and Analytical Methods Laboratory (MCEMA), Faculty of Sciences, Lebanese University, Hadath, Lebanon

Review published in MDPI-Pharmaceutical journal

Résumé : Le rose bengale (RB) est un photosensibilisateur (PS) utilisé dans la thérapie photodynamique (PDT) anticancéreuse et antibactérienne. L'excitation spécifique de ce PS permet la production d'oxygène singulet et d'espèces réactives de l'oxygène qui tuent les bactéries et les cellules tumorales. Dans cette revue, nous résumons l'histoire de l'utilisation du RB comme PS couplé de manière chimique ou physique à des nanoparticules (NPs). Les études sont divisées en PDT et PDT excitée par des rayons X (X-PDT) et subdivisées par type de NP. Dans l'ensemble des articles traités, le RB utilisé comme a montré une cytotoxicité remarquable sous l'effet de la lumière. Le RB chargé aux NPs est un excellent candidat pour la nanomédecine appliquée PDT et X-PDT.

Abstract: Rose Bengal (RB) is a photosensitizer (PS) used in anti-cancer and anti-bacterial photodynamic therapy (PDT). The specific excitation of this PS allows the production of singlet oxygen and oxygen reactive species that kill bacteria and tumor cells. In this review, we summarize the history of the use of RB as a PS coupled by chemical or physical means to nanoparticles (NPs). The studies are divided into PDT and PDT excited by X-rays (X-PDT), and subdivided on the basis of NP type. On the basis of the papers examined, it can be noted

that RB used as a PS shows remarkable cytotoxicity under the effect of light, and RB loaded onto NPs is an excellent candidate for nanomedical applications in PDT and X-PDT.

Keywords: photodynamic therapy; rose bengal; X-rays; nanomedicine; singlet oxygen; cancer;
nanoparticle.

I. Introduction

Photodynamic therapy (PDT) for cancer presents significant advantages over chemotherapy and radiation therapy [1]. PDT does not cause any of the side effects reported for other types of cancer treatment [2]. PDT was first applied clinically on humans in 1978 [3]. PDT is based on the principle of the excitation of a drug, called a "photosensitizer" (PS), with a light beam [4]. This PS is not toxic in the dark, but induces the production of highly reactive oxygen species (ROS), such as singlet oxygen ($^1O_2$), upon light illumination [5]. Upon light illumination, the PS is activated into a singlet excited state and then into a triplet state following intersystem crossing. In its triplet state, the PS undergoes electron or proton transfer to produce superoxide anion and hydroxyl radical, or transfers its energy into oxygen to produce $^1O_2$. Around 20 PSs have been commercialized to date, or are currently in clinical trials, including porphyrin, chlorin and phthalocyanine [6,7]. There are still some improvements to be made, such as the achievement of better absorption in the near-IR range, as well as achieving better solubility and increased selectivity. The coupling of these PSs to nanoparticles (NPs) can be used to achieve passive targeting of the PS to cancer cells, thus decreasing health cells being attacked [8]. One of the limitations of PDT is the poor penetration of light into the tissue. To overcome this problem, PDT excited by X-rays (X-PDT) can be used, owing to the fact that X-rays penetrate more deeply into the tissue [9].

Rose Bengal (4,5,6,7-tetrachloro-20,40,50,70-tetraiodofluorescein disodium, RB) is a dye belonging to the fluorescein family [10]. This amphiphilic chemical molecule is already used in medical applications to test the activity of the liver [11] and to diagnose corneal lesions [12]. Subsequently, it had been discovered by researchers that RB stimulates the immune system, and making it possible to reduce the risk of certain cancers [13].

For X-PDT applications, it is necessary to couple RB with NPs containing lanthanides [14]. Since RB absorbs within the visible range, the principle involves the excitation of lanthanides using X-rays; following the luminescence of the lanthanide, energy transfer towards RB takes place. In most cases, this is a non-radiative FRET (Förster resonance energy transfer)-type energy transfer [15]. Following this energy transfer, the RB is able to convert triplet oxygen to produce $^1O_2$ [16]. Thanks to its high $^1O_2$ quantum yield (Φ_Δ) and moderate fluorescence, RB can be used in anti-cancer and anti-bacterial PDT.

In this review, we collect all of the papers that describe the use of RB and NPs. These are divided in two parts: NPs excited by light (PDT), and NPs excited by X-rays (X-PDT). Then, the papers are classified on the basis of the type of NPs used. Finally, for each type of NP, the articles are presented in chronological order.

II. Photodynamic Therapy

II.1 Upconversion Nanoparticles (UCNPs)

Upconversion nanoparticles (UCNPs) are NPs that possess the ability to absorb two or more low-energy photons from infrared (IR) radiation and emit high-energy photons in the ultraviolet (UV) or visible area in between. The size of UCNPs is usually between 10 and 100 nm. A shift from high to low wavelengths is an anti-stock shift [17]. These NPs have attracted the attention of researchers due to several characteristics, including their photostability, low toxicity, no bleaching, high conversion efficiency, high light penetration into biological tissues, and long lifetime (from nanoseconds to milliseconds) [18]. UCNPs are composed of transition metals doped with rare earths (lanthanides or actinides) and incorporated deeply into cells. All of these characteristics allow their application in nanomedicine therapy, imaging and detection [19].

Liu et al. [20] were the first to synthesize and characterize hexagonal UCNPs $NaYF_4:Yb^{3+}$, Er^{3+}(Y:Yb:Er = 78:20:2) with a size of 20 nm. To replace oleylamine ligands, they used 2-aminoethyl dihydrogen phosphate (AEP) to introduce NH_2 functions (**Figure 69**). These amino groups of the NPs were coupled to the carboxylic group of the hexanoic acid ester of RB. They evaluated around 100 PS using NPs. Finally, they performed covalent coupling of folic acid (FA) via a dual functional PEG (NH_2-PEG-COOH).

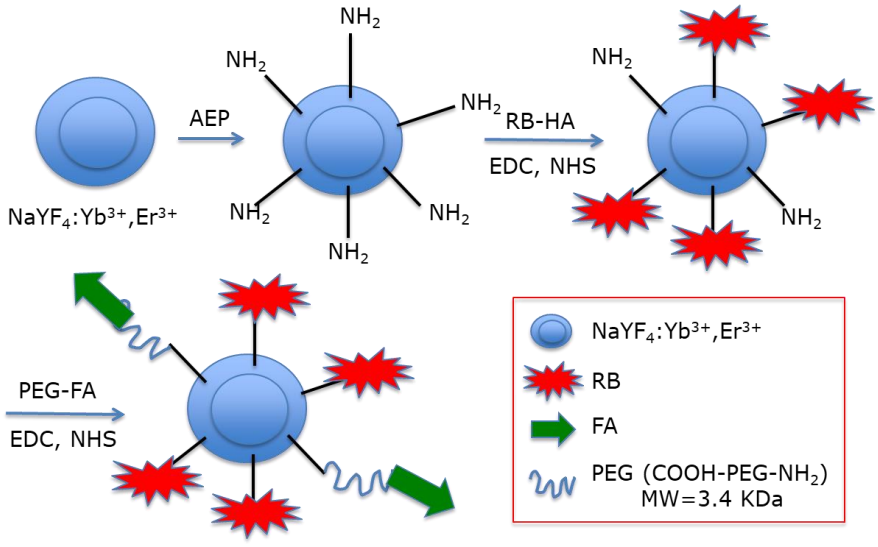

Figure 69 : Covalent coupling of NaYF4:Yb3+ and Er3+ UCNPs with RB and FA. Adapted from Liu et al. [20].

$^1O_2$ production was determined using the chemical probe 1,3-diphenylisobenzofuran (DPBF). A FRET energy transfer between this NP and RB reached 83% efficiency. $^1O_2$ production from UCNPs–RB nanoconjugates after excitation at wavelengths of 980 nm and 540 nm was observed, with a low difference between them. The authors performed irradiation at a wavelength of 980 nm (1.5 W/cm^2 for 10 min). The cell viability decreased with increasing UCNPs-PS concentration, showing the effectiveness of these biocompatible NPs (**Figure 70, left**). After the incubation of different concentrations of UCNPs in choriocarcinoma JAR cells

(FR+) and NIH 3T3 cells (FR−) as non-cancer cells and irradiation at a wavelength of 980 nm (1.5 W/cm^2 for 10 min), cell viability was measured (**Figure 70 right**). In NIH 3T3 cells, no killing was observed due to the non-incorporation of the UCNPs. In the JAR cells, 50% cell death was measured at 100 µg/mL.

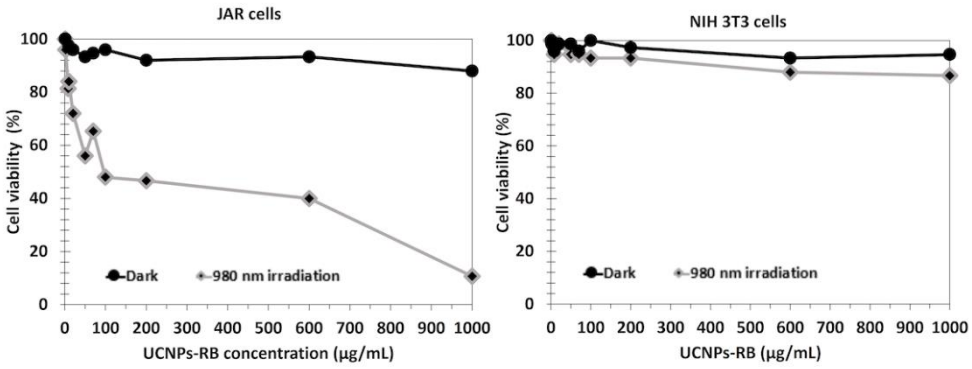

Figure 70 : JAR and NIH 3T3 cells viability in dark and after excitation at 980 nm (1.5 W/cm^2, 10 min) with increasing UCNPs-RB concentration. Adapted from Liu et al. [20].

Chen et al. [21] developed the multifunctional nano-platform UCNP@BSA-RB&IR825. The diameter of the NPs was around 60 nm. The UCNPs ($NaGdF_4$:Yb:Er (Gd:Yb:Er = 78:20:2)) were coated with polyacrylic acid (PAA) and conjugated using bovine serum albumin (BSA) protein. The hydrophobic pockets of the BSA protein enabled the effective loading of RB (≈ 7.6%, *w*/*w*) and a NIR-absorbing dye (IR825 ≈ 22%, *w*/*w*). The UCNPs showed excellent solubility both in water and physiological solutions. The resulting UCNP@BSA-RB&IR825 had the ability to produce both the PDT effect under excitation at a wavelength of 980 nm and a photothermal therapy (PTT) effect under 808 nm laser irradiation. Moreover, the presence of Gd^{3+} metal ions conferred these UCNPs with T1-weighted MRI (Magnetic Resonance Imaging) properties. $^1O_2$ production was confirmed using an $^1O_2$ Sensor Green (SOSG) probe. In vitro and in vivo experiments were performed on murine breast 4T1 cancer cells and 4T1 tumor-bearing mice irradiated with an 808 nm laser (0.5 W/cm² for 5 min) followed by 980 nm laser (0.4 W/cm² for 10 and 30 in for in vitro and in vivo experiments, respectively, with a 1 min interval after 1 min irradiation to avoid heating). UCNP@BSA-RB&IR825 showed no in vitro cytotoxicity at various concentrations (from 0 to 0.4 mg/mL) after 24 h incubation, and 4T1 cell viability was strongly decreased by the synergistic effect of PDT/PTT (**Figure 71a**). This synergistic effect was also observed in vivo with the inhibition of tumor growth (**Figure 71b**). The relative tumor volume (V/V_0) after 2 weeks was 7.3 for PDT, and the PTT effect was 7.5.

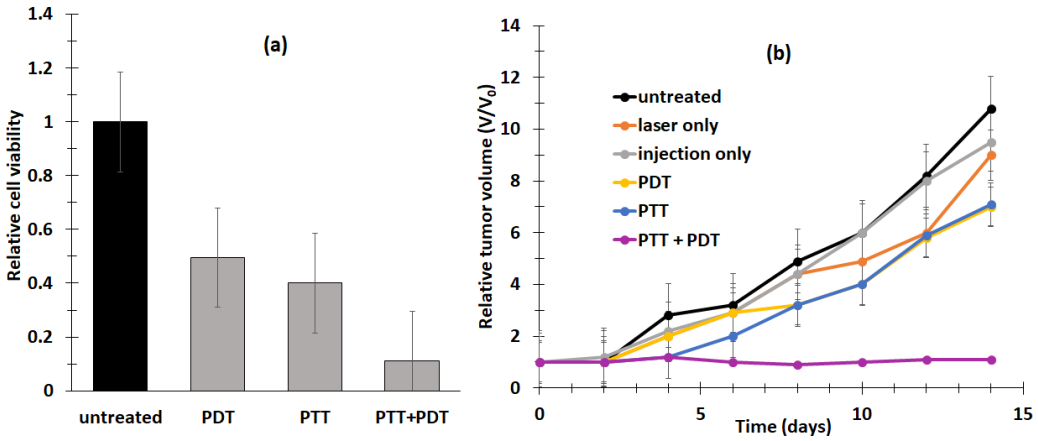

Figure 71 : (a) In vitro cytotoxicity effect of UCNP@BSA-RB&IR825 for PDT, PTT and combined PTT–PDT treatment. PDT (808 nm, 0.5 W/cm2) and PTT (980 nm, 0.4 W/cm2). (b) In vivo tumor growth in different groups of mice after various treatments, as indicated: 1: untreated; 2: laser only (808 nm and 980 nm); 3: injection only; 4: PDT; 5: PTT, 6: PTT + PDT. Wavelengths of 808 nm (0.5 W/cm2, 5 min) and 980 nm (0.4 W/cm2, 30 min) were used to separately trigger PTT and PDT, respectively. Adapted from Chen et al. [21].

Wang et al. [22] designed lipid nanovesicles combined with UCNPs ($NaYF_4$:Yb, Er(Y:Yb:Er = 78:20:2)) functionalized with PEG and RB (namely, RB-UPPLVs). RB-UPPLVs were modified with PEG on their surfaces. The nanosized PLVs presented high stability in blood. Once the RB-UPPLVs reached the tumor sites, they lost their PEG coating and the FA ligand was exposed under the acidic tumor environment. The average size was 62.1 nm. The biological tests were performed on HeLa cells. After treatment at 980 nm (2.5 W/cm^2, 20 min), cell viability for RB-UPPLVs pretreated with ABS (Acetate Buffer Solution) (22%) was lower than that of RB-UPPLVs incubated with PBS (Phosphate Buffer Solution) (50%), which was not the case in the dark.

In the same year [23], the same team synthesized UCNP ($NaYF_4$:Yb/Ho@$NaYF_4$:Nd@$NaYF_4$ (Yb/Ho(8/1%)@NaYF4:Nd(20%)) core–shell–shell nanostructures based on a thick Nd^{3+} sensitized shell. A ligand exchange approach was used to introduce NH_2 functions with poly(allylamine). The upconversion luminescence (UCL) of the UCNPs-RB was improved, compensating for the deleterious effect on UCL resulting from the decreased Nd^{3+} sensitized layer. The covalent conjugation of RB was realized in the same way as reported in Liu et al. [20]. In vitro experiments were performed in HeLa cancer cells with different concentrations of UCNPs-RB. After irradiation at 808 nm (0.67 W/cm^2, 10 min) with 600 µg/mL of UCNPs, only 10% of cells remained alive (**Figure 72**).

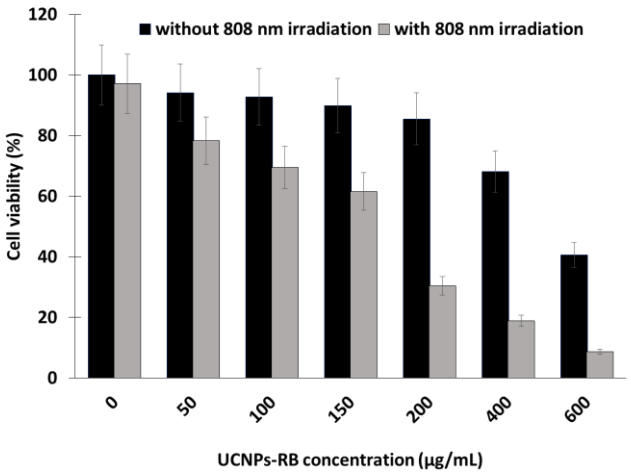

Figure 72 : HeLa cell viability when treated with different concentrations of UCNPs-RB with and without irradiation (808 nm, 0.67 W/cm^2, 10 min). Adapted from Wang et al. [23].

Lu et al. [24] designed organosilica-shelled β-$NaLuF_4$:Gd/Yb/Er (Lu/Gd/Yb/Er: 50/30/18/2 in mol%) UCNPsI with a rattle structure. NPs were adsorbed either with zinc β-carboxyphthalocyanine (ZnPc-COOH, 2.7 wt%) or RB (1.9 wt%). The NP core was β-$NaLuF_4$:Gd/Yb/Er and the shell was benzene-bridged organosilica. The size of these NPs was 10 nm. The rattle was used to introduce the storage of PSs and promote energy transfer. Moreover, the amino terminal fragment of urokinase plasminogen was finally conjugated in order to specifically target the urokinase plasminogen activator (UPA) receptor expressed in yeast cell. The synthesis route is shown in **Figure 73**.

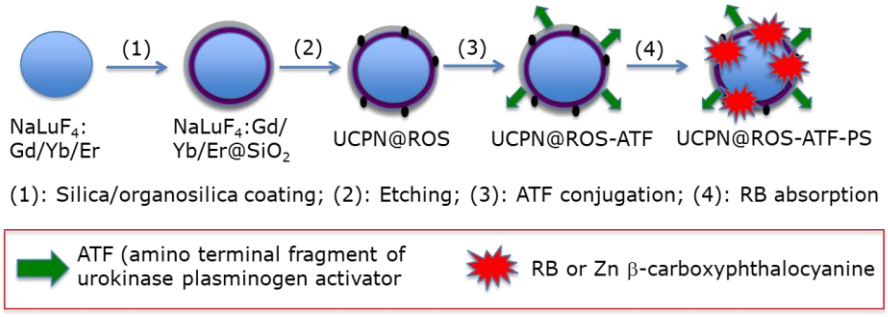

Figure 73 : Preparation of multifunctional UCNPs. Adapted from Lu et al. [24].

In vitro tests were performed on H1299 cells (human lung cancer cells). After irradiation at 980 nm (0.5 W/cm^2, 10 min), a viability of 10% was observed following incubation for 4 h with NPs (0.05 mg/mL).

Li et al. [25] developed UCNPs of luminescent lanthanide for Er doping with 20% Nd^{3+} and 10% Yb^{3+}. They coupled the hexanoic acid spacer to RB. The well-known EDC (*N*-ethyl-*N*′-(3-(dimethylamino)propyl)carbodiimide)/NHS *N*-hydroxysuccinimide couple was used for coupling the RB-HA to polyethylene imine PEI, and then to Er@$NdBF_4^-$ (**Figure 74**).

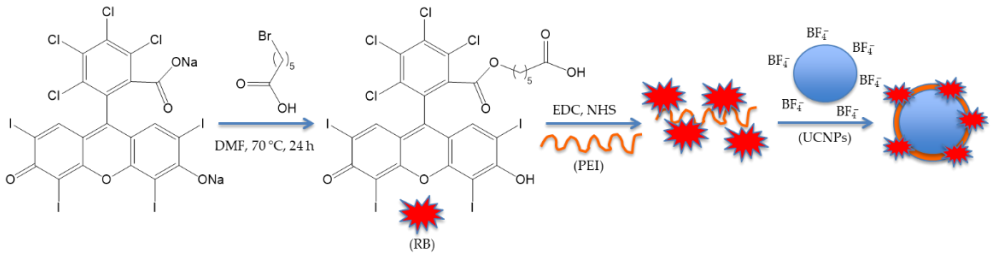

Figure 74 : Covalent coupling of RB onto Er@Nd UCNPs. Adapted from Li et al. [25].

$^1O_2$ production occurred as a result of the energy transfer from Nd^{3+} to Yb^{3+} to Er^{3+} to RB. The UCNPs had a size of 25.7 ± 1.4 nm, with a shell thickness of about 6 nm. In vitro tests on 4T1 cells showed the production of $^1O_2$ by means of DPBF. The amount of $^1O_2$ produced increased with increasing irradiation time (maximum 8 min), laser density (maximum 0.8 W/cm^2), and concentration (maximum 200 µg/mL) (**Figure 75**). Moreover, Er@Nd-RB conjugates did not enter the nucleus, but remained localized in the cytoplasm, inducing cellular oxidative stress and/or destroying proteins and breaking down organelle membranes.

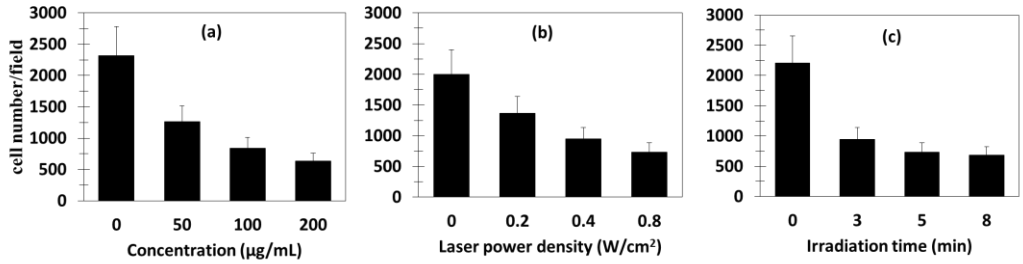

Figure 75 : In vitro PDT of Er@Nd-RB. Cell viability of 4T1 cells with different (a) concentrations, (b) laser power densities, and (c) irradiation times. Adapted from Li et al. [25]

The in vivo tests were performed on 4T1 breast cancer in BALB/c nude mice. Following 808 nm laser irradiation (520 mW/cm^2), Er@Nd-RB conjugates rapidly set upon the tumor region and remained at the tumor site for at least 45 min, while no signal was detected in other parts of the body. Mice treated with Er@Nd-RB NPs (100µL, 10 mg/mL) showed a greater decrease in tumor volume compared to the control with other NPs. (**Figure 76a**).

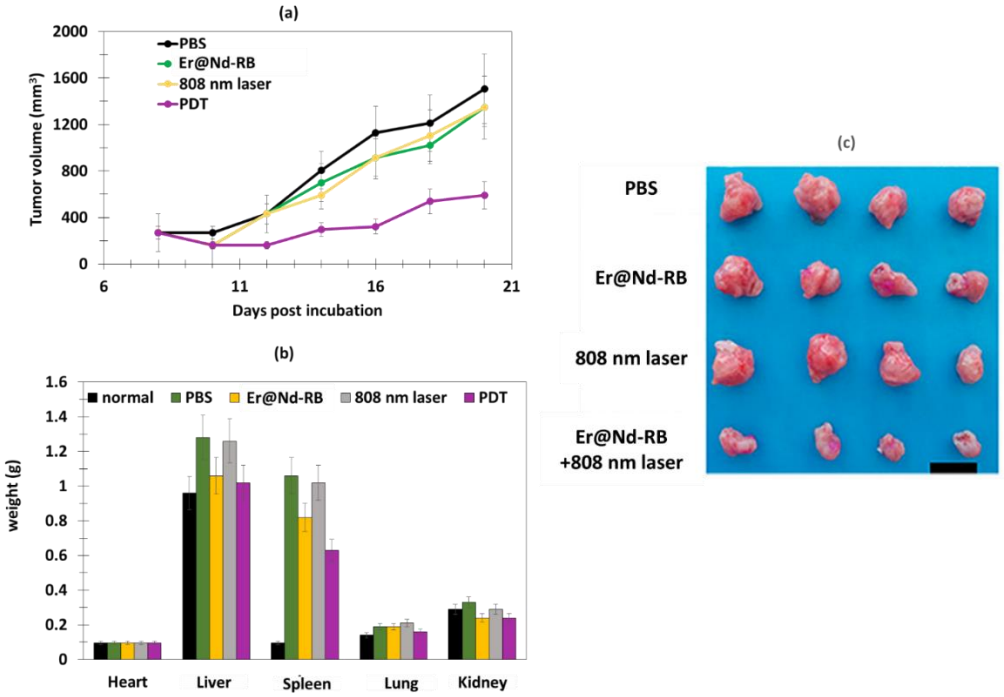

Figure 76 : PDT on 4T1 breast murine tumor after in vivo experiment (808 nm, 520 mW/cm2). (a) Tumor volume growth as a function of number of days of treatment, and (b) weight of heart, liver, spleen, lung and kidney for the four mice groups. (c) Digital photos of tumors for the four groups of mice. The mice were sacrified 14 days after treatment (808 nm, 520 mW/cm2). Figures (a) and (b) adapted from Li et al. [25]. Figure (c) reprinted with permission from Li et al. [25]. Copyright 2016 American Chemical Society.

The liver and spleen weights of the Er@Nd-RB-treated group 4 did not significantly change after PDT, which was not the case for the PBS group, demonstrating that PDT clearly attenuated the tumor-induced increase in volume in the liver and spleen.

Liang et al. [26] designed UCNPs based on a silica layer doped with RB. The particles were a core–shell ($NaYF_4$:Yb, Er@$NaGdF_4$ (Yb:Er 18%:2%)) doped with RB. A modified water-in-oil microemulsion method was employed to synthesize UCNP@SiO_2(RB). They were then functionalized with a fusion protein consisting of a binding peptide linker (L) genetically fused to *Streptococcus* Protein G, which in turn bound antibodies that were directed against cancer cells (**Figure 77**).

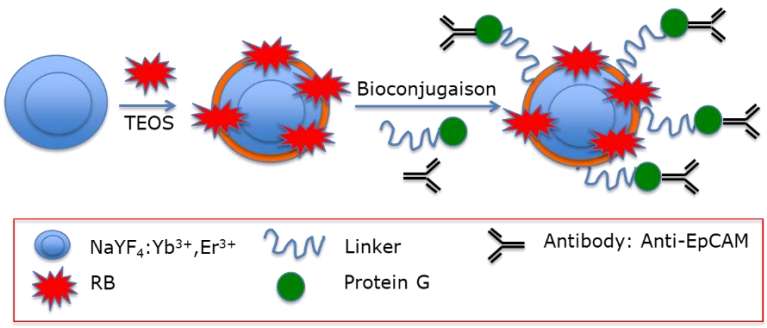

Figure 77 : Covalent coupling of RB and antibody through a bifunctional fusion protein G. Adapted from Liang et al. [26].

The average final size was around 43 nm. In particular, they tested antibodies against epCAM (FITC (Fluorescein isothiocyanate) labeled), which is overexpressed on the cell surface of many cancers, particularly colon adenocarcinoma cells. Antibodies bound epCAM and led to immune reaction, triggering cell death. In vitro experiments were performed on HT-29 cells with various concentrations of UCNP@SiO_2(RB)-LPG-Ab and irradiation times using 980 nm laser irradiation (1.5 W/cm^2). After 24 h incubation with UCNP@SiO_2(RB)-LPG-Ab, cell viability decreased to 38% (200 µg/mL, 15 min).

Ai et al. [27] synthesized biocompatible core–shell–shell UCNPs ($NaGdF_4$:Yb/Nd@$NaGdF_4$:Yb/Er@$NaGdF_4$ (50:50)). The UCNPs were covalently loaded with RB and Pt(IV) prodrug, in the form of *c*,*c*,*t*-[$Pt(NH_3)_2Cl_2(OCOCH_2CH_2NH_2)_2$] (Cisplatin), and PEGylated for biodisponibility. In vitro experiments were performed on the A2780 human ovarian carcinoma cell line and A2780cisR cells (A2780 cells resistant to cisplatin), at concentrations of 16, 80 and 400 µg/mL under near-infrared (NIR) laser irradiation (808 nm, 6 W/cm^2, 5 min). A2780 cell viability decreased to 70%, 10%, and 2%, respectively. Cell viability decreased with increasing concentration of A2780cisR (to 70%, 30%, and 5% at concentrations of 16, 80 and 400 µg/mL, respectively). (**Figure 78**).

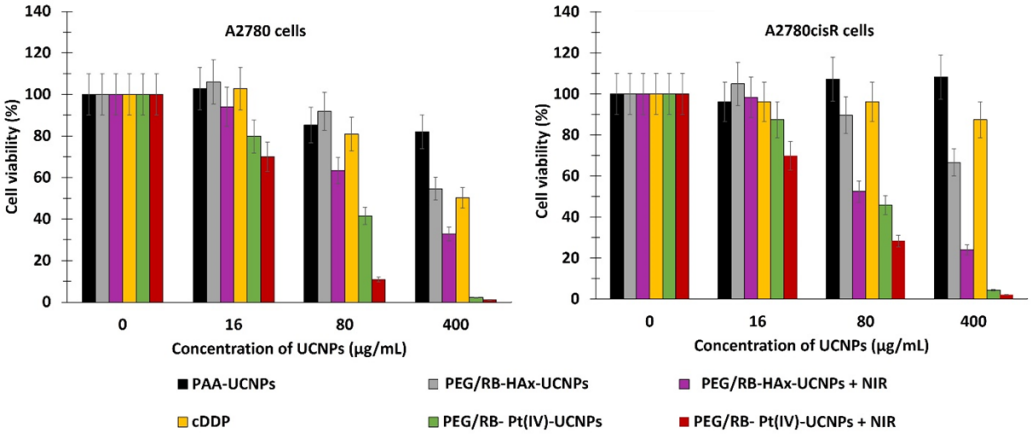

Figure 78 : Cell viabilities of A2780 and A2780cisR cells treated with various concentrations of PEG/RB-Pt(IV)-UCNPs, PEG/RB-HA-UCNPs, PAA-UCNPs and cDDP after NIR irradiation (808 nm, 6 W/cm^2, 5 min). Poly(acrylic acid) = PAA, Hexamethylenediamine = HAx, cisplatine or cis-diaminedichloroplatine(II) = cDDP. Adapted from Ai et al. [27].

Chen et al. [28] synthesized NIR-activated UCNPs to target neuroendocrine tumors (NETs) such as medullary thyroid cancer and carcinoids, which frequently 172ydrophobic to the liver, leading to a poor survival outcome. The size of these NPs was 29 nm, and they were composed of ($NaYF_4$:Yb^{3+}/Er^{3+}/Tm^{3+}(Y:Yb:Tm:Er(78:20:2:0.2)). On the UCNP surface, a photosensitive amphiphilic copolymer poly(4,5-dimethoxy-2-nitrobenzyl methacrylate)-polyethylene glycol (PNBMA-PEG) was covalently coupled with RB. Upon light illumination, there was a photoinduced polymer side-group cleavage leading to the release of the encapsulated drug AB3, which was loaded into the micelle. The mechanism is described in **Figure 79**.

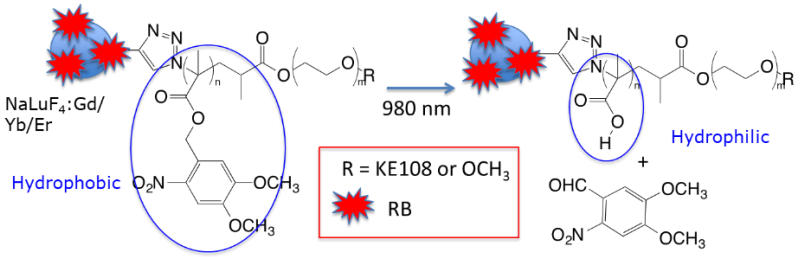

Figure 79 : Illustration of NIR-triggered hydrophobic-to-hydrophilic transition leading to the release of hydrophobic drug. Adapted from Chen et al. [28].

The targeting agent KE108 was coupled at the PEG extremity in order to target somatostatin receptors (SSTRs), which are overexpressed in many neuroendocrine cancers. The $^1O_2$ production under NIR irradiation was confirmed by the decrease in DPBF fluorescence. In vitro experiments were performed on NET (TT) cells incubated with T-RB-A3 (166 µg/mL) for 3 h. After NIR irradiation (980 nm, 0.5 W/cm^2, 10 min), these cells were re-incubated for 45 h. Cell viability decreased by 90%, compared to a decrease of 40% without illumination. This decrease in viability became less important when treating cells without the targeting agent, without AB3, or without RB. In vivo experiments were performed on TT-tumor xenograft mouse model grafted onto male athymic nude mice. Irradiation was performed at 980 nm (0.5 W/cm^2, 15 min, interval of 1 min after each 5 min of irradiation). At 7 days post injection of treatment, T-RB-AB3 showed a greater decrease in tumor volume compared to mice treated with T-RB and T-AB3 alone. These results indicated that the combination of chemotherapy with PDT was more effective than chemotherapy or PDT alone (**Figure 80**).

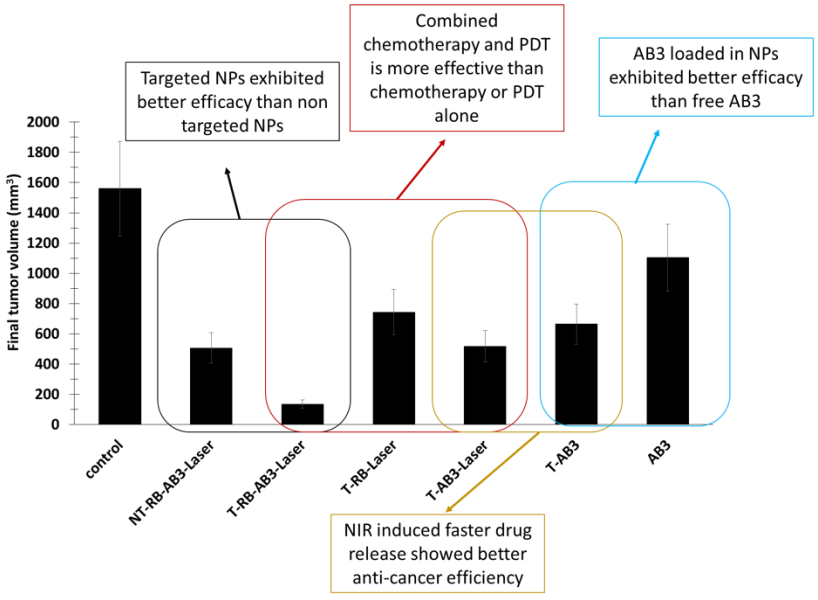

Figure 80 : Final tumor volumes, demonstrating the in vivo anti-cancer PDT efficacy of different formulations of UCNP-based theranostic micelles in NET xenografts. Tumor-bearing mice were treated in seven groups: (1) saline (control); (2) AB3 (conventional chemotherapy); (3) T-RB-Laser (targeted NIR-controlled PDT); (4) T-AB3 (targeted chemotherapy); (5) T-AB3-Laser (targeted NIR-controlled chemotherapy); (6) NT-AB3-RB (nontargeted chemotherapy; no PDT effect as no laser illumination); (7) NT-AB3-RB-Laser (nontargeted combination NIR-controlled chemotherapy and PDT). Each mouse received two intravenous injections (30 mg/kg of AB3) over a 7-day interval. A continuous wave fiber-coupled 980 nm laser (0.5 W/cm^2, 15 min, 1 min interval after every 5 min of irradiation) was applied at the tumor sites in the "Laser" groups 4 h post injection. Adapted from Chen et al. [28].

Chang et al. [29] designed core–shell (i.e., Yb^{3+}, Er^{3+}@ $NaYF_4$ (20:2)) UCNPs coated with poly(allylamine) and co-loaded with RB and zinc phthalocyanine (ZnPc). The size of these NPs was between 24 nm and 32 nm. RB and ZnPc were coupled covalently to the surface of the NPs in the shell, allowing an efficient resonance energy transfer of around 50%. The production of $^1O_2$, estimated on the basis of DPBF, was optimal for the co-loaded NPs (90%). The cellular uptake of the UCNPs was evaluated on A549 lung carcinoma cells, revealing an accumulation in the mitochondria after internal transport by lysosomes. After incubation for 24 h, the cell survival rate was 20% after irradiation (980 nm, 0.25 W/cm^2, 15 min). A mitochondrial apoptosis pathway was demonstrated. Hepa1-6 tumor-bearing mice after PDT treatment (980 nm, 0.25 W/cm^2, 15 min) showed a relative tumor inhibitory ratio of 90%.

Hou et al. [30] synthesized UCNPs ($NaYF_4$:Yb, Tm)@0.6($NaYF_4$: Yb, Er (Y:Yb:Tm = 75/25/0.3)) coated with tetraethyl orthosilicate (TEOS) (UCN@mSiO_2) coupled with azobenzene (Azo) and RB, and encapsulated with DOX. The size of these NPs was 120 nm. $^1O_2$ production was confirmed by ABDA (9,10-anthracenediyl-bis(methylene) dimalonic acid) probe. In vitro MTT tests were performed on HeLa cells at different concentrations. Cell viability decreased significantly when the cells were treated with UCN@mSiO_2-(Azo + RB) compared to when treated with UCN@mSiO_2-AZo and UCN@mSiO_2. When excited at 980 nm (2.0 W/cm^2, 10 min), HeLa cells treated with 100 µg/mL showed a decrease in cell viability of 60% with DoxUCN@mSiO_2-(Azo + RB) and of 40% with UCN@mSiO_2-(Azo + RB). The NIR excitation of these NPs activated the Azo molecules, allowing the release of the drugs and the PS (DOX and RB).

Kumar et al. [31] synthesized white emitting $NaYF_4$ upconversion nanocrystals (Y/Yb/Er:78/20/2). The UCNPs were composed of a hydrophobic core of oleic-acid-coated NPs and $NaYF_4$:Yb/Er/Tm (OA-WENs) coated with a layer of dense silica, followed by another layer of mesoporous silica, and with primary amine groups introduced on the external surface (WE-SiO_2). FA and RB were then alternatively covalently conjugated. The second PS (ZnPc) was loaded inside the mesoporous silica shell by physisorption. Finally, dPS-WE-SiO_2 NPs were obtained, with a hydrodynamic size of 91 nm. The FRET effect between the WEN core and the PSs was also confirmed on the basis of fluorescence and lifetime studies. DPBF was used to detect $^1O_2$ production. In vitro studies were conducted on HeLa cells. dPS-WE-SiO_2 NPs were found to be localized within the cytoplasm of the HeLa cells 48 h post incubation, and most of them were internalized. In the case of cells treated with 200 µg/mL of dPS-WE-SiO_2 NPs and irradiated with am NIR laser (980 nm, 2.5 W/cm^2, 20 min), number of dead cells was greater than in the cells treated with the single-PS-based nano-system. Early apoptosis was observed in 43% of dPS-WE-SiO_2-NP-treated cells, compared to 22.8% and 14.2% for RB-WE-SiO_2-NP- and ZnPc-WE-SiO_2-NP-treated cells, respectively. Late apoptosis and necrosis were observed in 51.5% of dPS-WE-SiO_2-NP-treated cells, compared to 16.7% and 13.3% of RB-WE-SiO_2-NP- and ZnPc-WE-SiO_2-NP-treated cells, respectively.

Sabri et al. [32] synthesized NIR-excited UCNPs. Lanthanide-doped UCNPs $NaGdF_4$:Yb^{3+}/Er^{3+} (Gd/Er/Yb:78/2/20)(Ln-UCNPs) were coated with BSA to increase

biocompatibility and stability in aqueous medium, resulting in BSA-Ln-UCNPs being obtained. RB was covalently conjugated onto the UCNPs with hexanoic acid spacer. RB-BSA-Ln-UCNPs were obtained, with a size of 78 nm. First, the energy transfer from the BSA-Ln-UCNPs to the RB was confirmed by the upconversion emission spectra, with a maximum energy transfer efficiency of 68% at a concentration of RB of 20 µM. DPBF was used to confirm the production of $^1O_2$. In vitro studies were conducted in mammalian cancer cell line A549. MTT (3-[4,5-dimethylthiazol-2-yl]-2,5 diphenyl tetrazolium bromide) assays were conducted to evaluate the effect of various concentrations of RB-BSA-Ln-UCNPs on the viability of A549 cells after a 980 nm irradiation (13 W/cm^2, 10 min). Dark cytotoxicity was observed, with cell viability decreasing by 15%. Cytotoxicity was observed upon irradiation, with a stronger effect at higher concentrations. At an RB-BSA-Ln-UCNP concentration of 250 µg/mL, 36% cell death was obtained after 10 min of exposure. These experiments confirmed the efficacy of these NPs when coupled to RB in PDT.

Buchner et al. [33] synthesized RB–lysine-functionalized UCNPs (UCNPs@K(RB)). RB was covalently attached to the lysine-modified UCNPs. The core–shell UCNPs were $NaYF_4$:Yb,Er,Gd@$NaYF_4$ (Yb/Gd/Er:20/20/2). The final solvodynamic diameter of these UCNPs was about 23.7 ± 8.4 nm, with a loading of RB estimated at 160 RB per NP. The $^1O_2$ production of UCNPs@K(RB) was evaluated using ABDA as a probe. An in vitro study was conducted on SK-BR-3 breast cancer cells at different concentrations of UCNPs@K(RB). After 3 h incubation with UCNPs@K(RB) (20 µg/mL), PDT treatment (980 nm, 200 mW/cm^2, 6 min) decreased the cell viability by more than 85% compared to the non-irradiated cells.

Xie et al. [34] developed a complex O_2-loaded pH-responsive multifunctional nanodrug carrier, UC@mSiO_2-RB@ZIF-O_2-DOX-PEGFA (NaYF$_4$:Yb/Er@NaYbF$_4$:Nd@NaGdF$_4$ (Yb/Er/Gd:18/2/80)), coating it onto silica in which RB was encapsulated. They added Zeolitic imidazolate framework-90 (ZIF-90) as an MOF (metal–organic framework) to act as an O_2 reservoir, in order to release O_2 into the tumor microenvironment to fight against hypoxia. NPs were conjugated to the chemotherapy drug DOX and PEG-FA (abbreviated URODF) to target the FA receptor (**Figure 81**).

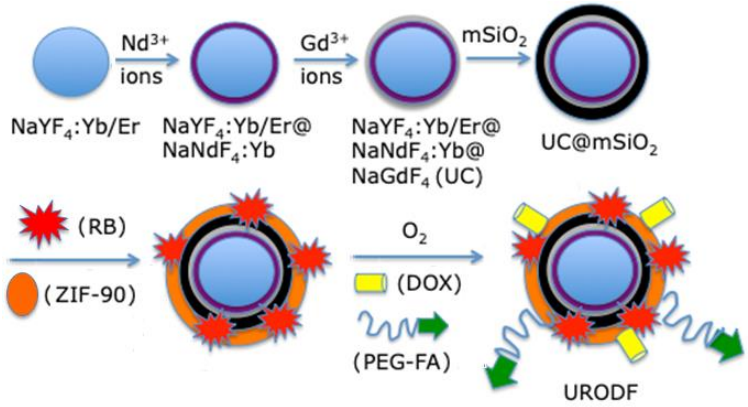

Figure 81 : Preparation of URODF NPs. Adapted from Xie et al. [34].

These NPs emitted a green light after having absorbed photons following illumination at a wavelength of 808 nm, as a result of a multi-photon process that activated the RB. The size of the URODF was 150 nm. $^1O_2$ production was quantified using DPBF. In vitro studies were performed on 4T1 and HeLa human cells. Eight groups were used in the study, with or without laser irradiation (808 nm, 0.5 W/cm^2, 10 min), as follows: (1) UC@mSiO$_2$@ZIF-PEG-FA (UF), (2) RB, (3) laser irradiation (+), (4) DOX, (5) UC@mSiO$_2$@ZIF-DOX/PEG-FA (UDF), (6) UC@mSiO$_2$-RB@ZIF-O$_2$-PEG-FA with laser irradiation, (7) (UROF+) UC@mSiO$_2$-RB@ZIF-DOX/PEGFA with laser irradiation (URDF+), (8) URODF with laser irradiation (URODF+). After incubation of 4T1 and HeLa cells for 14 days with URODF (100 µg/mL), and laser irradiation, the cell viability decreased from 100% to 20% (**Figure 82a,b**). These UCNPs were injected in vivo into H22 (murine hepatocarcinoma) tumor-bearing BABc mice with at a concentration of 4.0 mg/kg in DOX. The fluence was 0.5 W/cm^2 for 0 to 150 s. After 15 days of treatment with URODF, tumor volume decreased significantly (50%) (**Figure 82c,d**).

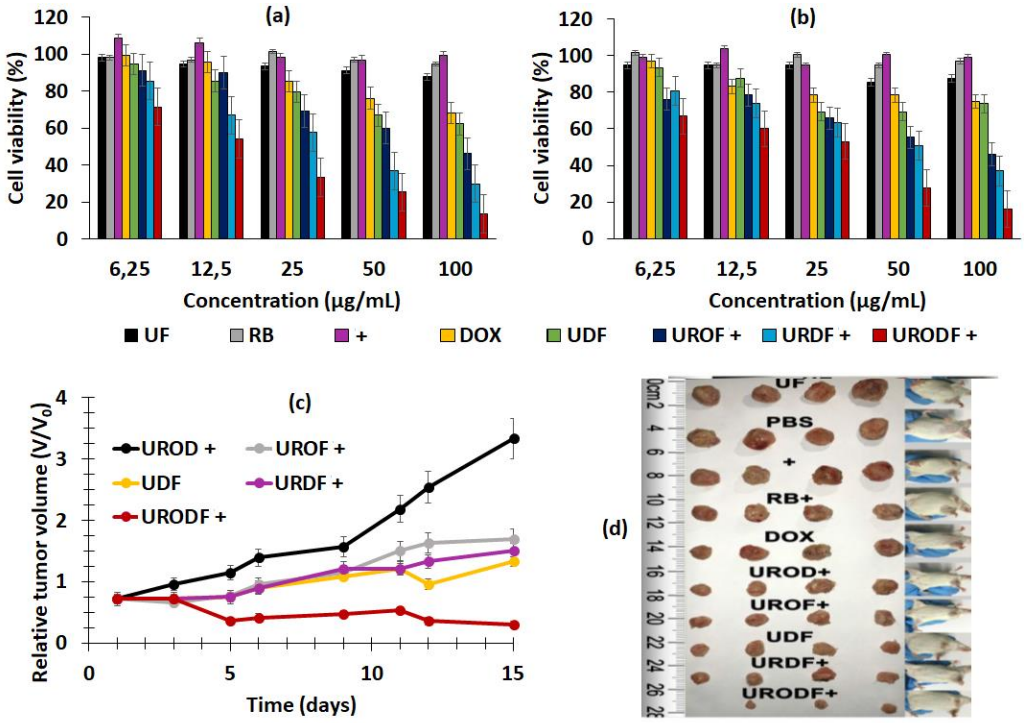

Figure 82 : MTT assays for cell viability of (a) 4T1 and (b) HeLa cells incubated with different products and concentrations for 24 h. (c) Tumor volume growth curves and (d) dynamic body change of mice in groups receiving UROD+, UROF+, UDF, URDF+ and URODF+ treatments over a period of 14 days (+ = laser irradiation (808 nm, 0.5 W/cm^2, 0 to 150 s)). Figures (a)-(c) adapted from Xie et al. [34]. Figure (d) reprinted with permission from Xie et al. [34]. Copyright 2019 American Chemical Society.

CSGUR-MSGG/5FU NPs were designed by Kumar et al. [35] to achieve dual chemotherapy and PDT, as well as enzyme-responsive drug release for treatment of colorectal cancer. The NaYF$_4$:Yb/Er (Yb/Er:20/2) core was shelled with NaYbF$_4$ and loaded with RB to produce UCNPs. Then, mesoporous silica loaded with FA for colorectal cancer targeting and 5-fluorouracil (5FU) drug was shelled. Finally, a gatekeeper layer for loading drug made with a guar gum (GG) polymer was added. Glycosidase enzymes in the colon can degrade GG to

produce enzyme-responsive drug release in the colon area. TEM (transmission emission microscopy) images of the NPs made it possible to measure their size (72.3 ± 7.1 nm). Under NIR irradiation (980 nm, 0.7 W/cm^2, 10 min), an energy transfer efficiency of 94.1% from UCNPs to RB was observed with the quenching of UCNP emission at 540 nm. Drug release was evaluated under different pH conditions, but no 5FU release was observed, confirming the stability of the NPs. When NPs were incubated with colonic enzymes, 5FU was released, with 82% being released after incubation for 72 h. Under NIR irradiation without colonic enzymes, 10% 5FU release was observed. A DPBF probe was used to confirm $^1O_2$ production under NIR irradiation. HT-29 cells were incubated with CSGUR-MSGG/5FU NPs for 48 h (200 µg/mL). A DCFH-DA (dichlorodihydrofluorescein-diacetate) probe made it possible to visualize intracellular ROS production. Under chemotherapy conditions, low green fluorescence was observed, showing a moderate production of ROS even without NIR irradiation. In PDT conditions, ROS was intensively generated, and the highest ROS production rate was observed in dual therapy conditions, demonstrating the synergistic effect of the combined treatment. In the dark, no cytotoxicity was observed. In the presence of colonic enzymes (chemotherapy conditions), CSGUR-MSGG/5FU NPs induced cell death in 22.5% of cells, and in 34.3% under NIR irradiation (PDT conditions), whereas combination therapy (enzymes + NIR) induced cell death in 74.8% of cells, confirming the synergistic effect of the dual treatment.

Sun et al. [36] synthesized Barium-Titanate NPs (BT) with RB (BT-RB NPs). The BT-RB NPs were capsulated with PAH (poly(allylamine hydrochloride). An NP size of 70 nm was determined using TEM. All in vitro experiments were performed on HeLa cells. First, they studied the cellular uptake of the NPs by comparing four different groups: RB alone, BT NPs, mixture of BT NPs with RB, and BT-RB NPs. Both SHG (second harmonic generation) and fluorescence signals were observed in the case of BT-RB NPs, confirming its cellular uptake. Intracellular ROS detection was performed using ABDA. It was shown that BT-RB NPs produced more ROS compared to RB alone, BT alone, or a mixture of RB + BT NPs. They conducted an in vitro cytotoxicity assay and demonstrated that BT-RB NPs did not induce dark cytotoxicity.

Song et al. [37] developed $Nd^{3+}/Yb^{3+}/Er^{3+}$-doped UCNPs co-encapsulated with Ag_2Se quantum dots (QDs) and RB into phosphatidylcholine (UCQRs). Ag_2Se QDs enhanced the photoluminescence of the upconversion system, which was excited at 808 nm and was able to perform resonance energy transfer (RET) to Yb^{3+} to improve UCL. The diameter of the UCQRs was 62.57 nm. The UCL of the UCQRs was quenched by 75% with respect to NPs-QDs without RB, demonstrating the energy transfer between the NPs and the RB. The $^1O_2$ generation capacity of the UCQRs was determined using an ABDA probe and a DCFH-DA probe in vitro. An in vitro viability assay was carried out using HeLa and HCT1116 cells incubated for 24 h with UCQRs (400 mg/mL) with or without light irradiation at a wavelength of 808 nm (1.6 W/cm^2, 10 min). Without irradiation, a viability of 85% was observed, compared to 10% with irradiation, at a concentration of 400 µg/L. In vivo PDT efficacy was determined using two mouse models: Lewis lung carcinoma tumor-bearing mice and 4T1 tumor-bearing mice. For the first model, intratumoral injection was performed, while intravenous injection was performed for the second mouse model. There were five groups: injected with PBS and

irradiated at a wavelength of 808 nm (1.6 W/cm^2, 10 min), UCQRs, UCRs with irradiation, and UCQRs (10 mg/mL) with irradiation. Tumor growth was greatly inhibited in mice treated with UCQRs with irradiation, whereas a moderate therapeutic effect could be observed for the fourth group, injected with NPs without QDs (**Figure 83a**). Body weight and tumor growth were monitored for 16 days **(Figure 83b**).

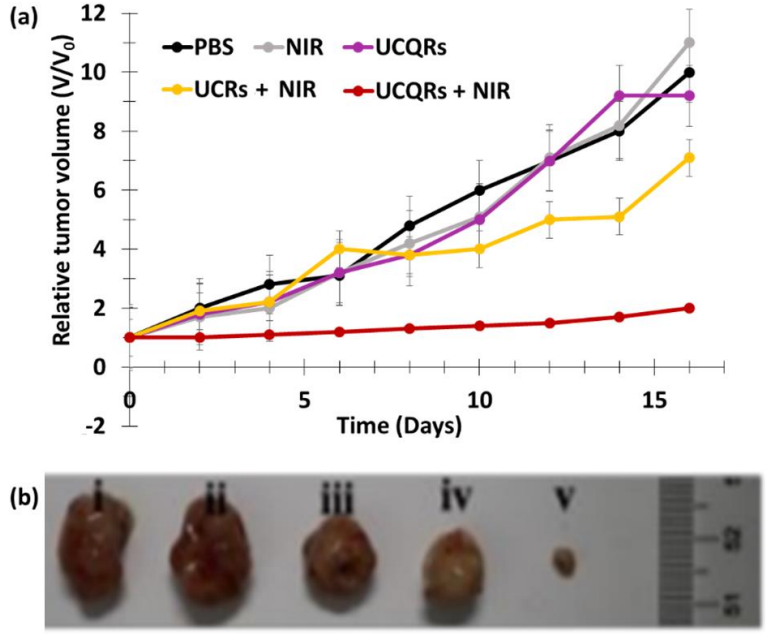

Figure 83 : (a) Relative tumor volume obtained from mice with various treatments. (b) Representative photographs of the corresponding excised tumors (i—PBS, ii—NIR, iii—UCQRs (10 mg/mL, 40 µL), iv—UCRs+NIR (10 mg/mL, 40 µL), and v—UCQRs+NIR) (10 mg/mL, 40 µL). NIR irradiation (808 nm, 1.6 W/cm^2, 10 min). Figure (a) adapted from Song et al. [37]. Figure (b) reprinted from Song et al. [37]. Copyright 2019 American Chemical Society.

Wawrzyńczyk et al. [38] developed smart and multifunctional nanocarriers (NCs) for theranostic applications. Co-encapsulation of Span 80 micelles containing RB and $NaYF_4:Er^{3+},Yb^{3+}$(Er/Yb:2/20) UCNPs in NCs was performed using a double core composed of a non-ionic surfactant Rosalfan A and poly(lactide-co-glycolide) (PLGA). A coron of cationic chitosan and PEG-HA was added to provide stealth and targeting properties. A hydrodynamic size of 154 ± 5 nm was measured for the (PEG-HA-NCs)-$NaYF_4:Er^{3+},Yb^{3+}$ + RB of. TEM images clearly showed NCs with a diameter of 150 nm loaded with UCNPs with an average diameter of 8 ± 3 nm. The determination of $^1O_2$ generation was performed using ABMDMA (9,10-Anthracenediyl-bis(methylene)dimalonic acid). No in vitro or in vivo tests were performed.

Wang et al. [39] designed FA/UCNPs-RB/HCPT/PFH@Lipid (named FURH-PFH-NPs) for multimodal imaging and combination therapy. These NPs were composed of a lipid shell modified with FA to target ovarian cancer cells, loaded with 10-hydroxycamptothecin (HCPT) with 72.6% encapsulation efficiency (EE) of HCPT in FURH-PFH-NPs, a cytotoxic drug for chemotherapy and UCNPs-RB for fluorescence imaging and PDT. RB was covalently coupled to UCNP via the classical EDC/NHS method to allow efficient FRET. In the shell, the core was composed of perfluorohexane (PFH), which is able to catch and release oxygen in order to prevent hypoxia in solid tumors (**Figure 84**).

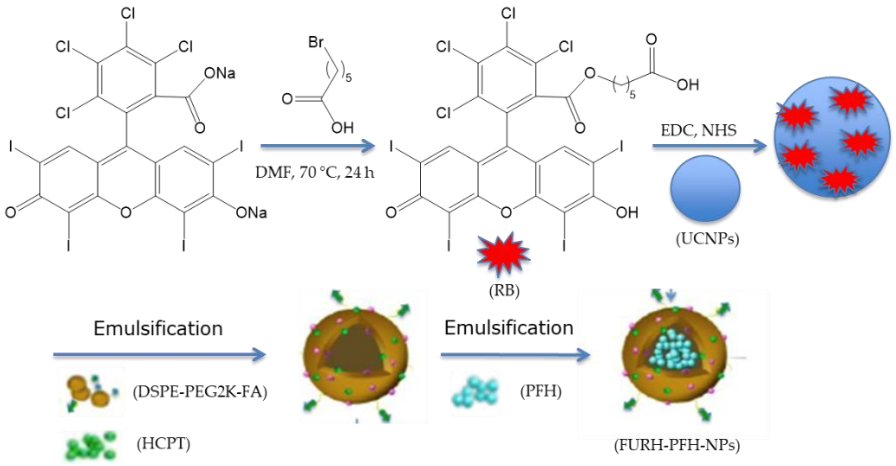

Figure 84 : Preparation of FURH-PFH-NPs. Adapted from Wang et al. [39].

The size of the NPs was measured on the basis of TEM images, and was found to be 223.6 ± 68.86 nm. $^1O_2$ formation was detected with DPBF. The low-intensity focused ultrasound (LIFU) technique was used to trigger the release of UCNPs-RB, oxygen, and HCPT. In fact, the PFH liquid enters liquid–gas transition state under irradiation, increasing the size of the particles and inducing ruptures in the NPs (2 W/cm^2, 2 min). Laser irradiation at 980 nm for 2 min was used at 2 W/cm^2 for DPBF, and 0.2 W/cm^2 for other tests. In vitro assays were performed using SKOV3 cells with FURH-PFH-NPs, demonstrating killing of 69.02 ± 1.42% of the total number of cells. SKOV3 cell apoptosis was observed in the presence of FURH-PFH-NPs (100 µg/mL) irradiated with LIFU or laser (approximatively 25%). Irradiation with LIFU + laser increased cell apoptosis to 42.8%. The PDT effect of FURH-PFH-NPs in SKOV3 cells was then evaluated. DCFH-DA was used as a green fluorescence indicator of ROS production. Fluorescence was observed for cells irradiated with LIFU or laser. The fluorescence was even more intense under LIFU + laser, showing the synergistic effect of oxygen and HCPT release by LIFU and PDT using RB. In vivo assays were performed on SKOV3 tumor-bearing mice. To determine the synergistic effect of HCPT (cytotoxic drug loaded in NPs and PDT), four groups of mice were employed: (1) saline + LIFU + laser, (2) HCPT + LIFU + laser, (3) FURH-PFH-NPs + laser, and (4) FURH-PFH-NPs + LIFU + laser. LIFU and laser treatments were performed every day for 28 days. No tumor growth inhibition was observed in groups 1 and 2. Tumor growth inhibition rate of 77.31% was observed for group 3, while an inhibition rate of 92.35% was observed for group 4, demonstrating a significant synergistic antitumoral effect (**Figure 85**).

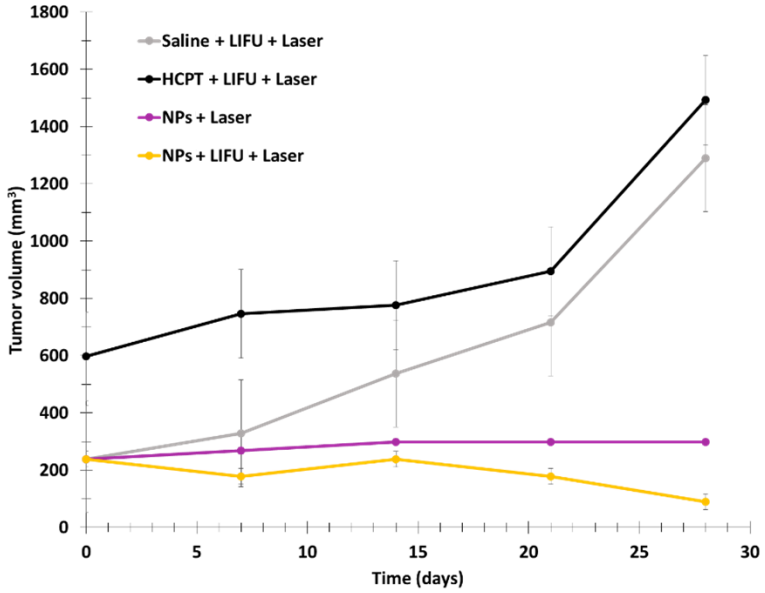

Figure 85 : Tumor growth of four groups of SKOV3 tumor-bearing mice treated with different conditions. Laser irradiation (980 nm, 2 W/cm², 2 min). Adapted from Wang et al. [39].

Li et al. [40] designed multi-shelled UCNPs (MUCNPs) for activable PDT. $NaYF_4$:Gd@$NaYF_4$:Er,Yb@$NaYF_4$:Nd,Yb (Y/Yb/Er:78/20/2) covalently modified with antenna 800 CW for NIR irradiation luminescence enhancement, RB for ROS generation, cyanine 3 (Cy3) for fluorescence imaging and pep-QSY7 (peptide labeled with a QSY7 quencher) for ROS generation quenching. Cathespin B (CaB), a lysosomal protease overexpressed in many cancers, could hydrolyze the peptide, releasing QSY7 quencher, which could activate RB and Cy3 for PDT and fluorescence imaging. MUCNPs/800WC/RB/Cy3/pep-QSY7 had a hydrodynamic diameter of 56.1 ± 1.0 nm. Energy transfer from MUCNPs to Cy3 was demonstrated by the suppression of the MUCNPs peak at 540 nm. The luminescence lifetime of the MUCNPs decreased from 118 µs without Cy3 to 77 µs with Cy3, confirming RET. $^1O_2$ generation was detected with DPBF (808 nm, 1.5 W/cm^2). No ROS was produced by MUCNPs/800WC/RB/Cy3/pep-QSY7, demonstrating the efficient quenching ability of RB and Cy3. In the presence of CaB, ROS generation was almost the same as for MUCNPs/800WC/RB/Cy3, demonstrating the catalytic cleavage of pep by CaB and the activatable PDT. A cytotoxicity assay was performed with HeLa and MCF-7 cells overexpressing CaB and NIH 3T3 as a negative control (6 h incubation, 808 nm, 1.5 W/cm^2 for 40 min). After 48 h, cell viabilities of 21.6, 26.0 and 91% were observed for HeLa, MCF-7, and NIH 3T3, respectively, demonstrating the therapeutic effect of MUCNPs/800WC/RB/Cy3/pep-QSY7. In vivo experiments were conducted using HeLa tumor-bearing BALB/c nude mice. Four groups were employed: groups 1 and 2 were used as a control with saline injection, and groups 3 and 4 were injected with MUCNPs/800WC/RB/Cy3/pep-QSY7 (300 µg/mL). Groups 2 and 4 were irradiated six times at a wavelength of 808 nm at 1.0 W/cm^2 for 40 min during the 14 days of the experiment, and no body weight fluctuation was observed (**Figure 86b**). Tumor growth inhibition was clearly observed for group 4 only, demonstrating the suitability of MUCNPs/800WC/RB/Cy3/pep-QSY7 for activatable PDT (**Figure 86a,c**).

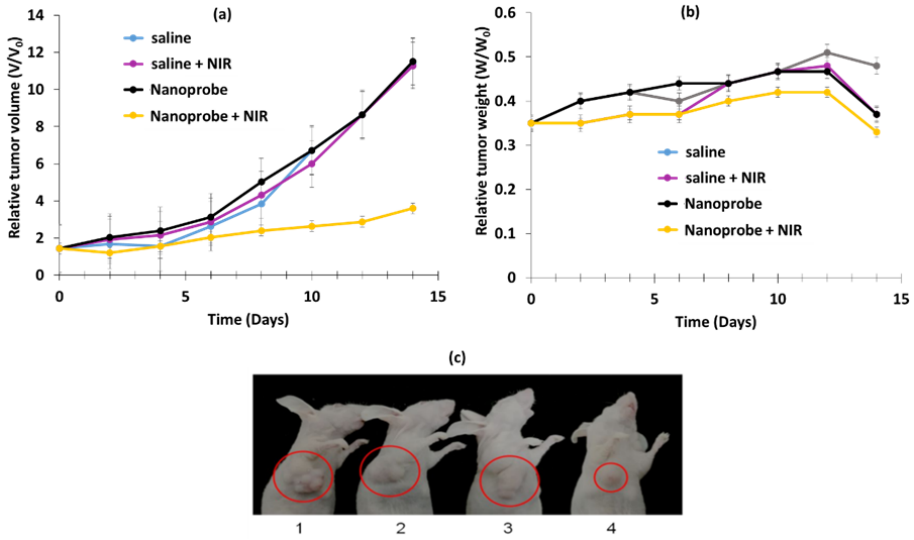

Figure 86 : Four groups of HeLa tumor-bearing BALB/c nude mice. (a,c) Relative tumor volume, (b) relative tumor weight when treated with (1) saline, (2) saline + NIR, (3) nanoprobe, (4) nanoprobe + NIR. NIR laser irradiation (808 nm, 1.0 W/cm^2, 40 min). The nanoprobe was MUCNPs/800WC/RB/Cy3/pep-QSY7. [Nanoprobe] = 300 µg/mL. Figures (a) and (b) adapted from Li et al. [40]. Figure (c) reprinted with permission from Li et al. [40]. Copyright 2020 American Chemical Society.

Han et al. [41] designed core–shell–shell NPs loaded with RB and methylene blue (MB) and DOX for dual pH-responsive chemotherapy and PDT. The UCNP core $NaYF_4$:Yb/Ho/Nd@$NaYF_4$:Nd was first shelled with silica containing MB, and second with boronic acid RB and DOX. Finally, cyclodextrin (CD) was conjugated onto the NP surface to obtain final NPs called DOX-RB-NH_2-UCMS-BA-CD. In the acidic environment of cancerous cells, the CD could be dissociated from the NPs, inducing the release of DOX for chemotherapy. The hydrodynamic diameter was 130 nm. $^1O_2$ production of NPs was observed using an ABDA probe, and NPs were irradiated at a wavelength of 808 nm, 0.5 W/cm^2, for 5 min. The NPs without MB and the NPs without RB showed no generation of $^1O_2$, but RB-MB-NPs showed the best $^1O_2$ production efficacy, highlighting a synergistic effect of the two PSs. The pH-responsive release of DOX was evaluated under pH values of 7.4, 5 and 3. After 24 h incubation of DOX-RB-NH_2-UCMS-BA-CD at different concentrations (0, 30, 60, 120 and 240 µg/mL), no significant DOX release was observed at physiological pH, whereas 61% release was observed at pH 5, confirming pH-responsive drug release. ROS generation was observed in HeLa cells incubated with NPs (100 mg/mL) under irradiation (808 nm, 0.5 W/cm^2, 10 min) thanks to DCFH-DA probe. A cytotoxicity assay was performed on HeLa cells incubated with RB-NH_2-UCMS-BA-CD (0.5 mg/mL). In the dark, no cell death was observed, confirming the biocompatibility of the NPs. Cell viability decreased to 64% and 55% when incubated with DOX-RB-NH_2-UCMS-BA-CD and RB-NH_2-UCMS-BA-CD, respectively, and irradiated at a wavelength of 808 nm, confirming their chemotherapeutic and PDT efficiency. Cell viability decreased by 95% with DOX-RB-NH_2-UCMS-BA-CD under light irradiation, demonstrating the significant synergistic effect of dual therapy. The efficiency of dual therapy was evaluated in vivo: six groups of HeLa tumor-bearing mice were employed: (1) control, (2) 808 nm irradiation for 5 min at 0.5 W/cm^2, (3) DOX-RB-NH_2-UCMS-BA-CD, (4) chemotherapy, (5) PDT, (6) chemotherapy + PDT. PDT was more efficient than chemotherapy, as tumor growth inhibition was higher for PDT. Moreover, the dual

chemotherapy and PDT group showed the best tumor growth inhibition, owing to the synergistic effect of the two treatments. No body weight loss was observed in the six groups, confirming the biocompatibility of the NPs and the non-toxic treatment (**Figure 87a,b**).

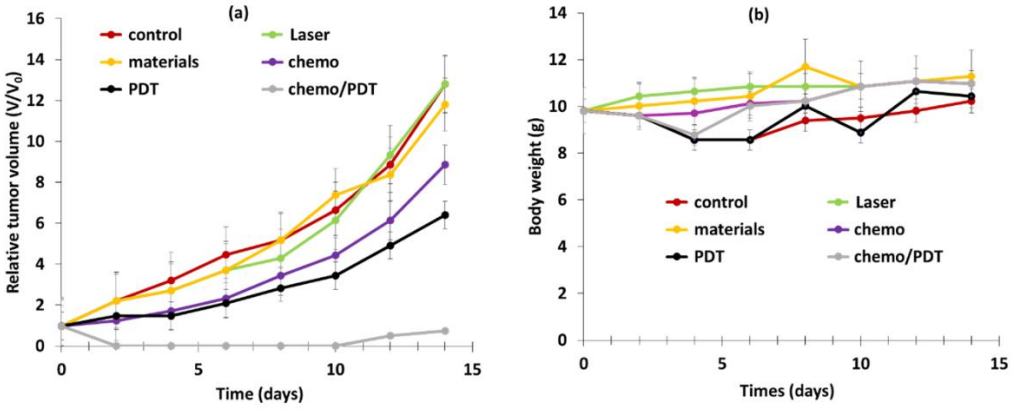

Figure 87 : (a) Relative tumor volume and (b) body relative weight of 6 groups of HeLa tumor-bearing mice under various conditions: control, laser (808 nm irradiation and 0.5 W/cm^2 for 10 min), DOX-RB-NH2-UCMS-BA-CD chemotherapy, PDT, chemotherapy + PDT. Adapted from Han et al. [41].

Jin et al. [42] designed SPTP@UCNP-RB-DOX NPs for dual chemotherapy and PDT. The β-$NaYF_4$:Yb/Er (Y/Yb/Er: 20/78/2) UCNP core was shelled with SPTP and loaded with RB and DOX. SA-PEG-TK-PLGA (SPTP) was composed of PLGA, a thioketal group, and sialic acid, targeting E-selectin, which is overexpressed on the surface of tumor cells, linked to the thioketal group by a PEG linker. Under NIR irradiation, UCNPs were able to activate RB via RET and produce $^1O_2$. A part of the ROS production was used to cut the thioketal group in two in order to induce self-destruction of the SPTP micelles and to release DOX into the tumor environment (**Figure 88**).

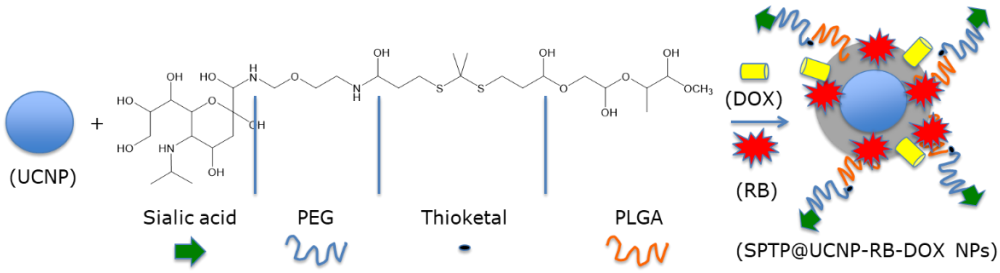

Figure 88 : Illustration of the synthesis of the SPTP@UCNP-RB-DOX NPs. Adapted from Jin et al. [42].

The hydrodynamic diameter of these NPs was 54.3 nm. DPBF probe was used to visualize the NIR (980 nm, 0.5 W/cm^2, 5–10 min)-controlled ROS generation of SPTP@UCNP-RB-DOX, confirming the RET ability between UCNPs and RB. Regarding chemotherapy, a 20% release of DOX after 14 h was observed without irradiation, whereas DOX release of 70% was observed under NIR irradiation, confirming the good self-destruction and drug release of the NPs. Incubation of 4T1 cells with SPTP@UCNP-RB-DOX and PTP@UCNP-RB/DOX revealed better cell uptake for the NPs containing sialic acid, demonstrating the ability of these NPs to target E-selectin owing to the presence of sialic acid. SPTP@UCNP-RB and STPT@UCNP-DOX (250 µg/mL) demonstrated no cytotoxic activity without irradiation,

whereas cell death of 47.2% and 24.5%, respectively, was observed under 980 nm irradiation (0.5 W/cm^2, 6 min). For SPTP@UCNP-RB-DOX, cell death of 19.6% was observed in the dark due to uncontrolled drug release, whereas cell death of 73.1% was observed under NIR irradiation. Thus, the combination of chemotherapy and PDT was more efficient than chemotherapy or PDT alone. A higher accumulation of NPs in the tumor was observed for SPTP@UCNP-RB-DOX, which had a better tumor targeting ability. Chemo-PDT efficiency was evaluated using 4T1 tumor-bearing TNBC mice. Eight groups of mice were employed: (1) saline, (2) NIR (980 nm, 0.5 W/cm^2 for 10 min), (3) DOX, (4) SPTP@UCNP-RB, (5) SPTP@UCNP-RB + NIR, (6) SPTP@UCNP-RB-DOX, (7) PTP@UCNP-RB-DOX + NIR, and (8) SPTP@UCNP-RB-DOX + NIR. Tumor growth was observed in groups 1, 2 and 4. Groups 3, 5 and 7 showed moderate tumor growth inhibition, and group 8 showed high tumor growth inhibition, demonstrating the high efficiency of PDT and chemotherapy, especially for dual application of chemotherapy and PDT. The survival rate of group 8 was the highest, confirming the efficiency of the treatment. (**Figure 89**).

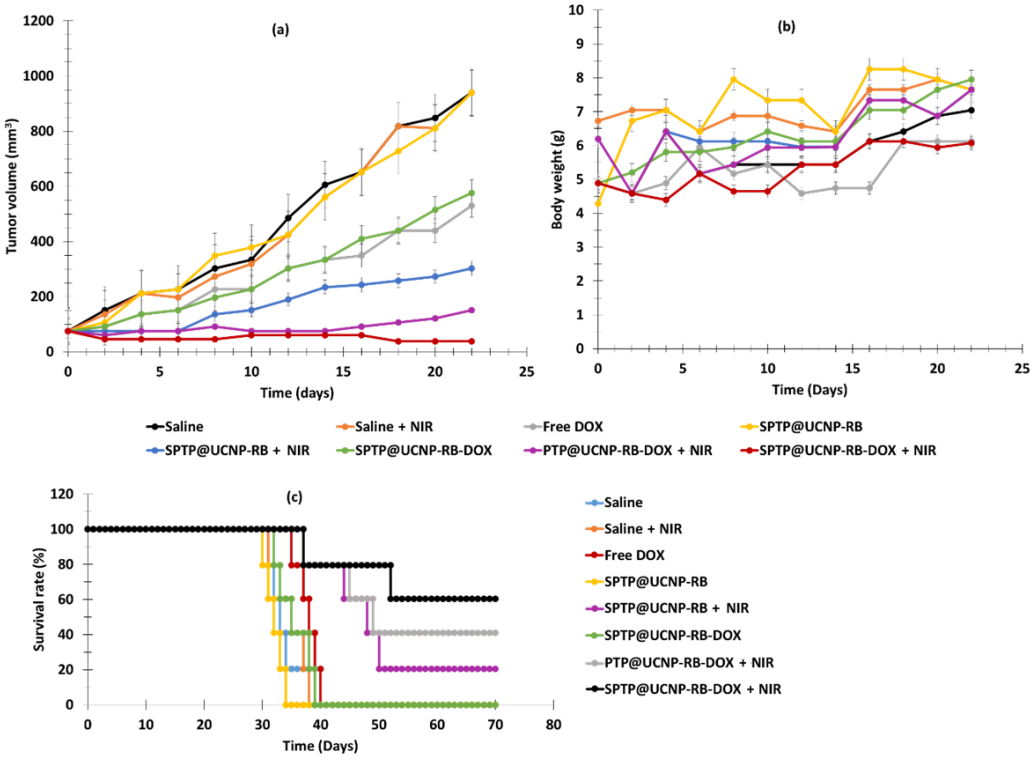

Figure 89 : In vivo antitumor effect. (a) Tumor volume for different treatment groups (n = 6). (b) Change in body weight of mice over 23 days. (c) Changes in survival rate in different groups. Light irradiation at a wavelength of 980 nm, 0.5 W/cm^2, for 5–10 min (SPTP: 50 μg/mL, DOX: 2.5 μg/mL and RB: 2.5 μg/mL). Adapted from Jin et al. [42].

Li et al. [43] also developed UCNPs based on Nd^{3+} metal ions consisting of electrostatically self-assembled core–satellite structures with single MOF NPs as the core and UCNPs (i.e., $NaGdF_4$:Yb,Er@$NaGdF_4$:Nd,Yb ; Gd:Yb:Nd = 5:1:4) as the satellite. The high porosity of MOF NPs allowed a high co-loading (i.e., loading efficiencies in weight ≈ 11%) of chlorin e6 (Ce6) and RB, producing a CR@MU nanotheranostic platform. The biocompatibility and biostability were improved by PEGylation of CR@MU (i.e., CR@MUP, hydrodynamic size of 216.0 ± 7.3 nm). In vitro and in vivo experiments were carried out on 4T1 cells and 4T1

tumor-bearing mice irradiated by the 808 nm laser (1 W/cm^2 and 1.25 W/cm^2 for in vitro and in vivo, respectively, for 5 min). These experiments highlighted the ability of the non-cytotoxic CR@MUP to exert a synergistic PDT effect under excitation at a wavelength of 808 nm (i.e., with a spectral overlap between UCNP emission and Ce6 and RB absorption). The cell viability at a concentration of 200 µg/mL under 808 nm excitation was very low (on the order of 10%). In addition, this was used as a trimodal imaging platform (i.e., UCNPs as MR and UCL maging agents, and Ce6 as a fluorescence imaging agent).

Borodziuk et al. [44] synthesized UCNPs ($NaYF_4$:Er,Yb (Er/Yb: 2/20)) with a diameter of 34.2 ± 3.1 nm. These UCNPs were coated with SiO_2, increasing the diameter of the UCNPs to 41.1 ± 4.7 nm. The UCNPs@SiO_2 NPs were covalently coupled to RB. A FRET between the NPs and RB was confirmed. The test in solution with DPBF confirmed the production of $^1O_2$. A Presto Blue viability assay was applied in vitro on 4T1 cells. After 1 and 24 h of incubation with UCNPs@SiO_2-RB NPs (250 µg/mL) in 4T1 cells, and following irradiation using 2 W/cm^2 for 10 min at a wavelength of 980 nm, cell viability decreased by 40% compared to the cells irradiated without incubation with NPs, indicating a decrease in ROS production by 60%.

Tezuka et al. [45] successfully synthesized an ultra-small biodegradable spherical UCNP (UC), $NaYF_4$:Yb^{3+},Er^{3+} (Yb/Er:18/2 in mol), and a hydrocarbonized RB dye (C_{18}RB). The UCNP and C_{18}RB were encapsulated in the hydrophobic core of the PEG-block-poly(ε-caprolactone) (PCL) micelle. The hydrodynamic diameter was 9.0 ± 3.2 nm. $^1O_2$ production was confirmed by DPBF probe. In vitro tests on cancer cells following 980 nm irradiation (2 W/cm^2 for 30 min) showed an increase in cytotoxicity with increasing RB concentration. Moreover, it is quite remarkable that RB alone was much more toxic than RB and C_{18}RB in HNPs (i.e., PEG-C_{18}RB-UCNPs). Then, the cell viability was compared between HNPs and the controls; HNPs under irradiation were the most toxic to cancer cells. Encapsulation of C_{18}RB with PEG-b-PCL in the hybrid NPs decreased the cytotoxicity of the dye without irradiation. Thus, NIR irradiation showed a PDT effect via the generation of $^1O_2$, decreasing the viability of deep cancer cells.

Table 15 summarizes the physical–chemical properties and PDT conditions for all references dealing with UCNP@RB.

Table 15 : Table summarizing all references dealing with UCNP@RB, including type of NPs, along with their size, excitation wavelength, type of detection of $^1O_2$, type of coupling between the NPs and the RB, and an indication of the type of biological tests performed.

PDT UCNPs									
References	**Type of NPs**	**Size of NPs (nm)**	**Irradiation Conditions**	**Type of $^1O_2$ Detection**	**Type of Coupling NP-RB**	**Biological Tests/In Vitro**		**Biological Test/In Vivo**	
						Cells Used	**Results**	**Mice Used**	**Results**
[20]	UCNPs@RB@FA-($NaYF_4$:Yb^{3+}, Er^{3+})	20 without RB	980 nm, 1.5 W/cm^2, 10 min	DPBF	Covalent	JAR NIH 3T3	Cytotoxicity (+)	nd	nd
[25]	UCNPs-RB	25 without RB	In vitro: 0.8 W/cm^2, 8 min In vivo: 808 nm, 520 mW/cm^2	DPBF	Covalent	4T1	Cytotoxicity (+)	4T1 breast cancer bearing mice	PDT (+)
[21]	UCNP@BSA-RB&IR825	60	980 nm, 0.4 W/cm^2 in vitro: 10 min in vivo: 30 min	SOSG	Encapsulation	4T1	Cytotoxicity (+)	4T1 tumor-bearing mice	PDT (+)
[43]	Er@Nd-RB Upconversion	216	808 nm laser (in vitro: 1 W/cm^2, in vivo: 1.25 W/cm^2), 5 min	DCFH-DA	Encapsulation	4T1 ~~cells~~	Cytotoxicity (+)	4T1 tumor-bearing mice- Healthy BALB/c	PDT (+)
[37]	UCNP@BSA-RB&IR825	16	In vitro: 808 nm, ~~,~~ 0.75 W/cm^2, 5 min In vivo: 808 nm, ~~15~~ 0.95 W/cm^2, 15 min	ABDA	Encapsulation	HeLa HCT116	Cytotoxicity (+)	4T1 tumor-bearing mice	PDT (+)
[29]	UCNPs-RB&ZnPc	24–32	980 nm, 0.25	DPBF	Encapsulation	A549	Cytotoxicity (+)	Hepa1-6 tumor-	PDT (+)

			W/cm^2, 15 min					bearing mice	
[30]	Nd^{3+}/Yb^3 UCNPs with Ag_2Se QD	120	980 nm, 2.0 W/cm^2, 10 min	ABDA	Covalent	HeLa	Cytotoxicity (+)	nd	nd
[28]	$NaYF_4$: 20%Yb^{3+}, 2% Er3+@ $NaYF_4$	29	980 nm, 0.5 W/cm^2, 10 min	DPBF	Covalent	NET	Cytotoxicity (+)	TT-tumor-bearing mice	PDT (+)
[27]	UCN@mSiO$_2$-(Azo + RB)	35.9	808 nm, 6 W/cm^2, 5 min	DPBF	Covalent	A2780 A2780cisR	Cytotoxicity (+)	nd	nd
[26]	PNBMA-PEG@ RB@AB3@ KE108	29	980 nm, 1.5 W/cm^2, 30 min	DPBF	Adsorption	HT-29	Cytotoxicity (+)	Mouse anti-human CD326 (EpCAM) (clone HEA-125)	PDT (+)
[22]	RB-UPPLVs	40	980 nm, 2.5 W/cm^2, 20 min	ABDA	Encapsulation	HeLa	Cytotoxicity (+)	nd	nd
[23]	$NaYF_4$:Yb/Ho@$NaYF_4$:Nd@$NaYF_4$	0.4 to 4.2	808 nm, 0.67 W/cm^2, 10 min	DPBF	Covalent	HeLa	Cytotoxicity (+)	nd	nd
[42]	SPTP@UCNP-RB-DOX	54.3	980 nm, 0.5 W/cm^2, 5–10 min,	DPBF	Adsorption	4T1	Cytotoxicity (+)	TNBC	PDT (+)
[35]	CSGUR-MSGG/5FU @RB@FA	72.3	980 nm, 30 min	DPBF	Covalent	HT-29	Cytotoxicity (+)	nd	nd
[40]	STPT@UCNP-RB-DOX	56.1 ± 1.0	808 nm, 1.5 W/cm^2, 40 min	DPBF	Covalent	HeLa MCF-7 NIH 3T3	Cytotoxicity (+)	BALB/c nude mice with HeLa tumor.	PDT (+)
[39]	FA/UCNPs-RB/HCPT/PFH@Lipid	223.6 ± 68.8	980 nm, 0.2 W/cm^2, 2 min	DPBF	Covalent	SKOV-3	Cytotoxicity (+)	SKOV3 tumor-bearing mice	PDT (+)
[41]	$NaYF_4$:Gd@ $NaYF_4$:Er,Yb@$NaYF_4$:Nd,Yb NPs @	130	808 nm, 0.5 W/cm^2, 10 min	ABDA	Covalent	HeLa	Cytotoxicity (+)	HeLa tumor-bearing mice	PDT (+)

	RB, Cy3 and pep-QSY7								
[37]	FA/UCNPs-RB/HCPT/PFH@Lipid	62.57 without RB	808 nm, 1.6 W/cm^2, 10 min	ABDA	Encapsulation	HeLa	Cytotoxicity (+)	Lewis lung carcinoma (LLC) tumor-bearing mice	PDT (+)
[36]	BT@PAH/RB/PAH, BT–RB	70	532 nm, 30 mW/cm^2, 3 min	DPBF	Loading	HeLa	Cytotoxicity (+)	nd	nd
[34]	Nd^{3+}/Yb^3 UCNPs) with Ag2Se QDs, RB	150	808 nm, 0.5 W/cm^2, 10 min	DPBF	Encapsulation	HeLa	Cytotoxicity (+)	tumor-bearing BALB/c mice	PDT (+)
[33]	Barium titanate NPs	23.7 without RB	980 nm, 200 mW/cm^2, 6 min	ABDA	Covalent	SK-BR-3	Cytotoxicity (+)	nd	nd
[32]	$NaGdF_4$:Yb^{3+}/Er^{3+}@BSA@RB	78	980 nm, 13 W/cm^2, 10 min	DPBF	Covalent	A549	Cytotoxicity (+)	nd	nd
[31]	$NaYF_4$:Yb,Er,Gd@$NaYF_4$@ SiO_2-RB	91	980 nm, 2.5 W/cm^2, 20 min	DPBF	Adsorption	HeLa	Cytotoxicity (+)	nd	nd
[44]	$NaGdF_4$:Yb^{3+}/Er^{3+} @ RB	41.1	980 nm, 2 W/cm^2, 10 min	DPBF	Covalent	4T1	Cytotoxicity (+)	nd	nd
[45]	PEG-block-Polymer/C18RB/$NaYF_4$:Yb^{3+}/Er^{3+}	8.7	980 nm, 2W/cm^2, 30 min	DPBF	Encapsulate	Colon-26	Cytotoxicity (+)	nd	nd
[32]	$NaYF_4$:2%Er,20%Yb)@ SiO_2 -RB	78	980 nm, 13 W/cm^2, 10 min	DPBF	Covalent	A549	Cytotoxicity (+)	nd	nd
[24]	UCNP@OS@RB	27	980 nm, 0.5 W/cm^2, 10 min	DPBF	Adsorption	HT1299	Affinity and Cytotoxicity (+)	nd	nd

nd: not determined; cytotoxicity (+): induced tumor cell death in vitro; PDT (+): induced tumor death in vivo.

II.2 Silica Nanoparticles

Under standard biological conditions, suspensions of silica NPs are stable if the salt concentration is low, but precipitate when this concentration increases beyond a critical threshold. Silica NPs are therefore all the more stable when the environment contains few salts and proteins, when they are few in number and larger in diameter, and when their surface is grafted by adequate groups. The mechanism of endocytosis, although it may differ from one cell line to another, always seems to be an active process, and the internalization of silica NPs is mainly done by clathrin or caveolae [46]. In addition, silica has the ability to combine imaging and contrast agents [47]. This has been used, for example, to incorporate or chelate rare earths (lanthanides) in these NPs [48].

Uppal et al. [49] synthesized silica NPs (SiNP) covalently or electrostatically coupled to RB (i.e., RB-SiNP electrostatic or covalent complexes, respectively). SiNP and the RB-SiNP electrostatic complex had similarly sized (35 ± 5 nm), while the size of the RB-SiNP covalent complex increased to 50 ± 5 nm. $^1O_2$ production was confirmed by SOSG probe. Cytotoxicity tests were performed on two different MCF-7 and 4451 cells at three concentrations of RB (10, 15 and 24 µM). With increasing concentration, cytotoxicity increased. Dark cytotoxicity was very low. The cytotoxicity on MCF cells at a wavelength of 480 nm for 1 h reached 87% for the RB-SiNP covalent complex NPs at a concentration of RB = 24 µM, and 94% under the same conditions in 4451 cells. The RB-SiNP electrostatic complex with a concentration of RB = 24 µM showed a cytotoxicity of 55% and 40%, respectively. The RB-SiNP covalent complex was more cytotoxic than the electrostatic complex.

Gianotti et al. [50] described the elaboration of mesoporous silica NPs (MSNs) with a size of 160–180 nm covalently coupled to RB through an amide bond. The average amount of RB per NP was about 4.20×10^4. They evaluated Φ_Δ using uric acid, and found a value of 0.74 in water. In vitro experiments were performed on melanoma cellular model (SK-MEL-28) with green light (green light, 5 min). Cell proliferation after 5 h incubation was 64.10 ± 8.79 cells/mm^2 in tumor-bearing mice in the absence of light and 47.85 ± 13.48 in presence of light. This diminution in cell proliferation confirmed the importance of PDT in melanoma treatment.

Martins Estevão et al. [51] incorporated RB into MSNs (with an average size of 150–180 nm) to optimize the efficiency of $^1O_2$ generation when illuminated with 540 nm green light (450 W Xenon lamp, 80 min). MSNs were functionalized using cetyltrimethylammoniumbromide (CTAB). No biological experiments were performed.

Adem et al. [52] proposed MSNs based on CTAB and RB (rMSN-ts). The length of rMSN-ts was 119 nm, and they had a width of 86 nm. In vitro experiments were performed in MCF-7 cells, and after incubation for 4 h with rMSN-ts (100 µg/mL), cell viability decreased from 100% to 25% with the application of green laser light irradiation (5 mV) for 30 min.

Liu et al. [53] designed polyglycerol MSNs with adsorbed FITC and RB (namely, FITC-PGSN-RB; average size of 100 nm) for two-photon-activated PDT. Two-photon-activated (TPA) dye-doped MSNs were synthesized using TEOS as a surfactant (**Figure 90**).

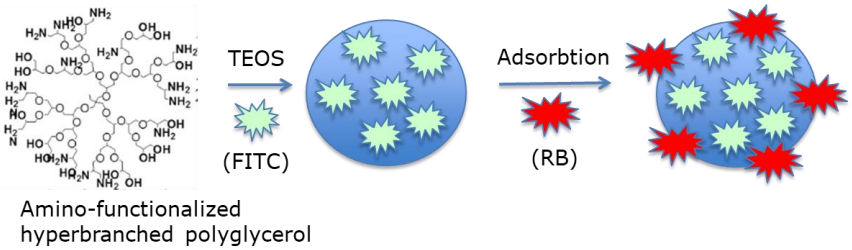

Figure 90 : Preparation of polyglycerol MSNs with adsorbed fluorescein isothiocyanate (FITC) and RB. Adapted from Liu et al. [53].

After 10 min irradiation with a two-photon laser (100 W xenon lamp) of HeLa cells incubated for 4 h with FITC-PGSN-RB (0.5 mg/mL), cell viability decreased to 30%.

Zhou et al. [54] synthesized $NaYF_4$:Yb, Er (Y:Yb:Er = 78:20:2) as UCNPs, surrounded by a silica shell (SiO_2) covalently coupled to RB, on which poly-(1,4-phenyleneacetone dimethylenethioketal) (PPADT) was self-assembled as a second outer shell contains the NPs and DOX. The size of UCN/SiO_2-RB was 38.2 ± 3.6 nm without DOX and PPADT. $^1O_2$ production was confirmed using ABDA. During NIR laser irradiation (980 nm, 1.0 W/cm^2, 20 min), DOX release was induced, with 40% of the DOX being released after 12 h of irradiation of (A + DOX)@PPADT. The $^1O_2$ production under NIR laser irradiation caused the biodegradation of the polymer and the release of DOX into the tumor. In vitro tests were performed on HeLa cells, and cell viability decreased to 25% and 15% for cells treated with 100 mg/mL and 200 mg/L (A + Dox)@PPADT, respectively, following NIR laser irradiation. This decrease was less significant in cells treated with A and A@PPADT, noting that cell viability was higher following treatment with A@PPADT than with A (**Figure 91**).

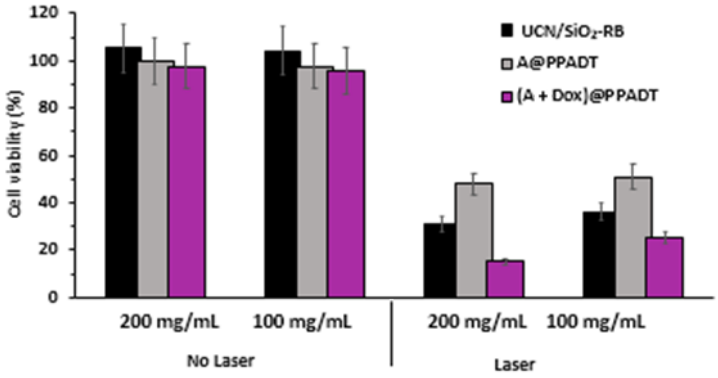

Figure 91 : Viability of HeLa cells incubated with UCN/SiO_2-RB, A@PPADT or (A + DOX)@PPADT) (100 and 200 µg/mL) with or without laser irradiation (980 nm, 1.0 W/cm^2, 20 min). Adapted from Zhou et al. [54].

Custodio de Souza Oliveira et al. [55] compared the efficiency of SiO_2 NPs functionalized with 3-(2-aminoethylamino)propyl groups (SiNP-AAP) either with covalently bound RB (SiNP-AAP-RB) or 9,10-anthraquinone-2-carboxylic acid (SiNP-AAP-OCAq) against human lung carcinoma A549 cells. Cell viability following incubation with SiNP-AAP-RB (50 µM) for 24 h decreased by approximately 80% under laser irradiation (410 nm, 1.6 J/cm^2, 15 min). Although RB alone showed very high photoxity, NPs coupled to RB allowed passive targeting.

Zhan et al. [56] synthesized a magnetic mesoporous silica NP (MMSN): (poly-ethylene glycol-b-polyaspartate-modified RB-loaded magnetic mesoporous silica Fe_3O_4@nSiO_2@mSiO_2@RB@PEG-*b*-PAsp (RB-MMSNs). Fe_3O_4 served as the magnetic core, and could be useful for application in contrast agents. nSiO_2 and mSiO_2 were added, respectively, to avoid Fe_3O_4 oxidation and for RB loading. Polyethylene glycol-*b*-poly(aspartic acid) (PEG-*b*-PAsp) was coupled for its pH-responsive properties. RB was pre-loaded on previously prepared Fe_3O_4@nSiO_2@mSiO_2 NPs (MMSNs), before grafting of PEG-*b*-PAsp (**Figure 92**).

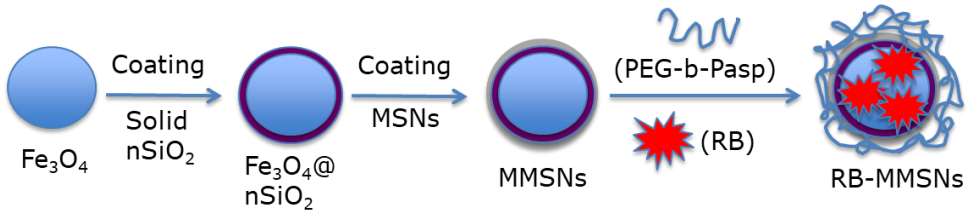

Figure 92 : Preparation of the synthesis of the core–shell RB-MMSNs. Adapted from Zhan et al. [56].

The size of the MMSNs was 190 nm. The loading efficiency of RB in MMSNs was about 35.74. In vitro experiments were performed on B16 cells. The best phototoxicity (i.e., with a 75% reduction in cell viability) was obtained after incubation of cells with RB-MMSNs (50 µg/mL) for 12 h followed by green light irradiation (535 nm, 25 mW/cm^2, 3 min) (**Figure 93a**). In vivo experiments were performed on C57BL/6J xenograft mice. After incubation for 18 days, the tumor volume decreased in all samples. The greatest decrease in survival was observed for cells treated with RB-MMSNs (**Figure 93b**).

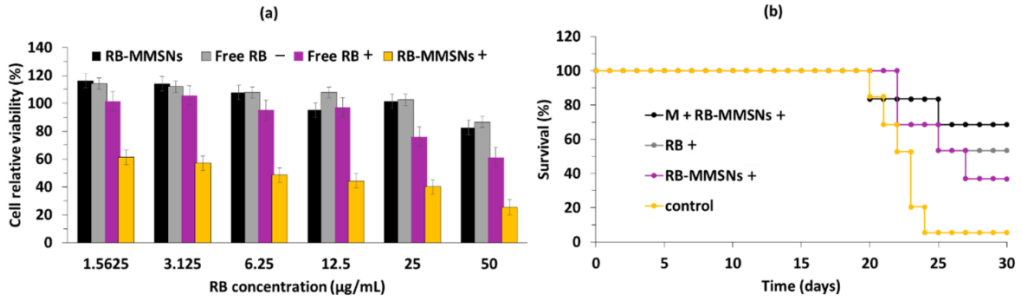

Figure 93 : (a) Relative cell viability of B16 cells treated with various concentrations of MMSNs, RB–MMSNs, and RB with (+) or without (−) green light irradiation (532 nm, 25 mW/cm^2, 3 min). (b) Survival curves of groups with different treatments (532 nm, 25 mW/cm^2, 3 min) (control, RB+, RB–MMSNs+ and M + RB–MMSNs+). Adapted from Zhan et al. [56].

Liu et al. [57] synthesized MSNs embedding carbon dots and RB in a core–shell structure with an average diameter of 104 nm. The core–shell structure prevented the self-aggregation of carbon dots and RB, enhanced the photoluminescence and $^1O_2$ production, and allowed drug loading. The in vitro cytotoxicity of the conjugate was evaluated on H1299 cancer cells by MTT assay using laser light irradiation (540 nm, 300 mW/cm^2, 5 min), and a reduction in cell viability of 90% was found. The conjugate presented a high capacity for imaging-guided chemo/PDT when DOX was incorporated into the NPs.

Yan et al. [58] designed MSNs conjugated with RB via an amide bond and with DOX via a pH-responsive linker (MSN-AH-DOX@RB) with a diameter of approximately 200 nm. The MSNs presented good biocompatibility and stability in an aqueous medium. DOX release in the acidic tumor microenvironment was highlighted when decreasing pH from 7.4 to 5.5. The cellular uptake of RB and DOX was demonstrated in MCF-7 cells. MSNs (0.5 mg/mL) showed minimal (~2%) dark cytotoxicity. MSN-AH-DOX@RB presented a higher cellular phototoxicity when evaluated by CCK-8 assays compared to control (RB or DOX or MSN-AH@RB or MSN-AH@DOX). $^1O_2$ production was observed via SOSG. A laser at a wavelength of 532 nm (0.5 W/cm^2) was used for 5 min at 1 min intervals for every 1 min of light exposure to illuminate MCF-7 incubated with MSN-AH-DOX@RB. The highest phototoxicity (90% efficiency) was observed for MSN-AH-DOX@RB plus laser irradiation for 5 min, showing a synergic chemo/PDT effect.

Jain et al. [59] reported the elaboration of silica-coated $Gd_3Al_5O_{12}:Ce^{3+}$ nano-platforms loaded with RB with a size of 74.13 ± 9.04 nm. $^1O_2$ production in water was detected using DPBF, and was higher for RB-loaded NPs than for RB. In vitro experiments were performed on the MDA-MB-231 cell line. After incubation with RB-loaded NPs (200 µg/mL) followed by illumination with blue light (470 nm, 20 mW/cm^2, 15–30–45 min), a decrease in cell viability (20%) was observed.

Jain et al. [60] synthesized magnetic-luminescent cerium-doped gadolinium aluminum NPs composed of $Gd_{2.98}Ce_{0.02}Al_5O_{12}$ (namely, GAG) coated with mesoporous silica ($mSiO_2$) and loaded with RB (RB loading concentration = 20 µM), namely, the nanocomposite GAG@$mSiO_2$@RB. The GAG core was synthesized using the sol–gel method and then loaded with RB. The average size of GAG was 18 nm, which increased to 110 nm following the addition of $mSiO_2$. Adsorption/loading of RB increased the size of the NPs to 147 nm. The photoluminescence emission intensity was strongly dependent upon the dopant concentration within a range of [Ce^{3+}] = 1–2% after excitation at 468 nm. The highest energy transfer was observed at an RB loading concentration of 20 µM. Upon excitation with X-rays (55 KV), GAG@$mSiO_2$@RB continuously produced ROS, which was detected via DPBF. In vitro experiments using breast MDA-MB-231 cancer cells revealed a low dark cytotoxicity, with a cell survival rate of around 70% at concentrations of GAG@$mSiO_2$@RB higher than 25 µM. The LC_{50} of GAG@$mSiO_2$@RB was 6.69, 11.2 and 6.56 mg/mL at a doses of 0.16, 0.33 and 0.5 J/cm^2, following irradiation at 15, 30 and 45 min respectively, at a wavelength of 470 nm, with 20 mW/cm^2. Cell viability decreased with increasing blue light dose and nanocomposite concentration. At a wavelength of 470 nm and 0.495 J/cm^2, and at a GAG@$mSiO_2$@RB concentration of 50 µg/mL, cell viability decreased by 80% (**Figure 94**).

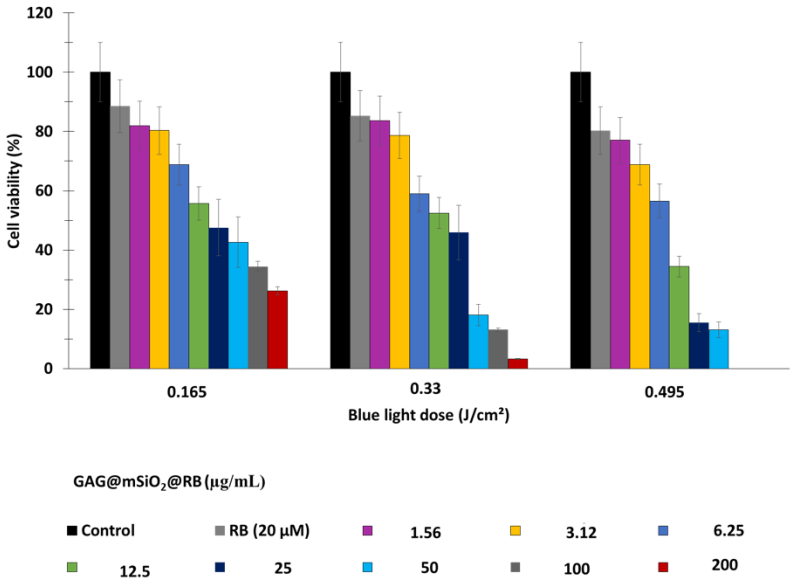

Figure 94 : Cell viability of MDA-MB-231 cells upon exposure to irradiation (470 nm, 20 mW/cm^2) for 15 min, 30 min and 45 min corresponding to energy densities of 0.165, 0.33, and 0.495 J/cm^2, respectively. Adapted from Jain et al. [60].

Hu et al. [61] synthesized drug-loaded ZIF-8@SiO_2 NPs using a thermal-assisted microfluidic system. They used ZIF-8 as the MOF. RB, DOX, and pyrene were coated onto the ZIF-8@SiO_2 (ZS) NPs in order to validate the universality of the microfluidic reactor system for the continuous fabrication of ZS nanocarriers, but only RB@ZS was used for cytotoxicity tests. The average size of RB@ZS particles was 93.8 ± 17.3 nm, and the drug loading was about 35.3 µg/mg. DPBF was used for the $^1O_2$ probe. In vitro studies were conducted on 4T1 cell lines. These cells were incubated for 24 h with various concentrations of RB@ZS. Following laser irradiation (532 nm, 100 mW/cm^2, 7 min), the viability of cells incubated with 100 µg/mL of RB@ZS decreased to 30% compared to cells treated with ZS only (~95%).

In vivo experiments (MTT) were performed on BALB/c female mice (aged 7–8 weeks). After incubation with RB@ZS (30 mg/mL), following exposure to 532 nm laser irradiation (500 mW/cm^2) for 10 min, the relative tumor volume decreased after 2 days and then remained constant after 14 days, in contrast to controls, which showed an increase in relative tumor volume without a variation in mass, whatever the conditions (Figure 95).

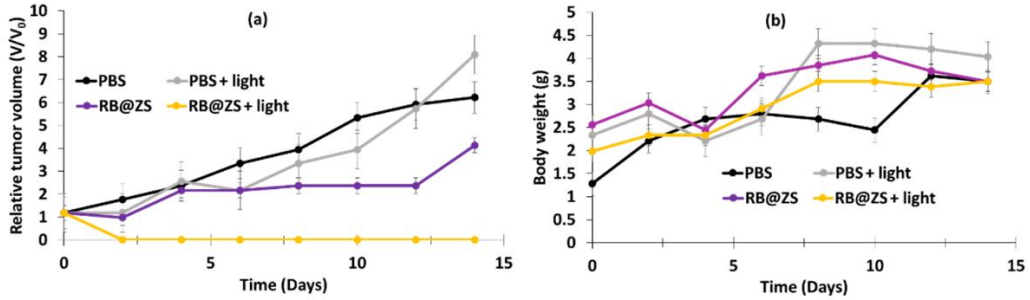

Figure 95 : (a) Relative tumor volume and (b) body weight of the tumor-bearing mice in different treatment groups (n = 6) during post-treatment with PBS or RB@ZS aqueous solution (30 mg/mL). Laser irradiation at 532 nm (500 mW/cm^2) for 10 min. Adapted from Hu et al.[61].

Chen et al. [62] developed a pH-responsive and tumor-targeted drug delivery system for chemo-PDT. The system RB-DOX@HMSNs-N=C-HA was composed of hollow mesoporous silica NPs (HMSNs) loaded with DOX and RB and coated with oxidized hyaluronic acid (HA). The average diameter of the NPs was determined using TEM (170 ± 10 nm). The drug loadings of DOX and RB were 15.30% and 12.78% (*w*/*w*%), respectively, and the drug entrapment efficiency of DOX and RB were 76.67% and 95.85%, respectively. An in vitro drug release study was performed at different pH values (7.4, 6.0 and 5.0), and showed that, after 80 h, significant RB and DOX releases from RB-DOX@HMSNs-N=C-HA occurred at pH 5.0 and 6.0 (DOX: 39.05% and 58.60%; RB: 27.30% and 48.86% at pH 6.0 and 5.0, respectively), while the releases were negligible at pH 7.4 (DOX: 12.23%; RB: 12.27%). After excitation at a wavelength of 532 nm, $^1O_2$ production was confirmed via DPBF. The targeted property provided by HA, which specifically recognizes the CD44 receptor, was confirmed by an in vitro 4T1 cellular uptake study. A study of in vitro cytotoxicity on 4T1cells was performed. At the maximum tested concentration (16 µg/mL, 4 h incubation), cell viability was 22.3% in the dark and 10.9% following laser irradiation (532 nm, 10 mW/cm^2, 5 min). The IC_{50} value of RB-DOX@HMSNs-N=C-HA upon irradiation was 0.23 µg/mL, compared to 0.70 µg/mL and 8.89 µg/mL for DOX@HMSNs-N=C-HA and RB-@HMSNs-N=C-HA, respectively.

Miletto et al. [63] designed Ln:ZrO_2@SiO_2 (Ln = Er, Pr or Yb) NPs covalently coupled to RB for PDT treatment. The size of the NPs was approximately 20–25 nm. $^1O_2$ production in water was determined using DPBF as the detector or using the spin tracking technique. In vitro experiments were performed on HeLa cells. After 10 min illumination (4 mW, 633 nm), a decrease in cell viability was observed (20–30%, depending on the type of lanthanide used).

Prieto-Montero et al. [64] synthesized biocompatible MSNs (with a size of 50 nm) with RB-PEG-FA covalently decorated onto their outer surface. Several sizes of PEG were tested, and the NPs that showed the highest stability in aqueous medium were the RB-PEG5000-NPs with a hydrodynamic diameter of 99 nm. The value of Φ_Δ in methanol was equal to 0.80–0.85. In vitro experiments on HeLa cells showed no dark cytotoxicity of RB-PEG-NPs and free RB in solution. When exposed to laser light irradiation (518 nm, 10 J/cm^2, 5 min), RB-PEG-NPs showed a higher phototoxicity compared to RB alone in PBS at the same concentration of RB. The presence of FA on the outer surface of RB-PEG-MSN also contributed to the stability of the NPs by reducing interparticle aggregation. In vitro tests on HeLa cells with different

concentrations of RB alone in PBS and RB-PEG-NPs upon exposure to laser irradiation showed that, when increasing the concentration from 0.1 µM to 10 µM, the cell viability decreased from 100% to about 10% following irradiation.

Table 16 summarizes the physical and chemical properties and PDT conditions presented in all references dealing with silica NPs@RB.

Table 16 : Table summarizing the references dealing with silica NPs@RB, including the type of NPs, as well as their size, excitation wavelength, type of detection of $^1O_2$, type of coupling between the NPs and the RB, and the type of biological experiments performed.

PDT Silica NPs									
References	**Type of NPs**	**Size of NPs (nm)**	**Irradiation Conditions**	**Type of $^1O_2$ Detection**	**Type of Coupling between NPs and RB**	**Biological Tests/In Vitro**		**Biological Test/In Vivo**	
						Cells Used	**Results**	**Mice Used**	**Results**
[63]	Ln:ZrO_2@ SiO_2@RB	20–25 thick	633 nm, 4 mW He-Ne laser, 10 min	DPBF	Covalent	HeLa	Cytotoxicity (+)	nd	nd
[50]	Mesoporous silica NPs@RB	160–180	green light, 5 min	nd	Covalent	SK-MEL-28	Cytotoxicity (+)	nd	nd
[59]	Silica coated ($Gd_3Al_5O_{12}$:Ce^{3+})-RB	74.13 ± 9.04	470 nm, 20 mW/cm^2, 15–30–45 min	DPBF	Loaded	MDA-MB-231	Cytotoxicity (+)	nd	nd
[58]	MSN@DOX@RB	200	532 nm, 0.5 W/cm^2, 5 min	nd	Covalent	MCF-7	Cytotoxicity (+)	nd	nd
[57]	MSN@C-dots/RB	104	540 nm, 300 mW/cm^2, 5 min	DPBF	Encapsulation	H1299	Cytotoxicity (+)	nd	nd
[54]	UCN/SiO_2-RB DOX)@PPADT	38.2 ± 3.6	980 nm, 1.0 W/cm^2, 20 min	ABDA	Covalent	HeLa	Cytotoxicity (+)	nd	nd

[55]	SiNP-AAP-RB	5–15	410 nm, 1.6 J/cm^2, 15 min	Direct	Covalent	A549	Cytotoxicity (+)	nd	nd
[52]	Silica capped rMSN-ts	Lenght 33 ± 27 and width 103 ± 15	5 mV green laser, 30 s	Direct	Covalent	MCF7 L269	Cytotoxicity (+)	nd	nd
[53]	FITC-PGSN-RB	100	480 nm, 100 W xenon lamp, 10 min	ABDA	Adsorption	HeLa	Cytoxicity (+)	nd	nd
[51]	RB-MSNs NPs	150–180	nd	Direct	Encapsulation	nd	nd	nd	nd
[62]	RB-DOX@HMSNs	170	532 nm, 10 mW/cm^2, 5 min	DPBF	Encapsulation	4T1	Cytotoxicity (+)	nd	nd
[61]	RB@ZIF-8@SiO_2@RB NPs (drug loaded MOFs@SiO_2 NPs)	93.8	532 nm, 200 mW/cm^2, 2 min or 100 mW/cm^2, 7 min	DPBF	Encapsulation	4T1	Cytotoxicity (+)	BALB/c mice bearing AT1 tumors	PDT (+)
[56]	RB–MMSNs	190	535 nm, 25 mW/cm^2, 3 min	Uric acid	Encapsultation	B16 HeLa L929	Cytotoxicity (+)	C57BL/6J mice	PDT (+)
[64]	RB-PEG5000-MSNs	50	518 nm, 10 J/cm^2, 5 min	Direct	Covalent	HeLa	Cytotoxicity (+)	nd	nd
[49]	RB-SiNP	electrostatic = 35 ± 5 covalent = 50 ± 5	480 nm, 1 h (fluence not cited)	SOSG	Covalent/Electrotatic	MCF-7 4451	Cytoxicity (+)	nd	nd

*nd: not determined; cytotoxicity (+): induced tumor cell death in vitro; PDT (+): induced tumor death in vivo.

II.3 Organic NPs (Polymers, Micelles, Peptides)

Organic NPs are mostly biocompatible and biodegradable. They can be formed as nanospheres or nanocapsules. To formulate these NPs, different types of polymers can be used: poly(lactic

acid) (PLA) [65], poly(glycolic acid) (PGA) [66] and poly(lactide-coglycolide) (PLGA) [67]. The use of hydrophilic and hydrophobic block copolymers in the formulation of these NPs improves their biodispersity. Natural or synthetic proteins are one type of polymer that can be used [68]. In addition, they can be used for coupling or encapsulating drugs, as well as as imaging and targeting agents.

II.3.1 Polymer NPs

Karthikeyan et al. [69] succeeded in encapsulating RB in nanoscale dendrimers (G2.5 PAMAM (Poly(amidoamine) + RB). The size of G2.5 PAMAM was 20 nm. They demonstrated values of RB release of 35%, 50%, 74% and 83% after 12, 24, 48 and 72 h, respectively. $^1O_2$ production was quantified by I^- in the presence of ammonium molybdate. In vitro experiments were performed on DLA cells, revealing that RB and G2.5 PAMAM + RB exhibited low dark cytotoxity. For cells incubated with G2.5 PAMAM + RB for 18 h, cell viability decreased by up to 24.9% at an RB concentration of 500 nM, and by up to 40% for cells incubated with RB alone at the same concentration upon exposure to a 150 W xenon lamp (540 nm, 10 min) (**Figure 96**).

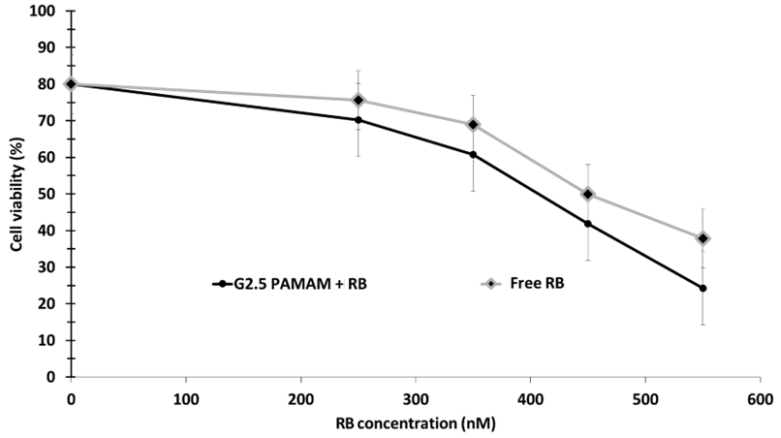

Figure 96 : DLA cell viability following incubation with G2.5 PAMAM + RB and free RB upon exposure to a 150 W xenon lamp (540 nm, 10 min). Adapted from Karthikeyan et al. [69].

Baumann et al. [70] developed polymer vesicles made of poly(2-methyloxazoline)–poly(dimethylsiloxane)–poly(2-methyloxazoline). These NPs were used to encapsulate RB-BSA conjugate (i.e., RB-BSA, hydrodynamic radius of 109 ± 5 nm). $^1O_2$ production was determined using 2,2,6,6-tetramethyl-4-piperidinol (TMP–OH) as $^1O_2$ scavenger. In vitro studies were performed on HeLa cancer cells and revealed no cytotoxicity of RB-BSA NPs at different concentrations (between 0 and 300 µg/mL) after incubation for 24 h. The light-controlled PDT effect of RB-BSA NPs was evaluated using irradiation doses of 30–135 J/cm^2 for 5–30 min with laser irradiation at wavelengths of 405 nm, 543 nm, and 633 nm. Visualization of the HeLa cells plasma membrane using confocal microscopy indicated the formation of blebs only upon laser irradiation at a wavelength of 543 nm, while the plasma membrane remained intact upon laser irradiation at wavelengths of 405 nm and 633 nm.

Bhattacharyya et al. [71] synthesized coumarin 153 (C153)-dye-doped poly(N-vinyl carbazole) (PVK) polymer NPs. The FRET efficiency was 60%. No biological experiments were performed.

Han et al. [72] successfully synthesized a PAH-modified UCNP/hyaluronate-RB covalently coupled (UCNP/PAH/HA-RB) in the form of a hexagonal (100) crystal lattice with a size of 30.34 ± 2.10 nm. The composition of UCNPs was 78:19:3 of Y:Yb:Er. The hydrodynamic diameter of these NP was 459.9 ± 98 nm. In vitro tests on NIH 3T3 cells showed that, by increasing the concentration of UCNP/PAH, cell viability decreased more significantly following laser irradiation (980 nm, 1.5 mW/cm^2, 30 min). Nevertheless, at a concentration of 200 µg/mL, cell viability was maintained at more than 90% (**Figure 97**).

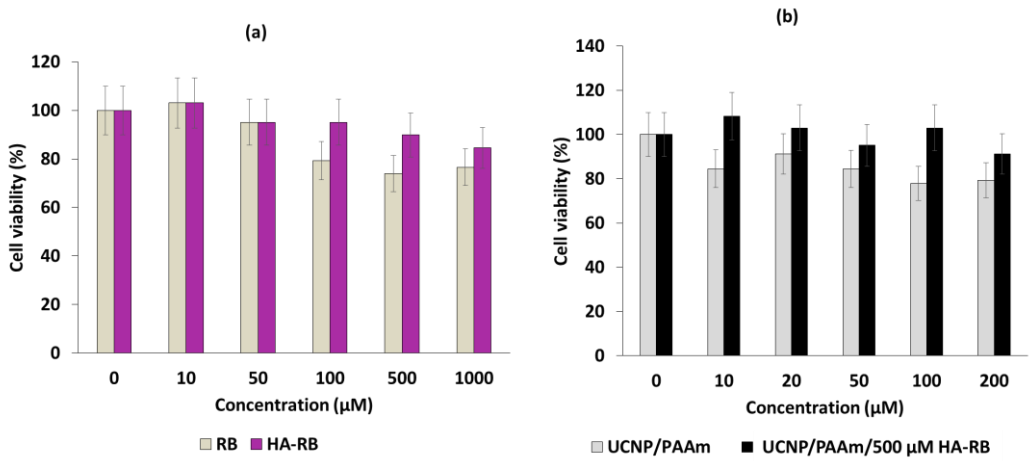

Figure 97 : NIH 3T3 cell viability following incubation for 24 h with various concentrations of (a) RB and HA-RB and (b) UCNP/PAH and UCNP/HA-RB after exposure to laser irradiation (980 nm, 1.5 mW/cm^2, 30 min). Adapted from Han et al. [72].

Yang et al. [73] synthesized PLGA NPs with a diameter of 28 nm, where RB was grafted via an amide bond. Firefly luciferin was then conjugated to the platform at a short distance from RB to allow efficient energy transfer (**Figure 98**).

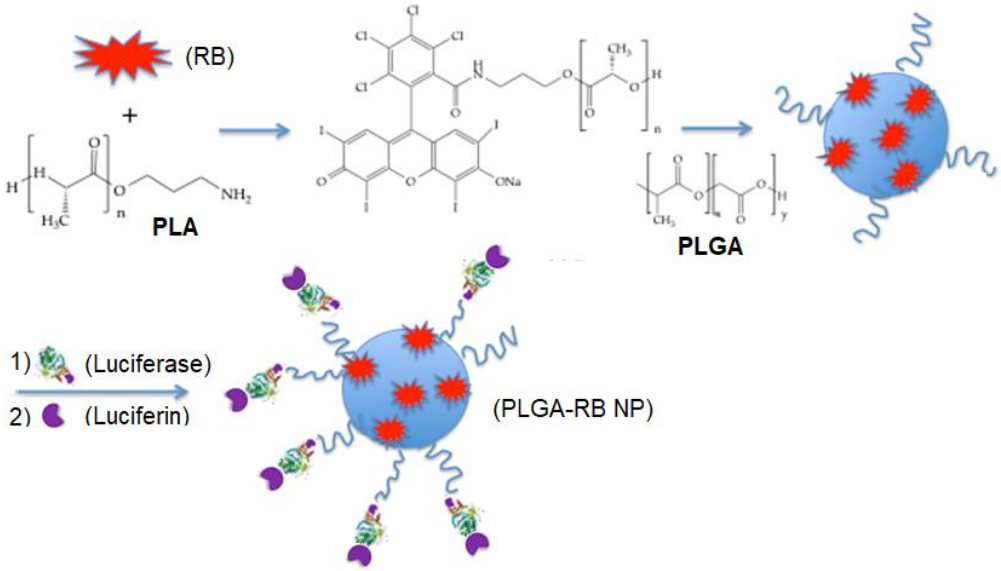

Figure 98 : Preparation of PLGA-RB NPs for BRET-PDT. Adapted from Yang et al. [73].

The NPs produced a fluorescent signal in the presence of luciferin that was able to excite RB with a bioluminescence resonance energy transfer (BRET) efficiency of around 58%. MTT assays performed on MCF-7 and HeLa cells showed no cytotoxicity of the NPs at a concentration of 50 µg/mL following incubation for 48 h. With increasing concentration of luciferin, cell viability estimated by MTT decreased to 45%, with the optimal value being reached at 60 µg/mL. In vivo experiments performed on H22 tumor-bearing mice demonstrated apparent tumor growth inhibition in the BRET-PDT group, whereas the tumors in the control group exhibited rapid growth (520 nm, 200 mW/cm^2, 30 min) (**Figure 99**).

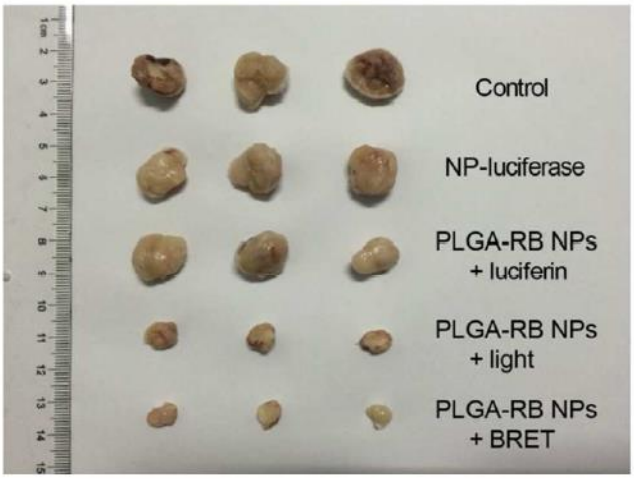

Figure 99 : Photographs of tumors excised from the BRET-PDT treatment group and other groups on day 14 following laser irrdiation (520 nm, 200 mW/cm^2, 30 min). Reprinted with the permission from Yang et al. [73]. Copyright 2018 American Chemical Society.

Chang et al. [74] developed photo-activated ROS-responsive nanocarriers (NCs) containing Paclitaxel (PTX) and RB for combinational chemotherapy and PDT. THe HA-BSA/CTS/PVA/bPEI-blended NCs (HBNCs) were composed of chitosan (CTS), poly(vinyl alcohol) (PVA) branched with polyethylenimine (bPEI), and BSA. The dual-functional drug

carriers RB/PTX-HBNCs were loaded with PTX and RB. This core was shelled with HA as a result of electrostatic bonds. The hydrodynamic diameter of HBNCs was 220 ± 14 nm. The encapsulation efficiencies (EE%) of RB and PTX were 60.7 7 ± 2.7% and 55.2 ± 8.9%, respectively. A DCFH-DA probe was used to determined ROS generation. It was found that 30% of PTX was released after an exposure time of 6 h, whereas negligible release was observed without light irradiation. Cellular uptake of RB/PTX-HBNCs in Tramp-C1 prostate cancerous cells expressing CD44 receptor was observed, confirming the HA-specific recognition and targeting ability of HBNCs. Significant intracellular ROS generation and PTX delivery was observed in Tramp-C1 cells following incubation with RB/PTX-HBNCs for 6 h after light irradiation for 1 h at a wavelength of 632 nm (15 mW/cm^2). A cell viability assay was performed to evaluate the antitumoral effect of RB/PTX-HBNCs. In the dark, cell death of 18% was observed, indicating that the NCs possessed a moderate toxic effect. After irradiation for 1 h at a wavelength of 632 nm (15 mW/cm^2), cell death increased to 24% for PTX-HNCs and to 40% for RB-HBNCs. RB/PTX-HBNCs showed an improved cytotoxic effect, with cell death increasing to 61%.

Bazylińska et al. [75] engineered double-core NCs for the co-delivery of RB and trioctylphosphine oxide (TOPO)-stabilized luminescent lanthanide-doped $NaYF_4$:2%Er^{3+}, 20%Yb^{3+} NPs to human melanoma for theranostic applications. The double core was composed of a non-ionic surfactant, Cremophor A25, and stabilized by PLGA copolymer. The loaded NCs had a hydrodynamic diameter of 158 nm. Under 980 nm laser excitation, $NaYF_4$:Er^{3+}, Yb^{3+} NPs showed three emission peaks, at 520, 540, and 660 nm. The green emission bands overlapped the RB absorbance spectra, leading to efficient energy transfer by FRET at a level of 25%. In vitro cytotoxicity assays were performed on two tumorous cell lines (human melanoma granular fibroblast (MeWo), lymph node metastasis of skin melanoma (Me-45)), as well as on non-tumorous human cutaneous keratinocyte (HaCaT) as control cells. Empty NCs under dark or light conditions (520–560 nm, 10 J/cm^2, 5 min) showed no cytotoxicity. Free RB presented moderate cytotoxicity under irradiation for the three cell types, while it presented high toxicity for MeWo (>90%) and Me-45 (55%) after incubation for 48 h, but not for HaCaT cells (25%) (**Figure 100**).

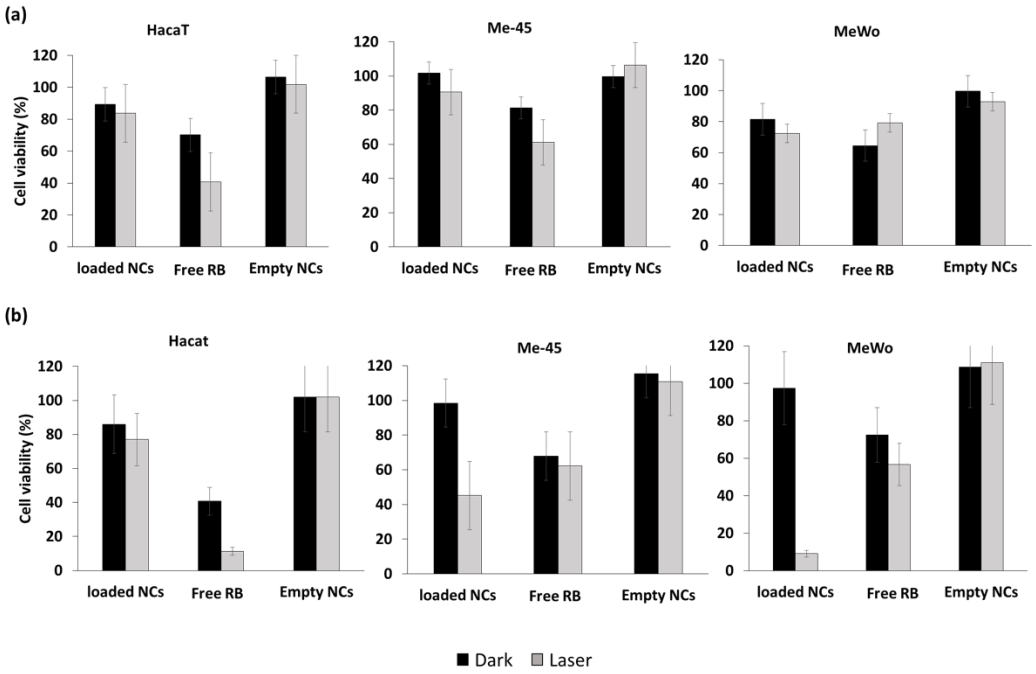

Figure 100 : Cell viability of Me-45, MeWo, and HaCaT in the dark or upon exposure to laser irradiation (980 nm, 10 J/cm², 6.2 W/cm², 5 min) after (a) 24 h and (b) 48 h. Adapted from Bazylińska et al. [75].

II.3.2 Peptide NPs

Sun et al. [76] designed cationic dipeptide NPs conjugated with bis-pyrene (BP) as an energy donor and RB as an acceptor. BP and RB were enveloped in spherical NPs with a diameter of 280 nm. The overlap between BP emission and RB absorption was high, allowing efficient energy transfer that was estimated to be 46%. The generation of $^1O_2$ was confirmed by means of an ABDA probe. Confocal laser scanning microscopy confirmed an internal uptake of the conjugate in MCF-7 cells, which presented good biocompatibility and low dark cytotoxicity. After co-culture for 48 h and irradiation at 480 nm (245 mW/cm^2) for 20 min, cell viability decreased to 27%. Irradiation (245 mW) at a wavelength of 810 nm for 50 min induced high two-photon photo-cytotoxicity.

Liu et al. [77] developed nanocapsules (PARN) that were composed of an amphiphilic peptide and RB for use in sonodynamic therapy and PDT. The amphiphilic peptide $C_{18}GR_7RGDS$ was composed of a carbonate chain and an RGD peptide for targeting the αvβ3 integrin receptor. This peptide was able to self-assemble owing to electrostatic interaction, and could be loaded with RB via weak interactions. The hydrodynamic diameter of PARN was 17.28 ± 0.88 nm. $^1O_2$ generation was confirmed by means of a DPBF probe. PARN was irradiated by laser at a wavelength of 808 nm, 1.5 W/cm^2 for 3 min, or by ultrasound (US) (50 MHz, 1 W/cm^2, 5 min). ROS generation was observed under both laser and US irradiation. B16 (melanoma cells) and HeLa cells were incubated for 24 h with PARN or RB and irradiated using either laser or US. In vitro ROS generation was determined using CLSM (confocal laser scanning microscopy) and DCFH-DA probes. Cells incubated with PARN under US or laser irradiation induced ROS production. Cytotoxicity tests were performed with B16 and HeLa cells incubated with PARN

(40 µg/mL). Without irradiation, cell viability was 30.2% and 29.7% in B16 and HeLa cells, respectively. After 5 min of US irradiation, cell viability decreased significantly to 4.7% and 4.1% in B16 and HeLa cells, respectively. Thus, both irradiation modalities were equivalent. In vivo sonodynamic therapy and PDT were evaluated using HeLa tumor-bearing mice, with five groups being used in this study, as follows: (1) control, (2) PARN, (3) PARN + laser, (4) PARN + US, and (5) PARN + laser + US (treatment for 18 days (US: frequency: 1.0 MHz; duty cycle: 50%; power density: 1.0 W/cm^2; wavelength: 808 nm; duration: 3 min). No tumor growth inhibition was observed for group 2, whereas, under US, laser or laser + US irradiation, moderate tumor growth inhibition was observed. Thus, the efficiency of PARN irradiated with US or laser needs to be improved before proposing treatment with highly promising results (**Figure 101**).

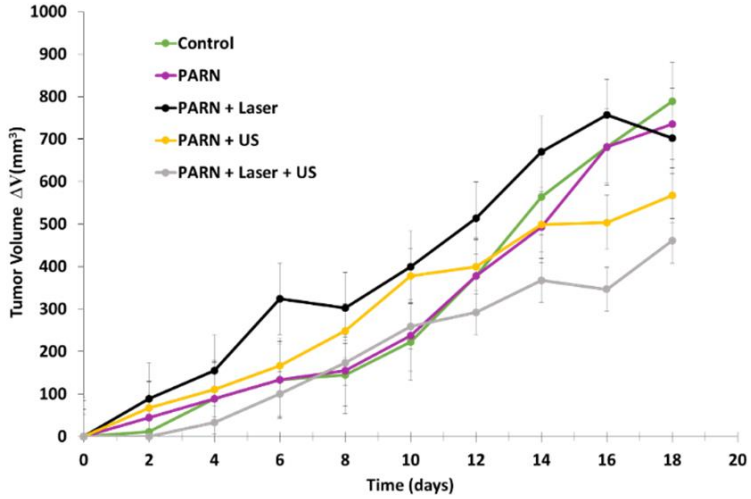

Figure 101 : Variations in tumor volume in HeLa-xenografted nude mice under various treatment conditions. Laser irradiation (808 nm, 1 W/cm^2, 3 min), US (frequency: 1.0 MHz; duty cycle: 50%; power density: 1.0 W/cm^2). Adapted from Liu et al. [77].

II.3.3 Micelle NPs

Korpusik et al. [78] reported the design of a targeted micelle-based PDT system (Sgc8 micelles, hydrodynamic diameter of 52 nm) based on azide-functionalized polymeric micelles decorated with protein tyrosine kinase 7 (PTK7)-binding DNA (Deoxyribonucleic acid) aptamer (Sgc8) via click chemistry. The covalent conjugation of RB to micelles provided quantitative and controlled RB loading. The use of ADPA revealed that Sgc8 micelles had a much higher $^1O_2$ production than free RB, and a controllable "on-off" release of $^1O_2$ using yellow light (590–595 nm, 0.2 mW/cm^2, 15 min). These RB-loaded micelles also exhibited better fluorescence emission than free RB. In vitro experiments were performed on PTK7-expressing HCT116 cancer cells and K562 cells lacking PTK7 receptors under 15 min of yellow light exposure. The cell targeting capacity of Sgc8 micelles compared to unlabeled ones was clearly demonstrated. The authors showed that Sgc8 micelles could be used to achieve selective PDT, but that it is necessary to be very careful regarding the concentration used (i.e., Sgc8 micelles exhibit significant cytotoxicity at high doses (e.g., 5.4 µM)).

Table 17 summarizes the physical and chemical properties and PDT conditions presented in all references dealing with organic NPs@RB.

Table 17 : References dealing with organic NPs@RB, including the type of NPs, as well as their size, excitation wavelength, type of detection of $^1O_2$, the type of coupling between the NPs and the RB, and the type of biological experiments performed.

PDT Organic NPs									
References	**Type of NPs**	**Size of NPs (nm)**	**Irradiation Conditions**	**Type of $^1O_2$ Detection**	**Type of Coupling between NPs and RB**	**Biological Tests/In Vitro**		**Biological Test/In Vivo**	
						Cells Used	**Results**	**Mice Used**	**Results**
[72]	UCNP/PAH/HA-RB	30.34	980 nm, 1.5 mW/cm^2, 30 min	nd	Covalent	NIH3T3	Cytotoxicity (+)	nd	nd
[78]	POEGMA-b-P(HPMA-co-RBMA)	52	590–595 nm, 0.2 mW/cm^2, 15 min	ADPA	Covalent	HCT116 K562	Cytotoxicity (+)	nd	nd
[70]	RB-BTSA	109 ± 5	490 nm, 30–135 J/cm^2, 5–30 min	TMP–OH	Encapsulation	HeLa	Cytotoxicity (+)	nd	nd
[73]	PLGA-NP-RB	28	520 nm, 200 mW/cm^2, 30 min	nd	Encapsulation	MCF-7 HeLa	Cytotoxicity (+)	H22 tumor-bearing mice	PDT (+)
[71]	PVK@C153@RB	340	No biological test	2-chlorophenol	Encapsulation	nd	nd	nd	nd
[75]	$NaYF_4$:Er^{3+},Yb^{3+} NPs@SPAN-20 micelles@RB@TOPO@Cremophor@PLGA copolymer	150	980 nm, 10 J/cm^2, 6.2 W/cm^2, 5 min	nd	Encapsulation	Me-45 MeWo HaCaT	Cytotoxicity (+)	Melanoma cells innoculated on monoclonal mouse	PDT (+)
[74]	HBNCs@RB	220	632 nm, 15	DCFH-DA,	Encapsulation	Tramp-C1	Cytotoxicity (+)	nd	nd

			mW/cm^2, 60 min						
[69]	PAPAM dendrimers G 2.5-RB	20	150 W xenon lamp 540 nm, 10 min	Iodure reaction	Covalent	DLA	Cytotoxicity (+)	nd	nd
[77]	polypeptide C18GR7RGDS	17.28	808 nm, 1.5 W/cm^2, 3 min	DPBF	Encapsulation	B16 HeLa	Cytotoxicity (+)	nd	nd
[76]	BP-CDPNP-RB	280	Two photons (810 nm, 245 mW/cm^2, 20 min	ABDA	Encapsulation	MCF-7	Cytotoxicity (+)	nd	nd
[77]	PARN@RB	17.28	808 nm, 1.5 W/cm^2, 3 min	DPBF DCF-DA	Encapsulation	B16	Cytotoxicity (+)	HeLa tumor-bearing mice	PDT (+)

*nd: not determined; cytotoxicity (+): induced tumor cell death in vitro; PDT (+): induced tumor death in vivo.

II.4 Gold Nanoparticles

Gold NPs are assemblies of 30 to 40 million gold atoms. The size of these NPs depends on their synthesis conditions, and mainly ranges between 1 and 100 nm [79]. For centuries, gold NPs have been used in clinical chemistry, laser phototherapy of cancer cells and tumors, targeted delivery of drugs, DNA and antigens, optical bioimaging, and monitoring of cells, tumors, and tissues using state-of-the-art detection systems. They are used in diagnosis, therapy, prevention, and hygiene. They can be used in these applications owing to their unique physical and chemical properties. In particular, the optical properties of gold NPs are determined by their plasmon resonance, which is associated with the collective excitation of conduction electrons and localized in the wide region, from visible to infrared (IR), depending on the size, shape, and structure of the particles. Having discovered the properties of biocompatibility and photostability possessed by gold NPs, scientists have also been attracted to their exceptional photophysical and optical properties [80,81]. These properties have led researchers to apply these NPs in cancer diagnosis and therapy [82].

Wang et al. [83] synthesized a gold nanorod with a diameter of 13 ± 2 nm and a length of 52 ± 4 nm in which RB was encapsulated (RB-GNRs) for application in PTT–PDT. The seed-mediated growth method was followed, and PAH was used to modify the surface of the CTAB-coated GNRs. RB was then adsorbed onto the surface. $^1O_2$ production was observed in vitor via ABDA in water (ABDA absorption decreased by 92% with light and RB-GNRs, while the reduction was only 15% without light or without RB, while a decrease of 85% was observed

with RB alone) and DCFH-DA. In vitro experiments were performed on Cal-27 cells and a home-made light-emitting diode at a wavelength of 530 ± 15 nm (170 mW/cm^2 for 90 s). Total cell survival after light illumination for 12 h was 19%, and 26.3% after light illumination for 24 h. In vivo experiments were performed on Male Syrian Golden hamsters with oral carcinomas induced by DMBA (7,12-dimethylbenz(a)anthracene) in acetone. After PDT (532 nm solid-state diode laser, 1.76 W/cm^2, for 10 min), an inhibition rate of 46.5% was observed on the 10th day, while 65.5% was observed after PTT (810 nm NIR light, 8.16 W/cm^2, 5 min), and 95.5% after combined PTT–PDT (**Figure 102**).

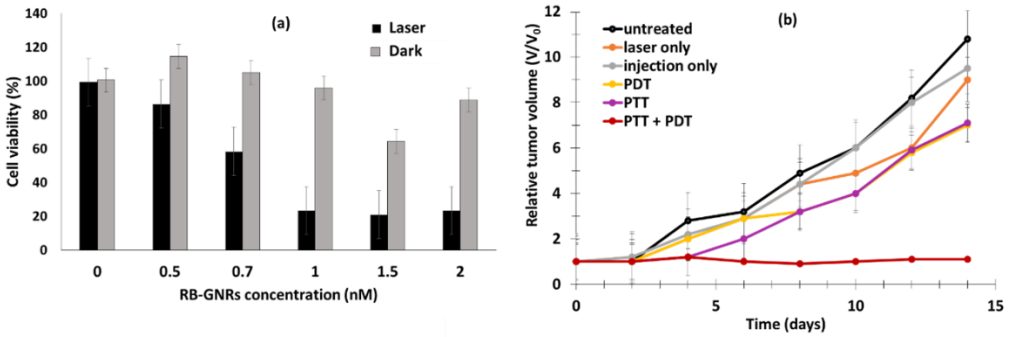

Figure 102 : (a) CaI-27 cell viability in the dark or upon exposure to green laser light irradiation (532 nm, 1.76. W/cm^2, 10 min). (b) Relative tumor volume under different treatment conditions (PDT: 532 nm, 1.76 W/cm^2, 10 min; PTT: 810 nm 8.16 W/cm^2, 5 min). Adapted from Wang et al. [83].

Prasanna et al. [84] designed glutathione (GSH)-capped gold NPs. RB was covalently attached via an amide bond between RB and GSH with EADC (1-Ethyl-3-(3-dimethylaminopropyl)carbodiimide) (**Figure 103**) or non-covalently coupled via electrostatic interactions.

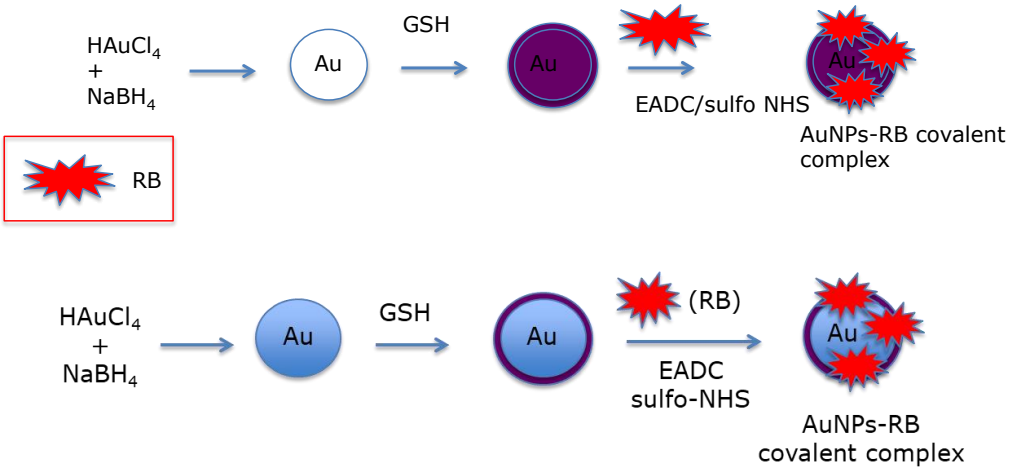

Figure 103 : Preparation of Au NPs covalently coupled to RB. Adapted from Prasanna et al. [84].

The size of the AuNPs-RB electrostatic complex was 53 nm, which is similar to the covalent complex, at 49 nm. PDT experiments were performed on Vero and HeLa cell lines using white LED light (500 nm, 5 J/cm^2). For assays in Vero cells, free RB and electrostatic and covalent AuNPs-RB complexes presented IC_{50} values of 19.53, 16.69, and 9.18 µg/mL (3 h), respectively. These values were 16.99, 14.47 and 8.24 µg/mL in HeLa cells. The AuNPs-RB

complexes were more toxic than free RB, and the covalent complex was more toxic than the electrostatic complex.

Kautzka et al. [85] synthesized a liposome of hydrogenated soy L-a-phosphatidylcholine (HSPC) and 1,2-dioleoyl-*sn*-glycero-phosphoethanolamine-*N*-(hexanoylamine) (PE-NH_2) encapsulating gold NPs, RB, and DOX. The size of the HSPC:PE-NH_2-gold NPs was dependent on the formulation (i.e., 130.1 ± 1.0 nm for 57:5:8.5; 124.6 ± 2.3 nm for 57:5:17; 131.1 ± 1.3 nm for 57:5:34). $^1O_2$ production was observed by means of an SOSG probe. For the HSPC:PE-NH2-gold NP formulation of 57:5:17, the relative Φ_Δ was found to be the highest, with a value equal to 1.33 ± 0.27, and an enhancement factor of 1.75 compared to liposomes without gold NPs. For the HSPC:PE-NH_2-gold NP formulation of 57:5:8.5, an enhancement factor of 1.53 was found. No enhancement was detected for the HSPC:PE-NH2-gold NP formulation of 57:5:34. Human colon adenocarcinoma (HCT116) and human breast cancer (MCF-7) cell lines were chosen for in vitro experiments following green light irradiation (532 nm, 14.3 mW/cm^2, 6 min) with the HSPC:PE-NH_2-gold NP formulation of 57:5:17. In HCT116, the highest cell mortality following illumination was obtained for HSPC:PE-NH_2-gold NP +RB+DOX, with 38% of cells being killed at a lipid concentration of 15.7 µg/mL. Similar results were observed in MCF-7. No dark cytotoxicity was observed in HCT116, MCF-7, or normal human colon epithelial cells (CCD 841 CoN).

Fu et al. [86] synthesized $CaTiO_3$:Yb,Er (CTO) nanofibers covalently conjugated with RB and gold nanorods (CTO-RB-AuNRs). The diameter distribution for CTO was 0.273 nm for nanofibers without AuNRs and RB. $^1O_2$ production was detected using a DPBF probe under laser irradiation at a wavelength of 980 nm (1.5 W/cm^2, 0–12 min). In vitro tests were performed on Hep G2 cells. The cells were incubated with CTO, CTO-RB, and CTO-RB-AuNRs and CTO-AuNRs. After incubation with CTO-RB-AuNR (200 µg/mL) for 24 h followed by illumination (980 nm, 1.5 w/cm^2, 6 min), the cell viability decreased to 15%.

Table 18 summarizes the physical and chemical properties and PDT conditions presented in all references dealing with gold NPs@RB.

Table 18 : References dealing with gold NPs@RB, including the type of NPs, along with their size, excitation wavelength, type of detection of $^1O_2$, the type of coupling between the NPs and the RB, and the type of biological experiments performed.

	PDT Gold NPs								
References	**Type of NPs**	**Size of NPs (nm)**	**Irradiation Conditions**	**Type of $^1O_2$ Detection**	**Type of Coupling Between NPs and RB**	**Biological Tests/In Vitro**		**Biological Test/In Vivo**	
						Cells Used	**Results**	**Mice Used**	**Results**
[84]	AuNPs-RB	AuNPs-RB complexes:	500 nm, 5 J/cm^2	nd	Covalent	Vero HeLa	Affinity (+)	nd	nd

		Electrostatic (53) Covalent (49)							
[85]	Gold NPs@RB@DOX	124.6	532 nm, 14.3 mW/cm^2, 6 min	SOSG	Encapsulation	HCT116 MCF-7 CCD 841 CoN	Cytotoxicity (+)	nd	nd
[86]	CTO-RB-AuNR	0.273	980 nm, 1.5 W/cm^2, 6 min	DPBF	Covalent	Hep G2	Cytotoxicity (+)	nd	nd
[83]	AuNRs @RB	13 ± 2	PDT: 532 nm, 1.76 W/cm^2, 10 min PTT: 810 nm NIR light, 8.16 W/cm^2, 5 min	ABDA	Covalent	Cal-27	Cytotoxicity (+)	Male Syrian Golden hamsters with oral carcinomas	PDT (+)

*nd: not determined; affinity (+): induced the affinity to tumor cells; cytotoxicity (+): induced tumor cell death in vitro; PDT (+): induced tumor death in vivo.

II.5 Polymer Dot Nanoparticles

Research has confirmed the importance of semiconducting polymer dots (Pdots) in biological applications. They are considered an essential tool for the diagnosis and treatment of certain diseases, thanks to their high luminosity, their long lifetime, their adjustable size, their narrow luminescence and their biocompatibility [87,88].

Haimov et al. [89] described the synthesis of polymer dots (Pdots) (chromophoric organic homo-polymers) using three types of phospholipids (phosphoethanolamine, PE): PEG350-PE, PEG2000-PE, and PEG5000-PE. Pdots have never before been used for PDT applications. RB or methylated RB was bound non-covalently but with high affinity. The sizes of the Pdot NPs were 43 ± 9 nm, 77 ± 0.3 nm, and 60 ± 0.15 nm for PEG350-PE, PEG2000-PE, PEG5000-PE, respectively. By using DMA (9,10-dimethylanthracene) the value of Φ_Δ in ethanol of RB was measured as 0.38, 0.24, and 0.16 for PEG350-PE, PEG2000-PE, PEG5000-PE, respectively, while that of methylated RB was determined to be 1.0, 0.81, and 0.76 for PEG350-PE, PEG2000-PE, PEG5000-PE, respectively. In vitro experiments were performed in MCF-7 (473 nm, 0.15 mJ/cm^2, between 1 h and 4 h). A decrease in cell viability was observed after illumination (with a reduction of 8.5% being observed after 1 h and 50% after 4 h) following incubation for 4 h with PF-PEG350 Pdots.

Hua et al. [90] developed fluorescent carbon quantum dots (CQDs) made of chitosan, ethylenediamine, and mercaptosuccinic acid, with RB being covalently grafted by means of amide bonds (CQDs-RB). Diameters of 33.1 ± 8.7 nm and 2.1 ± 0.3 nm for CQDs-RB and

CQDs, respectively, were determined. $^1O_2$ production was observed by means of SOSG probe. In MCF-7 cells, the CQDs-RB were localized in the mitochondria. After PDT (532 nm, 30 min, 20 mW/cm^2), CQDs-RB NPs were more effective than RB alone, with a decrease in cell viability from 100% to 11% being observed when the laser power was increased from 0 to 30 mW.

Table 19 summarizes the physical and chemical properties and PDT conditions presented in all references dealing with Pdots@RB.

Table 19 : References dealing with quantum dots NPs@RBs, including the type of NPs, along with their size, excitation wavelength, type of detection of $^1O_2$, the type of coupling between the NPs and the RB, and the type of biological tests performed.

PDT Polymer Dots NPs									
References	**Type of NPs**	**Size of NPs (nm)**	**Irradiation Conditions**	**Type of $^1O_2$ Detection**	**Type of Coupling between NPs and RB**	**Biological Tests/In Vitro**		**Biological Test/In Vivo**	
						Cells Used	**Results**	**Mice Used**	**Results**
[89]	Pdots-RB with: PEG350-PE, PEG2000-PE, PEG5000-PE	PEG350-PE: 43 ± 9 PEG2000-PE: 77 ± 0.3 PEG5000-PE: 60 ± 0.15	473 nm, 0.15 mJ/cm^2, between 1 h and 4 h	DMA	Encapsulated in the coating of Pdots	MCF-7	Cytotoxicity (+)	nd	nd
[90]	CQDS-RB	CQDs-RB: 33.1 ± 8.7 CQDs: 2.1 ± 0.3	532 nm, 20 mW/cm^2, 30 min	SOSG	Covalent	MCF-7	Cytotoxicity (+)	nd	nd

*nd: not determined; cytotoxicity (+): induced tumor cell death in vitro; PDT (+): induced tumor death in vivo.

II.6 Other Nanoparticles

II.6.1 Nanocapsules

A nanocapsule is composed of a core and a shell. The shell is composed of a polymer that can be coated with several types of targeting agents. The hydrophobic drug to be delivered is placed in the core. The size of the nanocapsules is between 10 and 1000 nm. The encapsulation of the drug serves to protect it from its environment during delivery. Lipid NPs have been suggested for use in cases of multidrug resistance in tumors [91]. The diffusion of drugs to the target is achieved by means of chemical, thermal or biological triggering.

Zhang et al. [92] successfully synthesized 300 nm bifunctional nanospheres (BFNS). The BFNS were a mixture of partially hydrolyzed α-lactalbumin (PHLA), RB, Gd^{3+} (for MRI), and

Ca^{2+}, coupled to RGD peptide. $^1O_2$ production was confirmed by DPBF. In vitro tests were performed on HepG2 cells. After irradiation at 550 nm (100 mW/cm^2, 15 min), cell viability decreased with increasing concentration of BFNS and BFNS-RGD (0, 6.25, 12.5, 25, 50, 100, 200 µg/mL). At a concentration of 200 µg/mL, cell viability was lower when treated with BFNS-RGD compared to with BFNS (with values of 19% and 49%, respectively, being observed).

II.6.2 Nanocomplexes

A nanocomplex [93] is an NP containing a chemical complex. A complex is a polyatomic structure consisting of one or more independent interacting entities.

Cao et al. [94] synthesized an organic nanocomplex composed of carboxylated bis(pyrene) molecules (BP) and RB-PAH. The core of the NPs consisted of BP, and the shell consisted of RB-PAH. Nanoaggregates of BP coated with RB-PAH provided the desired nanocomplex BP-RB, via the self-assembly method, for a use in two-photon PDT by exploiting the FRET effect. TEM images showed a diameter of about 70 nm for the BP-RB nanocomplexes. $^1O_2$ production was observed using ABDA. In vitro studies were conducted on MCF-7 cells. The lowest cell viability (21%) was observed for cells incubated with 36 µM for 4 h upon exposure to a 100 W xenon lamp (810 nm, 20 min).

II.6.3 Magnetic Nanoparticles

Magnetic NPs [95] have a size on the order of 1–100 nm. They are generally composed of a metal core (iron, cobalt, nickel, etc.) coated with other molecules. Magnetic NPs can be used as a contrast agent in biological imaging. They can improve image resolution and information content. Superparamagnetism finds application in data analysis and medicine, in particular, ferrofluids, owing to their viscosity [96].

Yeh et al. [97] synthesized magnetic nanoclusters (MNCs) coated with a tri-polymer and encapsulating RB using an oil-in-water emulsion method. The core consisted of iron oxide NPs (Fe_3O_4 NPs). The shell was composed of three polymers: CTS, PVA (poly(vinyl alcohol)), and bPEI, with a weight ratio of CTS:PVA:bPEI:Fe_3O_4 of 10:2:4:1. RB was incorporated into the polymeric coating by means of electrostatic interaction in order to give the final RB:MNCs. The encapsulation efficiency of RB was estimated to be about 87% (*w*/*w*%). The hydrodynamic size of RB:MNCs was about 108.6 ± 11.7 nm at pH 7.4. $^1O_2$ production was confirmed using DCFH-DA upon irradiation at a wavelength of 632 nm (15 mW/cm^2) for 1 h. A rate of cell death of 73 ± 3% was observed following illumination with a laser at a wavelength of 532 nm (15 mW/cm^2) for 5 min (7.5 µM of RB and 6 h). These strong PDT effects of RB:MNCs were also confirmed in mouse prostate cancer cell lines. No dark cytotoxicity was observed in Tramp-C1 cells or human ovary cancer cell line SKOV-3, but strong cell death was observed upon irradiation with a green laser (532 nm, 100 mW/cm^2, 5 min). Furthermore, PTX was also encapsulated with RB (74.4% EE%) to prove the combined chemo/PDT effect of such nanosystems. RB/PTX:MNCs (with an RB concentration of 7.5 µM) showed a cytotoxic effect on MCF-7 cells upon irradiation with a green laser (532 nm, 100 mW/cm^2) for 5 min, and cell viability decreased by almost 80%. In vivo studies were conducted in BALB/c nude mice. In this context, drug-resistant human breast cancer cells MCF-7/MDR were injected into nude

mice. At 4 h post injection with RB:MNCs and exposure to a green laser (532 nm, 100 mW/cm^2) for 5 min, a strong cytotoxic effect was observed. Tumor growth was significantly reduced (with an inhibition rate of 85% being observed). Moreover, RB:MNCs were not toxic to healthy tissues and organs in the 38 days following intratumoral injection. By conducting a TUNEL (terminal deoxynucleotidyl transferase dUTP nick end labeling) assay, at 4 h post injection, strong cell apoptosis was observed, induced by RB:MNCs (124 µg and 0.25 mg per mouse of RB and Fe_3O_4 NPs, respectively) in the treated mice 24 h after PDT treatment (**Figure 104**).

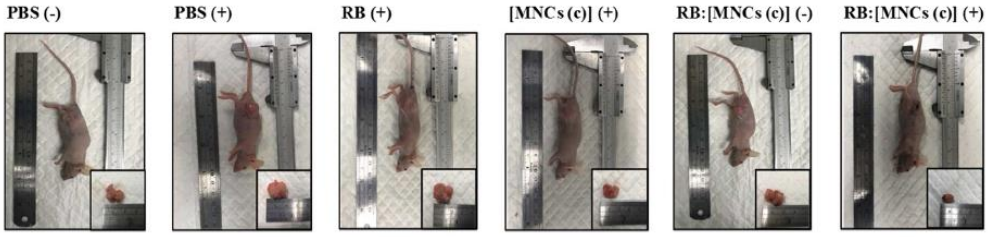

Figure 104 : Representative digital images of mouse tumor treated with PBS, RB, MNCs and RB:MNCs (124 µg and 0.25 mg per mouse of RB and Fe_3O_4 NPs, respectively) with (+) and without (−) green laser light irradiation (532 nm, 100 mW/cm^2, 5 min) for mice after 38 days under different treatment conditions. Reprinted with permission from Yeh et al. [97]. Copyright 2018 American Chemical Society

II.6.4 pH-Sensitive Nanoparticles

pH-sensitive NPs [98] make it possible to perform therapy by achieving either protonation or deprotonation of the NP system. The change in pH enables the delivery of the drug or the triggering of its application system.

Li et al. [99] worked on improving the phototoxicity of RB and enhancing tumor targeting using hypoxia/pH dual-responsive RB-NPs. Cs-Na/RB and Cs-Na/RBD were formed by the self-assembly of nitroimidazole-modified chitosan (Cs-Na) with RB or RBD (RB ω-carboxyheptyl ester) owing to electrostatic and intramolecular interactions. Chitosan was modified by nitroimidazole in order to obtain hypoxia-responsive NPs (nitroimidazole was transformed into its hydrophilic form by nitroreductases leading to the destabilization of NPs, and the release of dyes in cells). The modification of RB was carried out in order to adjust the amphiphilicity and to change the biodistribution of RB by increasing blood circulation time and tumor tissue distribution. The hydrodynamic diameters of Cs-Na/RB and Cs-Na/RBD were determined by DLS (with the values being found to be 86.9 and 115.4 nm, respectively), while their diameters were determined using AFM (50 and 60 nm, respectively). The drug loading capacity of Cs-Na was found to be 23.5 ± 2.5% for RB and 26.4 ± 1.9% (*w*/*w*%) for RBD. In vitro drug release in PBS was determined at pH 7.4 and 5.5 with and without $Na_2S_2O_4$ in order to simulate hypoxia conditions. Dye release was observed for both Cs-Na/RB and Cs-Na/RBD under normal conditions (pH 7.4), but significantly increases, by 22.5% and 19%, respectively, were observed under acidic conditions, by 14.5% and 14%, respectively, under hypoxia conditions, and by 25.5% and 30%, respectively, under acidic and hypoxic conditions. A cytotoxicity study was performed using PC9 cells. At 10 µg/mL under light irradiation (518 nm, 4.0 W/cm^2, 10 min), RB and RBD showed moderate cell inhibition (demonstrating cell

viability of 74.4% and 60.8%, respectively). Without light irradiation, Cs-Na/RB and Cs-Na/RBD exhibited moderate cell inhibition (cell viability of 80.7% and 80.6%, respectively), whereas they exhibited enhanced cell elimination upon light irradiation (with values of 68.8% and 62.2%, respectively). Under hypoxic conditions and under light irradiation, cell was enhanced even further for Cs-Na/RB and Cs-Na/RBD (60.1% and 50.2%, respectively). ROS production from RB, RBD, Cs/RBD, Cs-Na/RB and Cs-Na/RBD on PC9 cells was evaluated by means of a DCFH-DA probe. The results showed that, under the same concentration, RB, RBD, Cs/RBD, Cs- NA/RB, and Cs-NA/RBD with concentrations equivalent to 10 µg/mL of RB or RBD produced 4.1, 5.2, 7.2, 7.7 and 10.3 times more ROS compared to the control group without application of any of the samples.

II.6.5 Nanohybrid Nanoparticles

Hybrid NPs have both organic and inorganic compositions [100]. Su et al. [101] synthesized a multi-functional nanohybrid system, UCNPs@MF-RB/PEG. First, PAA was coated with UCNPs ($NaYF_4$,Yb/Er@$NaYF_4$ (Y/Yb/Er: 78/20/2). Second, $MnFe_2O_4$ (MF) was linked through an intermediate covalent bond and coated using PEI. Finally, PEG-COOH and RB were covalently bonded to this new hybrid system by means of the formation of amide bonds. UCNPs were used to convert photons from NIR into the 521/545 nm wavelength range, which could be further used to activate RB. $^1O_2$ production was observed by means of DPBF. In vitro studies were conducted on HeLa cells with four treatment groups: (1) RB, (2) RB+H_2O_2, (3) UCNPs@MF-RB/PEG, (4) UCNPs@MF-RB/PEG+H_2O_2. For groups 1 and 2, cell viability remained almost unchanged. Cell viability decreased significantly for groups 3 and 4, and this change was more pronounced for group 4 (**Figure 105**). This indicated the importance of the presence of H_2O_2 for the production of ROS.

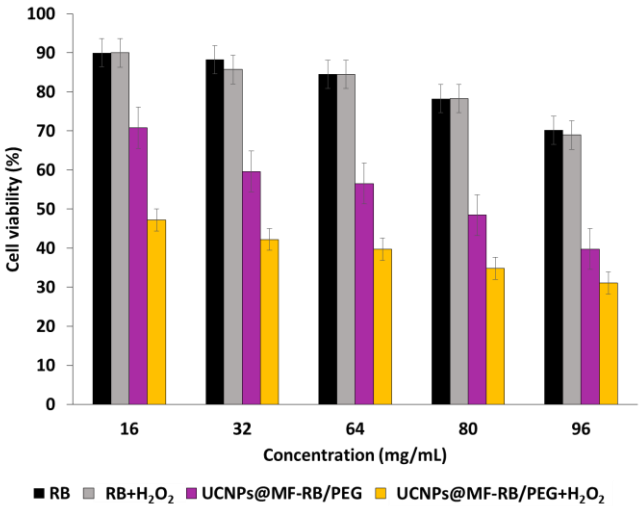

Figure 105 : Cell viability of HeLa cells incubated with various samples under laser irradiation (980 nm, 0.5 mW/cm², 15 min). Adapted from Su et al. [101].

II.6.6 Nanogels

A nanogel is composed of a hydrogel [102], a network of cross-linked hydrophilic polymers that is most often synthetic. These polymers can also be physically or chemically cross-linked

biopolymers. The size of a nanogel is usually 10–100 nm. The pores of the nanogels can be filled with small or large molecules.

Torres-Martínez et al. [103] showed that nanogels adapted for the intracellular transport of PDT agents such as RB did not show cytotoxicity in the dark. $^1O_2$ production was confirmed in water using an ABDA probe. In vitro tests were performed on HT-29 cells incubated for 24 h with RB alone, PBS, and RB@1 (PS-loaded nanogel) ([RB] = 2 μM) and irradiated with two 11 W LEDs (λ_{em} = 400–700 nm) for 2 min. The results showed that RB@1 induced apoptosis in more than 70% of cultured cells, while this value was only 15% for free RB. Under the same conditions, RB@1 showed no dark cytotoxicity.

Table 20 summarizes the physical and chemical properties and PDT conditions presented in all references dealing with nanogels, nanohybrid NPs, pH-sensitive NPs, magnetic NPs, nanocomplexes, and nanocapsules@RB.

Table 20 : References dealing with nanogel@RBs, nanogels, nanohybrid NPs, pH-sensitive NPs, magnetic NPs, nanocomplexes, nanocapsules, including type of NPs, along with their size, excitation wavelength, type of detection of $^1O_2$, the type of coupling between the NPs and the RB, and the type of biological tests performed.

PDT Nanogels, Nanohybrid NPs, pH-Sensitive NPs, Magnetic NPs, Nanocomplexes, Nanocapsules									
References	**Type of NPs**	**Size of NPs (nm)**	**Irradiation Conditions**	**Type of $^1O_2$ Detection**	**Type of Coupling NPs-RB**	**Biological Tests/In Vitro**		**Biological Test/In Vivo**	
						Cells Used	**Results**	**Mice Used**	**Results**
[92]	Ca^{2+}/Gd^{3+} - RB nanocapsules/RGD	300	550 nm, 100 mW/cm^2, 15 min	DPBF	Encapsulation	HepG2	Cytotoxicity (+)	nd	nd
[94]	BP-RB Bis(pyrene)-RB	70	100 W xenon lamp (810 nm, 20 min)	ABDA	Encapsulation	MCF-7	Cytotoxicity (+)	NIH mice (female)	PDT (+)
[97]	(MNCs)-RB	108.6	632 nm, 15 mW/cm^2 or 532 nm, 100 mW/cm^2 for 5 min	DCFH-DA	Electrostatic	MCF-7 Tramp-C1 SKOV-3	Cytotoxicity (+)	BALB/c nude mice bearing MCF-7/MDR	PDT (+)
[99]	Cs-Na/RB, Cs-Na-RBD	Cs-Na/RB: 50	518 nm, 4.0 W/cm^2, 10 min	DCFH-DA	Encapsulation	PC9	Cytotoxicity (+)	nd	nd

		Cs-Na/RBD: 60							
[101]	UCNPs@MF-RB/PEG	75	980 nm, 0.5 mW/cm^2, 15 min	DPBF	Covalent	HeLa	Cytotoxicity (+)	nd	nd
[103]	RB loaded in nanogel	218	11 W LEDs (400–700 nm), 2 min	ABDA	Encapsulation	HT-29	Cytotoxicity (+)	nd	nd

*nd: not determined; cytotoxicity (+): induced tumor cell death in vitro; PDT (+): induced tumor death in vivo.

III. X-Ray Photodynamic Therapy (X-PDT)

III.1 Silica Nanoparticles

Elmenoufy et al. [104] synthesized scintillating NPs (ScNPs) based on LaF_3:Tb coated with layers of silica. These ScNPs were covalently coupled to RB. $^1O_2$ production was confirmed using DPBF. No biological tests were performed.

Hsu et al. [105] designed an ScNP core–shell–shell, Eu(15%)@$NaLuF_4$:Gd(40%)@$NaLuF_4$:Gd(35%),Tb(15%) encapsulating RB and coupled to PEG-FA (ScNP-PAH-RB-PEG-FA). The production of $^1O_2$ following energy transfer was confirmed by ABDA probe (0–10 Gy). In vitro tests were performed on MCF-7 and MDA-MB-231 cells incubated for 24 h with ScNP-PAH-RB-PEG-FA (50 µg/mL). Cell viability decreased by 31% and 21% when MDA and MCF-7 cells, respectively, were treated with ScNP-PAH-RB-PEG-FA before X-ray irradiation (1, 3 and 5 Gy, 75 kV, 20 mA, 20 min) (**Figure 106**).

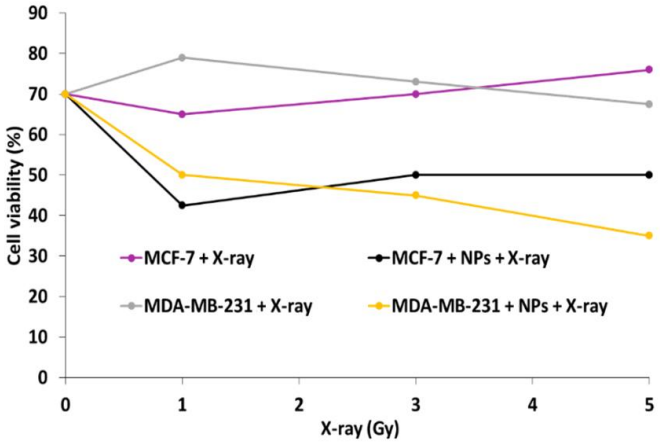

Figure 106 : MDA-MB-231 and MCF-7 cells incubated (50 µg/mL) with core−shell−shell ScNP-PAH-RB-PEG-FA (NPs) for 24 h followed by X-ray radiation with doses of 1, 3, 5 Gy of. Adapted from Hsu et al. [105].

Sun et al. [106] synthesized silicate nanoscintillators with controllable size and X-ray-excited optical luminescence (450–900 nm) using a general ion-incorporating silica-templating method. The NPs were conjugated to RB and RGD peptide (RGD-ZSM-RB). Both in vitro and in vivo experiments demonstrated that RGD-ZSM-RB incubated for 24 h increased the inhibitory effect on tumor progression under low-dose X-ray irradiation (1 Gy). The cell viability of U87MG decreased to half with RGD-ZSM-RB at a concentration of 80 µg/mL following X-ray irradiation of 1 Gy (**Figure 107a**). In vivo treatment in U87MG tumor-bearing mice induced tumor death following irradiation at 1.0 Gy, and an RGD-ZSM-RB concentration of 20 mg/kg (**Figure 107b**). After 48 h, the accumulation of RGD-ZSM-RB (20 mg/mL) was significant in the liver and spleen. Two hours after the injection of RGD-ZSM-RB (20 mg/kg) into the mice, strong fluorescence (ex/em: 570/585 nm) and CT imaging signals (1 Gy) of the RB were observed, and reaching their maximum values after 8 h.

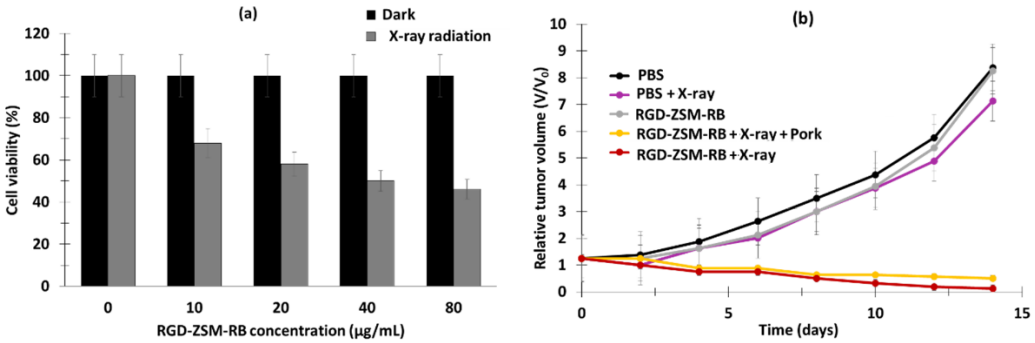

Figure 107 : (a) In vitro evaluation of X-PDT. Cell viability of U87MG cells incubated with different concentrations of RGD-ZSM-RB with or without X-ray irradiation (50 kV, 1 Gy, 10 min). (b) In vivo evaluation of X-PDT. Relative tumor volume obtained from mice under different treatment conditions (X-ray irradiation (1.0 Gy, RGD-ZSM-RB: 20 mg/kg) at different times (1, 2, 4, 6, 8 and 12 h) after injection). Adapted from Sun et al. [106].

Ahmad et al. [107] developed scintillation NPs of CeF_3 co-doped with Tb^{3+} and Gd^{3+} (CeF_3:Gd^{3+}, Tb^{3+}:CGTS), with Gd^{3+} (12.3 mol%) and Tb^{3+} (1.24 mol%) covered with a layer of mesoporous silica loaded with RB (CGTS-RB NPs). The size of the CGTS was 80 ± 1 nm. $^1O_2$ production was confirmed using SOSG. In vitro studies were performed on 4T1, Renca, and Mgc89 cells under several different X-ray doses (0–8 Gy). After incubation of these cells for 24 h with 50 µg/mL of CGTS-RB, irradiation of the cells at 2 Gy revealed decreased cell viability in the three cell lines (survival rates towards 41%) (**Figure 108**).

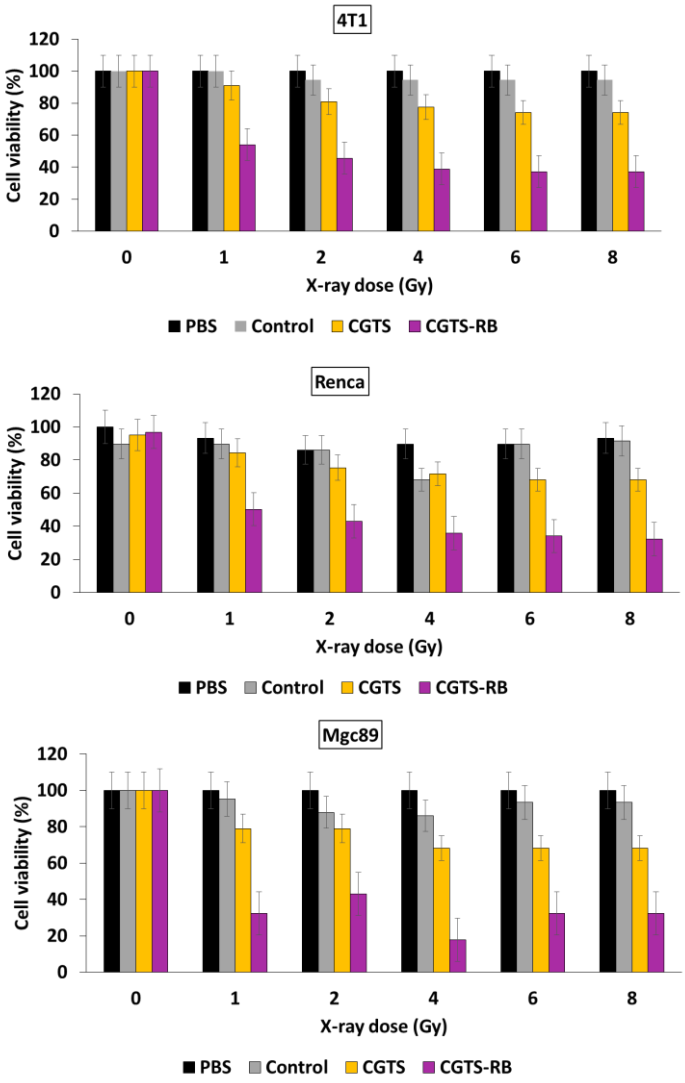

Figure 108 : Cell viability of 4T1, Renca, and Mgc89 cells incubated for 24 h with PBS, CGTS and CGTS-RB (50 µg/mL) under different X-Ray doses (1 Gy/min). Adapted from Ahmad et al. [107].

In vivo tests were performed on 4T1 tumor-bearing mice. Intravenous injection of CGTS-RB (2 mg/mL, 200 µL) and their X-ray irradiation (160 kV, 25 µA, 6 Gy) showed inhibition of tumor proliferation over 14 days (**Figure 109**).

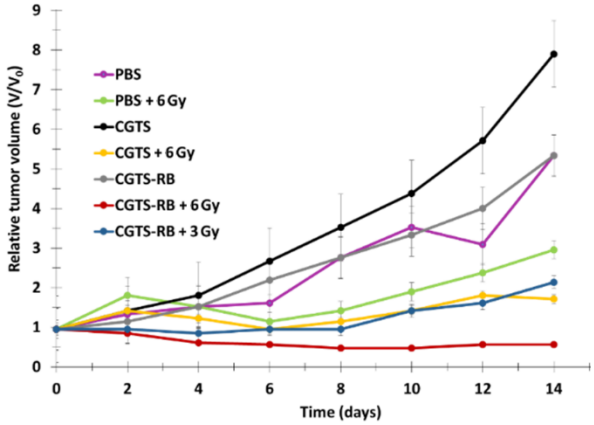

Figure 109 : Relative tumor volume under different treatment conditions (2 mg/mL, 200 µL, X-ray irradiation (160 kV, 25 µA, 1 Gy/min)). Adapted from Ahmad et al. [107].

Table 21 summarizes the physical and chemical properties and X-PDT conditions of nanocapsule@RB presented in all references dealing with magnetic NPs@RB and silica NPs@RB.

Table 21 : References dealing with silica NPs@RB under X-rays, including the type of NPs, along with their size, excitation wavelength, type of detection of $^1O_2$, the type of coupling between the NPs and the RB, and the type of biological tests performed.

X-PDT Silica NPs									
References	**Tpe of NPs**	**Size of NPs (nm)**	**Irradiation Conditions**	**Type of $^1O_2$ Detection**	**Type of Coupling NPs-RB**	**Biological Tests/In Vitro**		**Biological Test/In Vivo**	
						Cells Used	**Results**	**Mice Used**	**Results**
[104]	LaF_3:Tb@SiO_2-RB (ScNP-RB)	45	No biological test	DPBF	Covalent	nd	nd	nd	nd
[107]	CeF_3:Tb^{3+}, Gd^{3+} coated with MSN, loading with RB	89.2	160 kV (1 Gy/min)	Iodure reaction	Covalent	4T1 Renca Mgc893	Toxicity (+)	BALB/c, 4T1	PDT (+)
[105]	CSS ($NaLuF_4$:Gd,Eu@$NaLuF_4$:Gd@$NaLuF_4$:Gd,Tb)-CSS@$MSiO_2$@PAH-RB	27.5	160 kV, 25 mA, 1, 3, 5 Gy	nd	Adsorption	MCF-7/MDA-MB-231	Cytotoxicity (+)	nd	nd
[60]	$Gd_{2.98}Ce_{0.02}Al_5O_{12}$ NPs (GAG) coated with $mSiO_2$ and loaded with RB, GAG@$mSiO_2$@RB	147	Blue light (470 nm) 20 mW/cm^2 (55 kV),	nd	Adsorption	MDA-MB-231	Cytotoxicity (+)	nd	nd

[106]	RB-ZSM-RGD	80.8 ± 3.5	50 kV, 1.0 Gy, 10 min	SOSG	Covalent	U87MG	Cytotoxicity (+)	Nude mice U98 MG PDT (+)

nd: not determined; cytotoxicity (+): induced tumor cell death in vitro; PDT (+): induced tumor death in vivo.

III.2 Polymer Nanoparticles

Bekah et al. [108] synthesized LaF_3 NPs doped with either Ce^{3+}, Tb^{3+}, or both (size average of 4 nm). These NPs were surface modified with alendronate to covalently link PEG and PSs (either Ce6 or RB). No biological experiments were performed.

Maiti et al. [109] reported polyoxomybdate monoclusters loaded (68% (*w*/*w*%)) with RB, namely POMo NCs. These NPs were functionalized with chitosan and PEG and given a macro complex, namely a strawberry shape, with an estimated size of 5.9 nm. Moreover, chitosan formed a hollow into which RB was adsorbed. The POMo NCs were designed firstly for X-ray PDT producing $^1O_2$, and secondly for X-ray-inducible radiation generating auger electrons to induce DNA damage at low X-ray dose deposits of 2 Gy. The impact of the NPs was tested with mouse breast cancer 4T1 cells in vitro and in vivo, following the subcutaneous grafting of cells on BALB/c strain mice. In vitro, cell viability decreased with increasing amounts of NPs and RB. After treatment with 100 µg/mL POMo NCs@RB under 2 Gy/min, cell viability decreased from 100% to 20% (**Figure 110a**). In vivo, the application of POMo NCs@RB (25 mg of Mo/kg) in 4T1 tumor-bearing mice induced total inhibition of tumor volume proliferation (**Figure 110b**).

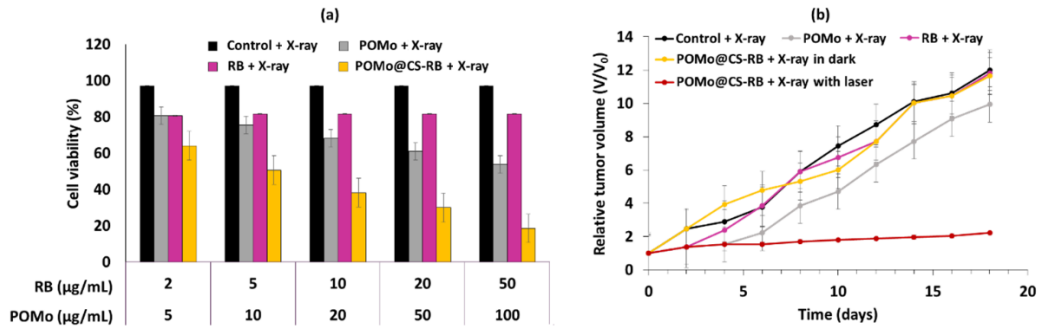

Figure 110 : (a) In vitro cell viability of 4T1 cells incubated for 24 h with various concentrations of RB, POMo and POMo@CS-RB under X-ray irradiation (2 Gy). (b) Relative tumor volume under different treatment conditions (X-ray irradiation (2 Gy), 25 mg/Kg). Adapted from Maiti et al. [109].

Sun et al. [110] explored the combination of PDT and radiation therapy using gadolinium-RB coordination polymer nanodots (GRDs) to treat breast tumor. The hydrodynamic diameter of GRDs was 7.7 ± 1.4 nm. RB and GRDs were excited at 525 nm and respective values of Φ_f of 0.11 and 0.97 were observed in ethanol. Thus, an increase in Φ_f by 7.7 times was observed, demonstrating that immobilization of RB in GRDs induced enhanced fluorescence due to the limitation of the rotation of the aromatic structure. Φ_Δ was also calculated to have values of 1.46 for GRDs and 0.75 for RB in water, showing an increase in Φ_Δ by 1.94 times for GRDs,

proving their suitability for PDT. The $^1O_2$ generation capacity of GRDs was determined by ABDA probe. 4T1 cells were incubated with 24 µg/mL of RB or GRDs for 24 h and irradiated at a wavelength of 532 nm for 5 min (30 mW/cm^2), and cell mortalities of 63.5% and 36.4% were obtained for GRDs, and 36.4% for RB. After irradiation (532 nm, 30 mW/cm^2, 10 min), cell viability was 37.4 ± 1.3%, demonstrating the synergistic effect of combined irradiations (**Figure 111a**). An in vivo therapy assay was performed on 4T1 tumor-bearing mice. Eight groups of mice were employed to evaluate the efficiency of PDT, radiation therapy, and combination therapy: (1) PBS, (2) PBS + light, (3) PBS + X-ray, (4) PBS + light + X-ray, (5) 10 mg/kg GRDs, (6) GRDs + light, (7) GRDs + X-ray, and (8) GRDs + light + X-ray (light = laser irradiation at 532 nm, 140 mW/cm^2 for 15 min and X-ray = 1Gy). No body weight loss was observed in any of the groups. Groups 6 and 7 exhibited good tumor growth inhibition rates (50.5 and 43.8%, respectively), while group 8 exhibited an excellent tumor growth inhibition rate of 98.8% and possessed the smallest tumor volume at the end of the study (**Figure 111b**).

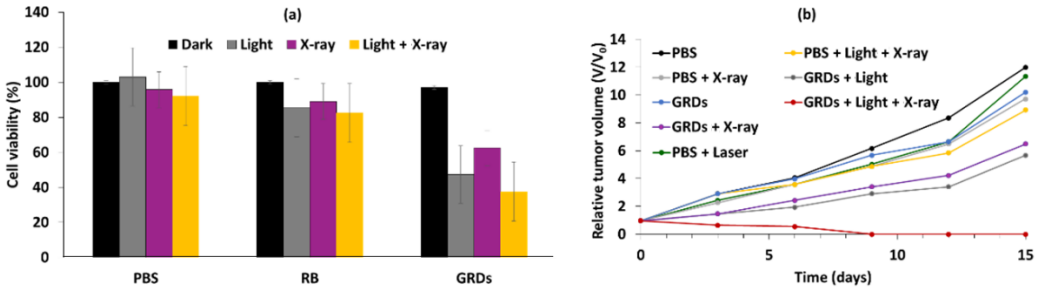

Figure 111 : (a) Cell viability of 4T1 cells incubated for 24 h with PBS, RB and GRDs (4.0 µg/mL) in the dark or following laser and/or X-ray irradiation (laser: 532 nm, 30 mW/cm^2, 5 min; and X-ray: 1 Gy). (b) Relative tumor volume under different treatment conditions (10 mg/kg). (Laser: 532 nm, 140 mW/cm^2, 15 min; X-ray: 1Gy). Adapted from Sun et al. [110].

Table 22 summarizes the physical and chemical properties and X-PDT conditions presented in all references dealing with polymer NPs.

Table 22 : References dealing with polymer NPs@RB under X-rays, including the type of NPs, along with their size, excitation wavelength, type of detection of $^1O_2$, the type of coupling between the NPs and the RB, and the type of biological tests performed.

X-PDT Polymer NPs									
References	**Type of NPs**	**NPs Size (nm)**	**Irradiation Conditions**	**Type of $^1O_2$ Detection**	**Type of Coupling NPs-RB**	**Biological Tests/In Vitro**		**Biological Test/In Vivo**	
						Cells	**Results**	**Mice Used**	**Results**
[110]	Gadolinium (Gd)–RB coordination polymer nanodots (GRDs)	3.3 ± 0.8	In vitro: 532 nm, 30 mW/cm^2, 5 min; 1 Gy In vivo: 532 nm, 140 mW/cm^2,	SOSG	Coordination	4T1	Cytotoxicity (+)	BALB/c mice, 4T1-tumor-bearing mice	PDT (+)

			15 min; 1 Gy						
[109]	POMo@CS–RB	80	2 Gy/min (160 kV)	SOSG	Adsorption	4T1	Cytotoxicity (+)	BALB/c mice, 4T1-tumor-bearing mice	PDT (+)
[108]	Ln NPs-PEG-RB	4	2 Gy (150 kV)	nd	Covalent	nd	nd	B16 murine melanoma cells	PDT (+)

nd: not determined; cytotoxicity (+): induced tumor cell death in vitro; PDT (+): induced tumor death in vivo.

III.3 Nanocomposites

Zhang et al. [111] designed β-$NaGdF_4$:Tb^{3+} NPs and RB (average size of 9 nm). RB was covalently coupled to the NPs. As the NPs were hydrophobic, they were functionalized with 2-aminoethylphosphonic. In this NPs-RB system, $^1O_2$ production was high, due to a high FRET efficiency. In vitro and in vivo biological studies were performed on human hepatocarcinoma HepG2 cells and mice bearing HepG2 cell tumors. Compared to NPs alone at different concentrations, NPs-RB demonstrated a decrease in cell viability from 100% to 20% (1 mg/mL after 90 min irradiation, 1.5 Gy, 24 h incubation) (**Figure 112**). The in vivo X-PDT (1.17 Gy/h, 80 kV, 0.5 mA) efficacy of NPS-RB following 1 h irradiation with 10 mg/mL after 24 h incubation was around 90% on HepG2 tumor.

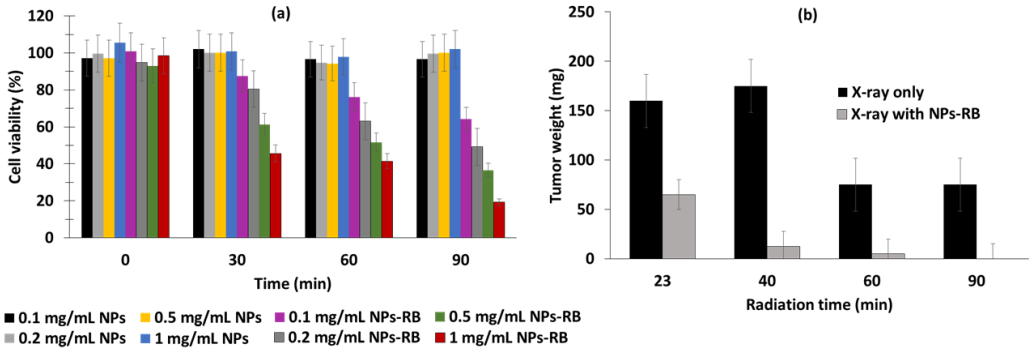

Figure 112 : Antitumor effect of NPs and NPs-RB on nude mice bearing HepG2 tumor cells subcutaneously. NPs or NPs-RB were injected intratumorally. (a) HepG2 cell viability after 90 min irradiation, 1.5 Gy, 24 h incubation. (b) Tumor weight with different irradiation times. Dissected tumor tissues were obtained from nude mice incubated for 24 h with 10 mg/mL NPs-RB. The X-ray tube was set at 80 kV, 0.5 mA and 1.17 Gy/h. Adapted from Zhang et al. [111].

Zhang et al. [112] designed X-ray-luminescent NPs (XLNPs-RB). The XLNPs-RB were composed of a β$NaLuF_4$:Tb^{3+} core with ultra-high FRET efficiency and RB covalently coupled to the core. The NPs were functionalized with AEP (2-aminoethyl dihydrogen phosphate) to increase water dispersity (**Figure 113**).

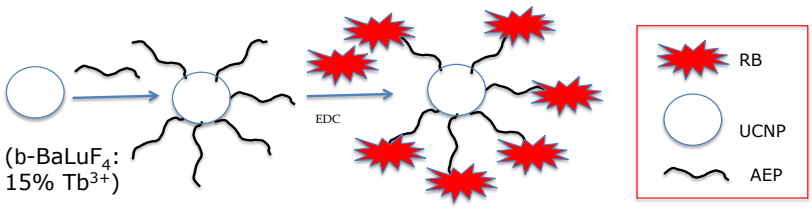

Figure 113 : Preparation of XLNPs-RB. Adapted from Zhang et al. [112].

As RB presented a high luminescence yield, the team evaluated the innovative XLNPs-RB for X-PDT under a lower X-ray dose (0.5 Gy) than other treatment strategies reported by other research teams. The average diameter of XLNPs-RB was 25.6 nm. FRET efficiency was guaranteed by the perfect match between the excitation spectrum of $\beta NaLuF_4:Tb^{3+}$ with the absorption spectrum of RB. XLNPs-RB were X-ray irradiated at 80 kV (0.5 mA) in the presence of a DPBF probe to evaluate $^1O_2$ production. The in vitro cytotoxicity of XLNPs and XLNPs-RB was evaluated on HepG6 cells. After X-ray irradiation for 1.5 h (80 kV, 0.5 mA for 20 min), cell death of 93% was observed at an XLNPs-RB concentration of 1 mg/mL after incubation for 10 h, with insignificant dark cytotoxicity. An in vivo X-PDT study was performed using HepG6 tumor-bearing nude mice injected with 20 mg/mL of XLNPs-RB. Following a single instance of irradiation for 20, 40 or 90 min (0.19, 0.38 and 0.87 Gy each time, respectively), significant tumor growth inhibition was observed, which was similar for the three tested conditions. Following four irradiations of 20, 60 or 90 min, significant tumor growth inhibition was observed, whereas no inhibition was observed in the control groups. Compared to a single instance of irradiation, being subjected to irradiation four times for 60 and 90 min showed better X-PDT efficiency. Nevertheless, with 60 min of irradiation, a significant loss of weight body was observed. In conclusion, successful X-PDT was achieved by performing irradiation four times for 90 min, but a single instance of irradiation of 20 min also gave good results, while requiring minimal X-ray exposure.

Polozhentsev et al. [113] synthesized a $GdF_3:Tb^{3+}$@RB nanocomposite with 10% chelated lanthanide. These NPs exhibited an orthorhombic structure in the form of a *"spindle"* with a length of 250 nm and a width of 60 nm. Following X-PDT (36 mGy/4 min), an efficient FRET energy transfer was observed between the lanthanides and the RB adsorbed onto the nanoparticle. In vivo studies were performed regarding biodistribution on intact BALB/c via CT imaging, revealing a significant improvement in the biodistribution contrast of NPs (200 µL of PEG-capped $GdF_3:Tb^{3+}$ quantified with 20 mg Gd), with 136 mGy after 5 min, 1 h, 2 h and 4 h injection being quantitatively estimated on the basis of CT imaging for the liver and spleen (Figure 114). This study showed enhanced contrast for the liver and spleen, but negative effects should be considered due to the prolonged accumulation times.

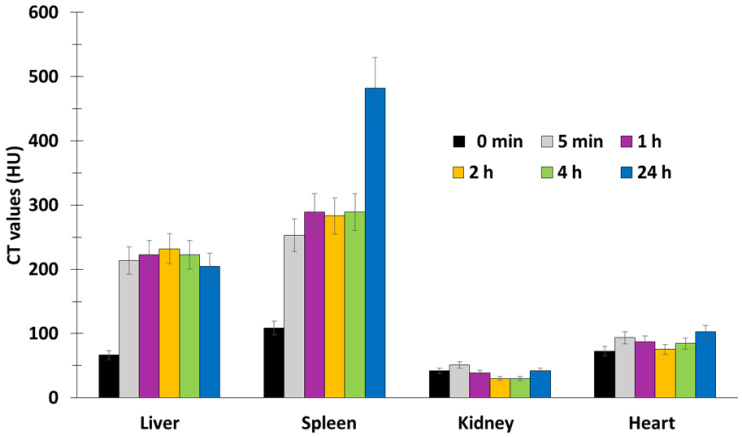

Figure 114 : CT values in the liver, spleen, kidney, and heart on BALB/c 5 min post injection of NPs (200 µL of PEG-capped $GdF_3:Tb^{3+}$ quantified with 20 mg Gd) with different radiation times (X-ray; 136 mGy/4 min). Adapted from Polozhentsev et al. [113].

Table 23 summarizes the physical and chemical properties and X-PDT conditions presented in all references dealing with nanocomposites@RB.

Table 23 : References dealing with nanocomposites@RB under X-ray, including the type of NPs, along with their size, excitation wavelength, type of detection of $^1O_2$, type of coupling between the NPs and the RB, and the types of biological tests performed.

X-PDT Nanocomposites									
References	**Type of NPs**	**Size of NPs (nm)**	**Irradiation Conditions**	**Type of $^1O_2$ Detection**	**Type of Coupling NPs-RB**	**Biological Tests/In Vitro**		**Biological Test/In Vivo**	
						Cells Used	**Results**	**Mice Used**	**Results**
[112]	β-$NaGdF_4:Tb^{3+}$-RB	25.6	80 kV, 0.5 mA (0,05–2 Gy), 20 min	DPBF	Covalent	HepG2	Cytotoxicity (+)	Nude Mice with subcutaneous HepG2 xenografts	PDT (+)
[111]	β-$NaGdF_4:Tb^{3+}$-RB	10	80 kV, 0.5 mA and 45 cm distance (1.17 Gy/h)	DPBF	Covalent	HepG2	Cytotoxicity (+)	Female BALB/c nude mice	PDT (+)
[113]	PEG-capped $GdF_3:Tb^{3+}$@RB nanocomposites	Length: 250 Width: 60	136 mGy/4 min	nd	Adsorption	nd	nd	BALB/c (ca. 3 months age, weight 34–35 g) male mice	PDT (+)

*nd: not determined; cytotoxicity (+): induced tumor cell death in vitro; PDT (+): induced tumor death in vivo.

III.4 Other Nanoparticles

III.4.1 Mesoporous LaF_3:Tb Scintillating Nanoparticles

Tang et al. [114] synthesized scintillating NPs (ScNPs = LaF_3:Tb). RB was encapsulated in these NPs. DPBF was used to confirm $^1O_2$ production. No biological experiments were performed.

III.4.2 Nanophosphors

Luminophores have attracted attention from researchers due to their optical properties [115]. They have important properties of organic phosphors, like its high absorption, good photoluminescence quantum yield, fast luminescence decay time and good processability [116].

Ren et al. [117] designed Tb-doped nanophosphors with a unique core–shell–shell (CSS) structure, referred to as $NaGdF_4$@$NaGdF_4$:Tb@$NaYF_4$ (0.85 mol of Gd and 0.15 mol of Tb). The nanoconjugate was successively covalently functionalized with polylysine, RB (namely, CSS-RB) and thiol-RGD peptide (RGD-CSS-RB), with an average size of 120 nm for CSS-RB. DPBF was used as a probe to confirm $^1O_2$ production. In vitro tests were performed on U87MG cells, showing that cell viability after 24 h incubation with RGD-CSS-RB (200 µg/mL) and X-ray radiation (4 Gy/min) decreased by up to 25%.

III.4.3 Lanthanide@MOF Nanoprobes

Zhao et al. [118] designed a new type of soft X-ray (tube voltage of 10–50 kV)-stimulated nanoprobe via in situ growth of Zr porphyrin-based MOFs—on lanthanide ($NaYF_4$:Gd,Tb@$NaYF_4$ (Gd/Tb: 40/15 (*w*/*w*%)) scintillator NPs (SNP with an estimated size of 30 nm). The nanoprobes exhibited a porous structure, enabling adsorption of RB, as well as porphyrin. In vitro experiments were performed on 4T1 cells following incubation for 24 h with SNPs@Zr-MOF@RB at at different concentrations (0, 50, 100, 200, 500, 1000 µg/mL). In vivo were performed in 4T1 tumor-bearing mice (BALB/c mice). The soft X-ray irradiation was performed at 45 kV for various durations (0, 3, 6, 9, 12, 15 min). A highly significant response was confirmed for the use of deep PDT in tissue and in immunotherapy for cancer cells.

Table 24 summarizes the physical and chemical properties and X-PDT conditions presented in all references dealing with lanthanide@MOF@nanoprobes@RB, nanophosphors@RB and ScNPs@RB.

Table 24 : References dealing with lanthanide@MOF, nanoprobes@RB, nanophosphors@RB and ScNPs@RB under X-ray, including the type of NPs, along with their size, excitation wavelength, type of detection of $^1O_2$, type of coupling between the NPs and the RB, and the type of biological tests performed.

X-PDT Lanthanide@MOF, Nanoprobes, Nanophosphors, ScNPs@RB									
Reference	**Type of NPs**	**Size of NPs (nm)**	**Irradiation Conditions**	**Type of $^1O_2$ Detection**	**Type of Coupling NP-RB**	**Biological Tests/In Vitro**		**Biological Test/In Vivo**	
						Cells Used	**Results**	**Mice Used**	**Results**
[118]	SNPs@Zr-MOF@RB-SNPs	30	45 kV (0, 3, 6, 9, 12, 15 min).	DPBF	Covalent	4T1	Cytotoxicity (+)	4T1 tumor-bearing BALB/c mice)	PDT (+)
[114]	ScNPs: LaF_3:Tb-RB	38.9	75 kV, 2.0 mA	DPBF	Encapsulation	nd	nd	nd	nd
[117]	$NaGdF_4$@ $NaGdF_4$:Tb @$NaYF_4$ (CSS)@RB @cRGD	18.8	4 Gy/min	DPBF	Covalent	U87MG HepG2 NIH-3T3	Cytotocity (+)	nd	nd

*nd: not determined; cytotoxicity (+): induced tumor cell death in vitro; PDT (+): induced tumor death in vivo.

IV. Conclusion

RB coupled to NPs is a good approach for PDT applications (**Figure 115**). RB is a xanthene dye that has interesting photo- and sono-sensitive properties. RB is already used for clinical applications, and an RB formulation for cancer known as PV-10 is currently undergoing clinical trials for use in different types of cancer (melanoma, breast cancer) or infection (clinicaltrials.gov). RB can be used alone, but can also be used as a PS in PDT applications. RB presents several advantages, including the ability to produce $^1O_2$ upon light illumination and solubility in water. One disadvantage is its absorption spectra, which have an absorption maximum wavelength in water of 550 nm, which does not allow great penetration of light into the tissue. Moreover, RB is not selective for cancer cells.

To improve the system, the use of NPs is an interesting strategy. Indeed, all types of NPs presented in this review were very efficient (UCNPs, Silica NPs, Organic NPs, Gold NPs, Pdots NPs, Nanocapsule, Nanocomplex, Magnetic NPs, pH sensitive NPs, Hybrid NPs, Nanogel, Nanocomposite, Nanophosphor, Lanthanide@MOF Nanoprobe). The use of NPs makes it possible to target RB to the tumor as a result of the passive targeting due to EPR effect. It should be noted that, on the basis of all of the papers reviewed here, the efficiency of RB is higher when RB is coupled with NP, and the best system is that in which RB is covalently coupled to NP, rather than encapsulated. From our point of view, UCNPs present many

advantages, since their size is small enough to allow passive targeting, and they can be easily functionalized by a vector, enabling active targeting, and they can be excited by both NIR and X-rays.

Another advantage of RB is that its absorption spectrum matches the emission of lanthanides such as Tb. It is therefore possible to excite Tb using X-ray, and following the energy transfer to RB, to induce the formation of $^1O_2$. The design in which NPs are coupled with RB and the targeted unit in order to target over-expressed receptors could be a nice option for treating deep tumor or melanoma, for example.

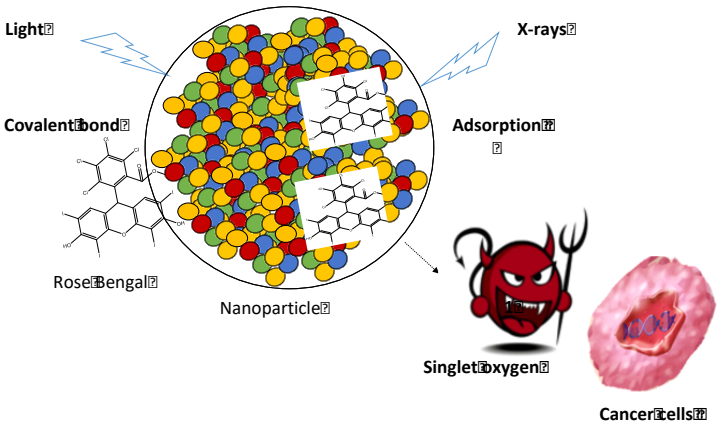

Figure 115 : Illustration of nanoparticle coupled to RB for PDT and PDT-X.

Abbreviations

AB3	Anti-cancer drug
ABDA	9,10-Anthracenediyl-bis(methylene) dimalonic acid
ABMDMA	9,10-Anthracenediyl-bis(methylene)dimalonic acid
ABS	Acetate buffer solution
ADPA	10-dipropionic acid, disodium salt
AEP	2-aminoethyl dihydrogen phosphate
AFM	Atomic force microscope
ATF	Amino terminal fragment of urokinase plasminogen activator
AuNPs	Gold nanoparticles
Azo	Azobenzene
BFNS	Bifunctional nanospheres
BP	Bis-pyrene
bPEI	Branched polyethylenimine
BRET	Bioluminescence resonance energy transfer
BSA	Bovine serum albumin
BTSA	Bis(trimethylsilyl)acetamide

BT	Barium–titanate
CaB	Cathepsin B
CD	Cyclodextrin
cDDP	Cis-diaminedichloroplatine(II)
Ce6	Chlorin e6
CLSM	Confocal laser scanning microscopy
CQDs	Carbon quantum dots
CR	Core satellite superstructure
C_{18}RB	Hydrocarbonized RB
Cs-Na	Nitroimidazole-modified chitosan
CTAB	Cetyltrimethylammoniumbromide
CTS	Chitosan
Cy3	Cyanine 3
DCFH-DA	Dichlorodihydrofluorescein-diacetate
DLS	Dynamic light scattering
DMA	9,10-Dimethylanthracene
DNA	Deoxyribonucleic acid
DOX	Doxorubicin
DPBF	1,3-diphenylisobenzofuran
EADC	1-Ethyl-3-(3-dimethylaminopropyl)carbodiimide
EDC	*N*-Ethyl-*N*′-(3-(dimethylamino)propyl)carbodiimide
EPR	Enhanced permeability effect
FA	Folic acid
FITS	Fluorescein isothiocyanate
FRET	Förster resonance energy transfer
5FU	5-Fluorouracil
GG	Guar gum
GRDs	Gadolinium-rose bengal coordination polymer nanodots
GSH	Glutathione
HA	Hyaluronic acid
HAx	Hexamethylenediamine
HCPT	10-Hydroxycamptothecin
HMSNs	Hollow mesoporous silica nanoparticles
HSPC	Hydrogenated soy L-a-phosphatidylcholine
IR	Infrared
IR825	NIR-absorbing dye
LIFU	Low-intensity focused ultrasound
Ln	Lanthanide
LNP	Luminescent lanthanide nanoparticles
MB	Methylene blue

MF	Multifunctional
MMSN	Magnetic mesoporous silica nanoparticle
MNCs	Magnetic nanoclusters
Mo	Oxymolybdate
MOF	Metal–organic frameworks
MRI	Magnetic resonance imaging
MS	Mesoporous silica
MSNs	Mesoporous silica nanoparticles
MTD	Maximum tolerated dose
MTT	3-[4,5-Dimethylthiazol-2-yl]-2,5 diphenyl tetrazolium bromide
MUCNPs	Multi-shelled upconversion nanoparticles
NCs	Nanocarriers
Nd	Not determined
NHS	*N*-Hydroxysuccinimide
NIR	Near infrared
NPs	Nanoparticles
OA	Oleic acid
$^1O_2$	Singlet oxygen
PAA	Polyacrylic acid
PAH	Poly(allylamine)
PAMAM	Poly(amidoamine)
PARN	Amphiphilic peptide nanocapsules
PBS	Phosphate buffer solution
PCL	PEG-block-poly(ε-caprolactone)
Pdots	Polymer dots
PDT	Photodynamic therapy
PE	Phosphoethanolamine
PEG	Polyethyleneglycol
PEG-*b*-PAsp	Polyethylene glycol-*b*-poly(aspartic acid)
PEI	Polyethylene imine
PE-NH_2	1,2-Dioleoyl-*sn*-glycero-phosphoethanolamine-*N*(hexanoylamine)
PFH	Perfluorohexane
PGA	Poly(glycolic acid)
PHLA	Partially hydrolyzed α-lactalbumin
p.i	Post injection
PLA	Poly(lactic acid)
PLGA	Poly(lactic-co-glycolic acid)
PPADT	Poly-(1,4-phenyleneacetone dimethylenethioketal)
PS	Photosensitizer
PTT	Photothermal therapy

PTX	Paclitaxel
PVA	Poly(vinyl alcohol)
PVK	Poly(*N*-vinyl carbazole)
QDs	Quantum dots
QSY7	ROS quenching
RB	Rose Bengal
RBD	Rose bengal ω-carboxyheptyl ester
RET	Resonance energy transfer
ROS	Reactive oxygen species
ScNPs	Scintillating ~~NPs~~ *nanoparticles*
SHG	Second harmonic generation
SOSG	Singlet oxygen sensor green
SSTRs	Somatostatin receptors
TEM	Transmission emission microscopy
TEOS	Tetraethyl orthosilicate
TMP–OH	2,2,6,6-Tetramethyl-4-piperidinol
TOPO	Trioctylphosphine oxide
TPA	Two-photon activation
TUNEL	Terminal deoxynucleotidyl transferase dUTP nick end labeling
UCL	Upconversion luminescence
UCNPs	Upconversion nanoparticles
UPA	Urokinase plasminogen activator
US	~~Ultrason~~ Ultrasound
UV	Ultraviolet
WEN	White emitting $NaYF_4$
XLNPs	X-Ray-luminescent ~~NPs~~ nanoparticles
X-PDT	Photodynamic therapy induced by X-ray
ZIF-90	Zeolitic imidazolate framework-90
ZnPc-COOH	Zinc β-carboxyphthalocyanine

References

1. Malik, R.; Manocha, A.; Suresh, D. Photodynamic therapy—A strategic review. *Indian J. Dent. Res.* **2010**, *21*, 285–291. https://doi.org/10.4103/0970-9290.66659.

2. Selvasekar, C.R.; Birbeck, N.; McMillan, T.J.; Wainwright, M.; Walker, S.J. Photodynamic therapy and the alimentary tract. *Aliment. Pharmacol. Ther.* **2001**, *15*, 899–915. https://doi.org/10.1046/j.1365-2036.2001.00990.x.

3. Stranadko, E.P.; Ponomarev, G.V.; Mechkov, V.; Ryabov, M.; Ivanov, A.V.; Reshetnickov, A.V.; Koraboyev, U.M. First experience of photodithazine clinical application for photodynamic therapy of malignant tumors. In Proceedings of the Optical Methods for Tumor Treatment and Detection: Mechanisms and Techniques in Photodynamic Therapy IX, 29 March 2000; pp. 138–144.

4. Macdonald, I.J.; Dougherty, T.J. Basic principles of photodynamic therapy. *J. Porphyr. Phthalocyanines* **2001**, *5*, 105–129. https://doi.org/10.1002/jpp.328.

5. Lan, M.; Zhao, S.; Liu, W.; Lee, C.S.; Zhang, W.; Wang, P. Photosensitizers for photodynamic therapy. *Adv. Healthc. Mater.* **2019**, *8*, 1900132. https://doi.org/10.1002/adhm.201900132.
6. Zheng, B.-D.; Ye, J.; Zhang, X.-Q.; Zhang, N.; Xiao, M.-T. Recent advances in supramolecular activatable phthalocyanine-based photosensitizers for anti-cancer therapy. *Coordin. Chem. Rev.* **2021**, *447*, 214155. https://doi.org/10.1016/j.ccr.2021.214155.
7. Li, D.; Pan, J.; Xu, S.; Fu, S.; Chu, C.; Liu, G. Activatable Second Near-Infrared Fluorescent Probes: A New Accurate Diagnosis Strategy for Diseases. *Biosensors* **2021**, *11*, 436. https://doi.org/10.3390/bios11110436.
8. Chatterjee, D.K.; Fong, L.S.; Zhang, Y. Nanoparticles in photodynamic therapy: An emerging paradigm. *Adv. Drug Deliv. Rev.* **2008**, *60*, 1627–1637. https://doi.org/10.1016/j.addr.2008.08.003.
9. Gunaydin, G.; Gedik, M.E.; Ayan, S. Photodynamic Therapy—Current Limitations and Novel Approaches. *Front. Chem.* **2021**, *9*, 400. https://doi.org/10.3389/fchem.2021.691697.
10. Chaudhuri, S.; Sardar, S.; Bagchi, D.; Dutta, S.; Debnath, S.; Saha, P.; Lemmens, P.; Pal, S.K. Photoinduced Dynamics and Toxicity of a Cancer Drug in Proximity of Inorganic Nanoparticles under Visible Light. *ChemPhysChem* **2015**, *17*, 270–277. https://doi.org/10.1002/cphc.201500905.
11. Mol, J.A.; Docter, R.; Hennemann, G.; Visser, T.J. Modification of rat liver iodothyronine 5′-deiodinase activity with diethylpyrocarbonate and Rose Bengal; Evidence for an active site histidine residue. *Biochem. Biophys. Res. Commun.* **1984**, *120*, 28–36. https://doi.org/10.1016/0006-291x(84)91409-8.
12. Machado, L.M.; Castro, R.S.; Fontes, B.M. Staining Patterns in Dry Eye Syndrome: Rose Bengal Versus Lissamine Green. *Cornea* **2009**, *28*, 732–734. https://doi.org/10.1097/ico.0b013e3181930c03.
13. Qin, J.; Kunda, N.; Qiao, G.; Calata, J.F.; Pardiwala, K.; Prabhakar, B.S.; Maker, A.V. Colon cancer cell treatment with rose bengal generates a protective immune response via immunogenic cell death. *Cell Death Dis.* **2017**, *8*, e2584. https://doi.org/10.1038/cddis.2016.473.
14. Zheng, B.; Zhong, D.; Xie, T.; Zhou, J.; Li, W.; Ilyas, A.; Lu, Y.; Zhou, M.; Deng, R. Near-infrared photosensitization via direct triplet energy transfer from lanthanide nanoparticles. *Chem* **2021**, *7*, 1615–1625. https://doi.org/10.1016/j.chempr.2021.03.008.
15. Wang, J.; Deng, R. Energy Transfer in Dye-Coupled Lanthanide-Doped Nanoparticles: From Design to Application. *Chem. Asian J.* **2018**, *13*, 614–625. https://doi.org/10.1002/asia.201701817.
16. Oar, M.A.; Serin, J.M.; Dichtel, W.R.; Fréchet, J.M.J.; Ohulchanskyy, T.Y.; Prasad, P.N. Photosensitization of Singlet Oxygen via Two-Photon-Excited Fluorescence Resonance Energy Transfer in a Water-Soluble Dendrimer. *Chem. Mater.* **2005**, *17*, 2267–2275. https://doi.org/10.1021/cm047825i.
17. Wilhelm, S. Perspectives for Upconverting Nanoparticles. *ACS Nano* **2017**, *11*, 10644–10653. https://doi.org/10.1021/acsnano.7b07120.
18. Huang, L.; Zhao, Y.; Zhang, H.; Huang, K.; Yang, J.; Han, G. Expanding Anti-Stokes Shifting in Triplet-Triplet Annihilation Upconversion for In Vivo Anticancer Prodrug Activation. *Angew. Chem.* **2017**, *129*, 14592–14596. https://doi.org/10.1002/ange.201704430.

19. Han, S.; Deng, R.; Xie, X.; Liu, X. Enhancing Luminescence in Lanthanide-Doped Upconversion Nanoparticles. *Angew. Chem. Int. Ed.* **2014**, *53*, 11702–11715. https://doi.org/10.1002/anie.201403408.
20. Liu, K.; Liu, X.; Zeng, Q.; Zhang, Y.; Tu, L.; Liu, T.; Kong, X.; Wang, Y.; Cao, F.; Lambrechts, S.; et al. Covalently Assembled NIR Nanoplatform for Simultaneous Fluorescence Imaging and Photodynamic Therapy of Cancer Cells. *ACS Nano* **2012**, *6*, 4054–4062. https://doi.org/10.1021/nn300436b.
21. Chen, Q.; Wang, C.; Cheng, L.; He, W.; Cheng, Z.; Liu, Z. Protein modified upconversion nanoparticles for imaging-guided combined photothermal and photodynamic therapy. *Biomaterials* **2014**, *35*, 2915–2923. https://doi.org/10.1016/j.biomaterials.2013.12.046.
22. Wang, S.; Zhang, L.; Dong, C.; Su, L.; Wang, H.; Chang, J. Smart pH-responsive upconversion nanoparticles for enhanced tumor cellular internalization and near-infrared light-triggered photodynamic therapy. *Chem. Commun.* **2015**, *51*, 406–408. https://doi.org/10.1039/C4CC08178A.
23. Wang, D.; Xue, B.; Kong, X.; Tu, L.; Liu, X.; Zhang, Y.; Chang, Y.; Luo, Y.; Zhao, H.; Zhang, H. 808 nm driven Nd^{3+}-sensitized upconversion nanostructures for photodynamic therapy and simultaneous fluorescence imaging. *Nanoscale* **2014**, *7*, 190–197. https://doi.org/10.1039/c4nr04953e.
24. Lu, S.; Tu, D.; Hu, P.; Xu, J.; Li, R.; Wang, M.; Chen, Z.; Huang, M.; Chen, X. Multifunctional Nano-Bioprobes Based on Rattle-Structured Upconverting Luminescent Nanoparticles. *Angew. Chem. Int. Ed.* **2015**, *54*, 7915–7919. https://doi.org/10.1002/anie.201501468.
25. Li, Y.; Tang, J.; Pan, D.-X.; Sun, L.-D.; Chen, C.; Liu, Y.; Wang, Y.-F.; Shi, S.; Yan, C.-H. A Versatile Imaging and Therapeutic Platform Based on Dual-Band Luminescent Lanthanide Nanoparticles toward Tumor Metastasis Inhibition. *ACS Nano* **2016**, *10*, 2766–2773. https://doi.org/10.1021/acsnano.5b07873.
26. Liang, L.; Care, A.; Zhang, R.; Lu, Y.; Packer, N.H.; Sunna, A.; Qian, Y.; Zvyagin, A.V. Facile Assembly of Functional Upconversion Nanoparticles for Targeted Cancer Imaging and Photodynamic Therapy. *ACS Appl. Mater. Interfaces* **2016**, *8*, 11945–11953. https://doi.org/10.1021/acsami.6b00713.
27. Ai, F.; Sun, T.; Xu, Z.; Wang, Z.; Kong, W.; To, M.W.; Wang, F.; Zhu, G. An upconversion nanoplatform for simultaneous photodynamic therapy and Pt chemotherapy to combat cisplatin resistance. *Dalton Trans.* **2016**, *45*, 13052–13060. https://doi.org/10.1039/c6dt01404f.
28. Chen, G.; Jaskula-Sztul, R.; Esquibel, C.R.; Lou, I.; Zheng, Q.; Dammalapati, A.; Harrison, A.; Eliceiri, K.; Tang, W.; Chen, H.; et al. Neuroendocrine Tumor-Targeted Upconversion Nanoparticle-Based Micelles for Simultaneous NIR-Controlled Combination Chemotherapy and Photodynamic Therapy, and Fluorescence Imaging. *Adv. Funct. Mater.* **2017**, *27*, 1604671. https://doi.org/10.1002/adfm.201604671.
29. Chang, Y.; Li, X.; Zhang, L.; Xia, L.; Liu, X.; Li, C.; Zhang, Y.; Tu, L.; Xue, B.; Zhao, H.; et al. Precise Photodynamic Therapy of Cancer via Subcellular Dynamic Tracing of Dual-loaded Upconversion Nanophotosensitizers. *Sci. Rep.* **2017**, *7*, 45633. https://doi.org/10.1038/srep45633.

30. Hou, B.; Yang, W.; Dong, C.; Zheng, B.; Zhang, Y.; Wu, J.; Wang, H.; Chang, J. Controlled co-release of doxorubicin and reactive oxygen species for synergistic therapy by NIR remote-triggered nanoimpellers. *Mater. Sci. Eng. C* **2017**, *74*, 94–102. https://doi.org/10.1016/j.msec.2017.02.016.
31. Kumar, B.; Rathnam, V.S.S.; Kundu, S.; Saxena, N.; Banerjee, I.; Giri, S. White-light-emitting $NaYF_4$ Nanoplatform for NIR Upconversion-mediated Photodynamic Therapy and Bioimaging. *ChemNanoMat* **2018**, *4*, 583–595. https://doi.org/10.1002/cnma.201800096.
32. Sabri, T.; Pawelek, P.D.; Capobianco, J.A. Dual Activity of Rose Bengal Functionalized to Albumin-Coated Lanthanide-Doped Upconverting Nanoparticles: Targeting and Photodynamic Therapy. *ACS Appl. Mater. Interfaces* **2018**, *10*, 26947–26953. https://doi.org/10.1021/acsami.8b08919.
33. Buchner, M.; García Calavia, P.; Muhr, V.; Kröninger, A.; Baeumner, A.J.; Hirsch, T.; Russell, D.A.; Marín, M.J. Photosensitiser functionalised luminescent upconverting nanoparticles for efficient photodynamic therapy of breast cancer cells. *Photochem. Photobiol. Sci.* **2019**, *18*, 98–109. https://doi.org/10.1039/C8PP00354H.
34. Xie, Z.; Cai, X.; Sun, C.; Liang, S.; Shao, S.; Huang, S.; Cheng, Z.; Pang, M.; Xing, B.; Al Kheraif, A.Z.; et al., O2-Loaded pH-Responsive Multifunctional Nanodrug Carrier for Overcoming Hypoxia and Highly Efficient Chemo-Photodynamic Cancer Therapy. *Chem. Mater.* **2019**, *31*, 483–490. https://doi.org/10.1021/acs.chemmater.8b04321
35. Kumar, B.; Murali, A.; Bharath, A.B.; Giri, S. Guar gum modified upconversion nanocomposites for colorectal cancer treatment through enzyme-responsive drug release and NIR-triggered photodynamic therapy. *Nanotechnology* **2019**, *30*, 315102. https://doi.org/10.1088/1361-6528/ab116e.
36. Sun, X.; Ji, Z.; He, S. SHG-enhanced NIR-excited in vitro photodynamic therapy using composite nanoparticles of barium titanate and rose Bengal. *RSC Adv.* **2019**, *9*, 8056–8064. https://doi.org/10.1039/c9ra00432g.
37. Song, D.; Chi, S.; Li, X.; Wang, C.; Li, Z.; Liu, Z. Upconversion System with Quantum Dots as Sensitizer: Improved Photoluminescence and PDT Efficiency. *ACS Appl. Mater. Interfaces* **2019**, *11*, 41100–41108. https://doi.org/10.1021/acsami.9b16237.
38. Wawrzyńczyk, D.; Cichy, B.; Zaręba, J.K.; Bazylińska, U. On the interaction between up-converting $NaYF_4:Er^{3+},Yb^{3+}$ nanoparticles and Rose Bengal molecules constrained within the double core of multifunctional nanocarriers. *J. Mater. Chem. C* **2019**, *7*, 15021–15034. https://doi.org/10.1039/c9tc04163j.
39. Wang, H.-Y.; Hou, L.; Li, H.-L.; Wang, X.; Cao, Y.; Zhang, B.-Y.; Wang, J.-T.; Wei, S.-J.; Dang, H.-W.; Ran, H.-T. A nanosystem loaded with perfluorohexane and rose bengal coupled upconversion nanoparticles for multimodal imaging and synergetic chemo-photodynamic therapy of cancer. *Biomater. Sci.* **2020**, *8*, 2488–2506. https://doi.org/10.1039/c9bm02081k.
40. Li, Y.; Zhang, X.; Zhang, Y.; He, Y.; Liu, Y.; Ju, H. Activatable photodynamic therapy with therapeutic effect prediction based on a self-correction upconversion nanoprobe. *ACS Appl. Mater. Interfaces* **2020**, *12*, 19313–19323. https://doi.org/10.1021/acsami.0c03432.
41. Han, R.; Tang, K.; Hou, Y.; Yu, J.; Wang, C.; Wang, Y. Fabrication of core/shell/shell structure nanoparticle with anticancer drug and dual-photosensitizer co-loading for synergistic

chemotherapy and photodynamic therapy. *Microporous Mesoporous Mater.* **2020**, *297*, 110049. https://doi.org/10.1016/j.micromeso.2020.110049.

42. Jin, F.-Y.; Qi, J.; Zhu, M.; Liu, D.; You, Y.; Shu, G.; Du, Y.; Wang, J.; Yu, H.; Sun, M.; et al. NIR-Triggered Sequentially Responsive Nanocarriers Amplified Cascade Synergistic Effect of Chemo-Photodynamic Therapy with Inspired Antitumor Immunity. *ACS Appl. Mater. Interfaces* **2020**, *12*, 32372–32387. https://doi.org/10.1021/acsami.0c07503.

43. Li, Z.; Qiao, X.; He, G.; Sun, X.; Feng, D.; Hu, L.; Xu, H.; Xu, H.-B.; Ma, S.; Tian, J. Core-satellite metal-organic framework@upconversion nanoparticle superstructures via electrostatic self-assembly for efficient photodynamic theranostics. *Nano Res.* **2020**, *13*, 3377–3386. https://doi.org/10.1007/s12274-020-3025-0.

44. Borodziuk, A.; Kowalik, P.; Duda, M.; Wojciechowski, T.; Minikayev, R.; Kalinowska, D.; Klepka, M.; Sobczak, K.; Kłopotowski, Ł.; Sikora, B. Unmodified Rose Bengal photosensitizer conjugated with $NaYF_4$:Yb,Er upconverting nanoparticles for efficient photodynamic therapy. *Nanotechnology* **2020**, *31*, 465101. https://doi.org/10.1088/1361-6528/aba975.

45. Tezuka, K.; Umezawa, M.; Liu, T.-I.; Nomura, K.; Okubo, K.; Chiu, H.-C.; Kamimura, M.; Soga, K. Upconversion Luminescent Nanostructure with Ultrasmall Ceramic Nanoparticles Coupled with Rose Bengal for NIR-Induced Photodynamic Therapy. *ACS Appl. Bio Mater.* **2021**, *4*, 4462–4469. https://doi.org/10.1021/acsabm.1c00213.

46. Quignard, S. *Silica Nanoparticles Behaviour in Biological Medium: From Cells to Biomaterials Comportement des Nanoparticules de Silice en Milieu Biologique: Des Cellules aux Biomatériaux*; Université Pierre et Marie Curie: Paris, France, 2012.

47. Natarajan, S.K.; Selvaraj, S. Mesoporous silica nanoparticles: Importance of surface modifications and its role in drug delivery. *RSC Adv.* **2014**, *4*, 14328–14334. https://doi.org/10.1039/c4ra00781f.

48. Soares-Santos, P.C.; Nogueira, H.I.; Félix, V.; Drew, M.G.; Sá Ferreira, R.A.; Carlos, L.D.; Trindade, T. Novel lanthanide luminescent materials based on complexes of 3-hydroxypicolinic acid and silica nanoparticles. *Chem. Mater.* **2003**, *15*, 100–108. https://doi.org/10.1021/cm021188j.

49. Uppal, A.; Jain, B.; Gupta, P.K.; Das, K. Photodynamic Action of Rose Bengal Silica Nanoparticle Complex on Breast and Oral Cancer Cell Lines. *Photochem. Photobiol.* **2011**, *87*, 1146–1151. https://doi.org/10.1111/j.1751-1097.2011.00967.x.

50. Gianotti, E.; MartinsEstevão, B.; Cucinotta, F.; Hioka, N.; Rizzi, M.; Renò, F.; Marchese, L. An Efficient Rose Bengal Based Nanoplatform for Photodynamic Therapy. *Chem. A Eur. J.* **2014**, *20*, 10921–10925. https://doi.org/10.1002/chem.201404296.

51. Martins Estevão, B.; Cucinotta, F.; Hioka, N.; Cossi, M.; Argeri, M.; Paul, G. Rose Bengal incorporated in mesostructured silica nanoparticles: Structural characterization, theoretical modeling and singlet oxygen delivery. *Phys. Chem. Chem. Phys.* **2015**, *17*, 26804–26812. https://doi.org/10.1039/C5CP03564C.

52. Yildirim, A.; Turkaydin, M.; Garipcan, B.; Bayindir, M. Cytotoxicity of multifunctional surfactant containing capped mesoporous silica nanoparticles. *RSC Adv.* **2016**, *6*, 32060–32069. https://doi.org/10.1039/C5RA21722A.

53. Liu, H.; Yang, Y.; Wang, A.; Han, M.; Cui, W.; Li, J. Hyperbranched Polyglycerol-Doped Mesoporous Silica Nanoparticles for One- and Two-Photon Activated Photodynamic Therapy. *Adv. Funct. Mater.* **2016**, *26*, 2561–2570. https://doi.org/10.1002/adfm.201504939.
54. Zhou, F.; Zheng, B.; Zhang, Y.; Wu, Y.; Wang, H.; Chang, J. Construction of near-infrared light-triggered reactive oxygen species-sensitive (UCN/SiO_2-RB + DOX)@PPADT nanoparticles for simultaneous chemotherapy and photodynamic therapy. *Nanotechnology* **2016**, *27*, 235601. https://doi.org/10.1088/0957-4484/27/23/235601.
55. Oliveira, R.C.D.S.; Corrêa, R.J.; Teixeira, R.S.P.; Queiroz, D.D.; Souza, R.D.S.; Garden, S.J.; de Lucas, N.C.; Pereira, M.D.; Forero, J.S.B.; Romani, E.C.; et al. Silica nanoparticles doped with anthraquinone for lung cancer phototherapy. *J. Photochem. Photobiol. B Biol.* **2016**, *165*, 1–9. https://doi.org/10.1016/j.jphotobiol.2016.10.008.
56. Zhan, J.; Ma, Z.; Wang, D.; Li, X.; Li, X.; Le, L.; Kang, A.; Hu, P.; She, L.; Yang, F. Magnetic and pH dual-responsive mesoporous silica nanocomposites for effective and low-toxic photodynamic therapy. *Int. J. Nanomed.* **2017**, *12*, 2733–2748. https://doi.org/10.2147/ijn.s127528.
57. Liu, Y.; Liu, X.; Xiao, Y.; Chen, F.; Xiao, F. A multifunctional nanoplatform based on mesoporous silica nanoparticles for imaging-guided chemo/photodynamic synergetic therapy. *RSC Adv.* **2017**, *7*, 31133–31141. https://doi.org/10.1039/c7ra04549b.
58. Yan, T.; Cheng, J.; Liu, Z.; Cheng, F.; Wei, X.; He, J. pH-Sensitive mesoporous silica nanoparticles for chemo-photodynamic combination therapy. *Colloids Surf. B Biointerfaces* **2018**, *161*, 442–448. https://doi.org/10.1016/j.colsurfb.2017.11.006.
59. Jain, A.; Koyani, R.D.; Muñoz, C.; Sengar, P.; Contreras, O.E.; Juárez, P.; Hirata, G.A. Blue light triggered generation of reactive oxygen species from silica coated $Gd_3Al_5O1_2$:Ce^{3+} nanoparticles loaded with rose Bengal. *Data Brief* **2018**, *20*, 1023–1028. https://doi.org/10.1016/j.dib.2018.08.072.
60. Jain, A.; Koyani, R.D.; Muñoz, C.; Sengar, P.; Contreras, O.E.; Juárez, P.; Hirata, G.A. Magnetic-luminescent cerium-doped gadolinium aluminum garnet nanoparticles for simultaneous imaging and photodynamic therapy of cancer cells. *J. Colloid Interface Sci.* **2018**, *526*, 220–229. https://doi.org/10.1016/j.jcis.2018.04.100.
61. Hu, G.; Yang, L.; Li, Y.; Wang, L. Continuous and scalable fabrication of stable and biocompatible MOF@SiO_2 nanoparticles for drug loading. *J. Mater. Chem. B* **2018**, *6*, 7936–7942. https://doi.org/10.1039/C8TB02308E.
62. Chen, K.; Chang, C.; Liu, Z.; Zhou, Y.; Xu, Q.; Li, C.; Huang, C.; Xu, H.; Xu, P.; Lu, B. Hyaluronic acid targeted and pH-responsive nanocarriers based on hollow mesoporous silica nanoparticles for chemo-photodynamic combination therapy. *Colloids Surf. B: Biointerfaces* **2020**, *194*, 111166. https://doi.org/10.1016/j.colsurfb.2020.111166.
63. Miletto, I.; Gionco, C.; Paganini, M.C.; Martinotti, S.; Ranzato, E.; Giamello, E.; Marchese, L.; Gianotti, E. Vis-NIR luminescent lanthanide-doped core-shell nanoparticles for imaging and photodynamic therapy. *J. Photochem. Photobiol. A Chem.* **2020**, *403*, 112840. https://doi.org/10.1016/j.jphotochem.2020.112840.
64. Prieto-Montero, R.; Prieto-Castañeda, A.; Katsumiti, A.; Cajaraville, M.; Agarrabeitia, A.; Ortiz, M.; Martínez-Martínez, V. Functionalization of Photosensitized Silica Nanoparticles for Advanced Photodynamic Therapy of Cancer. *Int. J. Mol. Sci.* **2021**, *22*, 6618. https://doi.org/10.3390/ijms22126618.

65. Berthet, M. *Nanoparticules Biodégradables et Multifonctionnelles pour la Régénération Tissulaire de Plaies Cutanées Profondes*; Lyon, France, 2017.
66. Castro, F.; Pinto, M.L.; Pereira, C.L.; Serre, K.; Barbosa, M.A.; Vermaelen, K.; Gärtner, F.; Gonçalves, R.M.; De Wever, O.; Oliveira, M.J. Chitosan/γ-PGA nanoparticles-based immunotherapy as adjuvant to radiotherapy in breast cancer. *Biomaterials* **2020**, *257*, 120218. https://doi.org/10.1016/j.biomaterials.2020.120218.
67. Bala, I.; Hariharan, S.; Kumar, M.N.V.R. PLGA Nanoparticles in Drug Delivery: The State of the Art;. *Crit. Rev. Ther. Drug Carr. Syst.* **2004**, *21*, 387–422. https://doi.org/10.1615/critrevtherdrugcarriersyst.v21.i5.20.
68. Chen, K.; Preuß, A.; Hackbarth, S.; Wacker, M.; Langer, K.; Röder, B. Novel photosensitizer-protein nanoparticles for photodynamic therapy: Photophysical characterization and in vitro investigations. *J. Photochem. Photobiol. B Biol.* **2009**, *96*, 66–74. https://doi.org/10.1016/j.jphotobiol.2009.04.006.
69. Karthikeyan, K.; Babu, A.; Kim, S.-J.; Murugesan, R.; Jeyasubramanian, K. Enhanced photodynamic efficacy and efficient delivery of Rose Bengal using nanostructured poly(amidoamine) dendrimers: Potential application in photodynamic therapy of cancer. *Cancer Nanotechnol.* **2011**, *2*, 95–103. https://doi.org/10.1007/s12645-011-0019-3.
70. Baumann, P.; Balasubramanian, V.; Onaca-Fischer, O.; Sienkiewicz, A.; Palivan, C.G. Light-responsive polymer nanoreactors: A source of reactive oxygen species on demand. *Nanoscale* **2012**, *5*, 217–224. https://doi.org/10.1039/c2nr32380j.
71. Bhattacharyya, S.; Barman, M.K.; Baidya, A.; Patra, A. Singlet Oxygen Generation from Polymer Nanoparticles–Photosensitizer Conjugates Using FRET Cascade. *J. Phys. Chem. C* **2014**, *118*, 9733–9740. https://doi.org/10.1021/jp4127094.
72. Han, S.; Hwang, B.W.; Jeon, E.Y.; Jung, D.; Lee, G.H.; Keum, D.H.; Kim, K.S.; Yun, S.H.; Cha, H.J.; Hahn, S.K. Upconversion Nanoparticles/Hyaluronate–Rose Bengal Conjugate Complex for Noninvasive Photochemical Tissue Bonding. *ACS Nano* **2017**, *11*, 9979–9988. https://doi.org/10.1021/acsnano.7b04153.
73. Yang, Y.; Hou, W.; Liu, S.; Sun, K.; Li, M.; Wu, C. Biodegradable Polymer Nanoparticles for Photodynamic Therapy by Bioluminescence Resonance Energy Transfer. *Biomacromolecules* **2017**, *19*, 201–208. https://doi.org/10.1021/acs.biomac.7b01469.
74. Chang, Y.-C.; Del Valle, A.C.; Yeh, H.-P.; He, Y.; Huang, Y.-F. Development of Photo-Activated ROS-Responsive Nanoplatform as a Dual-Functional Drug Carrier in Combinational Chemo-Photodynamic Therapy. *Front. Chem.* **2019**, *6*, 647. https://doi.org/10.3389/fchem.2018.00647.
75. Bazylińska, U.; Wawrzyńczyk, D.; Szewczyk, A.; Kulbacka, J. Engineering and biological assessment of double core nanoplatform for co-delivery of hybrid fluorophores to human melanoma. *J. Inorg. Biochem.* **2020**, *208*, 111088. https://doi.org/10.1016/j.jinorgbio.2020.111088.
76. Sun, B.; Wang, L.; Li, Q.; He, P.; Liu, H.; Wang, H.; Yang, Y.; Li, J. Bis(pyrene)-Doped Cationic Dipeptide Nanoparticles for Two-Photon-Activated Photodynamic Therapy. *Biomacromolecules* **2017**, *18*, 3506–3513. https://doi.org/10.1021/acs.biomac.7b00780.
77. Liu, Z.; Li, J.; Jiang, Y.; Wang, D. Multifunctional nanocapsules on a seesaw balancing sonodynamic and photodynamic therapies against superficial malignant tumors by effective

immune-enhancement. *Biomaterials* **2019**, *218*, 119251. https://doi.org/10.1016/j.biomaterials.2019.119251.

78. Korpusik, A.B.; Tan, Y.; Garrison, J.B.; Tan, W.; Sumerlin, B.S. Aptamer-Conjugated Micelles for Targeted Photodynamic Therapy Via Photoinitiated Polymerization-Induced Self-Assembly. *Macromolecules* **2021**, *54*, 7354–7363. https://doi.org/10.1021/acs.macromol.1c01276.

79. Calavia, P.G.; Bruce, G.; Pérez-García, L.; Russell, D.A. Photosensitiser-gold nanoparticle conjugates for photodynamic therapy of cancer. *Photochem. Photobiol. Sci.* **2018**, *17*, 1534–1552. https://doi.org/10.1039/c8pp00271a.

80. Dykman, L.A.; Khlebtsov, N.G. Gold nanoparticles in biology and medicine: Recent advances and prospects. *Acta Nat.* **2011**, *3*, 34–55.

81. Kalus, M.-R.; Rehbock, C.; Bärsch, N.; Barcikowski, S. Colloids created by light: Laser-generated nanoparticles for applications in biology and medicine. *Mater. Today: Proc.* **2017**, *4*, S93–S100. https://doi.org/10.1016/j.matpr.2017.09.173.

82. Sahoo, G.P.; Bar, H.; Bhui, D.K.; Sarkar, P.; Samanta, S.; Pyne, S.; Ash, S.; Misra, A. Synthesis and photo physical properties of star shaped gold nanoparticles. *Colloids Surfaces A: Physicochem. Eng. Asp.* **2011**, *375*, 30–34. https://doi.org/10.1016/j.colsurfa.2010.11.033.

83. Wang, B.; Wang, J.-H.; Liu, Q.; Huang, H.; Chen, M.; Li, K.; Li, C.; Yu, X.-F.; Chu, P.K. Rose-bengal-conjugated gold nanorods for in vivo photodynamic and photothermal oral cancer therapies. *Biomaterials* **2013**, *35*, 1954–1966. https://doi.org/10.1016/j.biomaterials.2013.11.066.

84. Prasanna, S.W.; Poorani, G.; Kumar, M.S.; Aruna, P.; Ganesan, S. Photodynamic efficacy of Rosebengal-gold nanoparticle complex on Vero and HeLa cell lines. *Mater. Express* **2014**, *4*, 359–366. https://doi.org/10.1166/mex.2014.1173.

85. Kautzka, Z.; Clement, S.; Goldys, E.M.; Deng, W. Light-triggered liposomal cargo delivery platform incorporating photosensitizers and gold nanoparticles for enhanced singlet oxygen generation and increased cytotoxicity. *Int. J. Nanomed.* **2017**, *12*, 969–977. https://doi.org/10.2147/IJN.S126553.

86. Fu, Y.; Liu, H.; Ren, Z.; Li, X.; Huang, J.; Best, S.; Han, G. Luminescent $CaTiO_3$:Yb,Er nanofibers co-conjugated with Rose Bengal and gold nanorods for potential synergistic photodynamic/photothermal therapy. *J. Mater. Chem. B* **2017**, *5*, 5128–5136. https://doi.org/10.1039/c7tb01165b.

87. Rosenthal, S.J.; Chang, J.C.; Kovtun, O.; McBride, J.; Tomlinson, I.D. Biocompatible Quantum Dots for Biological Applications. *Chem. Biol.* **2011**, *18*, 10–24. https://doi.org/10.1016/j.chembiol.2010.11.013.

88. Chen, D.; Wu, I.-C.; Liu, Z.; Tang, Y.; Chen, H.; Yu, J.; Wu, C.; Chiu, D.T. Semiconducting polymer dots with bright narrow-band emission at 800 nm for biological applications. *Chem. Sci.* **2017**, *8*, 3390–3398. https://doi.org/10.1039/c7sc00441a.

89. Haimov, E.; Weitman, H.; Ickowicz, D.; Malik, Z.; Ehrenberg, B. Pdots nanoparticles load photosensitizers and enhance efficiently their photodynamic effect by FRET. *RSC Adv.* **2015**, *5*, 18482–18491. https://doi.org/10.1039/c4ra15291c.

90. Hua, X.-W.; Bao, Y.-W.; Chen, Z.; Wu, F.-G. Carbon quantum dots with intrinsic mitochondrial targeting ability for mitochondria-based theranostics. *Nanoscale* **2017**, *9*, 10948–10960. https://doi.org/10.1039/c7nr03658b.

91. Subramani, K.; Mehta, M. Nanodiagnostics in microbiology and dentistry. In *Emerging Nanotechnologies in Dentistry*; Elsevier: Amsterdam, The Netherlands, 2018; pp. 391–419. https://doi.org/10.1016/b978-0-12-812291-4.00019-4.
92. Zhang, H.; Peng, S.; Xu, S.; Chen, Z. Bifunctional nanocapsules for magnetic resonance imaging and photodynamic therapy. *RSC Adv.* **2016**, *6*, 104731–104734. https://doi.org/10.1039/c6ra22831c.
93. Cao, H.; Wang, L.; Yang, Y.; Li, J.; Qi, Y.; Li, Y.; Li, Y.; Wang, H.; Li, J. An Assembled Nanocomplex for Improving both Therapeutic Efficiency and Treatment Depth in Photodynamic Therapy. *Angew. Chem.* **2018**, *130*, 7885–7889. https://doi.org/10.1002/ange.201802497.
94. Cao, H.; Qi, Y.; Yang, Y.; Wang, L.; Sun, J.; Li, Y.; Xia, J.; Wang, H.; Li, A.P.D.J. Assembled Nanocomplex for Improving Photodynamic Therapy through Intraparticle Fluorescence Resonance Energy Transfer. *Chem. Asian J.* **2018**, *13*, 3540–3546. https://doi.org/10.1002/asia.201800859.
95. Gravel, O. The emergence of liquid mixing from spinning magnetic nanoparticules in rotating magnetic fields: Visualisation and characterisation towards a better understanding of the underlying phenomena. 2014.
96. Colombo, M.; Carregal-Romero, S.; Casula, M.F.; Gutiérrez, L.; Morales, M.P.; Böhm, I.B.; Heverhagen, J.T.; Prosperi, D.; Parak, W.J. Biological applications of magnetic nanoparticles. *Chem. Soc. Rev.* **2012**, *41*, 4306–4334. https://doi.org/10.1039/C2CS15337H.
97. Yeh, H.-P.; Del Valle, A.C.; Syu, M.-C.; Qian, Y.; Chang, Y.-C.; Huang, Y.-F. A New Photosensitized Oxidation-Responsive Nanoplatform for Controlled Drug Release and Photodynamic Cancer Therapy. *ACS Appl. Mater. Interfaces* **2018**, *10*, 21160–21172. https://doi.org/10.1021/acsami.8b05205.
98. Peng, C.-L.; Yang, L.-Y.; Luo, T.-Y.; Lai, P.-S.; Yang, S.-J.; Lin, W.-J.; Shieh, M.-J. Development of pH sensitive 2-(diisopropylamino)ethyl methacrylate based nanoparticles for photodynamic therapy. *Nanotechnology* **2010**, *21*, 155103. https://doi.org/10.1088/0957-4484/21/15/155103.
99. Li, X.; Wang, J.; Cui, R.; Xu, D.; Zhu, L.; Li, Z.; Chen, H.; Gao, Y.; Jia, L. Hypoxia/pH dual-responsive nitroimidazole-modified chitosan/rose bengal derivative nanoparticles for enhanced photodynamic anticancer therapy. *Dye. Pigment.* **2020**, *179*, 108395. https://doi.org/10.1016/j.dyepig.2020.108395.
100. Francés-Soriano, L.; Zakharko, M.A.; González-Béjar, M.; Panchenko, P.A.; Herranz-Pérez, V.; Pritmov, D.A.; Grin, M.A.; Mironov, A.F.; García-Verdugo, J.M.; Fedorova, O.A.; et al. Nanohybrid for Photodynamic Therapy and Fluorescence Imaging Tracking without Therapy. *Chem. Mater.* **2018**, *30*, 3677–3682. https://doi.org/10.1021/acs.chemmater.8b00276.
101. Su, P.; Zhu, Z.; Fan, Q.; Cao, J.; Wang, Y.; Yang, X.; Cheng, B.; Liu, W.; Tang, Y. Surface ligand coordination induced self-assembly of a nanohybrid for efficient photodynamic therapy and imaging. *Inorg. Chem. Front.* **2018**, *5*, 2620–2629. https://doi.org/10.1039/c8qi00777b.
102. Yin, Y.; Hu, B.; Yuan, X.; Cai, L.; Gao, H.; Yang, Q. Nanogel: A Versatile Nano-Delivery System for Biomedical Applications. *Pharmaceutics* **2020**, *12*, 290. https://doi.org/10.3390/pharmaceutics12030290.

103. Torres-Martínez, A.; Bedrina, B.; Falomir, E.; Marín, M.J.; Angulo-Pachón, C.A.; Galindo, F.; Miravet, J.F. Non-Polymeric Nanogels as Versatile Nanocarriers: Intracellular Transport of the Photosensitizers Rose Bengal and Hypericin for Photodynamic Therapy. *ACS Appl. Bio Mater.* **2021**, *4*, 3658–3669. https://doi.org/10.1021/acsabm.1c00139.
104. Elmenoufy, A.H.; Tang, Y.; Hu, J.; Xu, H.; Yang, X. A novel deep photodynamic therapy modality combined with CT imaging established via X-ray stimulated silica-modified lanthanide scintillating nanoparticles. *Chem. Commun.* **2015**, *51*, 12247–12250. https://doi.org/10.1039/c5cc04135j.
105. Hsu, C.-C.; Lin, S.-L.; Chang, C.A. Lanthanide-Doped Core–Shell–Shell Nanocomposite for Dual Photodynamic Therapy and Luminescence Imaging by a Single X-ray Excitation Source. *ACS Appl. Mater. Interfaces* **2018**, *10*, 7859–7870. https://doi.org/10.1021/acsami.8b00015.
106. Sun, W.; Shi, T.; Luo, L.; Chen, X.; Lv, P.; Lv, Y.; Zhuang, Y.; Zhu, J.; Liu, G.; Chen, X.; et al. Monodisperse and Uniform Mesoporous Silicate Nanosensitizers Achieve Low-Dose X-Ray-Induced Deep-Penetrating Photodynamic Therapy. *Adv. Mater.* **2019**, *31*, 1808024. https://doi.org/10.1002/adma.201808024.
107. Ahmad, F.; Wang, X.; Jiang, Z.; Yu, X.; Liu, X.; Mao, R.; Chen, X.; Li, W. Codoping Enhanced Radioluminescence of Nanoscintillators for X-ray-Activated Synergistic Cancer Therapy and Prognosis Using Metabolomics. *ACS Nano* **2019**, *13*, 10419–10433. https://doi.org/10.1021/acsnano.9b04213.
108. Bekah, D.; Cooper, D.; Kudinov, K.; Hill, C.; Seuntjens, J.; Bradforth, S.; Nadeau, J. Synthesis and characterization of biologically stable, doped LaF3 nanoparticles co-conjugated to PEG and photosensitizers. *J. Photochem. Photobiol. A Chem.* **2016**, *329*, 26–34. https://doi.org/10.1016/j.jphotochem.2016.06.008.
109. Maiti, D.; Zhong, J.; Zhang, Z.; Zhou, H.; Xion, S.; Dong, Z.; Kumar, S.; Liu, Z.; Yang, K. Polyoxomolybdate (POM) nanoclusters with radiosensitizing and scintillating properties for low dose X-ray inducible radiation-radiodynamic therapy. *Nanoscale Horizons* **2019**, *5*, 109–118. https://doi.org/10.1039/c9nh00374f.
110. Sun, W.; Luo, L.; Feng, Y.; Qiu, Y.; Shi, C.; Meng, S.; Chen, X.; Chen, H. Gadolinium–Rose Bengal Coordination Polymer Nanodots for MR-/Fluorescence-Image-Guided Radiation and Photodynamic Therapy. *Adv. Mater.***2020**, *32*, 2000377. https://doi.org/10.1002/adma.202000377.
111. Zhang, W.; Zhang, X.; Shen, Y.; Shi, F.; Song, C.; Liu, T.; Gao, P.; Lan, B.; Liu, M.; Wang, S.; et al. Ultra-high FRET efficiency $NaGdF_4:Tb^{3+}$-Rose Bengal biocompatible nanocomposite for X-ray excited photodynamic therapy application. *Biomaterials* **2018**, *184*, 31–40. https://doi.org/10.1016/j.biomaterials.2018.09.001.
112. Zhang, X.; Lan, B.; Wang, S.; Gao, P.; Liu, T.; Rong, J.; Xiao, F.; Wei, L.; Lu, H.; Pang, C.; et al. Low-Dose X-ray Excited Photodynamic Therapy Based on $NaLuF_4:Tb^{3+}$–Rose Bengal Nanocomposite. *Bioconjugate Chem.* **2019**, *30*, 2191–2200. https://doi.org/10.1021/acs.bioconjchem.9b00429.
113. Polozhentsev, O.E.; Pankin, I.A.; Khodakova, D.V.; Medvedev, P.V.; Goncharova, A.S.; Maksimov, A.Y.; Kit, O.I.; Soldatov, A.V. Synthesis, Characterization and Biodistribution of $GdF_3:Tb^{3+}$@RB Nanocomposites. *Materials* **2022**, *15*, 569. https://doi.org/10.3390/ma15020569.

114. Tang, Y.; Hu, J.; Elmenoufy, A.H.; Yang, X. Highly Efficient FRET System Capable of Deep Photodynamic Therapy Established on X-ray Excited Mesoporous LaF_3:Tb Scintillating Nanoparticles. *ACS Appl. Mater. Interfaces* **2015**, *7*, 12261–12269. https://doi.org/10.1021/acsami.5b03067.
115. Darafsheh, A.; Najmr, S.; Paik, T.; Tenuto, M.; Murray, C.; Finlay, J.; Friedberg, J.S. Characterization of rare-earth-doped nanophosphors for photodynamic therapy excited by clinical ionizing radiation beams. In *Optical Methods for Tumor Treatment and Detection: Mechanisms and Techniques in Photodynamic Therapy XXIV*; SPIE: San Francisco, CA, USA, 2015.
116. Ponomarenko, S.A.; Surin, N.M.; Borshchev, O.V.; Luponosov, Y.N.; Akimov, D.Y.; Alexandrov, I.S.; Burenkov, A.A.; Kovalenko, A.G.; Stekhanov, V.N.; Kleymyuk, E.A.; et al. Nanostructured organosilicon luminophores and their application in highly efficient plastic scintillators. *Sci. Rep.* **2014**, *4*, 6549. https://doi.org/10.1038/srep06549.
117. Ren, Y.; Rosch, J.G.; Landry, M.R.; Winter, H.; Khan, S.; Pratx, G.; Sun, C. Tb-Doped core–shell–shell nanophosphors for enhanced X-ray induced luminescence and sensitization of radiodynamic therapy. *Biomater. Sci.* **2020**, *9*, 496–505. https://doi.org/10.1039/d0bm00897d.
118. Zhao, X.; Li, Y.; Du, L.; Deng, Z.; Jiang, M.; Zeng, S. Soft X-Ray Stimulated Lanthanide@MOF Nanoprobe for Amplifying Deep Tissue Synergistic Photodynamic and Antitumor Immunotherapy. *Adv. Health Mater.* **2021**, *10*, 2101174. https://doi.org/10.1002/adhm.202101174.

Matériels et Méthodes

I. Abbreviations

RB, Rose Bengale ; HA, acide 6-Bromohexanoïque, Ahx, acide 6-aminohexanoïque ; Maléimide DCM, dichlorométhane ; DMF, diméthylformamide; DO, densité optique ; EDCI, chlorhydrate de N–éthyl–N′–(3–diméthylaminopropyl)carbodiimide; HBTU, hexafluorophosphate de N,N,N′,N′–tétraméthyl–O–(1H–benzotriazole–1–yl)uranium); HO•, radical hydroxyle ; HPLC, chromatographie liquide à haute performance ; NHS, N-hydroxysuccinimide ; NMM, N-méthylmorpholine ; NMP, polymérisation médiée par les nitroxydes ; RMN, résonance magnétique nucléaire ; NRP-1, neuropiline-1 ; O_2, oxygène moléculaire ; $^1O_2$, oxygène singulet ; $O_2^{-\bullet}$, anion superoxyde ; PDT, thérapie photodynamique ; pipéridine; PS, photosensibilisateur ; ROS, espèces réactives de l'oxygène ; TFA, acide trifluoroacétique; TIPS, triisopropyléthylamine; CCM, chromatographie sur couche mince ; UV, ultraviolets ; SOSG, Singlet Oxygen Sensor Green™ ; Tb, Terbium ; Gd, Gadolinium, X-PDT, Thérapie photodynamique induite par les rayons X

II. Produits chimiques

De l'eau ultra pure (Milli–Q, ρ >18 MΩ·cm) a été utilisée dans toutes les expériences. Le dichlorométhane (DCM), le diméthylformamide (DMF) et l'éthanol (EtOH) ont été obtenus auprès de Sigma-Aldrich et ont été utilisés sans autre purification. Le RB (Sel de sodium de Rose Bengale 95%), acide 6-Bromohexanoïque (97%), Acide 6-Aminohexanoïque (Ahx) (98%), Chlorure de Terbium (III) hexahydraté (99,9%), Chlorure de Gadolinium (III) hexahydrate (99,9%), l'acide trifluoroacétique (TFA) et anhydride acétique et pipéridine, tous ces produits sont obtenus auprès de Sigma-Aldrich. Acide Fmoc-Aminohexanoïque (98%), triisopropylsilane (TIPS), –méthylpyrrolidinone (NMP), et N–méthylmorpholine (NMM), N (Alfa Aesar, Haverhill, MA, USA) sont obtenus auprès d'Alfa Aesar. La synthèse de tous les peptides a nécessité HBTU (Iris Biotech GmbH, Allemagne). Fmoc–L–Cys(Trt)–OH, Fmoc–L–Lys(Boc)–OH, Fmoc–L–Gly–OH, Fmoc–L–Thr(tBu)–OH et Fmoc–L–Arg(Pbf)– OH ont été obtenus auprès d'Iris Biotech GmbH (Allemagne). La résine Fmoc–L–Arg(Pbf)–Wang (100–200 mesh) et la résine Fmoc–L–Asn(Trt)–OH ont été achetées auprès de Novabiochem (Allemagne).

III. Synthèse peptidique

Les peptides ont été synthétisés avec un synthétiseur de peptides automatisé ResPepXL (Intavis AG, Bioanalytical Instruments).

IV. Purification

IV.1 CCM

Des chromatographies analytiques sur couche mince (CCM) ont été réalisées en utilisant des plaques Merck Kieselgel 60 F254 ; des tâches ont été détectées après illumination à la lumière UV et une solution d'acide phosphomolybdique. Les purifications de chromatographie sont faites sur colonne Gel de silice flash 60 H.granulo.40-63 microns (VWR).

IV.2 HPLC

Les composés ont été purifiés par HPLC (Shimadzu LC-10ATvp) avec une colonne Agilent Pursuit C18, colonne de 5 mm (5 µm, 150 × 21,2 mm) équipée d'un détecteur à barrette de photodiodes UV (Varian Prostar 335-190-950 nm) et d'un détecteur spectrofluométrique (Shimadzu RF–10AXL– 200–650 nm). La détection UV a été réalisée à 254 nm et 560 nm. La détection par fluorescence à 650 nm a été réalisée après une excitation à 415 nm. Les analyses par HPLC ont été réalisées avec le même équipement mais avec une colonne Agilent Pursuit 5 C18 (5 µm, 150 × 4,6 mm).

V. Caractérisation par RMN et spectrométrie de masse

Les spectres RMN ^{1}H ont été enregistrés à température ambiante (T = 298 K) sur un BRUKER Spectromètre AVANCE à 300 MHz au LCPM. Les déplacements chimiques (δ) sont donnés en parties par million (ppm) et en utilisant des solvants résiduels non deutérés comme référence interne pour les spectres RMN 1H. Les constantes de couplage (J) sont données en hertz (Hz) et les multiplicités sont rapportées comme suit : s = singulet, d = doublet, t = triplet, q = quadruplet, m = multiplet et large. Les échantillons ont été préalablement dissous dans du DMSO–d6 ou Chloroforme-d6.

Les chromatogrammes LC-MS sont enregistrés à l'aide d'un spectromètre de masse LCMS-2020 avec un quadripôle, de marque Shamdzu (electrospray ionisation ESI+, avec fenêtre de détection de 50 à 200). Il est couplé à une chaîne HPLC Shimadzu, pompes LC-20AB, mini d'un détecteur avec une barette de diodes SPD-M20A et un four CTO-20AC.

VI. Détermination des propriétés photophysiques

VI.1 Absorption

Les spectres d'absorption ont été mesurés avec un spectrophotomètre UV-visible double faisceau UV-3600 (SHIMADZU, MARNE LA VALLEE, France).

VI.2 Fluorescence

Les spectres de fluorescence ont été mesurés avec un spectrofluorimètre Fluorolog FL3-222 (HORIBA Jobin Yvon, LONGJUMEAU, France) équipé d'une lampe à arc xénon de 450 W, d'un compartiment porte-cuve thermostaté (25°C), d'un photomultiplicateur UV-visible R928 (HAMAMATSU Japon) et d'un détecteur infrarouge InGaAs refroidi à l'azote liquide (DSS-16A020L Electro-Optical System Inc, Phoenixville, PA, USA). Le faisceau d'excitation est diffracté par un monochromateur double réseaux SPEX (1200 traits/mm blasé à 330 nm). La fluorescence a été mesurée par le détecteur UV-Visible via le monochromateur d'émission double réseaux SPEX (1200 traits/mm blasé à 500 nm).

VI.3 Oxygène singulet ($^1O_2$) et rendement quantique

La production d'$^1O_2$ a été mesurée par le détecteur infrarouge *via* le monochromateur d'émission double réseaux SPEX (600 traits/mm blasé à 1 µm) et un filtre passe haut à 780 nm. Tous les spectres ont été mesurés en utilisant des cuves quartz à 4 faces. Tous les spectres d'émission (fluorescence et luminescence de l'$^1O_2$) ont été rapportés à la même absorbance (inférieure à 0,2) avec les corrections de lampe et de photomultiplicateur.

Le rendement quantique de fluorescence a été déterminé par l'équation (1) :

$$\Phi_f = \Phi_{f0} \cdot \frac{I_f}{I_{f0}} \cdot \frac{DO_0}{DO} \cdot \left(\frac{n}{n_0}\right)^2 \quad \text{(équation 25)}$$

où Φ_f et Φ_{fo}, I_f et I_{fo}, DO et DO_o, n et n_o sont les rendements quantiques, les intensités de fluorescence, les densités optiques, les indices de réfraction de l'échantillon et de la référence respectivement.

La référence utilisée pour le calcul du rendement quantique de fluorescence est la tétraphénylporphyrine dans le toluène avec un Φ_{fo} de 0,11.

Le rendement quantique de production d'$^1O_2$ est déterminé par l'équation (2) :

$$\Phi_\Delta = \Phi_{\Delta 0} \cdot \frac{I}{I_0} \cdot \frac{DO_0}{DO} \quad \text{(équation 26)}$$

où Φ_Δ et $\Phi_{\Delta o}$, I et I_o, DO et DO_o sont les rendements quantiques de production d'$^1O_2$, les intensités de production d'oxygène singulet et les densités optiques de l'échantillon et de la référence respectivement.

La référence utilisée pour le calcul du rendement quantique sont le TPP et l'éosine Y.

6.4 Durée de vie de fluorescence

Les expériences de durées de vie de fluorescence ont été réalisées en utilisant pour l'excitation une diode laser pulsée émettant à 407 nm (LDH-P-C-400M, FWHM < 70 ps, 1 MHz) couplée à un générateur d'impulsions PDL 800-D (PicoQuant GmbH, BERLIN, Germany) et pour la détection une photodiode à avalanche SPCM-AQR-15 (EG & G, VAUDREUIL, Canada) couplée à un filtre passe haut à 650 nm.

L'acquisition a été réalisée par un module PicoHarp 300 associé à un routeur 4 voies PHR-800 (PicoQuant GmbH, BERLIN, Germany). Les déclins de fluorescence ont été enregistrés en utilisant la méthode de comptage monophotonique (*Time Correlated Single Photon Counting* TCSPC). Les données ont été collectées jusqu'à obtenir 1000 coups accumulés dans un canal puis analysés en utilisant le logiciel de TCSPC Fluofit (PicoQuant GmbH, BERLIN, Germany) basé sur une reconvolution itérative utilisant un algorithme de Levensberg-Marquandt permettant l'obtention de déclins multi-exponentiels (principalement mono- ou bi-exponentiels dans notre cas).

6.5 Durée de vie d'$^1O_2$

Les mesures de durées de vie d'$^1O_2$ ont été réalisées avec un spectrophotomètre TEMPRO-01 (HORIBA Jobin Yvon, LONGJUMEAU, France) composé d'une diode d'excitation pulsée SpectraLED-415 émettant à 415 nm, d'un compartiment porte-cuve, d'un monochromateur d'émission de type Seya-Namioka (600 – 2000 nm) et d'un tube photomultiplicateur proche infra-rouge régulé thermoélectriquement H10330-45 (HAMAMATSU, Japon). Le montage est piloté par le module de comptage FluoroHub-B et les logiciels DataStation et DAS6 (HORIBA Jobin Yvon).

Les spectres d'émission et les mesures de durées de vie de phosphorescence ont été réalisés avec un spectrofluorimètre Fluorolog FL3-22 (HORIBA Jobin Yvon, LONGJUMEAU, France) équipé d'une lampe xénon continue 450 W, d'une lampe flash xénon, d'un compartiment porte-cuve thermostaté (25°C) et d'un photomultiplicateur UV-visible R928 (HAMAMATSU Japon). Le montage est piloté par le module de comptage FluoroHub-B. Le logiciel FluorEssence (HORIBA Jobin Yvon) a été utilisé pour les spectres d'émission ; les logiciels DataStation et DAS6 (HORIBA Jobin Yvon) ont été utilisés pour la mesure des durées de vie de phosphorescence.

6.6 Spectroscopie infra-rouge

Les mesures FTIR ont été réalisées sur un spectromètre Alpha-P de Bruker, avec une accumulation de 32 scans, une résolution 4 cm^{-1} et une exploitation sous Opus v 6.5.

VII. Tests d'affinité

La liaison des composés pour la protéine NRP-1 a été attribuée en termes de concentration inhibitrice demi-maximale (valeurs IC50) par un test compétitif en utilisant les solutions suivantes : rr Npn-1/Fc chimera recombinant rat 566-N1-025 (-20°C) R&D Systems, Tween, BSA, Héparine, VEGF biotinylé, VEGF non biotinylé, streptavidine-HRP, Color Reagents A et B, Plaque ELISA Fluoronunc Maxisorp et parafilm.

VIII. Mesure de la taille des nanoparticules par TDA-ICP-MS

La taille des NPs a été mesurée par TDA-ICP-MS (Analyse par Dispersion de Taylor couplé à un ICP-MS). L'analyse par dispersion de Taylor permet de mesurer le coefficient de diffusion et donc la taille hydrodynamique d'une espèce en solution. Pour résumer, l'échantillon est injecté dans un capillaire et une pression est appliquée. Toutes les espèces présentes sortent ensemble sous la forme d'un pic gaussien si les conditions expérimentales sont bien optimisées. Dans la théorie de la dispersion de Taylor, plus la NP est grosse, plus le pic est large, et s'il y a un mélange de tailles, une superposition de pics de différentes largeurs est obtenue. En fittant le pic, il est possible de remonter à la taille moyenne des espèces présentes. Le TDA est couplé à l'ICP-MS. En ICP-MS, l'acquisition du (Z+N=158) Gd et 159Tb sont sur 500 ms.

IX. Potentiel zêta

Les mesures des potentiels Zêta des nanoparticules ont été effectuées sur un Zetasizer Nano-Z (Malvern) équipé d'un laser He-Ne à 633 nm.

Chapitre II :
Etude du transfert d'énergie en solution entre le Terbium/Gadolinium et le Rose Bengale

I. Introduction

Les recherches actuelles orientées dans le développement de NPs pour des applications médicales mettent en exergue le potentiel applicatif de NPs dites multifonctionnelles [1], à savoir la possibilité de conférer au même nano-objet des propriétés thérapeutiques et d'imagerie comme agent de contraste. En effet, la nano-composition peut permettre une utilisation bimodale : (i) le gadolinium augmente fortement l'intensité de contraste de l'IRM et (ii) peut conduire également à des effets très prometteurs comme radiosensibilisant (les cations lanthanide ayant un numéro atomique élevé).

L'originalité de notre approche est de conjuguer des molécules de PS à des NPs pouvant contenir du gadolinium ou du terbium et rendues luminescentes après excitation aux rayons X. Quand le conjugué NP-PS est excité par rayons X, la particule génère de la lumière capable d'engendrer des réactions de photo-oxydation des molécules photo-activables couplées. Il a déjà été démontré que sous exposition à des rayons X, les NPs émettaient une scintillation ou une luminescence persistante qui, convertie, pouvait activer le PS par transfert d'énergie [2].

L'absorption des rayons X est directement dépendante de Z^4. Ainsi, les matériaux lourds facilitent le phénomène d'absorption. La démonstration récente de l'élaboration de scintillateurs de taille nanométrique a suscité l'intérêt dans la combinaison de l'utilisation des rayons X et de la PDT [3].

La bibliographie concernant le transfert d'énergie est reproduite d'après les références [4-8].

II. Transfert d'énergie

II.1 Définition de l'énergie

L'énergie est une « force en action ». C'est la capacité à produire un mouvement de travail ou changer un état. Plusieurs types d'énergie peuvent être mises en place par divers phénomènes : mécanique, gravitationnelle, thermique, chimique, électrique, nucléaire, radiative ou luminescente. Dans notre cas, nous nous intéressons à l'énergie lumineuse pour des applications en PDT.

II.2 La nature de la lumière

Depuis des siècles, la nature de la lumière est discutée. Dans la moitié du XVII^{e} siècle, Christian Huygens considérait que la lumière était composée d'une onde uniquement. A la même époque, Isaac Newton pensait que la lumière était un flux de particules. La révolution de la lumière a été introduite par Albert Einstein en 1909, lorsqu'il a annoncé que la lumière est une onde électromagnétique et un flux de particules en même temps. C'est la dualité de la lumière. Cette théorie a ouvert l'horizon à la physique quantique à l'égard de la physique moderne [9].

II.2.1 Propriétés ondulatoires de la lumière

La lumière est une onde électromagnétique (électrique et magnétique). Le champ électrique est perpendiculaire à l'axe de propagation du champ magnétique. Cette onde, comme toute onde, est caractérisée par une fréquence (v), une longueur d'onde (λ) et une polarisation. La polarisation précise la direction de propagation du champ électrique et sa trajectoire (circulaire, linéaire ou aléatoire) (**Figure 116**).

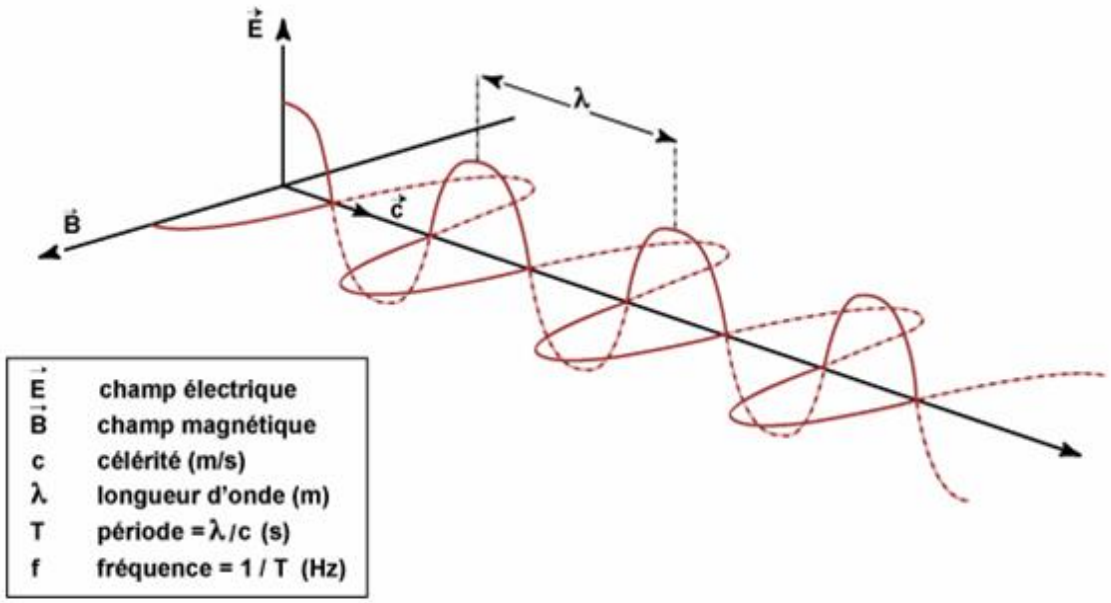

Figure 116 : Schéma d'une onde. Adapté de la page officielle de l'UVED (Université Virtuelle Environnement et développement)

II.2.2 Propriétés des photons

Le photon est l'assemblage de l'onde et d'une particule. La masse de cette particule est nulle, et elle se déplace à la vitesse c, définie comme célérité de la lumière. Un photon a une énergie spécifique E=hν ; pour cette énergie, une onde est associée. La propagation de plusieurs photons dans l'espace permet de les quantifier comme flux lumineux, qui est défini comme un nombre de photons par unité de temps (Energie = nhν).

III. Diagramme de Perrin-Jablonski

Les divers processus photophysiques sont regroupés dans un diagramme de Perrin-Jablonski. Il visualise : l'absorption d'un photon, les relaxations vibrationnelles, la fluorescence, la conversion intersystème, la phosphorescence, (représenté dans la **figure 9 du chapitre I**) [10].

Ces processus sont rapides. Les transitions électroniques se produisent sans changement de la position du noyau d'après Franck-Condon. L'absorption est la plus rapide des processus (10^{-15}s). Les valeurs moyennes des durées de vie de différents phénomènes sont : relaxation

vibrationnelle (10^{-12}-10^{-10} s), la fluorescence (10^{-10}-10^{-7} s), le croisement intersystème (10^{-11}-10^{-9} s) et la durée de vie de phosphorescence (10^{-6} - 1 s) [11].

IV. L'absorption des photons

L'intensité de la lumière absorbée par un échantillon est représentée dans l'équation 27.

$$I = I_0.e^{-kl} \quad \text{(équation 27)}$$

I_0 est la lumière monochromatique émise par la source de lumière qui traverse un milieu d'épaisseur l, I représente la lumière transmise par la solution et k est le coefficient d'extinction en cm^{-1}. Le coefficient d'extinction dépend de la concentration des solutés en solution. C'est la capacité de cette molécule à absorber des photons.

Selon la loi de Beer-Lambert [12] :

$$I= I_0 10^{\varepsilon.C.l} \quad \text{(équation 28)}$$

$$A= \varepsilon.C.l = \log (I_0/I) \quad \text{(équation 29)}$$

L'absorption est proportionnelle à l'intensité de la lumière absorbée, donc inversement proportionnelle à l'intensité de la lumière transmise.

V. Principe et mécanisme d'émission de la lumière

L'absorption d'un photon par un atome ou une molécule, leur permettent de passer à un niveau d'énergie supérieur, qui peut être électronique pour l'atome, et ou vibrationnel pour une molécule. Les atomes et les molécules, dans leur état excité, ne sont pas stables thermodynamiquement, ils tendent à revenir à l'état fondamental. Le temps prit entre le moment d'absorption et le retour à l'état fondamental est la durée de vie de luminescence. La molécule excitée peut être dans un état singulet ou triplet, la luminescence donc est nommée fluorescence et phosphorescence respectivement [13].

Le retour à l'état fondamental peut être radiatif par émission de la lumière (photon). Ce retour à l'état fondamental peut être aussi non radiatif par émission de chaleur ou relaxation vibrationnelle par conversion interne.

L'émission de lumière est quantitative, elle correspond au nombre de photons par unité de temps. Le rendement quantique de luminescence correspond à une probabilité qu'une molécule excitée peut émettre des photons (voir la formule dans le chapitre Matériel et Méthodes). C'est le rapport donc entre le nombre de photons émis et le nombre de photons absorbés pendant le même temps. Si ϕ_F est égal à zéro, la molécule est non fluorescente. Si ϕ_F est égal à l'unité, il n'y a pas d'autre processus de désexcitation de l'état singulet S_0 que la fluorescence. La durée de vie de fluorescence est le temps moyen qu'un fluorophore reste à l'état excité. L'efficacité de fluorescence est égale à $\phi_F \times \varepsilon$.

La conversion interne est une transition non-radiative entre deux états électroniques de même multiplicité de spin. Après cette transition, une relaxation vibrationnelle vers le plus bas niveau vibrationnel de l'état électronique final a lieu. La conversion interne dépend du niveau énergétique des électrons. Elle est plus efficace entre S_2 et S_1 qu'entre S_1 et S_0 vue que l'énergie

entre ces derniers est plus grande que celle entre S_2 à S_1. La conversion interne entre S_1 et S_0 entre en compétition avec la fluorescence et la conversion intersystème.

La conversion intersystème est aussi une transition non-radiative entre deux états électroniques de multiplicités différentes. Ces électrons feront alors le passage vers le plus bas niveau vibrationnel du niveau électronique considéré. Le passage intersystème entre deux niveaux énergétiques de multiplicités différentes est interdit, mais le couplage spin-orbitale peut être suffisamment important pour permettre ce transfert. Au niveau énergétique T_1, une compétition entre la désexcitation non radiative et la phosphorescence a lieu. Cela dépend du nombre de collisions entre les molécules et le solvant. Le spectre de phosphorescence est décalé vers les plus hautes longueurs d'onde de celles de fluorescence parce que le plus bas niveau vibrationnel du niveau T_1 est situé en-dessous de celui de S_1.

VI. Effet de la structure et de la substitution sur les caractéristiques photophysiques

Les composés fluorescents en majorité sont aromatiques à part quelques composés aliphatiques saturés. L'augmentation du degré de la conjugaison nommé « extension des liaisons Π » induit un déplacement des spectres d'absorption et de fluorescence vers le rouge (grandes longueurs d'onde, déplacement bathochorome) et une augmentation de ϕ_F. Dans ce cas, les transitions de plus basses énergies sont de type Π --> Π^*. L'introduction d'un hétéroatome dans le système Π peut induire une transition de plus basse énergie de type n --> Π^*, pour cette raison il y aura une diminution du coefficient d'extinction et de ϕ_F.

La nature et le type de substituant jouent un rôle très important dans les caractéristiques photophysiques.

- La présence d'un atome lourd (Br, I) augmente la probabilité du passage intersystème et provoque une inhibition de fluorescence. Le couplage spin-orbitale qui augmente la possibilité du passage intersystème est proportionnel au numéro atomique de l'atome lourd.
- Si le substituant est électro-donneur (-OH, -OR, $-NH_2$, -NHR, $-NR_2$), un déplacement bathochrome des spectres d'absorption et de fluorescence aura lieu. Les spectres sont larges et peu structurés, avec une augmentation du coefficient d'extinction.
- Si le substituant est électro-accepteur (groupe carbonyle et nitro) les caractéristique sont difficile à prévoir.

Les atomes lourds augmentent la possibilité du passage intersystème et aussi la possibilité de production $^1O_2$. C'est l'une des raisons pour lesquelles le Rose Bengale possède un rendement quantique de production d'$^1O_2$ élevé.

VII. La désexcitation non-radiative

La désexcitation non-radiative entre en compétition avec la fluorescence. Ce processus de désactivation peut se faire par plusieurs voies, une voie intramoléculaire qui est indépendante de l'environnement et une voie intermoléculaire qui dépend des molécules voisines et de la diffusion dans le milieu.

Le quenching est une inhibition de fluorescence. Il dépend de la distance entre les molécules; deux types de quenching existent : le quenching "**statique**" est dû à la formation d'un complexe non fluorescent à l'état fondamental, c'est un quenching sans diffusion puisque la distance entre le donneur et le quencheur est fixe. Cette interaction entre donneur et quencheur est rapide, ce qui entraîne une diminution de la fluorescence du donneur quand la concentration de l'accepteur augmente, sans changement de la durée de vie de fluorescence du donneur

Le quenching "**dynamique**" est dû à la diffusion entre un chromophore excité (donneur) et un inhibiteur (quencheur). Ce dernier se diffuse dans une sphère dite sphère d'inhibition virtuelle qui entoure le donneur. Dans ce cas, la fluorescence et la durée de vie du donneur diminuent avec une augmentation de la concentration du quencheur.

Les inhibitions dynamique et statique peuvent se faire simultanément, causant une déviation de la linéarité de I_0/I et τ_0/τ.

Lors d'une inhibition statique, Perrin propose un modèle d'inhibition totale de fluorescence lorsque l'inhibiteur est dans un volume sphérique qui entoure le donneur. La probabilité de résider dans ce volume est suivant Poisson :

$$P_n = \frac{<n>}{n!} e^{-n} \quad \text{(équation 30)}$$

n est le nombre moyen d'inhibiteur dans un volume. $<n> = V_q N_A [Q]$

$$\text{Soit } P_0 = e^{-n} = \exp(-V_q N_A [Q]) \text{ (équation 31)}$$

Sachant que l'intensité de fluorescence est proportionnelle à P_0, le rapport I_0/I sera donc écrit comme suivant :

$$\frac{I_0}{I} = \exp(Vq\ NA\ [Q]) \quad \text{(équation 32)}$$

Cela justifie l'aspect exponentiel du rapport I_0/I dans le cas d'une inhibition statique.

Le deuxième type de quenching est le quenching dynamique qui aura lieu lors d'une interaction bimoléculaire par la diffusion du quencheur (accepteur) dans la zone de réaction photophysique. Dans ce cas-là, l'intensité de luminescence et la durée de vie sont fixes. Le rapport I/τ est donc fixe. La cinétique de la réaction est représentée par la **Figure 117** et les équations 11, 12 et 13.

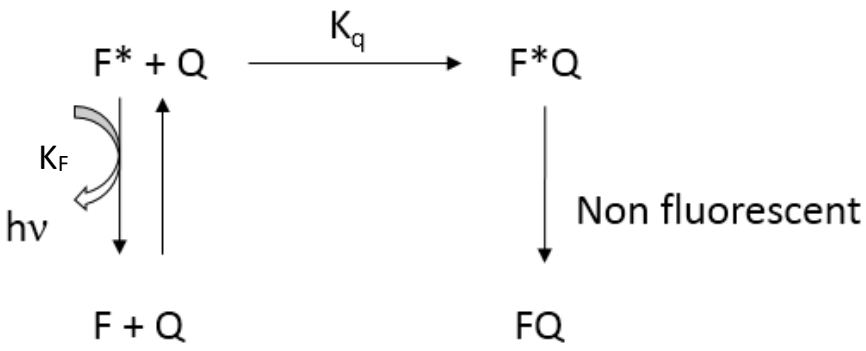

Figure 117 : Schéma représentant un quenching dynamique

$$I_0 = \frac{K_F}{K_F + K_{nf}} = K_F\ \tau_0 \quad \text{(équation 33)}$$

$$I = \frac{K_F}{K_F + K_{nf} + K_q\ [Q]} = K_F\ \tau \text{ (équation 34)}$$

$$\frac{I_o}{I} = 1 + K_q\ \tau_0\ [Q] = 1 + K_{SV}\ [Q] \quad \text{(équation 35)}$$

I_0 = intensité de fluorescence du donneur en absence d'inhibiteur

τ_0 = durée de vie moyenne du donneur en absence d'inhibiteur

I = intensité de fluorescence en présence d'inhibiteur

k_q = constante cinétique de la réaction

K_{nf} = constante cinétique de la réaction non fluorescente

K_F = constante cinétique de la réaction fluorescente

K_{SV} = constante de Stern-Volmer

VIII. Transfert d'énergie radiatif et non-radiatif

Le transfert d'énergie entre deux molécules est de deux types : radiatif et non radiatif (DEXTER/FRET).

- Le transfert d'énergie radiatif consiste en l'émission d'un photon par un donneur qui sera absorbé par un accepteur. Ce transfert d'énergie se fait sans interaction entre le donneur et l'accepteur. L'intensité de fluorescence du donneur diminue lorsque la concentration de l'accepteur augmente et la durée de vie de luminescence du donneur reste constante lorsque la concentration de l'accepteur augmente.
- Le transfert d'énergie non radiatif se fait par une interaction entre donneur et accepteur. Il ne se peut produire que s'il y a un recouvrement entre le spectre d'absorption de l'accepteur et le spectre d'émission du donneur. Ce recouvrement

signifie une correspondance entre la transition vibrationnelle du donneur et la transition vibrationnelle de l'accepteur. Dans ce cas, l'intensité de fluorescence du donneur diminue et la durée de vie de luminescence du donneur lorsque la concentration de l'accepteur augmente.

Le transfert d'énergie non-radiatif se fait par plusieurs mécanismes d'interactions : interaction coulombienne dipôle/dipôle à des distances moyennes (mécanisme de Förster) ou par une interaction multipolaire à courte distance (mécanisme de Dexter) (**Figure 118**).

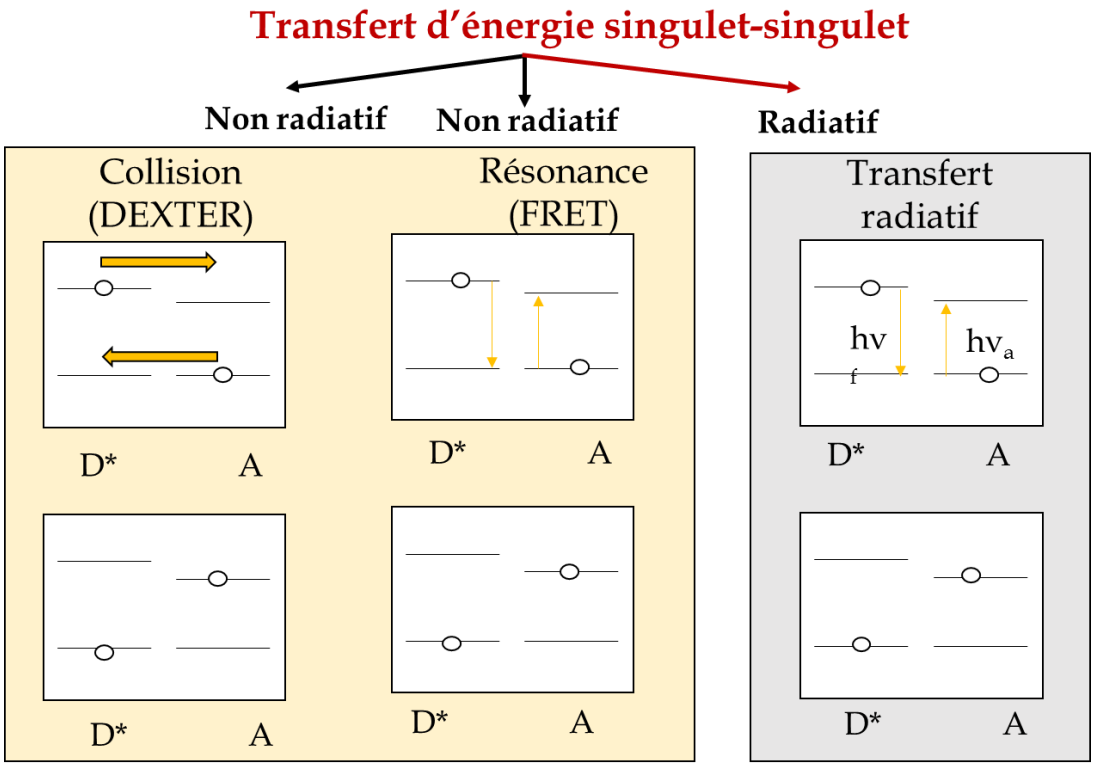

Figure 118: Différents types de transfert d'énergie (D : donneur, A : accepteur)

Pour avoir un transfert d'énergie entre le donneur et l'accepteur, il faut qu'ils soient « énergétiquement compatibles » (**Figure 119**). Cette comptabilité énergétique entre deux fluorophores est définie par l'intégrale de recouvrement J entre le spectre d'émission du donneur et le spectre d'absorption de l'accepteur. Cette valeur représente la capacité du fluorophore accepteur à absorber l'énergie provenant du fluorophore donneur à une longueur d'onde donnée.

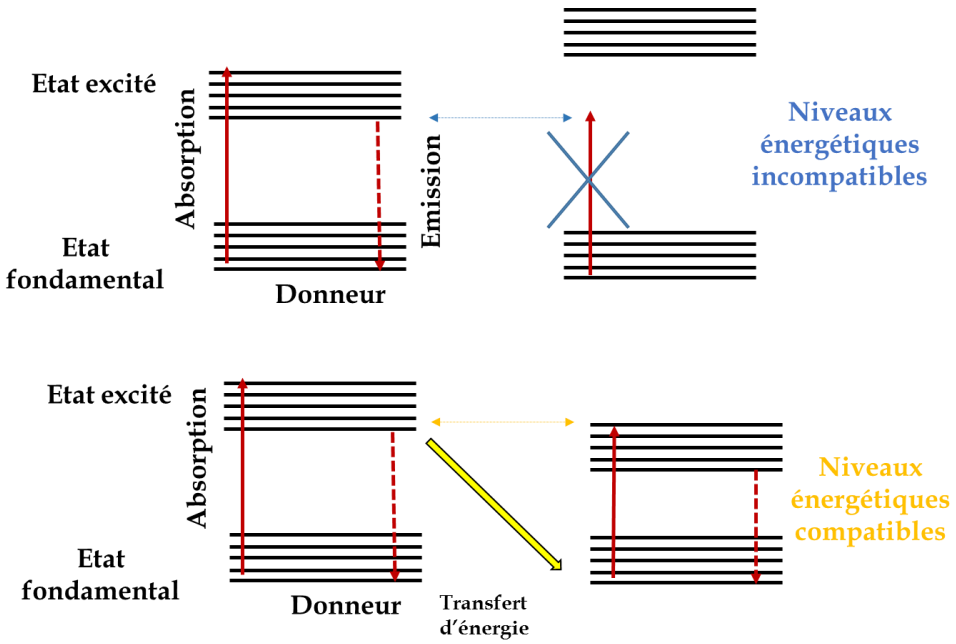

Figure 119 : Compatibilité énergétique entre un donneur et un accepteur pour un transfert d'énergie

Le recouvrement J représenté par la partie hachuré en jaune et noir (**Figure 120**) est calculé par l'**équation 36** :

$$J=\int f_D(\lambda)\varepsilon_A(\lambda)\lambda^4 d\lambda \quad \text{(équation 36)}$$

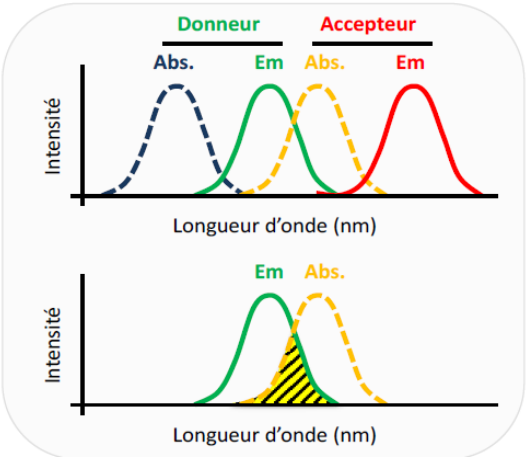

Figure 120 : Recouvrement entre spectre d'émission du donneur et spectre d'absorption de l'accepteur, la zone hachurée représente le recouvrement J. D'après J. R. Lakowitz, Principles of fluorescence spectroscopy.

R_0, le rayon Forster, est la distance donneur–accepteur pour laquelle l'efficacité de transfert d'énergie est de 50% **(Figure 121)**. Cette probabilité de désexcitation augmente en faveur du transfert d'énergie lorsque la distance entre les fluorophores donneur et accepteur diminue. R_0 est calculé par l'**équation 37** :

$$R_0 = (10^{-3}\, k^2\, n^{-4}\, Q_D\, J)^{1/6} \times 9730 \quad \text{(équation 37)}$$

Avec :

J : intégrale de recouvrement,
n : indice de réfraction du milieu (n^{-4} est généralement compris entre 1/3 et 1/5),
Q_D : ϕ_F du donneur en absence d'accepteur, Q_D de Tb et Gd = 10^{-2}.
k : facteur d'orientation qui est fonction de l'orientation des fluorophores l'un par rapport à l'autre, k^2 est assimilé à 2/3 lorsque le donneur et l'accepteur présentent un degré de liberté suffisant pour être aléatoirement orientés dans l'espace

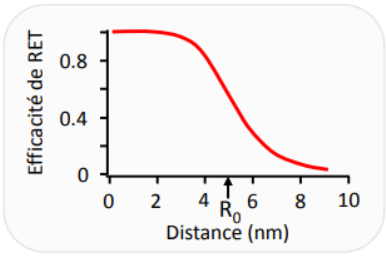

Figure 121 : Représentation du rayon de Förster. D'après J. R. Lakowitz, Principles of fluorescence spectroscopy.

L'efficacité du transfert d'énergie FRET est calculée par :

$$E = \frac{1}{1+(\frac{R}{R_0})^6} \quad \text{(équation 38)}$$

$$E = 1 - \frac{\tau}{\tau_0} \quad \text{(équation 39)}$$

La probabilité d'avoir un transfert d'énergie entre deux fluorophores est maximal si les moments dipolaires du donneur (émission) et de l'accepteur (absorption) sont parallèles. Si ces deux moments forment un angle de 90°, il n'y aura pas de transfert d'énergie. Ce principe provient du fait que la probabilité d'absorption de l'énergie d'un photon par un fluorophore est maximale lorsque son moment dipolaire d'absorption est aligné avec la direction de propagation de l'onde incidente. Si l'angle formé par ces deux vecteurs est égal à 90°, la probabilité d'absorption devient nulle (**Figure 122**).

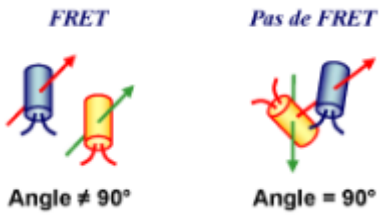

Figure 122 : Direction des moments dipolaire pour avoir ou non un transfert d'énergie. D'après J. R. Lakowitz, Principles of fluorescence spectroscopy.

Dans ce chapitre, nous allons étudier le transfert d'énergie en solution entre le $TbCl_3$/RB -$GdCl_3$/RB -AGuIX Tb/RB et AGuIX Gd/RB.

IX. Caractéristiques photophysiques du Rose Bengale

IX.1 Spectre d'absorption du RB

La **Figure 123** montre le spectre d'absorption du RB dans l'eau (concentration 18 µM). Le RB absorbe dans l'UV-Visible. Son maximum d'absorption est à 558 nm.

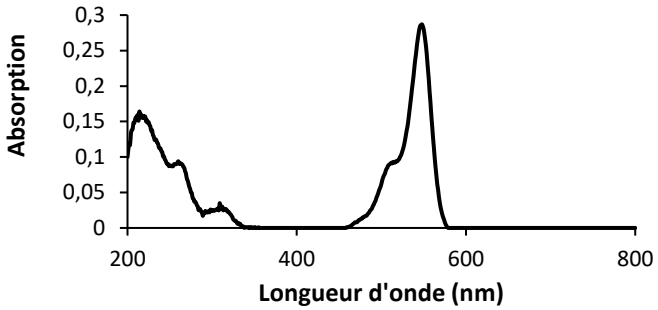

Figure 123 : Spectre d'absorption du Rose de Bengale [RB]=18 µM dans l'eau. $\varepsilon_{558\ nm}$ = 90400 ($cm^{-1}.M^{-1}$), $\varepsilon_{351\ nm}$ = 8492 ($cm^{-1}.M^{-1}$) et $\varepsilon_{273\ nm}$ = 3201 ($cm^{-1}.M^{-1}$).

IX.2 Emission de fluorescence du RB

La **Figure 124** montre les spectres d'émission du RB dans l'eau excité à 558 nm (sa longueur d'onde maximale d'absorption), 351 nm (longueur d'onde d'excitation du Terbium) et 273 nm (longueur d'onde d'excitation du Gadolinium).

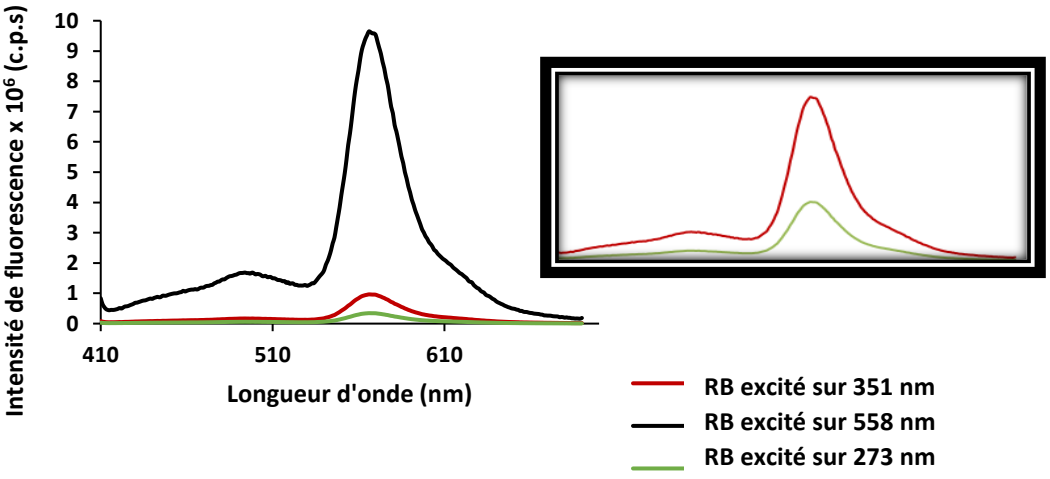

Figure 124: Spectre d'émission du RB excité à 558 nm (ε=90400 ($cm^{-1}M^{-1}$)), à 351 nm (ε=8492 ($cm^{-1}M^{-1}$)) et à 273 nm (ε=3201 ($cm^{-1}M^{-1}$)) avec [RB]=18 µM dans l'eau.

X. Etude du transfert d'énergie entre $TbCl_3$ et RB

X.1 Spectre d'absorption et d'émission de $TbCl_3$

La **Figure 125a** montre les spectres d'absorption du Terbium (Tb^{3+}) libre en solution en solubilisant le $TbCl_3$ dans l'eau. Le Terbium absorbe en UV à 218 nm. En revanche, son excitation à 218 nm ne montre aucune émission de fluorescence. Après avoir enregistré le spectre d'excitation (**Figure 125b**), plusieurs pics sont détectés. Après avoir testé toutes les

longueurs d'ondes détectées, l'excitation à 351 nm a été retenue. La **Figure 125c** montre le spectre d'émission du Terbium (Tb^{3+}) excité à 351 nm dans l'eau.

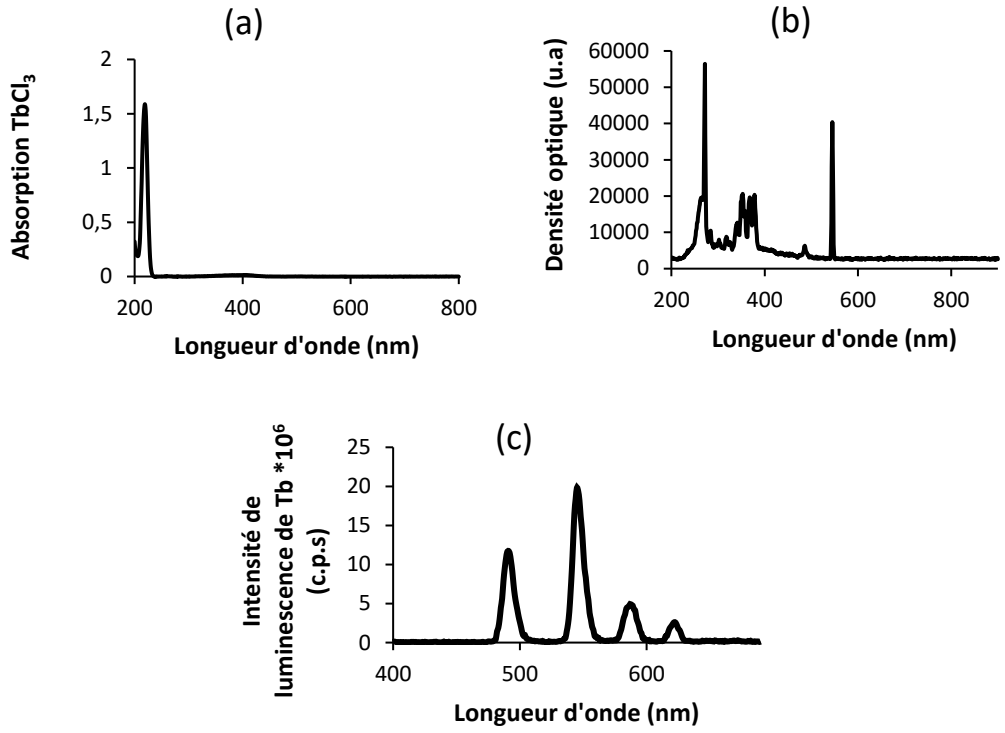

Figure 125 : (a) Spectre d'absorption du Terbium ($TbCl_3$) dans l'eau (b) spectre d'excitation de $TbCl_3$ à 351 nm (c) spectre d'émission du Terbium ($TbCl_3$) avec [$TbCl_3$]= 10 mM, dans l'eau, $\lambda_{excitation}$=351 nm

Les quatre pics d'émission du Terbium à 488 nm, 545 nm, 585 nm et 620 nm correspondent aux transitions électroniques entre le niveau $^5D_4$ et $^7F_6$, $^7F_5$, $^7F_4$ et $^7F_3$ respectivement (**Figure 126**).

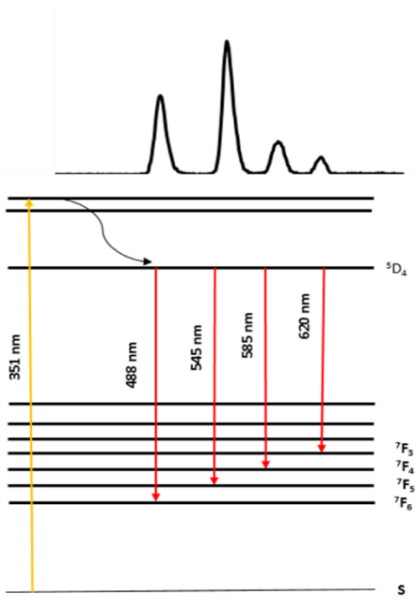

Figure 126 : Diagramme de niveau énergétique partiel de l'ion Terbium

X.2 Etude du transfert d'énergie

La **Figure 127** montre le recouvrement entre le spectre d'émission du Terbium et le spectre d'absorption du RB. Le recouvrement J et R_0 sont calculés d'après les équations 4 et 5 respectivement.

Il est trouvé $J_{Tb^{3+}/RB}$= 4,36*10^{15} ($M^{-1}.nm^4.cm^{-1}$) et R_0= 4,33 nm.

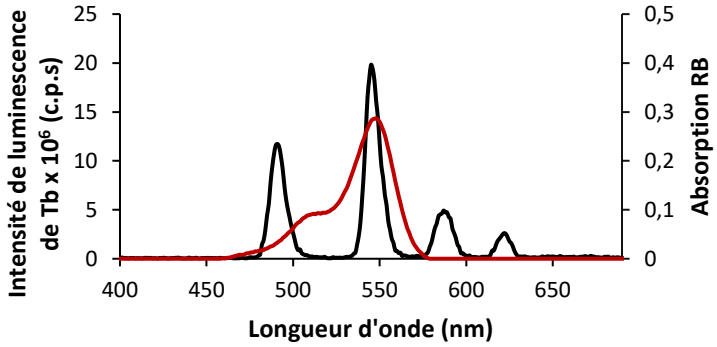

Figure 127 : Recouvrement entre le spectre d'émission du Terbium [Tb^{3+}]= 10 mM (noir) et le spectre d'absorption du RB [RB]= 18 µM (rouge), dans l'eau, $\lambda_{excitation}$=351 nm

Cette valeur J de recouvrement, ainsi que le R_0<10 nm suggère la possibilité d'avoir un transfert non radiatif de type FRET.

Pour justifier cette hypothèse, la variation de l'intensité et de la durée de vie de luminescence du Terbium en fonction de la concentration du RB, avec une concentration fixe de Tb [Tb^{3+}]=10 mM est étudiée. La figure 13 montre (a) I=f([RB]) et τ=f([RB]) (b)I_0/I= f([RB]) et τ_0/τ =f([RB]) dans l'eau. ($\lambda_{excitation}$= 351 nm, délai de 50 µs).

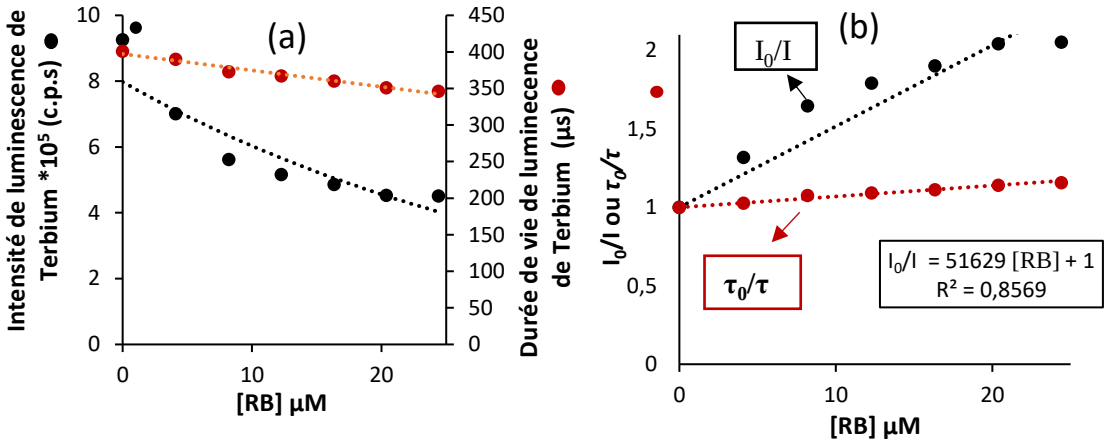

Figure 128 : (a) I=f([RB]) et τ=f([RB]), (b)I_0/I= f([RB]) et τ_0/τ =f([RB]) dans l'eau ($\lambda_{excitation}$= 351 nm- Délai 50 µs).

La constante de quenching (k_q) est calculée après avoir calculé la constante de Stern-Volmer (K_{SV}) suivant les équations suivantes :

$$\frac{F_0}{F} = 1 + K_{SV}[Q] \quad \text{(équation 40)}$$

$$K_{SV} = K_q \tau_0 \quad \text{(équation 41)}$$

D'après la **Figure 128**, la diminution linéaire et exponentielle de la durée de vie luminescence de Terbium et de son intensité de luminescence respectivement permettent de suggérer que le transfert non radiatif est de type FRET suite à des inhibitions dynamique et statique avec une constante de quenching égale à $1{,}2*10^8$ $M^{-1}.s^{-1}$ sachant que K_{sv} est égale à $5{,}16*10^4$ M^{-1}.

Dans la **Figure 129,** nous avons représenté le spectre d'émission de $TbCl_3$ (noir) seul ou en présence de RB en solution (rouge), après un délai de 50 µs. Nous pouvons observer une diminution de l'intensité de luminescence en présence de RB ainsi que l'apparition d'une bande d'émission à 560 nm dûe à la fluorescence du RB. Cela prouve l'existence d'un transfert d'énergie.

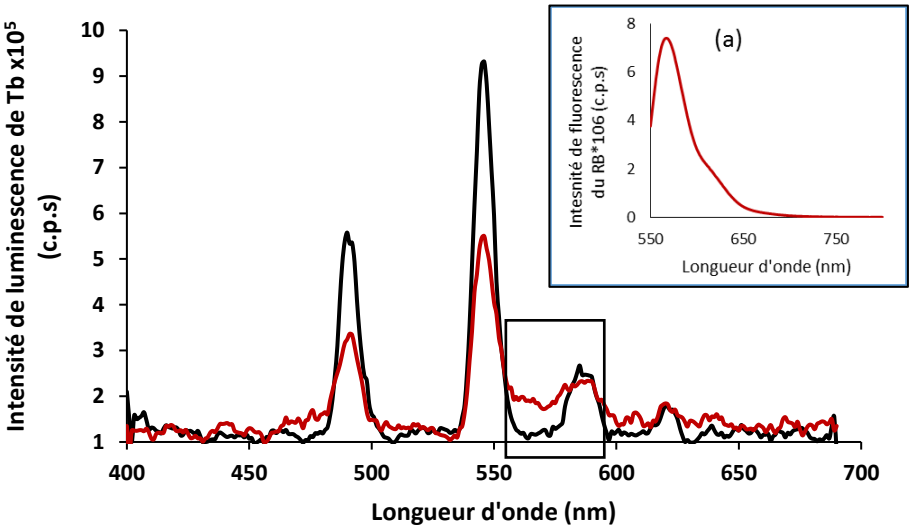

Figure 129 : Spectre d'émission du Terbium seul [Tb]=10 mM (noir) et du Terbium en présence de RB en solution [RB]= 3 µM (rouge) dans l'eau, ($\lambda_{excitation}$=351 nm - délai 50 µs). La figure (a) annexe est l'émission du RB dans l'eau après excitation à 558 nm.

La **Figure 130** représente le spectre d'émission du mélange $TbCl_3$ (0,1 mM) et RB (0,8 mM) dans l'eau ($\lambda_{excitation}$ = 351 nm, délai 50 µs). C'est l'émission du RB grâce au transfert d'énergie qui est illustré dans cette figure.

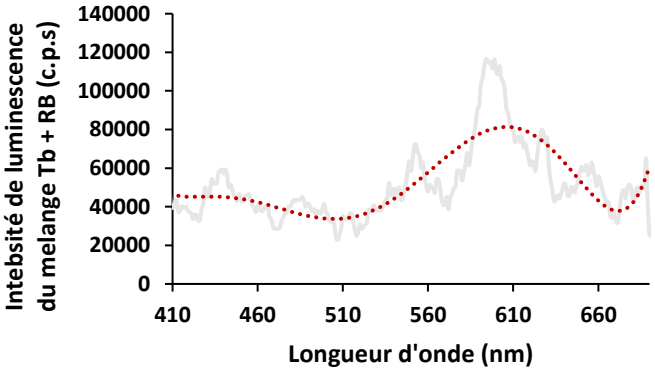

Figure 130 : Spectre d'émission du mélange $TbCl_3$ + RB dans l'eau ($\lambda_{excitation}$= 351 nm- délai 50 µs)

XI. Etude du transfert d'énergie entre AGuIX Tb et RB

XI.1 Spectre d'absorption d'AGuIX Tb

La **Figure 131** montre le spectre d'absorption du Tb chélaté dans les AGuIX. Son maximum d'absorption est à 294 nm. Le maximum d'absorption de Tb^{3+} (AGuIX Tb) est décalé de 76 nm par rapport à l'absorption de Tb^{3+} ($TbCl_3$). Ce déplacement bathochrome peut-être dû à l'influence de l'environnement.

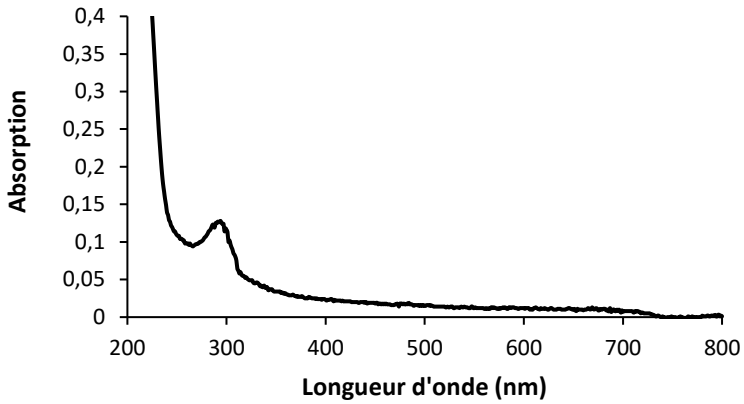

Figure 131 : Spectre d'absorption des AGuIX Tb dans l'eau. [Tb^{3+}]=10 mM

XI.2 Spectre d'émission d'AGuIX Tb

La **Figure 132** montre le spectre d'émission du Tb chélaté dans les AGuIX. Il est similaire à celui de Tb^{3+} ($TbCl_3$).

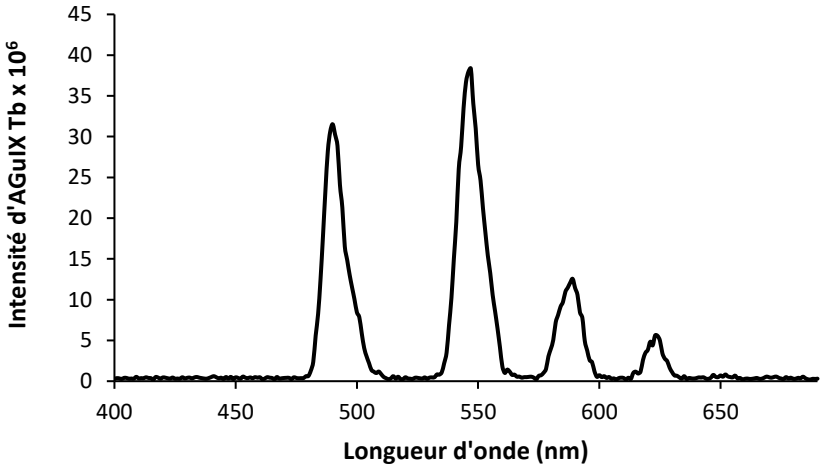

Figure 132 : Spectre d'émission des AGuIX Tb dans l'eau [Tb^{3+}]=10 mM. $\lambda_{excitation}$=351 nm

XI.3 Recouvrement AGuIX Tb+ RB et transfert d'énergie

La **Figure 133** montre le recouvrement entre le spectre d'émission de l'AGuIX Terbium et le spectre d'absorption du RB.

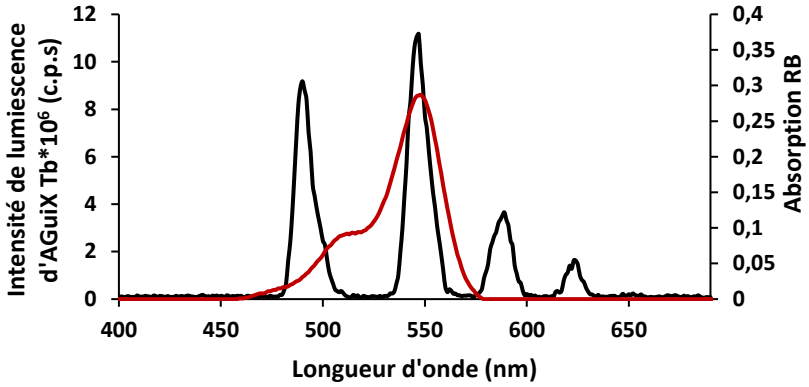

Figure 133 : Recouvrement entre le spectre d'émission d'AGuIX Tb et le spectre d'absorption du RB, [Tb]= 10 mM (noir) et le spectre d'absorption du RB [RB]=18 µM (rouge) dans l'eau ($\lambda_{excitation}$=351 nm, délai 50 µs)

Ce recouvrement J est évalué à $1,87*10^{15}$ $M^{-1}.nm^4.cm^{-1}$ avec un R_0 = 3,76 nm. Cela indique la possibilité d'avoir un transfert FRET. Le recouvrement J de $TbCl_3$ et AGuIX Tb avec le RB sont du même ordre de grandeur ($J=4,36*10^{15}$ $M^{-1}.nm^4.cm^{-1}$ et R_0=4,33 nm).

Pour vérifier le transfert FRET, la variation de l'intensité de la durée de vie de luminescence de l'AGuIX Tb en fonction de la concentration du RB, avec une concentration fixe de Tb [Tb^{3+}]=10 mM est étudiée. La **Figure 134** montre (a) I=f([RB]) et τ=f([RB]) (b)I_0/I= f([RB]) et τ_0/τ=f([RB]) dans l'eau ($\lambda_{excitation}$= 351 nm, délai 50 µs).

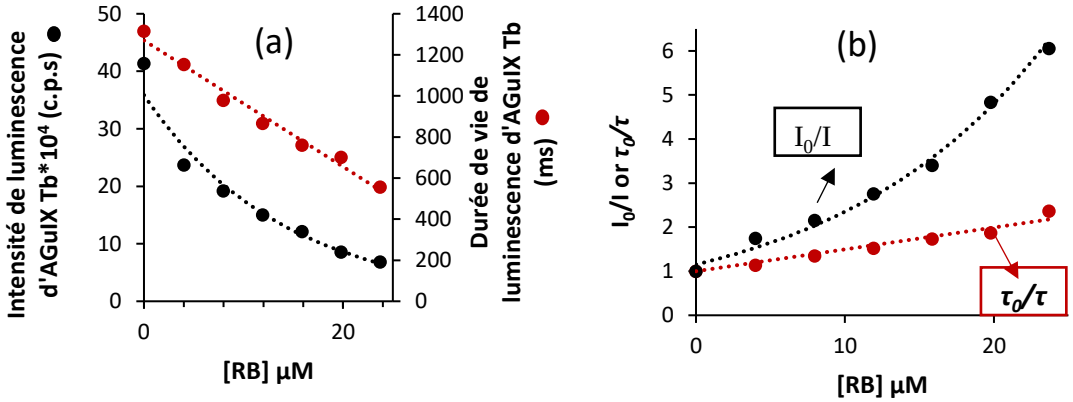

Figure 134 : (a) I=f([RB]) et τ=f([RB]), (b)I_0/I= f([RB]) et τ_0/τ =f([RB]) dans l'eau $\lambda_{excitation}$= 351 nm- délai 50 µs

La diminution exponentielle de l'intensité de luminescence du Terbium et la diminution linéaire de sa durée de vie de luminescence montre un transfert d'énergie non radiatif de type FRET avec des inhibitions dynamique et statique à la fois.

Ce résultat est compatible avec celui de $TbCl_3$/RB. Cela montre que la chélatation du Tb dans les AGuIX ne modifie pas ses caractéristiques photophysiques.

La **Figure 135** montre le spectre d'émission des AGuIX Tb seules ou en présence de RB. Après un délai de 50 µs, l'émission des AGuIX Tb (noir) en présence de RB (rouge) diminue et une émission de fluorescence du RB entre 550 nm et 600 nm apparaît. Cela est en faveur d'un transfert d'énergie entre le Terbium chélaté dans les AGuIX et le RB.

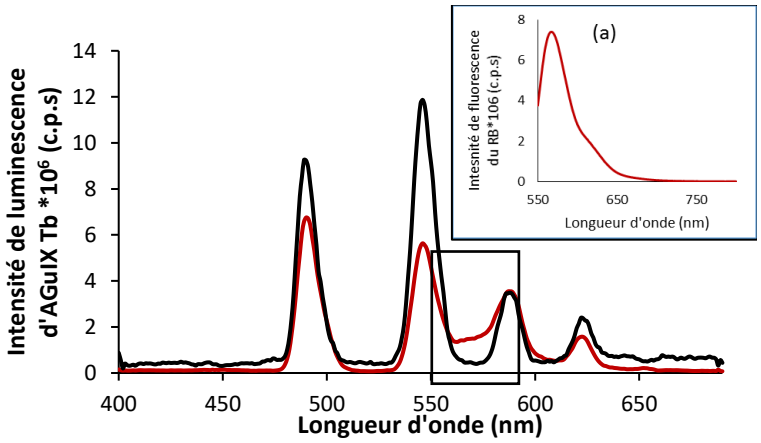

Figure 135 : Spectre d'émission des AGuIX Tb seules [Tb^{3+}]= 10 mM (noir) et d'AGuIX Tb avec RB en solution [RB]= 3 µM (rouge) avec un délai de 50 µs dans l'eau ($\lambda_{excitation}$=351 nm, délai 50 µs). La figure (a) annexe est l'émission du RB dans l'eau après excitation à 558 nm.

La **Figure 136** montre l'émission du Terbium soit sous forme $TbCl_3$, soit chélaté dans les NPs d'AGuIX. L'intensité de fluorescence du Terbium chélaté est plus grande que celle du Tb^{3+} libre. Cela peut être dû à la solvatation de l'ion Tb^{3+} par plusieurs molécules d'eau, ce qui n'est pas le cas pour les atomes de Tb chélatés.

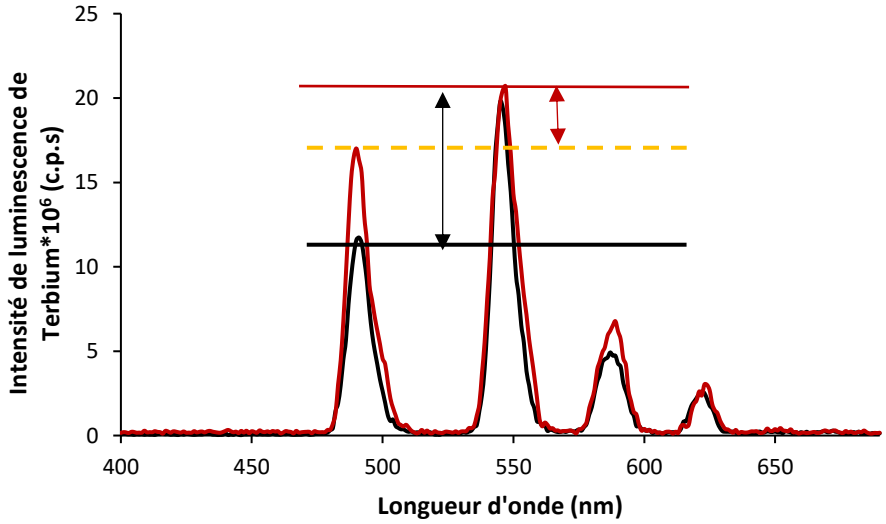

Figure 136 : Emission de $TbCl_3$, [Tb]= 10 mM (noir) et AGuIX Tb, [Tb]=10 mM (rouge).

XII. Etude du transfert d'énergie entre $GdCl_3$ et RB

XII.1 Spectre d'absorption du Gadolinium

La **Figure 137** montre le spectre d'absorption du Gadolinium dans l'eau. Son maximum d'absorption est situé à 273 nm.

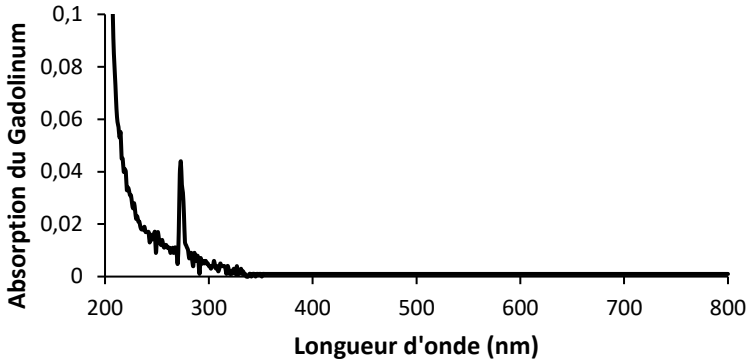

Figure 137 : Spectre d'absorption de Gadolinium, ($GdCl_3$) dans l'eau. [$GdCl_3$]=10 mM

XII.2 Spectre d'émission du Gadolinium

La **Figure 138** montre le spectre d'émission de Gd^{3+}($GdCl_3$) après excitation à 273 nm. Le maximum d'émission, après un délai de 50 µs est à 313 nm.

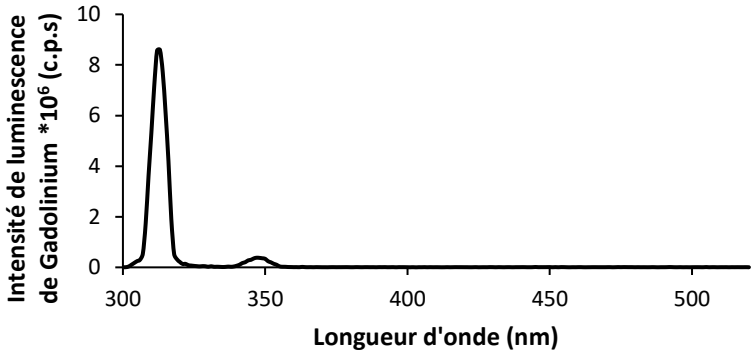

Figure 138 : Spectre d'émission du Gadolinium ($GdCl_3$) dans l'eau. [$GdCl_3$]=10 mM. $\lambda_{excitation}$= 273 nm - délai 50 µs

Cette émission à 313 nm correspond à la différence d'énergie entre les niveaux énergétiques ^6P_J et $^6S_{7/2}$. Le Gadolinium est le seul du groupe lanthanide qui a un premier état d'énergie trop haut, ce qui justifie l'unique pic d'émission étroit (**Figure 139**).

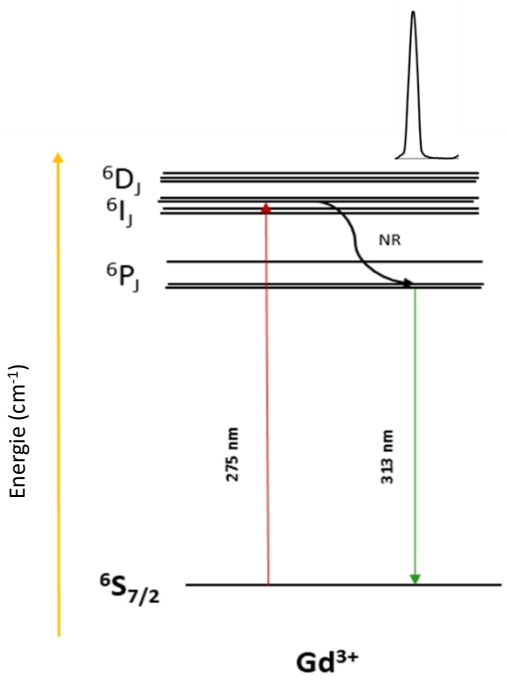

Figure 139 : Diagramme de niveau énergétique simplifié de l'ion Gadolinium

XII.3 Recouvrement AGuIX Tb+ RB et transfert d'énergie

La **Figure 140** montre le recouvrement entre les spectres d'émission du Gadolinium et le spectre d'absorption du RB. Le recouvrement J est de 2,72 *10^{14} ($M^{-1}.nm^4.cm^{-1}$) et R_0 = 2,73 nm.

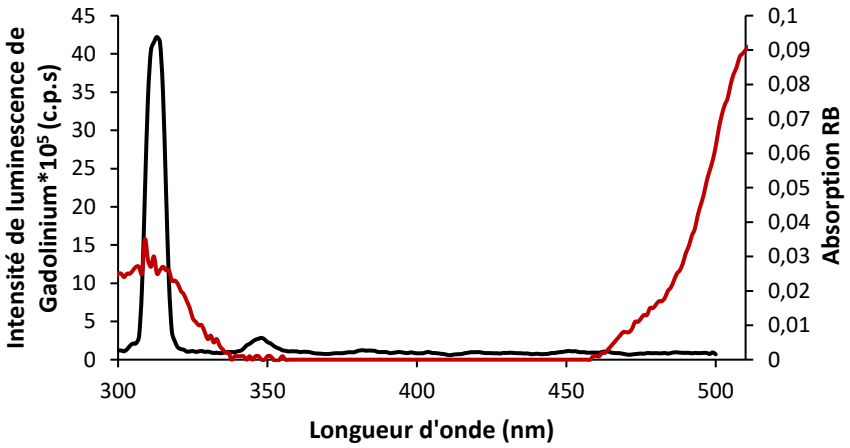

Figure 140 : Recouvrement entre le spectre d'émission de $GdCl_3$ et le spectre d'absorption du RB, [Gd]=10 mM (noir) et [RB]= 18 µM (rouge) dans l'eau ($\lambda_{excitation}$=273 nm, délai 50 µs).

Pour savoir s'il existe un transfert radiatif ou non entre le Gd et le RB, nous étudions la variation de l'intensité de luminescence et de la durée de vie de luminescence de Gadolinium en fonction de la concentration en RB, avec une concentration fixe de Gd / [Gd]=10 mM. La

Figure 141 montre (a) I=f([RB]) et τ=f([RB]) (b)I_0/I= f([RB]) et τ_0/τ=f([RB]) dans l'eau, $\lambda_{excitation}$= 351 nm avec un délai de 50 µs.

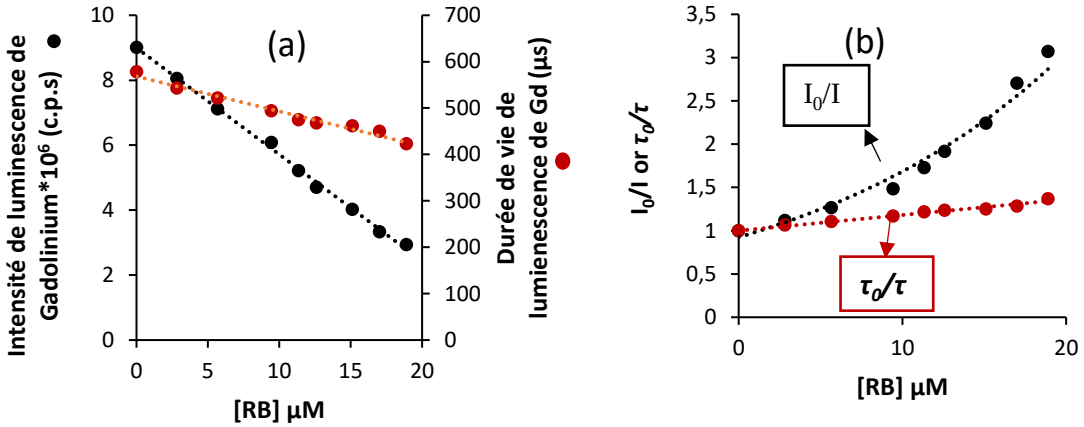

Figure 141 : (a) I=f([RB]) et τ=f([RB]), (b)I_0/I= f([RB]) et τ_0/τ=f([RB]) dans l'eau, $\lambda_{excitation}$= 273 nm, délai 50 µs

D'après la **Figure 141**, la diminution exponentielle de l'intensité de luminescence du Terbium et la diminution linéaire de durée de vie de Gadolinium montrent des inhibitions dynamique et statique. Les variations I_0/I= f([RB]) et τ_0/τ=f([RB]) montrent un transfert non radiatif de type FRET.

XIII. Recouvrement AGuIX Gd+ RB et transfert d'énergie

XIII.1 Spectre d'absorption de l'AGuIX Gd

La **Figure 142** montre le spectre d'absorption de l'AGuIX Gd dans l'eau. Son maximum d'absorption est à 291 nm. Le maximum d'absorption de Gd^{3+} (AGuIX Gd) est décalé de 18 nm par rapport à l'absorption de Gd^{3+} ($GdCl_3$). Ce déplacement bathochrome peut-être dû à la chélation des Gd^{3+}.

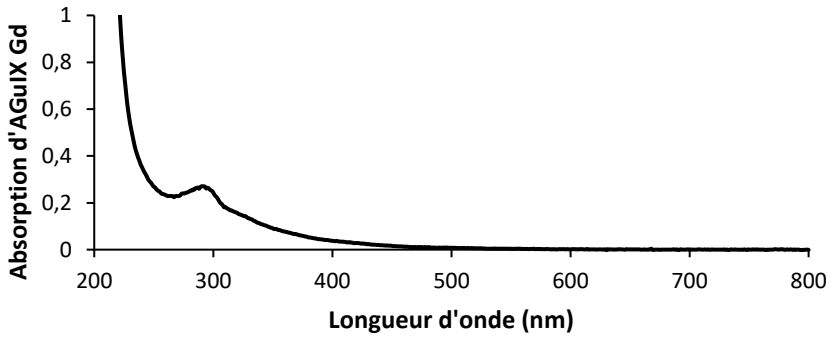

Figure 142: Spectre d'absorption des AGuIX Gd dans l'eau. [Gd^{3+}]=10 mM

XIII.2 Spectre d'émission de l'AGuIX Gd

La **Figure 143** présente le spectre d'émission, après excitation à 273 nm, des AGuIX Gd dispersées dans l'eau. Nous pouvons observer que le le maximum d'émission est à 313 nm.

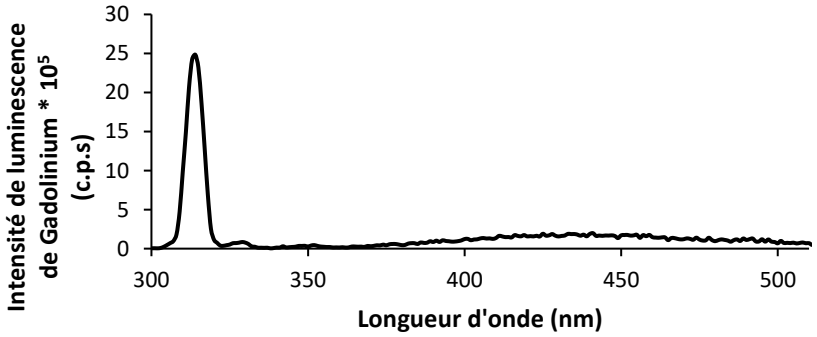

Figure 143 : Spectre d'émission des AGuIX Gd dans l'eau. [Gd^{3+}]=10 mM. $\lambda_{excitation}$= 273 nm, délai 50 µs.

XIII.3 Recouvrement entre AGuIX Gd et RB

La **Figure 144** montre le recouvrement entre le spectre d'émission d'AGuIX Gd (noir) et le spectre d'absorption du RB (rouge). Le recouvrement J est égale à 5,60 $*10^{14}$ ($M^{-1}.nm^4.cm^{-1}$) et R_0 = 3,08 nm, ces deux valeurs sont de même ordre de grandeur que $GdCl_3$/RB (J = 2,72 $*10^{14}$ ($M^{-1}.nm^4.cm^{-1}$) et R_0 = 2,73 nm). La chélation des Gd^{3+} ne modifie pas ses caractéristiques photophysiques.

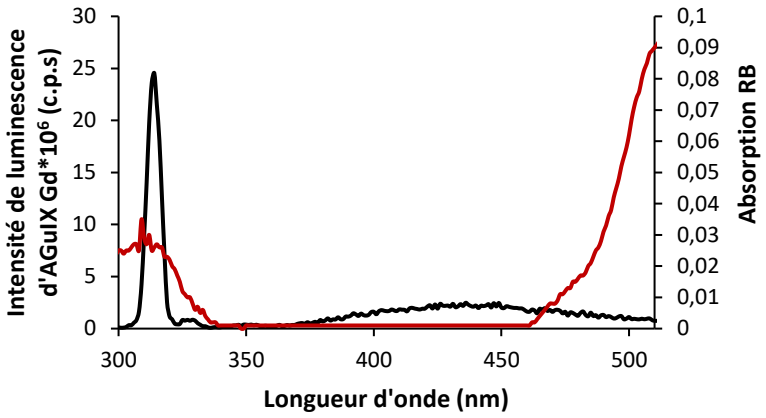

Figure 144 : Recouvrement entre le spectre d'émission de Gd^{3+} et le spectre d'absorption du RB, [Gd]=10 mM et [RB]=18 µM dans l'eau, $\lambda_{excitation}$=273 nm, délai 50 µs

Pour savoir s'il y a un transfert radiatif ou non, nous étudions la variation de l'intensité la durée de vie de luminescence de l'AGuIX Gd en fonction de la concentration du RB, avec une concentration fixe de Gd /[Gd]=10 mM. La **Figure 145** montre (a) I=f([RB]) et τ=f([RB]) (b)I_0/I= f([RB]) et τ_0/τ =f([RB]) dans l'eau, $\lambda_{excitation}$= 351 nm avec un délai 50 µs.

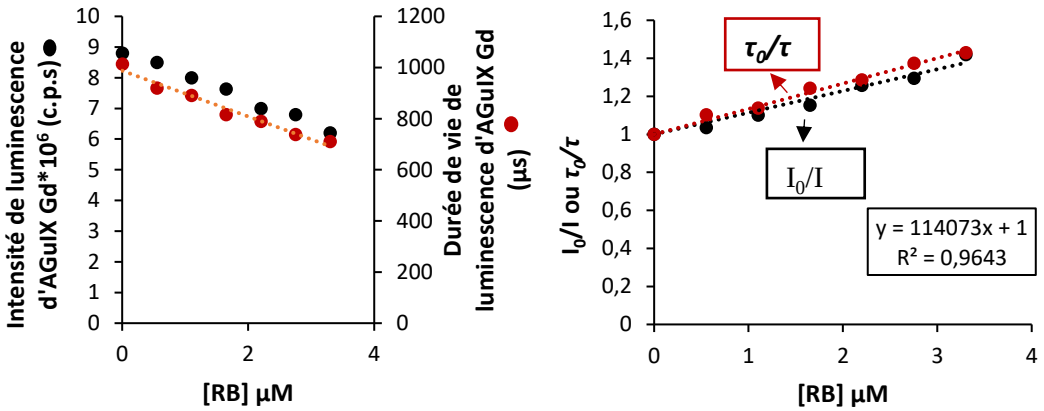

Figure 145 : (a) I=f([RB]) et τ=f([RB]) . (b)I_0/I= f([RB]) et τ_0/τ=f([RB]) dans l'eau. $\lambda_{excitation}$= 273 nm, délai 50 µs

Les résultats de la **Figure 145** montrent une diminution linéaire parfaite des deux variables I et τ. Cela peut indiquer un transfert FRET avec une inhibition dynamique avec une constante de quenching k_q égale à $0{,}57*10^8$ $M^{-1}.s^{-1}$ sachant que $K_{sv} = 11{,}40*10^4$ M^{-1}.

La **Figure 146** présente les spectres d'émission des AGuIX Gd seules ou en présence de RB. Dans l'intervalle 560 nm et 600 nm, nous observons une augmentation de l'intensité de luminescence pour l'échantillon avec RB ce qui peut indiquer un transfert d'énergie des AGuIX Gd.

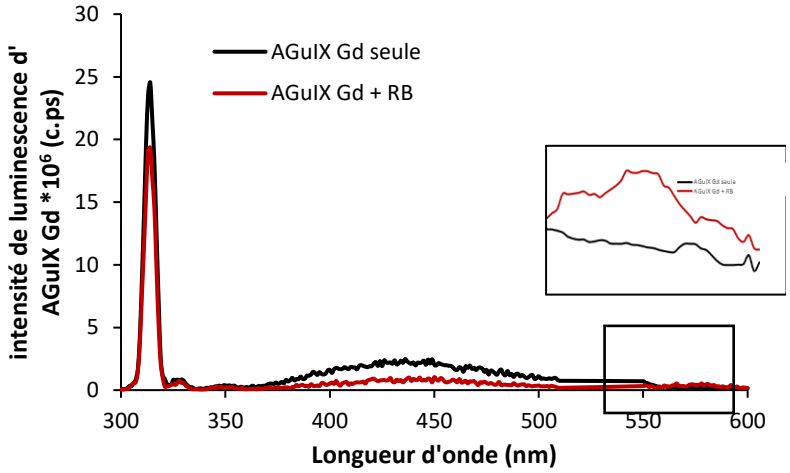

Figure 146: Spectre d'émission d'AGuIX Gd seul et AGuIX Gd +RB dans l'eau, $\lambda_{excitation}$=273 nm – délai 50 µs, [Gd^{3+}]=10 mM et [RB]=3 µM. La figure annexe est un zoom de l'émission entre 560 et 600 nm.

XIV. Nombre de molécules d'eau dans la première sphère de coordination des Lanthanides

En mesurant la durée de vie des lanthanides libres dans l'eau et les lanthanides chélatés dans les AGuIX, nous avons remarqué que la durée de vie des Ln^{3+} libres non chélatés est significativement plus petite que les Ln^{3+} chélatés dans les AGuIX (ms). Cela peut être dû à la solvatation des ions des lanthanides qui est plus favorable pour les ions libres que pour les ions chélatés.

Nous avons calculé le nombre de molécules d'eau dans la sphère de solvatation d'ions lantanides Ln^{3+} en solution ou chélatés dans du DOTA. Nous avons comparé les durées de vie des composés dans l'eau et dans D_2O. Ce nombre (n) est calculé par l'équation suivante suivant Horrocks/Sudnick [14, 15]:

$$\boldsymbol{n = A\left(\frac{1}{\delta_{H2O}} - \frac{1}{\delta_{D2O}} - B\right)} \quad \textbf{(équation 42)}$$

Avec A=5 et B=0,06 pour le terbium et le Gadolinium

Selon cette équation, le nombre de molécules d'eau dans la première sphère de coordination des Lanthanides est calculé (**Tableau 26**) pour : $TbCl_3$, $GdCl_3$, AGuIX Gd et AGuIX Tb sachant que les durée de vie de luminescence sont représentées dans le **Tableau 25**.

Tableau 25: Durée de vie de luminescence de $TbCl_3$, $GdCl_3$, AGuIX Gd et AGuIX Tb dans H_2O et D_2O

$TbCl_3$	Durée de vie (ms)
$TbCl_3$ dans l'eau	0,43
$TbCl_3$ dans D_2O	5,00
AGuIX Tb	Durée de vie (ms)
AGuIX Tb dans l'eau	2,40
AGuIX Tb dans D_2O	3,60
$GdCl_3$	Durée de vie (ms)
$GdCl_3$ dans l'eau	0,50
$GdCl_3$ dans D_2O	1,50
AGuIX Gd	Durée de vie (ms)

AGuIX Gd dans l'eau	2,00
AGuIX Gd dans D_2O	2,40

Tableau 26: Nombre de molécules d'eau dans la première sphère de coordination des Lanthanides de $TbCl_3$, $GdCl_3$, AGuIX Tb et AGuIX Gd

Echantillons	**Nombre de molécules d'eau dans la première sphère de coordination des Lanthanides**
$TbCl_3$	10
$GdCl_3$	7
AGuIX Tb	1
AGuIX Gd	2

Le **Tableau 26** montre que le nombre de molécules d'eau dans la première sphère de coordination des lanthanides est très supérieur pour $TbCl_3$ et $GdCl_3$ que pour Tb et Gd chélates dans les AGuIX. Cela explique les différences de durée de vie obtenue.

XV. Conclusion

En conclusion, pour tous les couples étudiés, nous avons pu observer un transfert d'énergie. Ce transfert d'énergie est de type non-radiatif FRET. L'efficacité est influencée par le recouvrement entre les spectres d'absorption de RB et d'émission des lanthanides. Les caractéristiques FRET de chaque couple sont résumés dans le **Tableau 27**.

Tableau 27 : Caractéristiques du transfert d'énergie entre les différents couples

Couples	**J recouvrement** ($M^{-1}.nm^4.cm^{-1}$)	**R_0** (nm)	**Type of transfer**	**Efficacité de transfert d'énergie**	**Constante de quenching kq** ($M^{-1}.s^{-1}$)
$TbCl_3$/RB	$4{,}36*10^{15}$	4,33	FRET	75%	$1{,}21*10^{8}$
AGuIX Tb/RB	$1{,}87*10^{15}$	3,76	FRET	66%	nd
AGuIX Gd/RB	$5{,}60*10^{14}$	3,08	FRET	27%	$0{,}57*10^{8}$
$GdCl_3$/RB	$2{,}72*10^{14}$	2,73	FRET	24%	nd

Références

[1] M. Ferrari, "Cancer nanotechnology: opportunities and challenges," *Nature Reviews Cancer,* vol. 5, pp. 161-171, 2005/03/01 2005.

[2] P. Juzenas, W. Chen, Y.-P. Sun, M. A. N. Coelho, R. Generalov, N. Generalova, *et al.*, "Quantum dots and nanoparticles for photodynamic and radiation therapies of cancer," *Advanced drug delivery reviews,* vol. 60, pp. 1600-1614, 2008.

[3] A. Vasudevarao, S. Denev, M. D. Biegalski, Y. Li, L.-Q. Chen, S. Trolier McKinstry, *et al.*, "Erratum:"Polarization rotation transitions in anisotropically strained SrTiO 3 thin films"[Appl. Phys. Lett. 92, 192902 (2008)]," *Applied Physics Letters,* vol. 94, p. 192902, 2009.

[4] G. v. Bünau, "J. B. Birks: Photophysics of Aromatic Molecules. Wiley-Interscience, London 1970. 704 Seiten. Preis: 210s," *Berichte der Bunsengesellschaft für physikalische Chemie,* vol. 74, pp. 1294-1295, 1970.

[5] E. L. Wehry, "Effects of molecular structure on fluorescence and phosphorescence," in *Practical fluorescence*, ed: CRC Press, 2020, pp. 75-125.

[6] "Effects of Intermolecular Photophysical Processes on Fluorescence Emission," in *Molecular Fluorescence*, ed, 2001, pp. 72-124.

[7] "Principles of Steady-State and Time-Resolved Fluorometric Techniques," in *Molecular Fluorescence*, ed, 2001, pp. 155-199.

[8] "Fluorescence Polarization. Emission Anisotropy," in *Molecular Fluorescence*, ed, 2001, pp. 125-154.

[9] C. Roychoudhuri, A. F. Kracklauer, and K. Creath, *The nature of light: what is a photon?*: CRC Press, 2017.

[10] R. Šípoš and J. Šima, "Jablonski Diagram Revisited," *Revista Cubana de Física,* vol. 37, pp. 125-130, 2020.

[11] H. Ta, "A Novel Method for Quantitative and Structural Determination of Molecular Complexes by Photon Antibunching," 2010.

[12] D. F. Swinehart, "The beer-lambert law," *Journal of chemical education,* vol. 39, p. 333, 1962.

[13] J. Delaire, J. Piard, R. Méallet-Renault, and G. Clavier, *Photophysique et photochimie: Des fondements aux applications*: EDP sciences, 2017.

[14] W. D. Horrocks Jr and D. R. Sudnick, "Lanthanide ion probes of structure in biology. Laser-induced luminescence decay constants provide a direct measure of the number of metal-coordinated water molecules," *Journal of the American Chemical Society,* vol. 101, pp. 334-340, 1979.

[15] S. Aime, A. Barge, M. Botta, J. A. Howard, R. Kataky, M. P. Lowe, *et al.*, "Dependence of the relaxivity and luminescence of gadolinium and europium amino-acid complexes on hydrogencarbonate and pH," *Chemical Communications,* pp. 1047-1048, 1999.

Chapitre III :
Etude du transfert d'énergie en solution entre Terbium/Gadolinium et le Photofrin

I. Introduction

Un projet de recherche a été mis en place durant ma thèse entre i) Gal Shafirstein, Professeur d'oncologie, directeur de la Recherche Clinique PDT au Centre de PDT à Roswell Park Comprehensive Cancer Center, Buffalo, aux Etats Unis, ii) NH TherAguix qui développe les AGuIX, et iii) notre équipe. Le but de ce projet est d'évaluer l'efficacité des AGuIX en présence ou non d'un PS, le photofrin, sous illumination à 630 nm ou sous irradiation X pour traiter le cancer du poumon. Dans ce nouveau projet, il est proposé d'améliorer le contrôle tumoral local et systémique en combinant la PDT interstitielle avec des NPs activées par rayons X à faible dose dans le traitement du cancer du poumon métastatique localement avancé.

L'étude du transfert d'énergie qui se produit après excitation de Gd/Tb chélatés dans les AGuIX en présence de Photofrin a été réalisée. Nous avons également utilisé des AGuIX Gd conjugués à la cyanine 5,5 (Cy5,5). Ce dernier est un fluorophore qui émet une couleur rouge et permet de visualiser la présence de NPs *in vivo*, notamment dans les cellules cancéreuses.

II. Le photofrin

II.1 Généralités

Le Photofrin est un mélange de plusieurs porphyrines. C'est un porfimère sodique utilisé en clinique dans la PDT pour le traitement des différents types de cancer comme le cancer de l'œsophage et le cancer endobronchique. La structure développée du Photofrin est donnée dans la **Figure 147**.

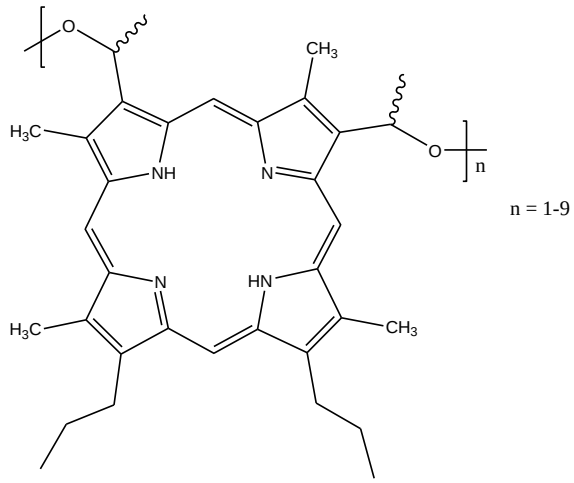

Figure 147 : Structure chimique du Photofrin®

À l'origine, les dérivés de l'hématoporphyrine étaient utilisés pour la PDT. Le Photofrin, un mélange mieux défini est désormais utilisé [1].

De nos jours, le Photofrin est utilisé en clinique pour traiter des maladies de la peau comme le psoriasis ainsi que certains types de cancers. En 1993, le Photofrin a été utilisé la première fois à Canada pour traiter le cancer de la vessie. Le Photofrin a ensuite été autorisé aux Etats-Unis pour traiter le cancer de l'œsophage et du poumon, qui, après une étude sur plusieurs patients, a montré une rémission complète pour 99% des patients [2].

Le Photofrin est utilisé pour traiter le cancer de l'œsophage, le cancer endobronchique et l'œsophage de Barrett. Il est aussi préconisé dans de nombreux cas de carcinomes baso- et spinocellulaires.

Le Photofrin® est injecté à la dose de 2 mg/kg par voie intraveineuse lente (3 à 5 minutes) 48 heures avant le traitement [3]. Après 48 h, le Photofrin est accumulé dans les cellules cancéreuses. La zone tumorale est illuminée à 630 nm permettant la production des ROS et d'$^1O_2$ détruisant les cellules tumorales.

II.2 Spectre d'absorption du Photofrin

La **Figure 148** montre le spectre d'absorption du Photofrin dans l'eau. Son maximum d'absorption (bande de Soret) est à 366 nm et il possède comme tous les porphyrines quatre bandes ($Q_{I-IV)}$ qui sont respectivement localisées à 618 nm, 568 nm, 540 nm, 507 nm. Les coefficients d'extinction molaires du Photofrin dans l'eau à 273 nm (longueur d'onde d'excitation du Gd), 351 nm (longueur d'onde d'excitation du Tb), 366 nm (sa longueur d'onde d'absorption maximale dans l'eau) sont 18078 $M^{-1}.cm^{-1}$, 114 194 $M^{-1}.cm^{-1}$, 147 206 $M^{-1}.cm^{-1}$ respectivement.

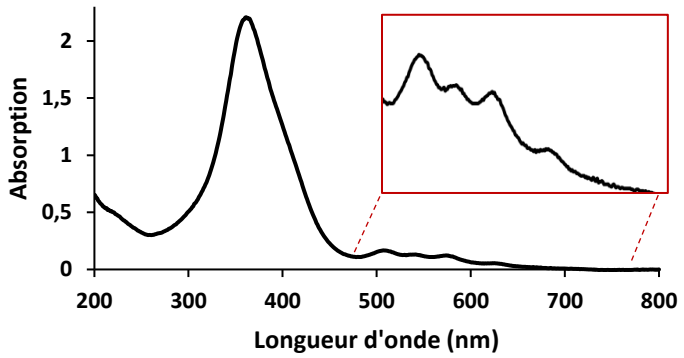

Figure 148 : Spectre d'absorption du Photofrin dans l'eau. [Photofrin] = 25 µM. ε_{505nm} (Q_{IV}) = 9544 $cm^{-1}.M^{-1}$, ε_{540nm} (Q_{III}) = 8084 $cm^{-1}.M^{-1}$, $\varepsilon_{559\,nm}$ (Q_{II}) = 7635 $cm^{-1}.M^{-1}$, $\varepsilon_{612\,nm}$ (Q_I) = 3593 $cm^{-1}.M^{-}$

II.3 Spectre d'émission de fluorescence du Photofrin

La **Figure 149** montre le spectre d'émission de fluorescence du Photofrin entre 590 nm et 700 nm dans l'eau, excité à 366 nm (sa longueur d'onde d'absorption maximale).

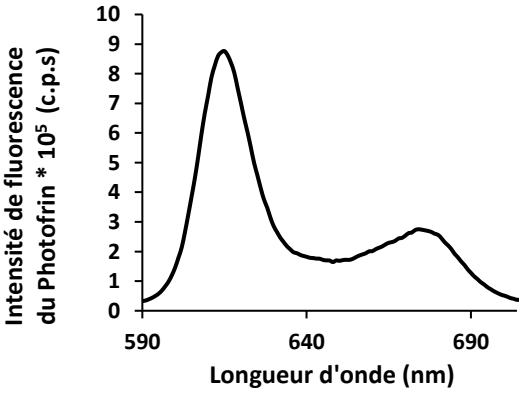

Figure 149 : Spectre d'émission du Photofrin dans l'eau. [Photofrin]=2,5 µM, $\lambda_{excitation}$ = 366 nm

Le spectre d'émission de fluorescence du Photofrin dans l'eau possède deux bandes maximales à 614 nm et 676 nm.

III. Etude du transfert d'énergie entre différent couples

III.1 $TbCl_3$ / Photofrin

III.1.1 Recouvrement entre les spectres de $TbCl_3$ et le Photofrin

La **Figure 150** montre le recouvrement entre les spectres d'émission de $TbCl_3$ (noir) et le spectre d'absorption du Photofrin (rouge) dans l'eau. Le recouvrement J est égale à $8{,}9*10^{14}$ ($M^{-1}.nm^4.cm^{-1}$) et $R_0 = 3{,}33$ nm. Cela indique la possibilité d'avoir un transfert d'énergie FRET.

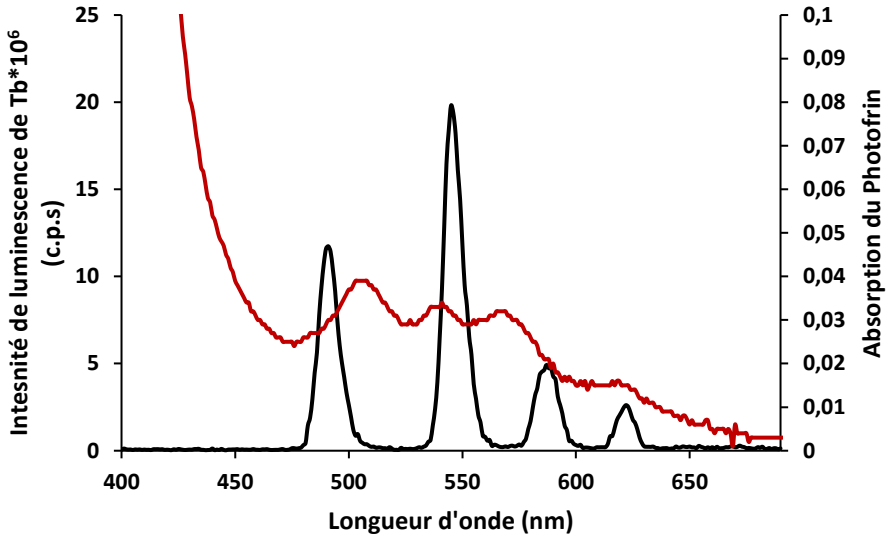

Figure 150 : Recouvrement entre le spectre d'émission de $TbCl_3$ (noir) et le spectre d'absorption du Photofrin (rouge), dans l'eau.

III.1.2 Etude du transfert d'énergie

Pour évaluer s'il existe un transfert d'énergie radiatif ou non, nous étudions la variation de l'intensité (I), et la durée de vie de luminescence (τ) du Terbium, en fonction de la concentration du Photofrin avec une concentration fixe de Tb /[Tb]=10 mM. La **Figure 151** montre (a) I=f([Photofrin]) et τ=f([Photofrin]) (b)I_0/I= f([Photofrin]) et τ_0/τ =f([Photofrin]) dans l'eau, $\lambda_{excitation}$= 351 nm avec un délai de 50 µs. En supposant que n=1, la masse molaire du Photofrin est considérée égale à 1179 g/mol.

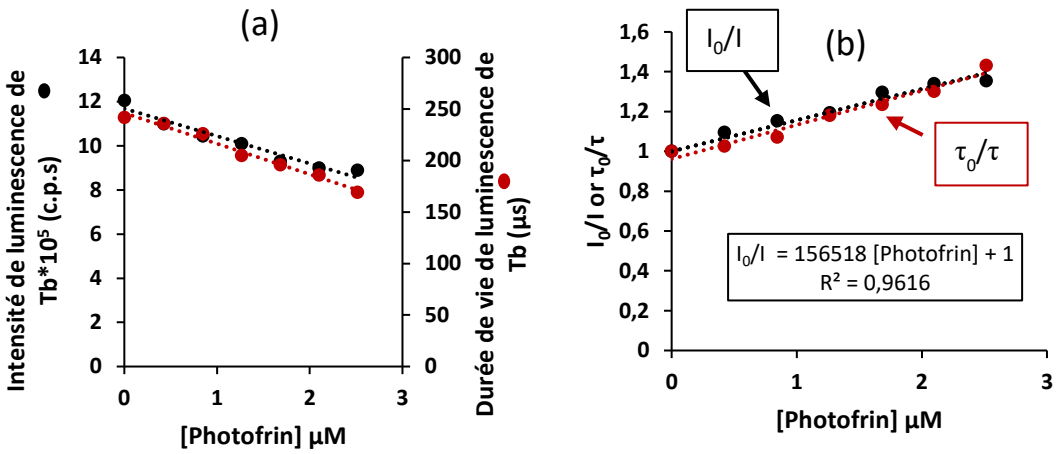

Figure 151 : (a) I=f(Photofrin]) et τ=f(Photofrin]), (b)I_0/I= f([Photofrin]) et τ_0/τ =f([Photofrin]) dans l'eau. $\lambda_{excitation}$= 351 nm, délai 50 µs

La superposition des deux courbes I_0/I= f([Photofrin]) et τ_0/τ =f([Photofrin]) montre un transfert d'énergie non radiatif FRET de constante de quenching k_q égale à 3,63 * 10^8 ($M^{-1}.s^{-1}$). Sachant que y = F/F_0 et x = [RB], la pente est la constante de Stern-Volmer (15,65 * 10^4 M^{-1}), la durée de vie de luminescence de Tb ($TbCl_3$) = 433 µs.

III.2 AGuIX Tb/Photofrin

III.2.1 Recouvrement entre spectre d'émission des AGuIX Tb et spectre d'absorption du Photofrin

La **figure 152** montre le recouvrement entre les spectres d'émission d'AGuIX Tb et d'absorption du Photofrin. Le recouvrement J est égal à 1,12*10^{15} $M^{-1}.nm^4.cm^{-1}$ et R_0 = 3,46 nm, sans différence avec le Tb non chélaté dans les AGuIX (8,9*10^{14} $M^{-1}.nm^4.cm^{-1}$ et R_0 = 3,33 nm).

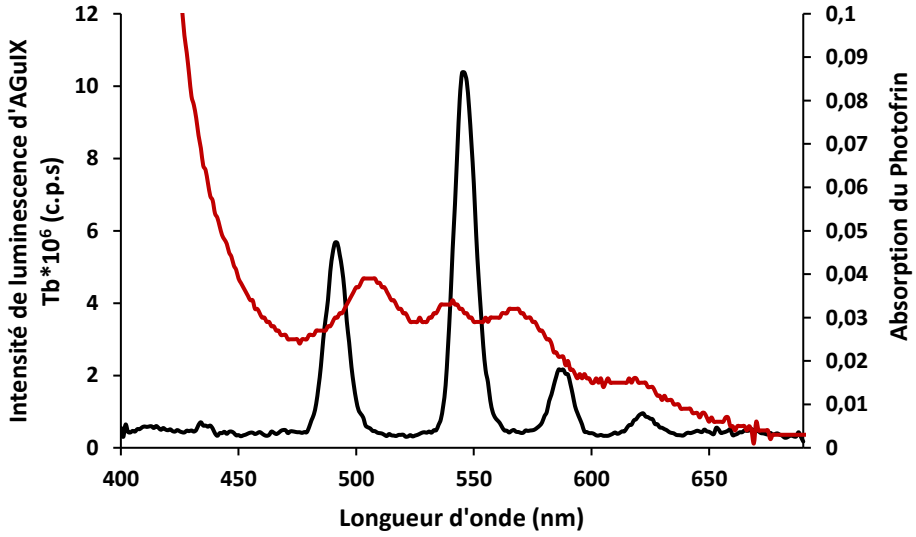

Figure 152 : Recouvrement entre les spectres d'émission de l'AGuIX Tb (noir) et d'absorption du Photofrin (rouge) dans l'eau. $\lambda_{excitation}$= 351 nm, délai 50 µs

III.2.2 Etude du transfert d'énergie

La **figure 153** montre (a)I=f([Photofrin]) et τ=f([Photofrin]) (b)I_0/I= f([Photofrin]) et τ_0/τ =f([Photofrin]) dans l'eau, $\lambda_{excitation}$= 351 nm avec un délai de 50 µs.

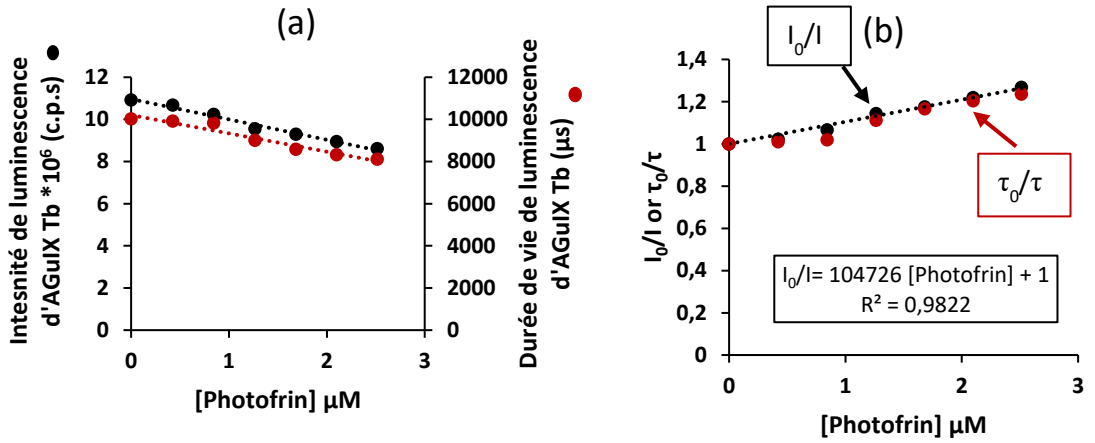

Figure 153 : (a) I=f(Photofrin]) et τ=f(Photofrin] , (b)I_0/I= f([Photofrin]) et τ_0/τ =f([Photofrin]) dans l'eau, $\lambda_{excitation}$= 351 nm, délai 50 µs

Les graphes de la **figure 153** montre un linéarité croissante de I_0/I= f([Photofrin]) et τ_0/τ=f([Photofrin]) confirmant un transfert d'énergie FRET avec une inhibition dynamique. La constante de Stern-Volmer est de 10,4726*10^4 M^{-1}, la durée de vie de luminescence de Tb (AGuIX Tb) = 2,4 ms, la constante de quenching k_q égale à 0,43 * 10^8 $M^{-1}.s^{-1}$.

La **figure 154** montre les spectres d'émission de l'AGuIX Tb seule (noir) et AGuIX Tb avec Photofrin (rouge) dans l'eau avec un délai de 50 µs. Nous pouvons observer que l'intensité de luminescence du Terbium diminue en présence du photofrin par rapport au Tb seul.

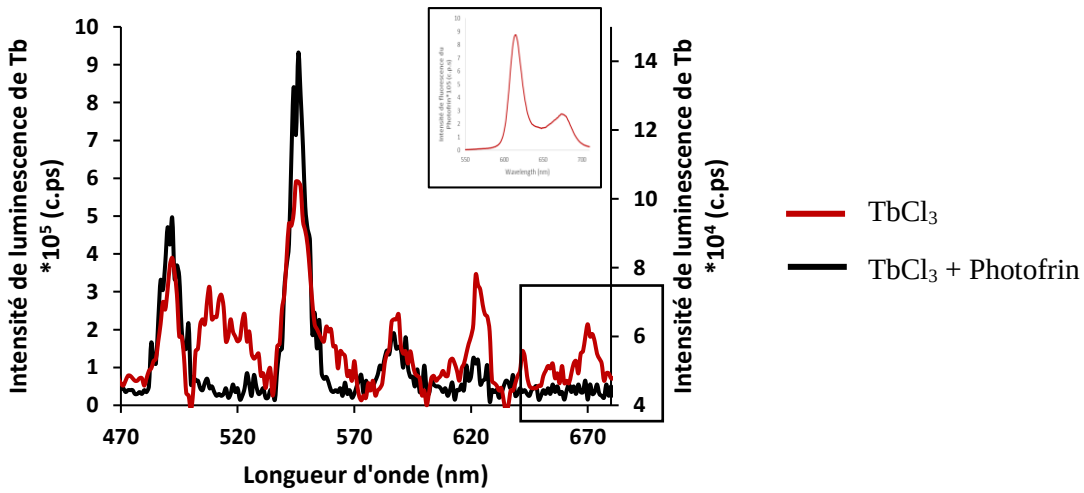

Figure 154 : Spectre d'émission du $TbCl_3$ seule et $TbCl_3$ en présence de Photofrin dans l'eau avec un délai de 50 µs [$TbCl_3$]=0,15 mM et [Photofrin]=22 µM et $\lambda_{excitation}$= 351 nm.

Nous observons également une augmentation de luminescence entre 600 et 650 nm due à l'émission du Photofrin.

Les couples $TbCl_3$ et AGuIX Tb avec le Photofrin montrent un transfert d'énergie FRET.

III.3 $GdCl_3$/Photofrin

III.3.1 Recouvrement entre le spectre d'émission de $GdCl_3$ et le spectre d'absorption du Photofrin

La **figure 155** montre le recouvrement entre le spectre d'émission du Gadolinium et le spectre d'absorption du Photofrin. Un recouvrement J= $3{,}433854*10^{14}$ $M^{-1}.nm^4.cm^{-1}$et un rayon FORSTER R_0=2,8 nm indiquent la possibilité d'avoir un transfert d'énergie non-radiatif.

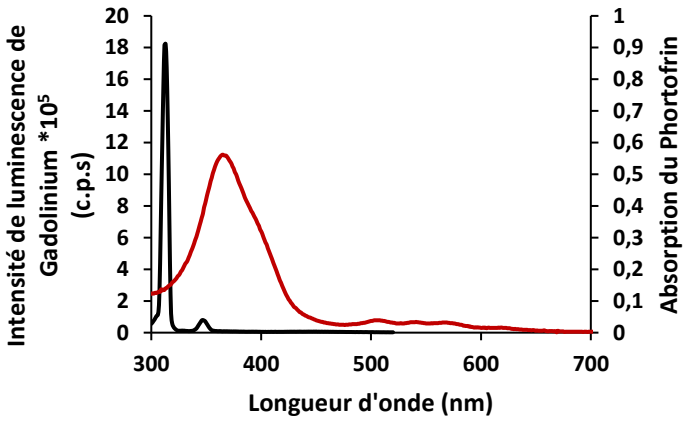

Figure 155 : Recouvrement entre l'émission de $GdCl_3$ (noir) dans l'eau excité à 273 nm, et le spectre d'absorption de Photofrin dans l'eau (rouge).

III.3.2 Etude du transfert d'énergie

La **figure 156** montre (a) I=f([Photofrin]) et τ=f([Photofrin]) (b)I_0/I= f([Photofrin]) et τ_0/τ =f([Photofrin]) dans l'eau, $\lambda_{excitation}$= 273 nm avec un délai de 50 µs.

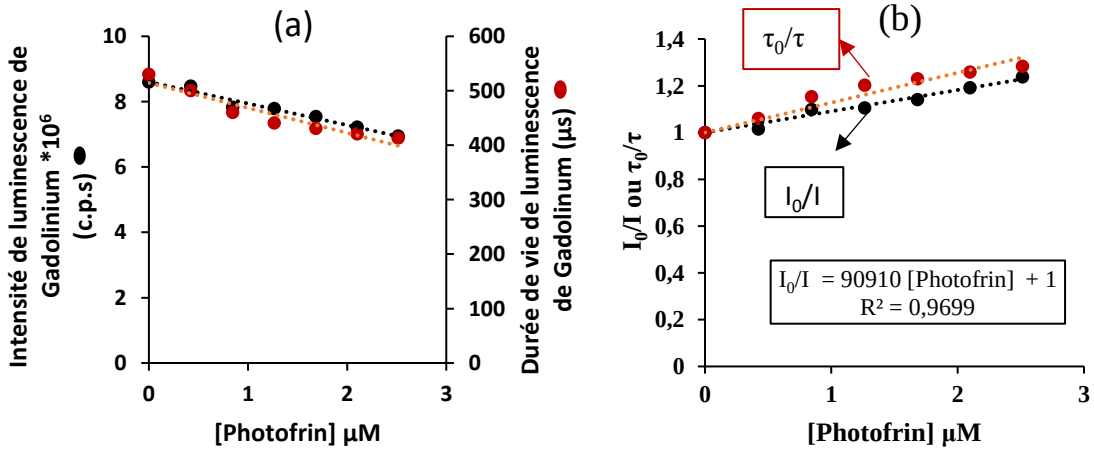

Figure 156 : (a) I=f([Photofrin]) et τ=f([Photofrin]) . (b)I_0/I= f([Photofrin]) et τ_0/τ =f([Photofrin]). L'eau est le solvant. $\lambda_{excitation}$= 273 nm- délai 50 µs

Une linéarité croissante de I_0/I= f([Photofrin]) et τ_0/τ=f([Photofrin]) confirmant un transfert d'énergie FRET avec une inhibition dynamique entre le Gd et le Photofrin avec constante de quenching k_q égale à $1{,}81*10^8$ $M^{-1}.s^{-1}$. La constante de Stern-Volmer est de $9{,}09 * 10^4\ M^{-1}$, la durée de vie de luminescence de Gd ($GdCl_3$) est de 500 µs.

III.4 AGuIX Gd/Photofrin

III.4.1 Recouvrement entre le spectre d'émission d'AGuIX Gd et le spectre d'absorption du Photofrin

La **figure 157** montre le recouvrement entre l'émission du Gadolinium chélaté dans les AGuIX et l'absorption du Photofrin. Un recouvrement $J=5{,}425214*10^{14}$ $M^{-1}.nm^4.cm^{-1}$ et un rayon Forster R_0=3,06 nm suggèrent la possibilité d'avoir un transfert d'énergie FRET.

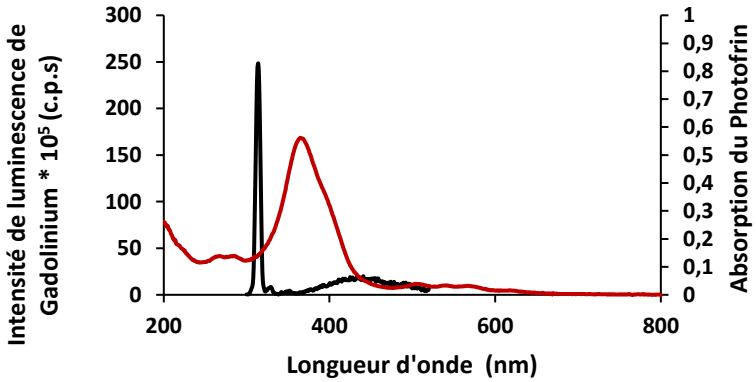

Figure 157 : Recouvrement entre le spectre d'émission de l'AGuIX Gd et le spectre d'absorption de Photofrin dans l'eau. Le Gd est excité à 273 nm.

III.4.2 Etude du transfert d'énergie

La **Figure 158** montre (a) I=f([Photofrin]) et τ=f([Photofrin]) (b)I_0/I= f([Photofrin]) et τ_0/τ =f([Photofrin]) dans l'eau, $\lambda_{excitation}$= 273 nm avec un délai de 50 µs.

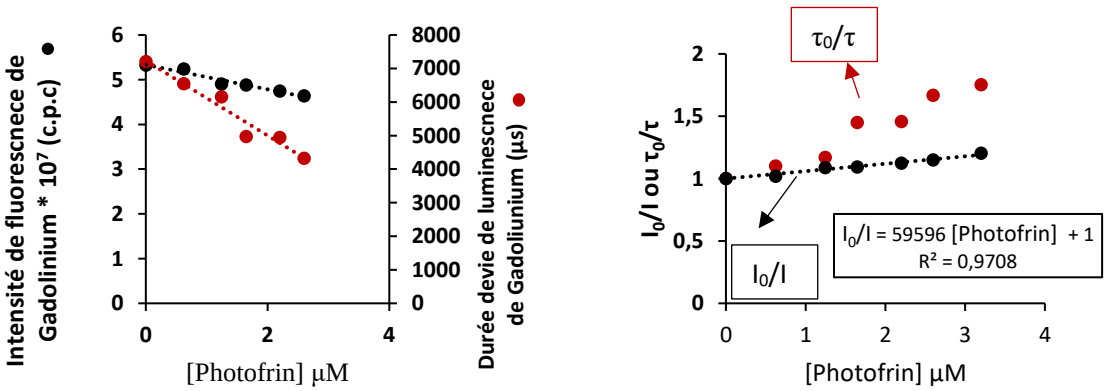

Figure 158 : (a) I=f([Photofrin]) et τ=f([Photofrin]), (b)I_0/I= f([Photofrin]) et τ_0/τ =f([Photofrin]) dans l'eau, $\lambda_{excitation}$= 273 nm, délai 50 µs.

La **Figure 158** montre aussi un transfert d'énergie FRET entre les AGuIX Gd et le Photofrin. La constante de Stern-Volmer est de $5{,}95*10^4$ M^{-1}, la durée de vie de luminescence de Gd (AGuIX Gd) = 2 ms, la constante de quenching k_q est de $0{,}29 * 10^8$ $M^{-1}.s^{-1}$.

Le **Tableau 28** résume les caractéristiques du transfert d'énergie FRET

Tableau 28 : Caractéristiques du transfert FRET pour les couples Ln/Photofrin.

Couple	Recouvrement ($M^{-1}.nm^4.cm^{-1}$)	R_0 (nm)	Type of transfert	Efficacité FRET	Constante de quenching k_q ($M^{-1}.s^{-1}$)
AGuIX Gd/Photofrin	$5{,}425214*10^{14}$	3,06	FRET	43%	$0{,}29 * 10^8$
$GdCl_3$/Photofrin	$3{,}433854*10^{14}$	2,80	FRET	39%	$1{,}81*10^8$
$TbCl_3$/Photofrin	$8{,}9*10^{14}$	3,33	FRET	40%	$3{,}63 * 10^8$
AGuIX Tb/Photofrin	$1{,}12*10^{15}$	3,46	FRET	42%	$0{,}43 * 10^8$

IV. Chélation des Ln^{3+} dans le Photofrin et adsorption du Photofrin sur les AGuIX

Lorsque nous réalisons le mélange du Photofrin avec $TbCl_3$ ou $GdCl_3$, une précipitation est observée 3 heures après, non observée dans le cas du mélange Photofrin, AGuIX Tb ou AGuIX Gd. Les ions trivalents favorisent la précipitation dans l'eau mais il se peut aussi que le Terbium et le Gadolinium s'adsorbe sur les molécules du Photofrin, les molécules deviennent plus lourdes et précipitent.

Une purification de ces échantillons par centrifugation et une lyophilisation ont été réalisées. Nous obtenons des poudres non dispersables dans l'eau. Une dispersion de ces échantillons dans le DMSO et la dilution 100 fois dans l'eau nous donne le spectre d'absorption de la **Figure 159**.

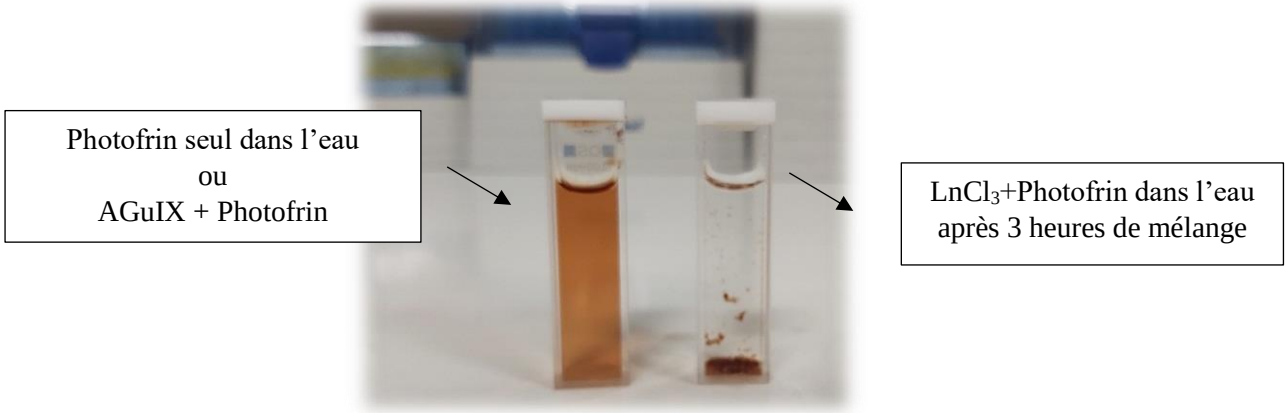

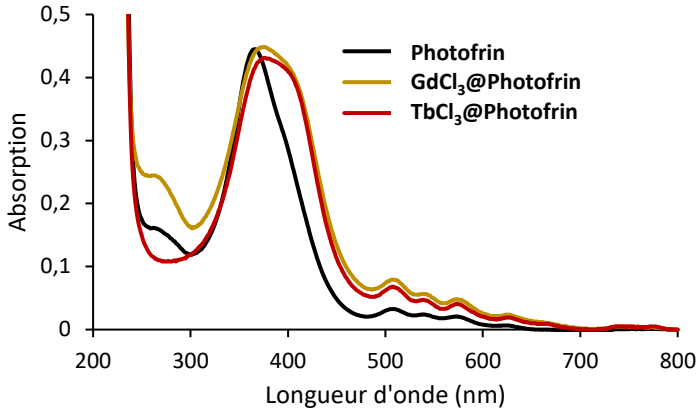

Figure 159 : Spectres d'absorption de $GdCl_3$@Photofrin, $TbCl_3$@Photofrin, Photofrin dans l'eau

Un shift batochromique est observé. Il est fort probable que Tb^{3+} et Gd^{3+} interagissent avec le Photofrin.

Après une journée d'agitation avec les AGuIX et le Photofrin, le spectre d'absorption du Photofrin subit également un shift bathochronique (**Figure 160**). Cela suggère qu'il y a adsorption du Photofrin sur les AGuIX Gd.

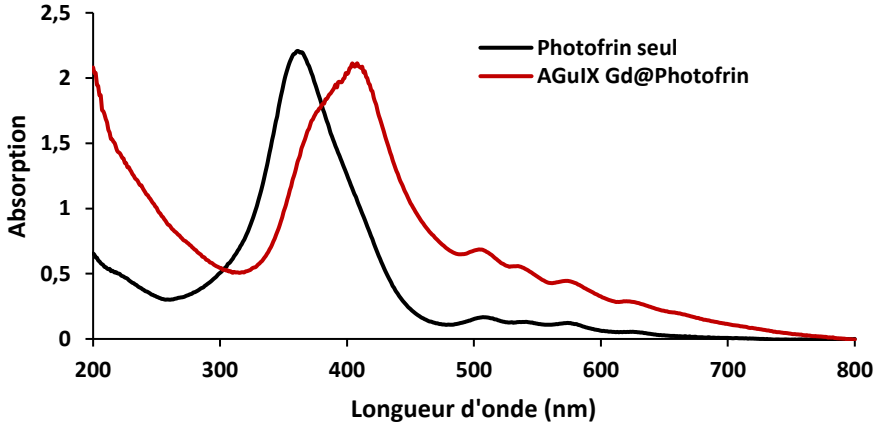

Figure 160 : Spectre d'absorption du Photofrin en solution et du Photofrin adsorbé sur l'AGuIX Gd dans l'eau. [Gd^{3+}]=10 mM et [Photofrin]=25 µM.

Nous nous sommes intéressés à la production d'$^1O_2$ du Photofrin. La **Figure 161** montre la luminescence d'$^1O_2$ du Photofrin en solution ou d'une solution en présence d'AGuIX Gd@Photofrin, dans l'éthanol après excitation à 273 nm. Aucune luminescence n'est observée pour le Photofrin qui n'absorbe quasiment pas à 273 nm. En revanche, le signal à 1270 nm observé en présence d'AGuIX démontre qu'il existe un transfert d'énergie entre Gadolinium et le Photofrin.

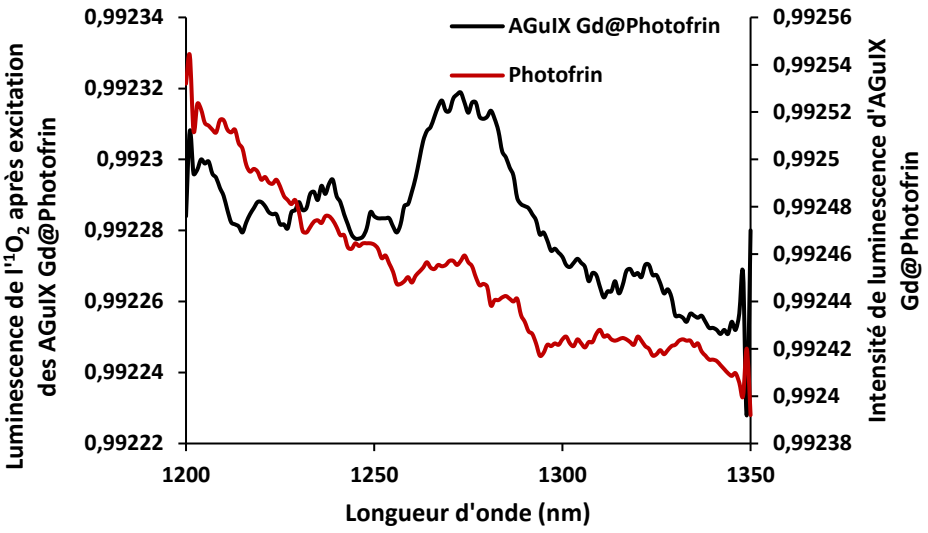

Figure 161 : Spectres de luminescence de l'$^1O_2$ après excitation du Photofrin seul et de l'AGuIX Gd@Photofrin dans l'éthanol. $\lambda_{excitation}$= 273 nm. [Gd^{3+}]=10 mM et [Photofrin]=2,5 µM.

V. Adsorption du Photofrin sur les AGuIX Gd

V.1 Synthèse

Afin de favoriser le transfert d'énergie, nous avons décidé d'adsorber au préalable le Photofrin sur les AGuIX Gd. Nous préparons les solutions en dispersant 20 mM d'AGuIX Gd dans l'eau pendant une heure afin d'avoir une bonne stabilité et dispersion. Cette solution est divisée en quatre et sont ajoutés dans chacune des solutions respectivement : 0,1 – 0,075 - 0,05 et 0,025 équivalent en nombre de mole de Photofrin, goutte à goutte.

Ces solutions sont laissées sous agitation 1 h à température ambiante. Une centrifugation est faite avec des vivaspin® 5 KDa de facteur, jusqu'à l'obtention d'un filtrat transparent (suivie par absorption jusqu'à l'arrêt de la détection de l'absorption du Photofrin). Dans notre cas, le filtrat ne contient aucune trace de Photofrin, l'adsorption est totale. Les solutions sont ensuite lyophilisées.

V.2 Spectre d'absorption

La **figure 162** montre les spectres d'absorption des différentes solutions de NPs ainsi que des AGuIX Gd seules et le Photofrin seul. Le spectre d'absorption du Photofrin adsorbé sur les AGuIX est décalé de 38 nm vers le rouge indiquant la réussite de l'adsorption.

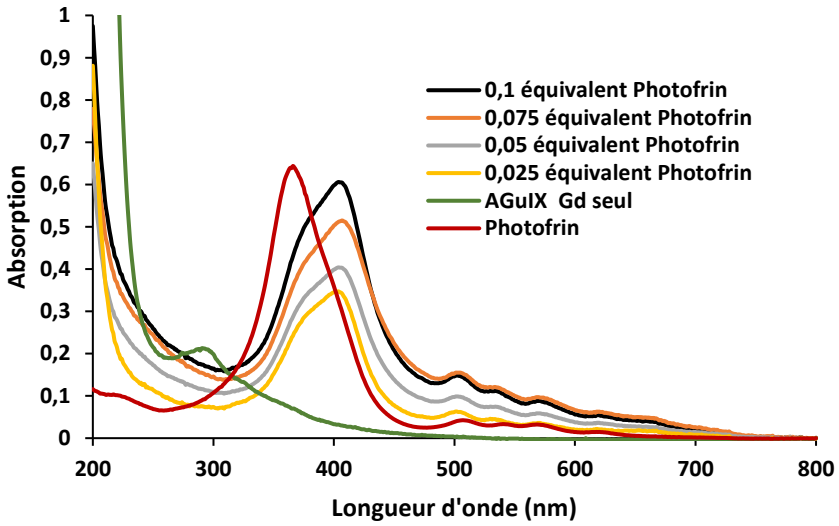

Figure 162 : Spectres d'absorption du Photofrin non adsorbé sur les AGuIX dans l'eau à différentes concentrations de Photofrin et une concentration fixe d'AGuIX Gd, [Gd] = 10 mM.

V.3 Transfert d'énergie

La **figure 163** montre (a) I=f([Photofrin]) et τ=f([Photofrin]) (b)I_0/I= f([Photofrin]) et τ_0/τ =f([Photofrin]) dans l'eau, $\lambda_{excitation}$= 273 nm avec un délai de 50 µs. Les concentrations de Photofrin sur les axes des abscisses sont exprimées en nombre de mole d'équivalent par rapport au Gd.

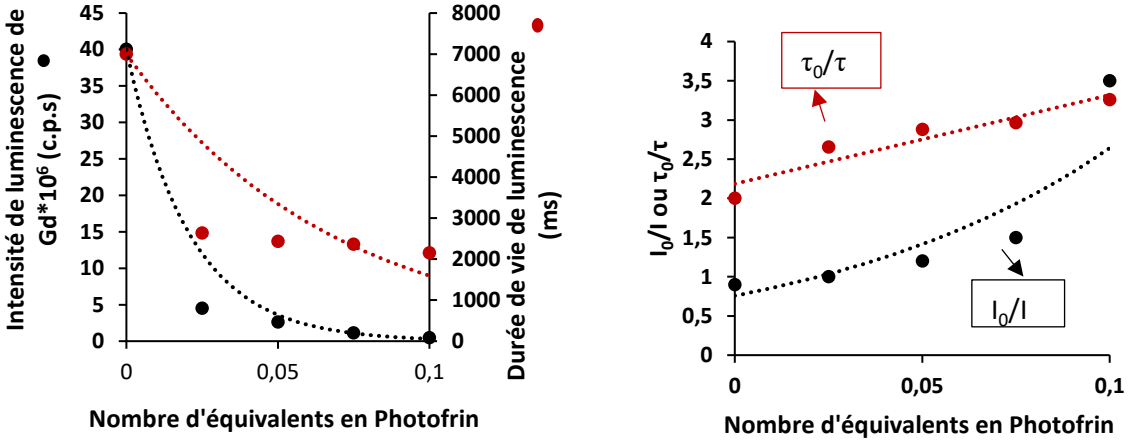

Figure 163: (a) I=f([Photofrin]) et τ=f([Photofrin]). (b)I_0/I= f([Photofrin]) et τ_0/τ =f([Photofrin]) dans l'eau$\lambda_{excitation}$= 273 nm, délai 50 µs.

L'allure des graphes de la **figure 163** montre un transfert d'énergie FRET mais avec un phénomème de saturation dès 0,025 équivalent en Photofrin adsorbé.

V.4 Rendement quantique d'oxygène singulet

La **figure 164** indique les rendements quantiques d'$^1O_2$ dans différents échantillons.Le rendement quantique de production d'oxygène singulet est déterminé par l'équation (26) :

$$\Phi_\Delta = \Phi_{\Delta 0} \cdot \frac{I}{I_0} \cdot \frac{DO_0}{DO} \quad \text{(équation 26)}$$

où Φ_Δ et $\Phi_{\Delta o}$, I et I_o, DO et DO_o sont les rendements quantiques de production d'oxygène singulet, les intensités de production d'oxygène singulet et les densités optiques de l'échantillon et de la référence respectivement. La référence utilisée est le TPP (Tétraphénylporphyrine).

Les AGuIX Gd sans Photofrin ne produisent pas d'$^1O_2$ après excitation à 273 nm. De 0,1 à 0,025 équivalent en Photofrin, les rendements quantiques d'$^1O_2$ augmentent progressivement de 25% à 32%.

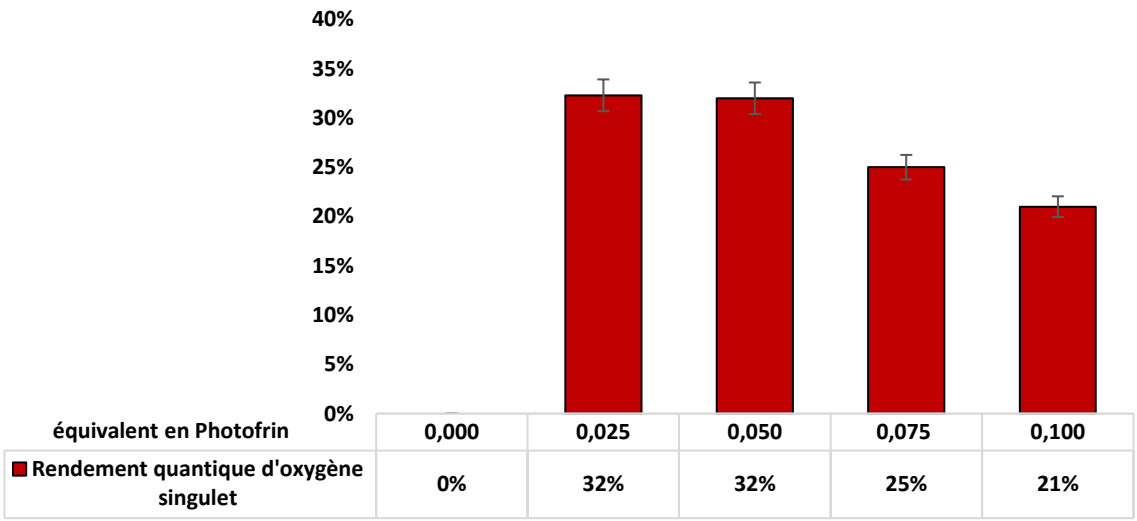

équivalent en Photofrin	0,000	0,025	0,050	0,075	0,100
Rendement quantique d'oxygène singulet	0%	32%	32%	25%	21%

Figure 164 : Rendement quantique d'$^1O_2$ des solutions de Photofrin adsorbé sur les AGuIX Gd dans le D_2O, excité à 273 nm.

L'augmentation de la quantité en Photofrin entraîne une diminution de la formation d'$^1O_2$ peut être dû à une agrégation, ou un quenching du fait de la grande proximité des PSs les uns par rapport aux autres.

V.5 Potentiel zêta

Le potentiel zêta représente la charge électrique d'une particule. Cette charge est le résultat de son acquisition des nuages d'ions suite à sa suspension dans une solution. En effet, lorsque les particules sont en mouvement dans un liquide, elles seront entourées par des ions organisés en une « double couche électrique » : une couche dense accrochée directement à la particule et une couche diffuse non liée à la particule.

Les deux couches dense et diffuse sont séparées par «plan de cisaillement ». La différence de potentiel entre le milieu de dispersion des NPs et le potentiel au plan de cisaillement est le potentiel Zêta (**Figure 165**).

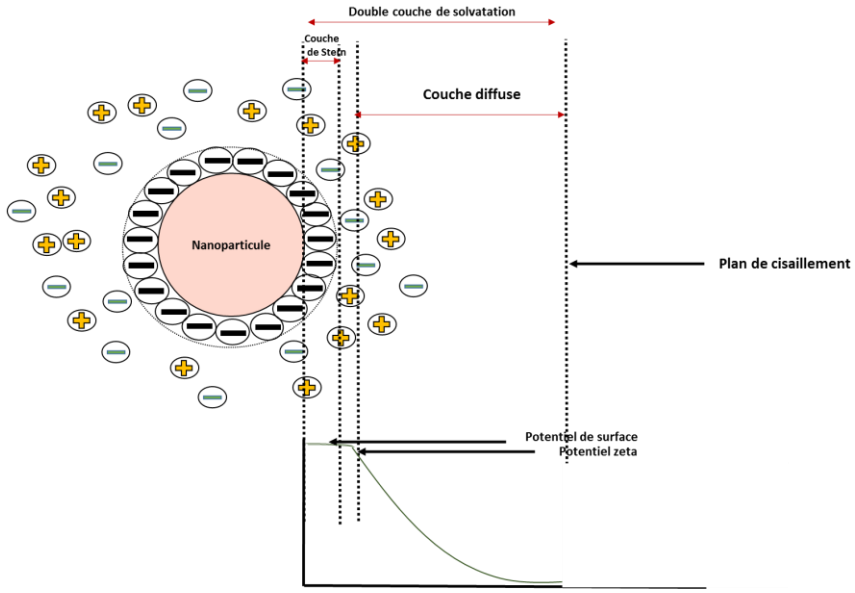

Figure 165 : Schématisation du principe du potentiel zêta.

Les NPs en suspension ont une tendance à s'agglomérer. Lorsque le potentiel zêta se rapproche de zéro, les forces inter-particulaires diminuent. Les forces attractives prédominent alors et les NPs s'agglomèrent. Le système devient instable. L'objectif est donc d'avoir le potentiel zêta le plus élevé (en valeur absolue) afin d'obtenir une suspension stable. Le potentiel zêta est affecté par plusieurs facteurs : pH, conductivité et la concentration ionique.

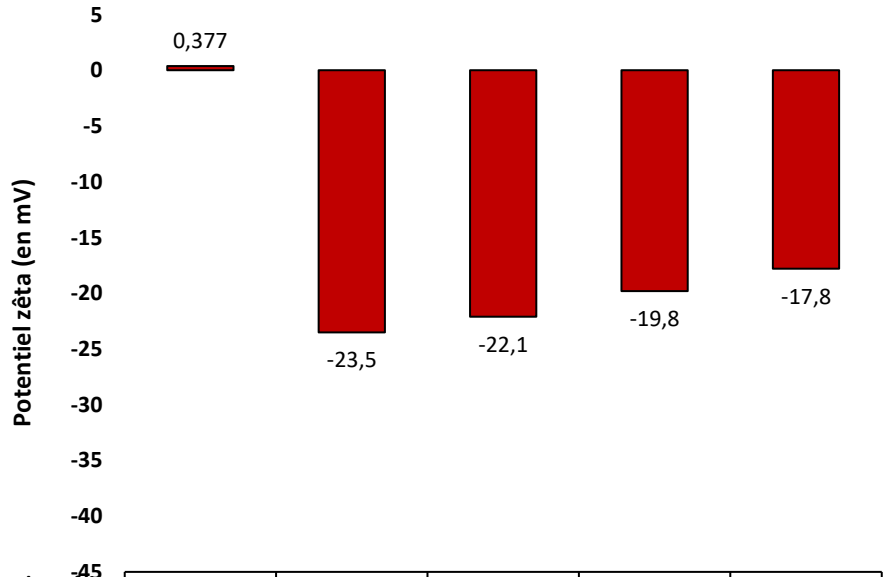

équivalent en Photofrin	0,000	0,025	0,050	0,075	0,100
Potentiel zêta (mV)	0,377	-23,5	-22,1	-19,8	-17,8

Figure 166 : Potentiel zêta des différentes NPs d'AGuIX Gd sur lesquelles le Photofrin a été adsorbé.

D'après la **Figure 166**, les quatre NPs sur lesquelles le Photofrin est adsorbé montrent une augmentation du potentiel zêta en valeur absolue par rapport à l'AGuIX seule qui est en faveur d'augmentation de stabilité.

VI. Etude des AGuIX Gd couplées à la cyanine 5,5

VI.1 Structure de la cyanine 5,5

La **figure 167** montre la structure développée de la cyanine 5,5-NHS.

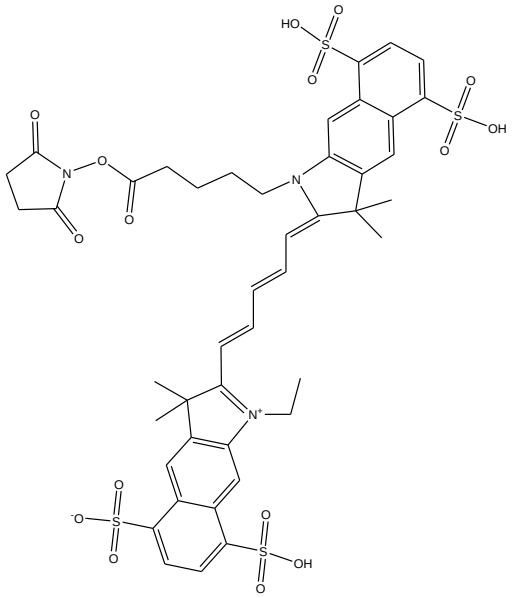

Figure 167 : Structure développée de la cyanine 5,5-NHS

VI.2 Spectre d'absorption

La **Figure 168** montre le spectre d'absorption de la cyanine 5,5 dans l'eau avec un maximum d'absorption à 670 nm.

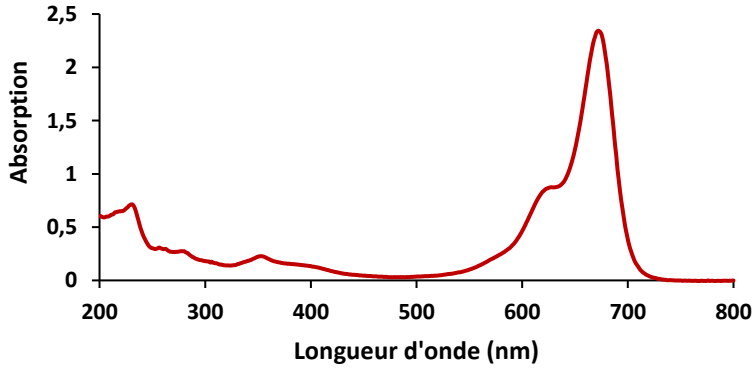

Figure 168 : Spectre d'absorption de la cyanine 5,5-NHS dans l'eau [10 µM]

VI.3 Caractérisation de l'AGuIX Gd@cyanine 5,5

VI.3.1 Spectre d'absorption

La **Figure 169** montre le spectre d'absorption des AGuIX Gd@cyanine 5,5 et celui de la cyanine 5,5. La bande maximale d'absorption en visible est à 670 nm pour la cyanine 5,5 et 678 nm pour la cyanine 5,5 couplée aux AGuIX montrant que le couplage n'influence pas le spectre d'absorption.

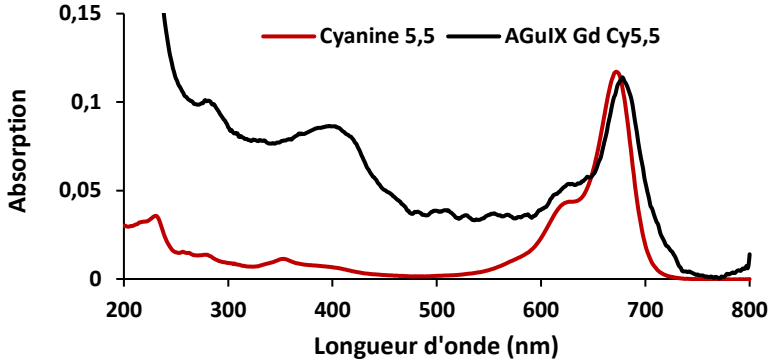

Figure 169 : Spectre d'absorption des AGuIX Gd@cyanine 5,5 et spectre d'absorption de la cyanine 5,5. [Gd] =10 mM et [cyanine 5,5] = 0,05µM.

VI.3.2 Transfert d'énergie entre le Gd dans les AGuIX Gd@cyanine 5,5 et le Photofrin non adsorbé

La **Figure 170** montre (a) I=f([Photofrin]) et τ=f([Photofrin]) (b)I_0/I= f([Photofrin]) et τ_0/τ =f([Photofrin]) dans l'eau, en présence de Photofrin. $\lambda_{excitation}$= 273 nm avec un délai de 50 µs.

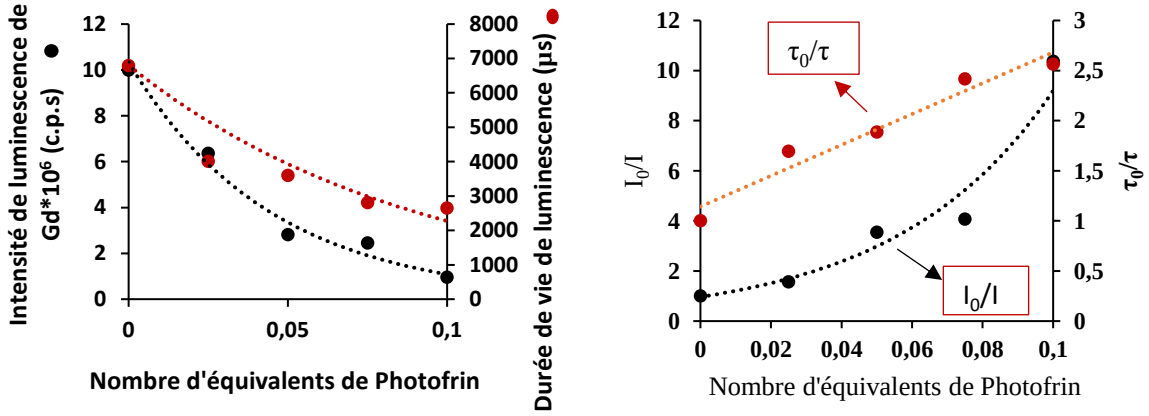

Figure 170 : (a) I=f([Photofrin]) et τ=f([Photofrin] . (b)I_0/I= f([Photofrin]) et τ_0/τ =f([Photofrin]) dans l'eau. $\lambda_{excitation}$= 273 nm, délai 50 µs.

D'après la **Figure 170**, le transfert d'énergie entre le AGuIX Gd@cyanine 5,5 et le Photofrin est un transfert FRET avec des inhibitions dynamique et statique.

VII. Adsorption du Photofrin sur les AGuIX Gd@cyanine 5,5

VII.1 Spectre d'absorption

Le protocole d'adsorption du Photofrin sur les AGuIX Gd@cyanine 5,5 est le même que celui sur des AGuIX non couplées à la cyanine 5,5. La **Figure 171** montre les spectres d'absorption des NPs d'AGuIX Gd@cyanine 5,5@Photofrin, de la cyanine 5,5 et du Photofrin.

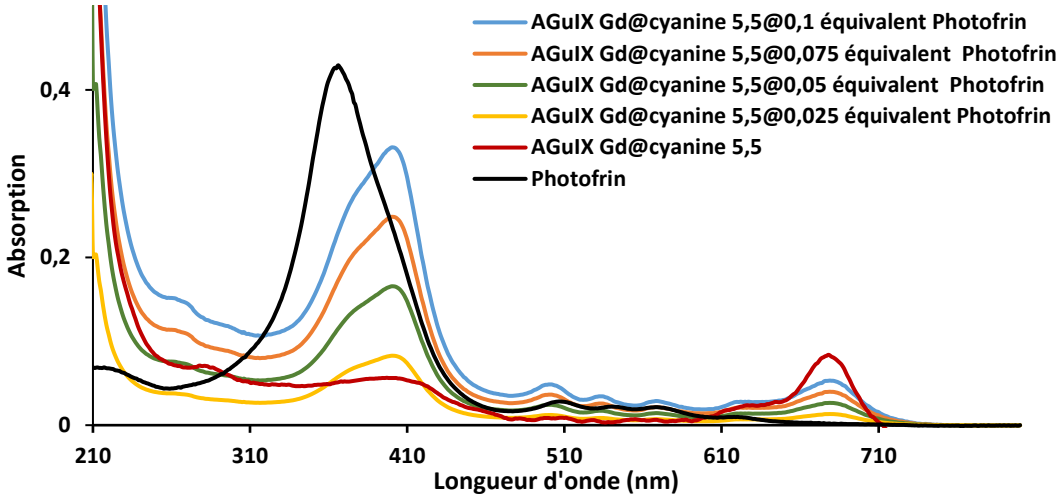

Figure 171 : Spectres d'absorption des AGuIX Gd@cyanine 5,5 et ceux du Photofrin adsorbé sur les AGuIX Gd@cyanine 5,5 dans l'eau. Différentes concentrations du Photofrin sont adsorbées, concentration d'AGuIX Gd, [Gd] = 10 mM.

Le décalage vers le rouge de 34 nm de la bande Soret du Photofrin confirme son adsorption sur les AGuIX. Le maximum d'absorption de cyanine 5,5 à 670 nm reste le même dans toutes les solutions.

VII.2 Transfert d'énergie entre AGuIX Gd@cyanine 5,5@photofrin après adsorption

La **Figure 172** montre (a) I=f([Photofrin]) et τ=f([Photofrin]) (b)I_0/I= f([Photofrin]) et τ_0/τ =f([Photofrin]) dans l'eau, $\lambda_{excitation}$= 273 nm avec un délai de 50 µs.

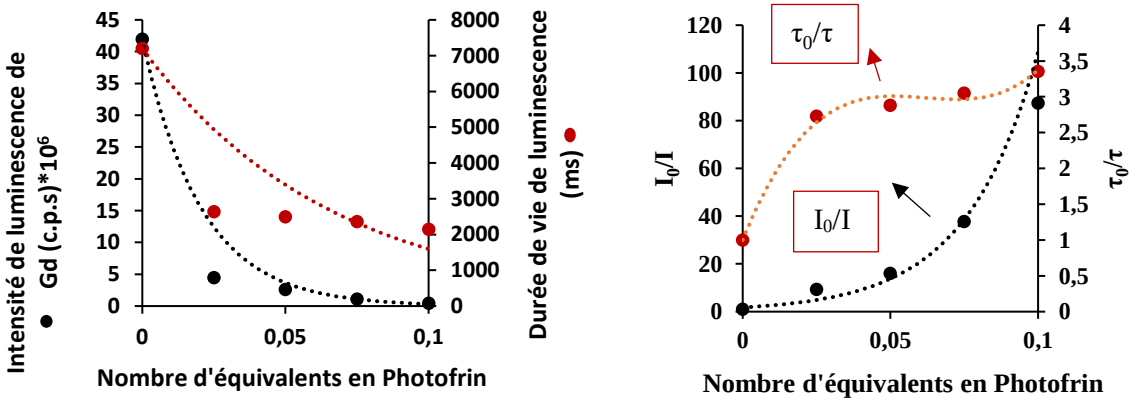

Figure 172 : (a) I=f([Photofrin]) et τ=f([Photofrin]), (b)I_0/I= f([Photofrin]) et τ_0/τ =f([Photofrin]) dans l'eau $\lambda_{excitation}$= 273 nm, délai de 50 µs.

Les graphes de la **figure 172** montrent un transfert d'énergie FRET avec des inhibitions dynamique et statique. Pour 0,025 équivalents en Photofrin une saturation de ce transfert est remarquée. Les durées de vie au-delà de cette concentration sont quasiment constantes.

VII.3 Formation d'oxygène singulet

Nous avons évalué la formation d'$^1O_2$ après excitation à 273 nm. Le rendement quantique d'$^1O_2$ des AGuIX Gd@cyanine 5,5@Photofrin est le double que celui sans cyanine 5,5. A ce jour nous n'avons pas d'explications, peut-être des impuretés dans la cyanine 5,5 commerciale. Une plus grande quantité de Photofrin adsorbé entraîne probablement une agrégation qui diminue la production de $^1O_2$ (79% pour 0,025 équivalent et 63 % pour 0,100 équivalent) (**Figure 173**).

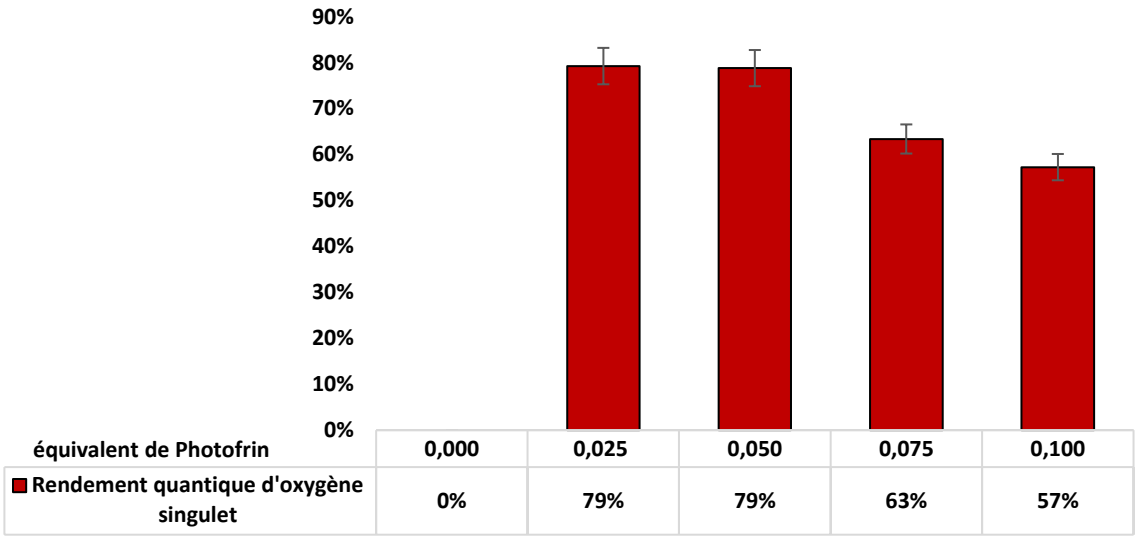

équivalent de Photofrin	0,000	0,025	0,050	0,075	0,100
Rendement quantique d'oxygène singulet	0%	79%	79%	63%	57%

Figure 173 : Rendement quantique d'$^1O_2$ des solutions de Photofrin adsorbé sur les AGuIX Gd@cyanine 5,5 dans le D_2O, excité à 273 nm.

VII.4 Potentiel zêta

Nous avons mesuré le potentiel zêta des AGuIX Gd@cyanine 5,5@Photofrin (**Figure 174**). En valeur absolue, les valeurs du potentiel zêta sont plus petites que ceux des AGuIX Gd@Photofrin, mais elles augmentent en augmentant la quantité du Photofrin adsorbé. Le couplage de la cyanine 5,5 diminue donc la stabilité des NPs. Cela peut être dû à la charge positive de la fonction N^+ de la cyanine 5,5.

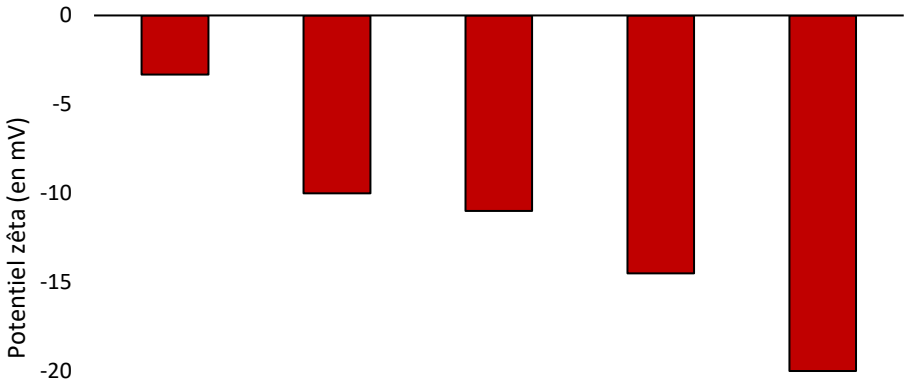

équivalent en Photofrin	0	0,025	0,05	0,075	0,1
Potentiel zêta	-3,33	-10	-11	-14,5	-20

Figure 174 : Potentiel zêta des différentes NPs d'AGuIX Gd@cyanine 5,5 avec le Photofrin adsorbé.

Les quatre solutions de NPs sur lesquelles le Photofrin est adsorbé présentent une augmentation du potentiel zêta en valeur absolue par rapport à l'AGuIX seule. Le potentiel zêta de l'AGuIX Gd@cyanine 5,5@0,1 Photofrin est plus élevé que les autres, le Photofrin augmenterait la répulsion grâce à la fonction COO- terminale. Ce résultat est confirmé avec celui des AGuIX Gd@photofrin sans cyanine 5,5.

VIII. Excitation par rayons X en solution

La **Figure 175** montre la production d'$^1O_2$ à l'aide du SOSG après excitation par rayons X (320 KV, 10 mA). Nous avons utilisé une sonde car il ne nous était pas possible, matériellement, de mesurer directement la luminescence de l'$^1O_2$ après irradiation X des AGuIX Gd.

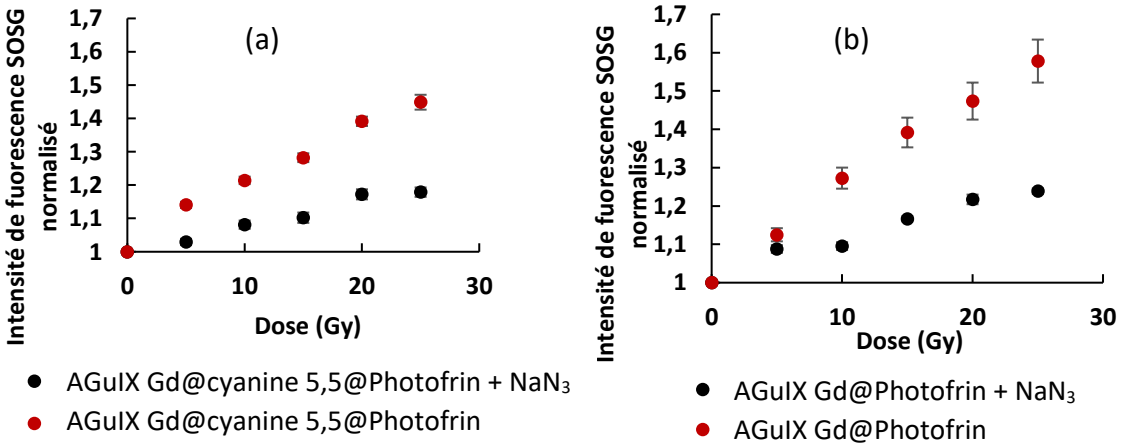

Figure 175 : Production d'$^1O_2$ après excitation (a) d'AGuIX Gd@cyanine 5,5@Photofrin (0,025 équivalent) (b) d'AGuIX Gd@Photofrin (0,025 équivalent)

Suivant le mécanisme de la **Figure 176**, l'augmentation de fluorescence du SOSG indique qu'il y a production d'$^1O_2$.

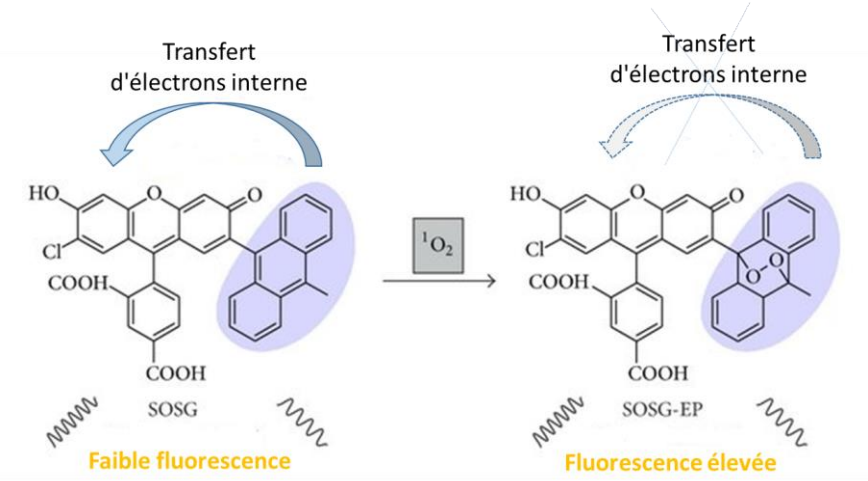

Figure 176: réaction entre le SOSG et $^1O_2$

L'ajout de NaN_3, quencheur d'$^1O_2$ re-instaure la fluorescence et confirme la production d'$^1O_2$.

Nous pouvons observer dans la **Figure 175** une augmentation de fluorescence du SOSG avec irradiation, montrant la formation d'$^1O_2$. Ceci est confirmé par l'ajout du NaN_3, qui entraîne une diminution de la fluorescence. Nous avons vérifié que les AGuIX Gd seules ne produisaient pas d'$^1O_2$. Il existe donc un transfert d'énergie entre les AGuIX Gd et le Photofrin sous rayon X en solution. La présence de la cyanine 5,5 n'influence pas ce phénomène.

IX. Taille des NPs par TDA-MS

La taille des NPs a été mesurée par TDA- ICP-MS (Analyse par Dispersion de Taylor couplé à un ICP-MS), (Collaboration avec l'Institut Lumière Matière - UMR5306 - UCBL – CNRS, Agnès HAGEGE, François LUX et Olivier TILLEMENT).

Nous avons mesuré les tailles des diamètres des AGuIX Gd@Photofrin et les résultats sont reportés dans le **Tableau 29**.

Tableau 29 : Diamètre des AGuIX Gd@Photofrin calculés par TDA

NPs	Diamètre en nm
AGuIX Gd	Population 1 : 1,8 nm (100%)
l'AGuIX Gd@0,1 Photofrin	Population 1 : 1,3 nm (74%) Population 2 : 3,7 nm (26%)
l'AGuIX Gd@0,075 Photofrin	Population 1 : 1,6 nm (63%) Population 2 : 4,0 nm (37%)
l'AGuIX Gd@0,05 Photofrin	Population 1 : 1,4 nm (80%) Population 2 : 4,5 nm (20%)
l'AGuIX Gd@0,025 Photofrin	Population 1 : 1,4 nm (52%) Population 2 : 3,5 nm (48%)

Pour toutes les NPs dont le photofrin a été adsorbé, deux populations sont observées : une population de petite taille (1,3-1,6 nm) et une population de plus grande taille (3,5-4,5 nm). Nous pouvons supposer qu'une partie des NPs ne contient pas de Photofrin, et une partie

contient des NPs adsorbées, ce qui entraîne une augmentation de la taille. La quantité de Photofrin ajouté ne semble pas avoir d'influence sur la taille des NPs.

X. Conclusion

En conclusion, un transfert FRET a été observé entre tous les couples étudiés Gd/Tb, AGuIX Tb/Gd et le Photofrin. Une simple adsorption du Photofrin sur les AGuIX montre un transfert d'énergie entre ces deux espèces (Gadolinium et Photofrin) et environ 40% en rendement quantique de production d'$^1O_2$.

La cyanine 5,5 qui est un fluorophore qui permet de visualiser le cancer, a été couplé sur les AGuIX et n'affecte pas le transfert d'énergie.

Les caractéristiques du transfert d'énergie entre les différents couples sont données dans le **Tableau 30**.

Tableau 30 : Caractéristiques du transfert d'énergie entre les différents couples

Couple	Recouvrement ($M^{-1}.nm^4.cm^{-1}$)	R_0 (nm)	Type of transfert	Efficacité FRET	Constante de quenching k_q ($M^{-1}.s^{-1}$)
AGuIX Gd/Photofrin	$5{,}425214*10^{14}$	3,06	FRET	43%	$0{,}29 * 10^8$
$GdCl_3$/Photofrin	$3{,}433854*10^{14}$	2,80	FRET	39%	$1{,}81*10^8$
$TbCl_3$/Photofrin	$8{,}9*10^{14}$	3,33	FRET	40%	$3{,}63 * 10^8$
AGuIX Tb/Photofrin	$1{,}12*10^{15}$	3,46	FRET	42%	$0{,}43 * 10^8$

Références

[1] C. S. Derkay and P. Campisi, "29 - Recurrent Respiratory Papillomatosis," in *Cummings Pediatric Otolaryngology (Second Edition)*, M. M. Lesperance, Ed., ed Philadelphia: Elsevier, 2021, pp. 421-440.

[2] J. Savary, "La photothérapie dynamique en dermatologie," *Les Nouvelles dermatologiques,* vol. 26, 2007.

[3] J. Étienne, P. Ducrotté, J.-M. Canard, and J.-C. Létard, "La photothérapie dynamique en cancérologie digestive," *Hegel,* vol. 1, pp. 20-25, 2011.

Chapitre IV:

Terbium-based AGuIX-design nanoparticle to mediate X-ray-induced photodynamic therapy

Terbium-based AGuIX-design nanoparticle to mediate X-ray-induced photodynamic therapy

Joël Daouk[1], Mathilde lltis[1], Batoul Dhaini[2], Denise Béchet[1], Philippe Arnoux[2], Paul Rocchi[3], Alain Delconte[1], Benoît Habermeyer[4], François Lux[3], Céline Frochot[2], Olivier Tillement[3], Muriel Barberi-Heyob[1]* and Hervé Schohn[1]

[1] Université de Lorraine, French National Scientific Research Center (CNRS), Research Center for Automatic Control (CRAN), UMR 7039, Department of Biology, Signals and Systems in Cancer and Neuroscience, F-54000 Nancy, France
[2] Université de Lorraine, French National Scientific Research Center (CNRS), UMR- 7274, Reactions and Chemical Engineering Laboratory (LRGP), F-54000 Nancy, France
[3] Université de Lyon, French National Scientific Research Center (CNRS), Light Matter Institute, UMR-5306, F-69000 Lyon, France
[4] Porphychem SAS, F21000- Dijon, France

Article publié dans Pharmaceuticals le 22 Avril 2021 (Impact factor : 5,6)

Comme nous l'avons montré dans le chapitre III, le recouvrement entre le spectre d'émission du Gadolinium ou Terbium et le spectre d'absorption du Photofrin permet un transfert d'éenrgie entre les deux espèces sous illumination ou par excitation par rayons X. Afin d'améliorer le transfert d'énergie, il serait intéressant de coupler de manière covalente le Photofrin aux AGuIX@Gd ou AGuIX@Tb. Cependant, la structure du Photofrin ne le permet pas. Aussi, l'étude décrite dans ce chapitre utilise la tétraphénylporphyrine monocarboxylique (P1) comme photosensibilisateur, dont la fonction carboxylique permet le couplage covalent sur les AGuIX. Dans ce chapitre les AGuIX@Gd-P1 et AGuIX@Tb-P1 sont synthétisées, caractérisées et leur activité PDT et PDTX sont évaluées.

L'effet PDT /X-PDT des nanoparticules a été étudié en utilisant des cellules de glioblastome humain U-251 MG. Nous avons montré qu'il existait un transfert d'énergie entre le Gd ou Tb et la P1 après excitation par rayons X. AGuIX@Gd-P1 et AGuIX@Tb-P1 ont une cytotoxicité dans le noir équivalentes et s'accumulent de façon similaire dans les cellules. L'exposition des cellules prétraitées aux rayons X est liée à la production d'espèces réactives de l'oxygène ($^1O_2$). En utilisant des tests clonogéniques, l'établissement des courbes de survie a permis de discriminer l'impact de la radiothérapie de l'effet photodynamique induit par les rayons X. Nous avons montré que l'arrêt de la croissance cellulaire était accru (augmentation de 35 %) lorsque les cellules étaient traitées avec AGuIX@Tb-P1 par rapport aux nanoparticules AGuIX@Gd-P1.

Abstract: X-ray-induced photodynamic therapy is based on the energy transfer from a nanoscintillator to a photosensitizer molecule, whose activation leads to singlet oxygen and radical species generation, triggering cancer cells to cell death. Herein, we synthesized ultra-small nanoparticle chelated with Terbium as a nanoscintillator and porphyrin as a photosensitizer (AGuIX@Tb-P1), the synthesis was based on the AGuIX@ plateform design. AGuIX@Tb-P1 was characterized for its photo-physical and physico-chemical properties. The effect of the nanoparticles was studied using human glioblastoma U-251 MG cells and was compared to treatment with AGuIX@ nanoparticles doped with Gadolinium and porphyrin (AguIX@Gd-P1). We demonstrated that the AGuIX@Tb-P1 design was consistent with X-ray photon energy transfer from Terbium to por-phyrin. Both nanoparticles had similar dark cytotoxicity and they were absorbed in a similar rate within the cells. Pre-treated cells exposure to X-rays was related to radical species production. Using clonogenic assays, establishment of survival curves allowed discrimination of the impact of radiation treatment from X-ray-induced photodynamic effect. We showed that cell growth arrest was increased (35%-increase) when cells were treated with AGuIX@Tb-P1 compared to the nanoparticle doped with Gadolinium.

Keywords: Glioblastoma multiforme, AGuIX@®, terbium, gadolinium, photodynamic therapy, X-ray-induced photodynamic therapy, singlet oxygen.

I. Introduction

Glioblastoma multiforme (GBM) is one of the main incurable brain tumours, mainly due to the presence of infiltrated cells within the parenchyma, responsible of GBM recurrence into the surrounding brain tissue [1]. The conventional treatment of GBM tumours consists of surgical resection followed by X-ray radiation and adjuvant temozolomide administration which improves modestly patient survival [2]. Brain exposure to X-ray involves the generation of radical species, which are responsible for DNA alteration, lipid peroxidation, protein oxidation and cell redox statue changes, triggering cells to cell death [3]. However, these effects are not limited to malignant cells, but alter also surrounding cells.

Alternative therapeutic strategies have been developed, notably photodynamic therapy (PDT). PDT appears as an innovative technology being investigated to fulfil the need for a targeted cancer treatment that may reduce recurrence and extend survival with minimal side effects [3,4]. It aims at selectively killing neoplastic cells by the combined action of a photosensitizer and visible light in the presence of oxygen, whose combined action mainly results in the formation of reactive species, especially singlet oxygen which is the main mediator of PDT reaction. To improve PDT efficiency, photosensitizer can be bound to ligands such as monoclonal antibodies or peptide moieties and be delivered by carrier systems such as nanoparticle [5,6]. Moreover, the nanoparticles can be modified by functional groups for additional biochemical properties. In addition, nanoparticles accumulation in the solid tumour site is improved by the enhanced permeability and retention effect (EPR) [7,8]. A number of clinical studies, including phase III randomized prospective clinical trials, have been reported for PDT, using alternative methods such as interstitial PDT and intraoperative PDT [9-20]. Interstitial PDT offers a localised treatment approach in which improvements in local control of GBM may result in significant enhanced survival [11,12,20]. Several photosensitizers have been used, including porfimer sodium (Photofrin®), 5-aminolevulinic acid (5-5-ALA, Gliolan®), m-tetrahydroxyphenylchlorin (mTHPC,

temoporfin, Foscan®) and benzoporphyrin derivative monoacids ring A (BPD-MA, verteporfin, Visudine®).

Compared to radiotherapy, the light irradiation used in PDT is less energetic and it cannot penetrate deeply enough into the tumour, as most tissue chromophores absorb visible light commonly used in clinical practice [4,6]. The penetration depth of 630 nm light in brain-adjacent-to-tumour is estimated at 2.5 mm. A breakthrough strategy to treat GBM *via* nanomedicine and X-ray has been suggested by combining the principles of radiotherapy and PDT, both clinically proven modalities, while maintaining their main benefits and decreasing their drawbacks. The principle of the so-named X-ray-induced PDT (X-PDT) is based on the conversion of X-ray photons into visible photons, known as X-ray excited optical luminescence, from the nanoscintillator embedded in the nanoparticle and linked to the photosensitizer, which, in turn, produces singlet oxygen and other oxygen reactive species [21,22]. X-PDT proof-of-concept with nanoparticles was first introduced by Cheng and Wang, who described simultaneous radiation and X-ray-induced photodynamic effects [23]. The strategy requires nanoparticles, exhibiting appropriated physical properties to establish energy transduction from the nanoscintillator to the photosensitizer, a high scintillation quantum yield and an optimal energy transfer from the scintillator onto the photosensitizer [24,25]. It must be pointed that only PDT can generate singlet oxygen which is highly cytotoxic to tumour tissue and to treat deeply lesions without invasive approach such as interstitial PDT. It is possible to use X-ray as an excitation source instead of light. Thus, the light penetration problem through the tumour tissue is overcome, and the activation of the photosensitizer within tumour tissue is performed by classical radiotherapy using X-ray. In addition, the synergistic effects between conventional radiotherapy and PDT should allow the use of conventional X-ray doses. In metal-hybrid system, the metal-based nanoparticle consists of a nanoscintillator coated with polyethylene glycol or a polysiloxane layers to ensure biocompatibility which allows covalently coupling of the photosensitizer [24,25]. Members of the lanthanide family have been used in nanoparticle synthesis, such as mesoporous lanthanum fluoride doped with Cerium or Terbium (Tb) and grafted with porphyrin (P1), Tb_2O_3 coated with a polysiloxane layer or silica-doped with lanthamide [26-31].

Among them, ultra-small Gadolinium (Gd) based nanoparticles, namely AGuIX®, were developed [32]. The nanoparticle design was first proposed for a non-toxic resonance magnetic agent and its imaging properties [33]. Moreover, *in vitro* and *in vivo* pre-clinic experiments demonstrated that AGuIX doped with Gd act as a theranostic agent, enhancing radiosensitization of tumour cells in diverse experimental conditions, notably, at different photon radiation energies (with a range from kiloelectron volts to million electron volts) and with different types of radiation [34]. The radiosensitizing effects are associated to diverse processes: Gd mediated generation of electrophotons and Auger photons amplifying the local production of reactive oxygen derived species, as demonstrated for Gold embedded nanoparticles [35,36]; or an impairment of DNA breaks reparation, as a consequence of irradiation, and reactive species production triggering cells to cell death [34,37]. In X-PDT, the main goal of the treatment consists on the transfer energy from irradiated nanoscintillator to the photosensitizer, limiting the delivery of high radiation energies and deposits to kill cancer cells without any alteration to adjoining normal cells. Recently, we demonstrated that AGuIX@ doped with Gd and P1 (5-(4-carboxyphenyl succinimide ester)-10,15,20-triphenylporphyrin) can be used to target Neuropilin-1, a transmembrane receptor localised in

endothelial cells within mouse grafted human GBM tumours [38]. The synthesized AGuIX@Gd-P1 behaved similar properties as the original AGuIX@Gd.

Therefore, in order to use the AGuIX plateform for X-PDT, we suggested the replacement of Gd in the Gd-based AGuIX nanoparticle by Tb as a nanoscintillator and the grafting of P1. In these conditions, an external light source will not be required to simultaneously support a photodynamic effect. The nanoparticles (referred herein as AGuIX@Tb and AGuIX@Tb-P1) were characterised for their photophysical and chemical properties. We evaluated the effect of X-PDT on human GBM U-251 MG cell survival after cell exposure to nanoparticles. In parallel, we tested AGuIX@ doped with Gd and P1 (referred herein as AGuIX@Gd and AGuIX@Gd-P1), which has been characterised previously [38]. We highlighted that chelated Tb-P1 nanoparticles can react linearly to X-ray energy and flow, and were able to activate P1 to produce singlet oxygen. *In vitro*, using human U-251 MG glioblastoma cells, experiments confirmed the interest of these AGuIX design, notably at a 3.0 Gy/min dose rate. Moreover, cell exposure to AGuIX@Tb-P1 improved the effect on cell growth arrest when it was compared to similar treatment with AGuIX@Gd or AGuIX@Gd-P1.

II. Results

II.1 Characteristics of the AGuIX@Tb-P1

We already demonstrated that the grafting of P1 on AGuIX doped with Gd induced a hydrodynamic diameter at about 11.1 nm, twice as large as the original AGuIX@Gd nanoparticle, with an estimated diameter at 4.9 nm on average [38]. Replacing Gd of the original AGuIX-designed nanoparticle by Tb did not induce any size modification. The hydrodynamic diameter of AGuIX@Tb and AGuIX@Tb-P1 were estimated respectively at 3.8 ± 1.0 nm and 11 ± 0.8 nm. Moreover, the zeta potential raised from -11.8 to -45.6 mV, when measurements were achieved with AGuIX@Tb and AGuIX@Tb-P1 respectively, supporting a high stability of the latter conjugate (Figure S1). AGuIX@Tb and AGuIX@Gd emission spectra after UV light excitation are presented in Figure 1 as well as P1 absorption spectrum, in water. An overlay between P1 absorption spectrum and Tb emission (**Figure 177a and b**) could be observed. In contrast, Gd emission did not overlay P1 emission spectrum. Calculation of the spectral overlap between Tb emission and P1 absorption was estimated at J = $1.15.10^{14}$ $M^{-1}.nm^4.cm^{-1}$. The corresponding Förster radius was found to be 2.5 nm (from 1 up to 10 nm). Moreover, Tb luminescence lifetime was 390 µs, long enough to allow energy transfer to P1. Thus, Tb luminescence in presence of P1 showed an exponential decay of its fluorescence intensity (**Figure 177c**), and a linear decrease of its fluorescence lifetime at PS concentration higher than 0.5 µM (**Figure 177d**). We recorded the luminescence exponential decay of AGuIX@Tb and AGuIX@Tb-P1 (Figure S2). AGuIX@Tb fluorescence lifetime was estimated at 1 ms whereas AGuIX@Tb-P1 fluorescence lifetime was 1 µs. This decrease of fluorescence lifetime of Tb in presence of P1 supported the concept of energy transfer between Tb and P1. Moreover, we measured the luminescence of both nanoparticles after excitation at 351 nm with a 50 µs delay between excitation and photon detection at 545 nm. As shown in figure S3, P1 luminescence was obtained between 630 and 690 nm, corresponding to the energy transfer between Tb and P1, concomitantly to the decrease of Tb emission. Collectively, the results obtained allowed us to conclude that Tb energy transfer to P1 is a FRET / non radiative transfer type characterised by a quenching constant, Kq = $0.045.10^9$ $M^{-1}. s^{-1}$.

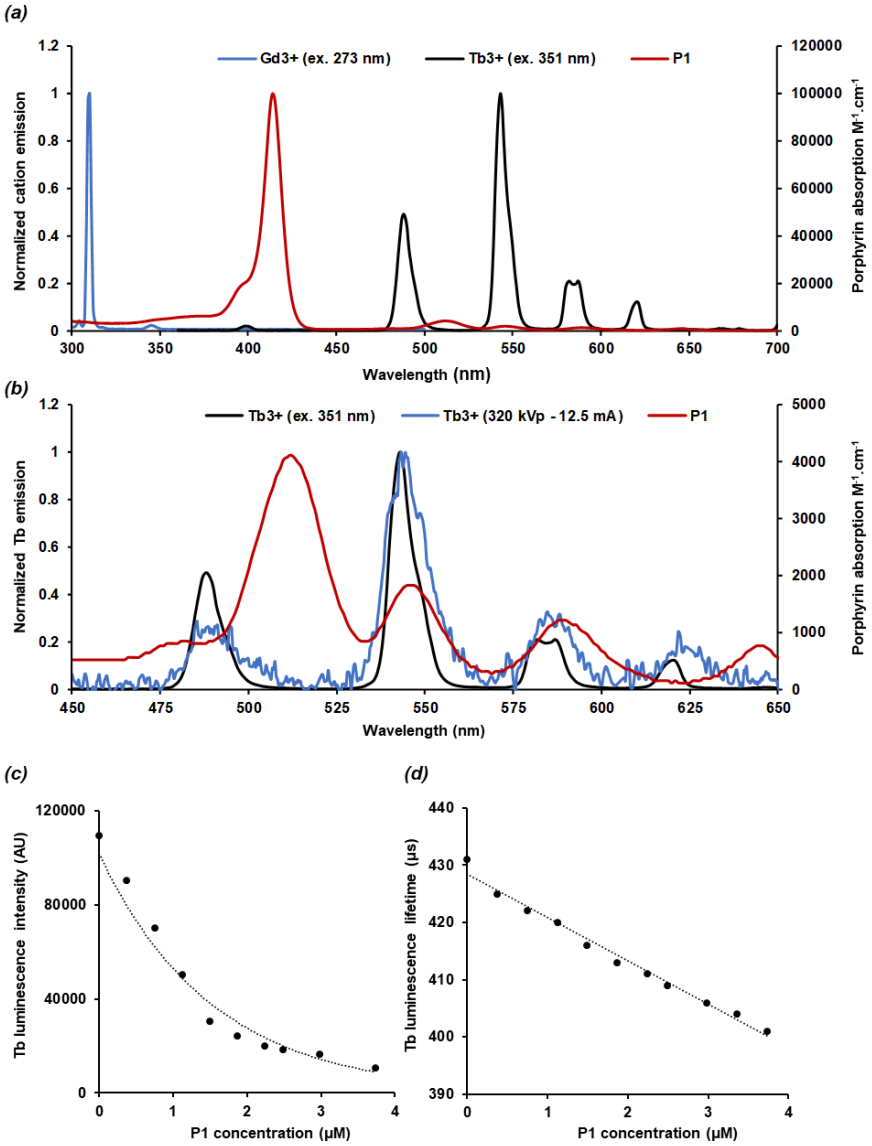

Figure 177 : Photophysical properties of AGuIX@Tb-P1 nanoparticle. (a), P1 absorption spectrum, AGuIX@Gd-P1 and AGuIX@Tb-P1 emission spectra (after 273 and 351 nm excitation, respectively, in water. Data presented in (b) is a zoomed view of the P1 Q bands, between 450 and 650 nm, Tb^{3+} emission overlap after UV (351 nm) or Tb^{3+} X-ray exposition; the tube parameters were set at 320 kVp, 12.5 mA and 3 Gy.min^{-1}). Tb^{3+} luminescence intensity (c) and lifetime (d) was estimated as a function of increasing concentration of P1. An exponential decay of luminescence intensity and a linear decreased of the fluorescence lifetime was respectively obtained.

II.2 Nanoscintillator response to X-ray excitation

AGuIX@Tb emission spectrum after X-ray excitation presented a similar profile compared with UV/visible light excitation (**Figure 178b**). To validate the pipeline acquisition setup under X-ray sessions, X-ray spectroscopy experiments were performed at different tube currents and voltages. Spectra intensities were positively related to tube current from 0.5 to 12.5 mA at 320 kVp (**Figure 178a**) and to tube voltage from 25 to 320 kVp at 12.5 mA (Figure 2b). For each condition, the four characteristic emission peaks of Tb cations (Tb^{3+}) were detected at 485, 545, 590 and 620 nm, respectively. For these different Tb cation emission peaks, the correlation coefficients between tube

currents and peak intensities were 0.97, 0.99, 0.99 and 0.84, respectively (**Figure 178c**). The maximum peak values were associated linearly with the tube voltage values (Figure 2d). Correlation coefficient values were found to be 0.96, 0.99, 0.99 and 0.96 for the four Tb peaks 485, 545, 590 and 620 nm, respectively.

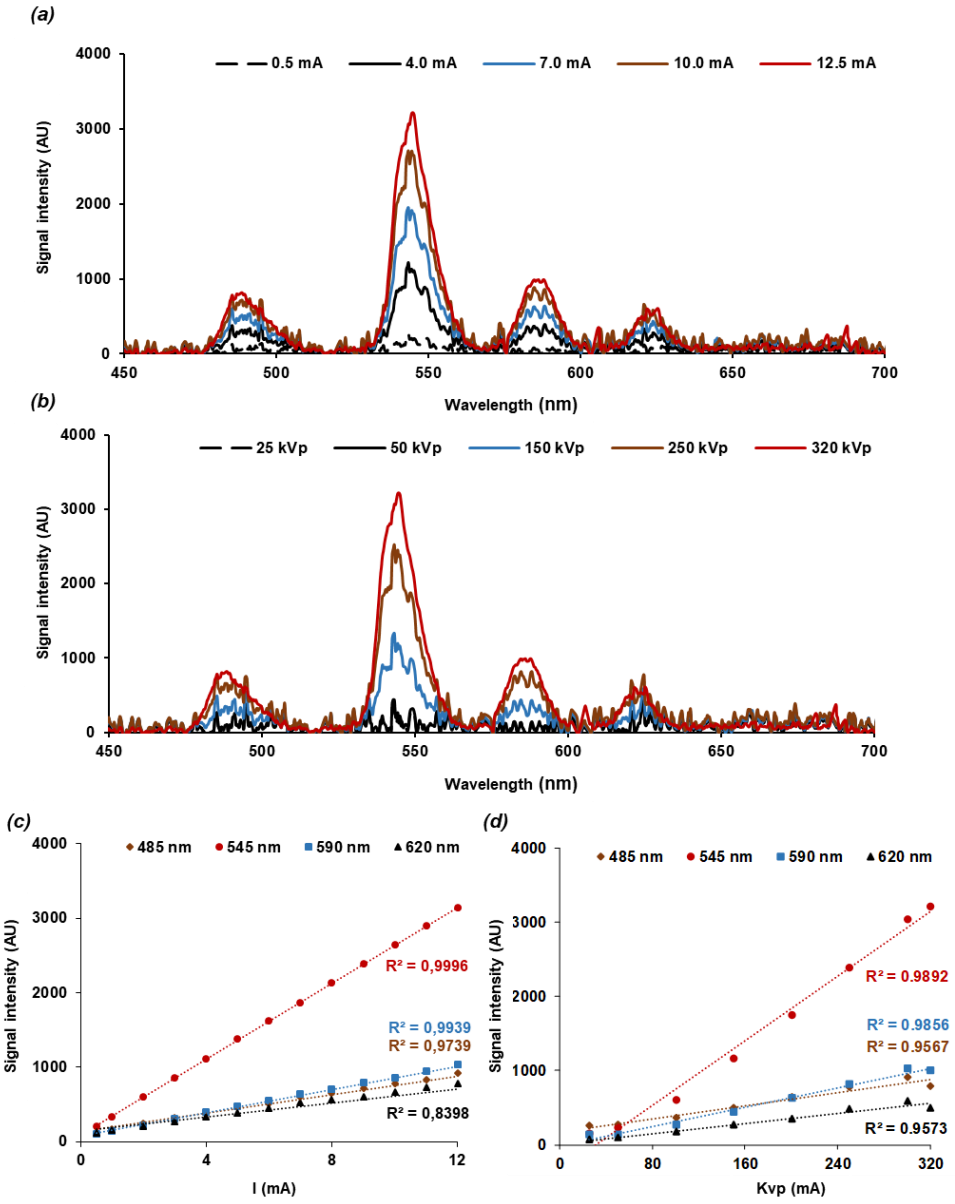

(a) **(b)**

Figure 178 : Tb scintillation response as a function of X ray parameters. (a). Tb^{3+} cation solution was irradiated by increasing tube intensity (mA) with a constant voltage set at 320 kVp. Tb^{3+} emission spectra were monitored in the range of 450 to 700 nm. The signal obtained (in arbitrary unit, AU) were plotted for each P1 Q band as a function of tube intensity (c). Similarly, the cation solution was irradiated by increasing tube voltages (KVp) with a tube current set at 12.5 mA (photons energy) (b). Luminescence signals were plotted for each P1 Q band as a function of tube voltage (d). In both cases, Tb luminescence was enhanced for each P1 Q band whatever tube intensity or voltage applied; the main increase variations were obtained for 545 nm P1 Q band.

II.3 Energy transfer and singlet oxygen production

We highlighted reactive species and singlet oxygen production using fluorescent probes, respectively, SOSG (**Figure 179a**) and APF (**Figure 179b**), during X-ray exposure. X-ray parameters were set to

320 kVp and 12.5 mA as it provided the highest Tb scintillation. Both APF and SOSG signals increased continuously during X-ray exposure. Addition of sodium azide (NaN_3), a singlet oxygen quencher, confirmed that the type II-PDT reaction (singlet oxygen generation) was mainly involved in X-PDT as SOSG and APF fluorescence signals were mostly inhibited.

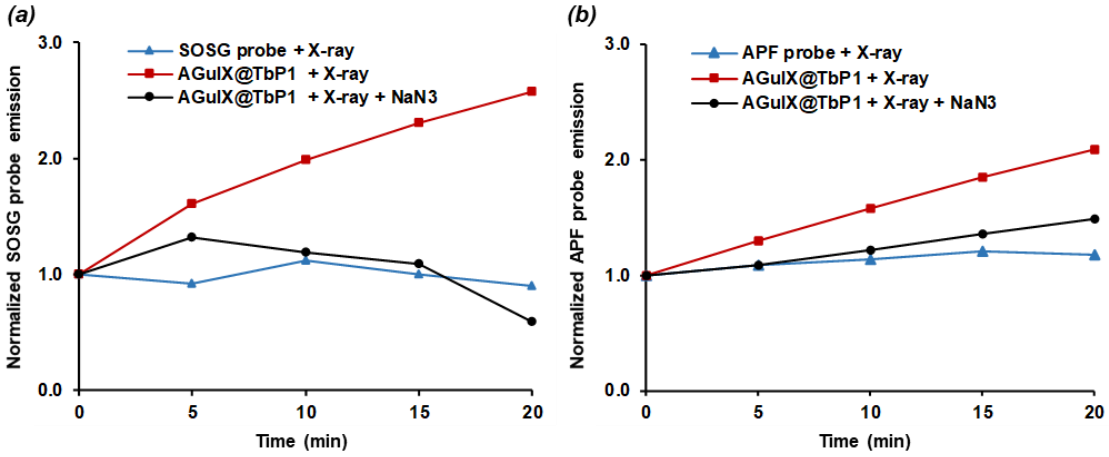

Figure 179 : Kinetics of reactive species and singlet oxygen production under X-ray irradiation in water. Experiments were performed with 400 µM P1 equivalent AGuIX@Tb-P1 solution and probe fluorescence signals were revealed every 5-min during continuous X-ray irradiation. ***(a)****, 10 µM SOSG probe was used to react specifically to singlet oxygen;* ***(b)****, 5 µM APF probe was used to assess reactive species production. Each fluorescence probe was irradiated alone. The production of singlet oxygen was inhibited by adding sodium azide (NaN_3) in the reaction mixture. Irradiation was performed with tube parameters set at 320 kVp, 12.5 mA and 3 Gy/min.*

II.4 Cytotoxicity of AGuIX@Tb-P1 on glioblastoma cell growth

We assessed whether treatment of P1 alone or AGuIX@Tb led to U-251 MG cytotoxicity, using the MTT procedure. Since P1 is hydrophobic, we choose ZnPy3P1 which is soluble in culture medium. IC_{50} was estimated at 34.8 ± 9.9 µM after 24h and 10.4 ± 3.4 µM after 72h-treatment duration. In addition, IC_{50} was similar when GBM cells were exposed to AGuIX@Tb with IC_{50} estimated at 1.73 ± 0.3 and 1.56 ± 01 mM, after 24 and 72 h exposition, respectively. We finally tested the effect t of increasing concentration (1.0 to 20.0 µM; – concentrations are expressed as P1 equivalent throughout the paper) of AGuIX@Tb-P1 and AGuIX@Gd-P1 (Figure S4). No cytotoxicity was observed whatever the dose tested and treatment duration.

II.5 NPs cell uptake

Cell uptake kinetics were established after cell exposure to 2.5 and 5 µM AGuIX@Tb-P1 over 48 h (Figure 4a). Cell uptake was quantified based on the fluorescence emission of P1. NPs accumulated within the cells, reaching a maximum at 48 h. Since the AGuIX doped with Gd or Tb are synthesized with a similar scheme and behave similar hydrodynamic diameter, we compared NP uptake after cell exposure to 1.0 or 2.5 µM AGuIX@Tb-P1 or AGuIX@Gd-P1 for 24 h. There was no significant difference suggesting that the replacement of Gd by Tb did not affect NP absorption within the cells, (**Figure 180b**). Moreover, when cells were treated with 1 µM AGuIX@-complexes for 24 h (**Figure 180b**), uptake was low as compared with cell absorption performed with 2.5 or 5.0 µM nanoparticles for the same culture delay (**Figure 180a**). Since NP absorption could lead to the increase of oxidative stress within the cells, we assessed whether nanoparticle uptake was related to reactive species generation. A slight but significant increase was observed after cell exposure to 2.5 µM nanoparticle.

However, cell exposure to 1 µM AGuIX@Gd-P1 (**Figure 180c**) was enough to modify redox statue within the cells. At least, we evaluated whether AGuIX@Tb-P1 uptake is associated to stress-mediated cell death by quantifying propidium iodide positive cells, after cell exposure to 2.5 or 5 µM over 48 h. No change was observed, supporting that the accumulation of AGuIX@Tb-P1was not related to cell death (**Figure 180d**).

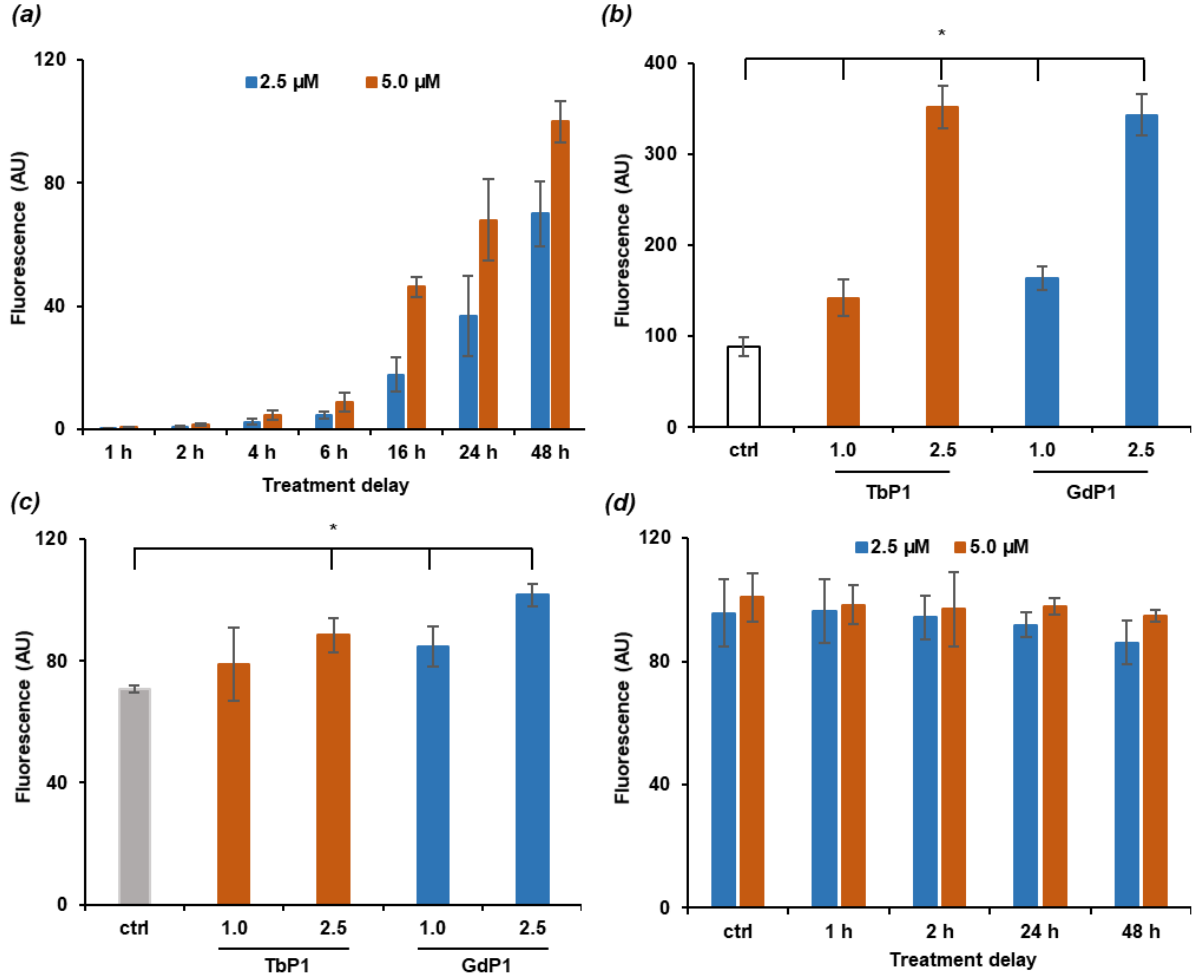

Figure 180 : AGuIX@ complexes uptake by U-251 MG cells. ***(a)****, U-251 MG cell uptake kinetics with AGuIX@Tb-P1 were performed over 48 h.* ***(b)****, cell uptake between AGuIX@Tb-P1 (TbP1) and AGuIX@Gd-P1 (GdP1) was compared for 24 h, for P1 equivalent concentration of 1.0 and 2.5 µM.* ***(c)****, reactive species content was quantified using DCF2-DA fluorescent probe after cell exposure to 1 or 2.5 µM nanoparticles for 24 h.* ***(d)****, AGuIX@Tb-P1 uptake-mediated cell death was estimated with propidium iodure dye after cell exposure to 2.5 and 5.0 µM AGuIX@Tb-P1 for 24 h. Results are means ± S.D. of triplicate determinations from three independent experiments. *, P<0.05, relative to control cells (Kruskal-Wallis test and post-hoc by the Dunn's test). Abbreviation: ctrl, untreated cells; AU, Arbitrary unit.*

II.6 Photodynamic effect on U-251 MG cell survival

We assessed whether cell exposure to photodynamic treatment led to cell growth inhibition after 24 h–exposure duration and could limit cell clone formation in anchorage-dependent clonogenic assays. U-251 MG cells were pre-treated with 1.0 and 2.5 µM AGuIX@Tb-P1 and exposed to a red light in a fluence range of 2.5 to 10.0 J.cm^{-2}. At the dose of 1 µM, cell growth inhibition was obtained with a fluence applied at 10.0 J.cm^{-2} (**Figure 181a**). We observed that clone formation was inhibited when the cells were pre-treated with 1 µM AGuIX@Tb-P1 and exposed to a fluence at 2.5 (50%-inhibition) or 5.0 J.cm^{-2} (90%-inhibition) (**Figure 181b**). Similarly, cell growth inhibition was observed in pre-treated U-251 MG cells with 2.5 µM nanoparticle and a fluence at 2.5 J.cm^{-2} (20%-inhibition). Inhibition increased with fluence up to 10.0 J.cm^{-2} (80%- inhibition) (**Figure 180a**). Since PDT is

associated with reactive species production, we quantified reactive species content immediately after cell exposure to red light (**Figure 181c**), when cells were pre-treated with 2.5 µM AGuIX@Tb-P1 and exposed to a fluence at 2.5 J.cm^{-2}, which corresponds to an immediate cell growth inhibition estimated at 20%. We found that reactive species content was enhanced 2 times over 30 min post light exposition supporting the concept that cell survival depends mainly on oxidative stress-mediated by light treatment. Finally, at nanoparticle concentrations higher than 2.5 µM (data not shown), and a fluence higher than 2.5 J.cm^{-2} (**Figure 181b**), the applied treatment killed all the cells.

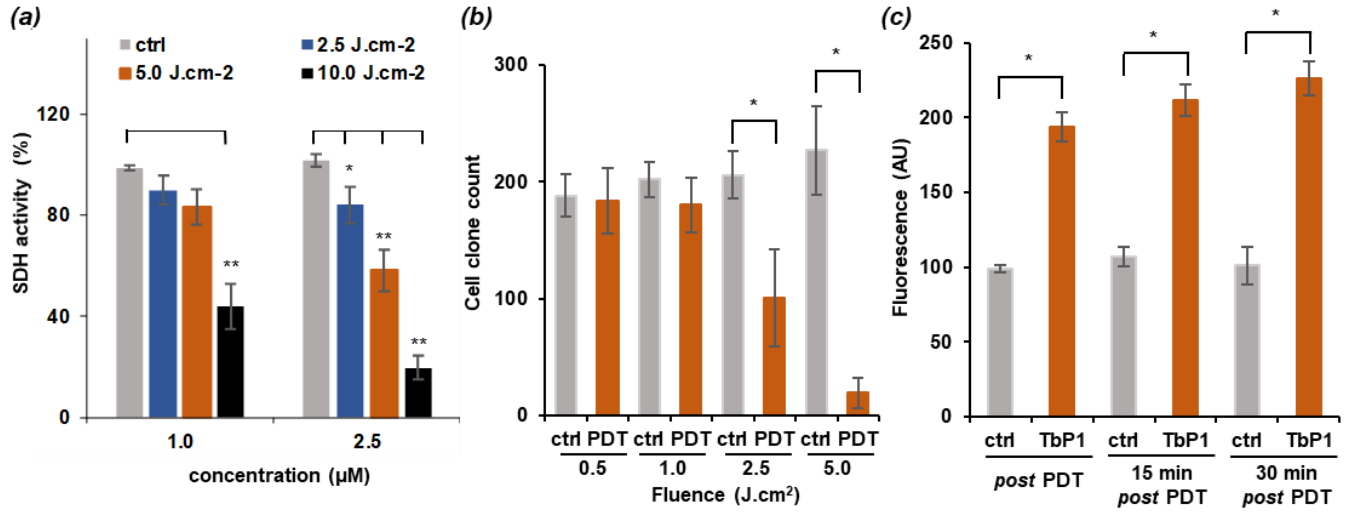

*Figure 181 : U-251 MG cell photodynamic effect. Cells were treated with AGuIX@Tb-P1 for 24 h before red-light exposition (2.5 to 10.0 J.cm^{-2}). **(a)**, cell viability was measured 24 h post treatment using the MTT assay. **(b)**, clonogenic assays after PDT treatment with increasing fluences. Clonogenic capabilities are expressed relative to control cells. Results are means ± S.D. (n= 12 wells/condition); *, P<0.05; (Kruskal-Wallis test and post-hoc by the Mann-Whitney test). **(c)**, reactive species content was quantified by flux cytometry after cell pre-treatment with 2.5 µM AGuIX@Tb-P1 (TbP1), followed by photodynamic treatment at 2.5 J.cm^{-2}. In **(a)** and **(c)**, results are means ± S.D. of three determinations from three independent experiments. *, P<0.05; **P<.0.001 (Kruskal-Wallis test and post-hoc by the Dunn's test). Abreviations: ctrl, cells treated with AGuIX@ congugates without light exposure; SDH, succinate dehydrogenase; UA, arbitrary unit.*

II.7 X-ray-induced photodynamic effect on U-251 MG cell survival

Similarly, we studied whether X-ray irradiation promoted U-251 MG cell growth arrest by photodynamic-mediated effect. Reactive species generation was quantified immediately after cell exposure to X-ray irradiation (**Figure 182a**). X-ray ionisation in itself generated reactive species and Tb scintillation could be involved in the redox change within the cells [5]. We assessed whether reactive species were generated in AGuIX@Tb and AGuIXTb-P1 pre-treated cells and irradiated at 2.0 Gy, with an energy set at 320kVp, over 1 h *post* irradiation (**Figure 182a**). Reactive species content was increased up to 1.5 time when cells were exposed to AGuIXTb-P1, whatever the delay. Conversely, at 30 min *post* exposition, reactive species content was enhanced in AGuIX@Tb pre-treated cells, but the increase was not significant when the results were compared to those obtained with untreated cells. Moreover, the obtained levels in pre-treated and untreated cells were close, after 1 h *post* irradiation.

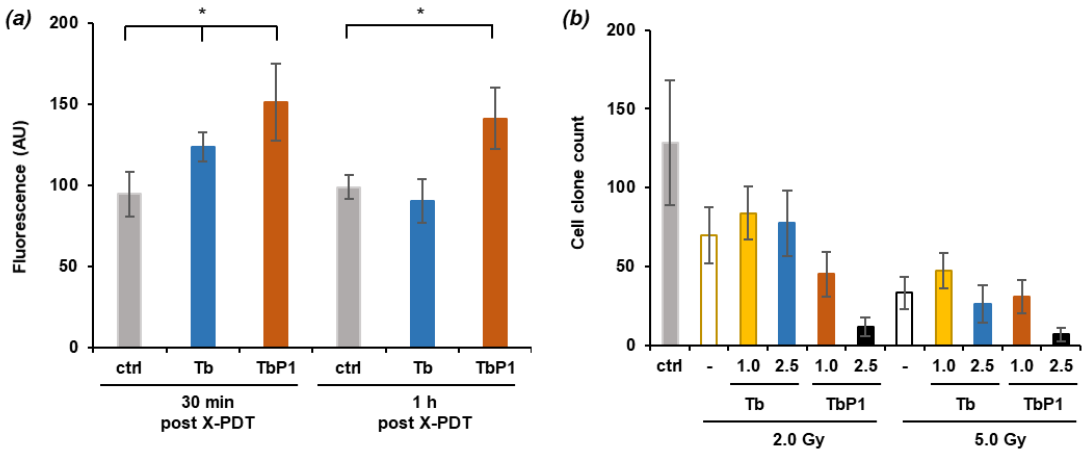

Figure 182 : Effect of X-PDT on U-251 MG cell survival and reactive species content. ***(a)****, Reactive species content in U-251 MG cells pre-treated with nanoparticles then exposed to X-ray irradiation at 2.0 Gy (320 Kev). Results are means ± S.D of triplicate determination from three independent experiments. *, P<.0.05 (Kruskal-Wallis test and post-hoc by the Dunn's test), comparison between nanoparticles-treated and -untreated cells (ctrl, control).* ***(b)****, U-251 MG cells were treated with 16.6 or 45.1 µM AGuIX@Tb, 1.0 or 2.5 µM AGuIX@Tb-P1 (TbP1) for 24 h, before X-ray irradiation at 2.0 or 5.0 Gy (320 kV). Results are means ± S.D. of clones counting from at least 12 wells Abbreviation: ctrl, irradiated cells without NPs pre-treatment. Abreviation: AU, arbitrary unit.*

In order to validate the concept of a photodynamic effect in X-PDT strategy, we performed anchorage-dependent clonogenic assays with AGuIX@NPs. Because Gd and Tb are neighbours in terms of atomic number, their behaviour regarding X-ray interaction is considered as similar. Cells were pre-treated with 1 µM AGuIX@NPs and irradiated at X-ray doses ranging from 0.5 up to 5.0 Gy, either at 160 or 320 kVp, corresponding to the dose rate of 1.5 or 3.0 $Gy.min^{-1}$, respectively. These conditions were chosen since cell clone formation was mainly inhibited when cells were pre-treated with 2.5 µM AGuIX@Tb-P1 and irradiated for X-ray doses higher than 2.0 Gy at 320 kV (**Figure 182b**). Experimental results were plotted in the quadratic semi log model (**Figure 183a**) and compared (**Figure 183b**). Curve parameters were computed for survival factor at 2.0 Gy (**Table 31**). Because we used X-ray dose exposures up to 5.0 Gy, which were close to those classically used in clinical practice (1.5 to 2.5 Gy), we considered the β -parameter equal to 0. In fact, β-parameter governs the slope for high dose exposure (sub-lethal damage), while the α-parameter reflects the enhanced benefit of X-ray-induced PDT on cell survival *id est* the direct lethal cell damage [42]. As shown in table I and **Figure 183b**, significant survival difference (p = 0.0018) was found at 2.0 Gy between scintillating (AGuIX@Tb-P1) and non-scintillating (AGuIX@Gd-P1) nanoparticles, when X-ray energies were set to 320 kVp corresponding to a mean 116 keV X-ray energy; DMF was estimated of 0.650 versus 0.876. The DER at 2.0 Gy was estimated at 1.54. Finally, for the same Gy dose, the enhanced factor was 35% when cells were treated with AGuIX@Tb-P1. Moreover, we did not find any significant change between results from cells treated with AguIX@Gd-P1 and those obtained of the cells treated with AGuIX@Gd for the same experimental conditions (**Figure 183b**). At energies set at 160 kVp, we did not found any difference between both nanoparticles either doped with Tb or Gd with or without P1. Accordingly, our results support the concept of AGuIX@Tb-P1 photodynamic-mediated effect, whereas nanoparticle chelated with Gd did not.

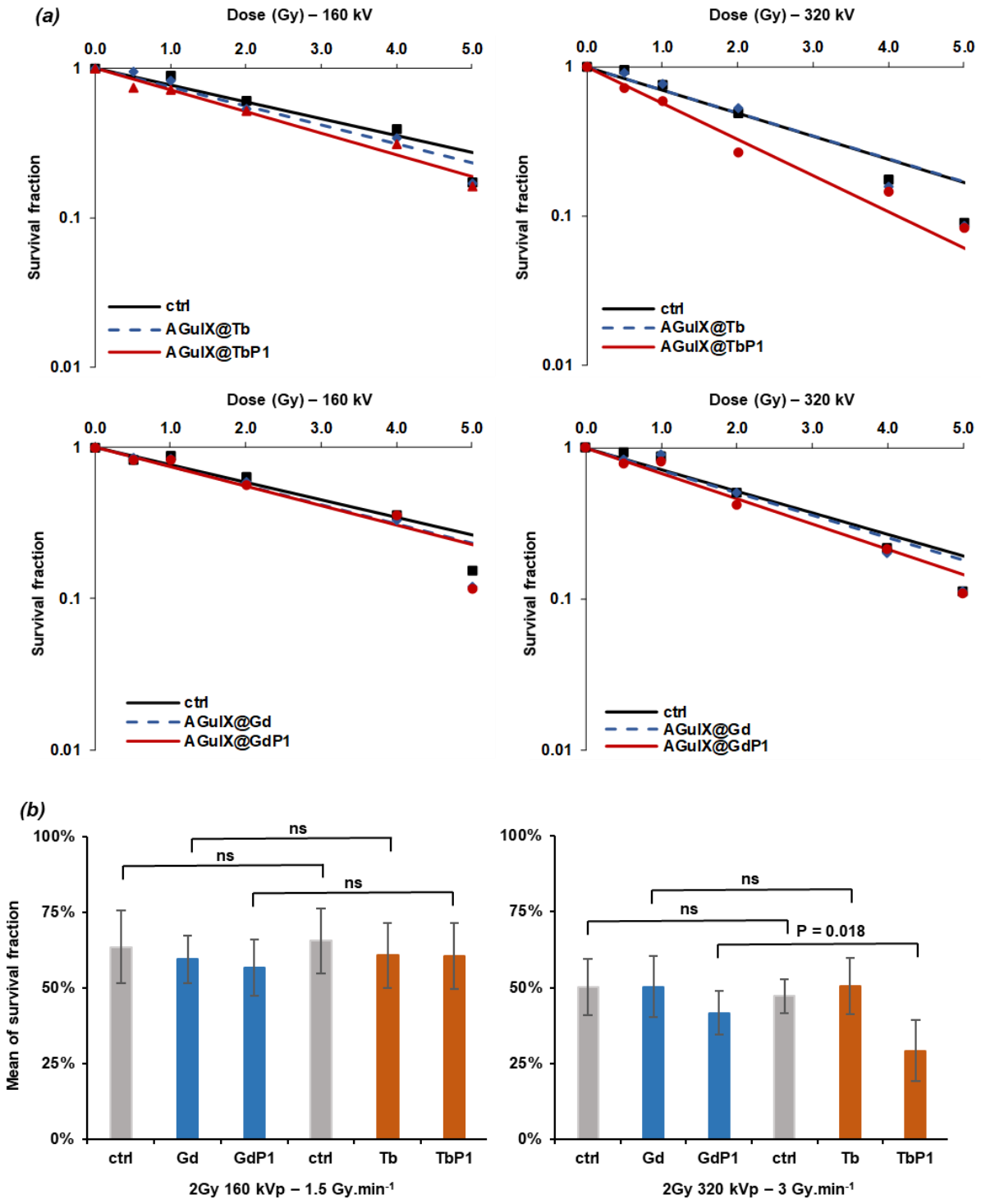

Figure 183 : Survival curve of pre-treated U-251 MG cells with AGuIX@Tb-P1 or AGuIX@Gd-P1 exposed to X-ray irradiation. (a), LQ model established after numeration of cell clones obtained for AGuIX@-complexes pre-treated cells, then irradiated at 160 and 320 KV for a range of 0.5 to 5.0 Gy. (b), means of survival fraction at 2.0 Gy were compared using the Kruskal-Wallis test (with α = 0.05), and post-hoc by the Mann-Whitney test (α = 0.05) for unpaired groups (n= 12 wells per condition from at least 4 independent experiments). Abbreviation: ctrl, irradiated cells without nanoparticles pre-treatment.

Table 31 : LQ model parameters for the range of 0 – 5.0 Gy irradiations

Condition tested	α parameter	Dose modifying factor (DMF)	Survival fraction ($SF_{2.0\ Gy}$)	Enhanced factor (%)	DER
160kV / 1.5 Gy.min^{-1}					
Control	0.263	1.000	0.592		
AGuIX@Gd	0.292	0.966	0.587		
AGuIX@GdP1	0.296	0.862	0.558		
AGuIX@Tb	0.291	0.885	0.559		
AGuIX@TbP1	0.333	0.769	0.515		
320kV / 3.0 Gy.min^{-1}					
Control	0.341	1.000	0.504		
AGuIX@Gd	0.340	1.000	0.507		
AGuIX@GdP1	0.385	0.876	0.463	8.1	1.08
AGuIX@Tb	0.354	1.000	0.493	2.2	1.02
AGuIX@TbP1	0.559	0.650	0.327	35.1	1.54

Two dose rates were assessed at 1.5 and 3.0 Gy.min-1. AGuIX@GdP1 or AGuIX@TbP1 concentrations were set to 1 µM Porphyrin equivalent (P1). Control, cells exposed to X-ray alone; DER, dose enhanced ratio.

III. Discussion

III.1 Gadolinium substitution by Terbium in the AguIX plateform

X-ray-induced PDT represents an alternative to PDT leading to the possibility to access to tumours localised in deep brain tissue. As shown herein, we proposed to replace Gd in the original AGuIX@Gd by Tb and grafted P1 to demonstrate the interest of such nanoparticle in X-PDT. This strategy is based on several lines of evidence: as demonstrated previously, AGuIX@Gd-P1 accumulate within human cell-grafted tumour by EPR in orthotopic site [38,39], even though the nanoparticle delivery depends mainly on the development of angiogenesis processes. Moreover, both AGuIX@Gd and AGuIX@Gd-P1 are eliminated from animal body by renal route [34,38]. However, in the latter, nanoparticle clearance was associated to the liver/feces body elimination. Moreover, we showed that the replacement of Gd by Tb in addition to the grafting of P1, did not change the hydrodynamic diameter of the nano-objects.

Tb was selected as a scintillating agent and we demonstrated the spectral overlap between Tb and P1, which is necessary for X-PDT (Figures 1 and 2). Thus, Tb can transfer the energy received after nanoparticle X-ray irradiation to P1 by FRET non radiative transfer. These results are consistent with previous findings, which highlighted the relation between the 545 nm Tb emission peak, P1 Q3 band and X-ray photons ranging from 20 to 130 kVp in activating photo-agents, through induced visible luminescence from rare-earth particles [31]. In PDT, a large part of visible light is absorbed by the photosensitizer which produces singlet oxygen, known as the PDT type II reaction [3]. In contrast,

when X-PDT is used, only a small fraction of the X-ray emitted photons will be converted into scintillations [21,22]. Indeed, the interaction between material and high energy photons depends on the Z atomic number *id est* electronic density and incident energy [4,21]. Usually, in medical imaging, scintillation crystals are designed thick enough to increase the probability to completely stop incident photons via the photoelectric effect [43]. Conversely, in aqueous media, the effective density will be lower than expected, leading only to a small fraction of X-ray energy converted into visible light. Moreover, the photodynamic efficiency can depend on various factors such as the distribution of the scintillating nanoparticles within the tumour tissue, the composition of the tumour stromal microenvironment, the level of molecular oxygen in this microenvironment and the illumination density resulting from the scintillating agents. Bulin *et al* and Abliz *et al* demonstrated the production of singlet oxygen via porphyrin X-ray-induced activation of Gd oxysulfide doped with Tb or Tb oxide, respectively [27,30]. However, low X-ray energies from 10 to 130 kVp (*id est* mean energies ranging from 5 to 70 keV at 20 mA) were tested, while energies used in radiotherapy are commonly from 160 to few hundred keV for preclinical *in vivo* experiments. In addition, clinical radiotherapy involves much higher energies, around 6 MeV. Scintillation yield is dramatically lower at such levels of keV energies since the probability of photoelectric interaction becomes minimal [43]. Therefore, X-PDT under conventional linear accelerators should be less effective than with radiograph tubes. On the other hand, the bioluminescence of Tb as a scintillating agent was demonstrated using high concentrations of the nanoscintillator and irradiation deposits without compatibility with the energies in pre-clinical studies or in the clinic [44-46].

III.2 Irradiation of AGuIX@Tb-P1 produces singlet oxygen

As shown in Figure 3, AGuIX@Tb-P1 produced singlet oxygen under X-ray irradiation, as demonstrated by the use of APF and SOSG probes. APF probe reacts with the hydroxyl radical and singlet oxygen; SOSG is specific to singlet oxygen [47,48,51,52]. Recently, it has been reported that the SOSG fluorescent signal occurs independently either of the presence of singlet oxygen or in the absence of photosensitizer during X-ray irradiation [49]. It has been also shown that the probe under UV excitation, generated an endoperoxide derivative which acts as a photosensitizer producing singlet oxygen [53]. No dramatic change was observed when the SOSG probe was tested without nanoparticles (Figure 3a), at a dose rate of 3.0 $Gy.min^{-1}$ and with an energy set up at 320 kVp. When NaN_3, as a quencher of singlet oxygen, was added in the reaction mixture, the changes observed were mainly due to the production of singlet oxygen generation from P1. Alternatively, the APF probe was used instead of SOSG in the same experimental conditions (Figure 3b). In the experimental conditions used, we could not exclude that during X-ray irradiation of AGuIX@Tb-P1, the APF fluorescence signal increase was associated to the generation of reactive species (especially hydroxyl radical), as observed by the slight but continuous increase of the slope curve, even though in the presence of sodiun azide (Figure 3a). Such an increase has been related to X-ray-mediated water radiolysis alone in the presence of the APF probe [53]. However, Bulin *et al* [27] hypothesised that P1 acts as a radiosensitizer and therefore the molecule could involve the generation of reactive species under X-rays exposition.

III.3 Irradiation of AGuIX@Tb-P1 induces a photodynamic effect on U-251 MG cell growth

We assessed whether AGuIX@Tb-P1 altered U-251 MG cell survival by PDT and X-PDT. We used U-251 MG cells whose behaviour is close to that of GBM *in situ* (54). Collectively, we demonstrated that P1 grafted into AGuIX@Tb limits the cytotoxicity of the molecule alone (Figure S4), in agreement

with previous findings [55,56]. AGuIX@Tb-P1 pre-treated cell exposure to photodynamic or X-ray irradiation triggered cell death and limited cell clone formation (Figures 6b and 7). Interestedly, we found that the treatment efficacy was enhanced with X-PDT relative to radiation treatment when cells were exposed to AGuIX@Tb-P1 instead of AGuIX@Gd-P1 at 2.0 Gy (320 keV), with a DMF estimated at 0.65 corresponding to an enhanced factor calculated at 35 %. The benefit of X-PDT relative to radiation treatment was obtained with diverse nanoparticle designs, for examples, with P1- and Ce-doped with titanium oxide on A549 human lung cancer cell; with P1-grafted silicium oxide nanospheres on Hela cervical cells; with rat L9 glioma cell exposed to LaF_3:Tb particles with adsorbed meso-tetra(4-carboxyphenyl)porphyrin with low irradiation source; or with $SrAl_2O_4$:Eu2+ nanoparticles; collectively, allowing to the conclusion that tumours cells undergo cell death by cumulative/synergistic effects of irradiation treatment and X-ray induced photo-treatment [57-60]. Finally, cancer cell exposure to AGuIX doped with Gd involved cell radiosensitization. However, we did not found any significant change when cells were treated with AGuIX@Gd, as compared to the results of untreated cells exposed to X-rays alone (Figure 7 and table I). This discrepancy could be explained since the radiosensitizing effects on cancer cells from diverse origin has been reported for Gd concentration from 100 µM up to 1 mM [34], whereas herein the concentration of lanthamide was 16 and 25 µM, for Tb and Gd respectively; in both cases, the P1 equivalent concentration tested was 1 µM.

Finally, we showed that replacement of Gd by Tb in the initial AGuIX design, leads to a promising nanoparticle for X-PDT in *in vivo* experimental. Moreover, we demonstrated that chelated Tb nanoparticles react linearly to X-ray energy (at least up-to 320 kV) and flow, and they were able to activate P1 to produce singlet oxygen. The constructed nanoparticle was not toxic, while remaining unexposed to light. *In vitro* experiments confirmed the interest of these AGuIX design, notably at a 3.0 $Gy.min^{-1}$ dose rate. However, it has to be noted that such strategy should not be considered with external radiotherapy but with low-energy devices (corresponding to a few hundred of keV), such as radiograph tubes to ensure high energy conversion and singlet oxygen production while lowering exposure dose. Such investigations are currently conducted in our group.

IV. Materials and Methods

IV.1 Reagents

Fluorescent probes, 3′-(p-aminophenyl) fluorescein (APF), 2',5'(di-acetate) dichlorofluorescein (DCF2-DA), Singlet Oxygen Sensor Green™ (SOSG) and propidium iodure (PI) were from Molecular Probe (Merck-Sigma, St Quentin Fallavier, France). 3-(4,5-dimethylthiazol-2-yl)-2,5-diphenyl tetrazolium (MTT) was purchased from Acros Organics (Thermo Fisher Scientific, France). 5-(4-carboxyphenyl succinimide ester)-10,15,20-triphenylporphyrin (P1) and zinc(II) 5-(4-carboxyphenyl)-10,15,20-(tri-N-methyl-4-pyridyl) porphyrin trichloride (ZnPy3P1) was were—purchased from Porphychem (Porphychem SAS, Dijon, France). Other reagents were of analytical grade.

IV.2 Synthesis and preparation of the AGuIX@-complexes

We used four different nanoparticles, based on the same AGuIX® polysiloxane core surrounded by 1,4,7,10-tetraazacyclododecane-1,4,7,10-tetraacetic acid (DOTA)/metal cation (3+) complexes, covalently grafted to the inorganic matrix. The cations used were Terbium (Tb^{3+}, Z=65, A = 159 $g.mol^{-1}$) and Gadolinium (Gd^{3+}, Z=64, A = 157 $g.mol^{-1}$). P1 was covalently grafted as a photosensitizer (AGuIX@Tb-P1 or AGuIX@Gd-P1).

Ultra-small siloxane particles were obtained in a two-step synthesis procedure as described previously [33]. In brief, 3-aminopropyl triethoxysilane (185 mmol) and 1,4,7,10-tetra-azacyclododecane-1-glutaric anhydride-4,7,10-triacetic acid (137 mmol, DOTAGA) were mixed to react in 630 mL of diethylene glycol (DEG) at room temperature for 20 h in order to create the DOTAGA silane. Tetraethyl orthosilicate (249 mmol) was added and the mixture was left for 1 h with stirring before addition of 6.3 L of ultrapure water for the condensation Sol-Gel reaction and hydrolysis. The mixture was heated successively at 80°C for 6h, then at 50°C for 18 h. After incubation, the pH was adjusted to 2.0 with HCl (12N). The ultra-small siloxane particles were purified by tangential filtration on Vivaflow® membranes with a cut-off at 5 kDa (Sartorius Stedim Biotech, Aubagne, France). The final volume was 400 mL with the purification factor of 1,000. The pH of the solution was adjusted to 7.4 with 1M NaOH solution. The final amount of free DOTA was measured by europium titration, as described previously [31]. Free DOTA groups were estimated at 100 mM DOTA. Tb chelation was performed by addition of 1.5 mmole trichloroterbium hexahydrate in 15 mL of the particle solution. The pH was adjusted at 6.0 with 1M NaOH, and the mixture heated until temperature raised 80°C. Each day, the pH was measured and adjusted to 6.0, until there was no pH change. The ultra-small particles were filtered onto VivaSpin® membranes (cut-off at 5 kDa, Sartorius Stedim Biotech). The volume obtained was 15 mL and the purification factor was 100. The Tb chelation yield was determined by Inductively Coupled Plasma – Mass Spectroscopy and was estimated at 60 %. Finally, the pH was adjusted at 7.4, before freeze-drying.

P1 was grafted following the protocol described previously [33,39]. In summary, 500 mM (1.5 g) of DOTA-free particles, obtained from the first step of particle synthesis, were dispersed in 3 mL of pure water and 1.5 mmol of trichloroterbium hexahydrate. The mixture's pH was adjusted to 6.0 with 1M NaOH solution and heated to 80°C for Tb chelation as described above. 12 mL of DEG pre-heated at 40°C was added to the solution. 150 µmol P1 diluted in DMSO was added drop-by-drop under stirring. The final solvent ratio H_2O/DEG/DMSO was 13/53/34. The mixture was left stirring at 40°C for 12 h in the dark and was filtrated through VivaSpin® membranes (cut-off at 5 kDa, Sartorius Stedim Biotech). The purification factor was 100 and the final volume was 15 mL. The Tb chelating yield, determined by Inductively Coupled Plasma – Mass Spectroscopy, was 47%. The P1 coupling yield was estimated at 29% by recording the absorbance at 520, 550 nm, 590 and 650 nm Q bands. The final Tb:P1 ratio was 16 moles Tb for 1 mole P1. All concentrations of nanoparticle containing P1 will be referred to thereafter as the concentration of P1. A stock AGuIX@Tb-P1 suspension was prepared in water and was 3 mM P1 equivalent; the solution of AGuIX@Tb was 37.5 mM (Tb equivalent) in water.

IV.3 Dynamic light scattering size

Direct measurements of the size distribution of the nanoparticles suspended in any medium were performed via Zetasizer NanoS DLS (Dynamic light scattering, laser He-Ne 633 nm, Malvern Instrument, Orsay, France). Prior to the experiment, the nanoparticles were diluted in 0.01 M NaCl (pH 7.4).

IV.4 zeta potential of the AGuIX conjugates

Potential zeta measurements were carried out with a Zetasizer Nano-Z (Malvern Instrument) equipped with a He-Ne laser at 633 nm. Before measurement, the nanoparticles were dispersed in 0.01 M NaCl and buffer solutions (Honeywell Fluka^{TM} Buffer Solution, ThermoFischer Scientific, Ilkirch, France).

IV.5 Synthesis of AGuIX@Gd and AGuIX@Gd-P1

The AGuIX@ complexes were synthesized and characterized as described previously [33], with a ratio of 1 mole of P1 for 25 moles of Gadolinium (Gd), as estimated by Inductively Coupled Plasma – Mass Spectroscopy analysis. Stock solution of AGuX@Gd or AGuX@Gd-P1 was respectively 50 mM Tb equivalent, and 4 mM P1 equivalent in water.

IV.6 Photophysical properties of AGuIX@Tb-P1

Absorption spectra were recorded on a UV-3600 UV-visible double beam spectrophotometer (Shimadzu, Marne-La-Vallée, France). Fluorescence spectra were recorded on a Fluorolog FL3-222 spectrofluorimeter (Horiba Jobin Yvon, Longjumeau, France) equipped with a 450 W Xenon lamp and thermostated cell compartment (25°C), a UV-visible photomultiplier R928 (Hamamatsu Photonics, Hamamatsu, Japan) and an InGaAs infrared detector (DSS-16A020L Electro-Optical System Inc, Phoenixville, PA, USA). The excitation beam was diffracted by a double ruled grating SPEX monochromator (1200 grooves/mm blazed at 330 nm). The emission beam was diffracted by a double ruled grating SPEX monochromator (1200 grooves/mm blazed at 500 nm). Singlet oxygen emission was detected through a double ruled grating SPEX monochromator (600 grooves/mm blazed at 1 µm) and a long-wave pass (780 nm). All spectra were measured in four-face quartz vials. All the emission spectra (fluorescence and singlet oxygen luminescence) have been displayed with the same absorbance (less than 0.2) with the lamp and photomultiplier correction.

Spectral overlap as well as Förster radius were computed to characterise the energy transfer from the Tb cation (Tb^{3+}) to P1. Moreover, Tb luminescence decay profile was recorded using a Fluorolog spectrofluorimeter; the excitation wavelength was set at 351 nm and the emission peaks were scanned in the 400-690 nm region. The luminescence lifetime of Tb alone or in mixture with P1 was recorded using lifetime Fluorolog. We assessed the 545 nm peak decay as it is the highest Tb fluorescence peak. If relevant, we computed the quenching constant (expressed as $L.mol^{-1}.s^{-1}$) as $Kq = K/\tau_0$, where K is the Stern-Volmer constant which was graphically determined; τ_0 is the Tb fluorescence lifetime without photosensitizer.

IV.7 Tb scintillation assessment under X-ray

Samples were irradiated using a biological X-ray Irradiator X-RAD 320 (Precision X-ray INC., North Branford, CT, USA) with a tungsten anode. Photons were produced by X-ray tubes and produced continuous energy distribution. The tube parameters were set from 25 up to 320 kVp (*id est* mean photon energies of 8 and 116 keV) with the current set from 0.5 up to 12.5 mA [40]. A 2 mm Al filter was used to remove low energy photons. For Tb scintillation assessment, irradiation time was set at 90 s for each parameter.

An optical fiber was inserted inside the irradiation chamber, in front of the vial containing AGuIX@Tb solutions to gather emission fluorescence photons. Emission spectra were recorded with an USB2000

spectrometer (Ocean Optics Inc, Dunedin, FL). This versatile high-resolution spectrometer (FWHM = 3.5 nm) is an optical instrument based on a diffraction grating and a one-dimensional CCD detector array. Integration time was set to 5 s, the spectrum bandwidth ranged from 340 to 820 nm and the optical fiber was placed across from a transparent vial (UVette® 220-1600 nm; cat.no. 952010051, Eppendorf, Hamburg, Germany). Emission spectra were recorded at different times to assess photonic density configurations on the Tb scintillation performance. Each measurement was repeated 7 times and all spectra were subtracted with the same solution spectrum obtained without irradiation. When varying X ray energy, we set the tube current to maximum and we set the voltage to 320 kVp when we assessed the tube current on the AGuIX@Tb response. A linear correlation coefficient was computed to characterise the relation between AGuIX@Tb peaks intensities, exciting photons energy (X ray kVp) and X ray flow (X ray mA), respectively. The energy transfer from the nanoparticles to a photo-agent was assessed with setting irradiation parameters to 320 kVp and 12.5 mA (a 3.0 Gy/min dose rate in our experimental conditions).

IV.8 Singlet oxygen production during red light exposition or X-ray irradiation

The reaction mixture was prepared in 30 mM Tris/HCl (pH 7.4) containing 400 µM AGuIX@Tb-P1 or 45 mM AGuIX@Tb and 5 µM APF or 10 µM SOSG probe. Singlet oxygen quenching was achieved by addition of NaN_3 (stock solution, 1 M) prepared in the same buffer, to a final concentration at 10 mM. Irradiation was set to 320 kVp, 12.5 mA and source-surface distance adjusted to yield a 3.0 Gy/min dose rate. Fluorescence emission was detected spectroscopically at 515 and 525 nm for APF and SOSG, respectively. Home-made software allowed long acquisition times and synchronization between laser illumination and signal recording. Integration time was set to 100 ms and time points were acquired every 5 min during 20 min. Moreover, P1 at 100 µM was irradiated without nanoscintillator with the same parameters to validate the absence of the~~ir~~ direct excitation by X-rays.

IV.9 Biological experiments

IV.9.1 Cell culture

Human U-251 MG (ECACC 09063001, Salisbury, UK) glioblastoma-derived cells were cultivated in Roswell Park Memorial Institute medium (RPMI) without phenol red, containing 10 % (v/v) heat-inactivated (30 min at 56 °C) fetal calf serum (Invitrogen, Paisley, UK), 1 % (v/v) non-essential amino acid (Invitrogen), 0.5 % (v/v) essential amino acid (Invitrogen), 1 mM sodium pyruvate (Invitrogen), 1 % (v/v) vitamin (Invitrogen) 0.1 $mg.mL^{-1}$ of L-serine, 0.02 mg/ml L-asparagine (Merck–Sigma) and 1 % (v/v) antibiotics (10,000 U/ml penicillin, 10 mg/ml streptomycin) (Merck-Sigma). The cells were seeded routinely at 105 cells/ml and cultivated at 37 °C in a 5% CO_2 humidified atmosphere (Incubator Binder, Tübingen, Germany).

IV.9.2 Cell growth assessment

Impact of AGuIX@Tb or ZnPy3P1 on U-251 MG cell survival was assessed by the MTT procedure, based on the measurement of mitochondrial succinate dehydrogenase activity (EC 1.3.5.1) [41]. Cells were seeded in 96 well-plates at 104 cells/well and left growing for 24 h. Cells were treated with increasing concentrations of P1 (up to 400 µM) and AGuIX@Tb (0.1 to 2 mM) over three days. In addition, glioblastoma cells were exposed to increasing concentrations of AGuIX@Tb-P1 or AGuIX@Gd-P1 (1 to 10 µM) for 72 h. At time, the medium was discarded and replaced by 100 µl of complete medium containing 0.5 $mg.mL^{-1}$ MTT. The plates were incubated for 2 h at 37 °C and formazan crystals obtained were dissolved by adding 100 µL of DMSO. The plates were read at 540

nm (Multiskan Ascent spectrophotometer, Thermo Fisher Scientific, Illkirch, France). Results are expressed relative to those obtained from untreated cells (control), taken as 100. They represented quadruplicate determinations from two independent experiments (n=8).

IV.9.3 Nanoparticles cell uptake

U-251 MG cells were seeded in 6 well-plates at 10^5 cells/well and left to grow over 48 h. Cells were treated with increasing concentrations of nanoparticles (0.5 to 5.0 µM AGuIX@Tb-P1 or AGuIX@Gd-P1) over 48 h. After incubation, cell layers were washed with 2 mL of Dulbecco's Phosphate buffer saline (DPBS, Merck–Sigma) and cells were suspended with 0.5 ml of 0.05% (w/v) Trypsin/0.02% (w/v) EDTA solution (Invitrogen) per well for 5 min at 37°C. Complete medium (0.5 mL; RPMI containing 10% (v/v) foetal calf serum) was then added. The cell suspension obtained was centrifuged at 1,000g for 5 min at 4 °C. Cell pellets were washed with 1 mL of DPBS and centrifuged again. Cells were suspended finally in 0.5 mL of DPBS and left on ice. Fluorescence of P1, was measured in 5,000 cells/sample by flow cytometry (Gallios Analyzer, Beckman Coulter France, Roissy, France), with excitation/emission settings at 638 nm and 660/30 nm. Results obtained from nanoparticle uptake were expressed relative to those obtained reaching the maximum of nanoparticle absorption taken as 100. Results are expressed as mean ± SD from triplicate determinations from 3 independent experiments.

IV.9.4 PDT and X-PDT conditions

Cell exposure to a red light was performed with a Laser diode (Biolitec, Biomedical Technology, Iena, Germany) at 0.7 W, corresponding to an irradiance at 4.54 $mW.cm^{-2}$. Cell layers were exposed to 0.5 to 10.0 $J.cm^{-2}$ corresponding to an exposition duration of 2 min to 38 min. X-ray irradiation was performed using the X-ray Irradiator X-RAD 320 (Precision X-Ray Inc), using tube parameters set at 160 and 320 kV (mean photons energies of 58 and 116 keV) with current set at 10 mA. A 2 mm Al filter was used to remove low energy photons. The dose rates were 1.5 and 3.0 $Gy.min^{-1}$ for 160 and 320 kVp respectively. The doses delivered were 0.5, 2.0, 4.0 and 5.0 Gy for both dose rates.

IV.9.5 Reactive species quantification during PDT or X-PDT

U-251 MG cells were seeded in 6 well-plates at 2.10^5 cells/well. Cells were left to grow over 48 h, then, treated in the presence of 1 µM AGuIX@-complexes for 24 h. Cells were washed with 2 mL of DPBS. Each well was filled again with complete medium before light exposition or X-ray irradiation. Reactive species generation measurements were achieved post treatment over 1 h. At each time point, cell medium was changed by 2 mL of pre-warmed medium containing 50 µM DCF2-DA for 30 min at 37 °C. Cells were then successively harvested by trypsination, washed with DPBS and suspended in 0.5 mL DPBS before flow cytometry analysis. Reactive species generation was measured in 5,000 cells/sample by flow cytometry with excitation/emission settings at 488 nm and 520/30 nm. Cell death was quantified also using propidium iodure in kinetic uptake experiments. Cells were treated with 20 µM propidium iodure (diluted in DMSO) added to the medium. Propidium iodure-positive cells were numbered by flow cytometric analysis with excitation/emission settings at 488 nm and 620/630 nm (FL3), respectively. Results represent the median of fluorescent peak. Results are expressed relative to those obtained from untreated cells, taken as 100. Results are expressed as mean ± SD of triplicate determinations from 3 independent experiments.

IV.9.6 Anchorage-dependent clonogenic assay

The clonogenic assay was performed in 6 well-plates with U-251 MG cells seeded at 500 cells/well. Cells were then treated in the presence of 16.6 µM of AGuIX@Tb, 25 µM AGuIX@Gd, 1 µM AGuIX@Tb-P1 or 1 µM AGuIX@Gd-P1 (P1 equivalent concentration) for 24 h at 37 °C. After incubation, cells were washed with 2 mL of DPBS. 2 mL of complete medium were added in each well before X-ray radiation or red-light exposition. Cells were left to grow at 37 °C for 7 days. At time, cell clones were successively washed with 2 mL DPBS, fixed with 1 mL of 4 % (v/v) formol (pH 7.4) at room temperature for 15 min, washed with 1 mL of DPBS, and stained for 30 min with 0.05 % (w/v) crystal Violet solution prepared in DPBS and containing 25% (v/v) methanol. Finally, cells were washed three times with 2 mL of bi-distilled water. Cell clones obtained were analysed after picture capture (GelCount™, Oxford Optronix, Abingdon, U.K.) and ImageJ quantification (N.I.H., Bethesda, Ma, USA). Image analysis was performed with well area taken as 862 mm². Cell clone counting was improved by background subtraction. Data from untreated and treated cell conditions were compared and expressed as the mean ± SD (n = 12).

Survival fraction (SF) was calculated using the linear quadratic (LQ) model, based on the equation: $SF_D = \exp(-(\alpha D + \beta D2))$, where survival fraction is defined as SF_D= (plating efficiency at the dose D) / (platting efficiency at 0 Gy); D corresponds to the Gy dose; α and β, are determined from the established semi log curve, as SF_D = f (Gy dose). The effects of radiation alone or X-PDT, related to untreated cells or exposed to each AGuIX@NP, were compared by calculating the dose modifying factor (DMF) and the survival fraction at 2.0 Gy (SF_2). We determined also the Dose Enhanced Ratio (DER) at 2.0 Gy. DER is defined as the ratio of $SF_{2.0\ Gy}$ calculated for untreated cells to that calculated of treated cells after irradiation (DER = $SF_{2.0\ Gy}$ (control cells)/ $SF_{2.0\ Gy}$ (treated cells)); We finally calculated the enhanced factor, expressed in percentage, as EF (%) = 100 x ($SF_{2.0\ Gy}$ (control cells) – $SF_{2.0\ Gy}$ (treated cells))/ $SF_{2.0\ Gy}$ (control cells)).

IV.9.7 Statistical analysis

Results obtained were analysed using the Kruskal-Wallis test (α = 0.05) and post-hoc Dunn's test (α = 0.05) for paired groups. Any difference was considered significant at $P<0.05$. Results obtained from clonogenic assays were analysed using the Kruskal-Wallis test (with α = 0.05), and post-hoc by the Mann-Whitney test (α = 0.05) for unpaired groups.

Supplementary Materials:

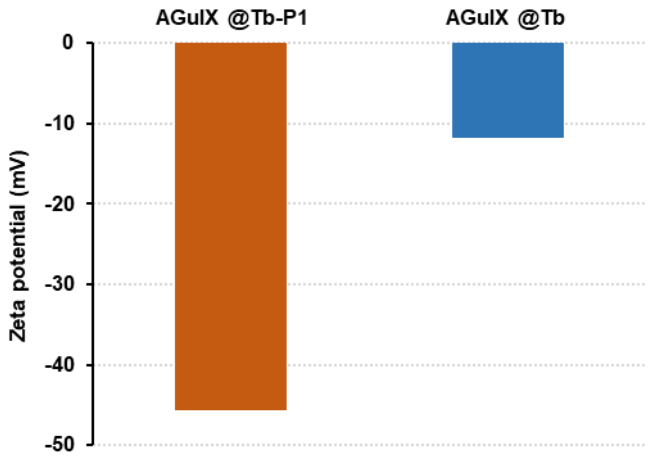

Figure S1: Determination of zeta potential of AGuIX@Tb-P1 and AGuIX@Tb. AGuIX were diluted in water in the presence of NaCl. zeta potential was measured in folded capillary zeta cell. It was estimated at - 46.5 and - 18.1 mV for AGuIX@Tb P1 and AGuIX@Tb, respectively.

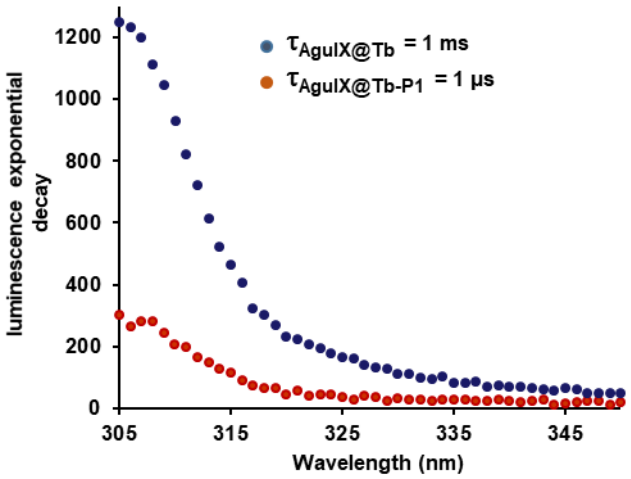

Figure S2 : *Luminescence decay of AGuIX@Tb and AGuIX@Tb-P1 in water. The fluorescence exponentiel decay at 545 nm was measured after excitation at 351 nm of sample diluted in water. Final concentration was 0.1 mM AGuIX@Tb and and 6.6 µM AGuIX@Tb-P1). The derivative of this decay gives the fluorescence lifetime of chelated Tb in AGuIX and was calculated at 1 ms, whereas fluorescence lifetime of AGuIX@-Tb-P1 was 1 µs.*

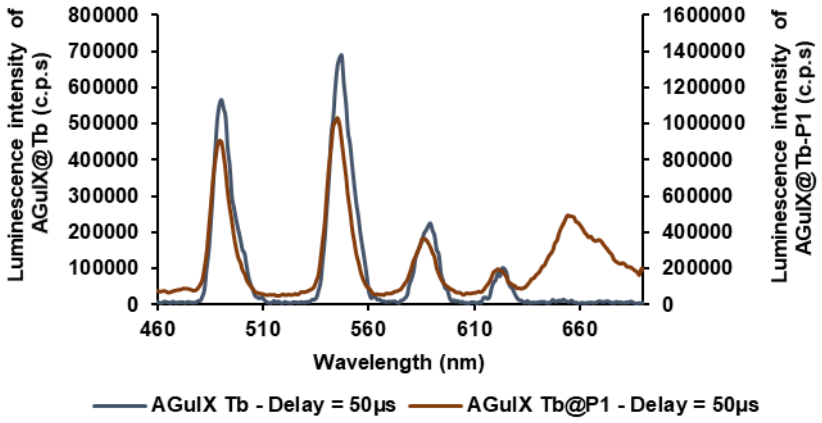

Figure S3: Luminescence of AGuIX@Tb-P1. The AGuIX@ nanoparticles were dispersed in water at a concentration of 140 µM equivalent porphyrin for AGuIX@Tb-P1 and 2.3 mM for AguIX@Tb. Each solution was illuminated at 351 nm and photon emission were monitored between 460 and 700 nm with a 50 µs delay. The decrease of Tb emission and increase of porphyrin luminescence between 630 and 690 nm is due to the energy transfer between Tb and porphyrin.

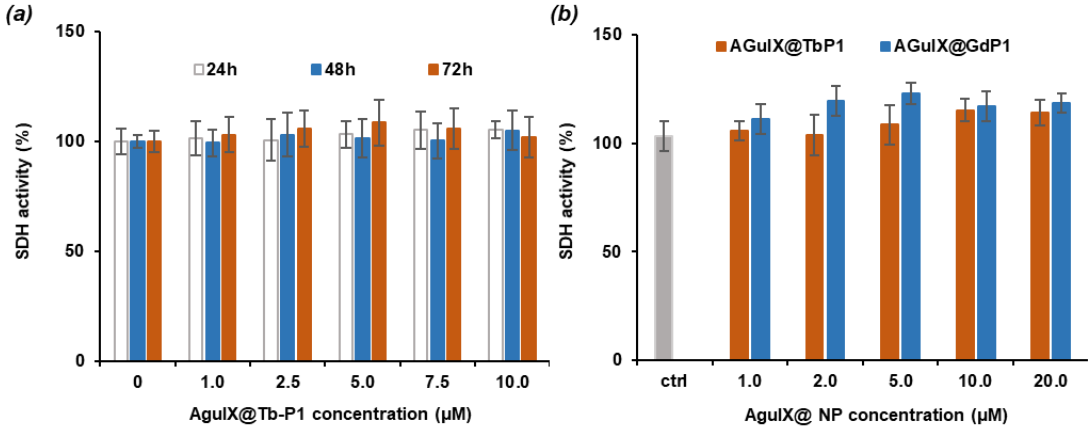

Figure S4: SDH activities after U-251 MG cell exposure to AGuIX@ nanoparticles (a) Cells were treated with increasing concentration (1.0 to 10.0 µM) of AGuIX@Tb-P1 (P1 equivalent concentration) over three days. (b) Similarly, cells were exposed to increasing concentrations (1.0 to 20.0 µM) of AGuIX@Tb-P1 or AGuIX@Gd-P1 for 72 h. In both experiments, succinate dehydrogenase activities (SDH) were evaluated by MTT assays. Results are means ± S.D. of at least quadruplicate determinations from two independent experiments (n = 8).

Abbreviations: AGuIX@Tb or Gd, Ultra small AGuIX-designed nanoparticle chelated with Terbium or Gadolinium; AGuIX@Tb-P1 or Gd-P1 Ultra small AGuIX-Tb or Gd grafted with Porphyrin; APF, 3′-(p-aminophenyl) fluorescein; DCF-2DA, 2',5'(di-acetate) dichlorofluorescein; DER, dose enhanced ratio; DMF, dose modified factor; DPBS, Dulbecco's phosphate buffer saline, Gd, Gadolinium; GBM, glioblastoma multiforme ; MTT, 3-(4,5-dimethylthiazol-2-yl)-2,5-diphenyl tetrazolium ; P1, 5-(4-carboxyphenyl succinimide ester)-10,15,20-triphenyl porphyrin; PDT, Photo Dynamic Therapy; RPMI, Roswell Park Memorial Institute medium; SOSG, Singlet Oxygen Sensor Green™; Tb, Terbium; X-PDT, X-ray-induced Photo Dynamic Therapy; Zn3PyP1, zinc(II) 5-(4-carboxyphenyl)-10,15,20-(tri-N-methyl-4-pyridyl) porphyrin trichloride.

References

1. Davis, M.E. Glioblastoma: Overview of Disease and Treatment. *Clin J Oncol Nurs* **2016**, *20*, S2-S8.
2. Stupp, R.; Hegi, M.E.; Mason,W.P.;van den Bent, M.J.; Taphoorn, M.J.; Janzer, R.C.; Ludwin, S.K.; Allgeier, A.; Fisher, B.; Belanger,K. *et al*. European Organisation for Research and Treatment of Cancer Brain Tumour and Radiation Oncology Groups; National Cancer Institute of Canada Clinical Trials Group. Effects of radiotherapy with concomitant and adjuvant temozolomide versus radiotherapy alone on survival in glioblastoma in a randomised phase III study: 5-year analysis of the EORTC-NCIC trial. *Lancet Oncol* **2007**, *10*, 459-466.
3. Calixto, G.M.; Bernegossi, J.; de Freitas, L.M.; Fontana, C.R.; Chorilli, M. Nanotechnology-Based Drug Delivery Systems for Photodynamic Therapy of Cancer: A Review. Molecules **2016**, *21*, 342.
4. Bechet D.; Mordon, S.R.; Guillemin F.; Barberi-Heyob, M. Photodynamic therapy of malignant brain tumours: a complementary approach to conventional therapies. *Cancer Treat Rev* **2014**, *40*, 229-241.
5. Larue, L.; Ben Mihoub, A.; Youssef, Z.; Colombeau, L.; Acherar, S.; André, J.C.; Arnoux, P.; Baros, F.; Vermandel, M.; Frochot, C. Using X-rays in photodynamic therapy: an overview. *Photochem Photobiol Sci* **2018**, *17*, 1612-1650.
6. Pinel, S.; Thomas, N.; Boura, C.; Barberi-Heyob, M. Approaches to physical stimulation of metallic nanoparticles for glioblastoma treatment. *Adv Drug Deliv Rev* **2019**, *138*, 344-357.
7. Maeda, H.; Sano, Y.; Takeshita, J.; Iwai, Z.; Kosaka, H.; Marubayashi, T.; Matsukado, Y. A pharmacokinetic simulation model for chemotherapy of brain tumor with an antitumor protein antibiotic, neocarzinostatin: Theoretical considerations behind a two-compartment model for continuous infusion via an internal carotid artery. *Cancer Chemother Pharmacol* **1981**, *5*, 243-249.
8. Maeda, H. Toward a full understanding of the EPR effect in primary and metastatic tumors as well as issues related to its heterogeneity. *Adv Drug Deliv Rev* **2005**, *91*, 3-6.
9. Beck,T.J.; Kreth, F.W.; Beyer, W.; Mehrkens, J.H.; Obermeier, A.; Stepp, H.; Stummer, W.; Baumgartner, R. Interstitial photodynamic therapy of nonresectable malignant glioma recurrences using 5-aminolevulinic acid induced protoporphyrin IX. *Lasers Surg Med* **2007**, *39*, 386-393.
10. Krishnamurthy, S.; Powers, S.K.; Witmer, P.; Brown, T. Optimal light dose for interstitial photodynamic therapy in treatment for malignant brain tumors. *Lasers Surg Med* **2000**, *27*, 224-234.
11. Stummer, W.; Beck, T.; Beyer, W.; Mehrkens, J.H.; Obermeier, A.; Etminan, N.; Stepp, H.; Tonn, J.C.; Baumgartner, R.; Herms, J., *et al*. Long-sustaining response in a patient with non-resectable, distant recurrence of glioblastoma multiforme treated by interstitial photodynamic therapy using 5-ALA: case report. *J Neurooncol* **2008**, *87*, 103-109.
12. Kostron, H.; Fiegele, T.; Akatuna, E. Combination of FOSCAN® mediated fluorescence guided resection and photodynamic treatment as new therapeutic concept for malignant brain tumors. *Medical Laser Application* **2006**, *21*, 285-290.
13. Stepp, H.; Beck, T.; Pongratz, T.; Meinel, T.; Kreth, F.W.; Tonn, J.C.; Stummer, W. ALA and malignant glioma: fluorescence-guided resection and photodynamic treatment. *J Environ Pathol Toxicol Oncol* **2007**, *26*, 157-164.
14. Eljamel, M.S.; Goodman, C.; Moseley, H. ALA and Photofrin fluorescence-guided resection and repetitive PDT in glioblastoma multiforme: a single centre Phase III randomised controlled trial. *Lasers Med Sci* **2008**, *23*, 361-367.
15. Zilidis, G.; Aziz, F.; Telara, S. ; Eljamel, M.S. Fluorescence image-guided surgery and repetitive Photodynamic Therapy in brain metastatic malignant melanoma. *Photodiagnosis Photodyn Ther* **2008**, *5*, 264-266.
16. Johansson, A.; Palte, G.; Schnell, O.; Tonn, J.C.; Herms, J.; Stepp, H. 5-Aminolevulinic acid-induced protoporphyrin IX levels in tissue of human malignant brain tumors. *Photochem Photobiol* **2010**, *86*, 1373-1378.

17. Aziz, F.; Telara, S.; Moseley, H.; Goodman, C.; Manthri, P.; Eljamel, M.S. Photodynamic therapy adjuvant to surgery in metastatic carcinoma in brain. *Photodiagnosis Photodyn Ther* **2009**, *6*, 227-230.
18. Jiang, F.; Robin, A.M.; Katakowski, M.; Tong, L.; Espiritu, M.; Singh, G.; Chopp, M. Photodynamic therapy with photofrin in combination with Buthionine Sulfoximine (BSO) of human glioma in the nude rat. *Lasers Med Sci* **2003**, *18*, 128-133.
19. Zimmermann, A.; Ritsch-Marte, M.; Kostron, H. mTHPC-mediated photodynamic diagnosis of malignant brain tumors. Photochem Photobiol **2001**, *74*, 611-616.
20. Stummer, W.; Pichlmeier, U.; Meinel, T.; Wiestler, O.D.; Zanella, F.; Reulen, H.J. ALA-Glioma Study Group. Fluorescence-guided surgery with 5-aminolevulinic acid for resection of malignant glioma: a randomised controlled multicentre phase III trial. *Lancet Oncol* **2006**, *7*, 392-401.
21. van Eijk, C.W.. Inorganic scintillators in medical imaging. *Phys Med Biol* **2002**, 47, R85-R106.
22. Ren,X.D.; Hao, X.Y.; Li, H.C.; Ke, M.R.; Zheng, B.Y.; Huang, J.D. Progress in the development of nanosensitizers for X-ray-induced photodynamic therapy. *Drug Discov Today* **2018**, *23*, 1791-1800.
23. Chen, W.; Zhang J. Using nanoparticles to enable simultaneous radiation and photodynamic therapies for cancer treatment. *J Nanosci Nanotechnol* **2006**, *6*, 1159-1166.
24. Kamkaew, A.; Chen, F.; Zhan, Y.; Majewski, R.L.; Cai, W. Scintillating Nanoparticles as Energy Mediators for Enhanced Photodynamic Therapy. *ACS Nano* **2016**, *10*, 3918-3935.
25. Retif P.; Pinel, S.; Toussaint, M.; Frochot, C.; Chouikrat, R.; Bastogne, T.; Barberi-Heyob, M. Nanoparticles for Radiation Therapy Enhancement: The Key Parameters. *Theranostics* **2015**, *5*, 1030-1044.
26. Tang, Y.; Hu, J.; Elmenoufy, A.H.; Yang, X. Highly Efficient FRET System Capable of Deep Photodynamic Therapy Established on X-ray Excited Mesoporous LaF_3:Tb Scintillating Nanoparticles. *ACS Appl Mater Interfaces* **2015**, *7*, 12261-12269.
27. Bulin, A.L.; Vasil'ev, A.; Belsky, A.; Amans, D.; Ledoux, G.; Dujardin, C. Modelling energy deposition in nanoscintillators to predict the efficiency of the X-ray-induced photodynamic effect. *Nanoscale* **2015**, *7*, 5744-5751.
28. Yang, C.C.; Wang, W.Y.; Lin, F.H.; Hou, C.H. Rare-Earth-Doped Calcium Carbonate Exposed to X-ray Irradiation to Induce Reactive Oxygen Species for Tumor Treatment. *Int J Mol Sci* **2019**, 20, pii: E1148.
29. Li, X.; Xue, Z.; Jiang, M.; Li, Y.; Zeng, S.; Liu, H. Soft X-ray activated NaYF(4):Gd/Tb scintillating nanorods for in vivo dual-modal X-ray/X-ray-induced optical bioimaging. *Nanoscale* **2017**, *10*, 342-350.
30. Abliz, E.; Collins, J.E.; Bell, H.; Tata, D.B. Novel applications of diagnostic X-rays in activating a clinical photodynamic drug: Photofrin II through X-ray induced visible luminescence from "rare-earth" formulated particles. *J Xray Sci Technol* **2011**, *19*, 521-530.
31. Elmenoufy, A.H.; Tang, Y.; Hu, J.; Xu, H.; Yang, X. A novel deep photodynamic therapy modality combined with CT imaging established via X-ray stimulated silica-modified lanthanide scintillating nanoparticles. *Chem Commun (Camb)* **2015**, *51*, 12247-12250.
32. Mignot, A.; Truillet, C.; Lux, F.; Sancey, L.; Louis, C.; Denat, F.; Boschetti, F.; Bocher, L.; Gloter, A.; Stephan, O.; *et al*. A top-down synthesis route to ultrasmall multifunctional Gd-based silica nanoparticles for theranostic applications. *Chemistry* **2013**, *19*, 6122-6136.
33. Le Duc, G.;, Roux, S.;, Paruta-Tuarez, A.; Dufort, S.; Brauer, E.; Marais, A.; Truillet, C.; Sancey, L.; Perriat, P.; Lux, F.; *et al*. Advantages of gadolinium based ultra-small nanoparticles vs molecular gadolinium chelates for radiotherapy guided by MRI for glioma treatment. Cancer Nanotechnol, **2014**, *5*, 4.
34. Sancey, L.; Lux, F.; Kotb, S. ; Roux, S.; Dufort, S.; Bianchi, A.; Crémillieux, Y.; Fries, P.; Coll, J.L.; Rodriguez-Lafrasse, C. *et al*. The use of theranostic gadolinium-based nanoprobes to improve radiotherapy efficacy. *Br J Radiol* **2014**, *87*, 20140134.

35. McMahon? S.J.; Hyland, W.B.; Muir, M.F.; Coulter, J.A.; Jain, S.; Butterworth, K.T.; Schettino, G.; Dickson, G.R.; Hounsell, A.R.; O'Sullivan, J.M.; *et al*. Biological consequences of nanoscale energy deposition near irradiated heavy atom nanoparticles. *Sci Rep* **2011**, *1*, 18.
36. Sicard-Roselli C.; Brun, E.; Gilles, M.; Baldacchino, G.; Kelsey, C.; McQuaid, H.; Polin, C.; Wardlow, N.; Currell, F. A new mechanism for hydroxyl radical production in irradiated nanoparticle solutions. *Small* **2014**, *10*, 3338-3346.
37. Du, Y.; Sun, H.; Lux, F.; Xie, Y.; Du, L.; Xu, C.; Zhang, H.; He, N.; Wang, J.; Liu, Y.; *et al*. Radiosensitization Effect of AGuIX, a Gadolinium-Based Nanoparticle, in Nonsmall Cell Lung Cancer. *ACS Appl Mater Interfaces*, **2020**, *12*, 56874-56885.
38. Gries, M.; Thomas, N.; Daouk, J.; Rocchi, P.; Choulier, L.; Jubreaux, J.; Pierson, J.; Reinhard, A.; Jouan-Hureaux, V.; Chateau, A.; *et al*. Multiscale Selectivity and in vivo Biodistribution of NRP-1 Targeted Theranostic AGuIX Nanoparticles for PDT of Glioblastoma. *Int J Nanomedicine* **2020**, *15*, 8739-8758.
39. Toussaint, M.; Pinel, S.; Auger, F.; Durieux, N.; Thomassin, M.; Thomas, E.; Moussaron, A.; Meng, D.; Plénat, F.; Amouroux, M.; *et al*. Proton MR Spectroscopy and Diffusion MR Imaging Monitoring to Predict Tumor Response to Interstitial Photodynamic Therapy for Glioblastoma. *Theranostics* **2017**, *7*, 436-451.
40. Huda, W.; Scalzetti, E.M.; Levin, G. Technique factors and image quality as functions of patient weight at abdominal CT. *Radiology* **2000**, *217*, 430-435.
41. Mosmann, T. Rapid colorimetric assay for cellular growth and survival: Application to proliferation and cytotoxicity assays. *J Immunol Methods* **1983**, *65*, 55-63.
42. Franken, N.A.; Oei, A.L.; Kok, H.P.; Rodermond, H.M.; Sminia, P.; Crezee, J.; Stalpers, L.J.; Barendsen, G.W. Cell survival and radiosensitisation: modulation of the linear and quadratic parameters of the LQ model (Review). *Int J Oncol* **2013**, *42*, 1501-1515.
43. Clement, S.; Deng, W.; Camilleri, E.; Wilson, B.C.; Goldys, E.M. X-ray induced singlet oxygen generation by nanoparticle-photosensitizer conjugates for photodynamic therapy: determination of singlet oxygen quantum yield. *Sci Rep* **2016**, *6*, 19954.
44. Kulmala, S.; Hakanen, A.; Laine, E.; Haapakka, K. X-ray irradiation-induced optical luminescence of terbium (III) chelates in aqueous solutions. *J. Alloys and Compounds* **1995**, *225*, 2279-2283.
45. Kulmala, S.; Laine, E.; Hakanen, A.; Raerinne, P.; Haapakka, K. Mechanism of terbium (III)-enhanced lyoluminescence of x-ray irradiated sodium chloride. *Anal Chim Acta* **1994**, *294*, 1-11.
46. Jürgensen A. XEOL spectroscopy of lanthanides in aqueous solution. *Can J Chemistry* **2017**, *95*, 1198-1204.
47. Setsukinai, K.; Urano, Y.; Kakinuma, K.; Majima, H.J.; Nagano, T. Development of novel fluorescence probes that can reliably detect reactive oxygen species and distinguish specific species. *J Biol Chem* **1998**, *278*, 3170-3175.
48. Price, M.; Reiners, J.J.; Santiago, A.M.; Kessel, D. Monitoring singlet oxygen and hydroxyl radical formation with fluorescent probes during photodynamic therapy. *Photochem Photobiol* **2009**, *85*, 1177-1181.
49. Liu, H.; Carter, P.J.H.; Laan, A.C.; Eelkema, R.; Denkova, A.G. Singlet Oxygen Sensor Green is not a Suitable Probe for $^1O_2$ in the Presence of Ionizing Radiation. *Sci Rep* **2019**, *9*, 8393.
50. Takahashi, J.; Misawa, M. Characterization of reactive oxygen species generated by protoporphyrin IX under X-ray irradiation. *Radiation Phys Chem* **2009**, *78*, 889–898.
51. Misawa, M.; Takahashi, J. Generation of reactive oxygen species induced by gold nanoparticles under x-ray and UV Irradiations. *Nanomedicine* **2011**, *7*, 604-614.
52. Gollmer, A.; Arnbjerg, J.; Blaikie, F.H.; Pedersen, B.W.; Breitenbach, T.; Daasbjerg, K.; Glasius, M.; Ogilby, P.R. Singlet Oxygen Sensor Green®: photochemical behavior in solution and in a mammalian cell. *Photochem Photobiol* **2011**, *87*, 671-679.

53. Popovich, K.; Tomanová, K.; Čuba, V.; Procházková, L.; Pelikánová, I.T.; Jakubec, I.; Mihóková, E.; Nikl M. LuAg:Pr^{3+}-porphyrin based nanohybrid system for singlet oxygen production: Toward the next generation of PDTX drugs. J Photochem Photobiol B 179: 149-155, 2018.

54. Jacobs, V.L.; Valdes, P.A.; Hickey, W.F.; De Leo, J.A. Current review of in vivo GBM rodent models: emphasis on the CNS-1 tumour model. *ASN Neuro* **2011**, *3*, e00063.

55. Luo, W.; Liu, R.S.; Zhu, J.G.; Li, Y.C.; Liu, H.C. Subcellular location and photodynamic therapeutic effect of chlorin e6 in the human tongue squamous cell cancer Tca8113 cell line. *Oncology letters* **2015**, *9*, 551-556.

56. Pavani, C.; Uchoa, A.F. ; Oliveira, C.S. ; Lamamoto, Y.; Baptista, M.S. Effect of zinc insertion and hydrophobicity on the membrane interactions and PDT activity of porphyrin photosensitizers. *Photochem Photobiol Sci* **2009**, *8*, 233-240.

57. Yang, C.C.; Sun, Y.J; Chung, P.H.; Chen, W.Y.; Swieszkowski, W.; Tian, W.; Lin, W.Y. Development of Ce-doped TiO_2 activated by X-ray irradiation for alternative cancer treatment. *Ceram Int* **2017**, *43*, 12675–12683.

58. Kuo, W.J.; Wang, Y.C.; Chen, M.H.; Tung, F.I.; Liu, T.Y. Study of a novel vehicle developed for enhancing the efficacy of radiation therapy. *Ceram. Int* **2017**, *43*, S789–S796.

59. Chen, M.H.; Jenh, Y.J.; Wu, S.K.; Chen, Y.S.; Hanagata, N.; Lin, F.H. Non-invasive Photodynamic Therapy in Brain Cancer by Use of Tb3+-Doped LaF3 Nanoparticles in Combination with Photosensitizer Through X-ray Irradiation: A Proof-of-Concept Study. *Nanoscale Res Lett* **2017**, *12*, 62.

60. Wang, G.D.; Nguyen, H.T.; Chen, H.; Cox, P.B.; Wang, L.; Nagata, K.; Hao, Z.; Wang, A.; Li, Z.; Xie, J. X-Ray Induced Photodynamic Therapy: A Combination of Radiotherapy and Photodynamic Therapy. *Theranostics* **2016**, *6*, 2295-2305.

Chapitre V :

Couplage covalent entre les AGuIX, le RB et un peptide pour un ciblage actif et passif

I. Introduction

Afin d'avoir un transfert d'énergie maximal entre le Terbium ou le Gadolinium comme donneur et le RB comme accepteur, nous avons décidé de coupler le RB de manière covalente à la surface des AGuIX.

Le couplage covalent est considéré meilleur que l'adsorption. En effet, il convient de noter que le lien entre le PS et la surface des NPs n'est qu'une faible adsorption physique (liaison de Van Der Wals) qui peut nuire à la stabilité à long terme. De ce fait, une liaison chimique est plus stable que l'adsorption.

Dans ce chapitre, nous décrivons la synthèse du RB couplé aux NPs d'AGuIX. Nous couplons dans un premier temps le RB activé par le NHS directement sur les AGuIX (AGuIX@RB) puis dans un deuxième temps *via* un bras espaceur pour étudier l'effet de la distance donneur-accepteur sur le transfert d'énergie. Deux bras ont été utilisés, HA (acide 6-Bromohexanoïque) et Ahx (acide 6-aminohexanoïque) pour donner 2 NPs : AGuIX@HA-RB et AGuIX@Ahx-RB.

D'autre part, nous avons couplé le RB sur deux peptides différents : DKPPR et XXXXX. Pour coupler ces peptides sur les AGuIX, les fonctions amines de la surface des AGuIX ont été transformées en fonctions thiols.

Nous décrivons dans ce chapitre les protocoles de synthèse et la caractérisation du RB activé, le couplage des bras espaceurs au RB, des peptides-RB. Ainsi que les protocoles de couplage des AGuIX avec le RB, l'étude photophysique de ces composés sous UV-visible, l'étude de la production d'$^1O_2$ sous rayons X, les études biologiques telles l'affinité pour NRP-1 et l'effet photodynamique *in vitro* sur la lignée U-251 MG.

II. Synthèse et caractérisation des AGuIX couplées au RB

II.1 Réaction d'activation du RB par du N-hydroxysuccinimide pour l'obtention du composé RB-NHS 1

Le RB (600 mg ; 0,60 mmol ; 1 équivalent), le *N*-hydroxysuccinimide (NHS) (276 mg ; 2,40 mmol ; 4 équivalents) et le *N*,*N*′-dicyclohexylcarbodiimide (EDC.HCl) (279 mg ; 1,80 mmol ; 3 équivalents) sont solubilisés dans du DMF (Diméthylformamide) anhydre (50 mL). Le milieu réactionnel est mis à température ambiante sous agitation et atmosphère inerte pendant une nuit à l'obscurité **(Figure 184)**. Le solvant est ensuite évaporé sous pression réduite. Le produit attendu RB–NHS **1** est obtenu avec une pureté de 90% sous forme d'un solide violet sombre. Le produit est extrait à l'aide d'un mélange $CHCl_3$ (Chloroforme)/H_2O dans un volume respectif de 50 et 20 mL. L'opération est répétée trois fois. La phase organique est collectée et le $CHCl_3$ est évaporé sous pression réduite. Le produit est purifié par chromatographie flash sur gel de silice (éluant : dichlorométhane (DCM)/EtOH, 90/10). Le composé **1** pur est isolé sous la forme d'un solide violet sombre de masse 580 mg (rendement 88 % et pureté de 98%).

La masse molaire de RB-NHS **1** est égale à 1070 g/mol. Par LC-MS, il est trouvé $[M+H]^+$ = 1071 g/mol, $[(M+3H)/3]^+$ = 357 g/mol.

La pureté est analysée par HPLC à une longueur d'onde de détection en absorption UV-Visible λ=560 nm, avec un gradient passant de 95/5 à 0/100 (A/B, v/v) pendant 15 minutes, suivi d'ACN isocratique 0/100 (A/B, v/v) pendant 10 minutes, puis un gradient de 0/100 à 95/5 (A/B, v/v) en 5 minutes (avec A = 95/5/0,1 (H_2O/acétonitrile (ACN)/méthanol (MeOH), v/v/v) et B = 100/0,1 (ACN/MeOH ; v/v)). Les données RMN sont situées en annexe.

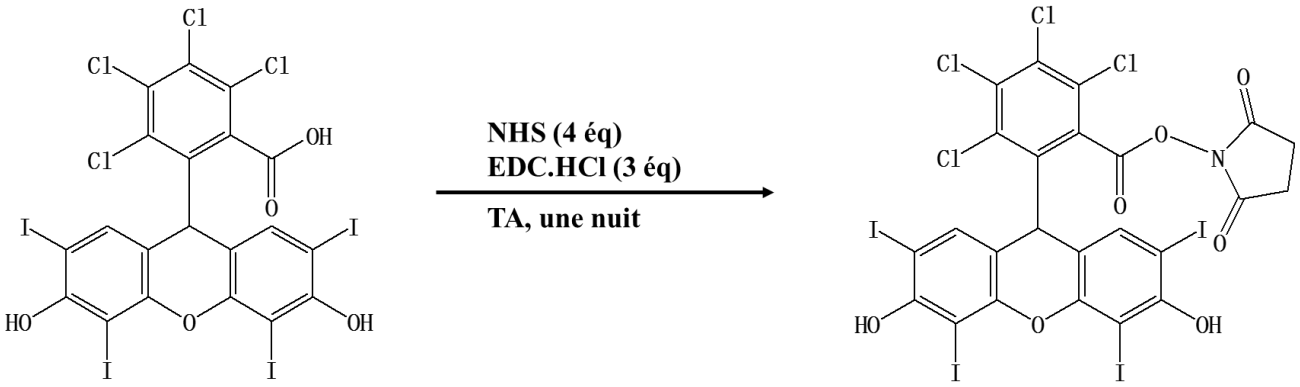

Figure 184 : Synthèse du RB activé (RB-NHS) 1.

II.2 Réaction de couplage du RB et de l'acide 6- Bromohexanoïque pour l'obtention du composé RB-HA 2

RB-HA a été préparé en suivant la méthode légèrement modifiée de Neckers [1]. Brièvement, le sel de sodium RB (500 mg, 0,50 mmol, 1 équivalent) et de l'acide 6-bromohexanoïque (284 mg, 1,5 mmoles, 3 équivalents) sont mis à réagir sous reflux (80 °C, 24 h) dans un ballon à fond rond (50 mL) contenant 20 mL de DMF (figure 2). La solution refroidie après 24 h est acidifiée avec du H_2SO_4 aqueux à 5 %, puis extraite et lavée à l'aide de $CHCl_3$ pour éliminer les sels de NaBr et autres produits n'ayant pas réagi. L'huile rouge résultante est séchée sous pression réduite et précipitée dans du diéthyl éther glacé. Le composé pur est isolé sous la forme d'un solide rouge (420 mg, 85 %). La masse molaire de RB-HA est égale à 1085 g/mol. Le résultat MS montre $[M+H]^+$ = 1086 g/mol, $[M+Na]^+$ = 1108 g/mol. Les données RMN sont situées en annexe.

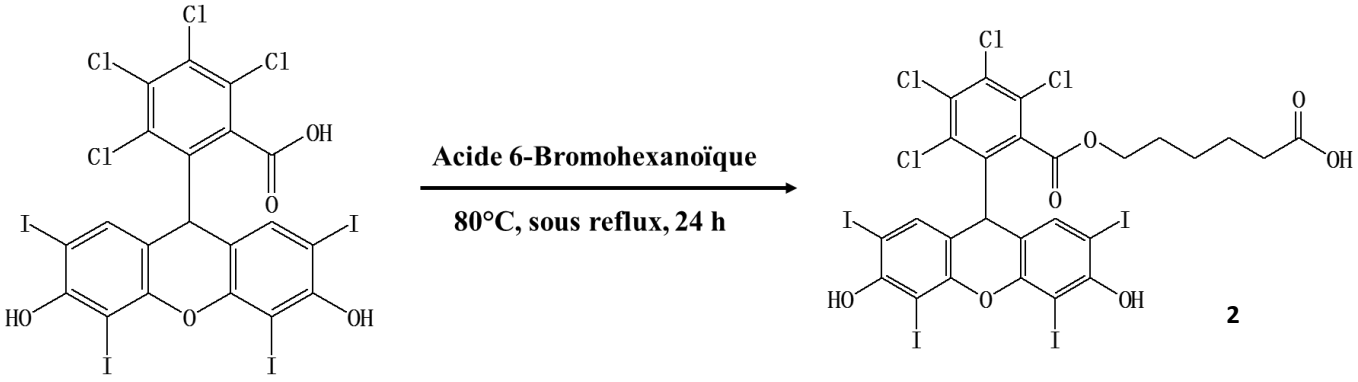

Figure 185 : Réaction de couplage du RB et de l'acide hexanoïque (RB-HA) 2

II.3 Réaction de couplage du RB-HA et du NHS pour l'obtention du composé RB-HA-NHS 3

RB-HA **2** (400 mg, 0,35 mmol) est dissous dans 3 mL de DMF anhydre et agité à l'obscurité et sous atmosphère d'azote. Une solution d'EDC (164 mg, 1,06 mmol, 3 équivalents) et du NHS (161 mg, 1,4 mmol, 4 équivalents) dilué dans 2 mL de DMF sont ajoutés **(figure 186)**. Après agitation à température ambiante pendant une nuit, le produit est extrait à l'aide de $CHCl_3/H_2O$ (10/20) trois fois. La phase organique est collectée et le $CHCl_3$ est évaporé sous pression réduite. Le produit est précipité dans du diéthyl éther glacé. Le produit est purifié par HPLC préparative utilisant un gradient ACN/H_2O (0,1 % de TFA; 5:95) à 100 % d'ACN en 20 min, suivi d'ACN isocratique pendant 15 min sur une colonne C18 varian (t_R=18,4 min). Après lyophilisation, le composé pur est isolé sous la forme d'un solide rouge (320 mg, 80 %). La masse molaire du produit attendue est égale à 1185 g/mol. Le résultat MS montre $[M+H]^+$ = 1186 g/mol. Les données RMN sont situées en annexe.

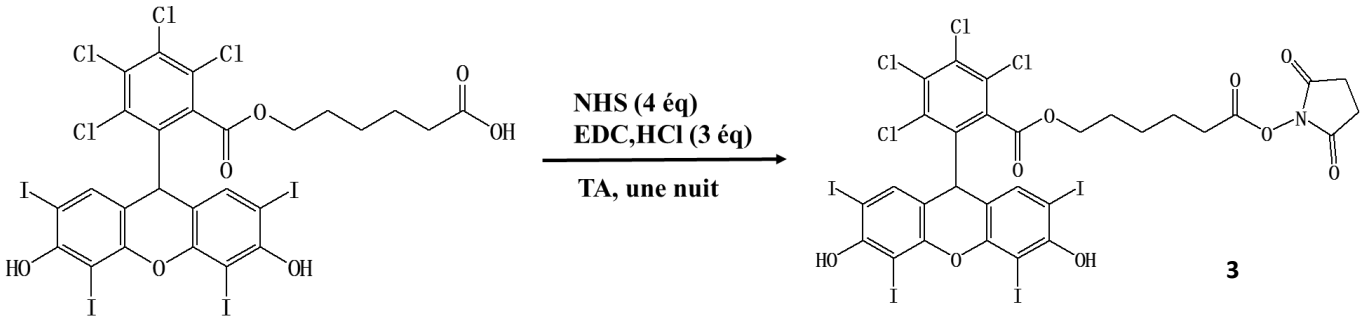

Figure 186 : Synthèse du RB-HA-NHS 3.

La liaison ester qui se forme entre l'acide carboxylique du PS et la fonction hydroxyle pourrait s'hydrolyser en milieu biologique. Nous décidons de coupler le bras sur le RB également avec une liaison amide. La liaison amide peptidique est plus stable en milieu biologique que la liaison ester.

II.4 Réaction de couplage du RB avec l'acide hexanoïque pour l'obtention du composé RB-Ahx 4

RB-NHS **1** (100 mg, 1 équivalent, 93 µmol) sont dissous dans 10 mL de DCM anhydre dans lequel la triéthylamine Et_3N (1 équivalent) est ajoutée. A cette solution, l'acide 6-aminohexanoïque (Ahx-OH) (83 mg, 2,5 équivalents, 0,23 mmol) solubilisé dans 4 mL de DMF est ajouté. Le mélange est laissé sous agitation 24 h, sous atmosphère inerte à température ambiante **(figure 187)**. Après 24 h, le solvant est évaporé sous pression réduite. Le produit attendu RB–Ahx est obtenu sous la forme d'un solide rouge sombre. Le produit est extrait à l'aide d'un mélange $CHCl_3/H_2O$ dans un volume respectif de 50 et 20 mL. L'opération est répétée trois fois. La phase organique est collectée et le $CHCl_3$ est évaporé sous pression réduite. Le composé **4** est isolé après extraction sous la forme d'un solide rouge sombre de masse 82 mg (rendement 82 % et pureté de 96%). La masse molaire de RB-Ahx **4** est égale à 1085 g/mol. Par LC-MS, il est trouvé $[M+H]^+$ = 1086 g/mol. Les données RMN sont situées en annexe.

La pureté est analysée par HPLC à une longueur d'onde de détection en absorption UV-Visible λ=560 nm, avec un gradient passant de 95/5 à 0/100 (A/B, v/v) pendant 15 minutes, suivi d'ACN isocratique 0/100 (A/B, v/v) pendant 10 minutes, puis un gradient de 0/100 à 95/5 (A/B, v/v) en 5 minutes (avec A = 95/5/0,1 (H_2O/ACN/MeOH, v/v/v) et B = 100/0,1 (ACN/MeOH ; v/v)).

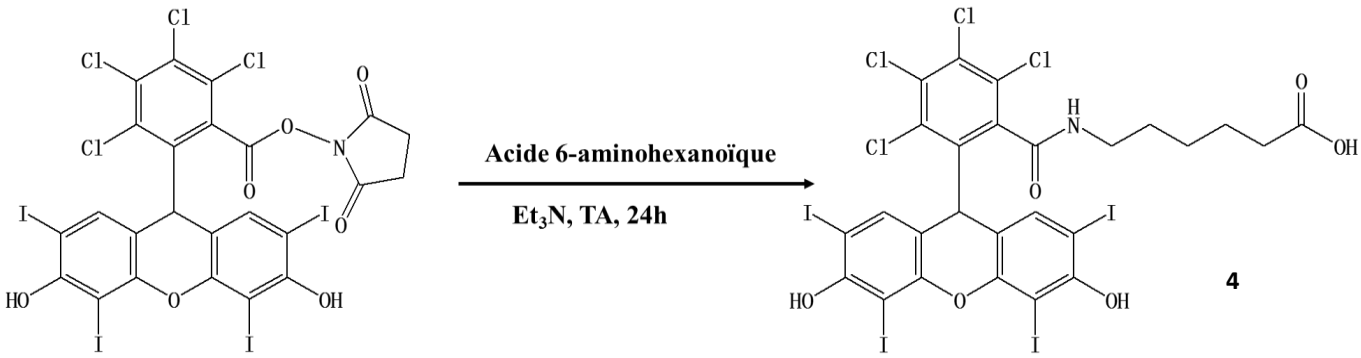

Figure 187: Réaction de synthèse du RB-Ahx 4

II.5 Réaction de couplage du RB-Ahx et du NHS pour l'obtention du composé RB-Ahx-NHS 5

RB-Ahx **4** (82 mg, 0,75 µmole, 1 équivalent) est dissous dans 2 mL de DMF anhydre est agité à l'obscurité et sous atmosphère d'azote. A cette solution, une solution d'EDC (1,05 mg, 2,25 µmol, 3 équivalents) et du NHS (1,035 mg, 3 µmol, 4 équivalents) dilué dans 1,5 mL de DMF sont ajoutés **(Figure 188)**. Après agitation à température ambiante pendant une nuit, le produit est extrait à l'aide dans le $CHCl_3$. La phase organique est collectée et le $CHCl_3$ est évaporé sous pression réduite. Le produit est extrait à l'aide d'un mélange $CHCl_3/H_2O$ dans un volume respectif de 50 et 20 mL. L'opération est répétée trois fois. La phase organique est collectée et le $CHCl_3$ est évaporé sous pression réduite. Le produit est purifié par chromatographie flash

sur gel de silice (éluant : DCM/EtOH, 90/10). Le composé **5** pur est isolé sous la forme d'un solide rouge sombre de masse 75 mg (rendement 91,5 % et pureté de 98%). La masse molaire de RB-Ahx-NHS **5** est égale à 1186 g/mol. Par LC-MS, il est trouvé $[M+H]^+$ = 1187 g/mol, $[(M\text{-}NHS+2Na^+)]^+$ = 1130 g/mol.

La pureté est analysée par HPLC à une longueur d'onde de détection en absorption UV-Visible λ=560 nm, avec un gradient passant de 95/5 à 0/100 (A/B, v/v) pendant 15 minutes, suivi de ACN isocratique 0/100 (A/B, v/v) pendant 10 minutes, puis un gradient de 0/100 à 95/5 (A/B, v/v) en 5 minutes (avec A = 95/5/0,1 (H_2O/ACN/MeOH, v/v/v) et B = 100/0,1 (ACN/MeOH ; v/v)).

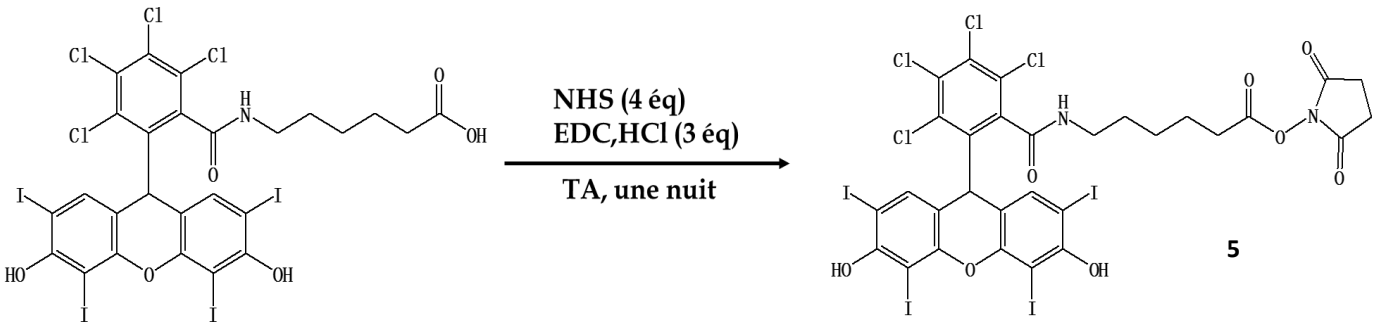

Figure 188: Synthèse du RB-Ahx-NHS 5.

II.6 Etude photophysique des précurseurs de couplage

II.6.1 Spectres d'absorption

La **figure 189** montre les spectres d'absorption du RB et de ses dérivés. A la même concentration, les trois dérivés montrent un décalage bathochrome dû à la modification de la fonction acide carboxylique. Une importante diminution du coefficient d'extinction molaire au maximum d'absorption (λ=570 nm) est observée pour RB-NHS.

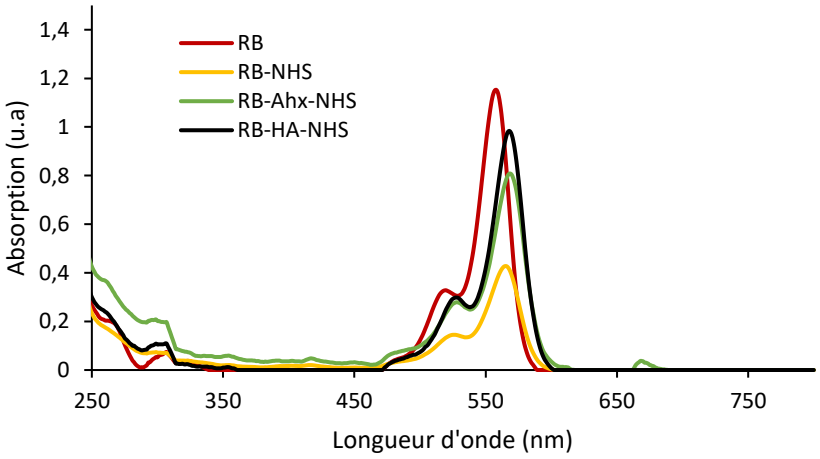

Figure 189 : Spectre d'absorption du RB et des dérivés dans l'éthanol, concentration = 10 µM.

II.6.2 Spectres d'émission de fluorescence

La **figure 190** montre les spectres d'émission du RB et de leurs dérivés avec une émission de fluorescence entre 550 nm et 700 nm. Ils présentent un aspect similaire mais des intensités différentes allant de RB> RB-HA-NHS> RB-Ahx-NHS> RB-NHS. Les rendements quantiques de fluorescence ont été calculés et sont présentés dans le tableau 1.

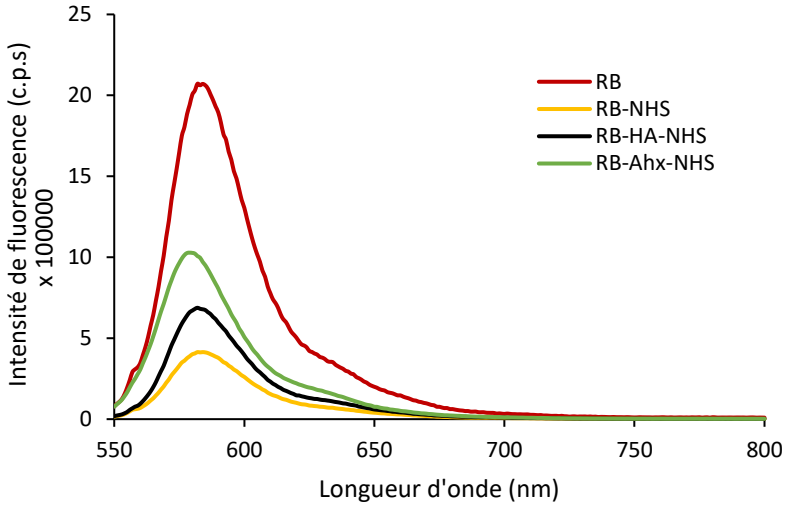

Figure 190: Spectre d'émission de fluorescence du RB et ses dérivés dans l'éthanol. $\lambda_{excitation}$= 560 nm, D.O = 0,2.

La diminution des coefficients d'absorption molaires et des rendements quantiques de fluorescence est due au remplacement de la fonction carboxylique par une fonction ester ou amide.

La durée de vie de fluorescence est très courte. C'est le cas des fluorescéines [2]. La courte durée de vie du RB et ses dérivés est due à la présence des atomes lourds qui favorisent le croisement intersystème vers l'état triplet.

Le **Tableau 32** regroupe les caractéristiques photophysiques du RB et de ses dérivés dans l'éthanol.

Tableau 32 : Caractéristiques photophysiques du RB et de ses dérivés dans l'éthanol

Echantillons	$\tau_{fluorescence}$ du RB (ns)	$\varepsilon\,\lambda max$ (L/mol.cm)	Φ_{fluo}	Φ_{Δ}
RB	0,63	126139 (λmax = 558 nm)	0,15	0,68
RB-HA-NHS	0,59	97487 (λmax = 570 nm)	0,07	0,76
RB-Ahx-NHS	0,60	75391 (λmax = 570 nm)	0,08	0,72
RB-NHS	0,50	43890 (λmax = 570 nm)	0,05	0,74

La durée de vie de fluorescence est enregistrée après excitation à 470 nm. Les spectres d'émission d'oxygène singulet sont obtenus après excitation à 558 nm (longueur d'onde d'absorption maximale du RB). Nous pouvons constater que la modification de la fonction carboxylique ne modifie pas beaucoup la durée de vie de fluorescence. En revanche, le rendement quantique de fluorescence est divisé par 2 entre le RB et ses dérivés. Les coefficients d'extinction molaires sont similaires pour RB et RB couplés au bras espaceur, en revanche, ils sont divisés par 2 par RB-NHS. Il est intéressant de noter que les rendements quantiques de formation d'$^1O_2$ sont meilleurs pour les dérivés que pour RB.

II.7 Couplage du RB et de ses dérivés avec les AGuIX.

Après l'étude photophysique des précurseurs RB, ils sont couplés sur les AGuIX. Les AGuIX Tb ou Gd sont dispersées dans l'eau (Tb=50 mM). Après une heure de stabilisation, la solution est ajustée à un pH=8 (NaOH (0,5 M)) puis 0,06 équivalent en mol % en lanthanide de RB-NHS ou RB-HA-NHS ou RB-Ahx-NHS dissous dans 5 % DMSO par rapport au volume total de la solution, sont ajoutés à la solution d'AGuIX Tb sous agitation, goutte à goutte (20 min, 5 ajouts). Après 3 heures d'agitation, les AGuIX Tb ou Gd sont diluées jusqu'à [Tb] ou [Gd]=10 mM.

La solution finale de NPs est purifiée par filtration tangentielle sur membrane Vivaspin® ayant un seuil de 5 kDa. Ces membranes conservent les particules au-dessus de 5KDa et éliminent les molécules plus petites dans le filtrat. Plusieurs cycles de filtration tangentielle sont effectués à 4500 tour/min à une accélération 5 jusqu'à l'obtention d'un filtrat transparent. Le filtrat est suivi par absorption. D'après une courbe d'étalonnage, le couplage des RB avec les AGuIX Tb ou Gd est considéré total lorsque le filtrat ne montre aucune absorption des précurseurs. Le rapport Tb ou Gd : RB (ou RB dérivé) est égal à 16 :1.

Six différentes NPs sont ainsi obtenues :

- AGuIX Tb@RB
- AGuIX Tb@HA-RB
- AGuIX Tb@Ahx-RB
- AGuIX Gd@RB
- AGuIX Gd@HA-RB
- AGuIX Gd@Ahx-RB

II.7.1 Etudes des AGuIX Tb

II.7.1.1 Spectres d'absorption

La **Figure 191** montre les spectres d'absorption du RB, AGuIX Tb et des AGuIX Tb couplées au RB et ses dérivés. Un décalage bathochrome par rapport à l'absorption du RB seule est observé avec un petit élargissement entre 460 nm et 620 nm. Cela est en faveur d'un couplage covalent du RB et de ses dérivées sur les AGuIX.

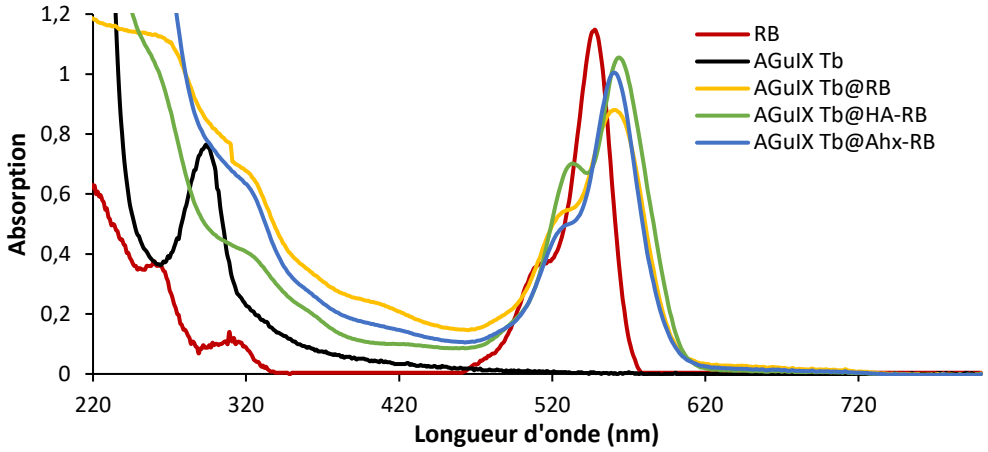

Figure 191 : Spectres d'absorption du RB, AGuIX Tb et des AGuIX Tb couplées au RB et ses dérivés dans l'eau. [RB : Tb] = [1 : 16] en mol

II.7.1.2 Spectres d'émission de luminescence

La **Figure 192** montre les spectres d'émission de luminescence des AGuIX Tb, et des AGuIX Tb couplé aux RB et ses dérivés à la même concentration.

Nous pouvons noter une diminution de l'intensité de luminescence des AGuIX Tb couplés au RB avec et sans bras espaceur comparée à celle des AGuIX seules. Ceci est en faveur d'un transfert d'énergie après excitation du Tb, entre le Tb et le RB. Ce transfert semble plus important pour les NPs dans lesquelles le RB est couplé *via* un bras espaceur (HA et Ahx).

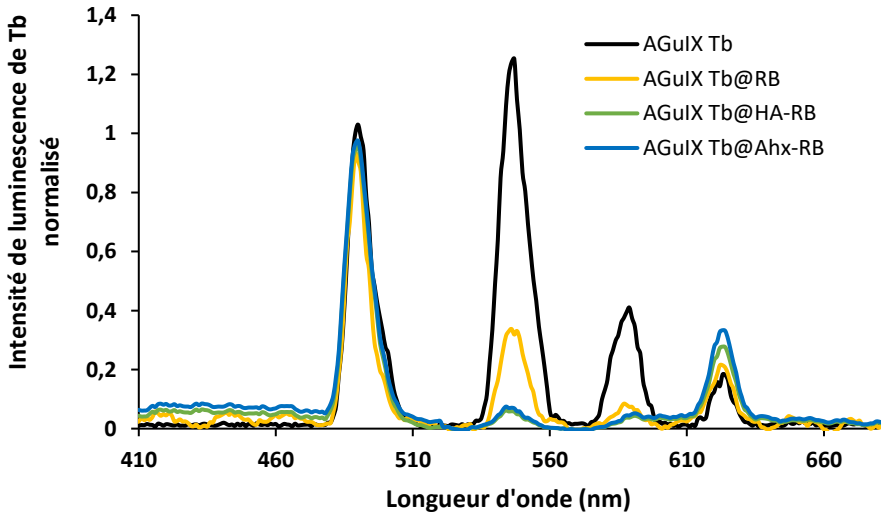

Figure 192 : Spectres d'émission de luminescence du RB, AGuIX Tb et des AGuIX Tb couplées au RB et de ses dérivés dans l'eau. [RB :Tb] = [1 : 16] en mol, délai 50 µs. $\lambda_{excitation}$ = 351 nm.

II.7.1.3 Durée de vie et rendement quantique de RB et des AGuIX Tb-RB

Le **Tableau 33** regroupe les caractéristiques photophysiques de RB, AGuIX Tb, AGuIX Tb@RB, AGuIX Tb@HA-RB, AGuIX Tb@Ahx-RB. $\tau_{luminescence}$ = Durée de vie de luminescence, et ΦΔ= rendement quantique d'$^1O_2$, et Φf= rendement quantique de fluorescence.

Tableau 33 : Caractéristiques photophysiques du RB, AGuIX Tb, AGuIX Tb@RB, AGuIX Tb@HA-RB, AGuIX Tb@Ahx-RB dans D_2O

Echantillons	$\tau_{fluorescence\ du\ RB}$ (ns)	$\tau_{luminescence}$ du Terbium (µs)	ΦΔ $\lambda_{excitation}$= 558 nm	ΦΔ $\lambda_{excitation}$= 351 nm	Φf $\lambda_{excitation}$= 558 nm
RB	0,63	-	0,67	0,00	0,15
AGuIX Tb	-	2000	0,00	0,00	0,00
AGuIX Tb@RB	6,3	650	0,68	0,35	0,13
AGuIX Tb@HA-RB	7,0	280	0,64	0,37	0,12
AGuIX Tb@Ahx-RB	6,1	310	0,67	0,34	0,13

La durée de vie de fluorescence est enregistrée après excitation à 470 nm. Les spectres d'émission d'oxygène singulet sont obtenus après excitation à 558 nm (longueur d'onde d'absorption maximale du RB) et 351 nm (longueur d'onde d'excitation du Terbium). Nous pouvons constater une augmentation d'environ un facteur 10 de $\tau_{fluorescence}$ du RB une fois qu'il est couplé aux NPs. Concernant les rendements quantiques de fluorescence enregistrés à 558 nm, nous ne remarquons pas de variation significative entre le RB seul et celui couplés aux AGuIX. La formation d'$^1O_2$ à 558 nm est identique pour le RB seul ou couplé aux NPs *via* et *sans* un bras espaceur indiquant la conservation de cette propriété après couplage au NPs. La formation d'$^1O_2$ à 351 nm, longueur d'onde d'excitation du Terbium, est identique pour toutes les NPs *via* et *sans* un bras espaceur, mais ces rendements sont la moitié de ceux après excitation à 558 nm obtenue après excitation. Mais vue que le RB n'absorbe pas sur 351 nm, et qu'il y a une production d'$^1O_2$, nous pouvons conclure qu'il y a un effet X-PDT.

II.7.2 Etude photophysique des AGuIX Gd

II.7.2.1 Spectres d'absorption

La **Figure 193** montre les spectres d'absorption de RB, AGuIX Gd et des AGuIX couplés au RB et ses dérivés. Un décalage bathochrome de 15 nm par rapport à l'absorption du RB seule ($\lambda_{excitation}$=558 nm) est observé avec un petit élargissement entre 460 nm et 620 nm. Un large élargissement dans l'UV est probablement dû au couplage avec les AGuIX chélatées au Gadolinium. Cela est en faveur d'un couplage covalent du RB et de ses dérivées sur les AGuIX.

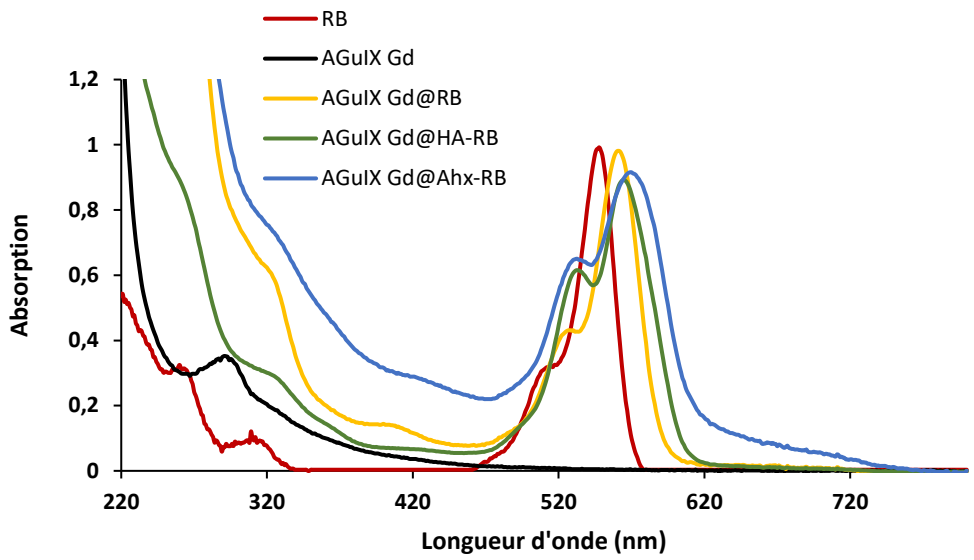

Figure 193 : Spectres d'absorption du RB, AGuIX Gd et des AGuIX couplées au RB et ses dérivés dans l'eau. [RB : Gd] = [1 : 16] en mol

II.7.2.2 Spectres d'émission de luminescence

La **Figure 194** montre les spectres d'émission de luminescence des AGuIX Gd, et des AGuIX Gd couplé aux RB et ses dérivés après excitation à 273 nm. Nous pouvons observer une diminution de luminescence du Gadolinium lorsque le RB est couplé aux NPs ce qui confirme un transfert d'énergie entre Gd et RB. Ce transfert semble plus important pour les nanoparticules dans lesquelles le RB est couplé *via* un bras espaceur (HA et Ahx).

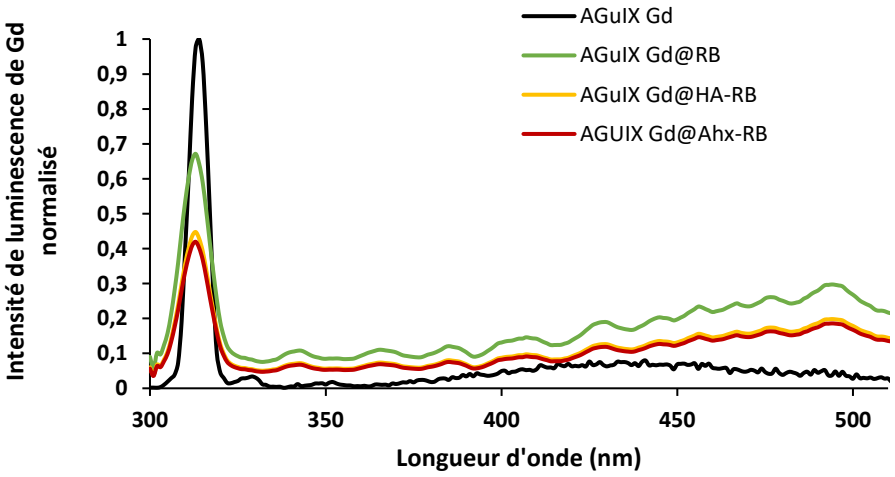

Figure 194: Spectre d'émission du RB, AGuIX Gd et des AGuIX couplé au RB et ses dérivés dans l'eau. [RB :Gd] = [1 :16] en mol,. $\lambda_{excitation}$ = 273 nm, délai 50 µs.

Le **Tableau 34** regroupe les caractéristiques photophysiques de RB, AGuIX Gd, AGuIX Gd@RB, AGuIX Gd@HA-RB, AGuIX Gd@Ahx-RB

Tableau 34 : Caractéristiques photophysiques de RB, AGuIX Gd, AGuIX Gd@RB, AGuIX Gd@HA-RB, AGuIX Gd@Ahx-RB dans D_2O

Echantillons	$\tau_{fluorescence\ du\ RB}$ (ns)	$\tau_{luminescence\ du\ Gadolinium}$ (µs)	ΦΔ $\lambda_{excitation}$= 558 nm	ΦΔ $\lambda_{excitation}$= 273 nm	Φf $\lambda_{excitation}$= 558 nm
RB	0,63	-	0,67	0,67	0,15
AGuIX Gd	-	2400	0,00	0,00	0,00
AGuIX Gd@RB	6,3	330	0,64	0,25	0,14
AGuIX Gd@HA-RB	6,6	290	0,60	0, 27	0,11
AGuIX Gd@Ahx-RB	6,8	330	0,61	0,31	0,10

La durée de vie de fluorescence est enregistrée après excitation à 470 nm. Les spectres d'émission d'oxygène singulet sont obtenus après excitation à 558 nm (longueur d'onde d'absorption maximale du RB) et 273 nm (longueur d'onde d'excitation du Gadolinium). Nous pouvons constater une augmentation d'environ un facteur 10 de $\tau_{fluorescence}$ du RB une fois qu'il est couplé aux NPs. Concernant les rendements quantiques de fluorescence enregistrés à 558 nm, nous ne remarquons pas de variation significative entre le RB seul et ceux couplés aux AGuIX. La formation d'$^1O_2$ à 558 nm est identique pour le RB seul ou couplé aux NPs *via* et *sans* un bras espaceur indiquant la conservation de cette propriété après couplage au NPs. La formation d'$^1O_2$ à 273 nm (longueur d'onde d'excitation du Gadolinium) est identique pour toutes les NPs *via* et *sans* un bras espaceur, mais ce rendement est la moitié de ceux obtenus après excitation à 558 nm. Nous pouvons conclure que la production d'$^1O_2$ est plus importante lorsque le RB est excité (effet PDT) que lorsque le Gd est excité (effet X-PDT).

II.7.2.3 Spectre Infra-rouge FT-IR

Les spectres FT-IR des NPs sont représentés dans la **Figure 195.** Nous ne pouvons pas observer des grandes différences entre les NPs non couplées et celles couplées. Cela est dû au fait que les bandes IR des NPs AGuIX Tb sont intenses dans les régions d'étirement des liaisons amides (1600-1800 cm^{-1} pour les C=O et 23200-3500 cm^{-1}) pour les NH), ce qui ne permet pas de mettre en évidence le couplage entre les NPs et les dérivés RB. Dans le futur, nous souhaitons réaliser une analyse en MALDI-TOF afin de bien caractériser le couplage.

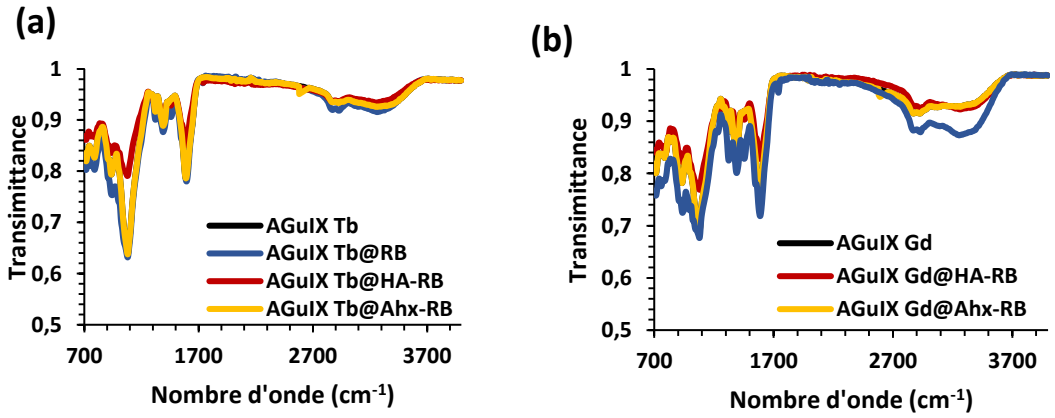

Figure 195 : Transformée de Fourrier FT-IR des NPs (a) AGuIX Tb, AGuIX Tb@RB, AGuIX Tb@HA-RB et AGuIX Tb@Ahx-RB (b) AGuIX Gd, AGuIX Gd@RB, AGuIX Gd@HA-RB et AGuIX Gd@Ahx-RB ..

II.7.2.4 Evaluation du potentiel zêta

La **Figure 196** montre le potentiel zêta des AGuIX Ln seules et celui des AGuIX Ln couplées au RB avec ou sans bras espaceur. Une augmentation du potentiel zêta en valeur absolue indique une augmentation de la stabilité des NPs en solution.

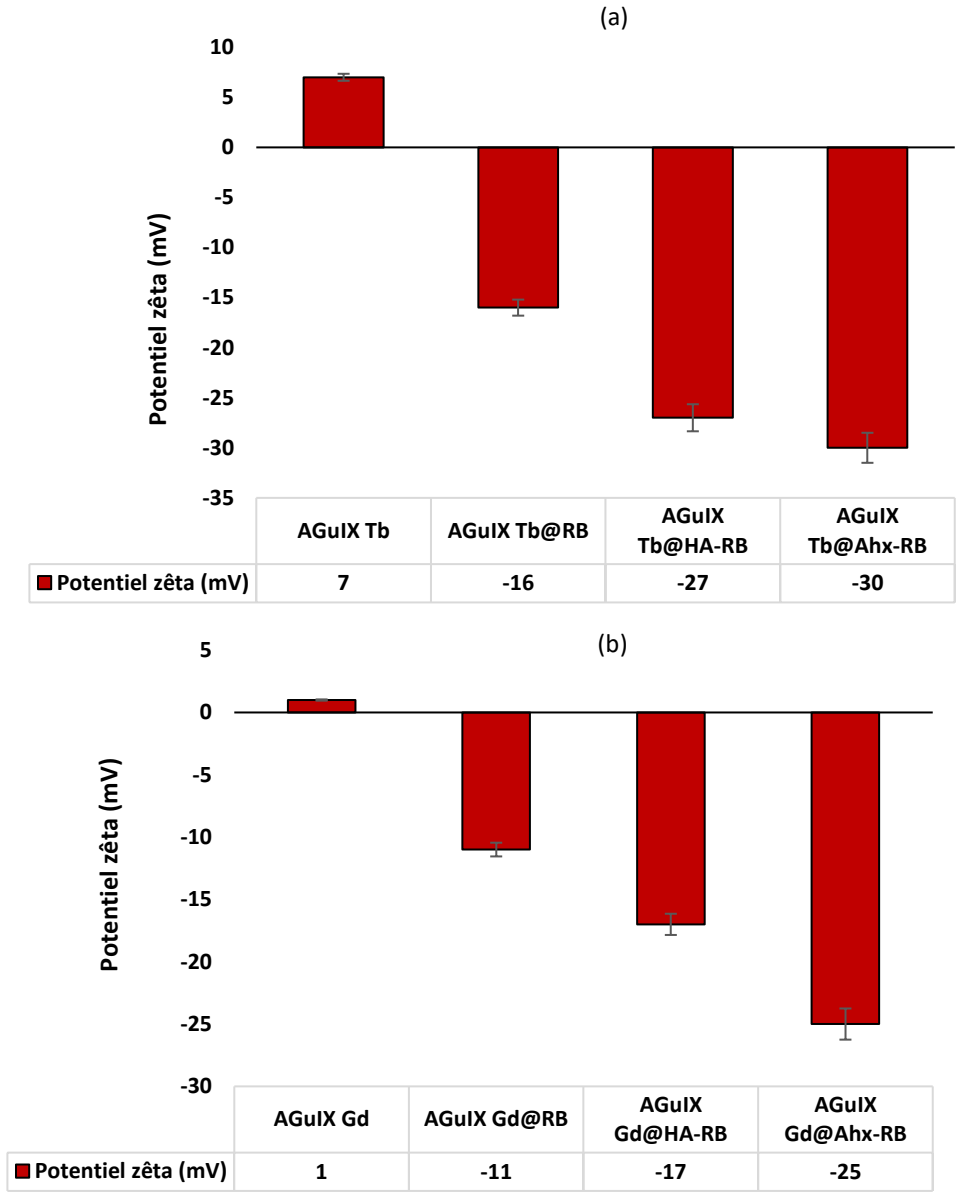

Figure 196 : (a) potentiel zêta des AGuIX Tb, AGuIX Tb@RB, AGuIX Tb@HA-RB et AGuIX Tb@Ahx-RB dans l'eau, (b) potentiel zêta d'AGuIX Gd, AGuIX Gd@RB, AGuIX Gd@HA-RB et AGuIX Gd@Ahx-RB dans l'eau, pH=7,2.

Le couplage du RB avec ou sans bras espaceur augmente la stabilité des NPs. L'augmentation de la charge négative est due au fait que pour un pH=7,2 les fonctions hydroxyles peuvent se transformer en anions (les fonctions hydroxyles du RB).

II.7.3 Taille des NPs par TDA-ICP-MS

La taille des NPs a été mesurée par TDA- ICP-MS (Analyse par Dispersion de Taylor couplé à un ICP-MS). Le TDA est couplé à l'ICP-MS. En ICP-MS, l'acquisition du $^{(158)}$Gd et ^{159}Tb

montre un pic à 500 ms (**Figure 197**). L'agrégation du RB entraîne un élargissement des pics correspondant aux Lanthanides. Les spectres sont représentés dans la **Figure 197** pour AGUIX Tb@RB et AGuIX Gd@RB comme exemple et les tailles indiquées dans le **Tableau 35**. Toutes présentent des diamètres inférieurs à 7 nm.

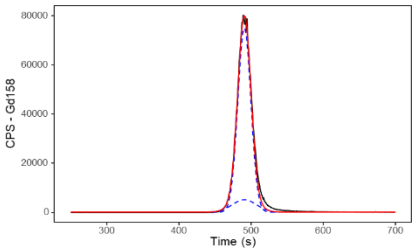

AGuIX Gd@RB

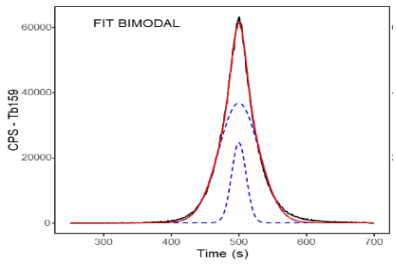

AGuIX Tb@RB

Figure 197 : Caractérisation TDA- ICP-MS des AGuIX Gd@RB, AGuIX Gd@HA-RB - AGuIX Tb@RB, AGuIX Tb@HA-RB

Tableau 35 : Diamètres des AGuIX Ln@RB, AGuIX Ln@HA-RB calculés par TDA

NPs	Diamètre en nm
AGuIX Tb@K(RB)	Population 1 : 4,9 nm (65,0%) Population 2 : 8,2 nm (35,0%)
AGuIX Gd@(RB)	Population 1 : 2,6 nm (98,3%) Population 2 : 0,2 nm (1,7%)
AGuIX Gd@HA-(RB)	Population 1 : 2,9 nm (97,0%) Population 2 : 30,0 nm (3,0%)
AGuIX Gd@Ahx-(RB)	Population 1 : 2,7 nm (94,6%) Population 2 : 12,0 nm (5,4%)
AGuIX Tb@(RB)	Population 1 : 3,1 nm (18,5%) Population 2 : 6,8 nm (81,5%)
AGuIX Tb@HA-(RB)	Population 1 : 3,7 nm (29,0%) Population 2 : 7,2 nm (71,0%)
AGuIX Tb@Ahx-(RB)	Population 1 : 3,0 nm (26,0%) Population 2 : 7,3 nm (74,0%)
AGuIX Tb	Population 1 : 1,0 nm (3,0%) Population 2 : 5,5 nm (97,0%)
AGuIX Gd	Population 1 : 1,8 nm (100%)

La taille des AGuIX Tb est inférieure à 10 nm. Nous observons 2 populations, tout comme l'AGuIX Tb. Une population serait composée d'AGuIX, l'autre serait composée d'un ensemble d'AGuIX. La différence entre les deux populations est peut-être due à un faible phénomène de stacking. Pour les AGuIX Gd avec le RB, il semblerait qu'il y ait des phénomènes d'agrégation entraînant une augmentation de la taille des NPs.

III. Ciblage actif

Dans cette partie nous nous intéressons au couplage de peptides sur les AGuIX pour un ciblage actif de NRP-1. Les deux peptides choisis sont le DKPPR et un peptide d'une séquence que nous nommerons XXXXX (pour des raisons confidentiel). Le DKPPR a déjà été déjà synthétisé par notre équipe et montre une affinité EC_{50}=11 µM pour NRP-1.

La synthèse se réalise en plusieurs étapes :

- Couplage de RB sur le NH_2 de la chaîne latérale d'une lysine
- Synthèse du peptide DKPPR sur support solide (SPPS)
- Couplage de la lysine(RB) sur le peptide en croissance sur support solide
- Couplage du bras maléimide au peptide en croissance
- Modification des fonctions amine en fonction thiol des AGuIX
- Couplage des AGuIX au peptide (**Figure 198**)

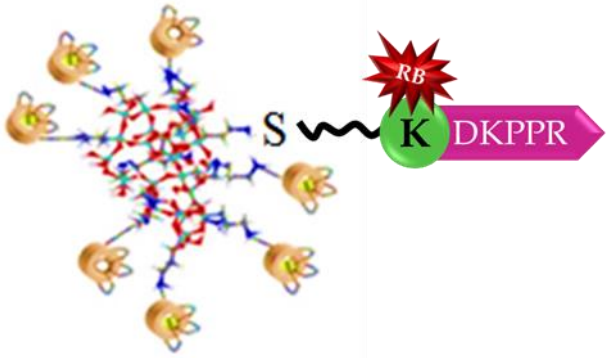

Figure 198: Représentation d'AGuIX RB@Maléimide-K(RB)DKPPR.

III.1 Synthèse du Fmoc-Lysine-(RB)

RB-NHS **1** (580 mg ; 0,54 mmol ; 1 équivalent) est solubilisé dans 30 mL de DCM anhydre. Une solution de Fmoc-Lys-OH.HCl (222 mg ; 0,54 mmol ; 1 équivalent) dans 3 mL de DMF anhydre et de la triéthylamine (168 µL ; 1,08 mmol ; 2 équivalents) est ajoutée au milieu réactionnel. Ce dernier est laissé sous agitation pendant 24 heures à température ambiante et sous atmosphère inerte à l'obscurité **(Figure 199)**. Le solvant est évaporé sous pression réduite. Le produit est ensuite purifié par chromatographie flash sur gel de silice (éluant : DCM/EtOH, 90/10). Le produit désiré Fmoc-Lys(RB) **6** est obtenu sous la forme d'un solide rouge, avec une masse m = 610 mg (rendement 85%, pureté 98%).

La masse molaire de Fmoc-K(RB) est égale à 1324 g/mol. Par LC-MS, il est trouvé $[M+H]^+$ = 1324 g/mol, $([M+2H)/2]^+$ = 663 g/mol.

La pureté est analysée par HPLC à une longueur d'onde de détection en absorption UV-Visible λ=560 nm, avec un gradient passant de 95/5 à 0/100 (A/B, v/v) pendant 15 minutes, suivi de ACN isocratique 0/100 (A/B, v/v) pendant 10 minutes, puis un gradient de 0/100 à 95/5 (A/B, v/v) en 5 minutes (avec A = 95/5/0,1 (H_2O/ACN/MeOH, v/v/v) et B = 100/0,1 (ACN/MeOH ; v/v)).

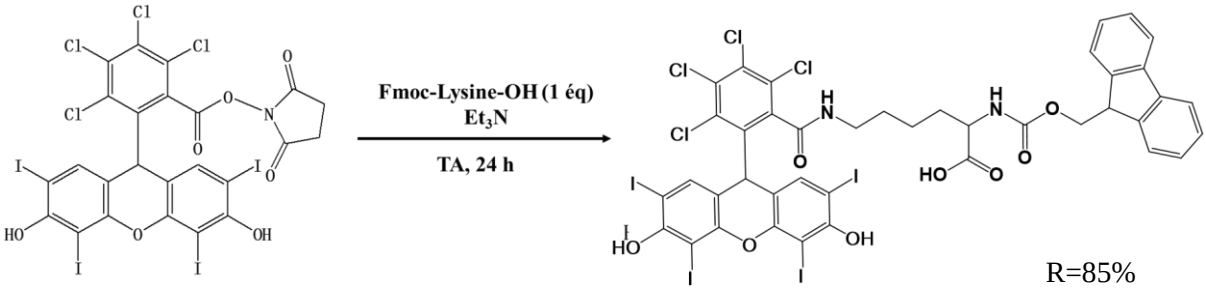

6

Figure 199 : Réaction de couplage entre RB-NHS 1 et Fmoc-Lys pour la synthèse de Fmoc-Lys(RB) 6.

III.2 Synthèse des peptides sur support solide (SPPS)

III.2.1 Protocole de synthèse de K(RB)DKPPR 8 et de K(RB)XXXXX 9

Les peptides H-K(Boc)D(OtBu)K(Boc)PPR(Pbf)-OH et XXXXX ont été synthétisés à l'aide du synthétiseur de peptides automatisé ResPepXL, avec une méthodologie Fmoc/tBu. Les chaînes latérales de l'arginine, de la lysine et de l'acide aspartique ont respectivement été protégées par des groupements 5-tert-butyl ester (O*t*Bu), *N*-tert-butyloxy carbonyl (Boc) et 2,2,4,6,7-pentamethyldihydrobenzofuran-5-sulfonyl (Pbf). Nous avons utilisé une résine Fmoc–Arg(Pbf)–Wang gonflée dans CH_2Cl_2. Pour éliminer le groupe Fmoc, nous avons utilisé de la pipéridine (20 % dans du DMF). Cette étape a été effectuée deux fois, une première pendant 4 min et une seconde pendant 7 min. Ensuite, l'acide aminé suivant a été greffé en ajoutant un excès de Fmoc-acide aminé-OH (6 équivalents), HBTU (5 équivalents), NMP (3 équivalents) et NMM (10 équivalents) dans du DMF. Cette étape a été répétée deux fois pendant 18 min. Les étapes de déprotection, de couplage ont été répétées jusqu'à la fin de la synthèse du peptide.

A l'issu de la synthèse, le peptide Fmoc-D(O*t*Bu)K(Boc)PPR(Pbf)-Wang a subi une déprotection de son extrémité *N*-terminale (Fmoc) par traitement avec une solution de DMF/pipéridine (80/20, v/v) sous agitation pendant 15 minutes. L'opération a été répétée deux fois supplémentaires afin de fournir le peptide sur résine D(O*t*Bu)K(Boc)PPR(Pbf)-Wang.

Le couplage de ce peptide D(O*t*Bu)K(Boc)PPR(Pbf)-Wang avec Fmoc- K(RB) **7** (2,00 équivalents) a été réalisé sous agitation pendant 4 jours.

Le peptide Fmoc-K(RB)-D(O*t*Bu)K(Boc)PPR(Pbf)-Wang a subi une déprotection de son extrémité *N*-terminale (Fmoc) par traitement avec une solution de DMF/pipéridine (80/20, v/v) sous agitation pendant 15 minutes. L'opération a été répétée deux fois supplémentaires afin de fournir le peptide sur résine K(RB)-D(O*t*Bu)K(Boc)PPR(Pbf)-Wang.

Enfin, le peptide sur résine K(RB)-D(O*t*Bu)K(Boc)PPR(Pbf)-Wang obtenu a été séché sous vide et son traitement avec une solution de TFA/TIPS/eau (92,5/5/2,5) pendant 2 h a permis la déprotection des chaînes latérales et le clivage du peptide de la résine. La résine a été filtrée et lavée avec 2 mL de TFA et 50 mL de DCM **(Figures 200 et 201)**. Le filtrat a été séché sous vide et lyophilisé.

Le peptide déprotégé brut K(RB)DKPPR **8** lyophilisé obtenu a été purifié par HPLC préparative (Rt = 11,2 min) en utilisant un gradient passant de 90/10 à 0/100 (A/B, v/v) pendant

15 minutes, suivi de ACN isocratique 0/100 (A/B, v/v) pendant 10 minutes, puis passage de 0/100 à 90/10 (A/B, v/v) en 5 minutes (avec A = 100/0,1 (H_2O/TFA, v/v) et B = 100/0,1 (ACN/TFA ; v/v)) pour une Masse molaire égale à 1695 g/mol vérifié par MS.

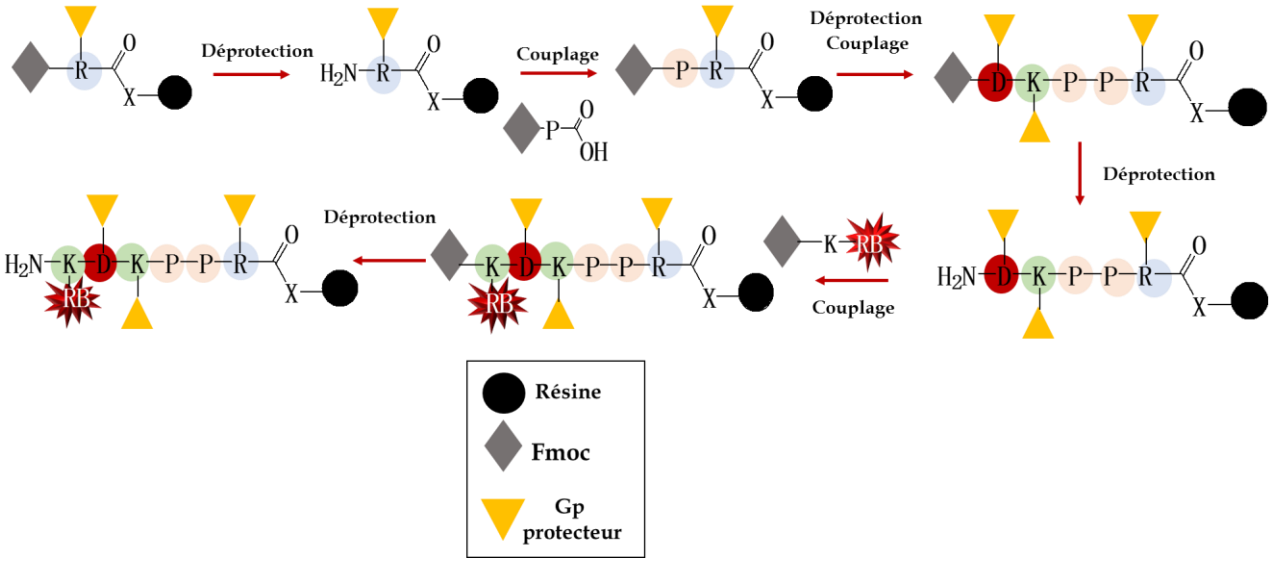

Figure 200 : Synthèse sur support solide du composé K(RB)DKPPR 8 : (a) N-déprotection : DMF/pipéridine (80/20, v/v), (b) couplage : HBTU/NMM/NMP et (c) clivage : TFA/TIPS/H_2O (92,5/5/2,5). Abréviations : TFA (acide trifluoroacétique) ; TIPS (triisopropylsilane)

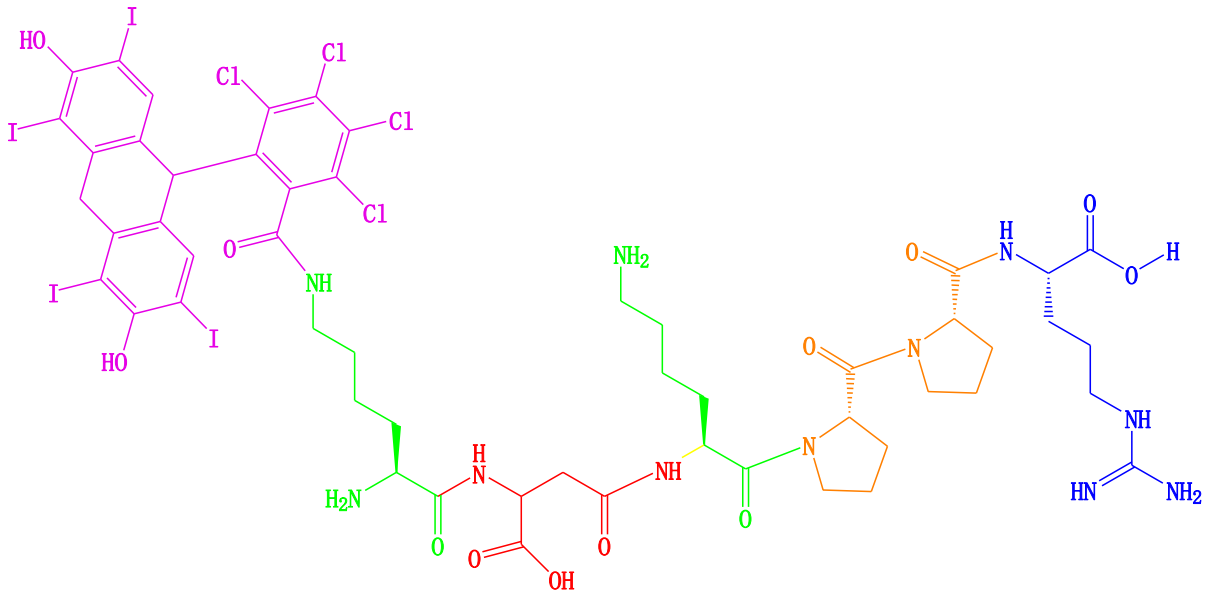

Figure 201 : Formule développée du composé K(RB)DKPPR 8

Le peptide déprotégé brut K(RB)XXXXX **9** lyophilisé obtenu a été purifié par HPLC préparative (Rt = 11,0 min) en utilisant un gradient passant de 90/10 à 0/100 (A/B, v/v) pendant 15 minutes, suivi de ACN isocratique 0/100 (A/B, v/v) pendant 10 minutes, puis passage de 0/100 à 90/10 (A/B, v/v) en 5 minutes (avec A = 100/0,1 (H_2O/TFA, v/v) et B = 100/0,1 (ACN/TFA ; v/v)).

Le produit pur K(RB)-XXXXX **9** a été isolé sous forme de poudre rose avec une masse m = 45 mg (rendement de 43% et pureté de 93%). L'analyse MS confirme l'obtention du produit **9**.

III.2.2 Protocole de synthèse de Maléimide-K(RB)DKPPR 10

Le peptide sur résine K(RB)-D(OtBu)K(Boc)PPR(Pbf)-Wang obtenu comme décrit dans la partie précédente a été séché sous vide puis couplé en utilisant un triple excès de l'acide maléimidohexanoïque (3 équivalents) et des réactifs d'activation HBTU (3 équivalents), NMP (3 équivalents) et NMM (9 équivalents) dans du DMF. Le mélange est laissé sous agitation pendant 48 h à température ambiante dans le noir.

Enfin, le peptide sur résine Maléimide-K(RB)-N(trt)K(Boc)R(Pbf)T(*t*Bu)R(Pbf)-Wang obtenu a été séché sous vide et son traitement avec une solution de TFA/TIPS/eau (92,5/5/2,5) pendant 2 h a permis la déprotection des chaînes latérales et le clivage du peptide de la résine. La résine a été filtrée et lavée avec 2 mL de TFA et 50 mL de DCM **(Figure 200)**. Le filtrat a été séché sous vide et lyophilisé.

Le peptide déprotégé brut Maléimide K(RB)DKPPR **10** lyophilisé obtenu a été purifié par HPLC préparative (Rt = 11,2 min) en utilisant un gradient passant de 90/10 à 0/100 (A/B, v/v) pendant 15 minutes, suivi ACN isocratique 0/100 (A/B, v/v) pendant 10 minutes, puis un gradient de 0/100 à 90/10 (A/B, v/v) en 5 minutes (avec A = 100/0,1 (H_2O/TFA, v/v) et B = 100/0,1 (ACN/TFA ; v/v)).

Le produit pur Maléimide-K(RB)-DKPPR **10** a été isolé sous forme de poudre rose avec une masse m = 50 mg (rendement de 56% et pureté de 92%). L'analyse MS confirme l'obtention du produit **10** avec des fragmentations correspondant à $[M+H]^+$=1887 g/mol, $[(M+2H)/2]^+$ = 945 g/mol.

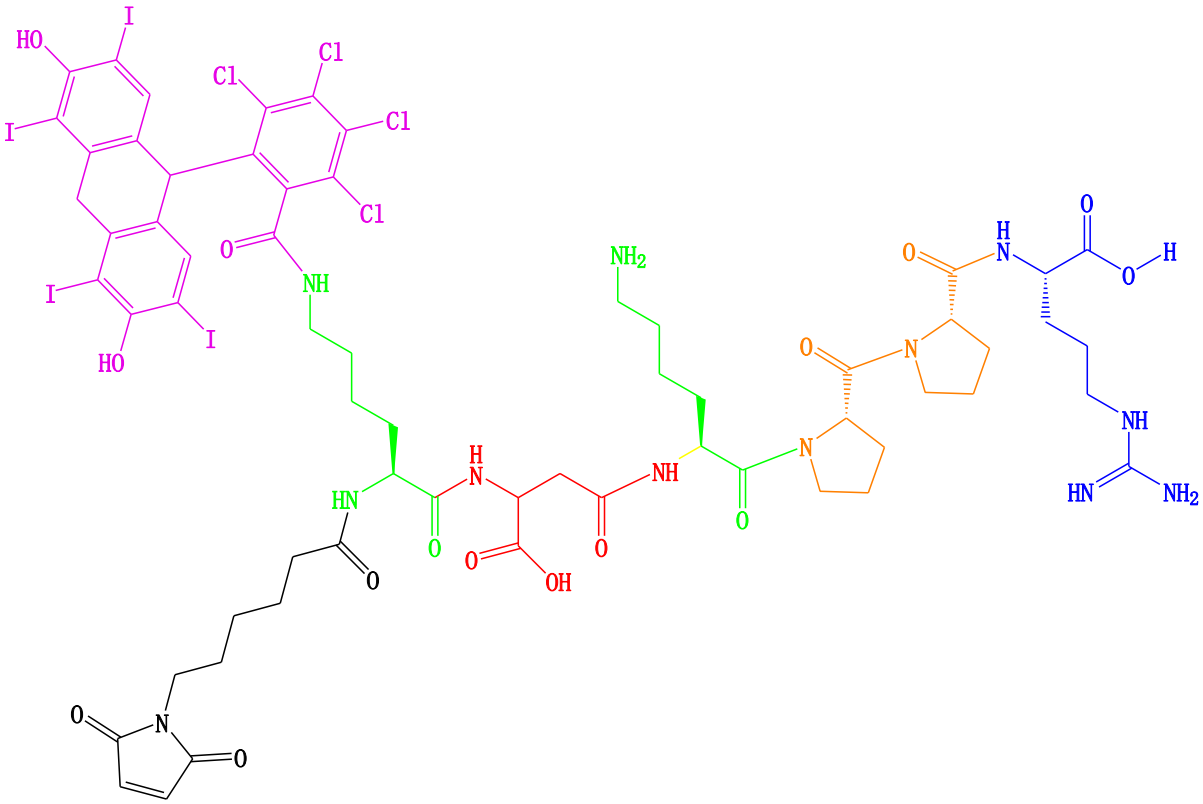

Figure 202 : Formule développée du composé Maléimide- K(RB)DKPPR 10

III.2.3 Protocole de synthèse de Maléimide-K(RB)XXXXX 11

La synthèse de Maléimide-K(RB)XXXXX est fait suivant le même protocole de synthèse de Maléimide-K(RB)DKPPR.

Le peptide déprotégé brut Maléimide K(RB)XXXXX **11** lyophilisé obtenu a été purifié par HPLC préparative (Rt = 10,08 min) en utilisant un gradient passant de 90/10 à 0/100 (A/B, v/v) pendant 15 minutes, suivi de ACN isocratique 0/100 (A/B, v/v) pendant 10 minutes, puis passage de 0/100 à 90/10 (A/B, v/v) en 5 minutes (avec A = 100/0,1 (H_2O/TFA, v/v) et B = 100/0,1 (ACN/TFA ; v/v)).

Le produit pur Maléimide-K(RB)-XXXXX **11** a été isolé sous forme de poudre rose avec une masse m = 40 mg (rendement de 45% et pureté de 91%). L'analyse MS confirme l'obtention du produit **11.**

III.2.4 Réaction de couplage de Fmoc-Lys(RB) avec l'acide maléimidohexanoïque

Fmoc-Lys(RB)-OH couple à l'acide maléimidohexanoïque est synthétisé pour être ensuite greffé aux àAGuIX. AGuIX@Maléimide-K(RB)-OH est considéré comme un contrôle par rapport à AGuIX@Maleimide-K(RB)-peptide-OH.

La fonction amine de la lysine est déprotégée à l'aide d'une solution 80:20, DMF:pipéridine (8 mL/2 mL). La solution est agitée pendant 4 h. Une extraction est réalisée avec un mélange eau/chloroforme (eau/chloroforme, 5 mL/10 mL). La phase organique est recueillie puis évaporée sous pression réduite.

Le H-Lys(RB)-OH (100 mg ; 93 µmol) est couplé à l'acide maléimidohexanoïque (3 équivalents) à l'aide des réactifs d'activation HBTU (N,N,N',N'-hexafluorophosphate tétraméthyl-O-(1H -benzotriazole-1-yl)uronium, 3 équivalents), NMP (N-méthylpyrrolidinone, 3 équivalents) et NMM (N-méthylmorpholine, 9 équivalents) dans le DMF qui sont agité 10 minute avant etre ajoute au H-Lys(RB)-OH. Le mélange est laissé sous agitation pendant 48 heures à température ambiante, à l'obscurité, dans un milieu inerte.

Le solvant est évaporé sous pression réduite. Le produit est purifié par HPLC préparative (Rt = 14,9 min) selon un gradient allant de 90/10 à 0/100 (A/B, v/v) pendant 15 minutes, suivi d'un isocratique 0/100 (A/B , v/v) pendant 10 minutes, puis passant de 0/100 à 90/10 (A/B, v/v) en 5 minutes (avec A = 100/0,1 (H2O/TFA, v/v) et B = 100/0,1 (ACN/TFA ; v/v)), A est H2O (0,1 % TFA) et B est ACN (0,1 %TFA).

Le produit pur Maléimide-K(RB)-OH, produit 12 (**Figure 203**) est isolé sous forme d'une poudre rose de masse m = 80 mg (rendement de 80 % et pureté de 95 %). L'analyse MS confirme l'obtention du produit avec des fragmentations correspondant à [M+H]+=1295 g/mol.

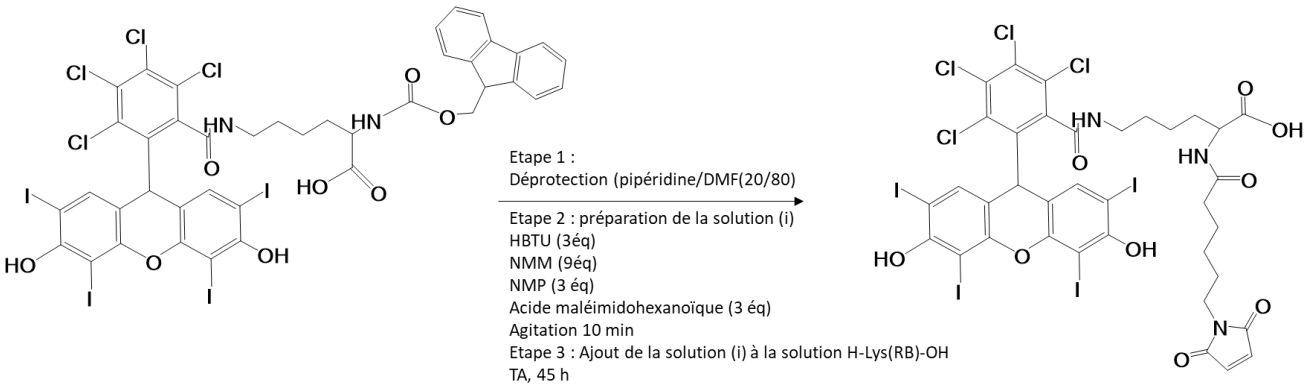

Figure 203 : Réaction de couplage entre l'acide-6-maléimidohexanoïque et la Fmoc-Lys(RB)-OH.

III.2.5 Etude photophysique des précurseurs de couplage

III.2.5.1 Spectres d'absorption

La **Figure 204** montre les spectres d'absorption du RB et des dérivés intermédiaires, K(RB)-DKPPR, K(RB)-XXXXX, maléimide-K(RB)-DKPPR, et maléimide-K(RB)-XXXXX. A une même concentration de 10 µM, ces composées montrent un décalage bathochrome de 6 à 10 nm dû à la modification de la fonction acide carboxylique. Une importante diminution du coefficient d'extinction molaire au maximum d'absorption (λ=558 nm) est observée. Le couplage des peptides au RB diminue ~25 fois le coefficient d'extinction molaire au maximum d'absorption (λ=570 nm). Cela peut être dû à la diminution de la vitesse de la libre rotation de ces composés et de l'encombrement à proximité du RB.

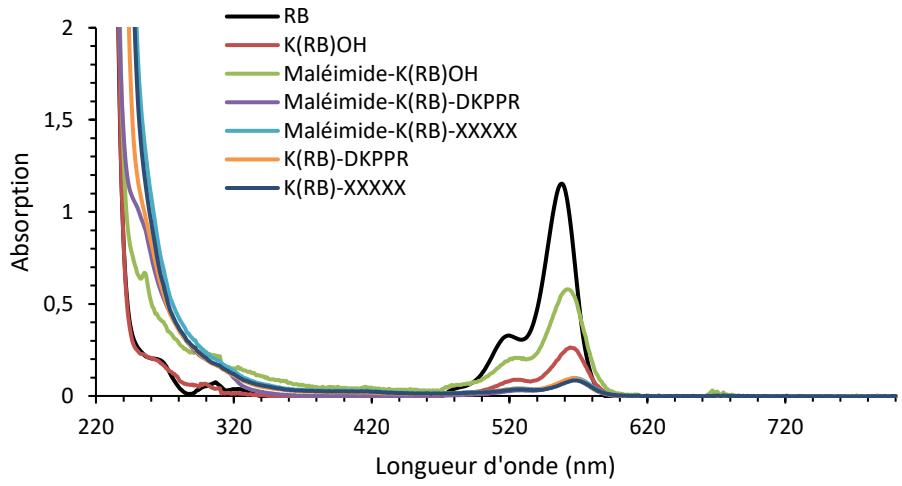

Figure 204 : Spectres d'absorption du RB et des dérivés dans l'éthanol, 10 µM.

III.2.5.2 Spectres d'émission de fluorescence

La **Figure 205** montre les spectres d'émission de fluorescence du RB et de ses dérivés. Les spectres d'émission de fluorescence entre 550 nm et 700 nm ont un aspect similaire sans aucun décalage mais avec une intensité décroissante allant de RB> K(RB)> Maléimide-K(RB)OH > Maléimide-K(RB)-DKPPR= Maléimide-K(RB)-XXXXX= K(RB)-DKPPR= K(RB)-XXXXX. Les rendements quantiques de fluorescence sont calculés et présentés dans le **Tableau 34**.

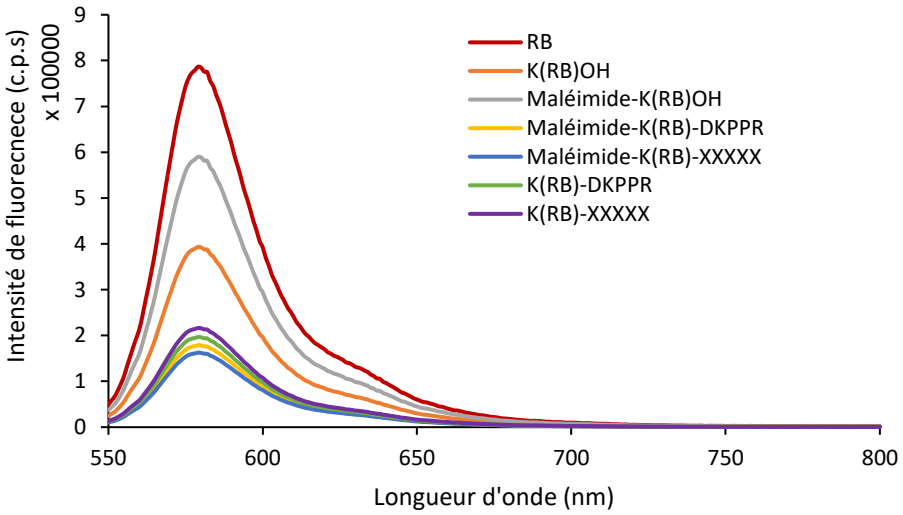

Figure 205 : Spectre d'émission de la RB et leurs dérivés dans l'éthanol. $\lambda_{excitation}$=558 nm à une concentration de 10 µM.

Le **Tableau 36** regroupe les caractéristiques photophysiques du RB, RB-peptide et de leurs dérivés dans l'éthanol.

Tableau 36 : Caractéristiques photophysiques du RB, RB-peptide et de leurs dérivés dans l'éthanol

Echantillon	$\varepsilon_{\lambda max}$ (L/mol.cm)	$\tau_{fluorescence}$ de RB (ns)	Φ_{fluo} $\lambda_{excitation}$= 558 nm	Φ_{Δ} $\lambda_{excitation}$= 558 nm
RB	126139 (λmax = 558 nm)	0,63	0,15	0,68
K(RB)OH	25954 (λmax = 570 nm)	0,62	0,10	0,88
Maléimide-K(RB)OH	55595 (λmax = 570 nm)	0,62	0,16	0,82
Maléimide-K(RB)DKPPR	2108 (λmax = 570 nm)	0,92	0,07	0,65
Maléimide-K(RB)XXXXX	3796 (λmax = 570 nm)	1,02	0,05	0,80
K(RB)DKPPR	6356 (λmax = 570 nm)	0,40	0,06	0,75
K(RB)XXXXX	4596 (λmax = 570 nm)	0,41	0,06	0,78

Le RB, le K(RB)OH et le Maléimide K(RB)OH présentent la même durée de vie de fluorescence ; cette durée de vie diminue de l'ordre de 0,2 ns pour le RB couplé aux peptides sans maléimide alors qu'il augmente de 0,27 ns avec le greffage du maléimide sans et avec peptide. Cela peut être dû à la dicarboxymide cyclique du maléimide.

Concernant les rendements quantiques de fluorescence, ils diminuent d'un facteur 2 lorsque le peptide est greffé. Les rendements quantiques d'$^1O_2$ sont très élevés et le greffage du peptide n'engendre pas de diminution.

III.3 Modification des nanoparticules

III.3.1 Synthèse des AGuIX SH@Maléimide-K(RB)OH

Les NPs AGuIX sont modifiées pour pouvoir greffer le peptide. Pour effectuer le couplage sur le bras maléimide des K-RB-peptide et K-RB, il est nécessaire de transformer les fonctions amine en fonctions thiol **(Figure 206)**. Nous utilisons pour ce faire l'agent traut (2-Iminothiolane). Les AGuIX Ln^{3+} ($[Ln^{3+}]$ = 50 mM) sont dispersées en solution dans l'eau pendant une heure. Elles sont ensuite ajustées à un pH=8 avec une solution NaOH (0,05 M). La solution traut (2-Iminothiolane hydrochloride) (1 équivalent en nombre de mole % au lanthanide) est dissoute dans l'eau puis ajoutée petit à petit à la solution AGuIX. Le mélange est laissé sous agitation pendant une heure. Une centrifugation tangentielle à 4500 tour/min accélération 5 est réalisée. La purification est finie lorsqu'aucun pic d'absorption spécifique du traut n'est observé à 248 nm. D'après une courbe d'étalonnage, il y aurait un SH pour 8 Ln^{3+}.

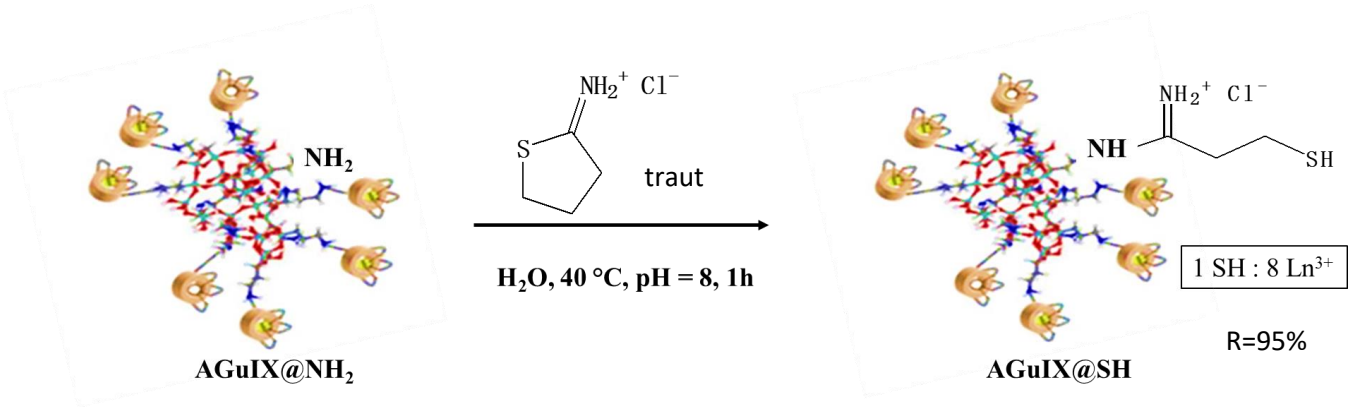

Figure 206 : Schéma de modification des fonctions amine des AGuIX.

III.3.2 Synthèse des AGuIX SH@Maléimide-K(RB)-DKPPR, AGuIX SH@Maléimide-K(RB)-XXXXX

Les NP AGuIX@SH sont dispersées dans l'eau distillée en milieu basique (0,5 M NaOH, pH 8), puis le maléimide-K(RB)-DKPPR dissous dans 5% en volume DMSO par rapport au volume total, est ajouté en cinq fois à l'obscurité et sous agitation pendant 30 min. La solution est laissée sous agitation pendant 2 heures supplémentaires ($[Ln^{3+}]$ = 50 mM).

La solution est ensuite diluée dans de l'eau pour atteindre un rapport DMSO/eau de 4 % et purifiée par filtration tangentielle comme décrit précédemment. La solution des NPs est concentrée à environ $[Ln^{3+}]$ = 100 mM, le pH est ajusté à 7,2 et, enfin, la solution est lyophilisée pour le stockage **(Figure 207)**.

Grâce à une courbe d'étalonnage en absorption, nous pouvons déterminer qu'il y a environ 1 RB@peptide pour 16 Ln^{3+}, soit 1 RB@peptide pour 1-2 NPs.

Le même protocole est utilisé pour la synthèse et la caractérisation des AGuIX SH@Maléimide-K(RB)-XXXXX.

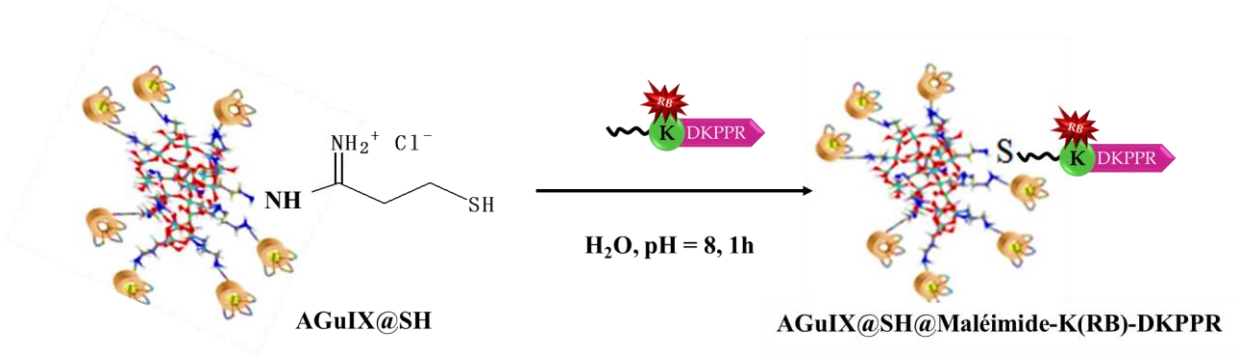

Figure 207 : Réaction de couplage entre AGuIX SH et Maléimide-K(RB)-DKPPR

III.3.2.1 AGuIX Tb

III.3.2.1.1 Spectres d'absorption

La **Figure 208** montre les spectres d'absorption de RB, AGuIX Tb et des AGuIX Tb couplées au RB et ses dérivés. Un décalage bathochrome d'environ 20 nm par rapport à l'absorption du RB seule est observé avec un petit élargissement entre 460 nm et 620 nm. Un large élargissement dans l'UV est probablement dû au couplage avec les AGuIX Tb. Cela est en faveur d'un couplage covalent du RB et de ses dérivées sur les AGuIX.

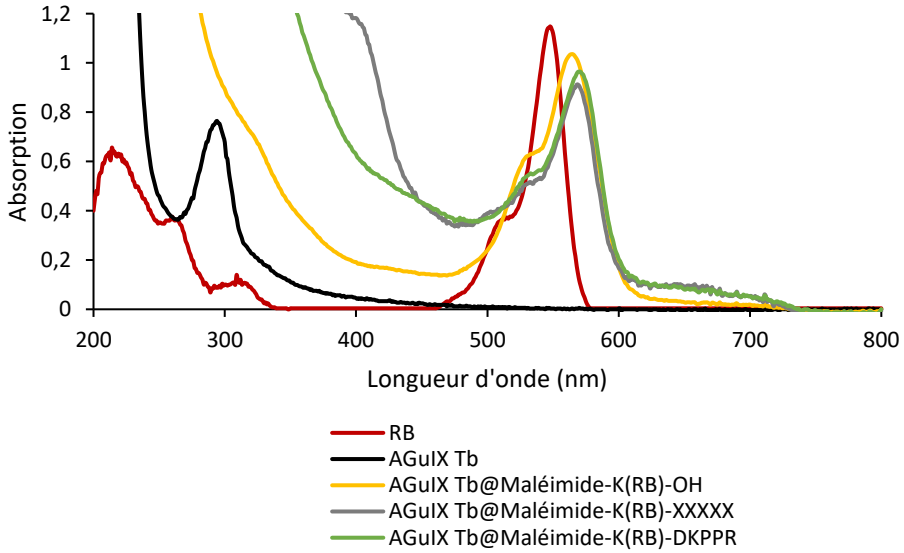

Figure 208 : Spectre d'absorption du RB, AGuIX Tb et des AGuIX Tb couplées au RB et ses dérivés dans l'eau. [RB :Tb] = [1 :16] en mol

III.3.2.1.2Spectres d'émission de luminescence

La **Figure 209** montre les spectres d'émission de luminescence d'AGuIX Tb, et des AGuIX Tb couplé aux Maléimide-K(RB)-peptide, K(RB)-peptide et Maléimide-K(RB)OH. La diminution de luminescence du terbium confirme la possibilité d'un transfert FRET entre Tb et RB. Une élongation d'émission de luminescence est observée entre 580 nm et 610 nm

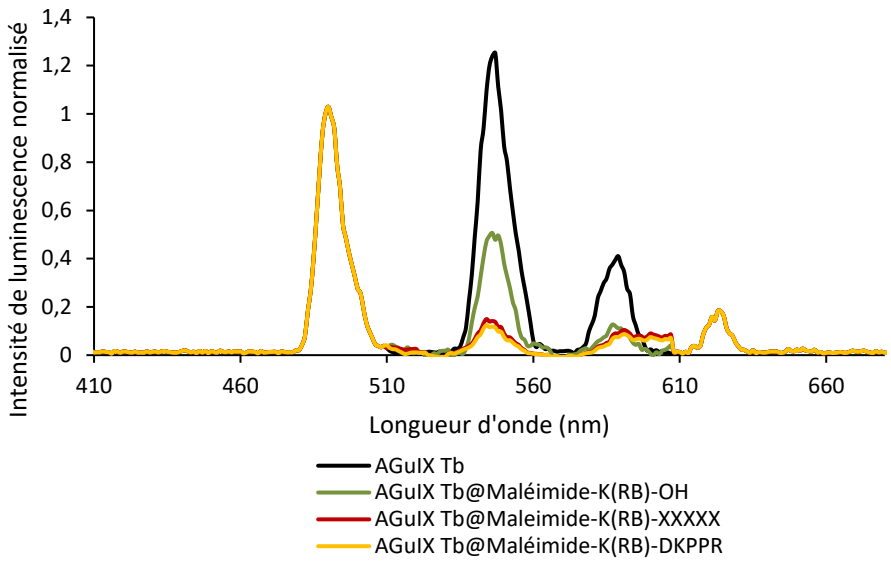

Figure 209: Spectre d'émission du RB, AGuIX Tb et des AGuIX Tb couplées au RB et ses dérivés dans l'eau. [RB :Tb]= [1 :16] en mol. $\lambda_{excitation}$=351 nm, délai 50 µs.

Le **Tableau 37** donne les caractéristiques photophysiques d'AGuIX Tb, et des AGuIX Tb couplées aux Maléimide-K(RB)-peptide, K(RB)-peptide et Maléimide-K(RB)-OH.

Tableau 37 : Caractéristiques photophysiques d'AGuIX Tb, et des AGuIX Tb couplé aux Maléimide-K(RB)-peptide, K(RB)-peptide et son intermédiaire Maléimide-K(RB)OH. $\lambda_{excitation\ de\ fluorescence}$ = 470 nm

Echantillons	$\tau_{fluorescence}$ (ns) RB	$\tau_{luminescence}$ (µs) Tb	ΦΔ $\lambda_{excitation}$= 558 nm	ΦΔ $\lambda_{excitation}$= 351 nm	Φf $\lambda_{excitation}$= 558 nm
RB	0,63	-	0,67	0,00	0,15
AGuIX Tb	-	2400	0,00	0,00	0,00
AGuIX Tb@maléimide-K(RB)-OH	3,1	470	0,65	0,34	0,13
AGuIX Tb@maléimide-K(RB)-DKPPR	2,8	345	0,68	0,36	0,11
AGuIX Tb@maléimide-K(RB)-XXXXX	5,6	259	0,62	0,31	0,10

La durée de vie de fluorescence est enregistrée après excitation à 470 nm.). Nous pouvons constater une augmentation de $\tau_{fluorescence}$ d'un facteur entre 5 et 10 du RB une fois qu'il est couplé aux NPs. Les rendements quantiques de fluorescence varient peu, que le RB soit seul ou couplé aux NPs. Les spectres d'émission d'oxygène singulet sont obtenus après excitation à 558 nm (longueur d'onde d'absorption maximale du RB) et 351 nm (longueur d'onde d'excitation du Terbium). La formation d'$^1O_2$ après excitation à 558 nm est identique pour le RB seul ou couplé aux NPs *via et sans* un bras espaceur, indiquant que le couplage covalent ne nuit pas à la formation d'$^1O_2$. Après excitation à 351 nm, ΦΔ est identique pour toutes les NPs mais deux fois moins importantes qu'après excitation à 558 nm après excitation. Nous pouvons

conclure que la production d'$^1O_2$ est plus importante lorsque le RB est excité (effet PDT) que lorsque le Tb est excité (effet X-PDT).

III.3.2.2 AGuIX Gd

III.3.2.3 Spectres d'absorption

La **Figure 210** montre le spectre d'absorption du RB, AGuIX Gd et des AGuIX Gd couplés au RB et ses dérivés. Un décalage bathochrome d'environ 20 nm par rapport à l'absorption du RB seule est observé avec un petit élargissement entre 460 nm et 620 nm. Un large élargissement dans l'UV est dû au couplage avec les AGuIX Gd. Cela est en faveur d'un couplage covalent du RB et de ses dérivés sur les AGuIX Gd.

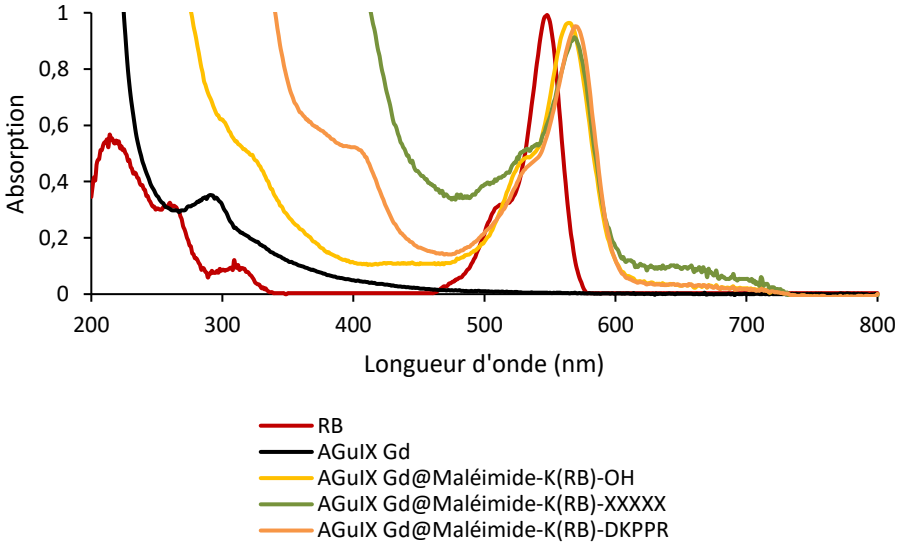

Figure 210 : Spectres d'absorption de RB, AGuIX Gd et des AGuIX Gd couplées au RB et aux peptides, 10 µM.

III.3.2.4 Spectres d'émission de luminescence

La **Figure 211** montre les spectres d'émission de luminescence d'AGuIX Gd, et des AGuIX Gd couplées aux Maléimide-K(RB)-peptide, K(RB)-peptide et son intermédiaire Maléimide-K(RB)-OH. La diminution de luminescence du gadolinium est en faveur d'un transfert d'énergie entre Gd et RB.

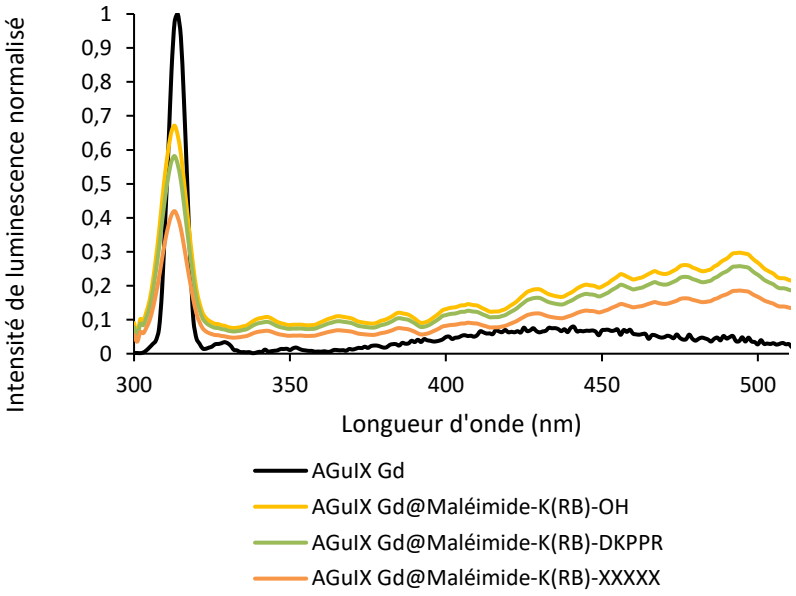

Figure 211 : Spectres d'émission du RB, AGuIX Gd et des AGuIX Gd couplées au RB et ses dérivés dans l'eau. [RB :Gd]= [1 :16] en mol. $\lambda_{excitation}$=273 nm, délai 50 µs.

Le **Tableau 38** présente les caractéristiques photophysiques d'AGuIX Gd, et des AGuIX Gd couplées aux Maléimide-K(RB)-peptide, K(RB)-peptide et l'intermédiaire Maléimide-K(RB)-OH.

Tableau 38 : Caractéristiques photophysiques d'AGuIX Gd, et des AGuIX Gd couplées aux Maléimide-K(RB)-peptide, K(RB)-peptide et son intermédiaire Maléimide-K(RB)OH

Echantillons	$\tau_{fluorescence}$ (ns) RB	$\tau_{luminescence}$ (µs) Gd	ΦΔ $\lambda_{excitation}$= 558 nm	ΦΔ $\lambda_{excitation}$= 273 nm	Φf $\lambda_{excitation}$= 558 nm
RB	0,63	-	0,67	0,68	0,15
AGuIX Gd	-	2400	0,00	0,00	0,00
AGuIX Gd@maléimide-K(RB)-OH	2,4	470	0,66	0,35	0,13
AGuIX Gd@ maléimide-K(RB)-DKPPR	3,8	345	0,67	0,35	0,11
AGuIX Gd@ maléimide-K(RB)-XXXXX	4,9	259	0,61	0,29	0,10

Les mêmes observations peuvent être faites qu'avec les AGuIX Tb, à savoir une augmentation de $\tau_{fluorescence}$ du RB lorsqu'il est couplé aux NPs, un Φf qui varie peu compris entre 0,10 et 0,15, de très bons ΦΔ en excitant à 558 nm qui sont divisés par 2 en excitant à 273 nm après excitation. Nous pouvons conclure que la production d'$^1O_2$ est plus importante lorsque le RB est excité (effet PDT) que lorsque le Gd est excité (effet X-PDT).

La **Figure 212** montre (a) le déclin de fluorescence du RB des échantillons après excitation à 470 nm, (b) le déclin de luminescence du Gadolinium en fonction du temps après excitation à 273 nm et (c) l'intensité de luminescence d'$^1O_2$ après excitation à 273 nm.

(a)

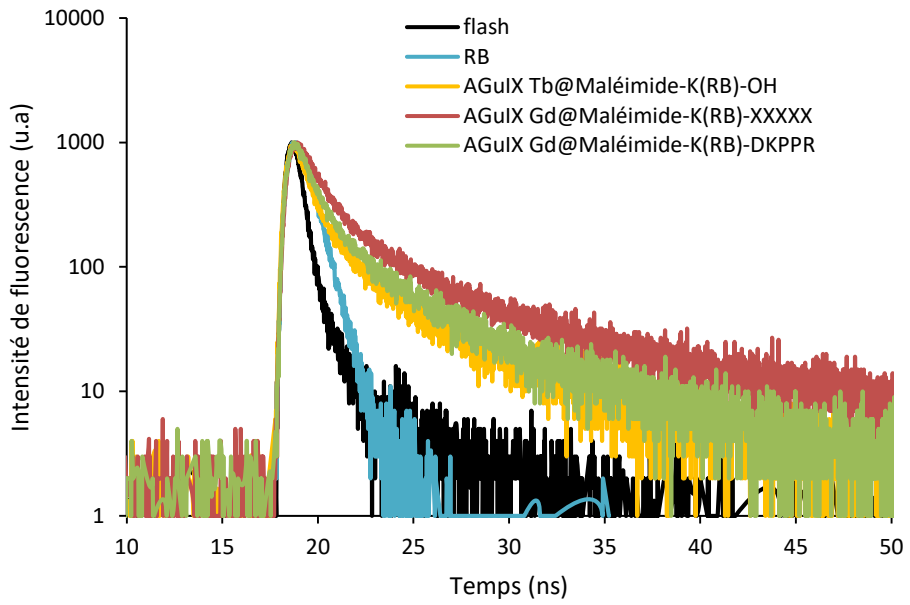
flash
RB
AGuIX Tb@Maléimide-K(RB)-OH
AGuIX Gd@Maléimide-K(RB)-XXXXX
AGuIX Gd@Maléimide-K(RB)-DKPPR
Intensité de fluorescence (u.a)
Temps (ns)
10000
1000
100
10
1
10
15
20
25
30
35
40
45
50

(b)

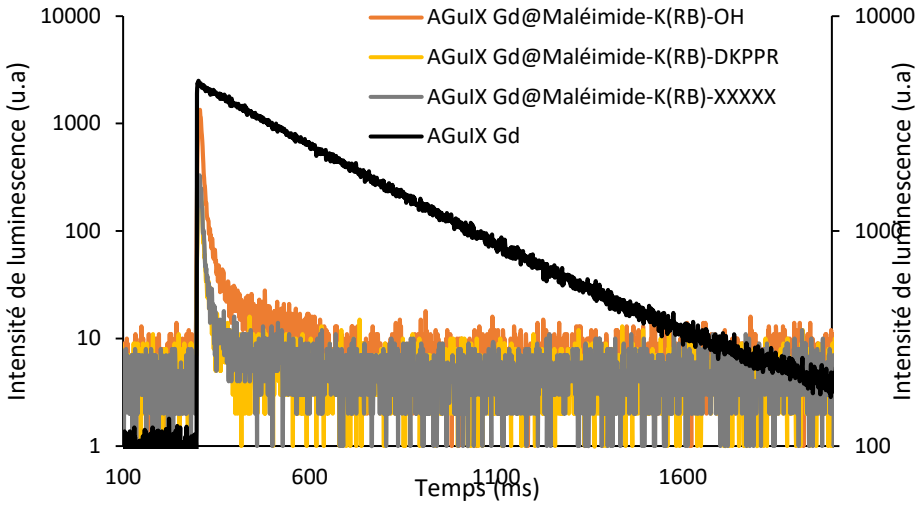
AGuIX Gd@Maléimide-K(RB)-OH
AGuIX Gd@Maléimide-K(RB)-DKPPR
AGuIX Gd@Maléimide-K(RB)-XXXXX
AGuIX Gd
Intensité de luminescence (u.a)
Intensité de luminescence (u.a)
Temps (ms)
10000
1000
100
10
1
100
600
1100
1600

(c)

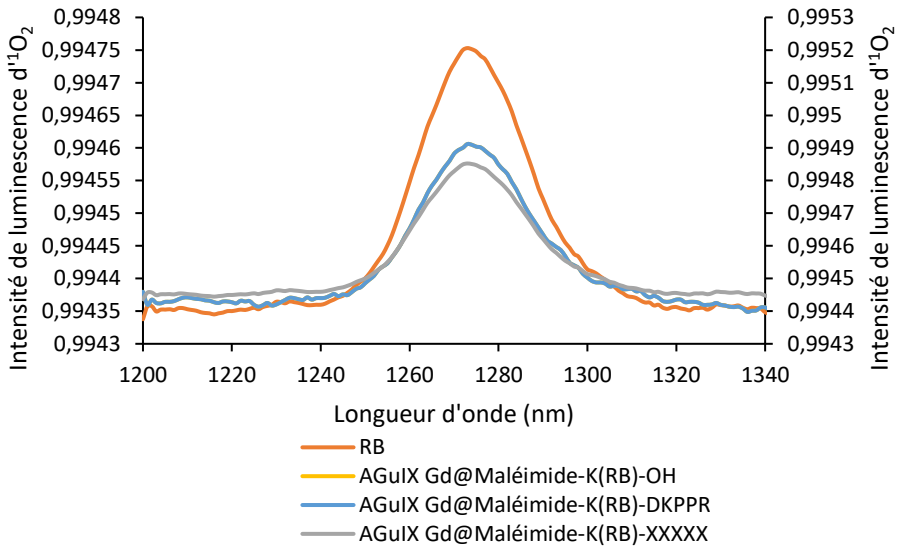

Figure 212: (a) Déclin de fluorescence du RB et du RB couplées au AGuIX Gd, $\lambda_{excitation}$ = 470 nm (b) le déclin de luminescence du Gadolinium en fonction du temps, $\lambda_{excitation}$ = 273 nm et (c) l'intensité de luminescence d'$^1O_2$, $\lambda_{excitation}$ = 273 nm.

Les déclins de fluorescence sont bi-exponentiels avec une espèce dont la durée de vie est plus petite que la ns qui en est très faible (<5%) que nous ne mentionnerons pas.

III.3.2.5 Spectres FT-IR

Pour les mêmes raisons énoncées pour la Figure 195, cette caractérisation ne permet pas de mettre en évidence le couplage entre les NPs et les conjugués RB-peptides. Nous envisageons dans le futur de réaliser une analyse en MALDI-TOF afin de bien caractériser le couplage.

III.3.2.6 Potentiel zêta

La **Figure 213** montre le potentiel zêta des AGuIX Ln (Tb/Gd) seules et celui des AGuIX Ln couplées au RB-peptide. L'augmentation en valeur absolu du potentiel zêta des NPs couplés au RB par rapport au NPs seule montre une augmentation de stabilité des NPs modifiées.

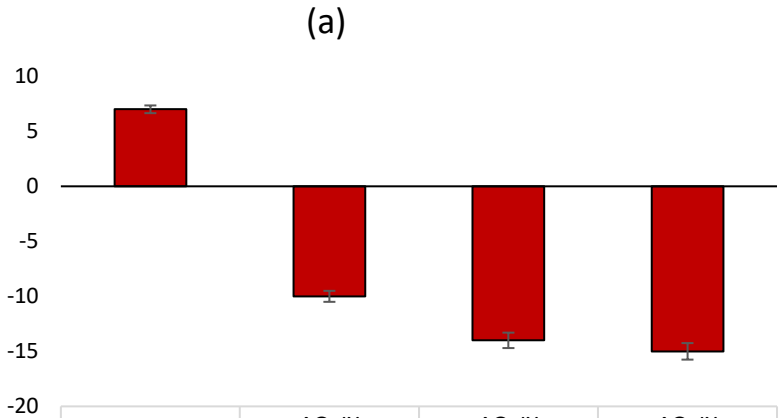

	AGuIX Tb	AGuIX Tb@Maléimide-K(RB)-OH	AGuIX Tb@Maléimide-K(RB)-DKPPR	AGuIX Tb@Maléimide-K(RB)-XXXXX
Potentiel zêta	7	-10	-14	-15

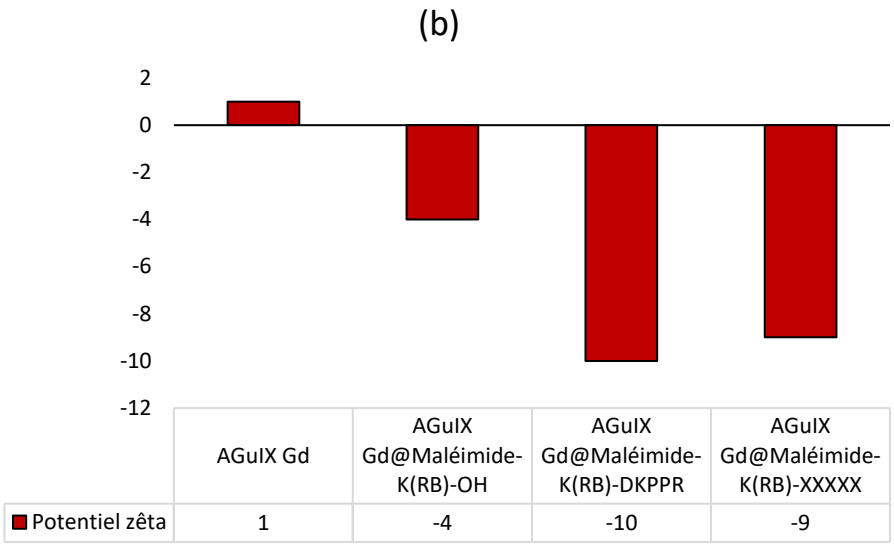

Figure 213 : (a) Potentiel zêta d'AGuIX Tb@Maléimide-K(RB)-OH, AGuIX Tb@Maléimide-K(RB)-DKPPR et d'AGuIX Tb@Maléimide-K(RB)-NKRTR dans l'eau, (b) Potentiel zêta d'AGuIX Gd@Maléimide-K(RB)-OH, AGuIX Gd@Maléimide-K(RB)-DKPPR et d'AGuIX Gd@Maléimide-K(RB)-XXXXX dans l'eau, pH=7,2.

III.3.3 Taille des NPs par TDA-ICP-MS

La taille des NPs a été mesurée par TDA- ICP-MS (Analyse par Dispersion de Taylor couplé à un ICP-MS). Les tailles sont indiquées dans le **Tableau 39**. La taille des NPs est inférieure à 40 nm. Nous observons 2 populations, tout comme l'AGuIX Tb. Une population serait composée d'AGuIX, l'autre serait composée d'un ensemble d'AGuIX. La différence entre les deux populations est peut-être due à un faible phénomène de stacking.

Tableau 39 : Diamètres des AGuIX Ln@ Maléimide- K(RB)-DKPPR, AGuIX Ln@ Maléimide- K(RB)-XXXXX et AGuIX Ln@ Maléimide-K(RB)-OH calculés par TDA

NPs	Diamètre en nm
AGuIX Gd@Maléimide- K(RB)-DKPPR	Population 1 : 2,9 nm (95%) Population 2 : 14,0 nm (5%)
AGuIX Gd@ Maléimide- K(RB)-XXXXX	Population 1 : 3,1 nm (100%)
AGuIX Gd@ Maléimide-K(RB)-OH	Population 1 : 3,2 nm (97%) Population 2 : 30,0 nm (3%)
AGuIX Tb@ Maléimide- K(RB)-DKPPR	Population 1 : 5,4 nm (46%) Population 2 : 32,0 nm (54%)
AGuIX Tb@ Maléimide- K(RB)-XXXXX	Population 1 : 4.5 nm (30%) Population 2 : 26 nm (70%)
AGuIX Tb@ Maléimide-K(RB)-OH	Population 1 : 4,9 nm (65%) Population 2 : 8,2 nm (35%)

IV. Production d'$^1O_2$ sous irradiation RX

Pour étudier la formation d'$^1O_2$, nous avons utilisé le SOSG. La **Figure 214** montre l'augmentation de l'intensité de fluorescence du SOSG en présence d'AGuIX Ln@RB et AGuIX Ln@bras espaceur-RB. Cette augmentation démontre la production d'$^1O_2$ qui n'est pas observé pour les contrôles AGuIX Tb, et AGuIX Gd et RB seul.

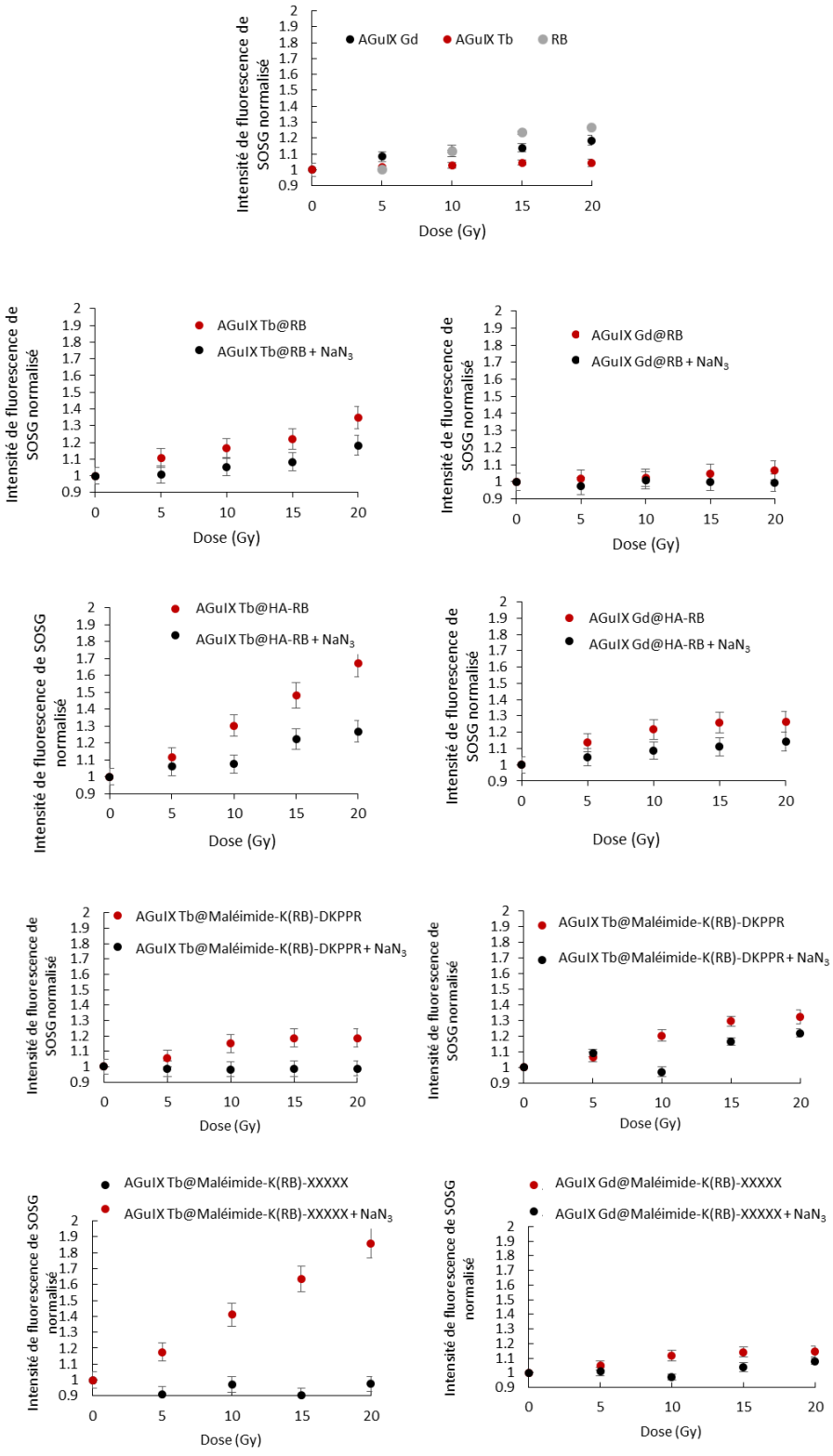

Figure 214: Fluorescence de SOSG sous rayon X (320 KV/12 mA) des AGuIX Tb, AGuIX Gd, RB, AGuIX Gd-Tb@RB et AGuIX Gd-Tb@HA-RB, des AGuIX Gd-Tb@Maléimide-K(RB)-DKPPR et des AGuIX Gd-Tb@Maléimide-K(RB)-XXXXX avec ou sans NaN_3. 320 KV, 10 mA.

Ces résultats montrent que, excepté pour que les AGuIX Gd@RB et les AGuIX Gd@maléimide-K(RB)-DKPPR, l'ajout de NaN_3 engendre une diminution de la fluorescence

du SOSG prouvant ainsi la formation d'$^1O_2$, due au transfert d'énergie entre le lanthanide et le RB ; en effet, les AGuIX seules ou le RB seul ne forment pas d'$^1O_2$ après excitation RX.

Nous pouvons constater que le Terbium est plus efficace comme donneur en transfert d'énergie que le Gadolinium, en adéquation avec le meilleur recouvrement entre le spectre d'émission du Tb par rapport spectre d'émission du Gd avec le spectre d'absorption du RB.

Les AGuIX Tb@HA-RB et AGuIX Tb@Maléimide-K(RB)-XXXXX montrent les plus importantes productions en $^1O_2$ à différentes doses en Gray (320 KV, 10 mA).

V. Affinité (Test Elisa)

Cette partie a été réalisée en collaboration avec Valérie Jouan-Hureaux, CRAN, UMR 7039 CNRS-Université de Lorraine.

L'affinité des peptides pour le récepteur NRP-1 a été évaluée par des tests Elisa. Brièvement, la surface des puits de la plaque ELISA 96 en polystyrène à haute capacité de liaison aux protéines (NUNC MaxiSorp™, Sigma-Aldrich, France) a été recouverte de NRP-1 à une concentration de 2 µg/mL dans une solution saline tampon phosphate (PBS) et maintenue pendant une nuit à température ambiante. Après 3 lavages, la plaque a ensuite été bloquée avec une solution d'albumine bovine (BSA) à 0,5 % dans du PBS pendant 1 h à 37 °C, afin d'inhiber les interactions non spécifiques. La liaison des peptides testés au NRP-1 a été évaluée en utilisant 5 ng/mL de VEGF-A-165 biotinylé dans un tampon de blocage contenant 2 µg/mL d'héparine. Le VEGF-A165 biotinylé est un ligand naturel de NRP-1 et entre en et entre en compétition, ou non, avec les différents peptides utilisés à différentes concentrations. Les plaques ont été incubées pendant 2 heures à température ambiante. Après cela, les plaques ont été lavées 3 fois et la quantité de VEGF-A-165 biotinylé lié a été évaluée en le marquant avec un conjugué de peroxydase de raifort couplé à la streptavidine. Après 20 min d'incubation à température ambiante avec le substrat de l'enzyme (tétraméthylbenzidine et H_2O_2), la réaction a été arrêtée par l'ajout d'acide sulfurique 2N. Les densités optiques correspondantes ont ensuite été mesurées à une longueur d'onde de 540 nm. Les résultats obtenus ont été exprimés en absorbance relative par rapport aux puits contenant uniquement le VEGF-A-165 biotinylé seul. Pour ce test, trois puits ont été utilisés par condition.

Nous avons observé une valeur d'IC50 de l'ordre du nM **(Figure 215)** pour les AGuIX couplé au RB-peptides. Cette affinité est beaucoup plus grande que celle de KDKPPR et XXXXX (IC50 KXXXXX = 8 µM ±4 et IC 50 KDKPPR = 2 µM ± 4) indiquant le potentiel efficace de ces NPs pour le ciblage du récepteur NRP-1. Les nano-RB sans le peptide ne semblent pas déplacer la liaison du VEGF-A-165 biotinylé et par conséquent ne sont donc pas affines vis-à-vis de ce récepteur. En notant qu'il faut comparer aussi avec le K(RB)-peptide puisque le PS joue un rôle important dans le changement de l'hydrophobie de la molécule.

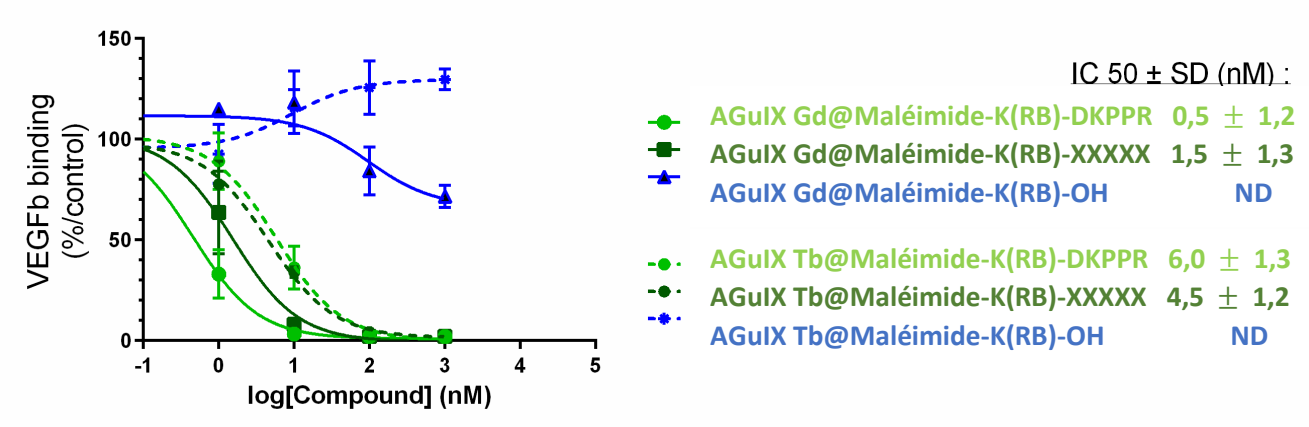

Figure 215 : Affinité des AGuIX couplées aux peptides DKPPR ou XXXXX pour NRP-1

VI. Test MTT

Afin de vérifier qu'il est possible de détruire des cellules de glioblastome, nous avons effectué des expériences *in vitro* sur des cellules U-251 MG qui expriment NRP-1 [3, 4]. Les U-251 MG sont dérivées d'un glioblastome malin humain multiforme. Cette partie a été réalisée en collaboration avec Joël Daouk et Hervé Schohn, CRAN, UMR 7039 CNRS-Université de Lorraine.

Le test MTT est utilisé pour mesurer l'activité métabolique cellulaire en tant qu'indicateur de la viabilité, de la prolifération et de la cytotoxicité des cellules. Ce test colorimétrique est basé sur la réduction du MTT (bromure de 3-(4,5-dimethylthiazol-2-yl)-2,5-diphenyl tétrazolium) en cristaux de formazan violet par cellules métabliquement active.

VI.1 Traitement des cellules

Les cellules U-251 MG sont ensemencées dans des plaques 6 puits (Falcon) et traitées le jour de l'ensemencement avec 1 µM d'AGulX@Tb-P1 pendant 24 h à 37°C. Après incubation, les tapis cellulaires sont lavés avec 2 mL de DPBS. 2 mL de milieu de culture sont ajoutés. Les cellules sont ensuite irradiée sous X à une dose de 2 Gy (320 kV, 10 mA - 3 Gy/min à 47 cm) dans un irradiateur biologique (XRAD 320, Précision X-rays, North Branford, CT).

VI.2 Fixation des cellules et coloration au cristal violet

Après 7 jours d'incubation, les clones cellulaires sont, successivement, lavés avec 2 mL de DPBS, fixés avec 1 mL de formol à 4 % (v/v) (pH 7,4) pendant 15 min, et lavés avec 1 mL de DPBS. 1 mL d'une solution de cristal violet à 0,05 % (v/v) dissous dans du DPBS et contenant 25 % (v/v) de MeOH est ajouté par puits. Après 30 min d'incubation, les clones formés sont lavés trois fois avec 1 mL d'eau distillée, et finalement comptés par acquisition d'images (GelCountTM, Oxford Optronix, Abingdon, UK). Les images obtenues sont analysées (application ImageJ, U.S. National Institutes of Health, Bethesda, Maryland, USA) en utilisant des paramètres définis : une surface de 862 mm^2 et un seuillage ne conservant que 20 % des pixels dans le puits (élimination du bruit de fond). Les résultats obtenus sont présentés par la moyenne ± SD, et correspondent à des duplicatas de 3 expériences indépendantes (n = 6).

La survie des cellules U-251 MG après irradiation X (2 Gy, 320 kV, 10 mA, 3 Gy/min à 47 cm) en présence de 1 µM de NPs est présentée dans la **Figure 216**.

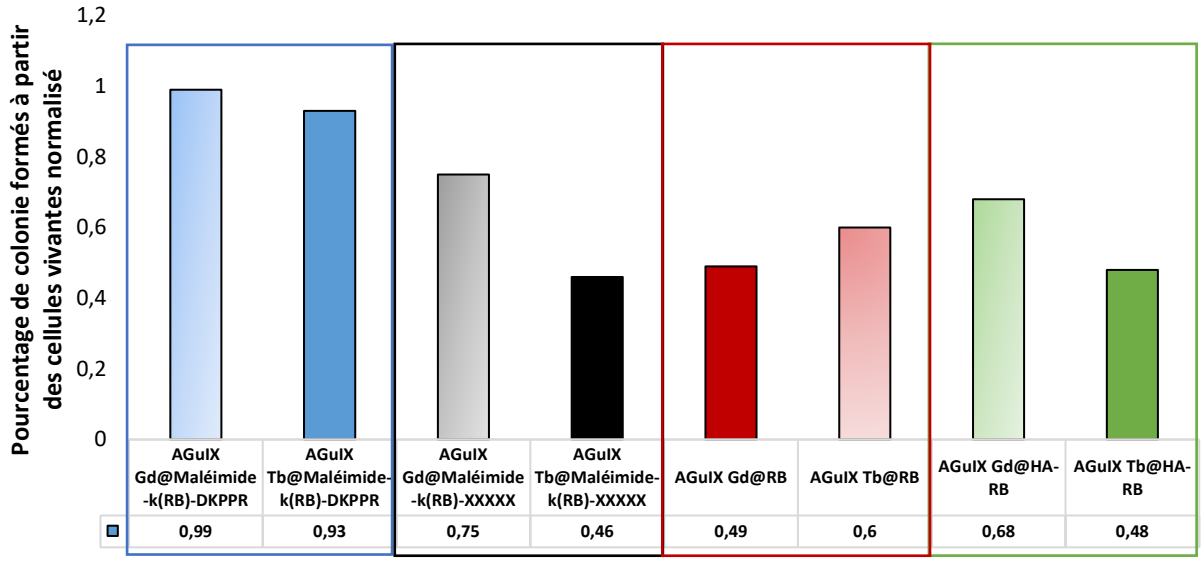

Figure 216 : Test MTT sur des cellules U-251 MG en présence des NPs AGuIX Gd@maléimide-K(RB)-DKPPR, AGuIX Tb@maléimide-K(RB)-DKPPR, AGuIX Gd@maléimide-K(RB)-XXXXX, AGuIX Tb@maléimide-K(RB)-DKPPR, AGuIX HA-RB, AGuIX Tb@HA-RB [NPs]=1 µM, sous 2 Gy (320 kV, 10 mA - 3 Gy/min à 47 cm)

Ces résultats préliminaires montrent les effets PDT-X les plus importants avec les AGuIX Tb@Maléimide-K(RB)-XXXXX (46% de survie) et AGuIX Tb@HA-RB (48% de survie). Il semblerait donc que, sur cette lignée, l'ajout de XXXXX n'ait pas d'influence sur l'efficacité X-PDT. Si l'on compare les NPs Gd et les NP Tb, les résultats montrent que la production d'$^1O_2$ est favorisée pour les NPs Tb, en adéquation avec le meilleur transfert d'énergie entre Tb et RB déjà observé en solution. Si l'on compare les peptides, les résultats sont meilleurs avec le peptide XXXXX que le peptide DKPPR. Ceci est en adéquation avec les IC50 obtenues pour les AGuIX Tb (IC50 AGuIX Tb@maléimide-K(RB)DKPPR = 6,0 µM ±1,3 et AGuIX Tb@maléimide-K(RB)DKPPR = 4,5 µM ± 1,2) mais pas en adéquation avec les IC50 obtenues pour les AGuIX Gd (IC50 AGuIX Gd@maléimide-K(RB)DKPPR = 0,5 µM ±1,2 et AGuIX Gd@maléimide-K(RB)DKPPR = 1,5 µM ± 1,3). Cela peut être dû à une incorporation non spécifique.

Si l'on compare les résultats en solution et *in vitro*, les conclusions sont les mêmes : Les AGuIX Tb@HA-RB et AGuIX Tb@Maléimide-K(RB)-XXXXX montraient les plus importantes productions en $^1O_2$ à différentes doses en Gray (320 KV, 10 mA).

Si l'on compare ces résultats avec ceux du chapitre 4 où nous utilisons des AGuIX Tb couplées à la porphyrine tétraphényle monocarboxylique P1, le RB couplé aux AGuIX montre de meilleurs résultats que les AGuIX couplé à la P1. En effet, le nombre de cellules vivantes normalisé pour AGuIX Tb@HA-RB est de 0,48 % pour 1 µ M à 2 Gy alors qu'il est de 0,515 % pour les AGuIX Tb@P1.

VII. Conclusions et perspectives

La synthèse de dérivés de RB a été réalisée avec succès. L'étude photophysique des précurseurs RB montre que le couplage du RB fait diminuer le coefficient d'extinction molaire du RB, les rendements quantiques de fluorescence et d'$^1O_2$. Ces dérivés ont été couplés aux AGuIX Tb et Gd. Les propriétés photophysiques du RB ont été réalisées et pour les deux types de NPs nous observons une augmentation de la durée de vie de fluorescence du RB lorsqu'il est couplé aux NPs, un Φ_f qui varie peu compris entre 0,10 et 0,15, de très bons rendements quantiques d'$^1O_2$.

En excitant les AGuIX Gd ou Tb couplées au RB avec ou sans bras espaceur, un transfert d'énergie est observé après un délai de 50 µs, avec la diminution de la luminescence du donneur (Gd ou Tb) et l'apparition de la fluorescence de l'accepteur (RB). Ce transfert d'énergie est confirmé sous irradiation par rayon X en solution.

Nous avons pu montrer également que les AGuIX couplées au RB-peptide (DKPPR ou XXXXX) sont très affins pour NRP-1 avec des affinités de l'ordre du nM.

Les expériences biologiques sous rayon X sur les cellules MG U-251 montrent un excellent effet X-PDT pour les AGuIX Tb@Maléimide-K(RB)-XXXXX (46% de cellules vivantes) et AGuIX Tb@HA-RB (48% de cellules vivantes) à une concentration 1 µM de RB.

Dans le futur, d'autres tests biologiques seront faits en faisant varier les conditions opératoires (concentration, doses rayon X…) pour optimiser les conditions afin d'obtenir une efficacité X-PDT maximale. D'autres lignées cellulaires pourraient être également utilisées, qui expriment plus ou moins NRP-1.

Références

[1] D. Neckers and J. Paczkowski, "Micro-organizational control of photochemical oxidations: Rose bengal and derivatives (XV)," *Tetrahedron,* vol. 42, pp. 4671-4683, 1986.

[2] J. R. Lakowicz, G. Laczko, and I. Gryczynski, "2 ‐ GHz frequency ‐ domain fluorometer," *Review of scientific instruments,* vol. 57, pp. 2499-2506, 1986.

[3] L. Chen, W. Miao, X. Tang, H. Zhang, S. Wang, F. Luo*, et al.*, "The expression and significance of neuropilin-1 (NRP-1) on glioma cell lines and glioma tissues," *Journal of biomedical nanotechnology,* vol. 9, pp. 559-563, 2013.

[4] H. Li, B. Lei, W. Xiang, H. Wang, W. Feng, Y. Liu*, et al.*, "Differences in protein expression between the U251 and U87 cell lines," *Turk Neurosurg,* vol. 27, pp. 894-903, 2017.

Annexe

RMN ^{1}H

1- RMN ^{1}H, RB-NHS

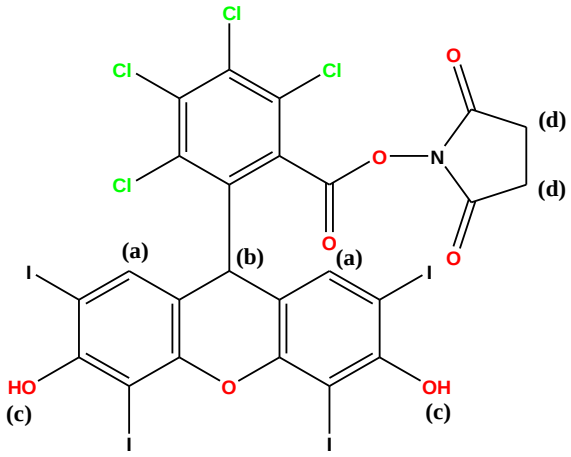

Figure S1: RMN ^{1}H RB-NHS (300 MHz, DMSO)

δ: 7,5 ppm (s, 3H, ArH (a), (b)), 6,0 ppm (s, 2H, ArH (c)), 2,8 ppm (t, J = 15,9 Hz, 4H, NHS, CH_2-C**H**$_{2\,(d)}$).

2- RMN ^{1}H, RB-HA-NHS

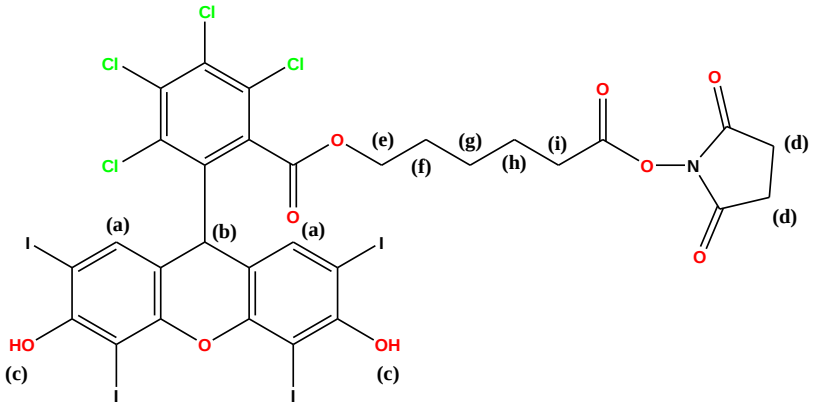

Figure S2: RMN ^{1}H RB-HA-NHS (300 MHz, DMSO)

δ : 7,7-7,4 ppm (s, 3H, ArH (a), (b)), 6,0 ppm (s, 2H, ArH (c)), 3,8 ppm (t, J = 7,2 Hz, 2H, CO-C**H**$_{2(e)}$-CH_2), 2,9 ppm (t, J = 7,2 Hz, 2H, CH_2-C**H**$_{2(i)}$ -C=O), 2,8 ppm (t, J = 4,5 Hz, 4H, NHS CH_2-C**H**$_{2(d)}$), 2,2 ppm (m, 2H, CH_2-C**H**$_{2(g)}$-CH_2), 1,6 ppm (m, 2H, CH_2-C**H**$_{2(f)}$-CH_2), 1,3 ppm (m, 2H, CH_2-C**H**$_{2(h)}$-CH_2).

3- RMN ^{1}H, RB-Ahx-NHS

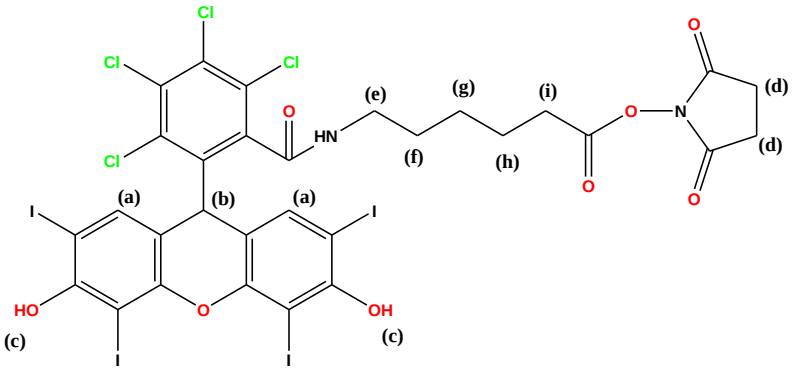

Figure S3: RMN ^{1}H RB-HA-NHS (300 MHz, DMSO)

δ : 7,2 ppm (s, 3H, ArH (a), (b)), 5,8 ppm (s, 2H, ArH (c)), 3,1 ppm (t, J = 7,4 Hz, 2H, NH-C**H**$_{2(e)}$-CH_2), 2,8 ppm (t, J = 5 Hz, 4H, NHS CH_2-C**H**$_{2\,(d)}$) 2,5 ppm (m, 2H, CH_2-C**H**$_{2(i)}$ -C=O), 2,0 ppm (m, 2H, CH_2-C**H**$_{2(g)}$-CH_2), 1,2 ppm (m, 2H, CH_2-C**H**$_{2\,(h)}$-CH_2), 1,5 ppm (m, 2H, acide hexanoïque (CH_2-C**H**$_{2\,(f)}$-CH_2)).

4- RMN ^{1}H, Fmoc-Lysine-RB

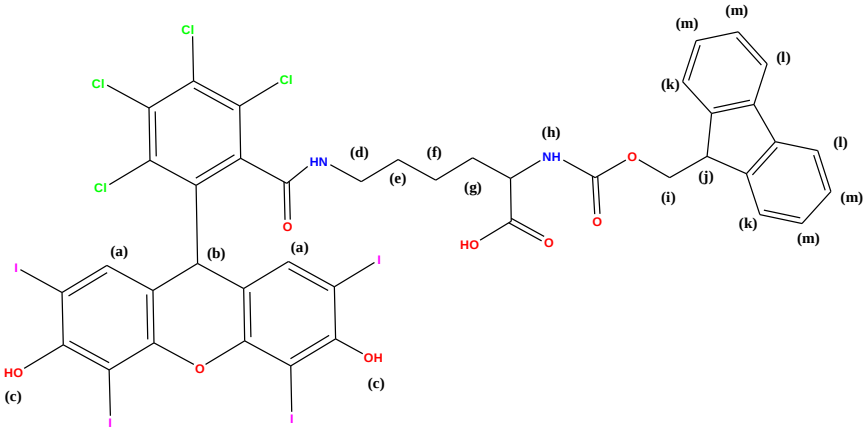

Figure S4: RMN ^{1}H Fmoc-Lys(Rose Bengal) (300 MHz, DMSO)

δ: 7,1-7,4 ppm (m, 4H, C**H**$_{(m)}$), 7,5 ppm (s, 2H, ArH $_{(a)}$), 7,2 ppm (m, 2H, C**H**$_{(l)}$), 4,5 ppm (m, 1H, C**H**$_{(j)}$), 3,9 ppm (m, CH_2-CH-N**H**$_{(h)}$), 3,1 ppm (m, 2H, NH-C**H**$_{2\,(d)}$-CH_2), 1,5 ppm (m, 6H, C**H**$_{2(e),\,(f),\,(g)}$).

5- RMN ^{1}H, Maléimide-K(RB)OH

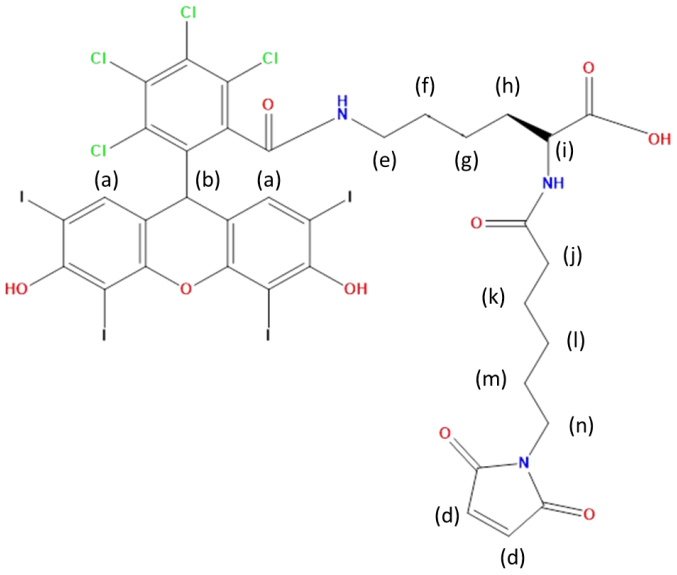

Figure S5 : RMN ^{1}H Maléimide-Lys(Rose Bengal)-OH (300 MHz, DMSO)

δ: 7,1 ppm (s, 2H, ArH **(a)**), 2,9 ppm (q, 2H, 8Hz, lysine CONH-C**H**$_{2(j)}$-CH_2), 3,4 (m, 2H, C**H**$_{2}$ $_{(n)}$-CH_2), 1,6 ppm (m, 4H, C**H**$_{2}$ $_{(m),\ (k)}$-CH2), 1,2 ppm (m, 2H, C**H**$_{2(l)-}$ CH2), 7,9 ppm (t, J = 6 Hz, 2H,CH_2-C**H**$_{2\ (d)}$), 4,3 ppm (m, 1H, C**H**$_{(i)}$), 1,3 ppm (m, 2H, C**H**$_{(g)}$), 1,8 ppm (m, 2H, C**H**$_{(h)}$), 3,1 ppm (t, 2H, C**H**$_{(e)}$), 1,6 ppm (m, 2H, C**H**$_{(f)}$).

q= quadruplet

6- RMN ^{1}H, Maléimide-K(RB)-DKPPR

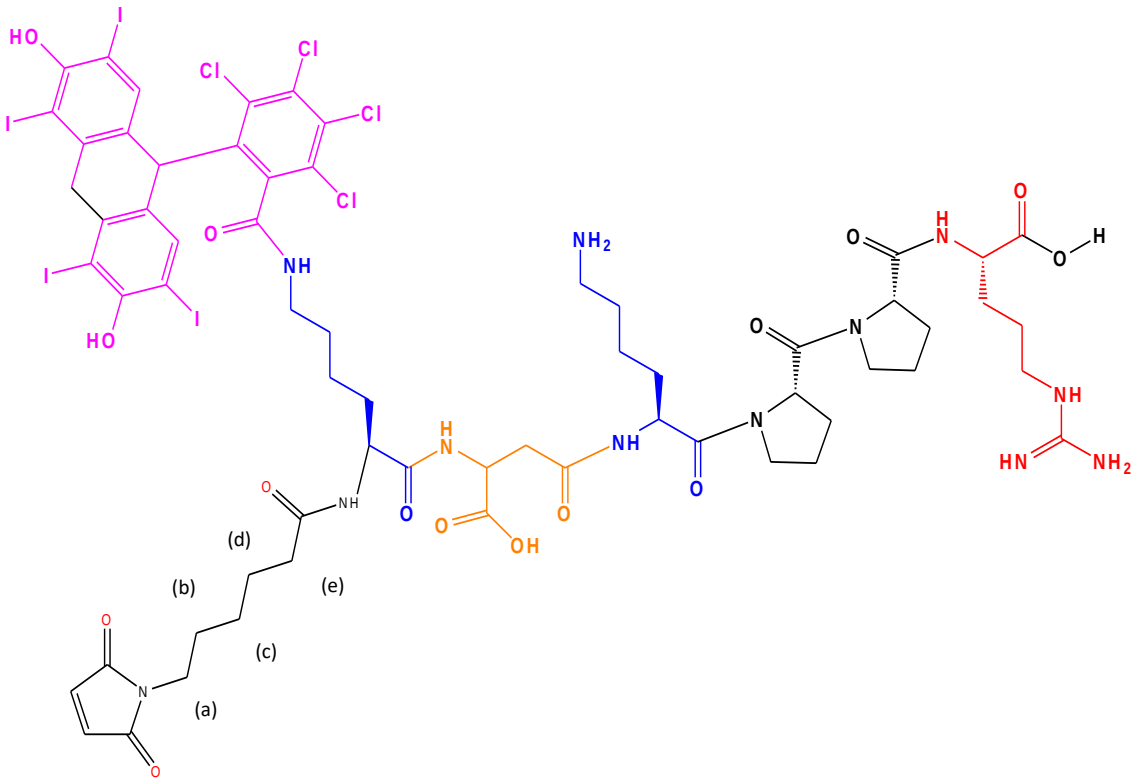

Figure S6 : ^{1}H NMR (400 MHz, DMSO–d6, δ)

	NH	αH	βH	δH	Autre
RB	-	-	-	-	7,8 (s, 3H, ArHmetaRB)
Bras-Maléimide	-	-	-	-	Maléimide: 6,8 (s, 2H, OC–CH=CH–CO), Bras: 3,1 (m, 2H, CH(a)), 1,37 (m, 4H, C**H**$_{(b),\ (d)}$) 1,09 (m, 2H, (C**H**$_{(c)}$), 2,08 (m, 2H, CH$_{(e)}$)
K	8,3	4,0	1,78	1,7	γCH$_2$=1,45 δCH$_2$=1,7 εCH$_2$=3,2 εNH$_3^+$=7,4
D	8,3	4,45	2,6 2,8	-	-
K	8,3	4,0	1,78	1,7	γCH$_2$=1,45 δCH$_2$=1,7 εCH$_2$=3,2 εNH$_3^+$=7,4
P	-	4,23	2,00 2,10	3,21 3,32	γCH$_2$= 1,7
P	-	4,23	2,00 2,10	3,21 3,32	γCH$_2$= 1,7
R	8,3	4,4	1,8 1,9	3,30	γCH$_2$= 1,7 εNH=7,10,

Conclusions et Perspectives

La thérapie photodynamique qui se base sur le principe d'exciter par la lumière un photosensibilisateur dans un milieu oxygéné pour produire des ROS dont l'$^1O_2$, rencontre plusieurs obstacles pour se développer à plus grande échelle. La limitation de la pénétration de la lumière et le manque de sélectivité de la plupart des PS utilisés en clinique envers les cellules cancéreuse font partie de ces limitations.

Au cours des trois années de thèse, nous avons développé des nouvelles plateformes pour surmonter les limitations de la pénétration de la lumière et le manque de sélectivité des PS. Dans ce but, nous avons choisi d'exciter avec les rayons X qui pénètrent profondément dans le corps humain. En revanche, la plupart des PS n'absorbent pas les rayons X. Pour cela, nous avons couplé ces photosensibilisateurs à des nanoparticules contenant des terres rares qui sont des antennes pour les rayons X. Nous avons étudié la possibilité d'avoir un transfert d'énergie entre le Terbium ou le Gadolinium et le Photofrin, une porphyrine P1 ou le Rose Bengale.

Nous avons étudié le recouvrement entre les spectres d'émission des donneurs (Tb/Gd) et d'absorption des accepteurs (P1, Photofrin et RB), puis nous avons étudié la variation de l'intensité de luminescence et de la durée de vie des lanthanides en fonction de la concentration des PS.

Nous avons pu :

- Confirmer le transfert non radiatif FRET entre les donneurs Terbium, Gadolinium et le RB en solution sous excitation UV-visible après un délai de temps entre l'excitation et la détection de la lumière de 50 µs en solution.
- Confirmer le transfert non radiatif FRET entre les donneurs Terbium, Gadolinium et le Photofrin sans et avec adsorption avec un délai de 50 µs en solution.
- Confirmer le transfert non radiatif FRET entre les donneurs Terbium, Gadolinium et le P1 avec un délai de 50 µs en solution.
- le remplacement de Gd par Tb dans la conception initiale d'AGuIX conduit à une nanoparticule prometteuse pour la X-PDT en expérimental in vivo. L'énergienous avons démontré que les nanoparticules de Tb chélaté réagissent linéairement à l'énergie des rayons X (au moins jusqu'à 320 kV) et au flux, et qu'elles étaient capables d'activer P1 pour produire de l'oxygène singulet. La nanoparticule construite n'était pas toxique, tout en restant non exposée à la lumière. Des expérimentations in vitro ont confirmé l'intérêt de ces conceptions AGuIX, notamment à un débit de dose de 3,0 $Gy.min^{-1}$.

Nous avons ensuite adsorbé le Photofrin sur les AGuIX Gd, et sur les AGUIX Gd couplé aux cyanine 5,5, et montré qu'il existe un transfert d'énergie entre le Gadolinium et le Photofrin avec un rendement quantique de production d'$^1O_2$ de 40%. L'efficacité du transfert d'énergie FRET est influencée par le recouvrement entre les spectres d'absorption de RB et d'émission des lanthanides : plus le recouvrement est plus large, plus l'efficacité augmente.

Nous avons couplé le RB de façon covalente aux AGuIX Tb et AGuIX Gd. Nous avons observé un transfert d'énergie entre les lanthanides des AGuIX et le RB après illumination UV-visible et irradiation sous rayons X.

Nous avons synthétisé les précurseurs RB (RB couplé à des bras espaceurs, et RB couplé aux peptides) pour les coupler aux AGuIX. Les études photophysiques des précurseurs RB montrent que la modification du RB fait diminuer coefficients d'extinction, rendements quantiques de fluorescence et d'oxygène singulet). Cela peut être dû à la diminution de la vitesse de la libre rotation des molécules du fait du couplage covalent sur la fonction acide carboxylique.

Les nanoparticules d'AGuIX couplées au PS/peptides sont bien dispersées dans l'eau. La taille des AGuIX couplés au RB est proche de celle des AGuIX seules, elle est d'environ à 6 nm. Toutes les AGuIX couplées au RB montrent un transfert d'énergie FRET non radiatif sous UV-visible et sous rayon X. Les AGuIX@RB avec le bras espaceur montrent un transfert d'énergie plus important en UV-visible et sous rayon X. Cela peut être dû à la diminution de l'encombrement stérique lorsqu'il y a un bras espaceur. Les AGuIX couplées aux peptide-PS montrent une excellente affinité pour le récepteur NRP-1 de l'ordre du nM. Parmi toutes les NPs synthétisées, c'est l'AGuIX Tb@Maléimide-K(RB)-OH avec une concentration de 1 µM (53%) qui montre les meilleurs résultats *in vitro* sur les cellules MG U-251 en termes de viabilité cellulaire (300 KV, 10 mA).

Dans le futur, il serait intéressant d'optimiser d'une part la composition des NPs et d'autre part les conditions d'irradiation afin d'avoir un transfert maximal. En ce qui concerne les NPs, le RB semble être le PS le plus efficace parmi RB, Photofrin, P1. De plus, il est déjà utilisé en clinique ce qui le rend d'autant plus attractif. Un plan d'expériences pourrait être envisagé pour étudier l'influence du nombre de RB, de la distance RB/NP, type de Ln. En effet, nous avons pu montrer que le Tb était un meilleur candidat que le Gd mais d'autres lanthanides pourraient également être envisagés. Les paramètres d'irradiation pourraient également être optimisés en changeant par exemple les doses utilisées. Nous avons testé une seule lignée cellulaire mais d'autres exprimant ou non NRP-1 pourraient être sélectionnées. De plus, NRP1 joue un rôle clé dans la survenue et le développement des tumeurs. Il est impliqué dans l'angiogenèse, la migration du cancer mais également l'immunité tumorale.

Liste des articles
et communication scientifiques

Articles

Joël Daouk, **Batoul Dhaini**, Jérôme Petit, Céline Frochot, Muriel Barberi Heyob, Hervé Schohn, « Can Cernekov light really induce an effective photodynamic therapy? » DOI: 10.3390/radiation1010002, MDPI Radiation Journal.

Joël Daouk, Mathilde ltis, **Batoul Dhaini**, Densie Bechet, Philippe Arnoux, Paul Rocchi, Alain Delconté, Benoit Habermeyer, Françcois Lux, Céline Frochot, Olivier tillement, Muriel Barberi Heyob, Hervé Schohn, « Terbium based AGuIX Design Nanoparticule to mediate X-ray Induced Phoodynamic therapy ». DOI: https://doi.org/10.3390/ph14050396, MDPI Pharmaceuticals journal. IF=5.8

Batoul Dhaini, Bibigul Kenzhebayeva,Amina Ben-Mihoub, Mickaël Gries, Samir Acherar, Francis Baros,Noémie Thomas,Joël Daouk,Hervé Schohn,Tayssir Hamieh and CélineFrochot. « Peptide-conjugated nanoparticles for targeted photodynamic therapy ». DOI: https://doi.org/10.1515/nanoph-2021-0275,Nanophotonics Journal. IF=8.4

Laurène Wagner, Bibiguk Kenzhebayeva, **Batoul Dhaini**, Samir Boukhlef, Albert Moussaron, Serge Mordon, Céline Frochot, Charlotte Collet and Samir Acherar. « Folate-based radiotracers for nuclear imaging and radionuclide therapy ». https://doi.org/10.1016/j.ccr.2022.214702. IF: 8,047.

Batoul Dhaini , Laurène Wagner, Morgane Moinard, Joël Daouk, Philippe Arnoux , Hervé Schohn , Perrine Schneller, Samir Acherar , Tayssir Hamieh and Céline Frochot. « Importance of Rose Bengal Loaded with Nanoparticles for Anti-Cancer Photodynamic Therapy ». https://doi.org/10.3390/ph15091093 IF: 5.8.

Conferences

Dhaini B, Arnoux P, Baros F, Daouk J, Schohn H, Acherar S, Barberi-Heyob M, Hamieh T, Frochot C. Development of addressed nanoparticles for X-ray induced anticancer photodynamic therapy. Photodynamic Therapy and Photodiagnosis Update E-CONGRESS 2020, Nancy, 2020 November 5-6th. Poster

Dhaini B, Arnoux P, Baros F, Daouk J, Schohn H, , Acherar S, Barberi-Heyob M, Hamieh T, Frochot C. Development of addressed nanoparticles for X-ray induced anticancer photodynamic therapy. French Swiss Photochemistry Symposium: FSPS – E-Symposuim - July 21-22, 2021.Flash presentation

Dhaini B, Arnoux P, Thomas N, Baros F, Daouk J, Schohn H, , Acherar S, Lux F, Tillement O, Hamieh T Barberi-Heyob M, , Frochot C. AGuIX nanoparticles coupled to a photosensitizer, excitable by light or X-ray: application in anti-cancer photodynamic therapy. Demi-journée scientifique du GDR MAPYRO-27 Mai 2021, Renne. Communication Orale

Dhaini B, Arnoux P, Daouk J, Schohn H, Baros F, Acherar S, Barberi-Heyob M, Hamieh T, Frochot C. Nanoparticles activated by X-rays to overcome limitation of in anticancer photodynamic therapy against cancer. International Conference on Photochemistry - 30th Edition, Geneva (Switzerland), July 19-23, 2021. Communication Orale.

Daouk J, Schneller P, Petit J, **Dhaini B**, Arnoux P, Pierson J, Collet C, Frochot C, Lux F, Tillement O, Schohn H, Barberi-Heyob M. The X-ray-induced photodynamic effect of AGuIX@Terbium-porphyrin ultrasmall nanoparticle can be substituted by Galium-68. 5th Photodynamic Day – SIFB, Acıbadem Mehmet Ali Aydınlar University, 18th May 2021, P10. Poster

Dhaini B, Arnoux P, Thomas N, Baros F, Daouk J, Schohn H, , Acherar S, Lux F, Tillement O, Hamieh T Barberi-Heyob M, , Frochot C. Modified AGuIX nanoparticles for X-ray induced anticancer

photodynamic therapy. Nanohybrides 17bis conference, June 20-24, 2021, Porquerolles. Communication Orale

Dhaini B, Daouk J, Arnoux P, Acherar S, Schohn H, Lux F, Rocchi P, Tillement O, Barberi-Heyob M, Hamieh T, Frochot C. X-ray photodynamic therapy (X-PDT): state of the art, development and clinical application parameters. journées conjointes GdR HappyBio-SFPb-SFPMed, Toulouse, November 24-26,2021. Communication Orale